The New Frontiers of Organic and Composite Nanotechnology

Editors
Victor Erokhin, Manoj Kumar Ram
and Ozlem Yavuz

The New Frontiers of Organic and Composite Nanotechnology

This page intentionally left blank

The New Frontiers of Organic and Composite Nanotechnology

Victor Erokhin, Manoj Kumar Ram and Ozlem Yavuz

ELSEVIER

Amsterdam • Boston • Heidelberg • London • New York • Oxford
Paris • San Diego • San Francisco • Singapore • Sydney • Tokyo

Elsevier
Linacre House, Jordan Hill, Oxford OX2 8DP, UK
Radarweg 29, PO Box 211, 1000 AE Amsterdam, The Netherlands

First edition 2008

British Library Cataloguing in Publication Data
A catalogue record for this book is available from the British Library

Library of Congress Cataloging-in-Publication Data
A catalog record for this book is available from the Library of Congress

ISBN: 978-0-0804-5052-0

For information on all Elsevier publications visit our website at books.elsevier.com

Printed and bound in Great Britain
08 09 10 11 10 9 8 7 6 5 4 3 2 1

Contents

Preface

Currently, the term nanotechnology is used to refer to the realized structures whose characteristic sizes are less than 100 nm. Nanotechnology has found special applications in most fields of modern science and technology. Realization of objects with decreased dimensionality (up to zero-dimensional quantum dots) provides new possibilities for fundamental researches connected to quantum phenomena, which cannot be observed on bulk materials. The applied aspects of nanotechnology are also very important. The method of modification of material surfaces with molecular layers has diverse applications such as corrosion inhibition, anti-friction, smart surface realization, etc. In electronics and communication systems, nanotechnology offers to increase the speed of information processing and integration. With respect to biomedical applications, new effective and reliable sensoristic systems have been developed based on the utilization of specific bioorganic molecular layers and conjugates of biomolecules with polymers and/or nanoparticles. Presently, new smart systems for directed drug release are under development.

The aim of this book is to review the current status and future perspectives of researches in different branches of nanotechnology, with the key focus on organic and composite systems. Organic materials attract increasing attention due to their unique properties, which allow the realization of a wide variety of working systems. Many of these properties, especially those connected to the functioning of biological molecules, cannot be reproduced with inorganic materials. In addition, organic materials are lightweight and have high flexibility. However, one serious drawback in them is decreased stability with respect to inorganic materials. Therefore, the current activities in this field are directed to the search of new compounds (mainly polymers), which are expected to significantly improve the stability, allowing, therefore, to widen the applications of organic materials. In parallel, organic–inorganic composites can produce hybrid structures, which combine the sound features of both types of compounds.

Each chapter of this book is connected to a unique aspect of nanotechnology. We begin with the description of layer-by-layer self-assembling,

which currently finds a lot of applications due to its simple realization process and the potential to develop a wide variety of functional molecular systems. Nanoengineered polymeric capsules have attracted a lot of attention immediately after it was first reported in 1998. These objects are very popular among researchers for several reasons. From a fundamental point of view, these systems allow to study growth processes and properties of space-confined matter. One of the most interesting properties of capsules is the possibility to open and close reversible pores in their shells. In particular, this property can be very useful for the development of smart drug-release systems. In the subsequent chapter, we describe the current status of applications of advanced optical spectroscopies to nanotechnology, including single-molecule spectroscopy and the latest achievements in the possibility of signal-pronounced enhancement. A separate chapter is dedicated to give an overview of compositions and properties of hybrid conducting materials formed from different guest molecules incorporated into the host matrix. One important feature of organic and composite materials is the possibility to vary their properties by redox reactions. Two chapters are dedicated to the utilization of these properties. One chapter demonstrates how it can be used in scanning probe microscopy, while the other describes the electrochemical elements that can be used for adaptive network realization. Two successive chapters deal with the biomedical applications of nanotechnology. In particular, the present developments of enzymatic and immunosensors are reviewed. Finally, electromagnetic applications are considered.

To my belief, each chapter of this book offers a critical approach to the description of the available techniques and investigation methods to provide a better understanding of their strong and weak points as well as their limits and areas of applications.

Victor Erokhin

List of contributors

Matt Aldissi
Fractal Systems Inc., Safety Harbor, FL, USA
maldissi@fractalsystemsinc.com

Andrea Alessandrini
Department of Physics, University of Modena and Reggio Emilia, Modena, Italy
alessandrini.andrea@unimo.it

Silvana Andreescu
Department of Chemistry and Biomolecular Science, Clarkson University, Potsdam, NY, USA
eandrees@clarkson.edu

Daria V. Andreeva
Max-Planck Institute of Colloids and Interfaces, Golm/Potsdam, Germany
daria.andreeva@mpikg.mpg.de

Tim Dubrovsky
BD Biosciences, San Jose, CA, USA
tim_dubrovsky@bd.com

Victor Erokhin
Department of Physics, University of Parma, Parma, Italy;
Institute of Crystallography, Russian Academy of Sciences, Moscow, Russia
erokhin@fis.unipr.it

Paolo Facci
Department of Physics, University of Modena and Reggio Emilia, Modena, Italy
facci.paolo@unimo.it

M. P. Fontana
Department of Physics, University of Parma, Parma, Italy
fontana@fis.unipr.it

Feng Hua
Electrical and Computer Engineering Department, Clarkson University, NY, USA
fhua@clarkson.edu

Cristina Ispas
Department of Chemistry and Biomolecular Science, Clarkson University, Potsdam, NY, USA

Oliver Kreft
Max-Planck Institute of Colloids and Interfaces, Golm/Potsdam, Germany
kreft@mpikg-golm.mpg.de

Yuri M. Lvov
Institute for Micromanufacturing, Louisiana Tech University, LA, USA
ylvov@latech.edu

John Njagi
Department of Chemistry and Biomolecular Science, Clarkson University, Potsdam, NY, USA

Manoj K. Ram
Fractal Systems Inc., Safety Harbor, FL, USA
manojkram@verizon.net

Esma Sezer
Department of Chemistry, Istanbul Technical University, Istanbul, Turkey
esezer@itu.edu.tr

Andrei G. Skirtach
Max-Planck Institute of Colloids and Interfaces, Golm/Potsdam, Germany
skirtach@mpikg.mpg.de

Gleb B. Sukhorukov
The Center for Materials Research, Queen Mary College, University of London, London, UK
g.sukhorukov@qmul.ac.uk

Olena Tsvirkunova
Align Technology, Inc., Santa Clara, CA, USA

Özlem Yavuz
Fractal Systems Inc., Safety Harbor, FL, USA
oyavuz@fractalsystemsinc.com

Chapter 1

Layer-by-layer assembly

Feng Hua
Electrical and Computer Engineering Department, Clarkson University, NY, USA
Yuri M. Lvov
Institute for Micromanufacturing, Louisiana Tech University, LA, USA

Abstract. Layer-by-layer self-assembly has several merits including low process temperature, molecular resolution of composition, thickness control and a wide variety of appropriate building blocks. From the time it was first demonstrated, it has been widely used by researchers in different disciplines. The alternate adsorption of oppositely charged macromolecules is able to produce complex heterogenuous architectures for optical devices, synthetic catalysts and especially man-made biological components. The principle, operation and characterization of this unique technique are discussed in the first part of this chapter. In the later part, the fabrication conditions and the current and future applications are addressed.

Keywords: layer-by-layer self-assembly, electrostatic interaction, nanostructured materials, nanocomposites, macromolecules

1.1. Introduction

It is always exciting to observe the miracles in living organisms through their unceasing, precise self-assembly of proteins, DNA and bones. In spite of its complexity, self-assembly is commonly recognized as one of the ultimate goals of nanoscience and nanotechnology. In the recent past, the semiconductor-based microfabricating technology helped people to produce structures at a length scale that has never been achieved before. Thin films could be made via molecular beam epitaxy, spin coating, thermal evaporation, sputtering and chemical vapor deposition. Micron-meter scale patterns can be reliably generated. However, with the constant reduction of

the feature size, self-assembly gradually reveals itself one of the ultimate means to manipulate the building blocks in a much smaller world.

So far, the existing self-assembly approaches are classified according to different processes and inter-molecular interactions. The Langmuir–Blodgett (LB) approach was mainly based on van der Waals interactions [1]. It allows to deposit multilayers by transferring a set of monolayers preformed on water surface onto solid substrate surfaces. Another approach, namely the self-assembled monolayer (SAM), was based on the attachment of thiol monolayers to the gold surface, which is due to strong bonds between the sulfur atoms of the thiol group and gold surface [1]. Even if both the above mentioned methods can control the molecular order in the film, they are limited by the thickness of the film, availability of building blocks, and substrates and versatility of the process. Layer-by-layer (LbL) self-assembly is an alternative approach to overcome the above drawbacks. It makes use of alternate adsorption of oppositely charged macromolecules resulting in the self-organization of films and new composites. It controls the precise order of deposition of molecular layers as well as thickness up to 1∼2 nm resolution. It significantly broadens the availability of building blocks and substrates because all charged macromolecules can be assembled onto the surfaces of charged substrates. The advantages enable the engineering of the macroscopic electrical, optical, magnetic, thermal and mechanical properties of the composites, which is important for many engineering devices and applications. There is no difficulty in constructing a c. 500 nm thick multilayer with a predesigned sequence of depositing different molecules. Its capability to self-organize a large number of biological substances such as proteins, including enzymes, and DNA allows a wide range of applications in the area of nanobiology. The regular dipping motion of the LbL assembly can be readily converted into the automatic manner for mass production.

The first report on electrostatically driven LbL self-assembly of inorganic colloidal particles can be traced to the work of Iler [2]. Iler showed that oppositely charged silica and alumina particles could be electrostatically self-assembled in multilayer structures by alternate successive immersing of the substrate into two colloidal solutions. In 1990s, Decher et al. had demonstrated the LbL self-assembly of cationic and anionic polyelectrolytes. Subsequently, they showed the possibility of the formation of similar multilayer structures consisting of combinations of charged colloidal particles and biomacromolecules such as DNA [3–5]. Soon, the method become very popular as different research groups had used this technique to realize assemblies containing charged polymers [4–8], proteins [6,7], nanoparticles [9–11], dyes [12–14] and clay nanoplates [15–17].

1.2. Layer-by-layer Self-assembly

1.2.1. Basic Principles

The alternate adsorption of molecular monolayers is mainly based on electrostatic interactions between the neighboring layers. Therefore, it is often referred to as electrostatic self-assembly (ESA). When the polyanion, such as poly(styrenesulfonate), is dissolved in water, the sodium cations are dissociated from the molecule backbone at appropriate pH that is away from the isoelectric point, leaving the long molecule chain negatively charged (Fig. 1.2). For the same reason, the ionized polycation chain is positively charged. Of course, the entire solution appears electrically neutral. The LbL self-assembly involves the alternate successive dipping of a solid substrate into solutions containing anionic and cationic molecules. When the polycationic molecules approach a negatively charged substrate within a sufficiently small distance (Debye length), the local electric field is so strong that it attracts molecules to the surface. The diffusion mechanism in the solution constantly provides the availability of molecules near the substrate surface. The surface is, therefore, completely covered by a layer of cationic molecules that compensate the charge of the previous layer and make the substrate surface positive with respect to the solution. The surface electrical polarity is completely reversed, and the sample can then be used as a template to attract negatively charged molecules during subsequent dipping.

The procedure of LbL self-assembly is illustrated in Fig. 1.1. In Fig. 1.1a, the negatively charged substrate is immersed into the polycation solution. The polycations are adsorbed on the substrate surface within an optimized duration depending on the type of molecules. Later, the substrate is taken out of the solution, rinsed in deionized water (DI water) for several minutes and then dried by a nitrogen jet. Subsequently, the substrate is immersed in a polyanion solution, rinsed and dried in the same way as above. Alternate dipping enables the formation of predefined polycation/polyanion multilayers. Fig. 1.1b illustrates the application of LbL self-assembly for the formation of composite films consisting not only polyions but also proteins, dyes and nanoparticles in a designed sequence.

Rinsing is quite important as it removes weakly attached, physically adsorbed components, thus preparing the surface for subsequent adsorption [18]. It also guarantees precise steps in the thickness growth of LbL self-assembled films, because only those attached with electrostatic

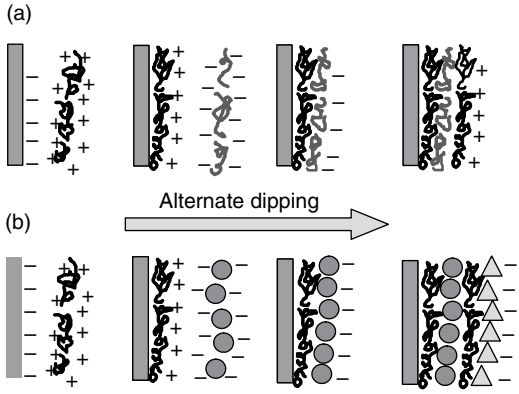

Figure 1.1: Schematic of the LbL self-assembly. (a) Alternate adsorption of polycations and polyanions on the solid substrate. (b) Alternate adsorption of polyions, proteins and nanoparticles on the substrate.

interactions of LbL self-assembly are likely to anchor on the support surface while those precipitated on the support are removed by rinsing.

It is interesting to note that the substrate surface need not necessarily be uniformly charged prior to LbL assembling. A uniformly charged substrate is critical for the successive steps which, in practice, can be achieved with strong oxidants or oxygen-containing plasma treatment, followed by the deposition of a few layers of polyion served as the precursor in order to increase the charge density over the substrate before the assembly begins.

1.2.2. Building Blocks for Layer-by-layer Self-assembly

A broad range of charged species are suitable for LbL self-assembly. The building blocks include:

(a) Polycations – poly(ethylenimin) (PEI), poly(dimethyldiallylammonium chloride) (PDDA) and poly(allylamine) (PAH).
(b) Polyanions – poly(styrenesulfonate) (PSS), poly(vinylsulfate) (PVS) and polyacrylic acid (PAA) (Fig. 1.2).
(c) Nanoparticles – Nanoparticles (NPs) must be functionalized with chemical groups to provide surface charging of particles. For example, nanoparticles may be carboxylate-modified or sulfonate-modified by coupling carboxylate or sulfonate groups on their surfaces (Fig. 1.3).

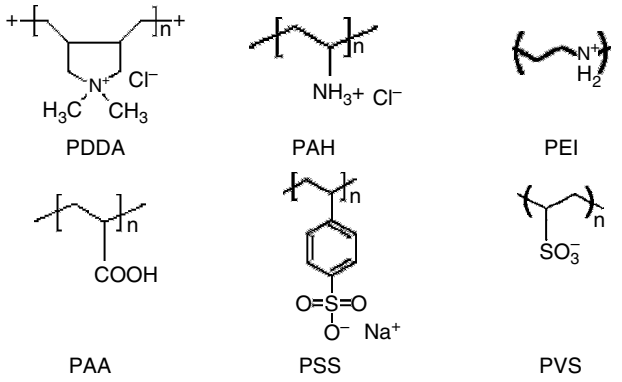

Figure 1.2: Structural schematic of frequently used polycations and polyanions.

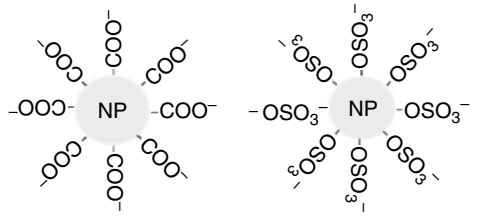

Figure 1.3: Schematic of carboxylate and sulfonate-modified nanoparticles.

(d) Proteins – Proteins can be self-assembled alternately with polycation or polyanion depending on their isoelectric point. This approach was successfully applied for the deposition of films with different proteins, such as pepsin, myoglobin and immunoglobulin [6,19,20].
(e) DNA, dyes, polyoxometalates, zeolite crystal and carbon nanotubes may also be used as building blocks.

The components used as building blocks can be adsorbed virtually on all types of substrates.

1.2.3. Kinetics of Multilayer Adsorption

The growth of the composite thin film can be monitored in situ by quartz crystal microbalance (QCM), which can detect a tiny mass adsorption on the surface. A QCM consists of a thin quartz disc sandwiched between a

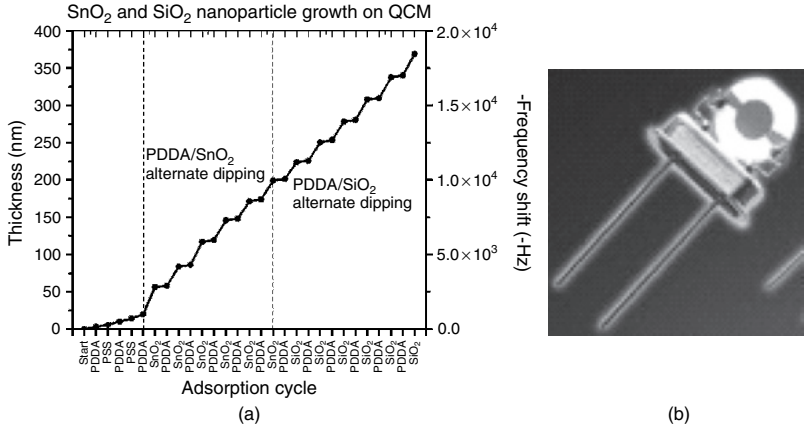

Figure 1.4: (a) QCM frequency shift and cycles of polyion-nanoparticle assembly. The left region is the alternate adsorption of PDDA/PSS. The middle is the alternate adsorption of PDDA/SnO_2 nanoparticles. The right is PDDA/SiO_2 nanoparticles. (b) Picture of a QCM.

pair of parallel electrodes (Fig. 1.4b). When the quartz crystal is excited by an AC voltage, it begins to oscillate due to the piezoelectric property of quartz. The resonant frequency is a function of the total oscillating mass, which decreases with the adsorption of mass on the crystal. The shift of resonant frequency is proportional to the mass of the film. As a result, QCM is sensitive to the adhering layer with a mass change. The mass is calculated according to the Sauerbrey equation [21]:

$$\Delta m = -K \cdot \Delta f$$

where Δm is variation of mass; Δf is variation of frequency; K is a constant depending on the geometry and property of the quartz.

Cumulative thickness can be calculated from the adhering mass by:

$$D = \Delta m / \rho$$

where D is thickness of the film; ρ is density of the adhering film.

Fig. 1.4a illustrates a typical frequency shift with the growth of the film. Beginning with the X-axis, the first five steps correspond to the coating with polyion precursor films necessary for successive adsorption. In the middle, there are six cycles of alternate PDDA/SnO_2 nanoparticle (about 15 nm

in diameter) adsorption. Note that the frequency shift corresponding to SnO_2 adsorption is significantly more than that of PDDA, because the SnO_2 film is thicker than PDDA. According to the curve, the thickness of a single layer of SnO_2 nanoparticles is about 25 nm, while that of PDDA is about 2 nm. On the right half of the figure, alternating deposition of PDDA and SiO_2 nanoparticles (45 nm in diameter) is reported. The curve indicates that, in general, the deposition of the polymer and nanoparticles is highly reproducible. Although most experiments show the linear growth of films made of polyions, proteins and nanoparticles, nonlinear growth may be observed in some situations.

It is believed that polyion adsorption occurs in two stages: quick anchoring to a surface and slow relaxation [22]. Adsorption in a single dipping is not a linear process. A large fraction of the mass is assembled shortly in a cycle and adsorption enters the saturation region [4,18]. In the saturation region, the growth of film significantly slows down until the surface charge is completely reversed, and no more molecules can be attracted. Figure 1.5 depicts a typical kinetic profile for two single steps of the assembly of polyanions (PSS) and polycations (PEI) in the range of concentrations of 1–3 mg/mL [4,18]. During the first 5 min, c. 87% of the surface is covered, and after 8 min, c. 95% is covered. Typically, in most of the reports, an adsorption time between 5 and 20 min for each polyion is used. It is not necessary to keep the dipping time to a high precision because the last one or two minutes are not so important. When the surface is completely covered, there is no purpose in immersing the substrate in the solution any longer.

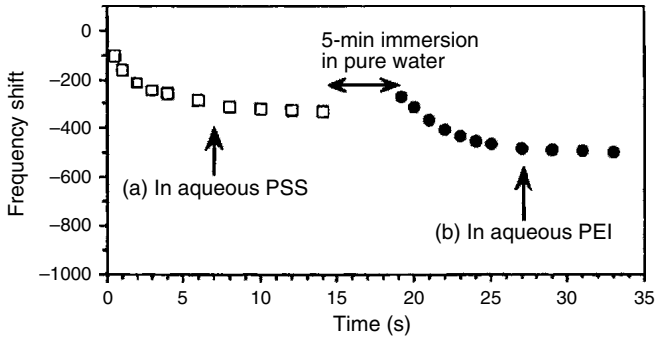

Figure 1.5: QCM frequency shift shows kinetics of two single adsorptions of PSS and PEI with 5-min intermediated rinsing in water, pH 6.5, 22 °C (Reprinted from *Colloids Surf. A.*, with permission from Elsevier.)

The dependence of polyion layer thickness on the concentration is not so important [22]; thus, the concentration range of 0.1–5 mg/mL yields similar bilayer thickness for the same incubation time. A further decrease in polyion concentration (about 0.01 mg/mL) decreases the layer thickness of the adsorbed polyion. An increase in the concentration to 20–30 mg/mL may result in nonlinear (exponential) enlargement of the growth rate with adsorption steps, especially if an intermediate sample rinsing is not long enough.

Unlike the later assemblies when the film mass and thickness increase linearly with the number of adsorption cycles, at the very beginning of the alternate assembly process, the film growth is always uneven [18,23]. In particular, at the first two or three layers, smaller amounts of polyion molecules are adsorbed. Tsukruk et al. have proposed that the very first polyion layer is adsorbed on a weakly charged solid support in an isolated manner, i.e., island-type [24]. In the following two to three adsorption cycles, these islands spread and cover the entire surface, and further multilayer growth occurs linearly. If the surface is well charged, then a linear growth with repeatable steps would occur. The precursor film approach [4,23] is usually employed to cover the substrate with a uniformly charged layer. Prior to the assembly, two to three layers of polyions are adsorbed on the substrate, forming a 'polyion blanket' with a well charged outermost layer. Then, the assemblies of proteins, nanoparticles or other components can be carried out in an improved way. In a typical procedure, precursor films are assembled by repeating two or three alternate adsorptions of PEI and PSS. The outermost layer becomes 'negative' or 'positive', respectively.

A detailed study of a multilayer structure derived from the neutron reflectivity analysis of films composed of deuterated PSS and hydrogen-containing PAH has revealed that the polyanion–polycation films possess a highly uniform thickness as well as a well-ordered multilayer structure. X-ray analysis, combined with neutron reflectivity analysis of polyion films, further proves the conclusion. The observed intensity oscillations, which are called Kiessig fringes due to the interference of radiation beams reflected from solid-support film and air-film interfaces, confirm the well-ordered internal structure [22]. The film thickness can be figured out from the periodicity of oscillations with the Bragg-like equation. In polyion/nanoparticle bilayer, the growth step of polyion is usually about 1–2 nm after one cycle of excess adsorption, and the thickness of nanoparticle–polyion bilayers is determined by the diameter of the particle. The values in Fig. 1.6 correspond to the curves of intensity of X-ray and

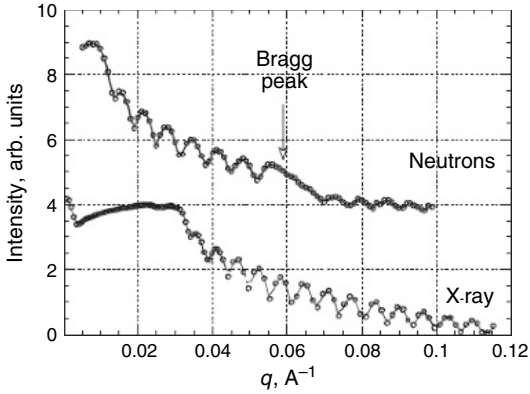

Figure 1.6: Intensity of X-ray and neutron reflection for (PSS/myoglobin/PSS-d/myoglobin)$_8$ film. (Reprinted from *Handbook of Surfaces and Interfaces of Materials* with permission from Elsevier.)

neutron reflection for (PSS-h/myoglobin/PSS-d/myoglobin)$_8$ films. Bragg reflection is not observed in X-ray reflectivity due to the small scattering contrast of polyanion and polycation layers. The concentration of polyion solutions is 3 mg/mL; the adsorption time is 15 min at pH 4.5. In order to achieve a distinct spatial separation of components, the intermediate polyion layer needs to be thicker.

Another simple analysis of a layered structure can be performed with UV-Vis absorbance spectroscopy. The amount of adsorbed layer can be estimated according to the Beer's law, provided that absorbance is proportional to the available material mass. The dependence of absorbance on the number of deposited bilayers (Fig. 1.7) reveals linear tendency. The four curves (from bottom to top) represent absorption spectra of 8, 12, 20 and 28 bilayers of PAH/PSS thin film, respectively. Inset shows the linear relationship between absorption of PSS at 230 nm and the number of deposited bilayers. The absorbance of UV light increases linearly with the growth of the film [25].

1.2.4. Tuning of Layer-by-layer Self-assembly

Although LbL self-assembly is a stable process, factors such as pH, ionic strength and temperature may influence self-assembly to a large extent.

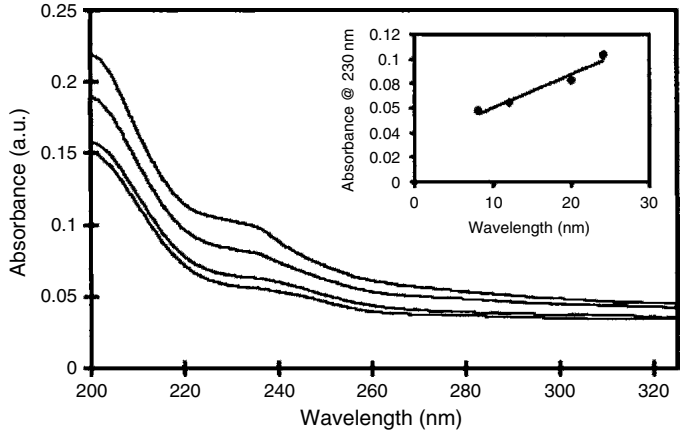

Figure 1.7: UV-Vis absorption spectra of an 8-, 12-, 20- and 28-bilayer PAH/PSS thin film. Inset shows the linear relationship between absorption of PSS at 230 nm and the number of bilayers deposited. (Reprinted from *Thin Solid Films* with permission from Elsevier.)

Taking nanoparticle–polyion self-assembly for instance, the packing density and adhesion of colloids to the polyion film can vary seriously, depending on specific interactions between colloids and surface of the film adjusted by process parameters.

In general, by adjusting the pH, we can control the deviation from isoelectric point as well as the variation of charge density on polyion chain and nanoparticle surface. By simply adjusting the pH, thin films with different thickness can be easily produced, but sometimes a sub-monolayer or no deposition is produced at all [26–30]. The packing density of nanoparticles adsorbed onto the polyion thin film may be dramatically influenced by pH. The pH determines the ionization degree of the incoming polyion or nanoparticle as well as the ionization of the uppermost surface of the existing polyion or nanoparticle multilayer. As a typical example, let us consider the adsorption behavior of 700 nm silica spheres on PAA/linear PEI (LPEI) polyion films at different pH [28]. At pH lower than the isoelectric point of LPEI (6.0∼7.0), LPEI is highly ionized so that the electrostatic force penetrates over one layer of the silica sphere, and a densely packed and clumped multilayer is formed above the polyion film. At pH 8.1, the ionization degree becomes lower, resulting in weak adsorption as seen from the weakly packed submonolayer of colloids. In the most extreme cases, at pH 9.0, LPEI ionization is practically stopped and the attraction force

between the LPEI film and colloids diminishes; therefore, adsorption is prohibited on the polyion film.

The addition of salt to change the ionic strength of incoming component solution is another effective way to adjust adsorption behavior [27–29,31]. In general, the electrolyte ions are attracted around the surface of the floating components, forming a double layer that screens surface charges. The effect of double-layer screening is multifold. It may reduce intermolecular repulsion, thus enhancing the aggregation of colloids. Moreover, it weakens the electrostatic attraction among self-assembled components. Furthermore, small charges in the adsorption solution break the ion-ion pairs between the polyelectrolytes in the existing multilayer, swell the film, and allow better penetration and incorporation of the incoming polyelectrolyte, thus increasing the amount of adsorbed material and multilayer thickness.

The effect of surfactant molecules on colloids during self-assembly is also observed [28,32–33]. At certain concentration, the surfactant molecules surround the particle, resulting in a shield layer that reduces the overall surface charge density. As a result, the addition of surfactant into the solution may weaken the attracting strength between the particle and polyelectrolyte. On the other hand, the interaction between the tails of the surfactant molecules may increase the degree of order of packed particles.

Temperature is another means of tuning self-assembly [34,35]. It has been observed that alternate adsorption of silica nanoparticles (45 nm) and PDDA is significantly influenced by the temperature of the solution in which the template is dipped. In particular, the growth rate of the polymer/nanoparticle bilayer is increased linearly with increasing temperature. The rate at 90 °C is nearly twice higher than at room temperature. It indicates a large potential upon the feasibility of mass production of self-assembly whose drawback is low throughput. For example, a 600-nm thick PDDA/silica film can be produced 2 h faster at 90 °C than at room temperature. The mechanism of rate improvement is still not clear, but it has been speculated that the increased mobility of self-assembly components and the expansion of the polyelectrolyte layer may contribute to it.

1.3. Fabrication of Nanocomposite Thin Films

Synthesis of nanostructures and hybrid organic–inorganic materials according to application requirements is one of the biggest achievements of modern chemistry. Recently, a number of nanoscale materials, exhibiting unique effects previously unidentified in the parent bulk materials owing

to confined quantum effects and large surface area, have been discovered. Appropriate techniques must be developed to organize various molecular- and nanometer-scale materials into ordered and functional nanostructures for the purpose of fully utilizing the new qualities as well as investigating their fundamental properties.

LbL self-assembly also helps to fabricate nanomaterials, incorporating different objects such as nanoparticles, dyes and virus into multilayer structures with a controlled sequence, which exhibit a number of interesting fundamentally new properties. Since the 1990s, the unique optical, magnetic, catalytic and mechanical characteristics of films made of nanomaterials have been widely reported by many research groups. Practically, a majority of these materials may have been incorporated into the multilayer by alternate adsorption with soft polyions, as shown in Fig. 1.1. The intermediate soft polyions act as 'chemical glue' that holds the multilayers more firmly because they make the interface smooth and surface charge uniform. In the following, the assembly of polyions/nanocomponents will be discussed. The alternate assembly of oppositely charged nanocomponents without using polyions is similar to the former one.

With fast developments in material sciences, many new materials have been continuously invented for thin-film fabrication, and large fractions of which have already become commercially available. In studying the feasibility of integrating new elements in the assembly, a standard procedure needs to be established in selecting the appropriate assembly substances and optimizing the assembly conditions. Many oxide nanoparticles have an isoelectric point at pH 4–5. They are negatively charged at pH 7–8. They must be assembled by means of alternate adsorption with polycations, such as PEI or PDDA, at a proper pH value, which should be known prior to the assembly. In general, the zeta potential analyzer, QCM and SEM can be used to analyse the surface charge, growth rate and film quality of the polyion/nanocomponent thin film, respectively.

The physical properties of colloids and suspensions are strongly dependent on the nature and extent of the particle–liquid interface. Almost all particulate materials, such as nanoparticles or proteins, in contact with a liquid acquire an electronic charge on their surfaces to prevent aggregation, thus improving the stability of dispersion [36,37]. Zeta potential is an important and useful indicator of this charge. The higher the zeta potential, the more the surface charges the colloids have. Therefore, the suspension is very likely to be stable due to the repulsion of charged particles helping to overcome the natural tendency to aggregate. Because of the electrostatic nature of LbL self-assembly, the measurement of zeta potential is always

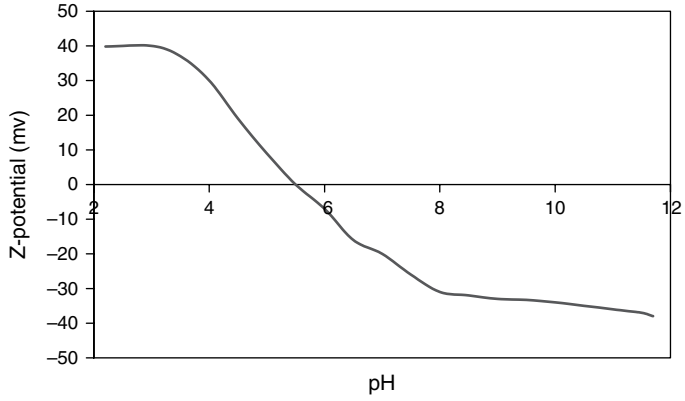

Figure 1.8: Typical Z-potential curve in dependence of pH.

the key parameter for understanding and designing process conditions. The polarity and value of charged groups on the surface of nanomaterials, as revealed by their zeta potential measurements, can directly affect their performance and processing characteristics.

A typical plot of zeta potential versus pH is shown in Fig. 1.8. In this example, the isoelectric point of the sample was at approximately pH 5.5. A plot can be used to predict that the sample should be stable at pH values less than 4 (sufficient positive charge is present) or higher than 7.5 (sufficient negative charge is present). The isoelectric point where the curve passes through zero zeta potential is normally the point where the colloidal particle has zero charge and colloidal system is not stable. Of course, the LbL self-assembly should be far away from this point because it represents the weakest electrostatic interaction.

A zeta potential analyzer usually supports the measurements of nanoparticle size, polarity and amount of surface charge. Once the materials and conditions for assembly are determined, the growth of the multilayer can be monitored by either QCM or UV-Vis spectra. Before we integrate the thin film into a device, its quality should be carefully checked. Films used in electronic or sensing devices must be closely packed, providing defectless structures and, therefore, preventing leaking currents or extra resistivity. SEM can be used to directly visualize the detailed structure of a self-assembled multilayer.

1.3.1. Silica/Polyion Multilayer

Silica assembly can be considered as a representative example of polyion/nanoparticle architecture. The negative surface charge of the silica nanoparticle demands alternate adsorbtion of polycations such as PDDA (3 mg/mL). Figure 1.9a shows the cross-sectional SEM image of three bilayers of PDDA/silica nanoparticle (45 nm in size and 8 mg/mL in concentration) adsorbed on silver electrode. Figure 1.9b illustrates six cycles of alternate adsorption of PDDA/silica as monitored by QCM. The film has a permanent thickness of 270 nm, corresponding to 45 nm for every bilayer close to the silica particle diameter. A film mass from QCM and film thickness from SEM gives the density of SiO_2/PDDA multilayers as $\rho = 1.43 \pm 0.05\,\mathrm{g\ cm^{-3}}$. To calculate the silica packing coefficient in the films, it is reasonable to assume that the dry film consists of SiO_2 nanoparticles, PDDA and air-filled pores. The total adsorbed mass equals to the sum of the mass of the three components, giving the equation

$$\rho(\mathrm{PDDA})\mathrm{V}(\mathrm{PDDA}) + \rho(\mathrm{SiO_2})\mathrm{V}(\mathrm{SiO_2}) + \rho(\mathrm{air})\mathrm{V}(\mathrm{air}) = \rho V$$

Given the component densities ($\rho = 1.43$, $\rho(\mathrm{SiO_2}) = 2.2$ and $\rho(\mathrm{PDDA}) = 1.1\,\mathrm{g\ cm^{-3}}$) and assume that the air term is very small, $\mathrm{V}(\mathrm{SiO_2})/\mathrm{V}$ works out to be 0.7. This is very close to the theoretical dense-packing coefficient for spheres (0.63), and consistent with details in the SEM micrographs. The PDDA/SiO_2 film's volume composition is 70% SiO_2 + 10% polycation +20% air-filled pores. These pores are formed by closely packed 45 nm SiO_2 with a typical dimension of 15 nm [38,39].

Saturation of adsorption can be attained very quickly. The growth of SiO_2 film remained nearly the same, as the adsorption time was changed from 20 min to 15 s. The assembly of SiO_2 particles with another polycation, PEI, gave similar kinetic parameters. The growth step for a PEI/SiO_2 multilayer was slightly less than that for PDDA/SiO_2 films. Height profiling of the image shows a height difference of 10–20 nm, in reasonable agreement with the actual particle radius of 23 nm.

1.3.2. Semiconductor Nanoparticle/Polyion Multilayers

The formation of polyion/semiconductor nanoparticle film is of great interest for exploiting the unique optical and electronic properties of such materials. A large variety of commercially available metal oxide semiconductor nanoparticles are functionalized so that they carry surface charges

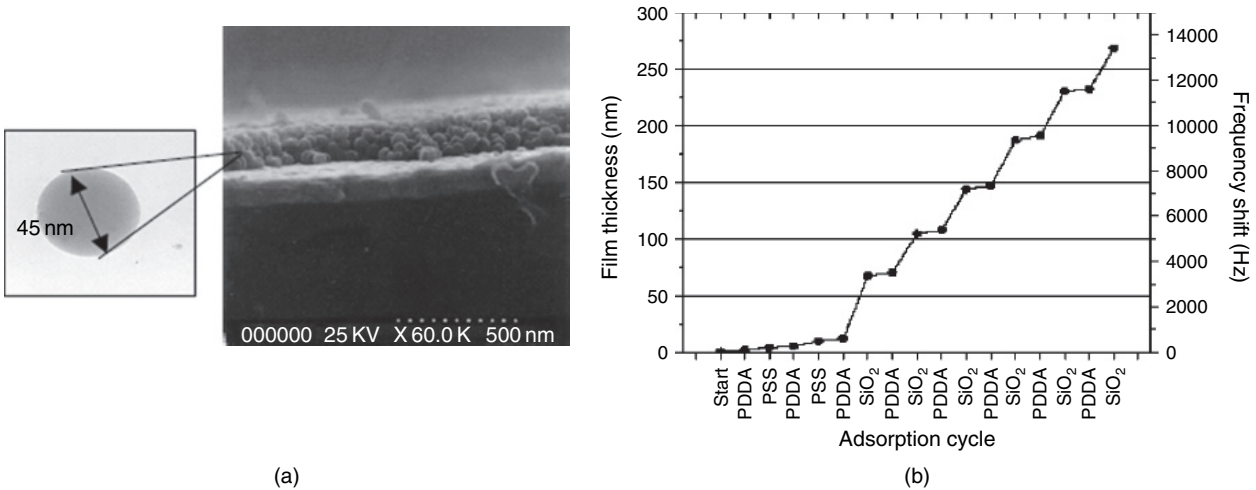

(a) (b)

Figure 1.9: (a) SEM image of the cross-sectional view of the PDDA/silica nanoparticle film. (b) Growth of six bilayers of PDDA/silica monitored by QCM. (Reprinted from *Nanotechnology* with permission of Institute of Physics.)

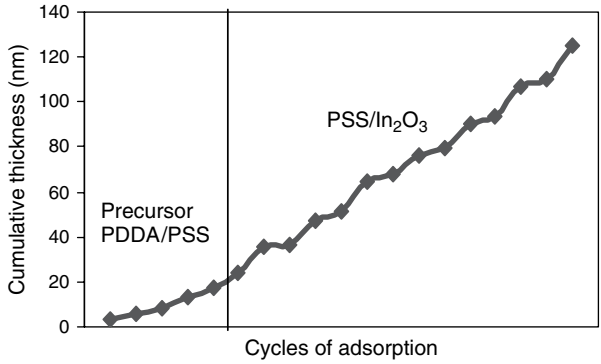

Figure 1.10: Growth of PDDA/In_2O_3 nanoparticle film monitored by QCM.

to prevent aggregation. As a result, they can be assembled in combination with linear polyions [39–41]. Figure 1.10 illustrates the steady growth of PDDA/In_2O_3 nanoparticle (45 nm) thin film. The concentration of nanoparticle dispersion ranges from 5 to 8 mg/mL. A precursor film consisting of PDDA/PSS layers on the solid substrate is still used to assist successive adsorption. The closely packed structure is readily obtained.

Growth of other nanoparticle films is possible if being alternately assembled with oppositely charged polyions. Multilayers of cationic CeO_2 nanoparticles, for example, at pH 3.5 were produced by sequential adsorption with anionic PSS. The growth step increased from 4 to 9.6 nm when the CeO_2 concentration is increased from 2 to 150 mg/mL.

Another type of semiconductor nanoparticles, the II-VI composites, can be integrated into the multilayer with polycations. For example, CdS and PbS nanoparticles can be alternately adsorbed on substrate with PDDA [41].

1.3.3. Au Nanoparticle/Polycation Multilayer

Alternate adsorption of Au nanoparticle with polycation such as PAH, is possible because of negative nanoparticle charge (surface potential c. −35 mV) due to the synthesis procedure. The saturation time necessary for the formation of closely packed gold nanoparticle monolayer ranges from a few to tens of hours, which is much longer than for other types of nanoparticles, because of the low particle concentration in solution. In order to obtain an ordered architecture, a vertical spatial separation of nanoparticle layers in such sandwich-like films was elaborated: three to

five polycation/polyanion interlayers were assembled between gold layers (e.g., Au/{PAH + $(PSS/PAH)_{3-5}$}/Au). The gold surface (with roughness of the order of the radius of nanoparticles) was covered and smoothened by 6–10 nm polyion layers. Further 'sandwiching' of gold nanoparticles with thick polyion interlayers resulted in ordered gold/polymer heterostructure. The low-angle X-ray reflectivity of these samples gave two to three orders of Bragg reflections with spacing corresponding to such complex unit cell [6,42].

1.3.4. Layered Ceramic Plates

The mica-type layered silicates can bear a natural negative charge because of the isomorphous substitution of silicon in octahedral sheets by aluminum or magnesium [22]. The charge is generally balanced by potassium cations that reside in the galleries between layers. The high lateral aspect ratios have rendered it suitable for the construction of ultrathin ceramic films. Alternating layers of polyion/ceramic sheet sandwich films can be constructed in a similar way as described above. Multilayers of anionic synthetic silicate-hectorite and cationic PDDA were produced by applying LbL adsorption [41,43]. In an experiment to build multilayers with alternating 1-nm thick montmorillonite sheets and cationic PEI, the film thickness increase was 1.1 nm for montmorillonite adsorption cycle and 2 nm for PEI. After 20 cycles, the resultant film had a permanent thickness of 63 nm (Fig. 1.11).

1.3.5. Conductive Polymers/Polyion Multilayer

LbL processing makes it possible to manipulate conducting polymers within multilayer thin films. Rubner et al. presented an approach to incorporate controllably highly conductive, p-type doped conjugated polymers into multilayer heterostructure films. In this case, the self-assembly process was based on induced electrostatic interactions between the negatively charged PSS and the positively charged p-type doped and electrically conductive chains of polypyrrole (PPY). The delocalized positive charges (polarons and bipolarons) of the doped conjugated polymer backbone provide the secondary forces required for LbL deposition with PSS. The p-doped conductive polymer dipping solution typically contains 0.006 M $FeC1_3$, 0.02 M pyrrole monomer and 0.026 M p-toluenesulfonic acid (PTS). The solutions

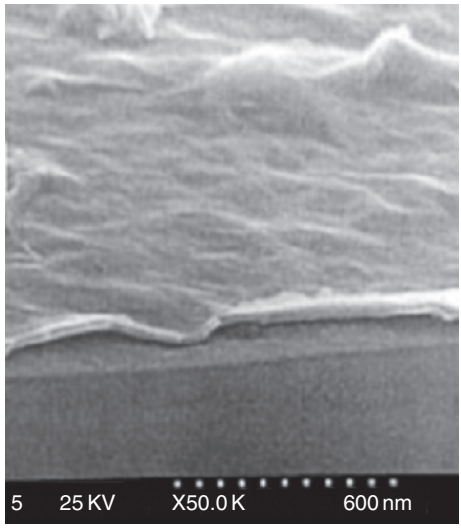

Figure 1.11: PEI/montmorillonite sheets multilayer (Reprinted from *Langmuir* with permission from American Chemistry Association.)

were stirred to assist the PPY-PTS reaction, continuously producing PPY by polymerization reaction to the solution during dipping. Therefore, in situ polymerized PPY can be self-assembled with suitable polyanions (PSS) into multilayer thin films [44].

Ozin demonstrated the synthesis of water-soluble organometallic polyelectrolyte, polyferrocenylsilanes (PFS). As a result, the organic polymer superlattice is fabricated based on the multilayer of organometallic PFS and polyanionic PSS, which offers interesting redox, conductive or preceramic properties [45].

1.3.6. Carbon Nanotube/Polyion Multilayer

Normally, carbon nanotubes are electrically neutral. In order to make them applicable for LbL fabrication, the nanotube must be chemically modified to carry some net surface charge [46–49]. Ionic groups can be covalently attached to either open tube ends or defect sites of oxidatively shortened or cut nanotubes. However, the covalent addition of the ionic group may destroy the unique electronic properties of the tube. Lukkari et al.

developed a technique to fabricate full-length, single-wall carbon nanotubes (SWNTs) that possess sufficient surface charge density based on the noncovalent modification of nanotubes by coupling several polyaromatic ionic molecules. These nanotube polyelectrolytes have a linear ionic charge density when electronic properties and high aspect ratio are retained. They are similar to that of highly charged polyelectrolytes and can form aqueous solutions with sufficiently high concentration and stability good enough to be used in LbL assembly. Depending on the ionic modifier, the neutral nanotube can be freely converted either to a highly charged polyanion or a polycation. Therefore, homogeneous tube/polyelectrolyte can be manufactured. Moreover, an extremely important finding is that tube/tube multilayers can be electrostatically assembled in multilayers without any polyion components.

SWNTs could be introduced into polyionic, water-soluble species via noncovalent adsorption of naphthalene and pyrene derivatives. To prepare tube/polyelectrolyte multilayers, anionic nanotubes were alternately assembled with poly(diallyldimethylammonium chloride) (PDADMA), MW 100 000–200 000, or PAH. The immersion time in tube water solution was about 30 min. For cationic SWNTs, PSS was used as the counter polyelectrolyte. SWNT/SWNT multilayers were prepared by alternately assembling anionic and cationic SWNTs [46]. The concentration of PDADMA, PAH and PSS solutions was 10 mM with respect to the monomer, and the ionic strength was adjusted with NaBr (PDADMA and PSS) or NaCl (PAH) to 0.1 M. Similarly to other polymer/nanoparticle multilayers, the adsorption of the tube is increased slowly during the first 5–10 bilayers, after which the growth process was accelerated and became linear.

1.3.7. Protein/Polyion Multilayer

Most of the protein species are suitable for LbL assembly. Ordered multilayers have been produced in a similar way as other polyion/nanocompenent structures. Protein multilayers were assembled with either positively charged PEI, PAH, PDDA, chitosan or negatively charged PSS, DNA and heparin [6,50–54]. Specific process conditions were developed to set the pH of the protein solutions apart from the isoelectric point so that proteins are sufficiently charged. So far, the assembly of different proteins was successfully achieved, including cytochrome [6,53], carbonic anhydrase [22], myoglobin [6], hemoglobin [6], bacteriorhodopsin [55], pepsin [6], peroxidase [56,57], alcohol dehydrogenase [57], glucoamylase [6], glucose

oxidase [6], immunoglobulin [19], catalase [53] and urease [58]. Homogeneous layers with proteins and strong polyions, such as PSS, PEI and PDDA, were insoluble in buffer for a pH range between 3 and 10 [6]. More importantly, assembled proteins are, in most cases, not denaturated [19,59]. The LbL immobilized enzyme in multilayers may both enhance its enzymatic stability and bioactivity linearly with the number of layers up to c. 10–15 protein layers, when the saturation of film bioactivity is reached. Bioactivity can be regulated by the compactness of protein multilayers. As it was shown, glucose oxidase, myoglobin and albumin multilayer films were compact, but immunoglobulin IgG/PSS multilayers had porous structure with areas as large as 100 nm in diameter unfilled in the upper layers of the film [19,20]. Figure 1.12 shows the SEM image of cross-section of $(PEI/glucose\ oxidase)_8$ multilayer on quartz [6].

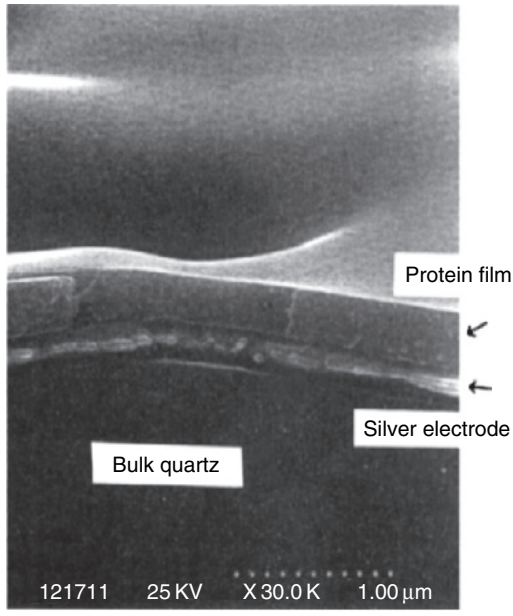

Figure 1.12: SEM image of $(PEI/glucose\ oxidase)_8$ film deposited onto the silver-coated resonator. (Reprinted from *J.A.C.S.* with permission from American Chemical Society.)

1.3.8. DNA Multilayer

LbL self-assembly has been extended to another important biological macromolecule – i.e., DNA. As an anionic polyelectrolyte with a unique double helix structure, DNA can be readily used to produce ultrathin films with cationic materials by the LbL technique. A lot of works has been successfully done to construct highly ordered structures of DNA films with different kinds of molecules, such as polycations, proteins, organic dyes, metal complexes and rare earth metals, through the LbL technique. For example, Jansen et al. fabricated and characterized the poly-D-lysine (PDL)/DNA multilayer coated on titanium with PDL as a polycation [60,61]. DNA immobilization into the coating was linear and approximated $3\,\mu g/cm^2$ for each double layer. Yinglin et al. produced thin films of alternating DNA and rare earth ion Eu(3+) layers from dilute aqueous solutions [62]. UV-Vis spectroscopy shows that a uniform layer of DNA can be fully adsorbed onto each alternate Eu(3+) layer.

1.4. Modified Procedures

1.4.1. Spin Layer-by-layer Self-assembly

Several procedures in LbL self-assembly may vary in view of either improving the property of thin film or satisfying specific design requirements.

One such modified procedure to mention is the spin LbL self-assembly [63–66]. Unlike the conventional dip self-assembly, the polycation, polyanion or nanoparticle solutions are spun cast on the template by a spin-coater with intermediate rinsing by spinning DI water on the template. Interestingly, the growth rate is at least one order of magnitude higher than that of the dipping process; the surface roughness of the multilayer is significantly decreased and the internal structure is highly ordered. These improvements may be attributed to the shearing effect. The dip self-assembly consists of slow diffusion of the components toward the surface with successive migration and conformation over the surface under electrostatic interaction. The weakly attached molecules are removed only during discrete rinsing. All the above steps are completed nearly simultaneously at a high rotating speed. In addition, water molecules are considered to somewhat hinder adsorption because it screens the electrostatic attraction when it stays between two oppositely charged components. In the spin self-assembly process, the water molecules are spun off the multilayer

surface at the same pace as adsorption so that adsorption is dramatically enhanced due to increasing electrostatic attraction. The spinning process also provides a well-ordered internal structure and consequently a smoother surface because the shearing effect assists the line-up of molecules among multilayer.

1.4.2. Spray Layer-by-layer Self-assembly

Another variation of spin LbL self-assembly is the spray self-assembly in which oppositely charged polyions and nanoparticles are sequentially sprayed onto the substrate within only a few seconds after each step [67,68]. Between every two depositions, the surface is washed by spraying DI water. Several measurements made by QCM, UV-Vis light absorbance, ellipsometry and X-ray diffraction (XRD) suggest that a highly uniform multilayer is produced in a large area within a short time interval while morphology, uniformity and chemical composition of the sprayed multilayer are nearly identical to the conventional ones.

1.4.3. Covalent Layer-by-layer Self-assembly

LbL composite materials constructed so far were mainly based on electrostatic interaction, hydrogen bonding, charge-transfer interactions and coordination bonding. However, these types of interactions may be insufficient to stabilize the composites for some applications such as high-speed spin coating of photoresist and etching by strong chemicals in lithographic process. The LbL composites can be strengthened by covalent cross-linking.

Sun et al. have reported the new type of LbL composite that is covalently bound [69,70]. The LbL multilayer was fabricated by depositing photoreactive films containing diazo-resins (DAR) as polycations and PSS as polyanions, which were held together by electrostatic interactions. The fabrication of the multilayer containing DAR and PSS was performed in the dark. The assembled films containing bilayers of DAR/PSS were irradiated with a medium-power mercury lamp. Upon UV irradiation, the adjacent interfaces of multilayer films reacted to form a crosslinking structure based on the photoreaction of diazonium and sulfonate groups in multilayer films. The infrared (IR) spectroscopy observed two adsorption peaks at 2166 and 1178 cm of 12 bilayers of DAR/PSS assembled on a CaF_2 substrate before UV irradiation, originated from the asymmetric stretching of CN_2 and symmetric stretching of SO_3, respectively. After UV irradiation, the adsorption

at 2166 cm disappeared completely, indicating the decomposition of diazonium group. Meanwhile, a new adsorption at 1162 cm appeared, which corresponds to the symmetric stretching of sulfonate coupled with phenyl group [69,70]. Owing to the formation of three-dimensional crosslinked structure based on covalent bonding, the resulting multilayer films are much more stable than those based on ionic interactions.

This technique of converting ionic LbL multilayer to covalently bonded multilayer has been extended to the fabrication of other robust LbL self-assembled thin films. Kotov et al. reported the fabrication of a LbL film constructed by cationic DAR and PSS-functionalized SWNTs [71]. The covalent linkages between SWNTs and PSS were formed by in situ free radical polymerization of sodium 4-styrenesulfonate (NaSS) in the presence of pristine HiPco SWNT. Multilayer films of DAR/SWNT-PSS were constructed using aqueous solutions. Multilayer films of DAR and anionic polyelectrolytes reacted to form covalent linkage upon UV irradiation. Moreover, diazonium groups can also react with SWNT thermally at room temperature in aqueous solution to form chemically functionalized SWNT. Therefore, LbL films from anionic polyelectrolyte-functionalized SWNT and DAR, having chemical crosslinking both between SWNT and DR and between polyelectrolytes and DAR, have excellent stability and strength.

1.5. Surface Patterning

LbL self-assembled multilayers have been used in various applications including light-emitting devices, biochemical sensors, multilayer actuator, etc. The capability of patterning the multilayer is the prerequisite of device fabrication. Since even the simplest device is made of more than one type of building block, the spatial separation of different building blocks both vertically and laterally must be achieved before thin films can be integrated into the device.

The patterning methods reported so far can be divided into three categories: selective adsorption, selective etching and photolithography method. Selective adsorption requires the fabrication of two types of functional regions on the surface before adsorption. The alternate functional regions either improve adsorption or resist it. The substances are preferentially attracted onto the adsorption-enhancing region while repulsed by adsorption-resisting regions. The adsorbates are self-assembled layer by layer only on adsorption-enhancing regions.

The formation of functional regions can be achieved by many ways. The microcontact printing method uses a surface patterned polydimethyl siloxane (PDMS) stamp to print chemicals onto the substrate [72,73]. At first, an adsorption-enhancing substance, such as acid (COOH) terminated self-assembled monolayer (SAM), is applied all over the surface. Then, an adsorption-resisting substance, such as oligoethylene glycol (EG) in the form of ink, is attached on the surface of PDMS and then printed onto the substrate, forming alternate adsorption-enhancing and resisting regions. The ink transfer makes use of low surface energy of PDMS ($19.8\,\mathrm{mJ/m^2}$). Once the template is immersed in the solution, the adsorbates are directed onto the COOH region, whereas they stay off the EG region. This method is simple and, at the same time, satisfies selectivity and biocompatibility requirements. So far, resolutions of sub-micrometer and even down to nanometer have been achieved [74].

Lateral separation of attractive and repulsive regions can be achieved by the electric field directed layer-by-layer assembly (EFDLA) method [75]. Electric fields accelerate and decelerate the deposition of charged species on an electrode, which is the basis of the electrophoretic deposition technique. The key advantages in the EFDLA method are achieving spatially selective deposition and controlling the start and stop points of ionic self-assembling on different areas of a substrate in order to eventually prepare spatially separated patterns. At first, an array of conductive electrodes must be laterally defined on the substrate. During successive deposition, the bias of different electrode regions is programmed in order to control the deposition of charged species. By delicate control of deposition, multi-components can be adsorbed onto the desired regions according to the design. If the distinction between accelerating and decelerating effects is sufficient, the control of growth or repulsion of thin film driven by electrostatic interaction can be realized on electrodes. Moreover, if a series of electrodes are placed on the same substrate and spatially separated, one can deposit different types of films on different electrodes by programming the polarities on each single electrode. Using successive depositions of different materials, spatially separated patterns can eventually be formed.

Another method to form regions with different chemical functionality is by way of microfluidic channels combined with the convective self-assembly process employing both hydrogen bonding and electrostatic intermolecular interactions. Microfluidic channels were formed by direct contact between an elastomeric PDMS mold and a hydrophilic substrate. PDMS stamp was obtained from a silicon master prepared by photolithography. The chemically patterned template was prepared by attaching polyion

bilayers within the confined space defined by microfluidic channels. In one report, $(PVP/PAA)_5$ multilayer films were sequentially deposited inside the channel region [76]. The patterning was performed in two steps. The polymer solution was first allowed to fill the microfluidic channels by capillary action. Channel filling enabled the polymer to adsorb onto the substrate. The removal of residual polymer solution was then carried out by the spinning process. These two steps were repeated for a predetermined number of bilayers. After the micropatterns of $(PVP/PAA)_5$ multilayer films were obtained, PDMS stamp was removed, leaving a chemically alternating template with blank substrate and $(PVP/PAA)_5$ multilayer. The carboxylic acid groups of PAA, an outmost layer of the template, are partially ionized and thus enable the adsorption of cationic polyelectrolytes. For example, an alternate deposition of poly(diallyldimethyl ammonium chloride) (PDAC) and PSS onto micropatterns was demonstrated by spin self-assembly. These multilayer micropatterns with vertical heterostructure reveal high line resolution and smooth surface. Perfect selectivity is given by the physical confinement of microfluidic channel. Sub-micron patterning is also possible using a mold with controlled geometric structure.

Selective etching makes use of different conditions under which LbL self-assembled multilayers are constructed and deconstructed. It has been found that, besides electrostatic interactions that have been utilized as the main driving force of assembly process, hydrogen-bonding interactions can be used for LbL processing. Hydrogen-bonded multilayers comprising weak polyacids could be assembled at low pH and subsequently dissolved at a higher pH as a consequence of increasing the degree of ionization of weak polyacid. New patterning schemes are derived from this mechanism by stabilizing hydrogen-bonded multilayers to high pH environments. Thermal treatment can be used to render normally soluble hydrogen-bonded multilayers insoluble at high pH. In one study [77], PAA and polyacrylamide (PAAm) ($MW = 5\ 000\ 000$) were alternately deposited at pH 3.0 for constructing multilayer films. Both dipping and rinsing solutions must be maintained at low pH to avoid dissolution of the film. The hydrogen-bonded PAA/PAAm multilayer films became completely soluble in water at pH 5.0 or higher in attribution to the ionization of PAA acid groups at high pH, which disrupts the hydrogen-bonded network and introduces electrostatic repulsive forces However, heating the film at 175 °C for 3 h (or at lower temperatures for longer time) introduces chemical cross-links that stabilize the multilayer assembly even at pH 7 in a buffered solution. The heated multilayer film remained unchanged on the substrate even after 24 h of immersion in the pH 7 buffer solution. In contrast, the as-prepared

multilayer film dissolved immediately when immersed in this solution. The ability to stabilize hydrogen-bonded multilayers via thermal reactions makes it possible to readily form patterns from these films with water as a developing agent. An ink-jet printer can be used to 'print' pH 7.0 water on a multilayer film, followed by heat treatment (95 °C) for 8 h and rinsing with water. The regions 'printed' with water are rendered noncross-linkable due to the ionization of acid groups of PAA, whereas the nonprinted regions become cross-linked by heat treatment.

As mentioned earlier, some diazo-resins (DARs) are photosensitive; therefore, a multilayer of DARs and polyions may have different solubility prior to and after UV irradiation. For example, covalently attached DAR/PAA multilayer can be fabricated by the LbL self-assembly of DAR and PAA in aqueous solutions, followed by UV irradiation. The reaction between DAR and PAA under UV exposure changes the interaction between films from ionic to covalent bonding, thus significantly improving the stability of the multilayer as compared to the unexposed film. Once the multilayer is fabricated, it is irradiated by UV light with a photomask between the light source and multilayer. The cross-linked and noncross-linked regions are generated after UV irradiation. The noncross-linked regions can be selectively etched by an aqueous solution with appropriate pH value [77].

Recently, a new technique, different from selective deposition and etching, was developed by combining the traditional photolithographic process with LbL assembly [74]. It allows a reliable patterning process on account of its compatibility with the existing technologies used for the production of traditional microelectronic devices. Figure 1.13 illustrates the patterning of LbL self-assembled polyion/nanoparticle multilayer. At first, a template with patterned photoresist is fabricated by photolithography. Then, the polyion and nanoparticles are alternately deposited on the entire surface. Finally, the template is immersed in acetone until the photoresist dissolves. This lift-off process removes both the photoresist and substances on top of it. However, during the lift-off process, sonification is necessary in order to break the polyion network; otherwise, substances above the photoresist settle down on the surface.

Reference [78] gives an example of the application of this kind of patterning. A 1 μm thick photoresist layer was lithographically patterned on silicon wafer. The feature that emerged consisted of alternate 5 μm-wide lines separated by spaces of same width. Then, the $(PDDA/PSS)_4 + PDDA$ precursor multilayer was adsorbed on the entire surface. Both PDDA and PSS solutions had a concentration of 3 mg/mL, ionic strength of 0.5 M

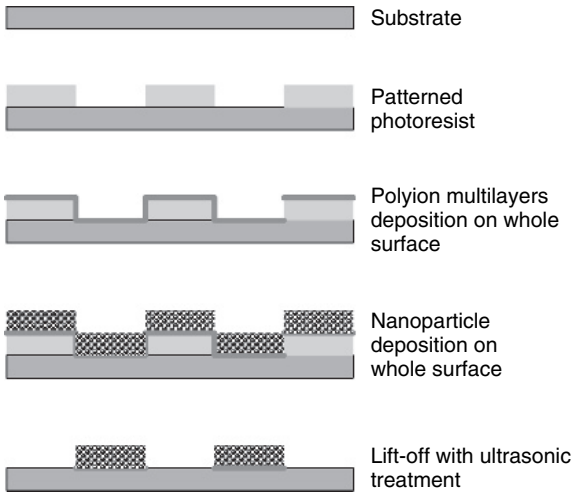

Figure 1.13: Schematic of lift-off to pattern layer-by-layer self-assembled nanoparticle thin film.

NaCl and pH 7. At this point, the outermost layer was positively charged PDDA. Silica colloids (300 nm diameter) in 0.02 M NaCl, 1 mg/mL, pH 9 whose surface was modified to be negatively charged, were adsorbed in the sequence of $[\text{PDDA (10 min)/silica (2 5 min)}]_3$. For each step, the substrate was rinsed in DI water for 1 min and dried by nitrogen flow between immersions. Finally, the substrate was put into acetone solution with ultrasonic treatment for 5 s to remove the photoresist. Figure 1.14 illustrates clear and distinct images of silica bead strips on the resulted wafer observed by SEM. The 5-μm strips containing the polyion precursor with nanoparticle multilayer are well shaped and have sharp borders. The silica particles are closely packed with few vacancy defects. The average roughness of the strip borders is less than one particle diameter (in this case 300 nm, but it could be lesser if smaller particles were used). There are no particles in the areas between strips.

This process has also been applied to fluorescent materials. In reference [78], negatively charged 45-nm diameter fluorescent nanoparticles were assembled over a similar precursor: $\{\text{PEI} + (\text{PSS/PDDA})_3 + \text{Fluoresbright/PDDA})_3\}$ following the same experimental procedure. Another mask with wider strips was used to make the pattern well visible through a fluorescent microscope (Fig. 1.15). One could see a sharp green

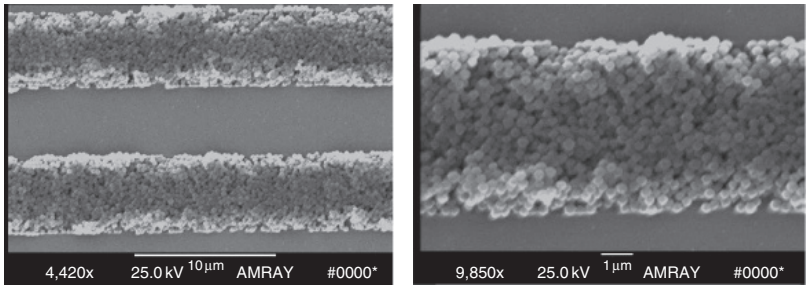

Figure 1.14: SEM pictures of self-assembly patterns. All with SiO_2 particles of 300 nm in diameter at the outermost layers. The line width is 5 µm. (Reprinted from *Langmuir* with permission of American Chemical Society.)

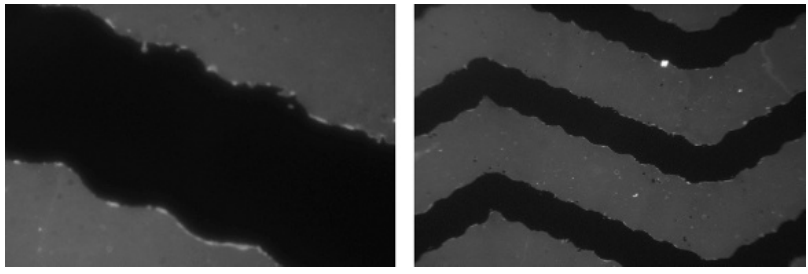

Figure 1.15: Fluorescent images of 25 µm wide multilayer of $\{PEI + (PSS/PDDA)_3 + (fluoresbright/PDDA)_3\}$ produced on silicon. (Reprinted from *Langmuir* with permission from American Chemical Society.)

pattern indicating permanent coverage fluorescent multilayers with strips 25 µm wide and dark areas 12 µm wide.

In order to incorporate two or more different elements within a pattern or array, the lift-off method may be extended with an addition of one more step. The 'two lift-off' method shown in Fig. 1.16 can separate two types of LbL self-assembled substances [79].

The desired geometry was lithographically defined on the photoresist layer [79]. After a coating with PDDA/PSS precursor multilayer, the negatively charged 64-nm polystylene nanoparticles were adsorbed onto the PDDA surface. Then, aluminum (90 nm thick) was coated on the nanoparticle layer. At this moment, the first lift-off process was carried out by immersing the sample into acetone. Another type of nanomaterial, a 150-nm polystylene nanoparticle, was adsorbed onto the entire surface

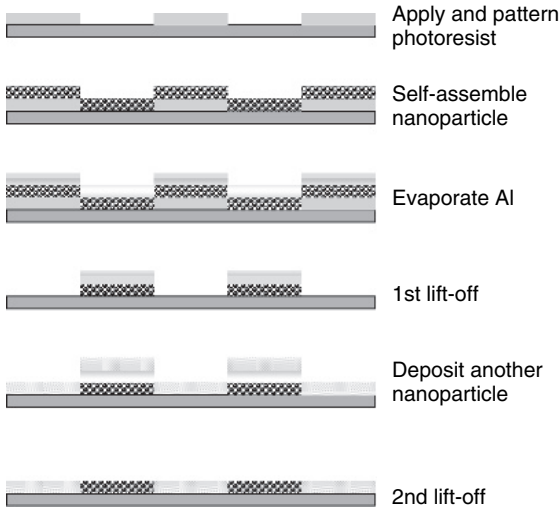

Figure 1.16: Schematic of 'two lift-off' method

alternately with polyions. The second lift-off process dissolved aluminum and removed the 150-nm nanoparticles above it. Figure 1.17a illustrates the photoresist template on silicon wafer with periodically arranged 5-μm squares. Figure 1.17b shows that polystylene nanoparticles, 64 and 150 nm in diameter, settle inside and outside the tiny square.

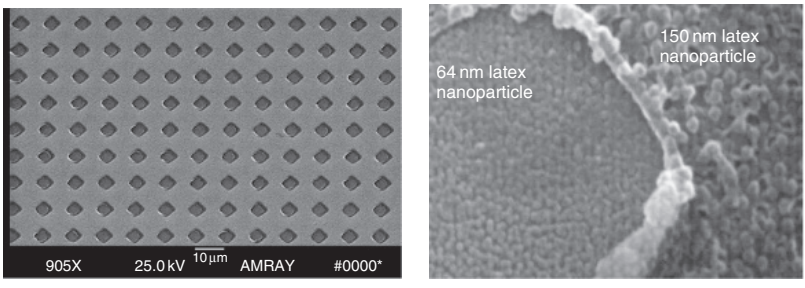

(a) (b)

Figure 1.17: SEM images of the spatial separation of two nanoparticles layers at different magnification: (a) matrix comprised of 5 μm squares; (b) 64-nm nanoparticles were filled in the square and 150-nm ones surrounding them. (Reprinted from *Thin Solid Films* with permission of Elsevier.)

1.6. Current and Potential Applications

Based on the numerous available charged species suitable for LbL self-assembly and the capability of spatially manipulating these species, the LbL self-assembly technique finds a wide range of applications, ranging from anticorrosion coatings, body armor and biomedical implants, to nanocoated microshells for drug delivery, fluorescence-based microsensors, and scaffolds for tissue growth. Let us discuss several examples of main applications of LbL technique. These include electronic devices, optical coatings, biomedical applications and self-assembly on nonplanar surface.

1.6.1. Current Applications

Electronic devices

LbL assembly has the capability to fabricate basic electronic devices including light-emitting diode (LED), rectifying diode, metal-oxide-semiconductor field effect transistor (MOSFET), MOS capacitor, MOSFET structured sensor, solar cell, etc.

Alivisatos et al. fabricated a rectifying p–n junction from a p-type semiconducting polymer (SCP) layer, poly(p-phenylenevinylene) (PPV), and an n-type semiconductor nanoparticle layer, CdSe [80]. These ultrathin films were constructed by alternate adsorption of layers of CdSe nanoparticles, 1,6-hexanedithiol and PPV. Later, Fendler et al. further demonstrated both rectifying behavior in the forward direction and Zener breakdown in the reverse direction by controlling the degree of p-doping in the SCP without affecting the properties of the n-type semiconductor nanoparticle layer [81]. Such Zener junction cannot be constructed exclusively from SCPs because p- and n-types of doping cannot be separately introduced to the neighboring layers. Additionally, the doping effect of n-doped SCP (polypyrrole or polythiophene, for example) tends to disappear upon exposure to air [81]. This problem can be overcome by coupling the p-type SCP to an n-type semiconductor nanoparticle layer.

New electroluminescent devices have been fabricated by polymer and inorganic semiconductor quantum dot layers. Chen et al. presented a nanoparticle LED (NLED) that was fabricated by LbL assembly of PPV and CdTe nanoparticles [82]. The turn-on voltage for electroluminescence is 4.0 V. Electroluminescence is exclusively from CdTe nanoparticles,

with a 30 nm red shift in the emission wavelength from photoluminescence and shifts to longer wavelengths at higher applied voltages. The red shift of electroluminescence may be attributed to the reabsorption of larger dots within the nanocrystal layer due to energy transfer from small to large dots or local Joule heating from the large current flux and poor thermal conductivity. Similarly, the voltage-tunable red shift may be attributed to trap filling or detrapping of surface states/interface states and the quantum confined Stark effect. LbL fabricated NLED may provide voltage-tunable multicolor emission with high contrast. The newly assembled multilayer enhances the efficiency of LED and hole transport performance [83].

One of the fundamental devices in modern integrated circuit (IC), the metal-oxide-semiconductor capacitor, was also realized by the LbL process [84]. In particular, capacitor arrays were constructed on both p- ($>1\,\Omega$cm) and n-type ($>1\,\Omega$cm) silicon wafers. The geometry of capacitor arrays was patterned on the photoresist. Then, six layers of 45-nm silica nanoparticles were adsorbed onto the silicon wafer alternately with PDDA. The sequence of alternate immersion was $[\text{PDDA} + \text{PSS}]_2 + [\text{PDDA} + \text{silica}]_6$ with necessary intermediate rinsing and drying after each immersion. Aluminum electrodes were evaporated in vacuum on the top. Finally, the photoresist was dissolved, leaving the capacitor arrays on silicon surface. The silicon wafer and vacuum-evaporated aluminum served as electrodes with silica nanoparticle sandwiched inbetween as the insulating layer. This process combining lithography and LbL assembly resulted in the high-resolution patterns of capacitor arrays with sharp borders. All 45-nm SiO_2 spheres were closely packed to form a dense structure, leading to a negligible leakage current. The surface roughness of the capacitor was 6.5 nm measured by a roughness step tester (RST). The fabricated device demonstrates the C–V curve of a typical MOS capacitor with distinct accumulation, depletion and inversion regions, as shown in Fig. 1.18. Since the inversion of a p-type MOS capacitor happens at a positive voltage and an n-type one at a negative voltage, the C–V curves move in opposite directions for p- and n-type MOS capacitors. For the given size of each square device, the dielectric constant of self-assembled oxide layer is 6, which is higher than that of the bulk silicon dioxide layer (3.9). The relatively high dielectric constant may be attributed to the precursor and intermediate polyion multilayer because the dielectric constant of polyion films is normally ten times higher than that of silica. The experimental results also show that the capacitance of each device is strictly proportional to the area of electrode, implying an extremely high reproducibility of the processes.

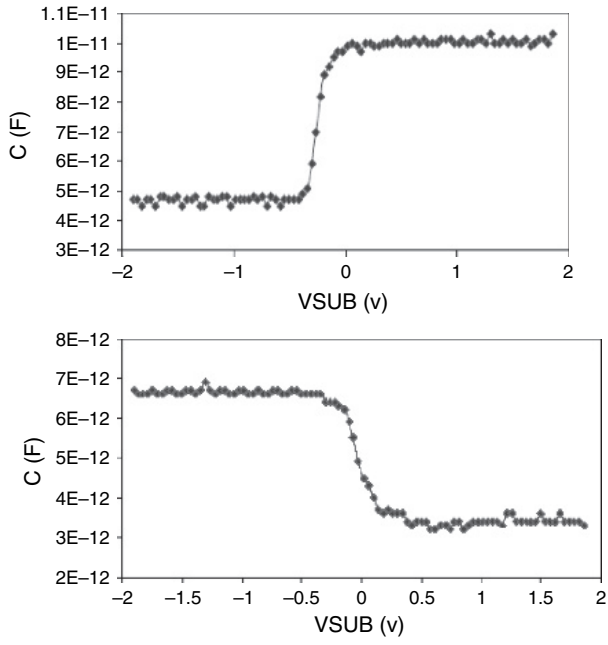

Figure 1.18: Capacitance versus voltage curves of MOS p- and n-type capacitors. (Reprinted from *Nanotechnology* with permission from Institute of Physics.)

MOSFET circuits are the most widely used active elements accounting for more than 90% of the IC market. A MOSFET transistor typically needs three functional layers, namely metal, oxide and semiconductor layers. It was reported that the oxide and semiconductor layers of a MOSFET were realized by LbL self-assembled nanoparticle layers instead of the conventional techniques based on evaporation and/or epitaxy processes [85]. As illustrated in Fig. 1.19, the metallic source and drain electrodes were initially formed on a silica layer. The second lithography step provided an opening of photoresist area just above the channel region. Then, six layers of 15-nm SnO_2 and 45-nm SiO_2 nanoparticles were LbL self-assembled on the surface. Aluminum was vacuum evaporated on top of the structure as the gate electrode. The final lift-off step generated the structure of MOSFET by dissolving the photoresist. The SEM image, Id–Vd drain voltage-current characteristics under different gate voltages and gate transfer characteristics of the MOSFET are shown in Fig. 1.19. The Id–Vd curve indicates that, when the gate voltage exceeds the threshold voltage and increase in

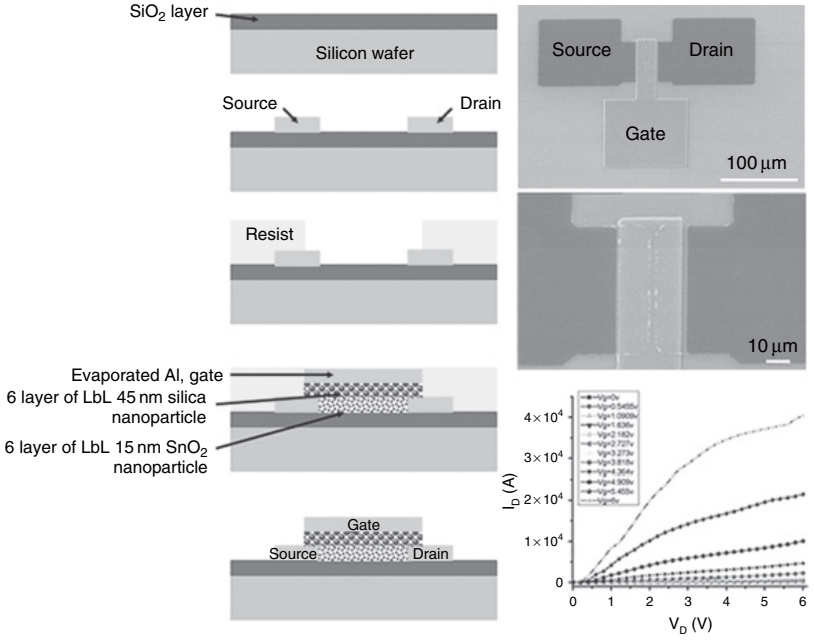

Figure 1.19: (Left column) Schematic of the MOSFET fabrication; (right column) from top to bottom: SEM image of the appearance of self-assembled MOSFET; Id–Vd characterization of MOSFET. (Reprinted from *IEEE Transactions on Electron Devices* with permission of Institute of Electrical and Electronics Engineers.)

positive polarity, drain currents rise more steeply at small drain voltages and show saturation tendency at high drain voltages. The threshold voltage is 3 V, on-off current ratio 10^4, and mobility 2.1×10^{-2} cm^2/V-s.

Note that the LbL fabricated electronic devices are inferior to the conventional ones in terms of performance. However, they show a high potential in special applications such as biological and chemical sensors where silicon technology is not adequate.

Optical coating

Low-cost and high-performance antireflection (AR) coatings can be realized by sequential deposition of polyelectrolytes and single-layer silica particle (110 nm in average diameter) coatings onto the glass substrate [86].

Reflectance of 0.07% can be achieved without scattering in the region of visible light. The coating is designed in a way that the relative phase shift between the beam reflected at the upper and lower boundaries of the thin film is 180°. Destructive interference between the two reflected beams occurs, canceling out both beams before they exit the surface. Optical thickness of the coating must be an odd number of quarter wavelengths ($\lambda/4$, where λ is the design wavelength). AR coating can also be achieved by polyion/polymer particle sequential adsorption. In this case, tuning the effective wavelength using deformation of the particles by heat treatment above the glass transition temperature is possible. Deformation of the particles seems to change both the refractive index and thickness of the coating.

Efforts have been made by Rubner et al. to produce low-cost antifog coating with layered composite films [87]. Glass fogs up when warm, moist air comes into contact with it, forming tiny water droplets on the hydrophobic glass surface. The droplets scatter light, causing the surface to become translucent. As a solution to this problem, a nanoporous and superhydrophilic multilayer composing of alternating layers of PAH and silica nanoparticles may be coated on the glass. It causes the water droplets to flatten into a thin uniform sheet rather than form the usual light-scattering beads. Finally, the coated glass substrate may be heated to 400 to 500 °C to burn off the polymer and make the coating more durable by fusing the silica nanoparticles.

Biomedical applications

LbL self-assembly has been widely used for the construction of biosensors [88,89,90]. A sensitive enzyme-based FET biosensor for lactate has been fabricated by the incorporation of MnO_2 nanoparticles onto the gate electrode surface by the LbL assembling method [88]. In particular, $(PDDA/MnO_2/PDDA/lactate\ oxidase\ (LOD))_3$ multilayer films were constructed above the gate surface. Figure 1.20 shows the idealized structure of multilayer films used in biosensor structures. LOD works as a catalyst for transferring lactate to pyruvate by oxidation, with O_2 being reduced to hydrogen peroxide. MnO_2 nanoparticles were introduced as an oxidant to react with H_2O_2, which results in a pH sensitive change in the active membrane of ion-sensitive field-effect transistor (ISFET) with the addition of lactate. The pH variation induced by hydrogen ions consumed during the reaction could be monitored by the ISFET. This biosensor is suitable

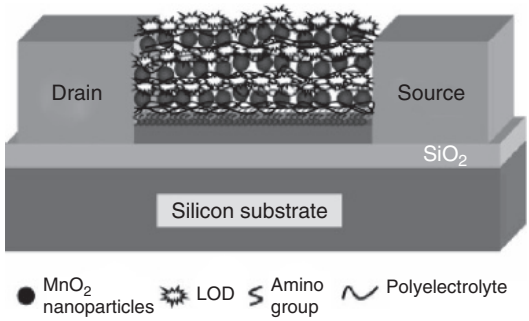

Figure 1.20: Schematic of an ISFET biosensor for lactate. MnO_2 nanoparticles are integrated into the multilayer structure. (Reproduced by permission of Royal Society of Chemistry.)

for monitoring very small pH variations occurring during enzyme reactions (such as LOD).

LbL-deposited thin film can provide additional functional elements, thus increasing the biological efficiency. Antimicrobial agents, often incorporated into the coatings, are important for sterility (e.g., hospital trays) and to prevent infection. These may be LbL assembled in a polymeric film or coating to provide a sustained release of medicine into a wound to prevent infection and thereby promote healing [91]. Polymeric films are prepared by alternately dipping a poly(ethylene terephthalate) (PET) substrate into dilute solutions of PEI and PAA. Prior to dipping, the antimicrobial ingredients are dissolved into the positively charged PEI. By using thin, more transparent coatings, it is possible to monitor wound healing without removing the bandage. Creating a film with the antiseptic already in its ionic form could produce greater effectiveness with lower concentration, which may also help to prevent side effects from overdose.

LBL assemblies have also exhibited wide utility in other important biomedical applications such as creation of biocompatible/bioactive surfaces. For example, LbL assembly was used to modify poly(L-lactic acid) (PLLA) surface and improve its cytocompatibility to human endothelial cells [92]. Chitosan and PSS were chosen as the polymer combination because of their cytocompatibility and layer stability in culture medium. At first, free amino groups were introduced onto polyester scaffolds via aminolyzing the ester groups with diamine. Next, the positively charged chitosan was deposited onto the aminolyzed PLLA membrane surface using PSS as a negatively charged polyelectrolyte. Later, the culture of HUVECs

in vitro showed that cytocompatibility of the modified PLLA was improved obviously [92].

LbL self-assembly on nonplanar templates

Initially, LbL self-assembly was performed on planar supports. Later, other supports such as fibers, carbon nanotubes and colloidals (with particles sizes ranging from hundred nanometers to a few microns, e.g., latex spheres, inorganic or protein microcrystals, and lipid microtubules) were introduced, and the coating layers replicate the shape of the support. After removal of the support by solvent extraction, chemical decomposition or calcination, hollow objects are formed. The assembly process elaborated for planar solid substrates can be adapted for micro- and nano-templates [93–95]. In the process of core-shell fabrication, c. 10^{10} core particles are added to a centrifuge tube; a polyion solution is added to a suspension of colloidal particles. After adsorption saturation, the particles are separated from free polyions in the solution by centrifugation or filtration, and the supernatant containing the unadsorbed species is removed. Then, an oppositely charged polyion solution is added to the suspension of particles, depositing another polyion layer around the particles. In the same manner, one can deposit any number of polyion layers on the template by repeating this procedure (Fig. 1.21). Furthermore, any charged material can be deposited

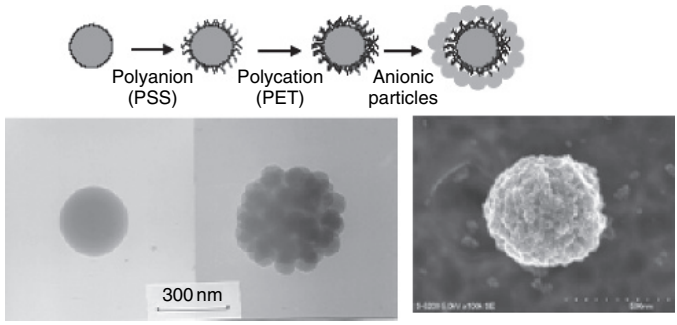

Figure 1.21: (Top) Schematic representation of core-shell synthesis and TEM image (bottom) of 45-nm diameter silica shell on 300-nm diameter core and SEM image of 400-nm diameter core coated with glucose oxidase multilayer and 12-nm magnetite nanoparticles. (Reprinted from *Langmuir* with permission of American Chemical Society.)

using this approach. Usually, the shell architecture contains the following sequence of layers: $(\text{polycation/polyanion})_{4–6}$. An example of a typical shell composition is $(\text{PSS/PAH})_{4–6}$. The core can be dissolved in many different ways to result in a hollow capsule. For example, $MnCO_3$ microcrystal cores can be dissolved by using EDTA. A solution of 0.1 M HF can dissolve silica core. Since nanoshell formation was first published in 1998–1999 by Möhwald and Sukhorukov et al., the structure of nanoshells was characterized in detail and the procedure of polymer, nanoparticle and enzyme incorporation into the capsule shell was significantly developed.

The core-shell technique was applied to different micro- and nano-encapsulated drugs, including furosemide, dexamethasone, insulin and nifedipine, providing enhanced colloidal stability and controlled release [96–101]. For example, furosemide microcrystals were encapsulated with polyions and gelatin to control the release of drug in aqueous solutions [96]. Sequential layers of PDDA and PSS were alternately deposited on 4-μm drug microcrystals, which was followed by adsorption from two to six (gelatin/PSS) bilayers with corresponding capsule wall thicknesses ranging from 45 to 115 nm. At both pH of 1.4 and 6, the release rate of furosemide from encapsulated particles was reduced by 50–300 times, as compared to uncoated furosemide. The results provide a method of achieving prolonged drug release through self-assembly of polymeric shells on drug microcrystals. Furthermore, if the capsules are coated with appropriate antibody, they can be targeted to specific regions in the body, which will reduce overall dosage requirements, increase drug concentrations in the appropriate regions and reduce side effects.

The core-shell technique is very useful for developing new-type nanoshell sensors. These sensors consist of the core with fluorescently labeled indicators and engineered micro- and nanoshell where enzymatically sensitive layers are embedded. Such composite bioparticles are capable of semi-quantitative detection of glucose, lactose, urea and other specific substances for the corresponding biocatalytical reactions. Embedding functional materials such as enzymes and dyes in the shell multilayer surrounding micro/nanoscale templates, sensors for chemical and biochemical compounds can be developed as tools for biological research, medical diagnostics and monitoring, and biodefense applications. One example is the ratiometric nanoscale probes that have been developed for intracellular and extracellular measurements of the presence of ions and oxygen [102–103]. The concentration can be measured by recording the

fluorescence intensity ratio, which is emitted by nanoparticles coated with fluorescent materials that respond selectively to the presence of specific species through binding with them or due to other interactions. These nanosensors have significant advantages with respect to the standard liquid-phase small molecule indicators as they provide a protective package for the encapsulated chemical compounds, separating the dyes from the biological environment, and therefore, reducing nonspecific responses, dye-protein binding and toxic effects. In addition, the immobilization of indicators within the nanofilms provides physical linkage with reference to fluorophores, allowing constant ratiometric monitoring without large shifts in calibrations otherwise seen.

LbL self-assembly also allows the deposition of nanostructures on other types of substrates with different shapes and sizes. With the aim to use carbon nanotube in practical devices, multilayer structures were coated noncovalently around individual nanotube. Initially, the tube surface was modified by a pyrene derivative to become charged. It was followed by LbL deposition of polyelectrolyte macroions on the tube. Transmission electron microscopy and scanning confocal fluorescence microscopy images confirm the formation of nanometer-thick amorphous polymer nanoshells around the nanotubes (Fig. 1.22) [104].

In another example, LbL assembly was applied to construct a nano-Fabry–Perot cavity at the end of an optic fiber pigtail that worked as the sensing element for H_2O_2. The deposited multilayer consisted of premixed Prussian Blue, PAH and PAA [105]. Prussian Blue serves as the redox indicator. When it is oxidized by H_2O_2, it causes a change in the absorbance.

Recently, Lvov et al. have demonstrated polyion LbL assembling onto the nonregular surface of lignocellulose pulp, leading to controlled modification of individual fiber surface charge and roughness [106,107]. Polycations (PDDA) and polyanions (PSS) were deposited around the pulp fibers, producing positively and negatively charged surfaces, respectively. Mixing the two different pulps revealed significantly stronger interactions between them. Handsheets made from mixing differently charged pulp fibers have showed improved strength. Handsheets made from original virgin fibers without any modification had an average tensile strength of $84.7 \pm 0.2\,\mathrm{Nm/g}$. Handsheets made by mixing positively and negatively LbL treated fibers had a 120% increase in tensile strength, giving a value of $184.6 \pm 0.3\,\mathrm{Nm/g}$. We can conclude that an attraction between oppositely charged pulp fibers would result in enhanced interaction and provide increased paper tensile strength.

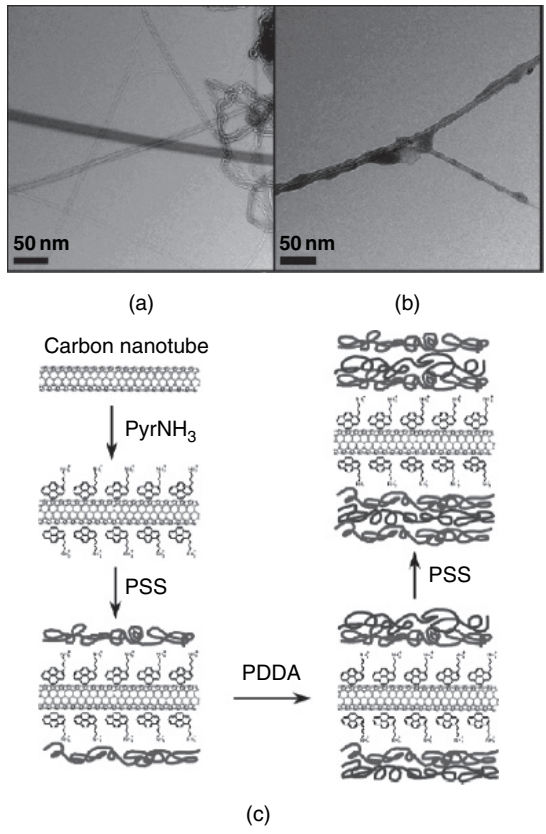

Figure 1.22: (a) TEM images of carbon nanotubes; (b) nanotubes coated with four alternating PSS/PDDA polyelectrolyte layers. (c) Schematic of the carbon nanotube modification using layer-by-layer electrostatic self-assembly. (Reprinted from *Langmuir* with permission of American Chemical Society.)

1.6.2. Potential Applications

LbL assembly will continuously find application in the following branches:

Surface modifications

Surface wetability, hardness, magnetic properties, lubrication and biocompatibility can be modified by the self-assembly of ultrathin nanostructured

coating. In biomaterials, the assembly is applicable directly to the tissue surfaces. The concept of 'smart' surface may be realized by including functional proteins in biocompatible films. Filter layers can be improved by coating with calibrated nano-pores. Chemical reactions can be assisted by LbL nanoparticle catalytic multilayers. The present researches are as follows: biocompatible coating of implants and eye lenses, biocompatible coating for fruit preservation, cotton fiber coating and lignocellulose wood microfiber for paper making [108–110].

Sensor layers and bioreactors

Protein films are able to contain precise number of monolayers, which is important for biosensor elements. The deposition of enzyme/polyion multilayers onto the carriers of biological reactors permits an increase in their performance proportionally to the number of immobilized enzyme layers. Sequential two- to three-step catalytic reactions can be realized in multiprotein films (cascade bioreactions). The enzymes in polyion films are stabilized and could work with nonaqueous substrate solutions. Polyions, which keep enzyme layers in the films together, can be doped by vitamins (cofactors), specific dyes or nanoparticles of metal catalysts to mediate reaction activity.

Nanoreactors

1. Construction of tiny catalytic units with ordered multilayer shells containing enzymes, nanoparticles and polymers.
2. Nanocoating of biological cells and microbes.

Pharmacy

Nanoencapsulation of drugs (including protein drugs such as insulin) for targeted and sustained release.

Electronics

The development of conductive thin films with electrical conductivity comparable to that of metallic thin film is under investigation. These films can be used as electrodes for lithium storage batteries based on graphite nanoplate/polycation multilayers. Magnetic nanoparticle mono- and multilayers, including the formation of magnetic/dielectric superlattices

and soft/hard magnet nanocomposites, may find applications in magnetic actuator and recording media.

1.6.3. Difficulties and Solutions

Low speed

The film grows at relatively low speed, largely depending on the diffusion of charged species. Typically, it takes about 1–5 min for every bilayer. Optimization of the process may alleviate the problem. Moreover, the automation of regular dipping procedures can aid mass production.

Stability

Anchoring the first monolayer to the substrate depends on the surface charge and sometimes demands preliminary surface treatment (e.g., plasma, thiol or silane compound treatment). Oxidized surfaces, such as SiO_2 and metal oxides, usually have good adhesion for polycations. Thermostability is restricted by c. 280 °C. In many cases, LbL assembly can be used as a nano-architectural method, which yields films with stability comparable to that of a polymer. For practical devices, a final fixation of the resultant assemblies with covalent cross-linking or thermal calcination may be necessary.

1.7. Conclusions

LbL self-assembly is a versatile tool in nanomaterial synthesis, device fabrication and biological research. An important aspect of this technique is its universal application to almost all charged element assemblies. Much of researches can benefit from its merits that ordered heterostructures can be produced in a predetermined manner. New properties have been discovered for LbL assembled thin films and devices.

Electrostatic LbL thin films are expected to continuously find new applications in future. The modified process and capability of patterning self-assembled micro- and nano-structures significantly broaden the prospective applications. The approaching challenges include the ability to find new building blocks, control of the formation of dimensional structures, exploitation of the numerous possibilities in their functionalization and use, and scaling up commercial production.

References

[1] Ulman, A. (1996) Formation and structure of self-assembled monolayers, *Chem. Rev*., **96**, 1533.
[2] Iler, R.K. (1966) *J. Colloid Interface Sci*., **21**, 569.
[3] Decher G. and Hong, J.D. (1991) *Makromol. Chem. Macromol. Symp*., **46**, 321.
[4] Lvov, Y., Decher, G. and Möhwald, H. (1993) *Langmuir*, **9**, 481.
[5] Decher, G. (1997) *Science*, **277**, 1232.
[6] Lvov, Y., Ariga, K., Ichinose, I. et al. (1995) *J. Am. Chem. Soc*., **117**, 6117.
[7] Onda, M. Lvov, Y., Ariga K. et al (1996) *J. Ferment. Bioeng*., **82**, 502.
[8] Ferreira, M., Cheung, J.H. and Rubner, M.F. (1994) *Thin Solid Films*, **244**, 806.
[9] Serizawa, T., Takeshita, H. and Akashi, M. (1998) *Langmuir*, **14**, 4088.
[10] Schmitt, J., Machtle, P. Eck, D. et al. (1999) *Langmuir*, **15**, 3256.
[11] Yonezawa, T., Onoue, S. and Kunitake, T. (1998) *Chem. Lett*. **10**, 689.
[12] Lenahan, K.M., Wang, Y.X., Liu, Y.J. et al. (1998) *Adv. Mater*., **10**, 853.
[13] Li, D., Ratner, M.A. and Marks, T.J. (1990) *J. Am. Chem. Soc*., **112**, 1789.
[14] Cooper, T., Campbell, A. and Crane, R. (1995) *Langmuir*, **11**, 2713.
[15] Kleinfeld, E. and Ferguson, G. (1994) *Science*, **265**, 370.
[16] J. Fendler, J. and Meldrum, F. (1995) *Adv. Mater*., **7**, 607.
[17] Schmitt, J., Decher, G., Dressik, W. et al. (1997) *Adv. Mater*., **9**, 61.
[18] Lvov, Y., Ariga, K. and Kunitake, T. (1999) *Colloids Surf. A*., **146**, 337.
[19] Caruso, F., Furlong, N., Ariga, K. et al. (1998) *Langmuir*, **14**, 4559.
[20] Onda, M., Ariga, K. and Kunitake, T. (1999) *J. Ferment. Bioeng*., **87**, 69.
[21] Sauerbrey, G. (1959) *Z. Phys*., **155**, 206.
[22] Lvov, Y. (2001) Thin film nanofabrication by alternate adsorption of polyions, proteins and nanoparticles. In *Handbook for Surfaces and Interfaces, Volume 3: Nanostructured Materials* (H. Nalwa ed.), NY: Academic Press, pp. 170–189.
[23] Lvov, Y. and Decher, G. (1994) *Crystallogr. Rep*., **39**, 628.
[24] Tsukruk, V., Rinderspacher, F. and Bliznyuk, V. (1997) *Langmuir*, **13**, 2171.
[25] Lowman, G.M. and Buratto, S.K. (2002) *Thin Solid Films*, **405, 135**.
[26] Shiratori, S. and Rubner, M.F. (2000) *Macromolecules*, **33**, 4213.
[27] Yoo, D., Shiratori, S.S. and Rubner, M.F. (1998) *Macromolecules*, **31**, 4309.
[28] Chen, K.M., Jiang, X.P., Kimerling, L.C. et al. (2000) *Langmuir*, **16**, 7825.
[29] Takeshi, S. and Satoko, K. (2000) *Colloids Surf*., **164**, 237.
[30] Richert, L., Arntz, Y., Schaaf, P. et al. (2004) *Surf. Sci*., **570**, 13.
[31] Liu, S., Volkmer, D. and Kurth, D.G. (2003) *J. Cluster Sci*., **14**, 200.
[32] Velikov, K.P., Durst, F. and Velev, O.D. (1998) *Langmuir*, **14**, 1148.
[33] Velev, O., Furusawa, D.K. and Nagayama, K. (1996) *Langmuir*, **12**, 2374.
[34] Shi, J.S., Hua, F., Cui, T. et al. (2003) *Chem. Lett*., **32**, 316.
[35] Tan, H.L. McMurdo, M.J. Pan G.Q. et al. (2003) *Langmuir*, **19**, 9311.

[36] Miller, J. Schatzel, F.K. and Vincent, B. (1991) *J. Colloid Interface Sci*., **143**, 22.
[37] Prescott, J., Shiau, H.S. and Rowell, R.L. (1993) *Langmuir*, **9**, 2071.
[38] Hua, F., Shi, J., Lvov, Y. et al. (2003) *Nanotechnology*, **14**, 453.
[39] Lvov, Y., Ariga, K., Ichinose, I. et al. (1997) *Langmuir*, **13**, 6195.
[40] Kotov, N., DCkiiny, A.I. and Fendler, J.H. (1995) *J. Phys. Chem*., **99**, 13065.
[41] Fendler, J.H. (1996) *Chem. Mater*., **8**, 1616.
[42] Schmitt, J. Decher, G., Dressik, W. et al. (1997) *Adv. Mater*., **9**, 61.
[43] Lvov, Y., Ariga, K. and Kunitake, T. (1996) *Langmuir*, **12**, 3038.
[44] Fou, C. and Rubner, M.F. (1995) *Macromolecules*, **28**, 7115.
[45] Ginzburg, M., Galloro, J., Jäkle, F. et al. (2000) *Langmuir*, **16**, 9609.
[46] Paloniemi, H., Lukkarinen, M., Areva, S. et al. (2006) *Langmuir*, **22**, 74.
[47] Qin, S., Qin, D., Ford, W.T. et al. (2005) *Chem. Mater*., **17**, 2131.
[48] Artyukhin, A.B., Bakajin, O., Stroeve, P. et al. (2004) *Langmuir*, **20**, 1442.
[49] Shimoda, H., Oh, S.J., Geng, H.Z. et al. (2002) *Adv. Mater*., **14**, 899.
[50] Lvov, Y., Ariga, K. and Kunitake, T. (1994) *Chem. Lett*., **10**, 2323.
[51] Kong, W., Wang, L., Gao, M. et al. (1994) *J. Chem. Soc., Chem. Comm*., **5**, 1297.
[52] Lvov, Y., Ariga, K., Ichinose, I. et al. (1995) *J. Chem. Soc., Chem. Commun*., **6**, 2313.
[53] Lvov, Y., Ariga, K., Ichinose, I. et al. (1996) *Thin Solid Films*, **284**, 797.
[54] Kong, J., Lu, Z., Lvov, Y. et al. (1998) *J. Am. Chem. Soc*., **120**, 7371.
[55] He, J.A., Samuelson, L., Li, L. et al. (1998) *J. Phys. Chem*., **B102**, 7067.
[56] Yangmei, L., Zhichun, C., Xiuming, J. et al. (2004) *Chem. Lett*., **33**, 564.
[57] Wenjun, Z. and Genxi, L, (2004) *Anal. Sci*., **20**, 603.
[58] Lvov, Y. and Caruso, F. (2001) *Anal. Chem*., **73**, 4212.
[59] Lvov, Y., Lu, Z., Zu, X. et al. (1998) *J. Am. Chem. Soc*. **120**, 4073.
[60] Beucken, J.J., Vos, M.R., Thune, P.C. et al. (2006) *Biomaterials*, **27**, 691.
[61] Beucken, J.J., Walboomers, X.F., Vos, M.R.J. et al. (2006) *J. Biomed. Mater. Res. A*, **77**A, 202.
[62] Zhou, Y. and Li, Y. (2004) *Langmuir*, **20**, 7208.
[63] Cho, J., Char, K., Hong, J.D. et al. (2001) *Adv. Mater*., **13**, 1076.
[64] Cho, J. and Char, K. (2004) *Langmuir*, **20**, 4011.
[65] Lee, S.-S., Hong, J.-D., Kim, C.H. et al. (2001) *Macromolecules*, **34**, 5358.
[66] Chiarelli, P.A., Johal, M.S., Casson, J.L. et al. (2001) *Adv. Mater*., **13**, 1167.
[67] Schlenoff, J.B., Dubas, S.T. and Farhat, T. (2000) *Langmuir*, **16**, 9968.
[68] Michel, A., Izquierdo, A., Decher, G. (2005) *Langmuir*, **21**, 7854.
[69] Shen, J., Sun, J. and Zhang, X. (2000) *Pure Appl. Chem*., **72**, 147.
[70] Sun, J., Wang, Z., Wu, L. et al. (2001) *Macromol. Chem. Phys*., **202**, 967.
[71] Qin, S., Qin, D., Ford, W.T. et al. (2005) *Chem. Mater*., **17**, 2131.
[72] Chen, K.M., Jiang, X.P., Kimerling, L.C. et al. (2000) *Langmuir*, **16**, 7825.
[73] Clark, S.L., Handy, E.S., Rubner M.F. et al. (1999) *Adv. Mater*., **11**, 1031.
[74] Hammond, P.T. (2004) *Adv. Mater*. **16**, 1271.
[75] Gao, M., Sun, J., Dulkeith, E. et al. (2002) *Langmuir*, **18**, 4098.

[76] Jang, H., Kim, S. and Char, K. (2003) *Mater. Res. Soc. Symp. Proc*., **775**, 121.
[77] Yang, S.Y. and Rubner, M.F. (2002) *J. Am. Chem. Soc*. **124**, 2100.
[78] Hua, F., Cui, T. and Lvov, Y. (2002) *Langmuir*, **18**, 6712.
[79] Hua, F., Cui, T. and Lvov, Y. (2004) *Thin Solid Films*, **449**, 222.
[80] Alivisatos, A.P. (1998) *MRS Bull*., **23**, 18.
[81] Cassagneau, T., Mallouk, T.E. and Fendler, J.H. (1998) *J. Am. Chem. Soc*., **120**, 7848.
[82] Chen, W., Grouquist, D. and Roark, J. (2002) *J. Nanosci. Nanotechnol*., **2**, 47.
[83] Khillan, R., Su, Y., Lvov, Y. et al. (2005) *IEEE Trans. Comp. Pack. Technol*., **28**, 748.
[84] Hua, F., Shi, J., Lvov, Y. et al. (2003) *Nanotechnology*, **14**, 453.
[85] Cui, T., Hua, F. and Lvov, Y. (2004) *IEEE Trans. Elec. Dev*., **51**, 503.
[86] Hattori, H. (2001) *Adv. Mater*., **13**, 51.
[87] Zhizhong, W., Walish, J., Nolte, A. et al. (2006) *Adv. Mater*., **18**, 2699.
[88] Xu, J.J., Zhao, W., Luo, X.L. et al. (2005) *Chem. Commun*., **10**, 792.
[89] Nohria, R., Khillan, R., Su, Y. et al. (2006) *Sens. Actuators B*, **114**, 218.
[90] Yan, X., Ji, H. and Lvov, Y. (2004) *Chem. Phys. Letts*, **396**, 327.
[91] Grunlan, J.C., Choi, J.K. and Lin, A. (2005) *Biomacromolecules*, **6**, 1149.
[92] Zhu, Y., Gao, C., He, T. et al. (2003) *Biomacromolecules*, **4**, 446.
[93] Caruso, F., Caruso, R.A. and Möhwald, H. (1998) *Science*, **262**, 1111.
[94] Donath, E., Sukhorukov, G., Caruso, F. et al. (1998) *Angew. Chem*., **37**, 2201.
[95] Sukhorukov, G., Dähne, L., Hartman, J. et al. (2000) *Adv. Mater*., **12**, 112.
[96] Ai, H., Jones, S., de Villiers, M. et al. (2003) *J. Control. Release*, **86**, 59.
[97] Shutava, T. and Lvov, Y. (2006) *J. Nanosci. Nanotechnol*., **6**, 1655.
[98] Li, N., Kommireddy, D., Lvov, Y. et al. (2006) *J. Nanosci. Nanotechnol*., **6**, 2114.
[99] Pargaonkar, N., Lvov, Y., Li, N. et al. (2005) *J. Pharm. Res*., **22**, 826.
[100] Shutava, T., Prouty, M., Kommireddy, D. et al. (2005) *Macromolecules*, **38**, 2850.
[101] Lu, Z., Prouty, M., Guo, Z. et al. (2005) *Langmuir*, **21**, 2042.
[102] Chinnayelka, S. and McShane, M.J. (2004) *J. Fluoresc*., **14**, 583.
[103] Brown, J.Q., Srivastava, R. and McShane, M.J. (2005) *Biosens. Bioelectron*., **22**, 212.
[104] Artyukhin, A.B., Bakajin, O., Stroeve, P. et al. (2004) *Langmuir*, **20**, 1442.
[105] Villar, I.D., Matías, I.R., Arregui, F.J. et al. (2005) *IEEE Trans. Nanotechol*., **4**, 187.
[106] Zheng, Z., McDonald, J., Khillan, R. et al. (2006) *J. Nanosci. Nanotechnol*., **6**, 624.
[107] Lu, Z., Eadula, S., Grozdits, G. et al. (2006) *Colloid Surf Engineering*, **253**, 344.
[108] Kommireddy, D., Sriram, S., Lvov Y. et al. (2006) *Biomaterials*, **27**, 4296.
[109] Li, M., Mills, D., Lvov, Y. et al. (2005) *J. Nanosci. Nanotechnol*., **5**, 1809.
[110] Kommireddy, D., Patel, A., Shutava, T. et al. (2005) *J. Nanosci. Nanotechnol*., **5**, 1081.

Chapter 2

Multifunctional microcontainers with tuned permeability for delivery and (bio)chemical reactions

Daria V. Andreeva, Oliver Kreft and Andrei G. Skirtach
Max-Planck Institute of Colloids and Interfaces, Golm/Potsdam, Germany

Gleb B. Sukhorukov
Department of Materials, Queen Mary, University of London, London, UK

Abstract. Small molecules (dyes, therapeutics, etc.) could be easily handled, stored, delivered and released from polyelectrolyte capsules. In order to make polyelectrolyte capsule a universe delivery platform, its permeability needs to be controlled. On the one hand, for efficient small-molecule encapsulation, the permeability of capsules should be significantly decreased. On the other hand, once the capsule reaches its target, the release of encapsulated materials needs to be triggered. These two functions – reducing permeability of capsules for encapsulation and subsequent release, collectively called tuning capsule permeability – are the subject of this chapter. Here, we demonstrate the possibility of entraping water-soluble molecular species into polyelectrolyte capsules modified by low-permeable dense polymers, e.g. polypyrrole, and various schemes for subsequent release of encapsulated materials. Future applications of polyelectrolyte capsules, such as carriers for gases, volatiles and biomedically relevant molecules in pharmacy, food and gas industries, agriculture and cosmetology, are also discussed.

Keywords: coatings, gases, microencapsulation, polyelectrolytes, polypyrrole, release, volatiles.

2.1. Introduction

Encapsulation of small molecules (gases), volatiles (fragrances, spice components, anesthetic drugs) and water-soluble compounds has been extensively developed during the recent years. Chemical, biomedical, and food industries widely use oxygen (O_2), carbon dioxide (CO_2), nitrogen (N_2), ammonium oxide (NH_3), chlorine (Cl_2), and ethylene (C_2H_4). CO_2 and nitrous oxide (N_2O) are major greenhouse gases, and huge amounts of CO_2 are released into the air by burning fuels such as oil, coal, wood, and natural gas [1,2]. Anesthetic gases and halogenated agents (vapors), such as halothane, enflurane, methoxyflurane, trichloroethylene, and chloroform [3], are released into the operating room during medical procedures and can cause nausea, dizziness, headache, fatigue, irritability as well as sterility, miscarriages, cancer, and liver and kidney diseases among operating room staff [4–9].

Controlling chemical retention during product manufacture and its release during consumption is of major interest to pharmaceutical, cosmetic and food manufacturers. The use of encapsulation to achieve this goal is well established. A few decades ago, a very convenient method of layer-by-layer (LBL) adsorption of oppositely charged PE on the surface of colloidal template particles of $0.1-20\,\mu m$ diameter was developed [10]. This technique allows step-wise adsorption of various components, as the layer growth is governed by their electrostatic attraction, to form multilayer shells with nanometer (thickness) precision. The modification of capsule shells by tailoring different functionalities and impregnating inorganic nanoparticles (fluorescent, magnetic, metal) provides multifunctional capsule application [10].

The capsule properties depend strongly on the capsule core and shell materials. The core materials can be used only as a template and, in this case, should be dissolved to yield hollow containers [11–13]. The template cores for fabrication of hollow capsules are desirable to be monodisperse and completely dissoluble. Weakly cross-linked melamine formaldehyde lattices (MF) [11,14], polystyrene lattices (PS) [15], silica particles [12], red blood cells [16], and inorganic carbonate crystals ($CaCO_3$, $MnCO_3$, and $CdCO_3$) [17] are promising agents for carrier formation. Shell polymers are classified in accordance to the type of external conditions causing their structure to change (pH and ionic strength [18,19], temperature [13], irradiation of light [20], etc.).

To entrap small molecules (e.g., gases, volatiles, fragrances) into PE capsules, novel shell and core materials should be found or developed.

We propose the following methods for small-molecule encapsulation into defined hollow volume cages: (a) bubble stabilization (PE layers are supposed to be formed on surfaces of surfactant-stabilized bubbles filled with a particular gas); (b) solidified volatiles can be used as cores for LBL (vanillin, naphthalene); (c) gases and volatiles might be trapped with molecular sorbents (cyclodextrin, cucurbit[7]uril, amylose) and then covered with polyelecrolytes.

Once encapsulated materials are delivered to a specific site, it is to be released. In an ideal situation, the release is induced by remote controlling in a way to have 'switching functions' in capsule contraction. Such permeability change is irreversible because it leads to irreversible permeability changes. It should be noted that remote permeability switching finds its application in the drug delivery area, in an environment where changing the biochemical characteristics of the sample is hindered. Several methods for such remote activation are possible: magnetic, ultrasound, enzyme and optical.

2.2. Novel Polymer Materials for Low Permeable Capsule Walls and Encapsulation

At present, the most important and interesting trend in encapsulation technology is the control of capsule permeability. As we know, the PE capsules are hydrophilic. The use of capsules, especially as drug carriers, occurs mostly in aqueous media, which can result in the swelling of PE shells or, sometimes, increase capsule permeability. Several attempts were made to encapsulate low-molecular-weight compounds by manipulating the shell polymer structure. Köhler et al. [21] have developed a method for sealing the PE capsules by temperature treatment. In this method, the PE capsules are saturated with encapsulated substance and subsequently temperature treated, which leads to polymer conformation changes and capsule shrinkage. However, the permeability of encapsulated macromolecules may slow down due to increased thickness.

We have suggested an alternative method to control capsule permeability. According to our method, the capsule surface should be coated by a low-permeable polymer [22]. The idea of coating came from gas separation membrane formation principles [23]. Highly selective polymers are usually characterized by very low permeability. To increase membrane efficiency, a nanometer gas selective working layer is formed on the surface of a high-permeable polymer support providing proper mechanical properties.

This type of membrane structure is known as a composite membrane. The coating material should exhibit water-resistant properties or low permeability. To obtain homogeneous and nonporous cover on PE capsules, the coating polymer should have affinity to one of the shell components and form dense and low permeable films.

Recently, conductive polymer coatings have been intensively developed and studied [23]. One of the conducting polymers, polypyrrole (PPy), was found to exhibit outstanding gas selectivity and low permeability [24].

Polypyrrole was widely studied mostly due to its electrochemical properties, easy synthesis and stability in air [25]. Furthermore, PPy films are characterized by outstanding density due to π-electron delocalization along the polymer chains and their high stiffness [26]. At the same time, PPy is a very high brittle material and not able to form films [25]. To overcome these drawbacks, in situ pyrrole polymerization on a supporting polymer was developed. This method would result in a composite membrane structure formed by two layers: selective skin PPy layer and polymer support. Andreeva et al. [27] have developed and characterized gas-separation composite membranes based on PPy and poly(phenylene) oxide as a polymer support. The PPy layer was homogeneous and defectless, and exhibited very high selectivity for gases. Furthermore, a PPy skin layer formed on the capsule surface might supply the desirable properties to PE shells. Besides low permeability, the transport properties of PPy coating can be changed by redox process [24]. It means that the polymer changes reversibly from a reduced (neutral) state to an oxidized (charged) state. As a result, important structural changes take place in the polymer, which passes from a compact (neutral) state to a gel (oxidized) state, because the polymer matrix swells during oxidation as water and counterions penetrate into the polymer matrix [24]. Due to this selective membrane-like behavior of PPy, controlled permeability through capsule shells can occur.

In our previous article [22], we have described a novel method of PPy coating on PE microcapsules. We have suggested a way of encapsulation of water-soluble compounds based on the formation of dense PPy coating on capsule surface. PPy deposition from 10 wt% aqueous polymer solution was found most effective for capsule modification. In this way, homogeneous and defectless PPy coatings can be formed. Magnetic microcapsules containing consequent layers of iron oxide and poly(allylamine hydrochloride) (PAH) with external poly(sodium 4-styrenesulfonate) (PSS) layers were used for encapsulation of water-soluble species. As a model compound, a water-soluble dye, tetramethylrhodamine isothiocyanate (TRITC), was used. To encapsulate water-soluble compounds by shell modification

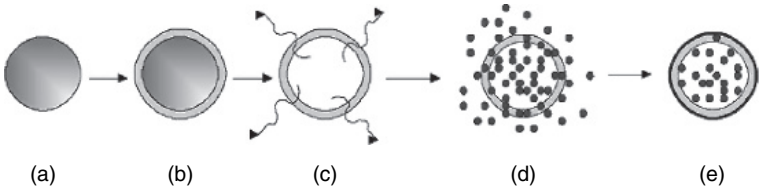

Figure 2.1: The sketch of capsule preparation and PPy modification.

method, both encapsulation and capsule sealing processes should be carried out simultaneously (Fig. 2.1).

First, the capsules are saturated with TRITC solution, and then a PPy layer is formed to trap encapsulated compounds inside the capsule cages. The magnetic properties of the capsule shell allow gentle capsule sedimentation with a constant magnet instead of a centrifugation process. Due to this, it is possible to avoid mechanical impact on the brittle PPy shell followed by shell rupture. As a result, low-permeable capsules with maximum concentration of magnetite nanoparticles are prepared.

In the next section, we shall discuss the release of encapsulated materials.

2.3. Release of Encapsulated Materials from Polyelectrolyte Capsules

The release of encapsulated materials can be realized by many methods. All of these methods can be applied to release low-molecular-weight materials described earlier. In this section, we provide an overview of these methods and further concentrate on the optical release method based on laser light-absorbing nanoparticles/dye interactions, because this method is fairly easy to use, completely remote, does not involve chemical changes in solutions, and can be used in real time.

Magnetic, ultrasound, and enzyme-based release are the general methods. Magnetic release is based on the interaction of a magnet with magnetic nanoparticles incorporated in the shells of microcapsules. In our experiments, ferromagnetic cobalt nanoparticles containing a layer of gold (Co/Au) were incorporated into the assembly of PSS and PAH polyelectrolyte multilayer shells of microcapsules. Subsequently, the application of alternating magnetic fields with frequencies of 100–300 Hz and 1200 Oe strength resulted in an increase of permeability leading to the release of the encapsulated content [28]. From this work, we observed that the magnetic

field affects the permeability of microcapsules by acting on the aggregates of nanoparticles. Recently, an easy method to control the aggregation condition of nanoparticles with different surface functionalization on microcapsules and planar surfaces has been proposed using polymers [29]. It should be noted that not all materials are compatible with magnetic particles: the solubility of magnetic particles at pH 1 makes MF unsuitable, leaving PS as a material of choice.

Ultrasound is widely used for synthesis of various nanomaterials, e.g., coating carbon nanotubes and noble metals. Several recent publications report that ultrasound can be used for the destruction of polyelectrolyte multilayer capsules [30,31]. Nanoparticles increase the density of the shells of microcapsules. Affecting the denser shell of microcapsules, ultrasound serves as a trigger to release encapsulated materials. The effect is attributed to cavitation microbubbles that occur as a result of the collapse of generated microbubbles and the shear forces, which cause the destruction of polyelectrolyte capsules. Powers in the range of 100–500 W at frequencies of 20 kHz are applied to destruct the capsules.

2.3.1. Enzyme-mediated Release of Encapsulated Materials

The use of enzymes for controlled release of encapsulated materials offers a promising route for a variety of biological applications [32,33]. Biodegradable polyelectrolyte multilayers from polysaccharides have been introduced previously by Picart et al. [33b]. Intracellular degradable capsules exhibit exciting potential, especially in drug delivery, as they are reliable for the delivery of drugs to diseased tissues. Moreover, intracellular targets, e.g., the cell nucleus or specific proteins, could be addressed. Therefore, destroying polyelectrolyte capsules by the action of enzymes reveals high practical importance [33]. De Geest et al. first demonstrated capsule degradation by enzymes [32]. Here, two types of biodegradable capsules fabricated on $CaCO_3$ templates were investigated. The first type was composed of poly-L-arginine (PArg) as the polycation and dextran sulfate (DEXS) as the polyanion. The second type comprised poly(hydroxypropylmethacrylamide dimethylaminoethyl) P(HPMA-DMAE) and PSS. In vitro tests conducted with Pronase®, a mixture of endo- and exo-proteases that cleaves proteins/peptides unspecifically down to single amino acids, demonstrated that DEXS/PArg microcapsules disintegrate completely within a few hours of incubation under given conditions.

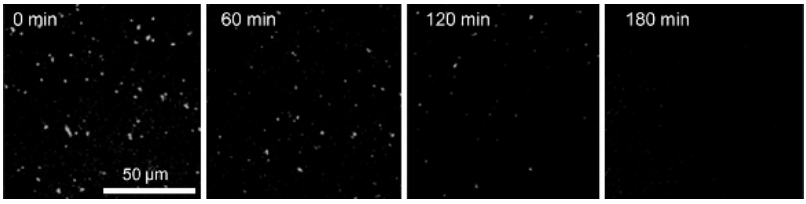

Figure 2.2: CLSM images recorded during the enzymatic degradation of polyelectrolyte capsules consisting of poly-L-arginine and poly-L-aspartic acid incubated in a Pronase solution (1 mg/ml) at 37 °C.

It is more exciting to know that both types of capsules are subject to intracellular degradation upon internalization by African green monkey kidney cells (VERO-1 cells). Figure 2.2 illustrates the Pronase-triggered degradation of a similar type of polyelectrolyte capsule fabricated from PArg as the polycation and poly-L-aspartic acid (PAsp) as the polyanion (O. Kreft, unpublished results). Even the leftovers of capsules could not be detected after 2 hr of incubation. Recently, Itoh et al. [33c] have introduced a similar type of biodegradable polyelectrolyte capsule fabricated from DEXS and chitosan. Here, sustained release of encapsulated substances was accomplished by capsule shell degradation with the enzyme chitosanase. However, this system is widely inapplicable for in vivo applications, because chitosanase is not available in mammalian cells.

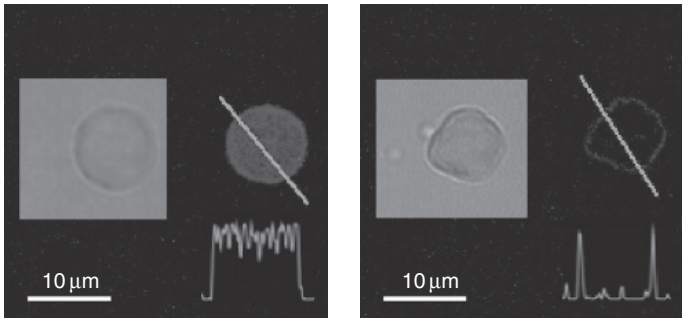

Figure 2.3: Remote release of encapsulated and rhodamine labeled polymer by laser. The images are shown before laser illumination (a) and after (b). (Reproduced with permission from Ref. [35]. Copyright ACS.)

2.3.2. Release by Laser

Laser has taken a prominent place as an external stimulus for remote release of encapsulated materials. It can be coupled with microscope to provide visualization – an important feature in research environment. Laser technology has so developed that it is possible to choose a source with desired wavelength of emission, mode of operation, power, etc. In addition, the area of illumination could be easily adjusted for any range from individual capsules to large clusters. In the context of drug delivery, lasers are used for remote activation and release of encapsulated materials [34].

The mechanism of remote release of encapsulated materials involves the conversion of light energy into thermal energy through interaction of laser with absorbing centers or nanoparticles on microcapsules. This phenomenon works on the principle that temperature increase is directly proportional to absorbed energy and the size of nanoparticles. The temperature increase is reciprocally dependent on the average distance between the nanoparticles, which in turn depends reciprocally on their concentration. Therefore, temperature increase will be proportional to the concentration of nanoparticles, while other factors affecting the release are the supplied energy and size of nanoparticles (Fig. 2.3) [35].

2.4. Applications and Perspectives

Our results highlight the principal possibility of using PPy in water-resistant capsule formulation. PPy is able to form homogeneous and defectless coatings on PE capsule surfaces, thus preventing capsule deformation or aggregation. This approach to capsule modification significantly expands capsule handling and application. PPy coatings provide control over capsule permeability by the PPy redox process. Furthermore, PPy is safe for medical applications, especially in pharmacology and cosmetology. The high surface energy of PPy films gives the possibility for direct sorption of some active molecules on the capsule surfaces.

The low permeability of capsules offers a wide range of potential applications in pharmacy, cosmetology, food and agricultural industry (Fig. 2.4). First of all, PPy-covered capsules can be used for gas encapsulation. Controlled storage, release and transportation of gases are desirable in a huge range of sectors. O_2 is of great importance in medicine and steel-making, while N_2 is utilized in space technology and in the production of NH_3.

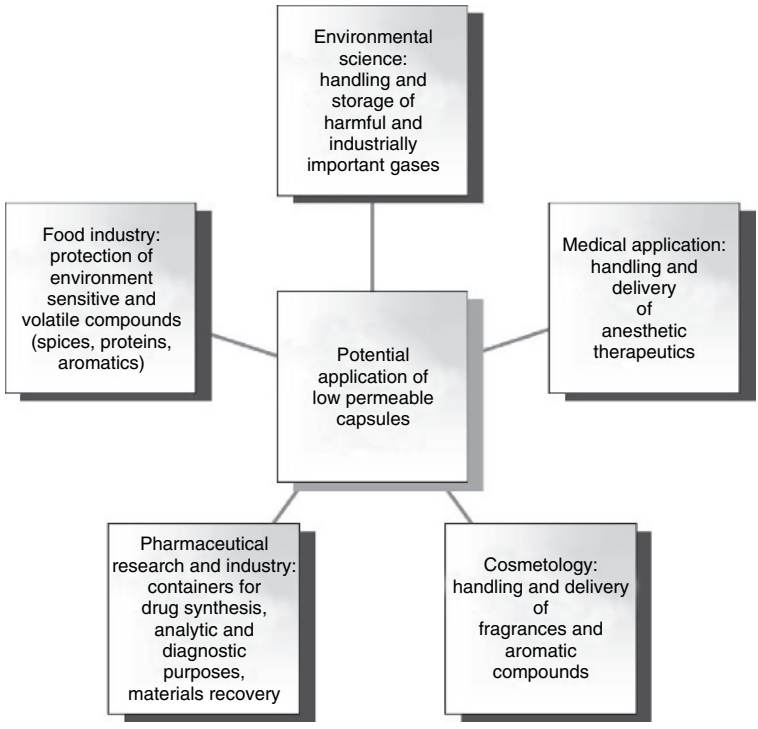

Figure 2.4: Potential applications of low-permeable capsules.

The use of H_2 as fuel in car engines or aircraft turbines is important for its safety and convenient storage and transportation [36–38].

The encapsulation of gases is based on the usage of nanoscale sorbents for gas trapping. Recently, Leontiev and Rudkevich [38,39] have demonstrated that a simple molecular container, a hemicarcerand, reversibly traps, stores and exchanges gases in the solid state at normal temperatures and pressures. The molecular complexes, gas–molecular trapper, can be used as a core for PE shells with barrier properties.

Another way of gas encapsulation is stabilization of hollow gas-filled microbubbles. Polymeric shells can be formed around the microbubbles and, therefore, stabilize them. Cavalieri et al. [40] have entrapped air in a polymer shell obtained by chemically cross-linking modified poly(vinyl alcohol) at the air–water interface. These bubbles exhibited unusual chemical and colloidal stability and could be used as potential drug-delivery

devices. Furthermore, as a dense polymer, PPy might form a barrier coating for gases on the surfaces of microbubbles filled with a particular gas. The bubbles can be generated by ultrasound method or by membrane emulsification and stabilized by in situ pyrrole polymerization.

One of the largest interests in volatile and gas encapsulation relates to pharmaceutical compounds. Several drugs, including some cancer therapeutics and volatile anesthetics, are highly fluorinated. Many of these fluorinated drugs cannot be safely delivered orally or intravenously [41]. We have suggested an encapsulation process to create nano/microcapsules of volatile drugs, allowing them to be delivered intravenously. The development of encapsulation technology provides the following benefits:

- allow intravenous delivery of gaseous anesthetics and other fluorinated compounds;
- provide a way to induce anesthesia in patients who cannot be incubated;
- intravenous injection of encapsulated anesthetics to quickly boost anesthesia;
- prolong the anesthetic effect;
- reduce possible side effects due to targeted delivery and controlled release;
- useful for drug synthesis, analytic and diagnostic purposes, sequestering molecules for materials recovery, and pollution abatement.

The methods described for possible gas encapsulation could also be applied for anesthetic gases. Formulations based on cyclodextrin–drug inclusion complexes enhance drug-delivery performance including improved drug stability, solubility, dissolution rate and, in some instances, reduction of adverse side effects [42]. These complexes could also be used as cores for PE shells and then sealed by PPy or other low-permeable polymers.

Encapsulation is widely employed in the flavor industry to protect volatile and/or labile flavoring materials during storage [43] (Fig. 2.5).

Encapsulation in food industry involves incorporation of food ingredients, enzymes, cells or other components in the coating materials. One of the largest areas in flavor encapsulation is that of food and cosmetic oils. Encapsulation can significantly prolong their aromatic properties. Spice flavors, for example, are incorporated in processed foods by essential oils or solvent-extracted spices' active components (oleoresin) [44]. Oleoresin is known to undergo oxidative degradation. Volatile encapsulation techniques are well known in food and cosmetic industry, including spray drying, spray chilling or spray cooling, extrusion coating, fluidized bed coating, liposome

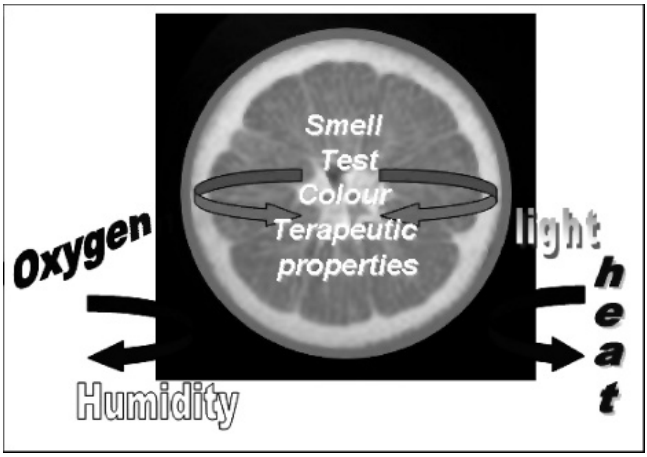

Figure 2.5: Protection of volatiles by using low-permeable coatings.

entrapment, conservation, inclusion complexation, centrifugal extrusion, and rotational suspension separation [43]. The applications of this technique have increased in food industry since the encapsulated materials can be protected from moisture, heat or other extreme conditions, thus enhancing their stability and maintaining viability. However, a disadvantage is that the properties of capsules are difficult to control. All the encapsulation techniques discussed so far will result in a simple coating of encapsulates by the shell material. In this case, the coatings are hardly modified and functionalized. Therefore, the capsules cannot be delivered to the target site. Volatiles and fragrances can be entrapped into PE shells as the above-described complexes or in solidified forms. Vanillin, for example, is a prospective model compound to study the encapsulation of volatiles. In an experiment, the vanillin crystals were successfully covered by one layer of PPy (Fig. 2.6). For this propose, 5 wt. % PPy solution in water was used. Optical microscopy observations showed that the PPy-covered vanillin crystals exhibited much higher stability as compared with pristine crystals.

Thus, PPy coating presents a new approach to control capsule permeability. The dense packing of PPy chains could easily seal off the low-molecular-weight encapsulates in nanometer capsule cages. PPy, along with a wide range of other polymer materials with hydrophobic (paraffin, wax) and water-resistant (polyurethanes) properties, opens an alternative area in

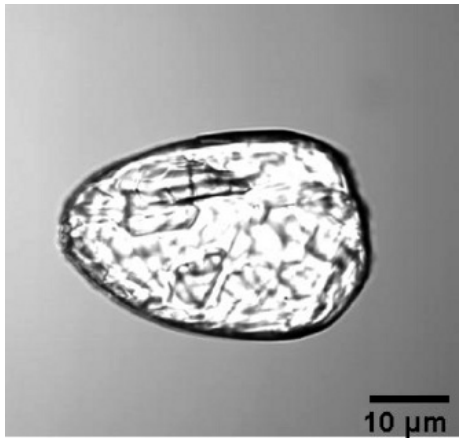

Figure 2.6: Optical microscopy image of vanillin crystals covered by one layer of PPy.

PE capsule application. Therefore, aromatic compounds, fragrances, and gases can be successfully encapsulated, targeted, delivered, and released.

Another vital application of nanoparticles is pharmaceutical and drug delivery areas. Remote activation and release of encapsulated materials inside living cells were reported [34]. Two types of nanoparticles were used: remote activation with silver and remote release with gold/gold sulfide nanoparticles in their walls. As mentioned earlier, the mechanism of laser release is thermal absorption, i.e., disruption of polymeric matrix around nanoparticles on the capsule shell; hence, noble metals are good candidates for this research. Potential adverse thermal side effects (high temperature rises) can be minimized by choosing the laser wavelength in the biologically 'friendly' near-IR window [34]. The spectral properties of water are a good criterion since water makes a large portion of eukaryotic cells. The temperature rise itself does not provide any threat; this is consistent with extremely small temperature rises in the focus of nonabsorbing materials.

Encapsulated AF-488 labeled dextran polymer was released by laser inside a living cell upon laser illumination (Fig. 2.7). Figure 2.7(a) demonstrates the fluorescence image of capsules, and Fig. 2.7(b) shows the fluorescence and transmission signals from the same cell and the same capsules before laser illumination. Before laser illumination, the capsule can be seen filled and its intensity profile is shown in Fig. 2.7(c). Images of the same capsule after laser illumination (Fig. 2.7(d–f)) show that polymers left

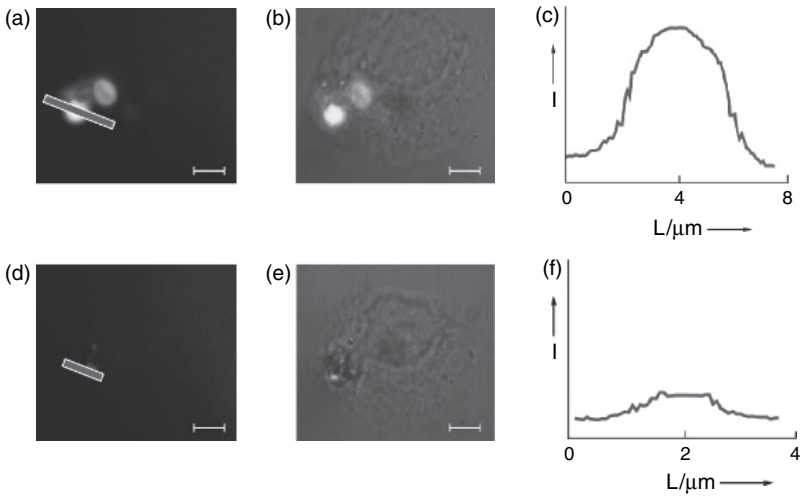

Figure 2.7: Intracellular remote release of encapsulated polymers by laser. The images are shown before laser illumination (top row) and after (bottom row). (Reproduced with permission from ref. [34]. Copyright Wiley-VHC.)

the interior of the capsule (Fig. 2.7(f)). The presence of a weak fluorescence signal in the shell of the microcapsule is consistent with the earlier reported experiments [35]. The temperature rise during remote release experiments is several degrees [35], and because the cells were found to adhere to the substrate both before and after the release of encapsulated polymers, this method can be regarded as feasible for delivery of encapsulated materials into cells.

References

[1] Frank, N.W. (1995) On problems of reducing energy consumption for irradiation of flue gas in the electron beam gas treatment technology. *Radiat. Phys. Chem.*, **45**, 989.

[2] Wang, Y.H. and Jacob, D.J. (1998) Anthropogenic forcing on tropospheric ozone and OH since preindustrial times. *J. Geophys. Res.*, **103**, 31123.

[3] Stachnik, J. (2006) Inhalant anesthetic agent. *Am. J. Health-Syst. Pharm.*, **63**, 623.

[4] Malekirad, A.A., Ranjbar, A., Rahzani, K. et al. (2005) Oxidative stress in operating room personnel: occupational exposure to anesthetic gases. *Human Exper. Toxicol*. **24**, 597.
[5] Cohen, E.N. (1974) Occupational disease among operating room personnel: a national study. *Anesthesiology*, **41**, 321.
[6] National Institute for Occupational Safety and Health (NIOSH) (1977) Criteria for a Recommended Standard: Occupational Exposure to Waste Anesthetic Gases and Vapors U.S. Cincinnati, Ohio: Department of Health and Human Services, Public Health Service, Centers for Disease Control and Prevention. DHEW Pub. No. 77B140.
[7] Cohen, E.N., Gift, C.H. and Brown, W.B. (1980) Occupational disease in dentistry and chronic exposure to trace anesthetic gases. *J. Am. Dent. Assoc*., **101**, 21.
[8] Hoerauf, K., Lierz, M. and Wiesner, G. (1999) Genetic damage in operating room personnel exposed to isoflurane and nitrous oxide. *Occup. Environ. Med*., **56**, 433.
[9] Decker, G. (1997) Fuzzy nanoassemblies: toward layered polymeric multicomposites. *Science*, **277**, 1232.
[10] (a) Sukhorukov, G.B., Möhwald, H., Decher, G. et al. (1996) Layer-by-layer assembly of DNA–dye complex films. *Thin Solid Films*, **285**, 220. (b) Lvov, Y., Ariga, K. and Kunitake, T. (1995) Assembly of multicomponent protein films by means of electrostatic layer-by-layer adsorption. *J. Am. Chem. Soc*., **117**, 6117. (c) Keller, S.W., Johnson, S.A., Brigham, E.S. et al. (1995) Photoinduced charge separation in multilayer thin films grown by sequential adsorption of polyelectrolytes. *J. Am. Chem. Soc*., **117**, 12879.
[11] Gu, Y.S., Decker, A.E. and McClements, D.Ju. (2005) Production and characteristics of oil-in-water emulsions containing droplets stabilized by β-lactoglobulin-ι-carrageenan-gelatin membranes. *Langmuir*, **21**, 5752.
[12] Antipov, A.A. and Sukhorukov, G.B. (2004) Polyelectrolyte multilayer capsules as vehicles with tunable permeability. *Adv. Colloid Interf. Sci*., **111**, 49.
[13] Gui, X., Laporatti, S., Donath, E. et al. (2001) Studies on the drug release properties of polysaccharide multilayers encapsulated ibuprofen microparticles. *Langmuir*, **17**, 5375.
[14] Ibarz, G., Dähne, L., Donath, E. et al. (2001) Smart micro- and nanocontainers for storage, transport, and release. *Adv. Mater*., **13**, 1324.
[15] Déjugnat, C. and Sukhorukov, G.B. (2004) pH-responsive properties of hollow polyelectrolyte microcapsules templated on various cores. *Langmuir*, **20**, 7265.
[16] Neu, B., Voigt, A., Mitlohner, R. et al. (2001) *J. Microencapsul*., **18**, 385.
[17] Sukhorukov, G.B., Volodkin, D.V., Günther, A.M. et al. (2004) *J. Mater. Chem*., **14**, 2073.
[18] Yoo, D., Shiratori, S.S. and Rubner, M.F. (1998) Controlling bilayer composition and surface wettability of sequentially adsorbed layers. *Macromolecules*, **31**, 4309.

[19] Sukhishvili, S.A. and Granick, S. (2000) Layered, erasable ultrathin polymer films. *J. Am. Chem. Soc*., **122**, 9550.
[20] Yager, K.G. and Barrett, C.J. (2001) All-optical patterning of azo polymer films. *Curr. Opin. Solid State Mater. Sci*., **5**, 487.
[21] Köhler, K., Möhwald, H. and Sukhorukov, G.B. (2006) Thermal behavior of polyelectrolyte multilayer microcapsules: 2. Insight into molecular mechanisms for the PDADMAC/PSS system. *J. Phys. Chem. B*., **110** (47), 24002–10.
[22] Andreeva, D.V., Gorin, D.A., Shchukin, D.G. et al. (2006) Magnetic microcapsules with low permeable polypyrrole skin layer. *Macromol. Rapid Commun*., **27**, 931.
[23] Kesting, R.E. and Fritzsche, A.K. (1993) *Polymeric Gas Separation Membranes*. New York: Wiley. p. 416S.
[24] Parthasarathy, R.V., Menon, V.P. and Martin, C.R. (1997) Unusual gas-transport selectivity in a partially-doped form of the conductive polymer polypyrrole. *Chem. Mater*., **9**, 560.
[25] De Jesus, M.C., Weiss, R.A. and Chen, Y. (1997) *Polym. Sci.: Part B: Polym. Phys*., **35**, 347.
[26] Conklin, J.A., Su, T.M., Huang, S.C. et al. (1986) In *Handbook of Conductive Polymer* (T.A. Skotheim, ed.) New York: Marcel Dekker Inc. p. 945.
[27] Andreeva, D.V., Pientka, Z., Brozová, L. et al. (2002) Effect of polymerization conditions of pyrrole on formation, structure and properties of high gas separation thin polypyrrole films. *Thin Solid Film*, **406**, 54.
[28] Lu, Z., Prouty, M.D., Guo, Z. et al. (2005) Magnetic switch of permeability for polyelectrolyte microcapsules embedded with Co@Au nanoparticles. *Langmuir*, **21**, 2042–50.
[29] Skirtach, A.G., Déjugnat, C., Braun, D. et al. (2007) Nanoparticles distribution control by polymers: aggregates versus non-aggregates. *J. Phys. Chem. C*, **111**, 555–64.
[30] Shchukin, D.G., Gorin, D.A. and Möhwald, H. (2006) Ultrasonically induced opening of polyelectrolyte microcontainers. *Langmuir*, **22**, 7400–4.
[31] Skirtach, A.G., De Geest, B.G., Mamedov, A. et al. (2007) Ultrasound stimulated release and catalysis using polyelectrolyte multilayer capsules. *J. Mater. Chem*., **17**, 1050–4.
[32] De Geest, B.G., Vandenbroucke, R.E., Guenther, A.M. et al. (2006) Intracellularly degradable polyelectrolyte microcapsules. *Adv. Mat*., **18**, 1005–9.
[33] (a) Berth, G., Voigt, A., Dautzenberg, H. et al. (2002) Polyelectrolyte complexes and layer-by-layer capsules from chitosan/chitosan sulfate. *Biomacromolecules*, **3**, 579–90. (b) Picart, C., Schneider, A., Etienne, O. et al. (2005) Controlled degradability of polysaccharide multilayer films in vitro and in vivo. *Adv. Funct. Mat*., **15**, 1771–80. (c) Itoh, Y., Matsusaki, M., Kida, T. et al. (2006) Enzyme-responsive release of encapsulated proteins from biodegradable hollow capsules. *Biomacromoleclues*, **7**, 2715–8.

[34] Skirtach, A.G., Munoz Javier, A., Kreft, O. et al. (2006) Laser-induced release of encapsulated materials inside living cells. *Angew. Chem. Int. Ed*., **45**, 4612–7.
[35] Skirtach, A.G., Dejugnat, C., Braun, D. et al. (2005) The role of metal nanoparticles in remote release of encapsulated materials. *Nano. Lett*., **5**, 1371–7.
[36] Brunner, G. (1994) Gas extraction: an introduction to fundamentals of supercritical fluids and the application to separation processes. *Darmstadt: Steinkopff*, 387S.
[37] Peschka, W. (1982) Operating characteristics of a LH_2-fuelled automotive vehicle and of a semi-automatic LH_2-refuelling station. *Int. J. Hydrogen Energy*, **7**, 661.
[38] Leontiev, A.V. and Rudkevich, D.M. (2001) Encapsulation of gases in the solid state. *Chem.Commun*., 1468–9.
[39] Rudkevich, D.M. (2004) Emerging supramolecular chemistry of gases. *Angew. Chem. Int. Ed*., **43**, 558.
[40] Cavallieri, F., Hamassi, A.E., Chiessi, E. et al. (2006) Tethering functional ligands onto shell of ultrasound active polymeric microbubbles. *Biomacromolecules*, **7**, 604.
[41] El-Aneed, A. (2004) An overview of current delivery systems in cancer gene therapy. *J. Controlled Release*, **94**, 1.
[42] Szejtli, J. (1998) Introduction and general overview of cyclodextrin chemistry. *Chem. Rev*. **98**, 1743.
[43] Desai, K.G.H. and Park, H.J. (2005) Recent developments in microencapsulation of food ingredients. *Drying Technol*., **23**, 1361.
[44] Shaikh, J., Bhosale, R. and Singhal, R. (2006) Microencapsulation of black pepper oleoresin. *Food Chem*., **94**, 105.

Chapter 3

Advanced optical spectroscopies in nanotechnology

M. P. Fontana
Department of Physics, University of Parma, Parma, Italy

Abstract. In this chapter, we shall discuss the application of advanced spectroscopic methods, especially those that have been developed during the last 10 years, to study matter on the nanoscale. After a brief introduction of the nanoworld, we shall introduce techniques such as single-molecule fluorescence spectroscopy, SERS (surface-enhanced Raman scattering)-based spectroscopies, including single-molecule Raman, infrared and fluorescence, and tip-enhanced Raman scattering, where the world of scanning probe microscopy meets with SERS; imaging derived from spectroscopic signals, also in a time-resolved mode. The final part of the chapter is devoted to some interesting applications of nanotechnologies, including nanobiotechnologies, materials nanoscience, nanomedicine and single-cell diagnostics, and new types of advanced instrumentation.

Keywords: nanospectroscopy; SERS; TERS; spectroscopic nanoimaging; single molecule spectroscopy

3.1. Introduction: Spectroscopy on the Nanoscale

Within the framework of linear response theory [1], a spectroscopic experiment probes the dynamics of the systems' internal degrees of freedom that couple to the external probe on the space–time scale, which is determined by the probe and space–time resolution of the experimental apparatus. In particular, the fluctuation–dissipation theorem connects the system complex susceptibility to the Fourier transform of an appropriate statistical correlation function and hence to the measured spectral density. In fact, following the Wiener–Khintchin theorem, a spectroscopic experiment can be performed either in the time domain or in the Fourier-transformed frequency domain.

Fundamentally, this equivalence is due to the validity of the ergodic hypothesis, from which it can be asserted that the time correlation function probed by the experiment is equal to an appropriate statistical correlation function. Thus, the choice is connected to the ease and convenience of the experimental set-up necessary to probe the system on the desired space–time scale. For instance, if one is interested in the diffusion dynamics of liquids in the hydrodynamic limit, the relevant time scale ($\tau \geq 10^{-6}$ s) would correspond to a frequency range that would necessitate a prohibitively high spectral resolution in the apparatus. In this case (Fig. 3.1), one could directly measure the time correlation function of density fluctuations using digital time correlators in a quasi-elastic scattering experimental configuration [2].

As we shall see later, photon correlation spectroscopy (PCS) is an important tool to analyse the statistics and dynamics of single molecules detected using single-molecule fluorescence spectroscopies (SMFS) and thus obtain fundamental parameters such as molecular mobility, electronic dynamics and their dependence on the local, nanoscale environment.

Electronic transitions in solids ($\tau \approx 10^{-15}$ s) often lead to broad spectral features at optical frequencies: in this case, a moderate to small spectral resolution is needed so that the measurement can be performed in the frequency domain using spectrographs and monochromators.

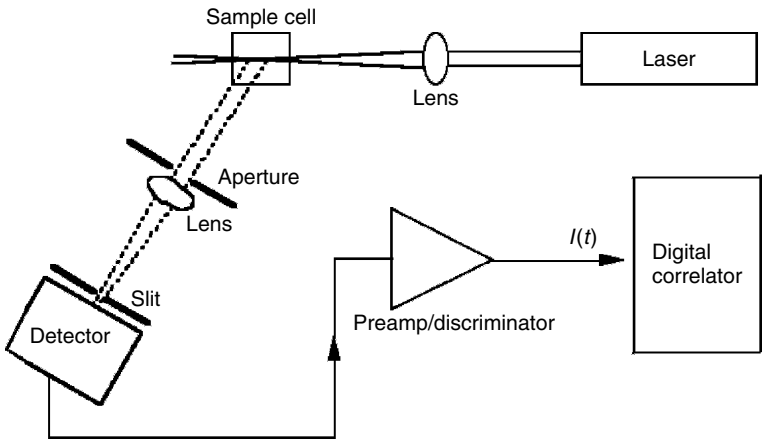

Figure 3.1: Scheme of a typical photon correlation spectroscopy (PCS) set-up in the photon counting mode. For characteristic fluctuation times longer than about 1 μs, the digital correlator can be avoided and the time correlation function determined directly by the computer software.

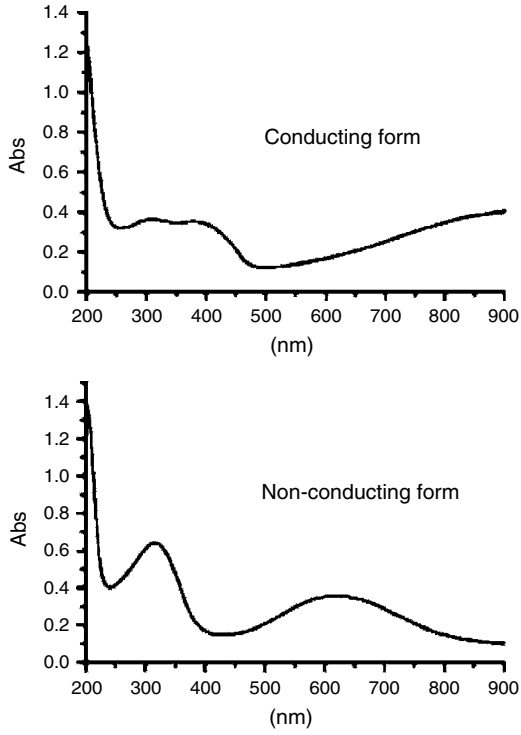

Figure 3.2: UV-Visible spectra of a Polyaniline Langmuir–Schaeffer multilayer (48 layers), before (lower panel) and after (upper panel) doping with HCl. (Reproduced with permission from T. Berzina, V. Erokhin, and M.P. Fontana, 'Spectroscopic investigation of an electrochemically controlled conducting polymer-solid electrolyte junction', *Journal of Applied Physics*, Vol. 101, 024501 (2007). Copyright 2007, American Institute of Physics.)

In Fig. 3.2, for instance, we have shown the optical absorption spectra of a well-known material belonging to the class of 'conducting polymers', i.e., polyanyline in its doped (conducting, green color) and undoped (insulating, blue color) states. The optical spectra are broad but, at the same time, extremely sensitive to the oxidation state of the polymer.

In all these, an underlying assumption is that of spatial homogeneity of the system on a scale greater than that of the fluctuations we wish to study. Thus, the formal apparatus at the foundation of spectroscopy may be found wanting at least in some aspects when the system under study is

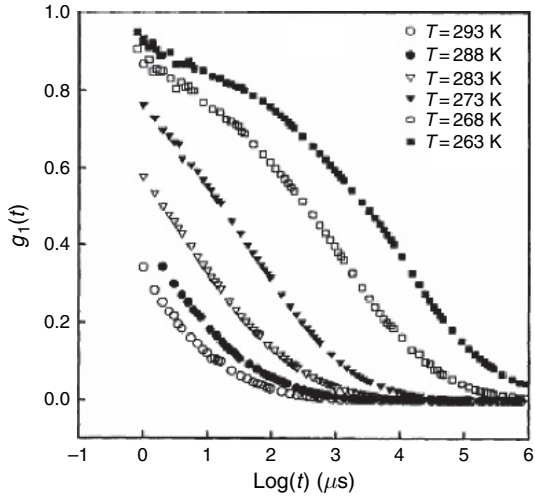

Figure 3.3: Density–density time autocorrelation function determined for a poliuretane gel in the neighbourhood of the glass transition at several temperatures. (Reproduced with permission from M. Tabellout, P.-Y. Baillif, H. Randrianantoandro, F. Litzinger, and J.R. Emery, *Phys. Rev. B*, 51, 12295 (1995). Copyright 1995, American Physical Society.)

on the nanoscale. A typical and important example is glasses, which are non-ergodic and characterized by space–time heterogeneities in the density correlation function on the nanoscale [3]. In Fig. 3.3, we show the results from quasi-elastic light scattering using PCS. The material studied was a polymer gel in the neighbourhood of glass transition. Note the strongly non-exponential behaviour of the measured time autocorrelation function upon the approach of glass transition.

In this case, heterogeneity is dynamical; in the nanosystems of interest here, we also have structural heterogeneity on a scale that interferes with the scale of physical processes such as electronic and vibrational transitions and electronic and ionic transport.

The best known, and historically the first, example of this can be found in the optical (absorption and luminescence) studies at very low temperatures in nanostructures such as inorganic quantum wells in one and two dimensions and quantum dots (Fig. 3.4) [4].

In this case, the optical spectra demonstrated profound modification in the electronic states of the material (mainly semiconductors) due to size confinement quantum effects [A1]. A very illustrative way of presenting

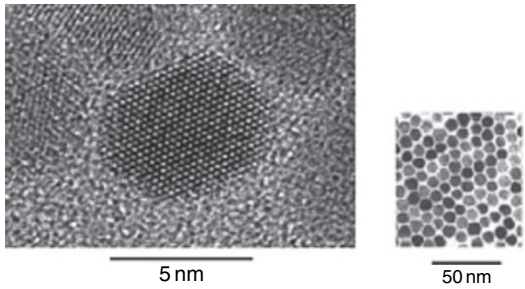

Figure 3.4: High-resolution TEM images of a single CdSe nanocrystal. The hexagonal symmetry is better seen in the low resolution image on the right. Note that the quantum dots are kept apart (i.e., they do not coalesce) by the surfactant coating on the surfaces. (Reproduced from *Journal of Cluster Science*, Vol. 13, 2002, pp. 521–532, 'Shape control of colloidal semiconductor nanoparticles', L. Manna, E.C. Scher, and A. P. Alivisatos, Figure 4. Copyright 2002, Springer, with kind permission from Springer Science and Business Media.)

this is the consideration of dimensionality induced changes in the density of electronic states (dos). Figure 3.5 shows the sketches of the corresponding structures. Note that the density of states in 0D (quantum dot) is similar to that of atomic energy level distributions, and hence the name 'artificial atoms' given to quantum dots or, more generally, nanoclusters.

The consequences of these changes on optical spectra are quite important, as can be seen from Figs 3.6 and 3.7. These data clearly show that optical spectroscopy is important for the study of electronic states in low-dimensionality structures and, at the same time, to the one who wishes to explore the new world of nanoscale.

When the knowledge and techniques from these studies were applied to the far more complex molecular nanostructures, it was quickly realized that more sophisticated theoretical and experimental approaches were necessary, mainly because of the strong structural and functional heterogeneity of these systems.

Later in this chapter, we shall discuss how spectroscopic techniques, in particular the optical ones, have been modified and adapted to study matter on the nanoscale. Without doubt, the greatest impact of advanced optical techniques has been in organic and biological nanosystems, and so we have drawn most of our examples from this field. For a general review of nanostructured materials with more emphasis on inorganic systems, we refer the reader to [A2], where much of work, including spectroscopic

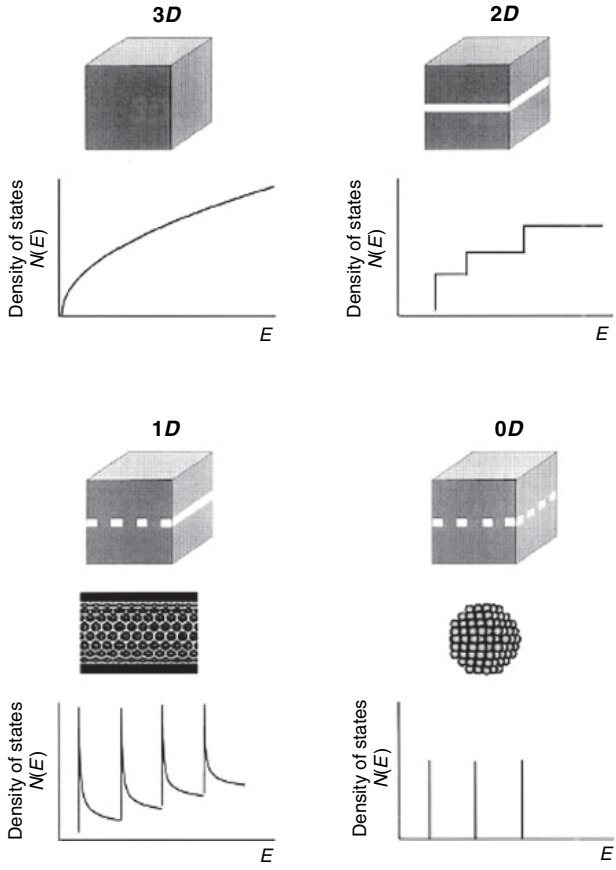

Figure 3.5: Schematic of the behaviour of electronic density of states as a function of system dimensionality, for the free electron model. We can clearly see the passage from the band structure of the 3D crystal to the atomic-like energy levels of the quantum dot. (Reproduced with permission from P. Moriarty, *Reports on Progress in Physics*, Vol. 64, pp. 297–381 (2001). Copyright 2001, IOP Publishing Limited.)

measurements, done from 1980 to 2000 is accessible. In this chapter, therefore, we shall mainly discuss the work done in the last decade.

After a brief description of the 'nanoworld', we shall introduce the novel techniques, beginning with the well-established SMFS and then going on to several other methods based of the SERS (surface enhanced Raman

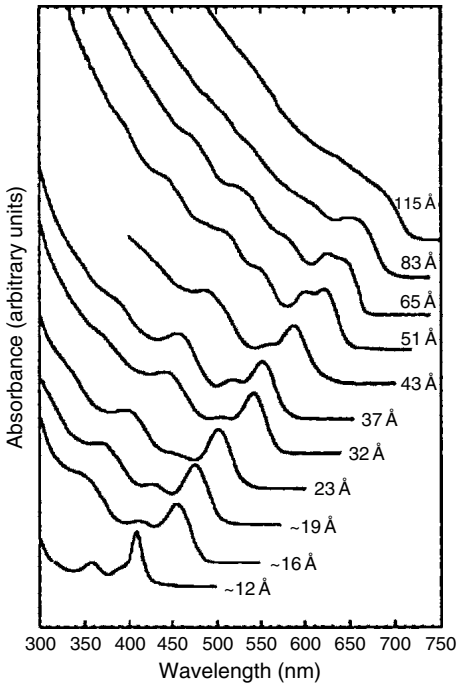

Figure 3.6: Optical absorption spectra of CdSe nanocrystals as a function of size. Note the blue shift as the size decreases, accompanied by a sharpening of the spectral structures. (Reproduced with permission from C.B. Murray, D.B. Norris, and M. G. Bawendi, *Journal of the American Chemical Society*, 115, 8706–8715 (1993). Copyright 1993, American Chemical Society.)

scattering) effect, which allow to perform Raman, infrared and time-resolved spectroscopies at the ultimate limit of single molecule or single nanostructure. Finally, we shall present some recent applications to nanotechnology.

The coupling of advances in optical techniques to the explosion of nanotechnologies has led to a very large number of publications, besides the traditional disciplines of physics and chemistry, in fields as diverse as materials science, nanomedicine, forensics and postgenomic biology. A large number of reviews have also appeared in the literature. Therefore, wherever possible, we shall refer the reader to the most recent or the most seminal work. To help the reader, we have grouped the reviews in

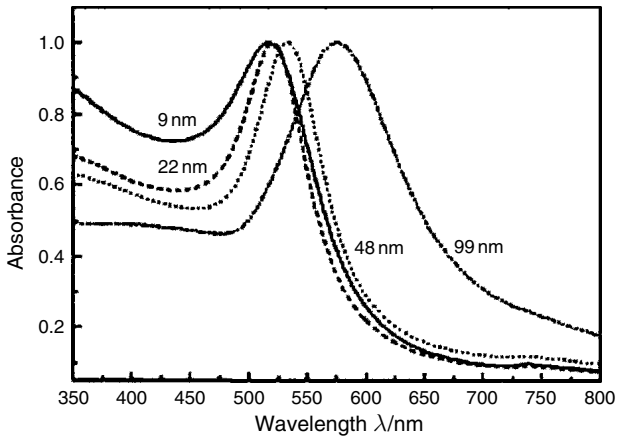

Figure 3.7: Optical absorption spectra of Au nanoparticles as a function of size. We are looking at the blue shift of the plasmon resonance peak. This behaviour is particularly relevant to the properties of SERS. (Reproduced with permission from S. Link and M.A. El Sayed, *Journal of Physical Chemistry B*, 103, 4212–4217 (1999). Copyright 1999, American Chemical Society.)

a dedicated Bibliographical Appendix (in which the reviews are labelled A#); other reviews of collateral interest are listed in the References section.

3.2. The Nanoworld

3.2.1. Small Objects

In the field of modern nanosciences, a favourite adage reads 'after all, molecules are the natural nanostructures'. Probably, the most used molecule in optical nanospectroscopies is the dye Rhodamine 6G (R6G) (Fig. 3.8).

An example of the use of R6G is reported in Fig. 3.9, where a functionalized carbon nanotube (CNT, see later) is shown. R6G is attached to the CNT through an appropriate linkage. It functions as a probe beacon of the CNT through its strong fluorescence, thus allowing biologically interesting processes such as CNT crossing the cell membranes and distribute to several crucial cell sites, where they may release specific drugs or other molecules [5].

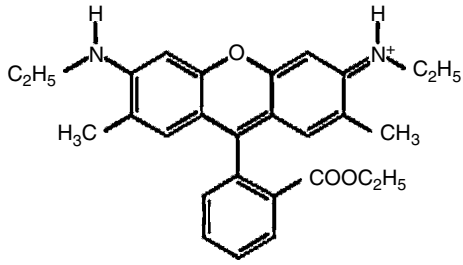

Rhodamine 6G

Figure 3.8: Chemical structure of a well known and used molecule, Rhodamine 6G. Geometrically, it can be decsribed as a triangle of 1.5 nm base and 0.8 nm height. Note the group N^+ which allows to bind the molecule to specific sites of other molecules – typically proteins or oligonuleotides – or nanocrystals, and to transport the molecule into biological cells.

Figure 3.9: Molecular model of CNT functionalized with a fluorescent probe (from A. Bianco, 'Nanowires: bridging the gap between materials science and biology', ESF PESC Exploratory Workshop, EW04-102, K. Nielsch, O. Hayden Convenors). (Reproduced with permission from Dr Alberto Bianco.)

The present scenario indicates that the overall scope of research in molecular nanoscience is to arrive at the single-molecule limit, where the molecule has been 'programmed' to perform a specific function, either because it has been synthetized or modified by molecular engineering techniques and/or because it has been placed in the appropriate physico-chemically and structurally controllable environments. We are still far from the 'routine' fabrication of single molecular devices, but small objects on a scale down to the nanometer abound in the recent literature. One classic example is colloids, which evolved as providers of one of the main pathways to the fabrication of nanodevices and new 'smart' drugs [6].

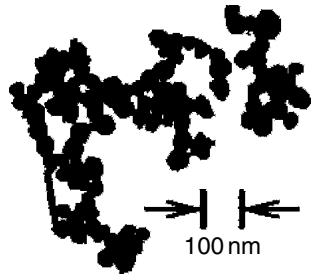

Figure 3.10: SEM image of a silver nanoparticle nanostructure, which shows extremely strong SERS enhancements. (Reproduced with permission from K. Kneipp, H. Kneipp, P. Corio, S.D.M. Brown, K. Shafer, J. Motz, L.T. Perelman, E.B. Hanlon, A. Marucci, G. Dresselhaus, and M.S. Dresselhaus, *Phys. Rev. Lett.* **84**, 3470–3473 (2000). Copyright 2000, American Physical Society.)

Figure 3.10 shows the electron micrograph of typical colloidal silver nanostructures.

Molecular Langmuir–Blodgett and self-assembled [7] films have been used as precursors and matrices for the production of arrays of semiconductor nanoclusters and nanocrystals, where new fundamental results have been demonstrated, such as Coulomb blockade and one-electron transistors [8]. In Fig. 3.11, we show a typical example of a nanodevice based on CdSe nanocrystal-functionalized STM tip. Nanocrystals were obtained by the Langmuir–Blodgett precursor method.

Clearly, the best example of 'programmed' molecules is the biological macromolecules, which is still the unequalled paradigm for research in this field. The greatest progress that 'nanospectroscopies' have allowed is our much better understanding of the very complex dynamics of proteins and nucleic acids both ex situ and in situ, i.e., during their biological function in living cells or other biological systems [9]. In Fig. 3.12, we have shown a sketch of the tertiary structure of lysozyme, an enzyme, which is probably one of the most studied and the simplest proteins.

The study of protein folding–unfolding [10] has led to a much better understanding of the process. For this, the fundamentals have been the single-molecule spectroscopies, such as single-molecule fluorescence and Raman scattering, which shall be discussed here, and AFM force microscopy, for which we refer the reader to [A3,11]; similarly, synchrotron radiation spectroscopies have given important contributions to the field of nanoscience and nanotechnology. Again, we must choose to refer the reader to the more recent reviews [A4] and some select literature [12].

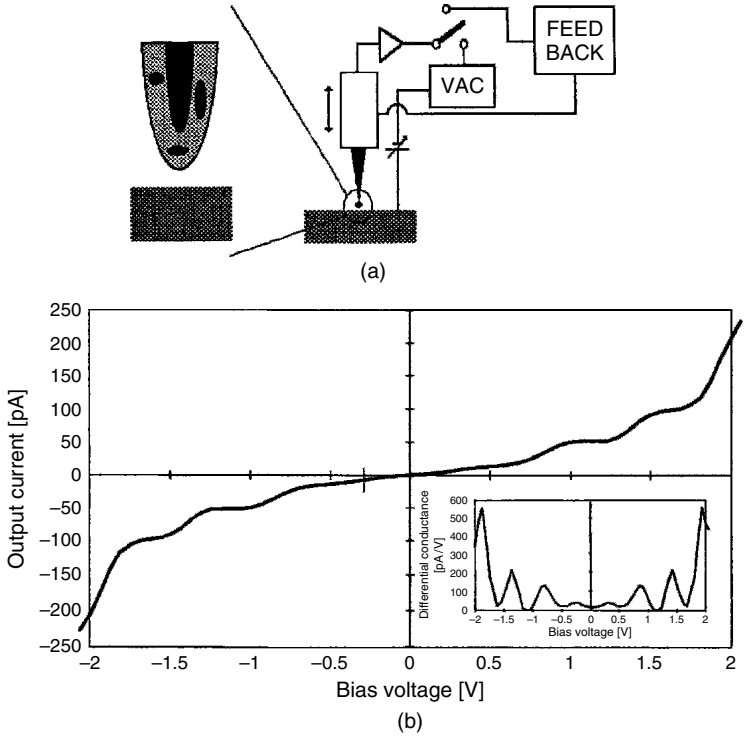

Figure 3.11: Experimental set-up (a) and voltage-current characteristics (b) demonstrating Coloumb staircase at room temperature (Insert – differential conductivity). The tip is functionalized with the active material, e.g., CdSe nanocrystals (from Facci et al., ref [8]).

Another quite important development in the field of nanoscience during the last decade was the synthesis of fullerenes, which sparked a revolution in materials science and the subsequent development of carbon nanotubes (Fig. 3.13).

These nanostructures, made up of rolled up graphene, have an amazing spectrum of functionalities and applications, mainly in nanocomposites with polymers yielding fibers of exceptional lightness and strength and in systems with modified optical, electrical and magnetic properties. Furthermore, CNTs can provide nanowires for molecular electronics, quantum dots used as fluorescence markers, single-electron transistors, high-surface-area sensors, nanoprobes for AFM, and hydrogen storage media. Interestingly,

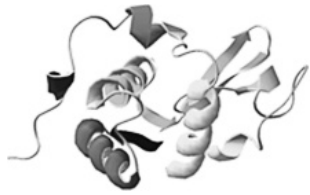

Figure 3.12: The tertiary structure of lysozyme: alfa-helices, beta-sheets, and random coil strands are clearly visible. Such a structure and its conformational changes are fundamental for the biological function of the protein (from Wikipedia, http://en.wikipedia.org/wiki/Lysozyme).

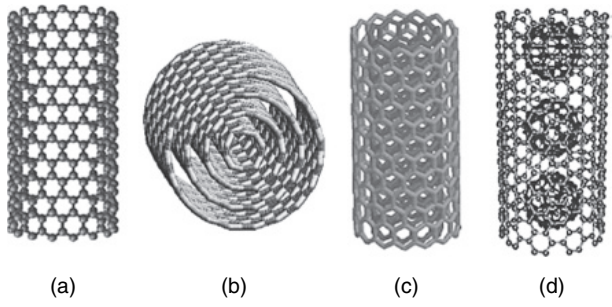

Figure 3.13: Carbon nanotubes: (a) single wall nanotube (SWNT); (b) multiwall nanotube (MWNT); (c) double wall nanotube (DWNT); (d) peapod, i.e., a SWNT filled with C60 or other fullerenes. (Reproduced from *Materials Science and Engineering C*, Vol.23, M.S. Dresselhaus et al., 'Nanowires and nanotubes', pp. 129–140. Copyright 2003, with permission from Elsevier.)

nanosystem optical spectroscopies have given important contributions. For reviews on several aspects of CNTs, see [A5]. Some select recent spectroscopic investigations are reported in [13].

3.2.2. Small Structures

We have already cited the classic example of quantum-size limited structures, such as quantum dots; these are an offshoot of the lithographic technology of microelectronics, which actually set the beginning of nanotechnologies. With electron beam lithography (EBL), it is possible to produce electronic components, such as FET, on a size of about 50 nm.

On the research level, the size can be made even smaller, but there may be many fundamental difficulties when the scale of 1 nm is reached: the presence of quantum effects due to the high localization, which may turn a semiconductor into an insulator; the tunnelling phenomenon, which may 'smear out' the electronic behaviour of an ultrasmall nanostructure; and the very high energy density, which poses an insurmountable obstacle to inorganic nanoelectronics.

Nanospectroscopies can be a very powerful tool in studying nanostructures and what happens to them in case of failure or damage. Here, we show an example of a fundamental inorganic nanostructure, the nanowire. In Fig. 3.14, we can see the ZnO nanowires and their arrays, which are grown by combining substrate patterning and catalyst-directed epitaxial growth of single crystal ZnO wires and pillars.

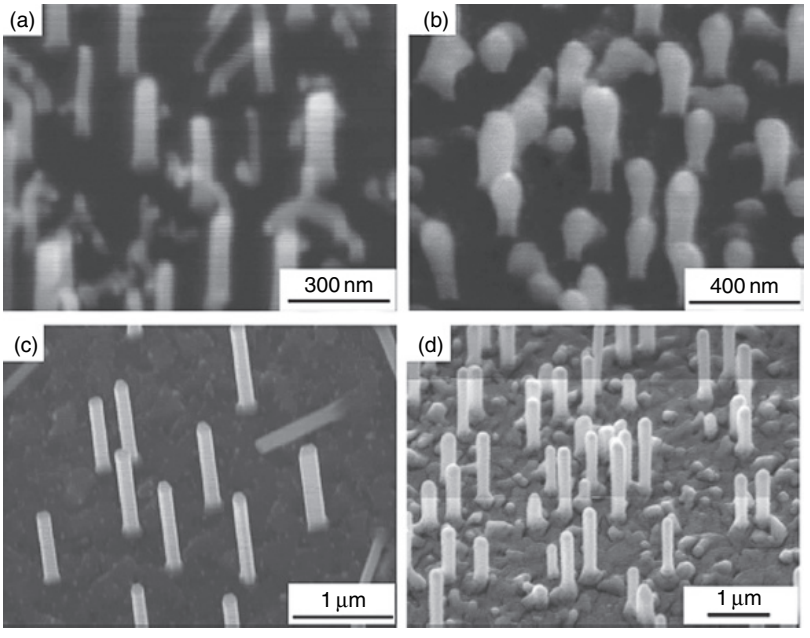

Figure 3.14: ZnO nanowires and nanowire arrays. (Reproduced with permission from M. Alexe, D. Hesse, V. Schmidt, S. Senz, H.J. Fan, M. Zacharias, and U. Gösele, 'Ferroelectric nanotubes fabricated using nanowires as positive templates', *Applied Physics Letters*, 89, 172907 (2006). Copyright 2006, American Institute of Physics.)

However, the aforementioned difficulties have increased interest in functional molecular nanostructures or molecular nanodevices, for which both quantum effects and heat dissipation problems do not appear to be as strong basically due to their 'soft' character, which yields strong responses to very small perturbations.

Thus, the field of molecular nanoelectronics opened up [A6]. However, the very advantages of soft matter also bring the fundamental difficulties of inadequacy of standard, hard-matter lithographic techniques, which would damage or destroy the molecular nanostructures and the intrinsic instability of fabricated structures, for which Langmuir–Blodgett deposition and self-assembly processes are used [6]. Thus, much of technological research is still necessary before organic nanoelectronics can become competitive with silicon-based electronics. In particular, some progress has been made in alternative soft lithographic techniques [14], which hold the potential of small damage to the materials.

The other frontier in this field is that of biological applications. Here, much of interest is in the fabrication of stable arrays of immobilized proteins or nucleic acid oligomers for biosensing or sequencing down to the molecular scale [15]. A typical example is the streptavidin-biotin technique, which is an important tool in immunocytochemistry, especially in the fabrication of arrays of immobilized proteins or DNA and its oligomers, etc. [16].

In all these, nanospectroscopies have been fundamental for progress. For instance, much detailed information on immobilized protein folding–unfolding and more generally conformational states has been obtained by SMFS; this technique has also yielded precious information on energy transfer and vibrational relaxation processes [17]. SERS-like confocal Raman spectroscopy has been used to study the interaction and complexing of DNA with mutagenic drugs, or for detection of minute amounts, or for sequencing [18]. The giant (up to about 10^{14} enhancement factor) SERS effect [A7] shown by molecules adsorbed to gold/silver nanoparticles or even better to their aggregated nanostructures [A8] has been used, among other applications, to detect time-resolved Raman spectra of biomolecules as their conformation changes, or to sample molecule by molecule the statistical distribution of conformations through their effect on the Raman spectra of single biomolecules, such as for instance, the well-known green fluorescent protein [19]. For an excellent general review of the SERS work on biosystems before 2002, see Kneipp et al. [A9].

In Fig. 3.15, we show an example of what can be achieved with nanofluorescence spectroscopy. In this particular case, the interest was in

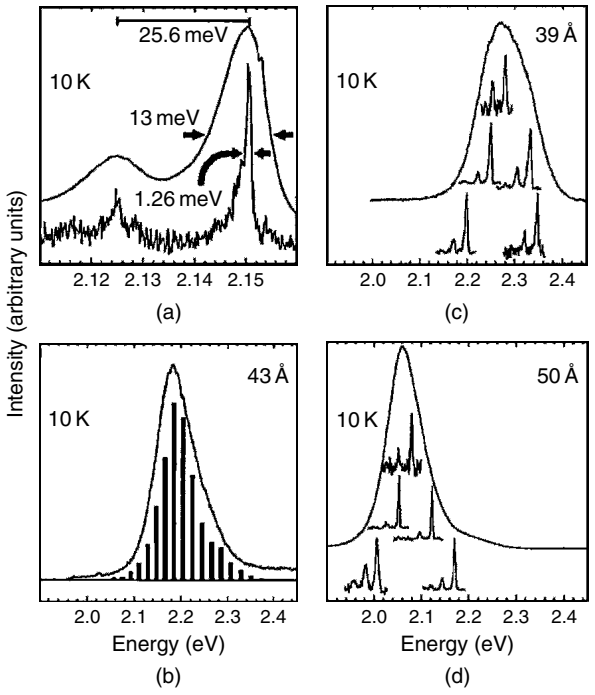

Figure 3.15: Nanofluorescence of CdSe nanocrystals. (a) Comparison between the spectra obtained with FLN (upper trace) and SDL (lower trace). Ensemble spectra and single nanocrystal spectra for everage sizes of 3.9 nm (c), 4.3 nm (b) and 5 nm (d). In (b), the histogram corresponds to the emission spectra of 513 single nanocrystals (Reproduced with permission from S.A. Empedocles, D.J. Norris, and M.G. Bawendi, *Phys. Rev. Lett.* 77, 3873 (1996). Copyright 1996, American Physical Society.)

deconvoluting the real spectra of single nanocrystals from the normally observed spectrum, i.e., the emission from an ensemble of nanocrystals. In panel A, a comparison is made between the fluorescence spectrum detected using the fluorescence narrowing technique (upper trace) with that obtained from the single quantum dot (lower trace); note the impressive narrowing. This result can then be used to disentangle the broadening due to ensemble average. The possibility of getting the signal from each individual nanocrystal allows to quantify the heterogeneity of the size distribution and environment of nanocrystals. It also confirms the line structure expected for a quantum dot, which would otherwise be hidden in the broad, featureless

emission band of the ensemble. Note the displacement to higher energies of the emission peak positions as the nanocrystal size is reduced.

The combination of ultrahigh space and time resolution can be achieved by using scanning tunnelling microscopy with femtosecond (fs) light excitation [20] This new technique is very useful in studying fast relaxational dynamics in organized nanostructures. As an example, we show in Fig. 3.16 some data taken on GaN_xAs_{1-x} $(x = 0.36)$. The imaging is performed through the differential scanning tunnelling current, i.e., the difference between the current during the downstroke and the upstroke of the STM tip at a given instant in time, as a function of delay time between the pump and probe pulses of a titanium-doped-sapphire (Ti:S) laser. The analysis of time dependence of the integrated current identifies two relaxation times of $\sim$1 and $\sim$50 ps (picoseconds), respectively, for space resolution of 10 nm.

3.3. Advanced Optical Spectroscopies

3.3.1. Single-molecule Fluorescence Spectroscopies

Certainly, the most popular spectroscopic techniques to explore the nanoworld are SMFS, which in general combine a high space resolution confocal microscope with high sensitivity CCD (charge coupled devices) arrays or APDs (avalanche photodiodes) for luminescence detection (Fig. 3.17) [21].

The basic principle is simple: in the focal volume of the microscope, there should be either one molecule or none. This can be simply obtained by a sufficient decrease in the concentration of the molecule of interest in a solution, or by a parallel decrease of the active volume. In both cases, however, there is no control on which molecule is seen; furthermore, molecules will go in and out of the useful volume. Actually, at room temperature, the transit time of a typical fluorescent molecule through the active volume is about 10^{-3} s; so for a radiative decay time of 1 ns, utmost 10^6 absorption-emission cycles (hence photons) could be observed. However, the luminescence, hence the molecule, disappears much sooner because of photodecomposition or other photoeffects (self-bleaching effect, quantum efficiency 10^{-5}–10^{-8}). Considering that the detection efficiency is of the order of a small percentage, the actual signal that detects the single molecule is a burst of about 10–100 photons. In Fig. 3.18, we show an example of the bursts, which signal the passage of one molecule, in our example rhodamine 6G, through the active volume. It is worth noting

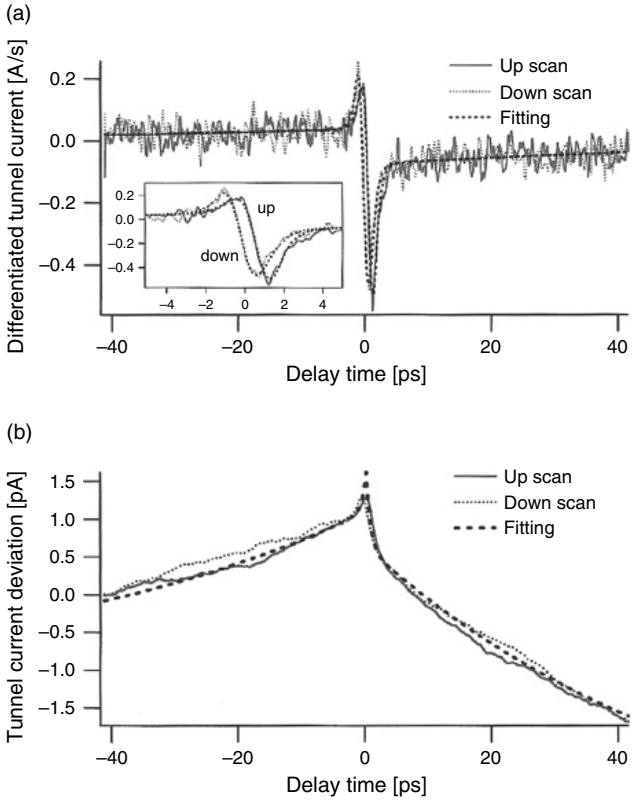

Figure 3.16: (a) Differential tunnelling current as a function of delay time between pump and probe laser pulses for a sample of GaN_xAs_{1-x} ($x = 0.36$) annealed at 600°C; (b) integral tunnelling current obtained from the data in (a). The best fit is a two-exponential function. The asymmetry between negative and positive delays is due to the different intensities of the two laser pulses. The data correspond to an active area of a few nanometers. (Reproduced with permission from O. Takeuchi, M. Ayoama, R. Oshima, Y. Okada, H. Oigawa, N. Sano, R. Morita, M. Yamashita, and H. Shigekawa, 'Probing subpicosecond dynamics using pulsed laser combined scanning tunnelling microscopy', *Appl. Phys. Lett.* Vol. 85, pp. 3268–3270 (2004). Copyright 2004, American Institute of Physics.)

that the mother solution – water-glycerol – had a R6G concentration of 15 femtomoles! While the upper trace shows the bursts of fluorescence due to the passage of solution microdroplets, the lower trace shows the control signal: identical microdroplets but of the water–glycerol solvent only [22].

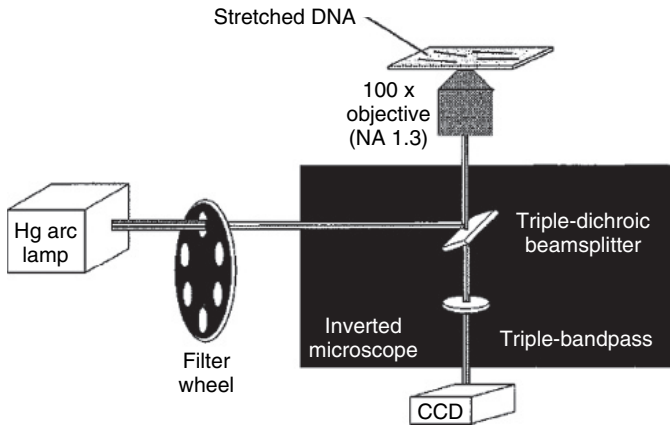

Figure 3.17: The simplest experimental set-up to view single molecules through their fluorescence. In this case, a normal multiline lamp is used with an inverted microscope. (Reproduced with permission from J.R. Taylor, M.M. Fang, and S. Nie, *Analytical Chemistry*, 72, 1979–1986 (1999). Copyright 1999, American Chemical Society.)

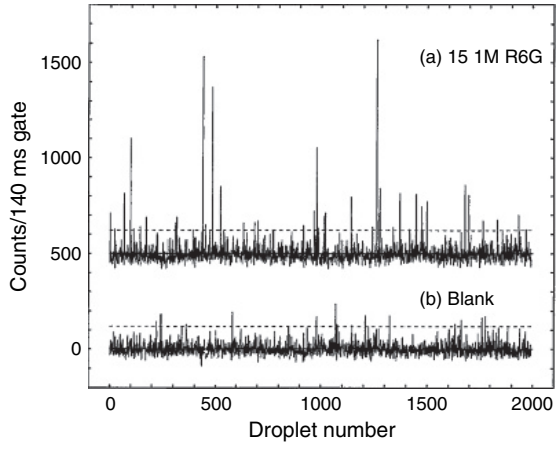

Figure 3.18: Detection of single R6G molecules dissolved in free-falling glycerol water microdroplets; the dashed line indicates the noise fiduciary level. (Reproduced with permission from M.D. Barnes, N. Lermer, C.Y. Kung, W.B. Whitten, J.M. Ramsey, and S.C. Hill, *Optics Letters*, Vol. 22, pp. 1265–1267 (1997).)

The very low concentrations necessary for the single-molecule limit imply a particularly vexing problem that the system will detect, beside the wanted signal, a diffuse background due to the luminescence of excited molecules outside the target volume; impurity luminescence too is an increasingly difficult problem to overcome as the fluorophore concentration is reduced. In spite of these difficulties, SMFS in its simplest form is now a routine tool for studying dynamics and relaxation of single molecules in a variety of applications; we shall discuss some representative examples later. For general reviews and experimental details, see [A10]. Here, we wish to briefly discuss the more advanced versions of SMFS, in which some of the aforementioned problems are eliminated or at least minimized.

An obvious improvement can be obtained using a confocal microscope, which would reduce the active volume and also reduce the intensity of 'stray fluorescence' through the spatial filtering of the pinhole. Nowdays, this confocal geometry is almost universally used.

More sophisticated excitation schemes can be used. In Fig. 3.19, we show methods based on total internal reflection and evanescent wave excitation.

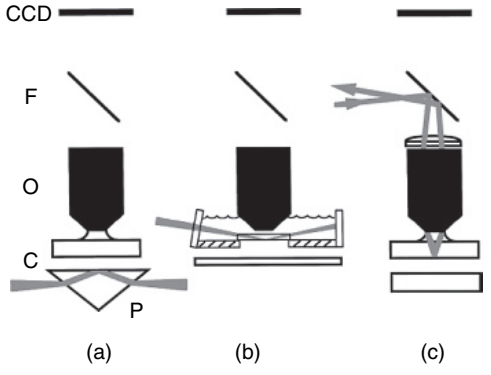

Figure 3.19: Schematic view of several total internal reflection and evanescent wave excitation schemes: (a) total internal reflection (TIR) prism using evanescent wave coupling; (b) the same, but without prism; (c) TIR using large angle (due to the high objective aperture) input rays, which focus at angles beyond the critical angle for the silica surface of the sample cell. (Reproduced from W.P. Ambrose, P.M. Goodwin, and J.P. Nolan, 'Single-molecule detection with total internal reflection excitation: Comparing signal-to-background and total signals in different geometries', *Cytometry*, Vol. 36, pp. 224–231 (1999). Copyright John Wiley and Sons Limited; reproduced with permission.)

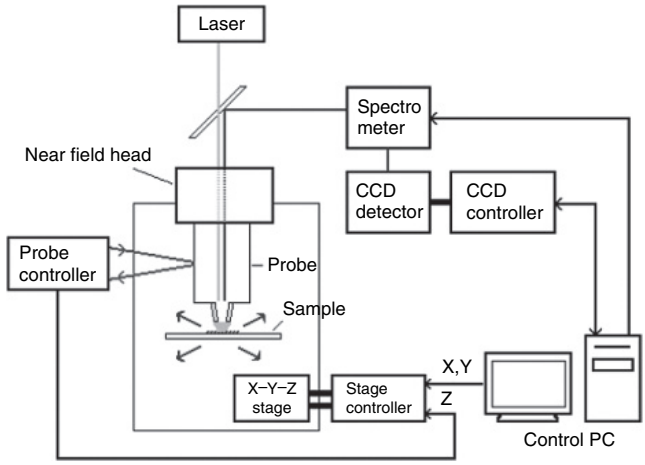

Figure 3.20: Schematic view of the spectroscopic version of NSOM, realizing a suggestion made originally by Synge [23]. (Reproduced with permission from S. Nagata, K. Kaga, and O. Karthaus, *e-J. Surf. Sci. Nanotech* 3, 94 (2005).)

A more spectacular improvement derives from the use of the tip of the NSOM to excite fluorophore (Fig. 3.20). In this case, the lateral dimension of the spot will be reduced from about 1 μ to 50 nm, yielding a reduction of the active volume from about $1\,\mu^3$ (1 femtoliter, fl) to 0.05 fl. This reduction, coupled with the confocal geometry, reduces the unwanted luminescence considerably. Another and perhaps the most important advantage of using a sub-wavelength excitation spot is the possibility of studying molecules localized in some specific nanostructure. In this case, the NSOM is used in the dual role of imaging microscope, yielding the sample topography down to a scale of about 50 nm (the aperture limit due to the tip size) and excitation source localized well beyond the diffraction limit. Using this, it is possible to study fluorophores localized in specific sites in a larger nanostructure, which can be a biological macromolecule or a semiconductor nanocrystal [A11].

Up to now, we focussed our attention on excitation and emission optics. Another important point concerns the detectors, such as the CCDs and APDs, which have allowed the quantum limited sensitivity and high time resolution necessary for most advanced applications. This, for instance, has allowed the application of PCS techniques (for a general introduction

to the subject see [2]) to obtain the time correlation functions of intensity fluctuations due to single-molecule photon bursts [24]. This is an important development since it allows the measurement of fundamental quantities of direct physical interest, such as diffusion coefficients, concentrations, reaction kinetics, etc., on the single molecule instead of relying on the normally measured ensemble averages, which, especially in the spatially heterogeneous systems we are considering here, could lead to a considerable loss of precious information; for a review see [A12].

A further approach to improving the experimental situation uses nonlinear optical effects. Two-photon excited fluorescence is particularly useful because of its relative simplicity [25]. Here, the trick is to use the dependence of the effect on the square of the incoming intensity to restrict the active volume considerably. Let us recall that the intensity distribution along the direction of propagation in the focal region has a clessidra-like shape, i.e., the power density strongly increases as the focal point is approached, and then decreases as strongly. Another advantage of this technique is that the excitation light is generally in the spectral region where the material is transparent; this avoids unwanted heating effects and allows probing the material further in the bulk.

The required excitation intensity is high (greater than 1 MW cm^{-2}). Usually, a mode-locked Ti:S laser is used, which allows pulse widths of about 100 fs and hence single-molecule time resolved fluorescence spectroscopy with fast time resolution. This, by the way, allows an interesting imaging method, which involves the determination of the fluorescence lifetime of the single molecules. Such lifetime, as was the case of the fluorescence spectrum (Fig. 3.15), depends on the single-molecule local environment, which can be imaged by this technique (see f.i. Benda et al., ref [26]; see also Fig. 3.25).

Using the near-infrared wavelengths available with the laser source in two-photon single-molecule spectroscopy, it is possible to achieve radial and axial space resolution of less than 500 and 1000 nm, respectively. This space resolution is similar to what can be obtained with a confocal microscope, and allows 3D imaging of the sample.

As an example, we show in Fig. 3.21 a Z-scan (2-μ step, scale bar 10 μ) of images of two dividing HEK293 cells. The 3D profiling possible with two-photon fluorescence microscopy is evident. Here, the fluorophore is EGFP bound to a Calmodulin protein, which in turn binds to the enzyme myosin light chain kinase at the cell membrane.

A final improvement shall be discussed in the following paragraph since it involves the SERS effect.

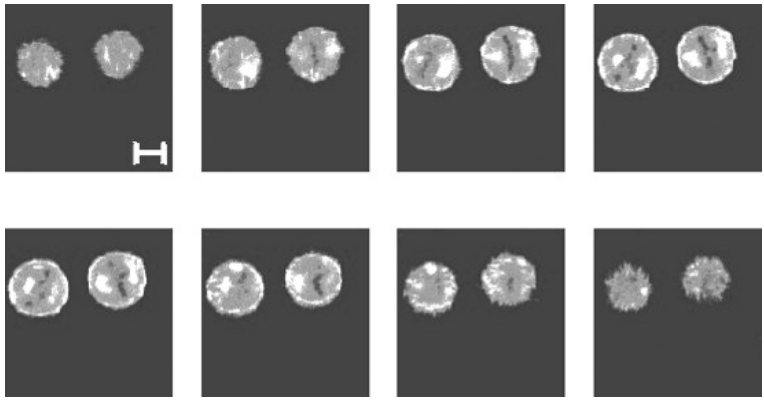

Figure 3.21: Two-photon fluorescence microscopy imaging of a cell division process, profiled along the z direction (Z-scan). The color codes are: blue = low intensity; red = medium intensity; yellow = high intensity (from t.gensch@fz-juelich.de, with permission from Dr Thomas Gensch)

3.3.2. The SERS Effect and Enhanced Spectroscopies

One of the most important developments in spectroscopy is SERS, discovered by Fleishmann et al. in 1974 [27] while studying electrode reactions. A confirmation and rough understanding of the effect came a few years later [28,29].

Basically SERS is an enormous increase of the non-resonant Raman cross-section of certain molecules when adsorbed 'near' a rough metallic surface. Originally this was the sponge-like silver electrode of an electrochemical cell [27]. The purpose of the experiment was to try and increase the Raman signal by increasing the surface/volume ratio and hence the density of molecules in the useful scattering volume. The signal increase was then attributed to such effect. It was quickly realized [28,29] that the effect was instead due to an increase of the Raman cross-section itself, connected with the strong local electric field enhancement near a metallic surface, sufficiently rough to feature a high density of localized surface plasmons. Later the effect was seen in island silver and gold (and other metals) thin films (about 50 nm average thickness). For a general review of the early work and theories on SERS, see [A7]. More recently, micro- and nanocolloidal metallic particles, in solutions or especially deposited on a solid substrate forming fractal-like aggregates, have shown the highest enhancement factors (10^{14}–10^{16}) [A9,A13]. In a way, the original intuition

of Fleischmann et al. was somewhat vindicated in the later years. In fact, the 'surface enhanced' locution in SERS is somewhat of a misnomer. Flat metallic surfaces do not show the effect (or at least they show only a small increase, less than one order of magnitude). It is the space heterogeneity on nanoscale that affects both the surface plasma excitations of the metal and the near field distribution the molecules see near the surface, which is responsible for the effect. SERS is an important example of how life on the nanoscale can be full of surprises, i.e., impressive new physical and chemical effects; thus SERS, which for over a decade had become a so-called 'mature' sub-field of surface sciences, was resurrected in the late 1990s as a revolutionary field in nanosciences [30–32]. For an up-to-date account of research in this field, see [A14].

In Fig. 3.22, we show the sketch of a typical experimental configuration to determine SERS spectra with high enhancement factors.

With a relatively simple set-up, the sensitivity level of single-molecule Raman spectrum can be reached. We can understand why this is so by closely considering the actual enhancement factors provided by the SERS substrate.

In Fig. 3.23, we show a direct measurement of intensity enhancement due to SERS. Here, the method was to measure in precisely the same experimental conditions the SERRS (resonance SERS) spectra of a solution of colloidal gold nanoparticles containing R6G at about 10^{-10} M concentration, and in the same solution to which 5-M methanol was added. Methanol does not show any SERS enhancement, and has the typical Raman cross-section of about $10^{-30}\,\mathrm{cm}^2$. By subtracting the two spectra, the spectrum of pure methanol was obtained; the intensities and known concentrations yielded an estimated enhancement factor of 10^{10}. In this particular case, an additional enhancement contribution was due to the fact that R6G was resonantly excited by the 514.5 nm argon laser line, and hence the acronym SERRS.

However, the real maximum enhancement was actually much higher. This was seen in several experiments. In particular, in Fig. 3.24, we show the Stokes and Anti-Stokes SERS spectra of crystal violet adsorbed on colloidal silver particles of different sizes. The Stokes–Anti-Stokes intensity ratio was clearly anomalous. At room temperature, the high wavenumber lines in the Anti-Stokes spectrum should be considerably weaker. The extra strength of the Anti-Stokes lines was due to the pumping of higher vibrational levels due to very strong SERS [31]. This non-linear process allows to estimate the actual maximum SERS cross-section from the difference between the equilibrium and SERS pumped Stokes–Anti-Stokes ratios. The

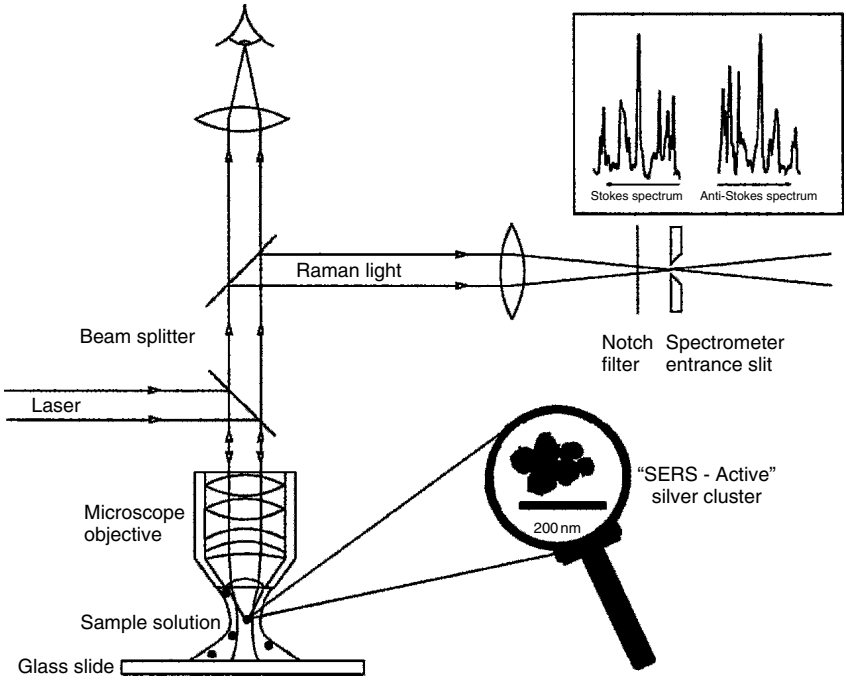

Figure 3.22: Schematic experimental set-up for single molecule SERS in a colloidal solution. Inserts are an electron micrograph of a typical colloidal cluser and the Raman spectrum of a single molecule adsorbed on such cluster. (Reproduced from K. Kneipp, H. Kneipp, R. Manoharan, I. Itzkan, R. Dasari, and M.S. Feld, *Bioimaging* 6, 104 (1998). Copyright 1998, John Wiley and Sons Limited; reproduced with permission.)

value obtained was about $10^{-16}\,cm^2$, i.e., an enhancement of 10^{14}! However, a perusal of Fig. 3.23 will clearly indicate that, for such enhancement, the SERRS lines of R6G should be much stronger than they are. The conclusion is that not all adsorbed molecules have the same enhancement, i.e., strong substrate heterogeneity implies a wide distribution of sites with strongly different enhancement factors. If a homogeneous distribution is assumed, it would lead to an underestimation of the maximum enhancement factor. The highest enhancements (up to 10^{16}) are due to the so-called 'hot spots', whose existence and morphology became quite an active research subject on its own [33].

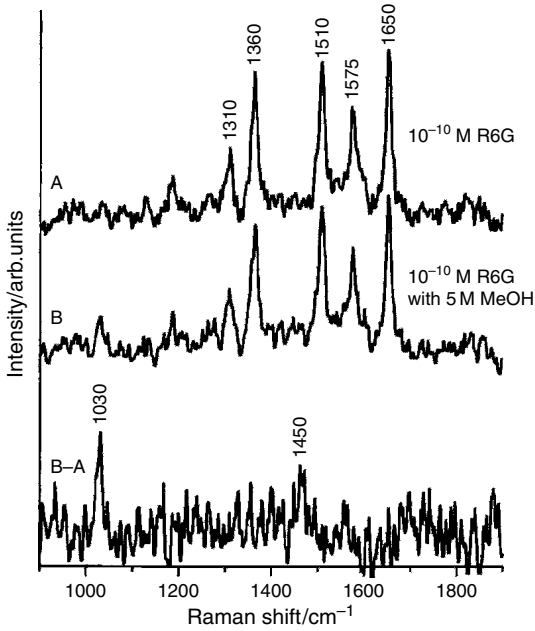

Figure 3.23: SERRS spectra of R6G solution with and without the presence of methanol. (Reproduced with permission from K. Kneipp, Y. Wang, R. R. Dasari, and M.S. Feld, *Appl. Spectrosc*. 49, 780 (1995).)

The existence of hot spots is evident in Fig. 3.25, where AFM images of highly efficient SERRS particles are presented together with inefficient ones (A). Under higher magnification (B, C, D), the hot particles were revealed to be either nanorods or linear clusters of a few particles, or so-called 'faceted' particles, i.e., with a strong spatial heterogeneity on the nanoscale.

Referring to Fig. 3.22, the relatively simple set-up shown could be complicated by using a confocal microscope for excitation. However, due to the space selective nature of SERS, i.e., most of the signal comes from the hot spots that are localized on the scale of about 10 nm, the actual resolution of the experiment does not depend on the excitation and detection optics, but instead on the nanoscale morphology of the substrate. In this sense, SERS not only enhances the Raman intensity but also allows an imaging space resolution on 10-nm scale!

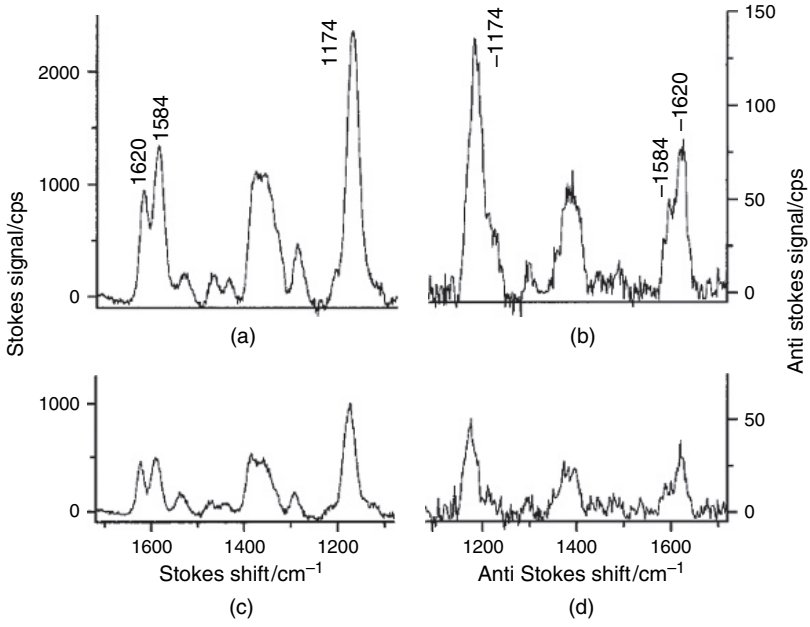

Figure 3.24: Stokes and Anti-Stokes SERS from cresyl violet adsorbed on colloidal silver particles of different sizes. (Reproduced with permission from K. Kneipp, H. Kneipp, I. Itzkan, R.R. Dasari, and M.S. Feld, *Chemical Reviews*, 99, 2957–2975 (1999). Copyright 1999, American Chemical Society.)

In spite of its obvious interest on a fundamental level as well as a highly sensitive and innovative analytical tool, the large amount of theoretical work has yet to arrive to a definitive theory of SERS effect. Although its ultimate explanation is not clear yet, it is certainly connected with nanoscale non-homogeneities on a metallic surface or more generally a surface with strongly inhomogeneous and sufficiently high electronic density. In particular, the Raman spectrum – but also other optical effects such as fluorescence and infrared absorption from a molecule adsorbed ('physical' SERS) or bound ('chemical' SERS) to such a surface – can be increased by several orders of magnitude, reaching the enormous value of 10^{16} in the most favourable cases.

Basically, the present understanding is that SERS is a consequence of nanostructuration of materials, which induces electronic effects that not only produce enhancement but also other important characteristics of SERS,

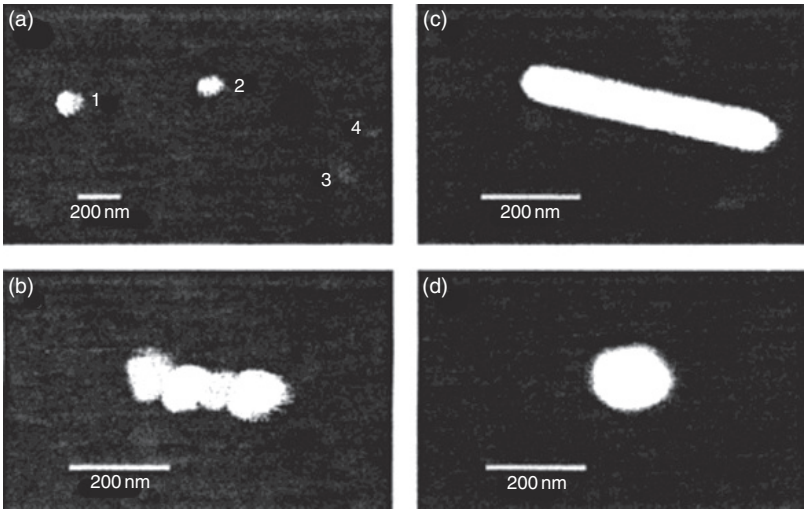

Figure 3.25: AFM images of colloidal silver particles: (a) four isolated particles of which particles 1 and 2 showed a very strong SERS effect, whereas 3 and 4 did not; (b–d) higher magnification images of some hot particles. (Reproduced from S. Nie and S.R. Emory, *Science*, Vol. 275, p. 1102 (1997); reproduced with permission from AAAS.)

such as its potentially high space resolution, way beyond the diffraction limit for visible light.

From the very beginning, two schools of thought appeared, claiming a physical or a chemical nature of the effect. This author never liked this division since, as it is now clear, there is a strong correlation feedback between chemical effects (i.e., changes in the electronic structure of molecules which then bind the molecule to the metallic nanostructure) and physical effects (i.e., the strong local electric fields due to excitation of the localized surface plasmons in the metal which add to the incoming light field and influence the scattering from molecules simply adsorbed or 'sufficiently near' the surface).

In fact the local field also couples the plasma electronic states to the LUMO states of the molecule. This generates a sort of resonant tunnelling effect, which will also depend on the nature of wavefunctions of the molecular electronic states ([34], [A13]).

The several strong possible interactions that we discussed so far should also have an effect on the fluorescence of a fluorescent molecule adsorbed

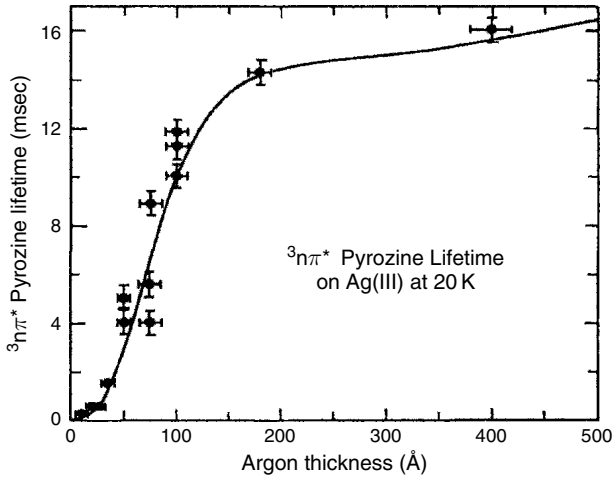

Figure 3.26: Phosphorescence decay time of pyrazine at 20°K as a function of distance from an Ag island film. The spacer is provided by an argon film. (Reproduced with permission from M. Moskovits, *Rev. Mod. Phys*., 57, 783 (1985). Copyright 1985, American Physical Society.)

on a SERS substrate, both on its intensity and its decay time. We shall discuss fluorescence enhancement later; here, we show the interesting effect on the lifetime. In Fig. 3.26, we present the behaviour of phosphorescence decay time of pyrazine at 20 K as a function of distance from a silver surface. Clearly, the decay time decreases with decreasing distance, which implies a strong increase in radiationless transitions and/or change in the electronic wavefunctions due to the 'chemical' part of SERS.

Furthermore, it is known that SERS works well in molecules with π states that are more delocalized; conversely, it will not work at all on others, such as f.i. the simple hydrocarbons or alcohols. An important consequence of this is that, contrary to the older assumptions, the SERS spectrum in many cases is not the same as the ordinary non-resonant Raman spectrum: some peaks that are almost absent in this are prominent in SERS; in fact, in some cases, the symmetry selection rules are broken so that the SERS spectrum will include forbidden vibrations. In Fig. 3.27, for instance, we show the case of C_6F_6 adsorbed on a silver island film [A7]. The strongest peak in the SERS spectrum (the totally symmetric C-F stretching vibration) is totally absent in the normal Raman spectrum from a polycrystalline sample. The reverse is true for a peak at 630 cm^{-1} in the polycrystalline sample.

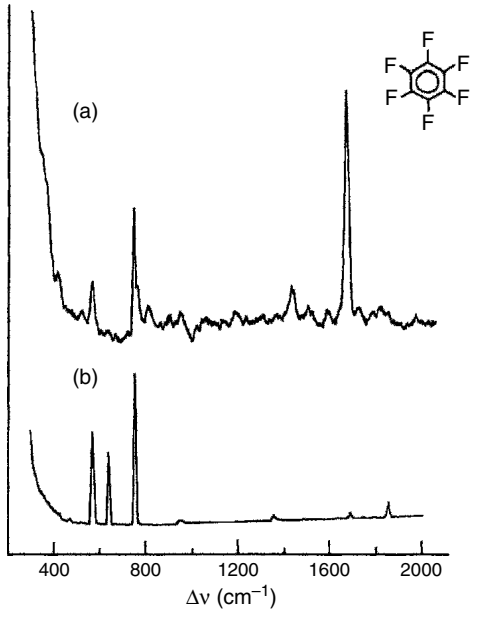

Figure 3.27: SERS spectrum of C6F6 adsorbed on a silver island film; normal Raman spectrum of a solid polycrystalline layer. (Reproduced with permission from M. Moskovits, *Rev. Mod. Phys*., 57, 783 (1985). Copyright 1985, American Physical Society.)

A general remark on SERS effect is that, the enhancement due to resonance with localized surface plasmon polaritons enhances not only the Raman scattering cross-section but also that of any optical effect, such as optical absorption and, more importantly, fluorescence. Thus, as in the case of Raman scattering, SERS enhancement can be used to increase the sensitivity and space resolution of single-molecule fluorescence.

Finally, SERS-like effects can also enhance infrared absorption, thus providing a useful complement to Raman scattering. In fact, depending on the incoming light wavelength, another contribution to the enhancement originates from localized surface phonon polaritons, i.e., mixed electronic-vibrational excitations. This greatly extends the scope and applications of the technique [35]. In particular, nanostructures of polar or dielectric materials can be studied. One interesting way to produce infrared, spectroscopically weighed images on the nanoscale is to use s-NSOM, i.e., scattering NSOM [36]. Here, a CO_2 laser is focussed onto a Si tip

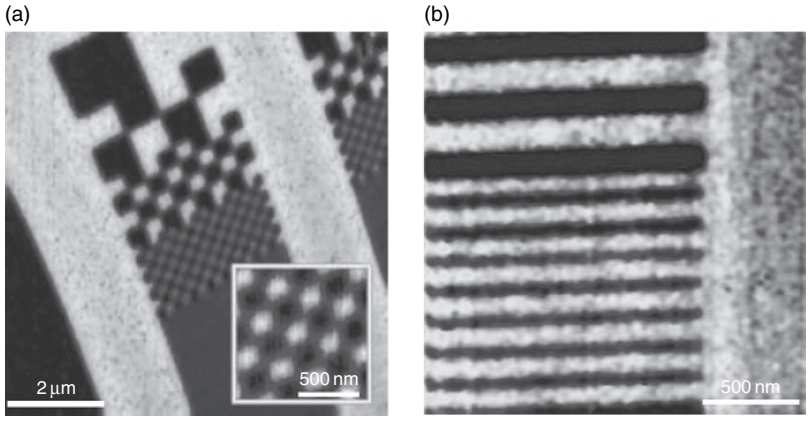

Figure 3.28: s-NSOM amplitude imaging of Ga^+-implanted SiC nanostructures: (a) imaging taken at 891 cm^{-1}; the inset zooms in a scan of 200 nm squares; (b) images of implanted stripes taken at 920 cm^{-1}; the stripe widths are 100 and 200 nm. (Reproduced from N. Ocelic and R. Hillenbrand, *Nature Materials*, Vol. 3, p. 606 (2004). Copyright 2004, Macmillan Publishers Ltd; reproduced with permission.)

covered with a thin platinum layer. The backscattered light is spectrally analysed interferometrically. When resonance of a sample (e.g. SiC) vibrational frequency with the tip is achieved, strong enhancement takes place and there will be a peak at that frequency in the backscattered light. Such a peak can be used to image the local dielectric properties of the sample. In Fig. 3.28, we show the IR imaging of a Ga^+ ion-implanted SiC using s-NSOM. The effect of 40 KeV Ga^+ ions on the SiC sample is clearly evident through the changes in vibrational spectra.

An experiment more closely related to the SERS effect is reported in [37]. Her,e the infrared detection of nano-objects is accomplished through three different types of nanostructures (Fig. 3.29): (a) a nanogap between two metal antennas, (b) the final part of metal probe tip, (c) the gap formed by the tip dipole and its mirror image on a highly reflecting substrate. Through enhancement due to the near field in these nanostructures, it is possible to selectively image particles (in this case gold) down to a size of 8 nm. By changing the substrate from metallic to dielectric, the contrast can be varied by a factor of 10. Furthermore, for different nanoparticles, resonance with different vibrational modes of the substrate can be used.

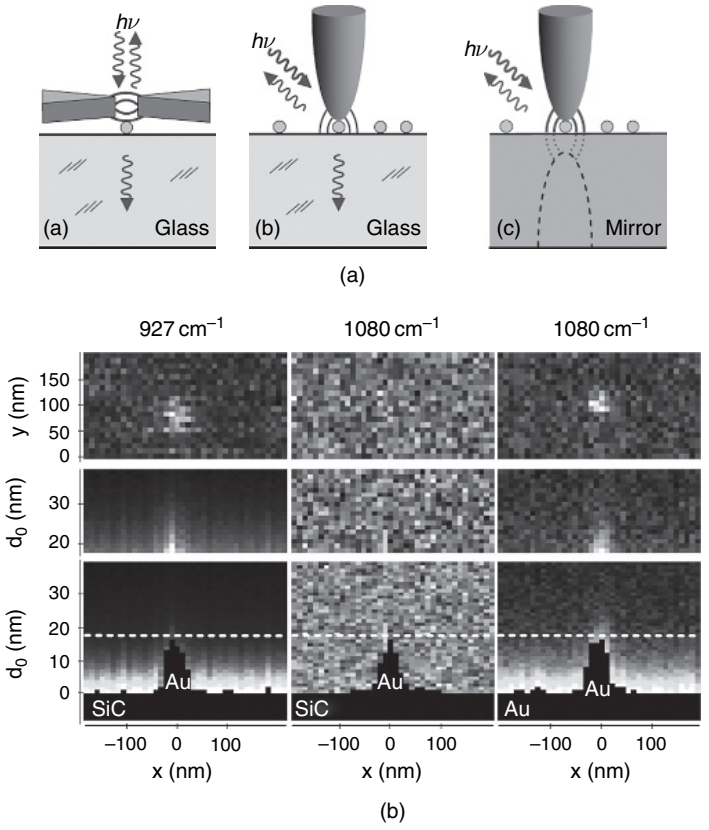

Figure 3.29: Detection of nanoparticles in different nanostructured environments and substrates using the s-NSOM technique (a); (b) imaging of a Au nanoparticle on different substrates using three different IR frequencies as probes. The lower panels are slices in the x direction (d_0 is the gap size), whereas the upper panel shows an x-y map of the particle. Note the total disappearance of the particle from the x-y map referring to the 1080 cm^{-1} frequency. (Reprinted with permission from A. Cvitkovic, N. Ocelic, J. Aizpurua, R. Glukenberger, and R. Hillenbrand, *Phys. Rev. Lett*., 97, 060801 (2006). Copyright, 2006, American Physical Society.)

3.3.3. Tip-enhanced Spectroscopies

As was the case for SMFS, subwavelengh excitation of SERS spectra can be achieved by illuminating the SERS sample through the tip of a NSOM.

Thus, it is possible to study a specific molecule in a solid structure, the molecule being chosen from the microscopic image. In this case, the space resolution of the system is limited by the aperture of the tip, yielding a minimal space scale of about 50 nm [38]. Thus, if single-molecule resolution was expected, the concentration of the molecule must be appropriately reduced. However, we would discuss another more sophisticated form of nanospectroscopy in which scanning probe microscopies are coupled with the SERS effect, which in a sense is brought to its limit. In this case, the strongly non-homogeneous environment is provided by the tip of the scanning microscope, i.e., STM, NSOM, AFM, the latter two being appropriately functionalized by a thin (about 50–100 nm) metal coating. More recently, electrochemically etched simple gold tips have been used with impressive results [39]. The resulting electric field in immediate vicinity of the point of the tip will be as high as the highest found in the 'rough' metallic surfaces of metal nanoparticles (i.e., the hot spots). At the same time, in contrast to normal SERS, the substrate metallic surface is flat.

In many cases, what we look for is the signal from a typical area of the nanostructure. In this apertureless geometry, both space resolution and system sensitivity can be increased to the ultimate limit of the single molecule [40]. In Fig. 3.30, we show a typical experimental geometry for

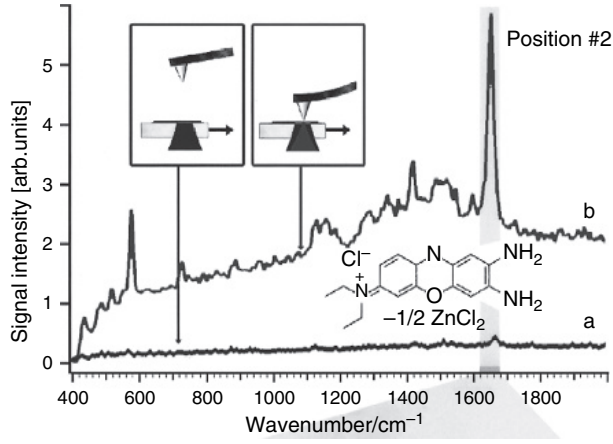

Figure 3.30: Raman spectra of brilliant cresyl blue (BCB) with the tip in contact with the sample (b) and with the tip removed from the sample (a). (Reproduced from R.M. Stocle, Y.D. Suh, V. Deckert, and R. Zenobi, 'Nanoscale chemical analysis bu tip-enhanced Raman spectroscopy', *Chemical Physics Letters*, Vol. 318, pp. 131–136. Copyright 2000, Elsevier; reproduced with permission.)

what has now come to be called TERS (tip enhanced Raman scattering), together with the tip-enhanced Raman spectrum and the unenhanced one.

A good example of TERS is reported in Fig. 3.31, in which the Raman spectra of one single-walled carbon nanotube are shown with the tip in contact with the single wall nanotube (SWNT) (solid line) and removed

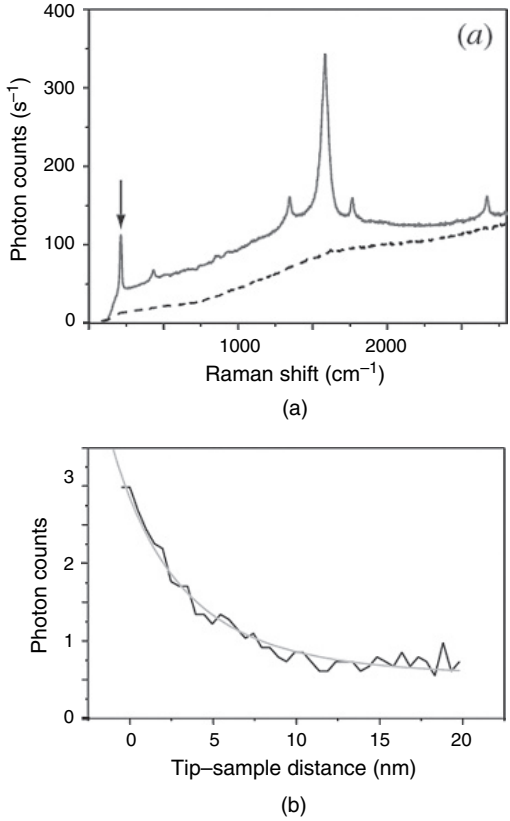

Figure 3.31: TERS of SWNT; (a) solid line tip in contact with sample, dashed line spectrum with tip removed; (b) tip-to-sample distance dependence on the intensity of the radial breathing mode (evidenced by the arrow in (a)). (Reproduced with permission from A. Hartschuh, M.R. Beversluis, A. Bouhelier, and L. Novotny, 'Tip-enhanced optical spectroscopy', *Philosophical Transactions of the Royal Society A*, Vol. 362, pp. 807–819, Figure 7 (2004). Copyright 2004, Royal Society.)

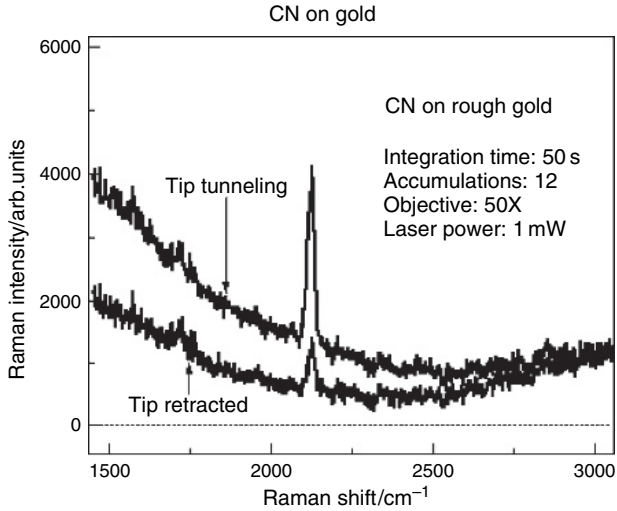

Figure 3.32: Raman spectra of isothiocyanate (CN stretching mode) molecules on a rough gold substrate, with and without TERS enhancement (from B. Pettinger, http://w3.rz-berlin.mpg.de/pc/shg/shg_sers/Tip_enhanced_RS.html, with permission from Dr. Bruno Pettinger).

from it by 2 μm (dashed line). In the right panel (b), the dependence of the Raman signal (monitored by the radial breathing mode) on the tip–sample distance is shown [41].

It may be argued that some of the enhancement may still come from inhomogeneities in the metallic substrate. In Fig. 3.32, we show the TERS spectrum of isothiocyanate taken on a rough gold substrate, with and without the tip. Clearly, the tip near field proximity to the sample yields an important additional enhancement.

In fact the optimal conditions for TERS enhancement are an atomically flat metallic surface and a well-defined sharp metal tip [42]. In Fig. 3.33, we show a comparison between the RRS of a single monolayer of isothiocyanate on Au(111) monocrystalline substrate with the TERRS spectrum in the same conditions.

Even if a relatively large area of the sample is illuminated (usually a confocal microscope is used so that the typical area is of the order of $1\,\mu^2$), only the molecules located in the immediate vicinity of the tip will experience the largest enhancement and, therefore, will dominate the signal at the sensitivity level of their spectrum. If only one molecule is attached to

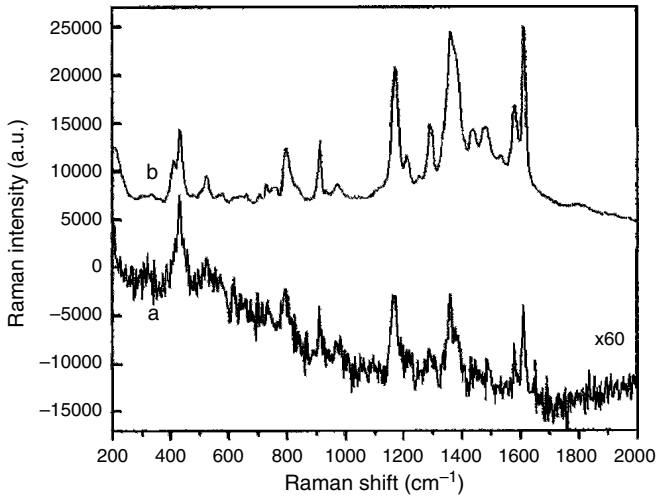

Figure 3.33: RRS (a) and TERRS (b) of malachite green isothiocyanate on Au(111). For (a), the acquisition time was 30 s, and the spectrum was enlarged 60 times; for (b), the acquisition time was 10 s. (Reproduced with permission from B. Ren, G. Picardi, and B. Pettinger, 'Preparation of gold tips suitable for tip-enhanced Raman spectroscopy and light emission by electrochemical etching', *Review of Scientific Instruments*, Vol. 75, pp. 837–841 (2004). Copyright 2004, American Institute of Physics.)

the tip, then TERS will yield the Raman spectrum of that single molecule at that specific position in the examined structure. Thus, TERS allows the sensitivity of the single molecule as well as a space resolution well beyond the diffraction limit or, in favourable cases, the imaging capabilities of the scanning probe microscope itself. This, for instance, permits the study of Raman spectrum of single specific subunits of a given macromolecule or, in the case of biomolecules, the study of the dependence on the location within the protein of the Raman spectrum of a given aminoacid or active site. For a general review of recent work, see [A15].

We have already pointed out the general character of SERS as an optical signal amplifier. In particular, SERS-like amplification has been used in SMFS. In Fig. 3.34, we show fluorescence enhancement as a function of tip-to-sample distance for single photon emission from single quantum dots and rods. Note the very fast spatial decay of the enhancement, which indicates that, in order to fully use the SERS effect, the tip must be almost in contact with the sample [43].

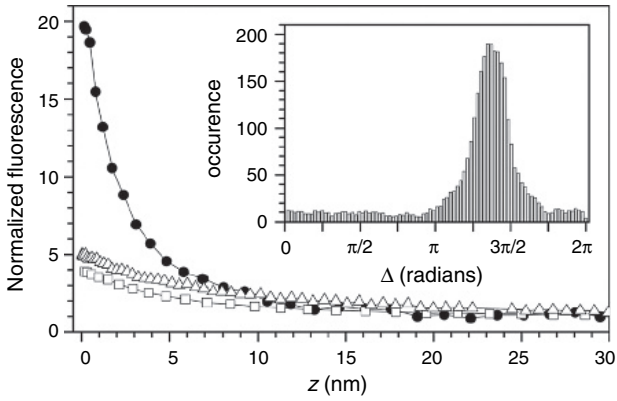

Figure 3.34: Fluorescence enhancement near a sharp Si tip as a function of tip-sample separation. The samples were quantum dots and rods of CdSe-ZnS. Solid circles: 5 nm quantum dot; open squares: 5×20 nm nanorod. The open triangles are for dye-doped latex spheres of 20 nm diameter. Clearly, the small quantum dot shows by far the largest enhancement. The inset shows the phase delays histogram for the quantum dot. (Reproduced with permission from J.M. Gerton, L.A. Wade, G.A. Lessard, Z. Ma, and S.R. Quake, *Phys. Rev. Lett*., 93, 180801 (2004). Copyright 2004, American Physical Society.)

We conclude this brief introduction to TERS with some experimental considerations. The scheme of a typical experimental configuration is shown in Fig. 3.35.

The laser excitation powers are always below 1 mW, and the excitation lines are chosen to be at resonance either with the electronic transitions of the sample and/or the localized surface plasmons of the SERS substrate or the tip material. For TERS enhancement, an axial polarization of the incoming electric field is usually necessary. To achieve this in the backscattering axial geometry shown in Fig. 3.35, it is necessary to displace the tip laterally or use higher order or radial laser modes with longitudinal fields. Otherwise, an oblique incidence of the laser beam can be used; this allows to observe enhancement for the planar component of laser polarization (see [44]).

With a surface density of 10^{14} mol cm^{-2} and a tip radius of 10 nm, one single dye (such as R6G) molecule could in principle be detected underneath the tip, given a TERRS enhancement of 10^{11}. This brings the Raman cross-section close to that for photoluminescence from the same dye [45].

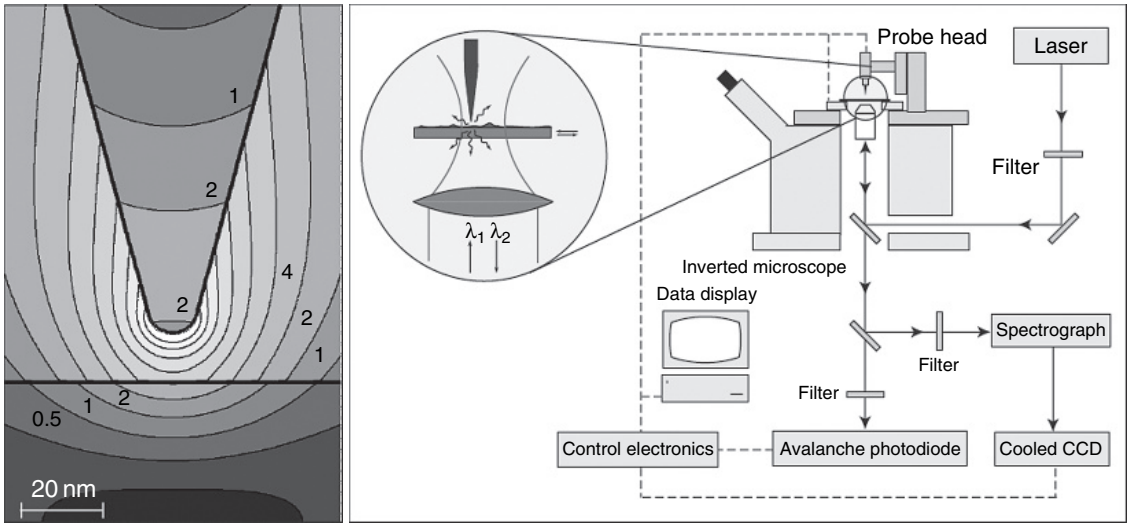

(a) (b)

Figure 3.35: An experimental set-up to study TERS using an STM base. The sharp metal tip is scanned through the focus area of the laser beam. The signal can either be detected without spectral analysis with the APD or with the spectrograph-CCD combination. The objective of the inverted microscope is usually a long working distance objective with NA of about 0.5–1.5. In the left panel is a scheme of calculated local field distribution at the tip which is irradiated on axis. (Reproduced with permission from A. Hartschuh, M.R. Beversluis, A. Bouhelier, and L. Novotny, 'Tip–enhanced optical spectroscopy', *Philosophical Transactions of the Royal Society A*, Vol. 362, pp. 807–819, Figure 1 (2004). Copyright 2004, Royal Society.)

3.4. Some Applications

3.4.1. Blinking, Statistics and PCS

The probing of single nanostructure and its immediate environment leads to the well-known phenomenon of fluorescence 'blinking' [46], i.e., the random discontinuous jumps of the detected intensity in single nanocrystals [47] or single molecules [48]. This has been proposed as a sure signature that the signal originated from a single molecule/nanostructure [21]. The blinking phenomenon involves the intensity as well as the spectrum and the luminescence lifetime. There are several possible causes for this, connected in one way or other to the heterogeneity of the local environment of the chromophore: conformational changes of the host macromolecule, radical formation and photoeffects such as photobleaching and photoionization, interlevel system crossing (singlet to triplet state, leading to phosphorescence at the expense of fluorescence or vice versa) and changes in the density of final photonic states (PSD) in the emission process [49]. If the non-homogeneous environment is due to a SERS substrate or a tip, the PSD modifications can be quite large and lead to substantial enhancements of the luminescence [50].

Here, we would bring in an important fundamental point, which has been successfully addressed using nanospectroscopy techniques: the connection between time averaging, i.e., following the single nanocrystal or molecule in time, and ensemble averaging. In an ergodic system, the two averages should coincide. Single molecule spectroscopy can yield profound insights into this matter. Since the typical intermittency time is about 0.1–0.5 s, and the single molecule/nanocrystal observation time for each point is about 120 s, it is clear that intermittency may strongly influence the experimental observations and conclusions.

In Fig. 3.36, we show the intermittency luminescence signal from a single CdSe quantum dot of about 2 nm. Note the two-level, on-off appearance of the signal and the long time scale of the process. Because of the broad distribution of on-off intervals, the signal appears to be dominated by a few long time events. This implies using a statistical analysis of time interval distributions based on Lévy statistics [51], from which statistical aging and ergodicity breaking can be observed [52].

In Fig. 3.37, we show the results obtained for CdSe nanocrystals, which imply a power law dependence of probability density $s(\theta)$ that a nanocrystal jumps to the ON state after having spent time θ in the OFF state (Fig. 3.37a). The value of the exponent α is fitted to be 0.5. This strongly

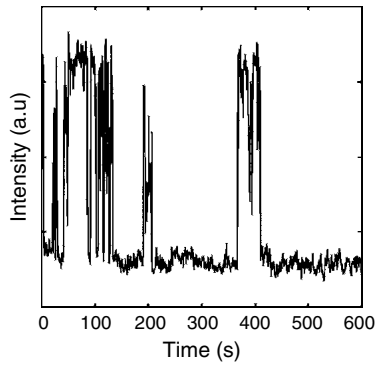

Figure 3.36: Typical fluorescence blinking signal. In this case, it was from a single CdSe nanocrystale. (Reproduced with permission from X. Brokmann, J.P. Hermier, G. Messin, P. Desbiolles, J.-P. Bouchaud, and M. Dahan, *Phys. Rev. Lett*., 90, 120601 (2003). Copyright 2003, American Physical Society.)

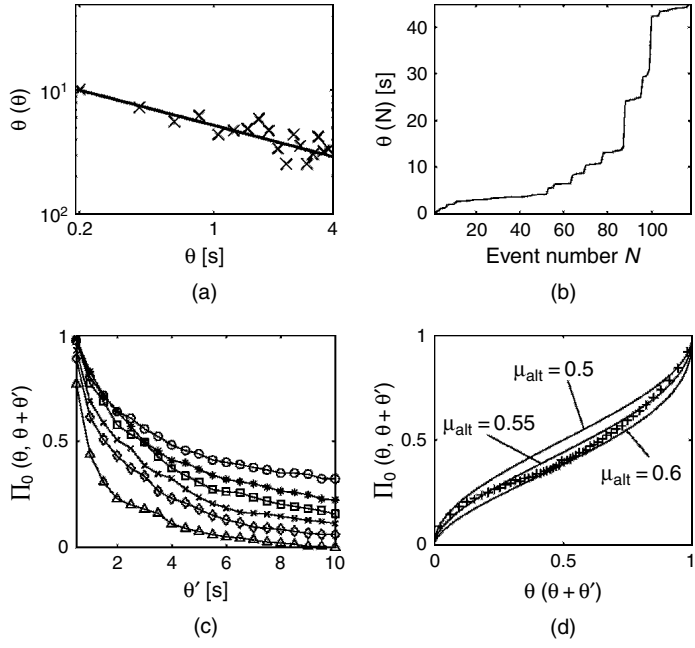

Figure 3.37: Statistical aging and Lévy power law for a sample of 215 quantum dots. (Reproduced with permission from X. Brokmann, J.P. Hermier, G. Messin, P. Desbiolles, J.-P. Bouchaud, and M. Dahan, *Phys. Rev. Lett*., 90, 120601 (2003). Copyright 2003, American Physical Society.)

non-exponential behaviour is typical of Lévy flights. In the figure, we can see the statistical aging of the system from the behaviour of persistence probability at different values of time intervals $\theta + \theta' - \theta$ (Fig. 3.37c), which shows a dependence on θ; in panel Fig. 3.37d, the same data are shown as a function of $\theta/\theta + \theta'$ together with the appropriate theoretical fits.

It is interesting to note that blinking effects are a general occurrence at the nanoscale. For instance, they are also observed in single-molecule SERS [53]. Although the basic cause of blinking remains the strong space dishomogeneity that characterizes nanoparticles observable at the single particle level, the actual specific mechanism may be different for SERS relatively to fluorescence. In particular, proposals for them indicate adsorbed molecular mobility on the SERS substrate [53, Weiss and Haran] or charge transfer [54]. For instance, in Fig. 3.38, we show data obtained for 'blinking' SERS, which clearly show transfer from ferrous to ferric ion during measurement time in a single iron-protoporphirin IX molecule adsorbed on a silver colloidal surface.

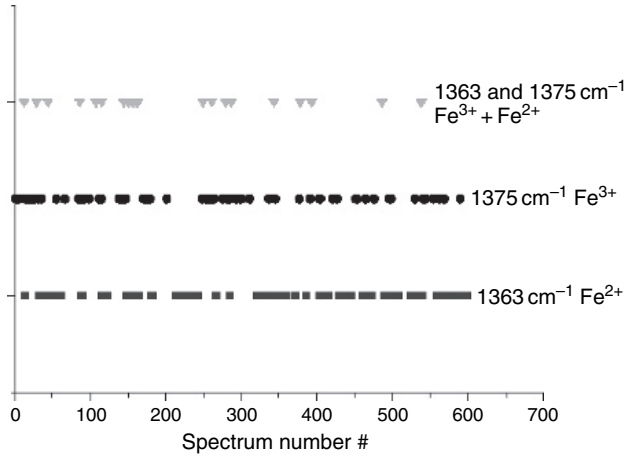

Figure 3.38: Data from 600 SERS spectra. Each point indicates the appearance of the Raman peak of marked frequency in the time sequence of the spectra from silver colloids incubated with 10^{-11} M FePP. The 1363 and 1375 cm^{-1} frequencies correspond to the ferrous and ferric oxidation state in the protoprotein (from ref. [54]). (Reproduced from A.R. Bizzarri and S. Cannistraro, 'Evidence of electron-transfer in the SERS spectra of a single iron-protoporphyrin IX molecule', *Chemical Physics Letters*, Vol. 395, pp. 222–226. Copyright 2004, Elsevier; reproduced with permission.)

From this point of view, it is interesting to note that the tip/substrate–molecule/macromolecule contacts, which are based on the thiol group capacity of forming strong bonds with gold, also 'blink', i.e., fluctuate between closed (ON) and open (OFF) circuits in a manner that is very similar to the fluctuations observed in single-molecule fluorescence and SERS. An example is provided by stochastic conductance switching between simple molecules such as octane, decane and dodecane-dithiols bonded to an Au(111) surface or even with the top gold contact pressed at constant force against the tip of an AFM [55] (see also [53], Bizzarri and Cannistraro). In this case, the effect seems to be due to the swing mobility of molecules attached to the gold surface, which allows them to explore different local environments on the nanoscale.

The generality of the blinking phenomenon extends to its statistics. A particularly detailed SERS study of the blinking statistics in Fe-protoporphirin IX demonstrates that the vibrational mode time fluctuations obey Lévy statistics and show aging and non-ergodicity characteristics [56].

The blinking effect contains important and detailed information on the nanoparticle dynamics as well as the fluctuations of its environment, the coupling between the tip (or SERS substrate) and the adsorbed molecule, and on the photoinduced effects during an optical measurement. On the other hand, blinking may pose strong limitations to the use of single molecules or nanoparticles as sensors or other applications, since its time scale is on the same scale as that of the sensing activity. See [49] for a remedial pathway to the blinking problem; in this case, fluorescence blinking is removed by engineering the rate constants for the intersystem crossing between singlet and triplet states, one of the main mechanisms for blinking. The engineering was accomplished by decreasing the PSD of the triplet states, which increases the singlet state fluorescence and 'fills up' the OFF time slots, as can be seen in Fig. 3.39.

We wish to conclude by reporting on a measurement which allows the separation of blinking from photobleaching in single-molecule spectroscopy. Since the time scales of the two processes are similar, when performing a statistical analysis of the data, the two may interfere, leading to erroneous estimates. An interesting modification of single-molecule imaging, which involves the use of wide-field illumination, allows the identification of the two channels [57]. The image field is about $100 \times 100\,\mu^2$, which allows to observe many fluorescent molecules simultaneously and follow them in a time series of images. Using the fact that bleaching is irreversible and taking into account the initial dark states of the molecules, the two processes can be separated and, therefore, the correct values of the relevant

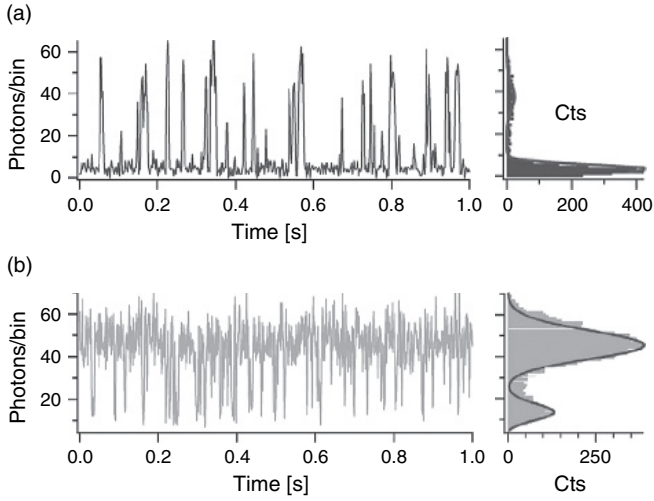

Figure 3.39: Fluorescence time traces (1 s measurement time) for a standard molecule (upper trace) and 'engineered' molecule (lower trace). The corresponding histograms are shown on the right. (Reprinted with permission from F.D. Stefani, K. Vasilev, N. Bocchio, F. Gaul, A. Pomozzi, and Kreiter, *New Journal of Physics*, Vol. 9, p. 21 (2007). Copyright (2007) IOP Publishing Limited.)

parameters (decay times, rate constants, statistics) determined. This, by the way, provides an improved experimental technique to study single-molecule fluorescence since it features the multiplex advantage of getting information for each frame from many single molecules simultaneously instead of a single one.

Another issue of relevance here is single-molecule fluorescence, which uses PCS techniques for analysing data [58]. For instance, Fore et al. [58] showed that using sophisticated experimental and statistical analyses the discrete distribution of DNA-conjugated dyes could be precisely determined, together with their stoichiometry, at the single molecule level in protein–protein and protein–nucleic acid complexes. Antibunching photon correlations and the second-order time correlation function of fluorescence intensity fluctuations were obtained from nanosecond resolved determination of the time of arrival distribution of single photons. It is interesting to note that the photon coincidences were assessed using the Hanbury-Brown and Twiss stellar interferometer [59], originally developed to determine the size of distant stars!

Photon antibunching (a 'dead' time due to the finite fluorescence lifetime of excited electronic states) yields a precise determination of the small number of fluorescent molecules in the excitation volume, and hence it allows to distinguish between a discrete number of different molecules in individual complexes. The technique was tested on DNA hairpin complexes labelled with one, two or three Atto655 fluorescent dyes. In Fig. 3.40, we show typical results.

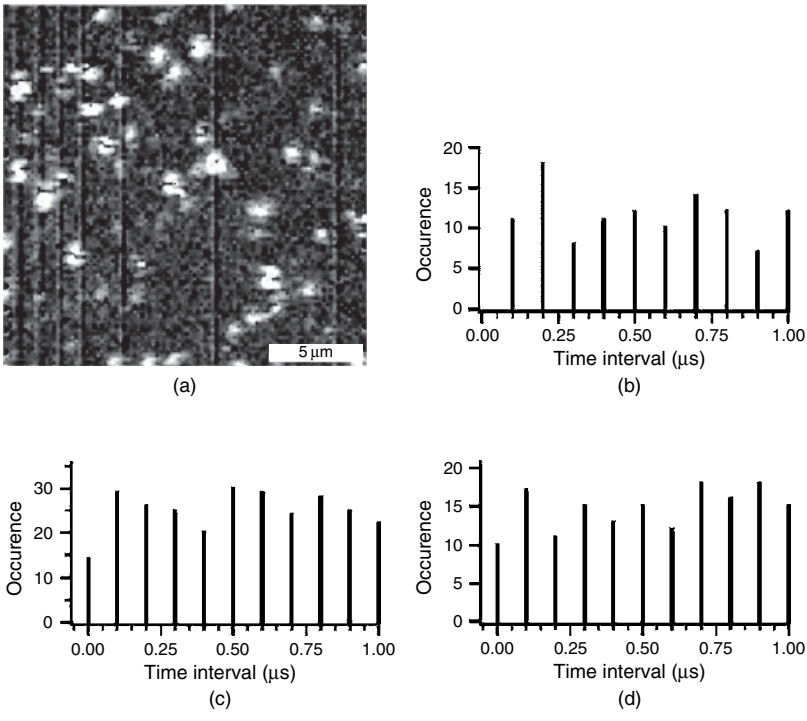

Figure 3.40: Typical single-molecule image of labelled (one dye molecule) DNA hairpin complex (a); the lower panels show the antibunching correlation plots: (b) from image (a); (c) and (d) from images similar to (a) but with DNA complexes containing two and three dye molecules respectively. (Reproduced with permission from S. Fore, T.A. Laurence, Y. Yeh, R. Balhorn, C.W. Hollars, M. Cosman, and T. Huster, 'Distribution analysis of the photon correlation spectroscopy of discrete numbers of dye molecules conjugated to DNA', *IEEE Journal of Selected Topics in Quantum Electronics*, Vol. 11, pp. 873–880 (2005). Copyright 2005, IEEE.)

From the correlation plots, it is clear that, with only one dye molecule, the area of the peak for coincident events (zero time) is zero and so is the ratio between it and the average area of the time delayed peaks; such ratio grows to 0.58 for two molecules and 0.71 for three molecules, thus allowing a precise measure of stoichiometry at the single-molecule level.

The PCS techniques can be also applied when fluorescence lifetime fluctuations are considered instead of the more typical intensity fluctuations. In [26], this technique coupled with lifetime tuning was used to study diffusional dynamics of fluorophores in lipid membranes. The technique allows the simultaneous determination of diffusion coefficients of identical molecules localized in different environments. Lifetime tuning to obtain the maximum contrast is accomplished by locating some of the chromophores close to a light absorbing surface (metal or semiconductor), such as f.i. ITO glass; the tuning is obtained by using different quenching effects of different surfaces. The strong dependence of the quenching effect on distance from the surface allows to differentiate diffusion in two and three dimensions respectively.

Photon correlation spectroscopy techniques have also been used when the sources are synchrotron radiation X-rays. In this case, for instance, the diffusion and relaxation in a carbon black filled elastomer under an applied stress were studied [60].

3.4.2. Surface Plasmon Engineering and Sensors

One important application of nanosystems is the development of devices that are potentially capable of sensing to the level of single molecules and in a space-resolved way down to the nanoscale. Here, we shall discuss a few applications involving advanced spectroscopic techniques.

Certainly the electronic states in granular or nanostructured metallic surfaces are the most important material ingredients in nanospectroscopies. Thus, it is natural to expect that, with appropriate ‘engineering’, localized surface plasmon or phonon polaritons could be a useful probe. In Figs 3.41 and 3.42, we show a good example of ‘engineering’ possibilities, which are based on the strong sensitivity of optical spectra of colloidal nanoparticles on shape, anisotropy and composition [A8]. Figure 3.41 presents the absorption spectra of gold nanospheres and nanorods (panel a), and the absorption spectrum and Mie theory fit for a gold–silver nanoparticle alloy (panel b). Clearly, all the important resonance behaviours can be strongly

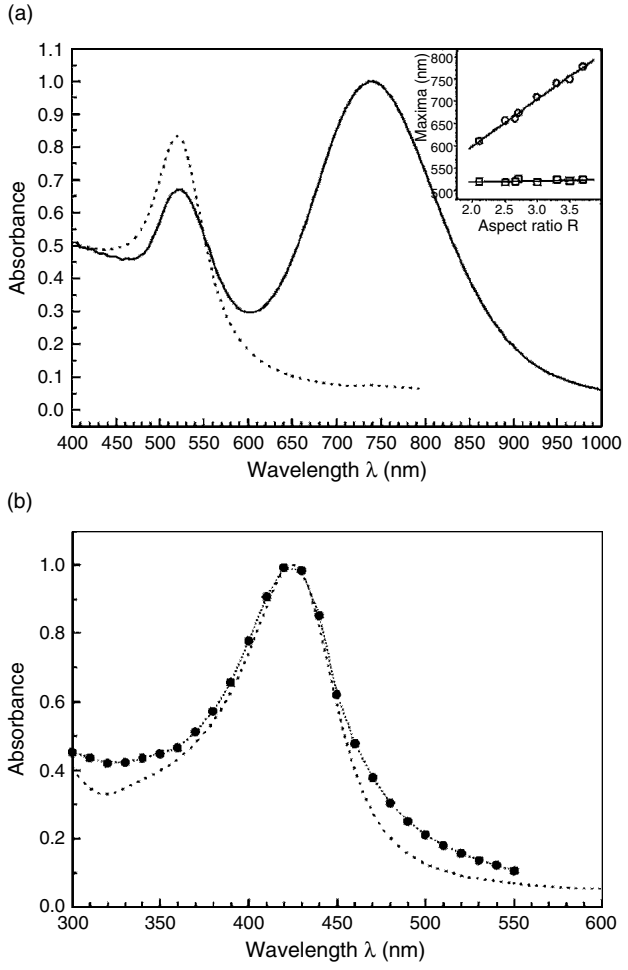

Figure 3.41: Absorption spectra of 22 nm gold nanodots (dotted line) and rods (aspect ratio $R = 3.3$, solid line). The dependence of the absorption maximum for the rods on R is shown in the inset (a); absorption spectrum of Au-Ag alloy nanoparticles with a gold mole fraction concentration of 0.27 and the calculated spectrum from Mie theory (b). (Reproduced with permission from the *Annual Review of Physical Chemistry*, Vol. 54. Copyright 2003, Annual Reviews, www.annualreviews.org).

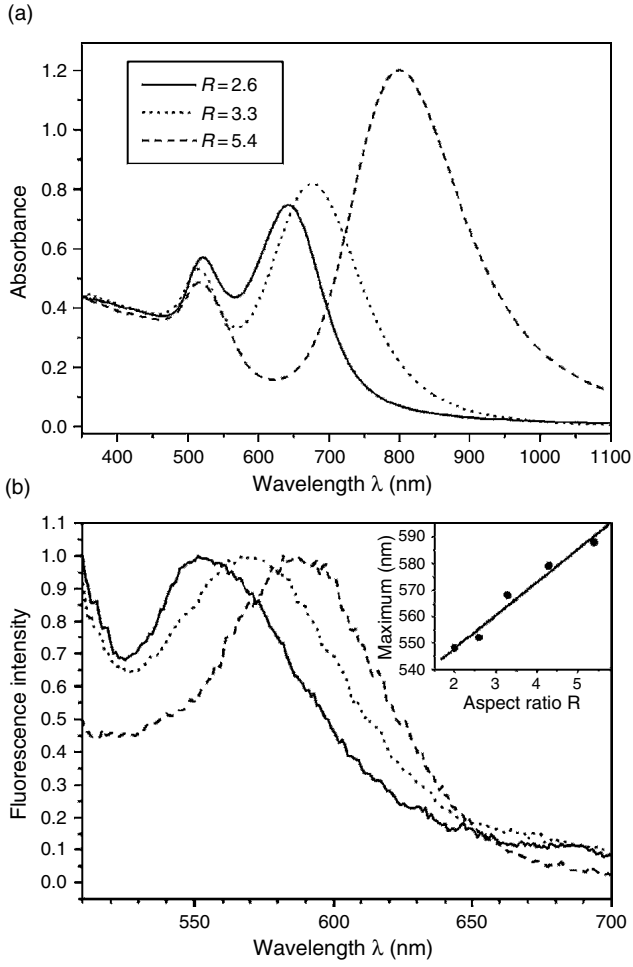

Figure 3.42: Dependence of absorption (a) and luminescence (b) spectra of gold nanorods on the aspect ratio *R*. The inset shows that the luminescence maximum depends linearly on *R*. (Reproduced with permission from the *Annual Review of Physical Chemistry*, Vol. 54. Copyright 2003, Annual Reviews, www.annualreviews.org.)

modified to suit the specific requirements of experiments (such as SERS or SMFS) and applications.

A good review of how to prepare SERS-effective nanostructured substrates with an eye to sensor applications can be found in [61]. As an

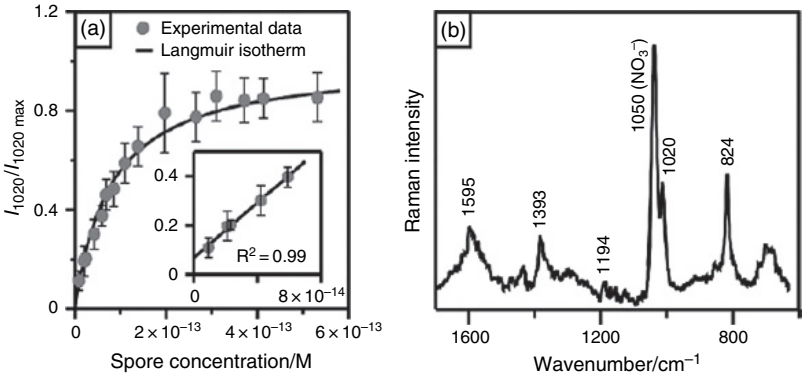

Figure 3.43: Adsorption isotherm (yielded by the Raman intensity at $1020\,cm^{-1}$) of a *Bacillus subtilis* spore suspension on an AgFON (Ag film over (gold) nanosphere) substrate. Note the extremely low range of spore concentrations (left panel); SERS spectrum of a 2.1×10^{-14} M spore suspension on AgFON. Excitation at 750 nm, power 50 mW, acquisition time 60 s. (Reprodued from C.L. Haynes, C.R. Yonzon, X. Zhang, and R.P. Van Duyne, 'Surface-enhanced Raman sensors: early history and the development of sensors for quantitative biowarfare agent and glucose detection', *Journal of Raman Spectroscopy*, Vol. 36, pp. 471–484 (2005). Copyright John Wiley and Sons Limited; reproduced with permission.)

example, in Fig. 3.43, we have shown a Raman sensor that can detect deadly bacterial spores at extremely low concentrations; here the actual experiment was performed – may be for safety – on a harmless look-alike of *Bacillus anthracis*.

The combined results of experimental preparation and theory have recently led to novel ways of employing SERS in Raman nanospectroscopic sensors [62].

For instance, using an adaptive SERS substrate, a sensitive protein sensor has been proposed to separate two isomers of insulin: human insulin and its analogue insulin lispro. The two differ only for the interchange of two neighbouring aminoacids; such small difference may have important clinical consequences in the treatment of diabetes. Under protein deposition, the nanostructured adaptive silver substrate modifies the local morphology so that SERS is optimized and the conformational state of the protein is preserved. In Fig. 3.44, we show the SERS spectra of two forms of insulin, wherein the differences allow their separation. The spectra were taken at

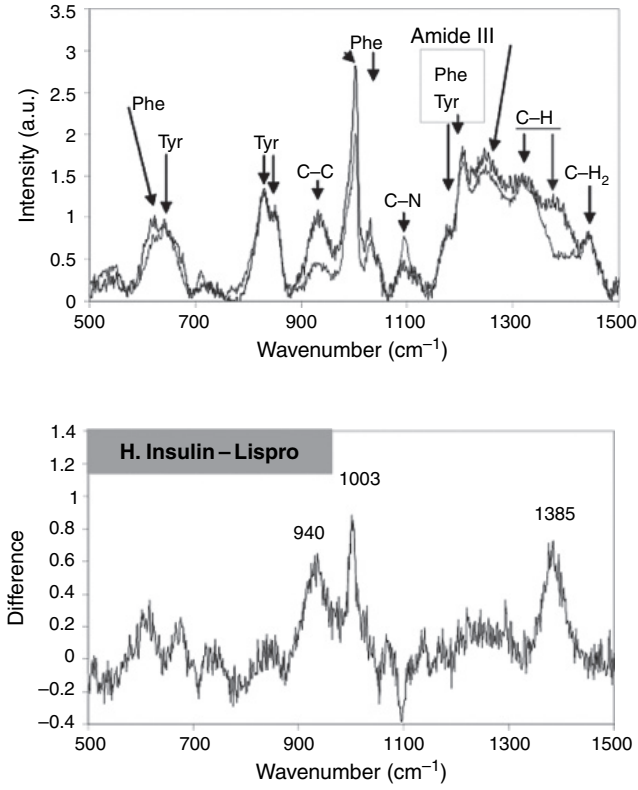

Figure 3.44: SERS spectra of H. insulin and Lispro, upper panel; difference spectra, lower panel. (Reproduced with permission from V.P. Drachev, M.D. Thoreson, E.N. Khaliullin, V.J. Davisson, and V.M. Shalaev, *Journal of Physical Chemistry B*, 108, 18046–18052 (2004). Copyright 2004, American Chemical Society.)

the submonolayer density of 80 fmol mm^{-2} (i.e., 20 attomol in the probed area) with an enhancement factor of 3×10^6 [63].

As a final example, we shall discuss a spectroscopic sensor in which the active part is an AFM acting as a local infrared absorption probe [64]. This sensor is capable of performing chemical mapping with nanoscale lateral resolution. Here the process involves the detection by the AFM tip of enhanced lateral deformation when the excitation laser is tuned to

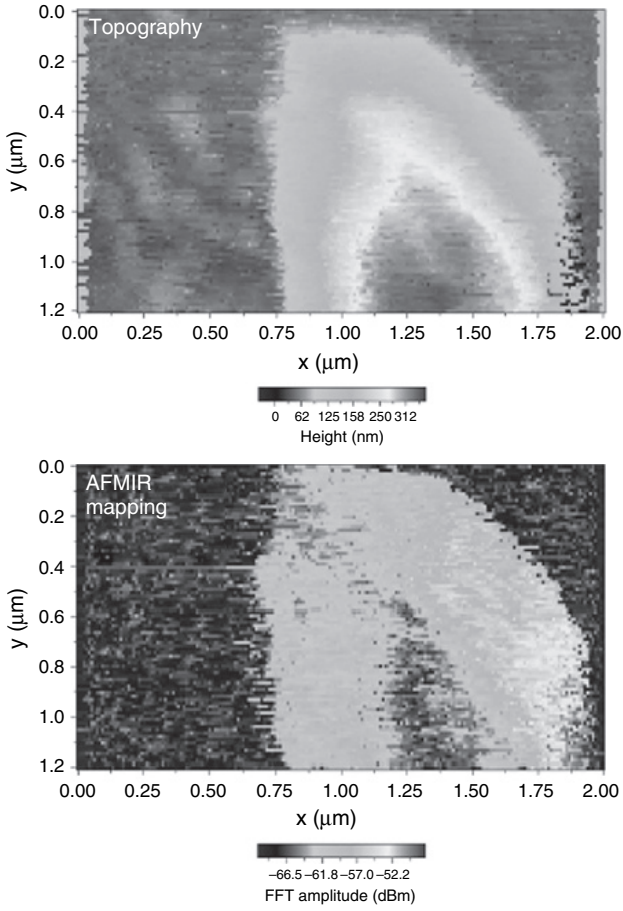

Figure 3.45: Bacterium AFM topography (top panel) and corresponding chemical map using the 1550 cm^{-1} amide I band as the spectroscopic probe. (Reproduced from A. Dazzi, R. Prazeres, F. Glotin, and J.M. Ortega, 'Subwavelength infrared spectromicroscopy using an AFM as a local absorption sensor', *Infrared Physics and Technology*, Vol. 49, pp. 113–121, Copyright 2006, Elsevier; reproduced with permission.)

one of the infrared oscillation frequencies of the material under study. Figure 3.45 shows the chemical mapping of *Eschirichia coli* bacteria with this sensor. By changing the resonance wavelength of excitation, different space chemical structures can be resolved of the scale of AFM.

3.4.3. Quantum Dots and Nanoparticles

Here we present some interesting applications of nanoparticles to nanotechnologies.

A typical example is a more than 10-fold increase of photoluminescence from a light emitting diode. An InGaN quantum well is taken over which, on one side, a rough layer of either Ag or Al was deposited [65]. The layer roughness was estimated to be about 40 nm. Au films did not show the effect, probably because gold generally quenches luminescence. The luminescence data are shown in Fig. 3.46.

Nanocrystals and nanoclusters can be quite useful as sensing elements (Fig. 3.47). A particularly important application of these is in biological systems [66]. Here we show an example of the use of enhanced luminescence [67] in gold nanoparticle (GNP) arrays or rods [68].

These systems feature a tuneable plasmon resonance in the near-infrared. Colloidal gold nanoparticles functionalized with surfactant reorcinarene

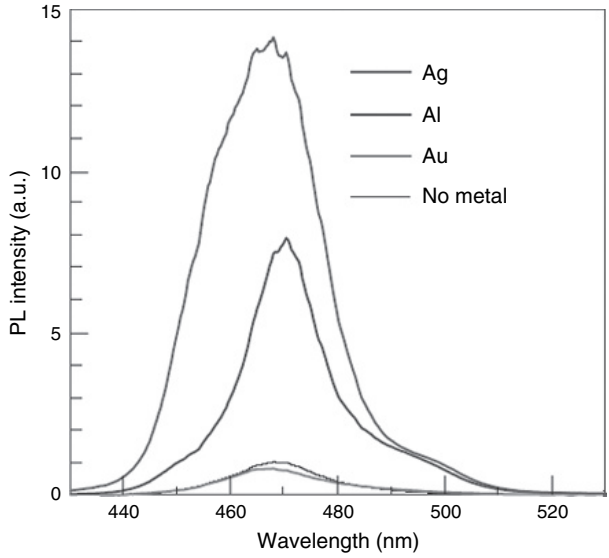

Figure 3.46: Luminescence from an InGaN quantum well as a function of metal film covering on one side. (Reproduced from K. Okamoto, I. Niki, A. Shvartser, Y. Narukawa, T. Mukai, and A. Scherer, *Nature Materials*, Vol. 3, p. 601 (2004). Copyright 2004, Macmillan Publishers Ltd; reproduced with permission.)

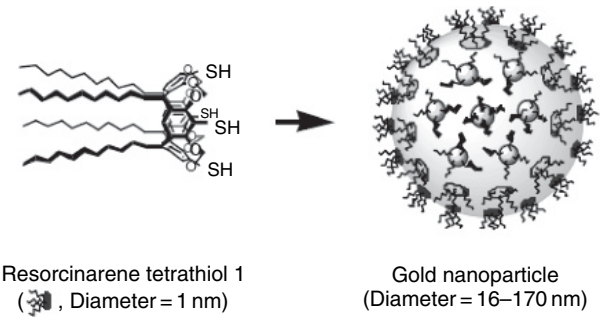

Figure 3.47: Resorcinarene functionalized GNPs. (Reproduced with permission from A. Wei, *e-J. Surf. Sci. Nanotech* 4, 9 (2006).)

tetrathiol (in order to avoid aggregation) of sizes up to 170 nm were self-assembled in regular 2D arrays. These arrays can attach to cells and form excellent substrates for SERS for cell detection (Fig. 3.48).

Another useful nanosystem is gold nanorods, which features a strong two-photon luminescence. Images of single rods have been produced in vivo inside the blood vessels of a mouse using this property [69]. The gold particles were injected at picomolar concentration into an anaesthetized mouse by tail vein injection. After a few minutes, the two-photon monitoring signal from the earlobe began to be seen as intermittent bursts of an intensity at least a factor of three greater than the autofluorescence background from the blood and the vessel. Another advantage of this technique is that the nanorod luminescence does not seem to show any bleaching. A magnificent image is shown in Fig. 3.49.

Finally, we present an application of GNPs to the fabrication of a high-sensitive, inexpensive DNA sequencer [70].

GNPs are functionalized with thiolated DNA probe strands, which can recognize complementary DNA targets. The solution of such particles is red in color due to a sharp plamon resonance of the GNPs. If a solution of DNA target molecules is mixed with the targets, besides hybridizing the GNP, surface-immobilized DNA strands act as linkers between different GNPs, producing a network of correlated GNPs, which turn the color of the solution to purplish-blue (λ_{max} shifts from 520 to 574 nm). This yields a sensitive colorimetric assay of hybridization, as shown in Fig. 3.50.

Single-molecule sensitivity is in principle obtainable using the SERS effect. In Fig. 3.51, a possible scheme for heterogeneous GNP detection assay is shown.

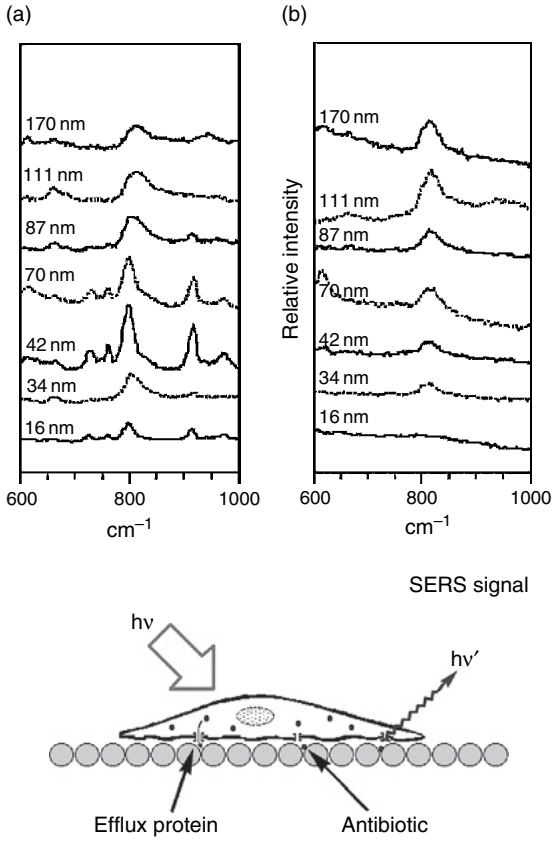

Figure 3.48: Tunable SERS from the GNP arrays (left panels); the spectra were excited at 647 nm (left) and 1064 nm (middle); on the right is a sketch of the SERS detection of biochemical transport with such device. (Reproduced with permission from A. Wei, *e-J. Surf. Sci. Nanotech* 4, 9 (2006).)

Here, the functionalized GNPs are immobilized onto a glass substrate target sequence array, in which a laser probe light is scattered by the GNPs via evanescent wave total reflection coupling. Using the size dependence of light scattering intensity, hybridization can be monitored from the intensity variation of the scattered light (whichcan be seen with the naked eyes for high target concentrations). At low concentrations (attomolar to picomolar), the GNP signal is amplified by electrochemical deposition of Ag onto the GNPs. A further improvement – to add color (i.e., multispectral

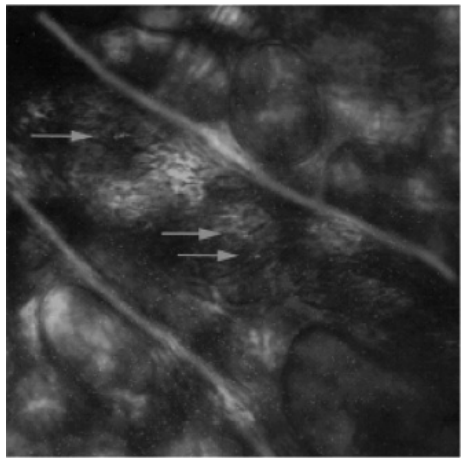

Figure 3.49: Still image of two-photon excited luminescence ($\lambda = 830\,\text{nm}$) from single gold nanorods (red dots) as they flow through the blood vessel in a mouse ear. (Reproduced from C.S. Thaxton, D.G. Geogranopoulou, and C.A. Mirkin, 'Gold nanoparticle probes for the detection of nucleic acid targets', *Clinica Chimica Acta*, Vol. 363, pp. 120–126. Copyright 2006, Elsevier; reproduced with permission.)

fingerprints) to the ensuing grey scale readout and eventually reach single-molecule sensitivity – is to detect the SERS-amplified Raman scattering signal from the hybridized complex. This requires a further encoding of the DNA complex with an appropriate Raman active molecule. The assay demonstrated a sensitivity of $1\,\text{fmol}\,\text{l}^{-1}$ target concentration. Above all, there were no photobleaching effects. Hence, there is very high specificity contrast and high discrimination against single nucleotide polymorphisms (mismatches). Finally, the very high sensitivity may make enzymatic amplification (e.g. PCR) unnecessary.

3.4.4. Polarization and Anisotropy Effects

Let us discusse the polarization characteristics of single-molecule fluorescence or Raman spectra. The polarization of emitted light is connected with the local anisotropy of polarizability tensor and system symmetry. The degree of polarization yields information on molecular (or nanoparticle) orientation and its dynamics [71]. A typical example was provided

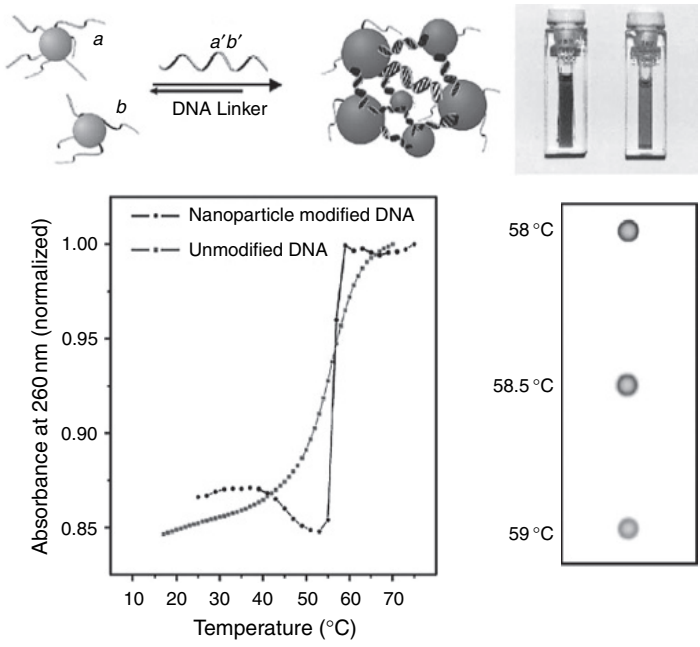

Figure 3.50: Absorbance modification of DNA-functionalized GNPs according to their aggregation state. If the GNPs are functionalized with non-complementary strands a and b, there is no aggregation and the color is red. If instead a solution of complementary a′, b′ strands is added, the color turns to bluish-purple. In the lower left panel, the temperature dependence of absorption in the DNA-sensitive UV range shows a striking sharpening of the reverse transition. This is clearly evidenced in the lower right panel. (Reproduced from C.S. Thaxton, D.G. Geogranopoulou, and C.A. Mirkin, 'Gold nanoparticle probes for the detection of nucleic acid targets', *Clinica Chimica Acta*, Vol. 363, pp. 120–126. Copyright 2006, Elsevier; reproduced with permission.)

by the micro-photoluminescence study of anisotropic confinement of excitons in GaAs/AlGaAs quantum dots [72]. Using a modified epitaxial growth technique, larger and strongly anisotropic quantum dots can be produced, and single-dot photoluminescence spectra can be taken at 10 K. The crystalline quality of the samples was such that very sharp exciton recombination fluorescence spectra could be obtained and studied as a function of excitation intensity and emission spectra polarization. In Fig. 3.52, such polarized spectra are shown, which demonstrate strong anisotropic quantum confinement in these quantum dots.

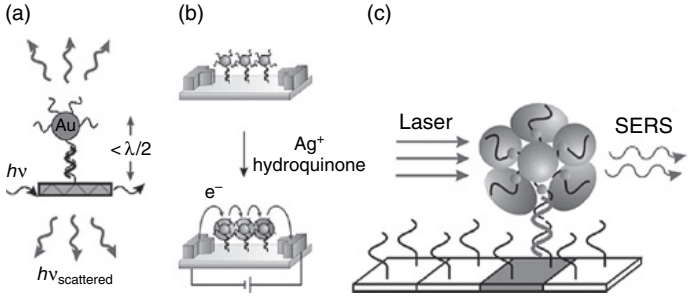

Figure 3.51: Heterogeneous GNP detection assays: (a) size dependent Rayleigh scattering from functionalized GNP complexes (note the evanescent wave excitation); (b) electrochemical covering of GNPs with silver shells, and conductometric assay detection; (c) SERS readout which selects different targets through the appropriate Raman fingerprints and increases the assay sensitivity. (Reproduced from C.S. Thaxton, D.G. Geogranopoulou, and C.A. Mirkin, 'Gold nanoparticle probes for the detection of nucleic acid targets', *Clinica Chimica Acta*, Vol. 363, pp. 120–126. Copyright 2006, Elsevier; reproduced with permission.)

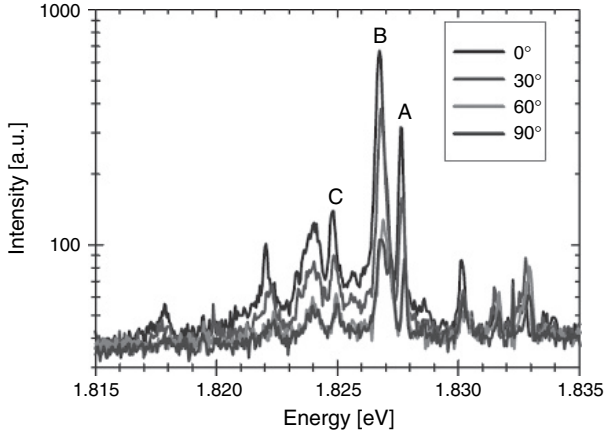

Figure 3.52: Spectral dependence of the linear polarization of exciton luminescence in a single GaAs quantum dot. A, B and C label single (a) and multiexciton (b, c) recombination lines. Note the logarithmic intensity scale. (Reproduced with permission from M. Yamagiwa, N. Kogucji, F. Saito, Y. Ogawa, and F. Minami, *e-J. Surf. Sci. Nanotech* 4, 446 (2006).)

An interesting imaging study of the orientation of single molecular transition dipole moments is reported in [73]. Here single-molecule polarized luminescence photoexcitation spectra were taken at 1.7 K in n-hexadecane polycrystalline matrices; the fluorophores dissolved in the matrix were terrylene or diperinaphthylenpyren. The experimental set-up was designed to take advantage of the multiplex detection of many single molecules within the field of view. In Fig. 3.53, we show the single-molecule transition dipole imaging.

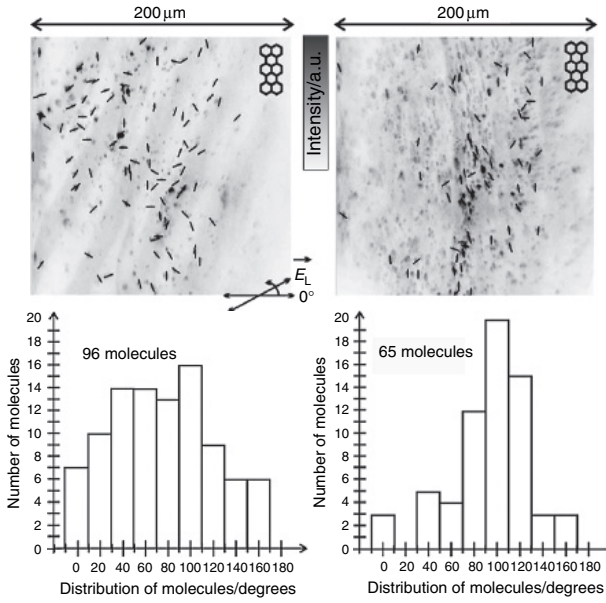

Figure 3.53: Polarization microscopy from single-molecule polarized photoexcitation spectra of terrylene in an n-hexadecane matrix. The single molecules appear as dark spots (inverted intensity scale). Superimposed on each molecular image is a dark bar that indicates the transition dipole moment orientation of the photoluminescence transition. The two panels refer to two different experiments, one performed in an area of the matrix where the fluorophores were more randomly oriented (left), the other where there was more anisotropy and hence orientation (right). The corresponding orientation histograms are shown in the lower panels. (Reproduced from T.Y. Latychevskaia, A. Renn, and U.P. Wild, 'A single-molecule study of polycrystalline microstructure by fluorescence polarization spectroscopy', *Journal of Luninescence*, Vol. 118, pp. 111–122. Copyright 2006, Elsevier; reproduced with permission.)

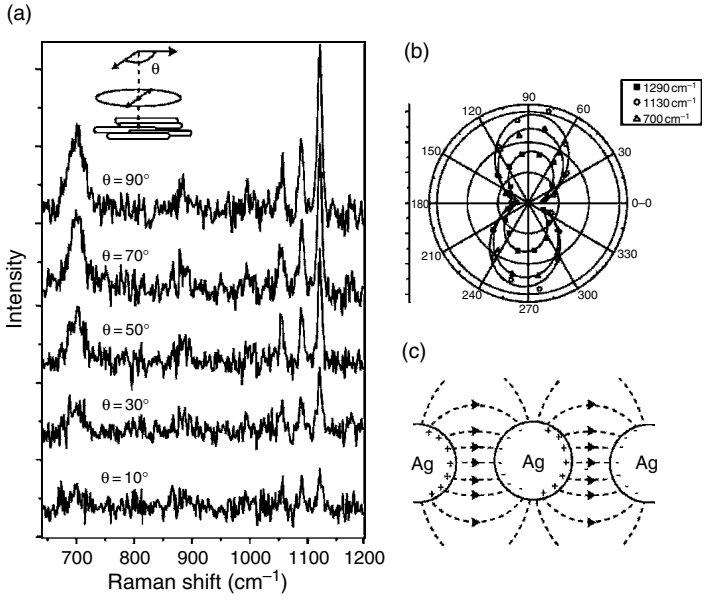

Figure 3.54: Polarized SERS spectra of adsorbed 1-isodecanethiol on a silver nanowire monolayer. The spectra were taken for different orientations of incident light polarization relative to the nanowire long axis. (Reproduced with permission from A.R. Tao and P. Yang, *Journal of Physical Chemistry B*, 109, 15687–15690 (2005). Copyright 2005, American Chemical Society.)

It is well known about TERS that maximum enhancement can be obtained if the electric field polarization of the incident light is parallel to the tip axis; this is a simple consequence of tip symmetry, and other polarizations can be enhanced only if the experimental symmetry is somewhat changed. In Fig. 3.54, we show the polarized SERS spectra of 1-hexadecanethiol on a monolayer of aligned Ag nanowires [74]. The spectra were taken for different polarization orientations of the incident electric field relative to the nanowire long axis. Clearly, the spectra are well polarized, and the intensity of the main peaks decreases strongly as the angle θ changes by 90°. The anisotropy is clearly evidenced in the polar diagram, which refers to the intensities of three selected peaks. The explanation to why maximum signal is obtained for $\theta = 90°$ becomes apparent from the symmetry of field distribution in part (c) of the figure.

3.4.5. Innovative Methods and Results

Here we shall discuss some select recent developments in nanoscience in which advanced optical spectroscopies play a central role. We start with the description of an interesting instrumentation – a versatile, multifunctional microscope that features both far-field Raman and TERS capabilities [75]. It combines an atomic force microscope, an inverted confocal microscope and a piezo stage to perform fast and accurate tip–laser alignment and characterize large areas under constant illumination across the surface (Fig. 3.55). The instrument allows simultaneous measurements (and hence comparison under the same environment conditions) of far-field micro-Raman and TER spectra on nano-objects and single molecules with short exposure times.

The instrument is calibrated using SWCNT and BCB molecules dispersed onto a glass substrate. AFM images and far-field and near-field Raman spectra could be taken simultaneously. In Fig. 3.56, we show the BCB spectra in normal and TERS configurations. As shown in the figure, the estimated enhancement was about two orders of magnitude, but with better tip functionalization much higher enhancements are expected.

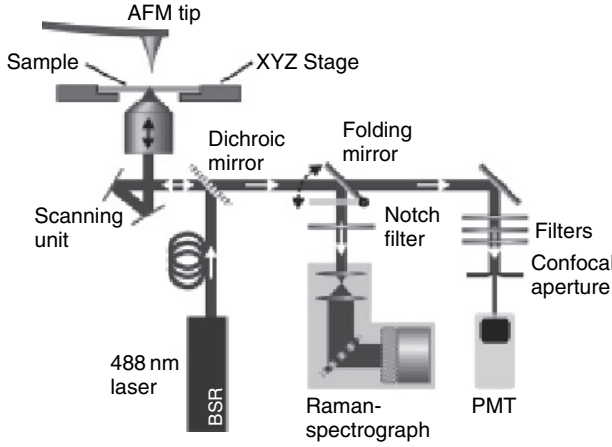

Figure 3.55: Scheme of the multifunctional AFM-Raman microscope. (Reproduced with permission from C. Vanner, B.-S. Yeo, J. Melanson, and R. Zenobi, 'Multifunctional microscope for far-field and tip-enhanced Raman spectroscopy', *Review of Scientific Instruments*, Vol. **77**, 023104 (2006). Copyright 2006, American Institute of Physics.)

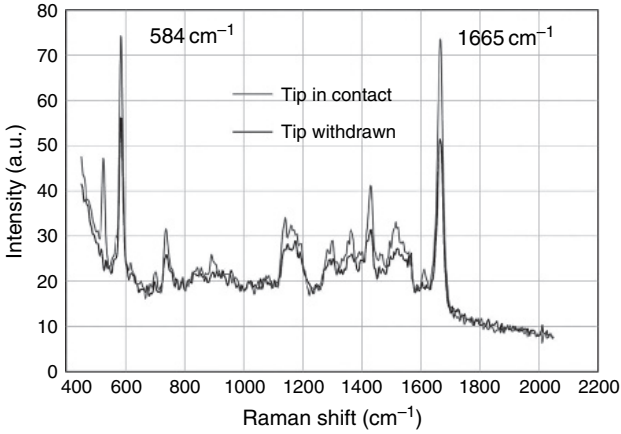

Figure 3.56: Normal (black line) and tip-enhanced (grey line) Raman spectra of BCB. (Reproduced with permission from C. Vanner, B.-S. Yeo, J. Melanson, and R. Zenobi, 'Multifunctional microscope for far-field and tip-enhanced Raman spectroscopy', *Review of Scientific Instruments*, Vol. **77**, 023104 (2006). Copyright 2006, American Institute of Physics.)

Besides, the instrument is versatile in that it allows the measurements to be taken on a simple glass substrate, which greatly simplifies the procedures.

In the following, we shall discuss an application of single quantum dot two-photon excited fluorescence to minimally invasive optical microendoscopy. This is an example of the impressive progress these techniques have contributed to very diverse fields, namely neurophysiology and nanomedicine. In Fig. 3.57, we show a schematic of the apparatus used.

The endoscope ends with a GRIN (three-layer GRaded INdex) lens, which acts as a large-aperture microscope inside the animal. Its size generally varies between 300 and 1000 μm, and it helps to take images within a micron-scale field. A great advantage of this technique is the possibility of real-time probing of neuronal processes deep (up to several millimeters) into the cerebral cortex, thus minimizing the need for invasive surgery or tissue excision. For simpler and faster imaging (albeit losing in-depth imaging), one photon microfluorescence can be used. In this case, the cellular activity can even be video-recorded. For two-photon spectroscopy, the laser used for excitation is a Ti:S femtosecond pulse laser. For linear spectroscopy, other types of lasers may be used, depending on the optics of fluorescent labels.

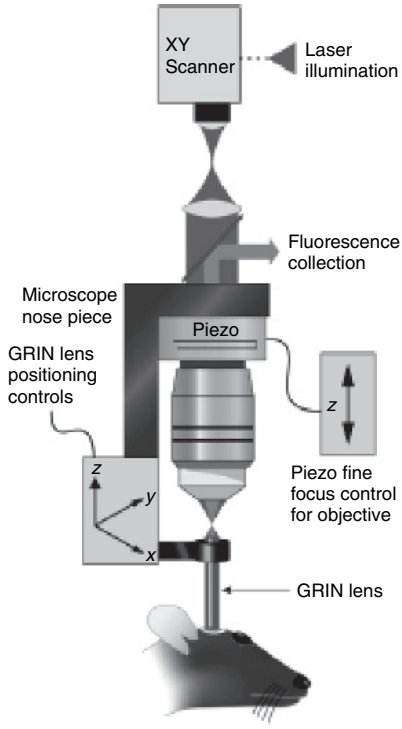

Figure 3.57: Typical experimental arrangement for multiphoton fluorescence microspectroscopy used in conjunction with a GRIN lens based endoscope. Note the two focus arrangement with fine positioning controls for both the endoscope and the microscope objective, yielding a confocal type geometry (from ref. [76]).

In Fig. 3.58, we show in vivo imaging deep (about 1 mm or more) inside the cerebral cortex of single cells (neurons, dendrites). In panels (a–c), we show the images of cell bodies containing yellow fluorescent protein in the area of layer V neurons of the cortex; observe the neuron body, the dendrites and the axon issuing from it. In panel D, the details of an axon are shown; scale bar: 10 μm [76].

The faster frame rate possible with one-photon-excited fluorescence allows to probe the cellular activity in real time. In Fig. 3.59, we show some images taken with this technique using the confocality of the system due to the two focus set-up; this allows good depth resolution, without

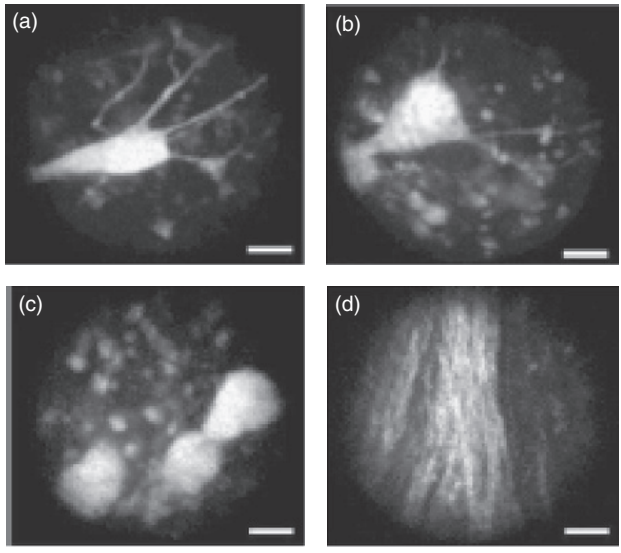

Figure 3.58: In vivo imaging, deep into the cerebral cortex of line H anesthesized mice, of single cell bodies in neuronal cells by two-photon excited single quantum dot fluorescence (adapted from ref. [76]).

moving the endoscope; the system focus inside the animal is instead varied by the fine z- scan of the microscope objective [77].

The type of microendoscopy possible with single nanodot and single-molecule one-photon and two-photon microfluorescence should provide a robust experimental tool to meet the new challenges posed to in vivo cellular imaging by new synthetic or genetically encoded fluorophores that label specific locations in the brain.

An interesting development in single-molecule near-field spectroscopy is the use of free electron laser (FEL) as the infrared source [78]. Such a source couples the tunability of an ordinary continuous spectrum source with the intensity, directionality and monochromaticity of a laser. The experimental set-up is shown in Fig. 3.60.

Although the work uses the aperture NSOM instead of the more advanced apertureless techniques, it still shows the potential for the use of FEL, by producing chemically resolved images of single biological cells; furthermore, it allows the measurements of samples in water, which is a desirable characteristic for biological systems. In any case, the shear force resolution achieved is 50 nm, and the optical resolution is 100 nm,

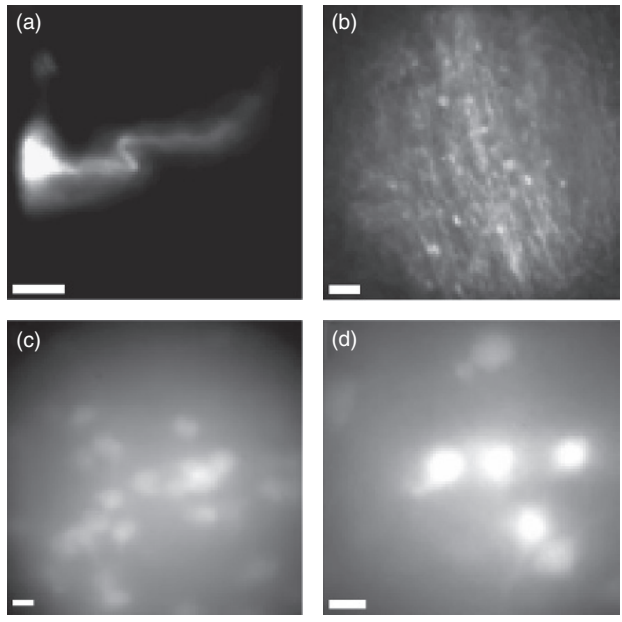

Figure 3.59: Mammalian neurons imaged in vivo by one-photon fluorescence microspectroscopy: (a) neuron in the infragranular somatosensory complex of an anesthesized rat; the GRIN lens had a working distance of 130 μm, 0.48 NA, 1000 μm diameter. For the frames B, C, D, the working distance was longer (390 μm) and this allowed probing deeper regions; in particular, without moving the endoscope, the system was focussed on basal dendrites in stratum oriens (b), or on pyramidal cells in stratum pyramidale (c, d). Scale bar 10 μm (from ref [77]).

which corresponds for the wavelengths used to about $\lambda/70$. In Fig. 3.61, we show the NSOM reflection images of rat panchreatic β line (INS-1) cell as compared with the topographic images [79]. The left panel shows the topographic images, which are independent of the IR excitation wavelength. In the right panel, we can observe the chemical contrast images: the darker areas correspond to absorption at the incoming radiation wavelength. Note that there is no constrast in image (d), since at a wavelength of 6.45 μm there is no absorption. At the wavelengths of 6.1 μm (b) and 6.95 μm (f), the absorption corresponds to the vibrational modes of amide I and amide II, respectively. Clearly, the dark distribution is different for the two images, showing the chemical contrast imaging capabilities of the technique.

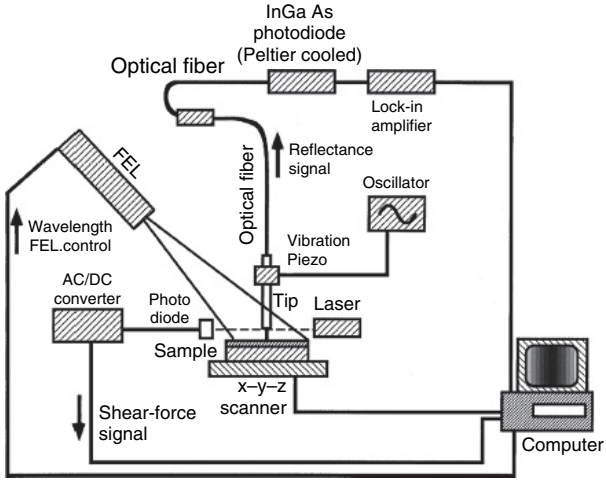

Figure 3.60: Schematic of the FEL-NSOM instrument. (Reproduced with permission from A. Cricenti, R. Generosi, P. Perfetti, J.M. Gilligan, N.H. Tolk, C. Coluzza, and G. Margaritondo, 'Free-electron-laser near-field nanospectroscopy', *Applied Physics Letters*, Vol. 73, pp. 151–153 (1998). Copyright 1998, American Institute of Physics.)

Although in this chapter we have mainly discussed linear spectroscopies (apart from the two-photon fluorescence), we wish to present an application of one of the most well known non-linear optical effects, namely coherent Anti-Stokes Raman spectroscopy (CARS) [80]. CARS was detected in the TERS mode, i.e., TE-CARS. It is related to the third-order non-linear susceptibility and is due to a four-wave mixing process. This implies the use of three incoming light frequencies: ω_1 (pump), ω_2 (stokes) and again ω_1 (probe), chosen such that $2\omega_1 - \omega_2 = \omega_{CARS}$, the frequency of induced oscillation of non-linear susceptibility. When the difference $\omega_1 - \omega_2$ equals a Raman frequency of the sample, the Anti-Stokes Raman signal is generated in a direction depending on precise phase-matching conditions. The use of tip enhancement, which implies an active volume of size much smaller that light wavelength, relaxes these conditions, allowing Raman imaging of the sample. Thus, the tip not only enhances the signal but also, due to its high space localization, simplifies the conditions which otherwise would strongly limit the usefulness of the technique.

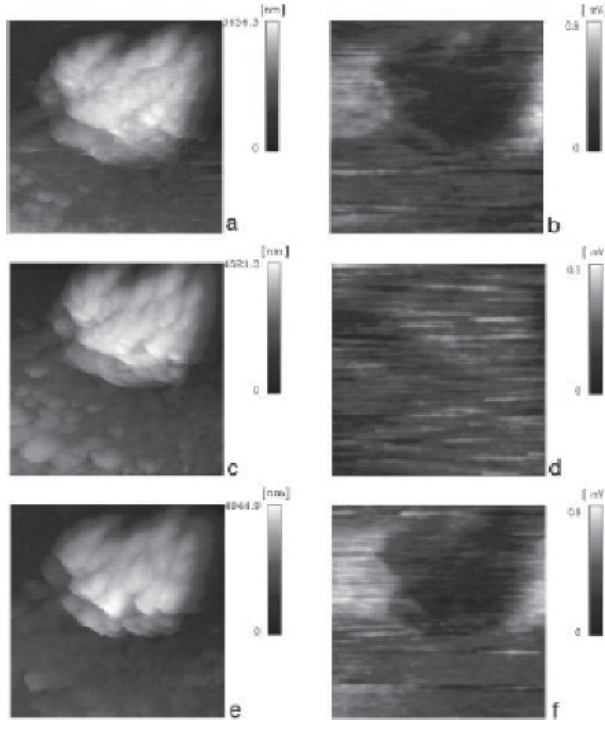

Figure 3.61: FEL excited NSOM reflection images of a single INS-1 cell at different wavelengths in the infrared (right panels); corresponding topographic images (left panel); the area covered by the image is $20\,\mu m^2$. (Reproduced with permission from A. Cricenti, R. Generosi, M. Luce, P. Perfetti, G. Margaritondo, D. Talley, J.S. Sanghera, I.D. Aggarwal, N.H. Tolk, A. Congiu-Castellano, M.A. Rizzo, and D.W. Piston, *Biophysical Journal*, 85, 2705 (2003). Copyright 2003, Biophysical Society.)

The experimental setup is shown in the Fig. 3.62 [81].

The sample studied with TE-CARS were DNA oligomer bundles about 20 nm thick and 100 nm wide. The Ti:S lasers were tuned to yield $\omega_1 - \omega_2 = 1337\,cm^{-1}$, i.e., the Raman frequency of the diazole ring breathing mode of adenine. The imaging background was determined by shifting the frequencies to a non-resonant range, where no CARS should be seen.

In Fig. 3.63, we show some images of TE-CARS.

The figure clearly shows the position of adenine in the DNA helix strand at 370 and 700 nm (the latter being well defined). The estimated

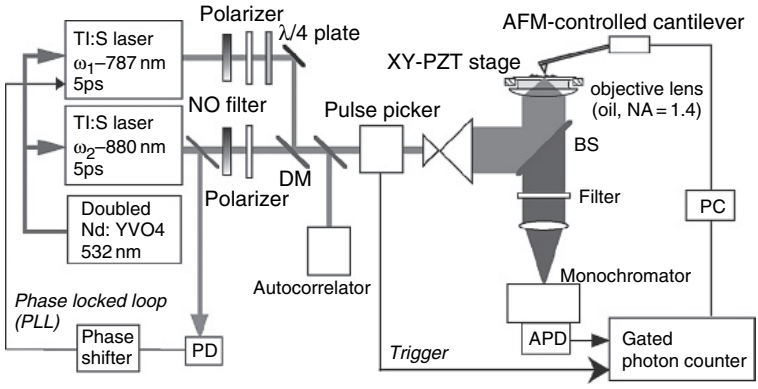

Figure 3.62: Experimental set-up for TE-CARS. For the experiment, the two Ti:S lasers were tuned at 787 and 880 nm respectively. The third laser, Nd-YAG, was frequency doubled yielding 532 nm to pump the Ti:S lasers. (Reproduced with permission from T. Ichimura, N. Hayazawa, M. Hashimoto, Y. Inouye, and S. Kawata, *Phys. Rev. Lett*., 92, 220801 (2004). Copyright 2004, American Physical Society.)

enhancement factor was nearly 100, and the sampled volume was nearly 1 zeptoliter (zl)! Clearly, the 'ordinary' tip enhancement, coupled with the smallness of the probed volume and the stronger Raman signals that the CARS technique inherently provides, makes this technique powerful. The main disadvantages of this technique include higher complexity and cost of the apparatus.

In recent years, with the development of third and fourth generation synchrotron radiation sources, full advantage could be taken of specific characteristics such a brilliance, continuous spectrum from the hard X-ray to the far-infrared regions, beam collimation and ultrashort pulse time structure. Although it is beyond the scope of this chapter to cover many of the other applications, we would like to conclude with an interesting example in advanced spectroscopies using synchrotron radiation. For other interesting work, we refer the reader to the reviews [A4] and the papers listed in [12].

Let us discuss the development of subnanosecond, time-resolved, broadband infrared spectroscopy using a pump-probe configuration in which the pump is a Ti:S laser pulse of 2 ps duration and the probe is a synchrotron radiation pulse (100 ps duration) in the infrared. Due to the broadband spectrum of synchrotron emission, a very extended spectral

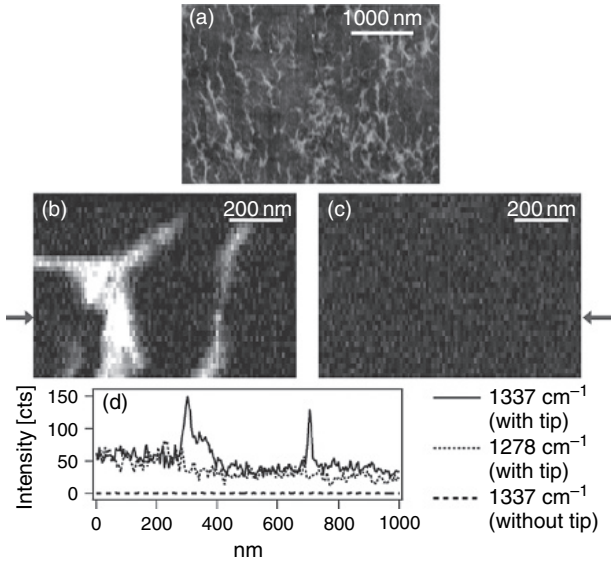

Figure 3.63: TE-CARS imaging of the DNA network: (a) topographic AFM image; (b) on-resonant image; (c) off-resonant image (background); (d) line profiles at position 270 nm; the scanned area was 1000 nm × 800 nm, acquisition time was 12 minutes per image and the average excitation powers were 45 and 23 μW for ω_1 and ω_2, respectively. (Reproduced with permission from T. Ichimura, N. Hayazawa, M. Hashimoto, Y. Inouye, and S. Kawata, *Phys. Rev. Lett*., 92, 220801 (2004). Copyright 2004, American Physical Society.)

range (20–20 000 cm^{-1}) can be probed with the same set-up [82,83]. A block diagram is shown in Fig. 3.64. The pump–probe configuration allows to determine the time dependence of spectra after perturbation, and hence to study the photoinduced phenomena in the samples. Furthermore, due to the high collimation of synchrotron radiation infrared pulse, the spectra can be taken with diffraction limited spatial resolution.

The confocal optics, coupled with the high collimation and brilliance of synchrotron radiation, allows to push the space resolution limit to about 5 μ, i.e., to perform single-cell scans in biological systems (Fig. 3.65). A very interesting application can be seen in Fig. 3.66.

One of the clear features of the Alzheimer's disease is the presence of amyloid plaque in the diseased tissues, which limits the blood flow and eventually causes atrophization of the neurons. The space-resolved spectra clearly demonstrate this in a chemically sensitive mapping of the area. In

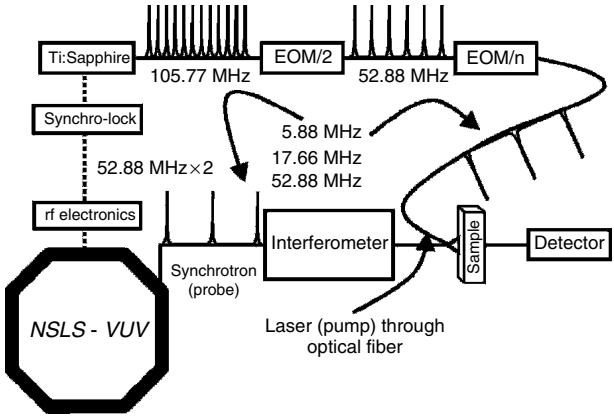

Figure 3.64: Block diagram of the IR spectrometer facility at NSLS. (Reproduced with permission from R.P.S.M. Lobo, J.D. LaVeigne, D.H. Reitze, D.B. Tanner, and G.L. Carr, 'Subnanosecond, time-resolved, broadband infrared spectroscopy using synchrotron radiation', *Review of Scientific Instruments*, Vol. 73, pp. 1–10 (2002). Copyright 2002, American Institute of Physics.)

particular, the β-amyloid protein amide I band, essentially due to α-helix amide I vibration, in the pathological area is found to split with a strong extra component at $1626\,cm^{-1}$ due to the formation of β sheets; this is a clear indication of protein misfolding, which is thought to lead to plaque build-up.

3.4.6. 'Normal' Spectroscopy on Nanostructured Systems

It is advisable to exploit the impressive enhancements of SERS, TERS, etc., wherever possible. However, in many real-life cases where a material, or a device, must be studied 'as is' on the microscopic scale, it may not be possible to use the enhancements to arrive at the single molecule or single nanostructure level; in some cases, it may not even be interesting. Toward the end of this chapter, we would like to report on some interesting results obtained with 'conventional' optical spectroscopies.

Recently, an electrochemically controlled conducting polymer device with asymmetric non-linear behaviour was described [84]. Such a device was constructed by fabricating a structure composed of two electrodes connected to the active channel of a thin (50 nm) film of polyaniline (PANI)

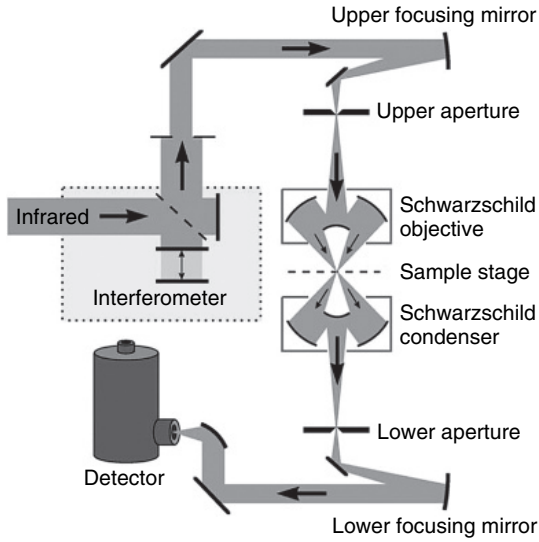

Figure 3.65: Scheme of the Spectra-Tech Irμs™ scanning infrared microinterferometer used in the NSLS facility. Note the confocal-like arrangement, which allows to perform microspectroscopy on a few microns scale, even at the long infrared wavelengths studied. (Reproduced from L.M. Miller, G.D. Smith, and G.L. Carr, 'Synchrotron-based biological microspectroscopy: from the mid-infrared through the far-infrared regimes', *Journal of Biological Physics*, Vol. 29, 2003, pp. 219–230, Figure 3. Copyright 2003, Springer; reproduced with kind permission from Springer Science and Business Media.)

covered in the central part by a stripe of $LiClO_4$-doped polyethylene oxide (PEO) with attached third (gate) electrode. The heart of its functioning was the modification of electronic conductivity of doped PANI by a voltage driven ionic flux into and out of the polymeric conductor through a heterojunction with solid electrolyte. The device showed strong nonlinear behaviour and out-of-equilibrium oscillations. This was connected with spatial heterogeneity of the system, which passed from conducting to insulating as the ions crossed the interface in a way that was dependent on the applied polarity and hence the position along the long axis of the interface. Since resonant Raman spectroscopy can distinguish between oxidized and reduced states of PANI, Raman spectra were taken as a function of applied voltage and time in micron-sized areas of the sample, and maps were obtained both in-plane and out-of-plane using a confocal Raman

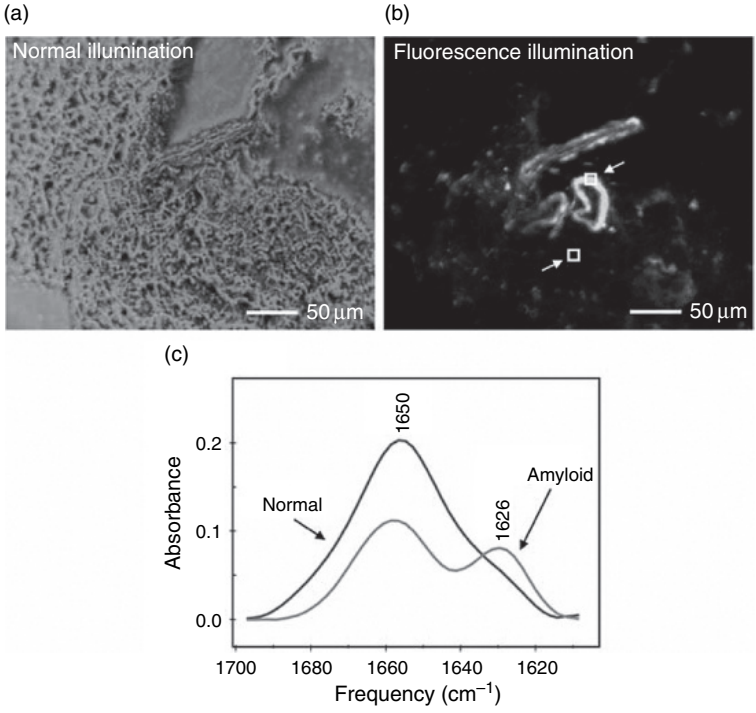

Figure 3.66: Normal microscope image of the diseased brain section of an Alzheimer patient (a) and the corresponding fluorescence microscopy image. The thioflavin-S fluorophore used stains positive to the plaque (b). In (c), the IR microspectra taken in a healthy brain tissue (lower square in (b)) and diseased tissue (upper square in (b)) clearly show important differences in the amide I spectral range. (Reproduced from L.M. Miller, G.D. Smith, and G.L. Carr, 'Synchrotron-based biological microspectroscopy: from the mid-infrared through the far-infrared regimes', *Journal of Biological Physics*, Vol. 29, 2003, pp. 219–230, Figure 2. Copyright 2003, Springer; reproduced with kind permission from Springer Science and Business Media.)

microscope [85]. In Fig. 3.67, we report the confocal micro-Raman spectra taken in the PANI-PEO junction focussing in three different characteristic areas of the device. The spectral range (about $1600\,cm^{-1}$) is sensitive to the conductive state of the material, and the spectra clearly indicate that the PANI area immediately below the PEO layer has reduced conductivity due to the Li^{+}influx. Note the strong sharp perchlorate peak, absent in

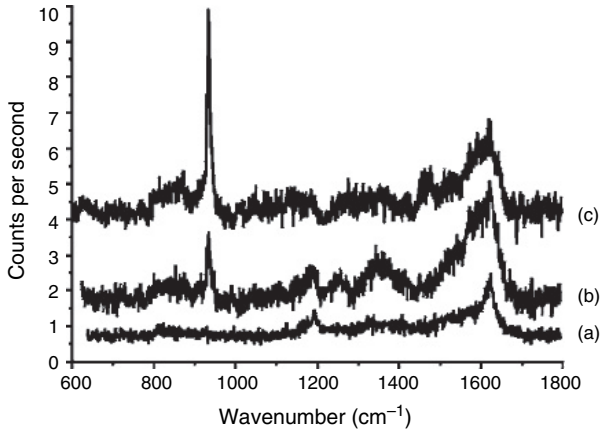

Figure 3.67: Raman spectra taken for the fully doped device; spectra acquired in the PANI-only area near the drain electrode (a); in the PEO-PANI interface but far from the Ag electrode (b); very close to the Ag electrode (c). The sharp peak at 930 cm^{-1} is due to the $(ClO_4)^-$ ion. (Reproduced with permission from T. Berzina, V. Erokhin, and M.P. Fontana, 'Spectroscopic investigation of an electrochemically controlled conducting polymer-solid electrolyte junction', *Journal of Applied Physics*, Vol. 101, 024501 (2007). Copyright 2007, American Institute of Physics.)

the PANI-only area; its intensity behaviour may be connected to SERS-like enhancement due to the silver gate electrode.

The space-resolved microspectra could be taken in real time as a function of applied voltage in the three-electrode device. In Fig. 3.68, we show the spectra taken in the PEO-PANI area in the region of the perchlorate peak taken over four voltammetric cycles of the source-drain voltage. The spectral changes are due to ionic fluxes across the interface and the ensuing changes in PANI oxidation state.

As already mentioned, the discovery of carbon nanotubes has given a boost to materials science and nanotechnology. Here we shall discuss an application of Raman spectroscopy in studying a CNT/polymer nanocomposite [86]. In order to understand the exceptional properties of CNT-based nanocomposites, it is important to assess the CNT dispersion in polymeric matrices and their interactions. This can be done by using the sensitivity of Raman spectroscopy not only to vibrational dynamics, but also to electronic states, through the resonance effects, and to local symmetry changes due

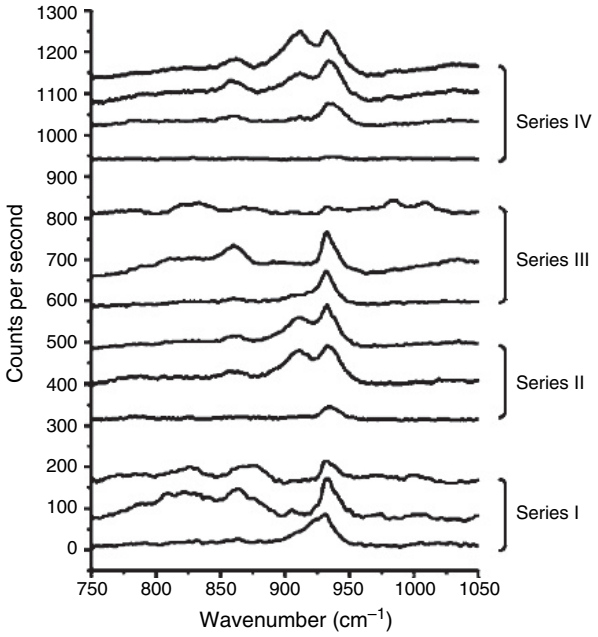

Figure 3.68: Raman spectra of the PANI-PEO heterojunction under the cyclic application of voltages of different polarity between the source and drain electrodes. (Reproduced with permission from T. Berzina, V. Erokhin, and M.P. Fontana, 'Spectroscopic investigation of an electrochemically controlled conducting polymer-solid electrolyte junction', *Journal of Applied Physics*, Vol. 101, 024501 (2007). Copyright 2007, American Institute of Physics.)

for instance to stresses or to structural transitions, through the polarization analysis of specific Raman bands.

In Fig. 3.69, we report the Raman spectrum from one nanotube of a film deposited over a Si/SiO_2 substrate and the corresponding AFM image showing isolated SWNTs [87]. As is the case with other nanoparticles whose electronic properties depend on their sizes, here too the spectrum is selected by a size-dependent resonant Raman effect. Thus, the only CNTs that are actually observed are those whose electronic states are at resonance with the excitation laser wavelength. From this effect, combined with the frequency of the radial breathing mode (RBM), it is possible to determine the CNT diameter, and from other peaks other characteristics, such as orientation and interaction with the polymeric matrix, can be determined.

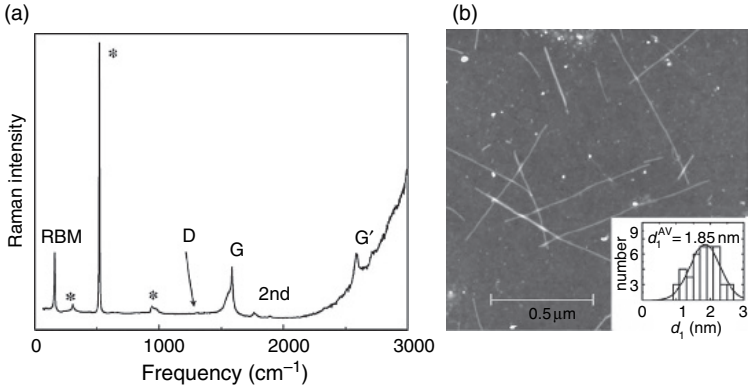

Figure 3.69: Resonant Raman spectrum of a single nanotube. The RBM is clearly evident at about 160 cm^{-1}. The very sharp intense line at 523 cm^{-1} is due to the Si in the substrate. In the right panel, the AFM image of the single nanotubes is shown. The insert shows the CNT diameter dispersion obtained by AFM imaging over 40 samples, the average being 1.85 nm. (Reproduced from M.S. Dresselhaus, A. Jorio, A.G.S. Filho, D. Dresselhaus, and R. Saito, 'Raman spectroscopy on one isolated carbon nanotube', *Physica B*, Vol. 323, pp. 15–20. Copyright 2002, Elsevier; reproduced with permission.)

It is important to note that the observed peaks are so sharp because the spectrum is taken on a single nanotube.

Clearly, such sharp and characteristic spectra can be used as microscopic probes of the composite material. As an example, in Fig. 3.70, we show the determination of micromaps of stress distribution in a CNT/polymer nanocomposite [88]. In this case, the Raman fingerprint was the $D^*(G')$ band at 2600 cm^{-1}. This band is a symmetry sensitive overtone of the D band and can be used to probe the stress state of the material. The 'calibration' of the technique was done by studying the frequency shift of the D^* band (which can be as high as 20 cm^{-1}) in a nanocomposite under an applied mechanical stress.

If the internal strain state of the material (i.e., without the action of the applied stress) is desired, the technique must be modified using the symmetry sensitivity of the D^* band, i.e., use polarized Raman scattering: the D^* band is strongly polarized along the single CNT main axis, and this implies the sensitivity to internal strain in samples with randomly oriented CNTs. Using this, a map of the strain spread from the location, where a

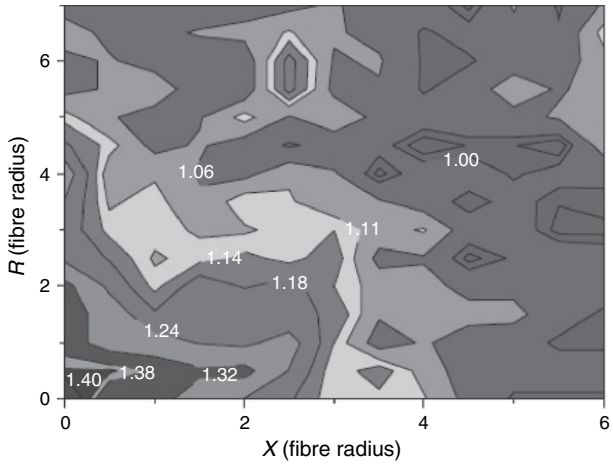

Figure 3.70: Two-dimensional contour map of stress near a single fiber break in an E-glass. The break is located at the origin; the X axis runs along the fiber length and the Y axis is perpendicular to the fiber length, the unit of length being the fiber radius (some microns). The colors code the stress intensity from red to gray. (Reproduced from Q. Zhao and H.D. Wagner, 'Two-dimensional strain mapping in model fiber-polymer composites using nanotube Raman sensing', *Composites: Part A*, Vol. 34, pp. 1219–1225. Copyright 2003, Elsevier; reproduced with permission).

small break was made in a CNT/PUA (polyurethaneacrylate) fiber glass, could be obtained as shown in Fig. 3.70.

3.5. Conclusions and Perspectives

Spectroscopic techniques have contributed extraordinary developments to nanosciences and nanotechnologies. Single-molecule sensitivity and nanoscale space resolution has been made possible by concomitant developments in imaging optics and detectors and the renaissance of research on enhancement effects due to nanostructured metallic surfaces or sharp tips. It is now possible to obtain single nanoparticle spectra that are space resolved far below the diffraction limit, time resolved to the fraction of a picosecond scale and cover not only the visible and near-UV spectral ranges but also the infrared. The very detailed studies on the nanoscale

with the new advanced techniques have had an enormous impact on our knowledge in such strategic fields as nanostructured materials and biological systems, and have allowed the emergence of absolutely new types of applications in nanomedicine, materials science and biology.

Bibliographical Appendix

[A1] (a) U. Woggen, *Optical Properties of Semiconductor Quantum Dots*, Springer, Berlin (1997). (b) A. D. Yoffe, 'Semiconductor quantum dots and related systems: electronic, optical, luminescence and related properties of low dimensional systems', Adv. Physics. 50, 1–208 (2001).

[A2] (a) P. Moriarty, 'Nanostructured materials', Repts. Progr. Phys. 64, 297–381 (2001). (b) M. J. Zehetbauer and Y. T. Zhu (eds), *Bulk Nanostructured Materials*, Wiley-VCH, Weinheim (2007).

[A3] (a) H. Takano, J. R. Kenseth, S. S. Wong, J. C. O'Brien and M. D. Porter, 'Chemical and biochemical analysis using scanning force microscopy', Chem. Rev. 99, 2845–2890 (1999). (b) D. Leckband, 'Measuring the forces that control protein interactions', Ann. Rev. Biophys. Biomolec. Struct. 29, 1–26 (2000). (c) More recent work is reviewed in H. Janovjak, A. Kedrov, D. A. Cisneros, K. T. Sapra, J. Struckmeier and D. J. Muller, 'Imaging and detecting molecular interactions of single transmembrane proteins', Neurobiol. Aging 27, 546–561 (2006).

[A4] (a) S. K. Sinha, 'Application of synchrotron radiation techniques to nanoscience', Rad. Phys. Chem. 70, 633–640 (2004). (b) G. Shenoy and P. J. Viccaro (eds), 'Applications of synchrotron radiation techniques to materials research (Special Issue)', J. Synchrotron Rad. 12, 123–253 (2005). (c) P. Suortti and W. Thomlinson, Phys. Med. Biol., 48, R1–R35 (2003). (d) A. J. Miles and B. A. Wallace, 'Synchrotron radiation circular dichroism spectroscopy of proteins and applications in structural and functional genomics', Chem. Soc. Rev. 35, 39–51 (2006).

[A5] (a) H. Dai, 'Carbon nanotubes: opportunities and challenges', Surf. Sci. 500, 218–241 (2002). (b) R. C. Haddon (ed.), 'Special issue on carbon nanotubes', Acc. Chem. Res. 35, 997–1113 (2002). (c) R. Saito, G. Dresselhaus and M. S. Dresselhaus: *Physical Properties of Carbon Nanotubes*, Imperial College Press, London, (1998). (d) For a interesting application of CNTs to AFM imaging, see J. H. Hafner, C. Cheung, A. T. Wooley and C. M. Lieber, 'Structural and functional imaging with carbon nanotube AFM probes', Progr. Biophys. Mol. Biol. 77, 73–110 (2001). (e) For a brief review on single CNT Raman spectroscopy, see M. S. Dresselhaus, G. Dresselhaus, A. Jorio, A. G. Souza Filho, M. A. Pimenta and R. Saito, 'Single nanotube Raman spectroscopy', Acc. Chem. Res. 35, 1070–1078 (2002).

[A6] (a) M. C. Petty, M. R. Bryce, and D. Bloor (eds), *An Introduction to Molecular Electronics*, E. Arnold, London (1995). (b) J. Jortner and M. Ratner, *Molecular Electronics*, Blackwell Science, New York (1997).

[A7] (a) M. Moskovits, 'Surface enhanced spectroscopy', Rev. Mod. Phys., 57, 783 (1985). (b) See also, A. Otto, 'Surface-enhanced Raman scattering: 'classical' and 'chemical' origins', in *Light Scattering in Solids IV. Electronic Scattering, Spin Effects, SERS and Morphic Effects*, M. Cardona and G. Guntherodt (eds), Springer, Berlin (1984).

[A8] S. Link and M. A. El-Sayed, 'Optical properties and ultrafast dynamics of metallic nanocrystals' Ann. Rev. Phys. Chem. 54, 331–366 (2003)

[A9] K. Kneipp, H. Kneipp, I. Itzkan, R. R. Dasari and M. S. Feld, 'Surface-enhanced Raman scattering and biophysics', J. Phys.: Condensed Matter 14, R597–R624 (2002)

[A10] (a) V. P. Ambrose, P. M. Goodwin, J. H. Jell, A. Van Orden, J. H. Werner and R. A. Keller, 'Single molecule fluorescence spectroscopy at ambient temperature', Chem. Rev. 99, 2929–2956 (1999). (b) X. Michalet, A. N. Kapanidis, T. Laurence, F. Pinaud, S. Doose, M. Pflughoefft and S. Weiss, 'The power and prospects of fluorescence microscopies and spectroscopies', Annu. Rev. Biophys. Biomol. Struct., 32, 161–182 (2003). (c) For earlier work, see X. S. Xie and J. K. Trautman, 'Optical studies of single molecules at room temperature', Annu. Rev. Phys. Chem. 59, 441–480 (1998). (d) S. Nie and R. N. Zare, 'Optical detection of single molecules', Annu. Rev. Biophys. Biomol. Struct. 26, 567–596 (1997). (e) T. Plakhotnik, E. A. Donley and U. P. Wild, 'Single-molecule spectroscopy', Ann. Rev. Phys. Chem. 48, 181 (1997).

[A11] B. Hecht, B. Sick, U. P. Wild, V. Deckert, R. Zenobi and O. J. F. Martin, 'Scanning near-field optical microscopy with aperture probes: fundamentals and applications', J. Chem. Phys. 112, 7761–7774 (2000).

[A12] S. T. Hess, S. Huang, A. A. Heikal and W. W. Webb, 'Biological and chemical applications of fluorescence correlation spectroscopy: a review', Biochemistry 41, 697–705 (2002).

[A13] (a) A. Campion and P. Kambhampati, 'Surface enhanced Raman scattering', Chem. Soc. Rev. 27, 241–250 (1998). (b) K. Kneipp, H. Kneipp, I. Itzkan, R. R. Dasari and M. S. Feld, 'Ultrasensitive chemical analysis by Raman spectroscopy', Chem. Rev. 99, 2957–2975 (1999). (c) R. F. Aroca, R. A. Alvarez-Puebla, N. Pieczonka, S. Sanchez-Cortez and J. V. Garcia-Ramos, 'Surface-enhanced Raman scattering on colloidal nanostructures', Adv. Coll. Inter. Science 116, 45–61 (2005).

[A14] L. F. Cohen (ed.), *Surface Enhanced Raman Spectroscopy*, Faraday Discussions vol. 132, RSC London (2006).

[A15] S. Kawata and V. Shalaev, *Tip Enhancement*, Elsevier, Lausanne (2006).

Bibliography

[1] (a) Zwanzig, R. (1965). Time-correlation functions and transport coefficients in statistical mechanics. *Annu. Rev. Phys. Chem*. **16**, 67–102. (b) Berne, B.J. (1971) *Physical Chemistry: An Advanced Treatise*, Vol. VIIIB (D. Henderson, ed.), New York, NY: Academic Press. (c) Gordon, R.G. (1968) Correlation functions for molecular motion. *Adv. Magn. Reson*., **3**, No. 1. (d) Wang, C.H. (1985) *Spectroscopy of Condensed Media: Dynamics of Molecular Interactions*. Orlando, FL: Academic Press.

[2] Berne, B.J and Pecora, R. (1976) *Dynamic Light Scattering with Applications to Chemistry, Biology and Physics*. New York: Wiley-Interscience.

[3] Donth, E. (2006) *The Glass Transition*. Berlin: Springer.

[4] (a) Brus, L. (1986) *J. Phys. Chem*., **90**, 2555. (b) Esaki, L. (1992) *Nanostructed Mat*., **12**, 1–8. (c) Alivisatos, A.P. (1996) *Science*, **271**, 933. (d) Xia, Y. (2003) *Adv. Mat*., **15**, 353.

[5] (a) Shi Kam, N.W., Jessop, T.C., Wender, P.A. et al. (2004) *J. Am. Chem. Soc*., **126**, 6850. (b) Pantarotto, D., Briand, J., Prato, M. et al. (2004) *Chem. Commun*., **1**, 16.

[6] For general reviews, see (a) Caruso, F. (ed.), (2003). *Colloids and Colloid Assemblies*. Weinheim: Wiley-VCH. (b) Rotello, V. (2004) *Nanoparticles*. Berlin: Springer. (c) For some biomedical applications, see (d) Fujimoto, K. Iwasaki, C. Arai, C. et al. (2000) *Biomacromolecules*, **1**, 515. (e) Hiller, R.S., Leporatti, S., Schnackel, A. et al. (2004) *Biomacromolecules*, **5**, 1580. (f) Park, J.-S., Akiyama, Y., Winnik, F.M. et al. (2004) *Macromolecules* **37**, 6786. (g) Sawant, M., Hurley, J.P., Salmaso, S. et al. (2006) *Bioconjug. Chem*., **17**, 943. (h) Roh, K.-H., Martin, D.C. and Lahann, J.J. (2006) *Am. Chem. Soc*., **128**, 6796. (i) Adiga, S.P. and Brenner, D.W. (2007) *Macromolecules* **40**, 1342.

[7] (a) Roberts, G. (ed.), (1990) *Langmuir–Blodgett Films*. New York: Plenum Press. (b) Ulman, A. (1991) *An Introduction to Ultrathin Organic Films*. Boston: Academic Press. (c) Huck, W.T.S. (ed.), (2005) *Nanoscale Assembly Techniques*. New York: Springer.

[8] For reviews, see: (a) Carter, F.L. (ed.), (1987) *Molecular Electronic Devices II*. New York: Dekker. (b) Metzger, R.M. (1994) *Adv. Chem. Ser*., **240**, 81–129. (c) McCreery, R.L. (2004) *Chem. Mater*., **16**, 4477–96. (d) Facci, P., Erokhin, V., Carrara, S. et al., (1996) *Proc. Natl. Acad. Sci. USA*, **93**, 10556. (e) Yu, L.H., Keane, Z.K., Ciszek, J.W. et al. (2004) *Phys. Rev. Lett*., **92**, 266802. (f) Flatt, A.K., Chen, B. and Tour, J.M. (2005) *J. Am. Chem. Soc*. **127**, 8918. (g) Natsui, Y., Miyoshi, Y., Ooike, N. et al. (2006) *e-J. Surf. Sci. Nanotechnol*., **4**, 180–3. (h) Natelson, D. Yu, L.H., Ciszek, J.W. et al. (2006) *Chem. Phys*., **324**, 267.

[9] (a) Kneipp, K., Kneipp, H., Bhaskaran Kartha, V. et al. (1997) *Phys. Rev*., **57**, R6281. (b) Byassee, T.A., Chan, W.C.V. and Nie, S. (2000) *Anal. Chem*.,

72, 5606–11. (c) Taylor, J.R., Fang, M.M. and Nie, S. (2000) *Anal. Chem*., **72**, 1979.

[10] For introductory reviews, see (a) Tanford, C. (1970) *Adv. Protein Chem*., **24**, 1–95. (b) Onuchic, J.N., Lutey-Schulten, Z. and Volynes, P.G. (1997) *Ann. Rev. Phys. Chem*., **48**, 545–600.

[11] (a) Kuhner, F. and Gaub, H.E. (2006) *Polymer*, **47**, 2555. (b) Zhang, Q. and Marszalek, P.E. (2006) *Polymer* **47**, 2526. (c) Sapra, K.T., Besir, H., Oesterhelt, D. et al. (2006) *J. Mol. Biol*., **355**, 640. (d) Kransnoslobodtsev, A.V., Shlyakhtenko, L.S., Ukraintsev, E. et al. (2005) *Nanomedicine* **1**, 300. (e) Sandal, M., Grandi, F. and Samorì, B. (2006) *Polymer* **47**, 2571.

[12] (a) Dumas, P. and Miller, L. (2003) *J. Biol. Phys*., **29**, 201. (b) Pechkova, E., Roth, S.V., Burghammer, M. et al. (2005) *J. Synchrotron Radiat*., **12**, 713. (c) Saito, A., Maruyama, J., Manabe, K. et al. (2006) *J. Synchrotron Radiat*., **13**, 216. (d) Azuma, J., Itoh, M., Koike, M. et al. (2006) *J. Synchrotron Radiat*., **13**, 464.

[13] (a) Dou, X., Takama, T., Yamaguchi, Y. et al. (1998) *Appl. Opt*., **37**, 759. (b) Kneipp, K., Kneipp, H., Corio, P. et al. (2000) *Phys. Rev. Lett*. **84**, 3470. (c) Puretzky, A.A., Geohegan, D.B., Fan, X. et al. (2000) *Appl. Phys. Lett*., **76**, 182. (d) Pantarotto, D., Partidos, C.D., Hoebeke, J. et al. (2003) *Chem. Biol*., **10**, 961. (e) Wong Shi Kam, N., Jessop, T.C., Wender, P.A. et al. (2004) *J. Am. Chem. Soc*. **126**, 6850. (f) Zhao, Q. and Wagner, H.D. (2004) *Phil. Trans. R. Soc. Lond. A*, **362**, 2407. (g) Dyke, C.A. and Tour, J.M. (2004) *J. Phys. Chem. A*., **108**, 11151. (h) Saito, Y., Yanagi, K., Hayazawa, N. et al. (2006) *Jpn. J. Appl. Phys*. **45**, 9286. (i) Yano, T., Verma, P. and Kawata, S. (2006) *Appl. Phys. Lett*., **88**, 93125.

[14] (a) Xia, Y. and Whitesides, G.M. (1998) 'Soft Lithography'. *Annu. Rev. Mater. Sci*., **28**, 153–84. (b) Quake, S.R. and Scherer, A. (2000) *Science* **290**, 1536. (c) Herminghaus, S. (2003) *Nat. Mater*., **2**, 11. (d) Erokhin, V., Berzina, T. and Fontana, M.P. (2004) Electron beam irradiation for structuring of molecular assemblies. *IEEE Trans. Nanobiosci*., **3**, 6.

[15] For reviews, see (a) Sleytr, U.B., Györvary, E. and Pum, D. (2003) Crystallization of S-layer protein lattices on surfaces and interfaces. *Prog. Org. Coatings* **47**, 279–87. (b) Yeates, T.O. and Padilla, J.E. (2002) Designing supramolecular protein assemblies. *Curr. Opin. Struct. Biol*., **12**, 464–70. (c) Besteman, K., Lee, J.-O., Wiertz, F.G.M. et al. (2003) *Nano Lett*., **3**, 727. (d) Berganza, J., Olabarria, G., García, R. et al. (2007) Biosens. Bioelectron. **22**, 2132. (e) Krieg, A., Ruckstuhl, T. and Seeger, S. (2006) *Anal. Biochem*. **349**, 181. (f) Shim, J.W. and Gu, L.Q. (2007) *Anal. Chem*. **79**, 2207.

[16] (a) Buckland, R.M. (1986) Nature, **320**, 557. (b) Weber, P.C., Ohlendorf, D.H., Wendoloski, J.J. et al. (1989) *Science*, **243**, 85. (c) Chilkoti, A., Tan, P.H. and Stayton, P.S. (1995) *Proc. Natl. Acad. Sci. USA*, **92**, 1754. (d) Freitag, S., Le Trong, I., Klumb, L. et al. (1997) *Protein Sci*. **6**, 1157. (e) Gonzalez, M., Bagatolli, L.A., Echabe, I. et al. (1997) *J. Biol. Chem*., **272**, 11288. (f) Li, M. and Mann, S. (2004) *J. Mat. Chem*., **14**, 2260. (g) Pincet, F.

and Husson, J. (2005) *Biophys. J*., **89**, 4374. (h) Holmberg, A., Blomstergren, A., Nord, O. et al. (2005) *Electrophoresis*, **26**, 501.

[17] (a) Bonnet, G., Krichevsky, O. and Lichaber, A. (1998) *Proc. Natl. Acad. Sci. USA*, **95**, 8602. (b) Weiss, S. (2000) *Nature Struct. Biol*., **7**, 724–9. (c) Deniz, A.A., Laurence, T.A., Beligere, G.S. et al. (2000) *Proc. Natl. Acad. Sci. USA*, **97**, 5179–84. (d) Schuler, B., Lipman, E.A. and Eatin, W.A. (2002) *Nature* **419**, 743. (e) Lipman, E.A., Schuler, B., Bakajin, O. and Eaton, W.A. (2003) *Science* **301**, 1233. (f) Rhoades, E., Gussakowsky, E. and Haran, G. (2003) *Proc. Natl. Acad. Sci. USA*, **100**, 3197. (g) Schuler, B. (2005) *Chemphyschem* **6**, 1206. (h) Kuzmenkina, E.V., Heyes, C.D. and Nienhaus, G.U. (2005) *Proc. Natl. Acad. Sci. USA* **102**, 2754. (i) Cannone, F., Bologna, S., Campanini, B. et al. (2005) *Biophys. J*., **89**, 2033. (j) Antia, M., Islas, L.D., Boness, D.A. et al. (2006) *Biomaterials*, **27**, 679. (k) Kim, D.Y., Gray, J.K. and Barbara, P.F. (2006) *Synth. Metals* **156**, 336.

[18] (a) Murza, A., Sanchez-Cortes, S. and Garcia-Ramos, J.V. (1998) *Biospectroscopy*, **4**, 327. (b) Vo-Dinh, T., Stokes, D.L., Griffin, G.D. et al. (1999) *J. Raman Spectr*., **30**, 785. (c) Ke, W., Zhou, D., Wu, J. et al. (2005) *Appl. Spectr*., **59**, 418. (d) Cao, Y.W.C., Jin, R. and Mirkin, C.A. (2002) *Science*, **297**, 1536. (e) Bell, S.E.J. and Sirimutu, N.M.S. (2006) *J. Am. Chem. Soc*., **128**, 15580.

[19] (a) Habuchi, S., Cotlet, M., Gronheid, R. et al. (2003) *J. Am. Chem. Soc*., **125**, 8446.

[20] (a) Takeuchi, O., Ayoama, M., Oshima, R. et al. (2004) *Appl. Phys. Lett*., **85**, 3268. (b) Shigekawa, H., Takeuchi, O. and Ayoama, M. (2005) *Sci. Technol. Adv. Mater*., **6**, 582–8.

[21] (a) Weiss, S. (1999) *Science*, **283**, 1676. (b) Moerner, W.E. and Orrit, M. (1999) *Science* **283**, 1670. (c) Ishijima A. and Yanagida, T. (2001) *Trends Biochem. Sci*., **26**, 438.

[22] Barnes, M.D., Lermer, N., Kung, C.Y. et al. (1997) *Opt. Lett*. **22**, 1265.

[23] Synge, E.H. (1928) *Philos. Mag*., **6**, 356.

[24] Elson, E.L. and Madge, D. (1974) *Biopolymers* **13**, 1.

[25] Diaspro, A. (ed.) (2001) *Confocal and Two-Photon Microscopy: Foundations, Applications and Advances*, Wiley, London.

[26] Benda, A., Fagul'ova, V., Deyneka, A. et al. (2006) *Langmuir* **22**, 9580.

[27] Fleishmann, M., Hendra, P.J. and McQuillan, A.J. (1974) *Chem. Phys. Lett*., **26**, 163.

[28] Albrecht, M.G. and Creighton, J.A. (1977) *J. Am. Chem. Soc*., **99**, 5215.

[29] Jeanmarie, D.L. and Van Duyne, R.P. (1977) *J. Electroanal. Chem*. **84**, 1.

[30] Kneipp, K., Wang, Y., Kneipp, H. et al. (1996) *Phys. Rev. Lett*., **76**, 2444.

[31] Kneipp, K., Wang, Y., Kneipp, H. et al. (1997) *Phys. Rev. Lett*., **78**, 1667.

[32] Nie, S. and Emory, S.R. (1997) *Science*, **275**, 1102.

[33] (a) Novotny, L., Pohl, D.W. and Hecht, B. (1995) *Opt. Lett*., **20**, 970. (b) Gadenne, P., Quelin, X., Ducourtieux, S. et al. (2000) *Physica*, **B279**, 52. (c) Ducourtieux, S., Podolskiy, V.A., Gresillon, S. et al. (2001) *Phys. Rev*.,

B64, 165403. (d) Podolski, V.A., Sarychev, A.K. and Shalaev, V.M. (2003) *Opt. Express*, **11**, 735. (e) Notingher, J. and Elfick, A. (2005) *J. Phys. Chem. B*, **109**, 15699. (f) Tao, A.R. and Yiang, P. (2005) *J. Phys. Chem. B Lett*., **109**, 15687.

[34] Han, W., Durantini, E.N., Moore, T.A et al. (1997) *J. Phys. Chem. B*, **101**, 10719.

[35] (a) Hillenbrand, R., Taubner, T. and Keilman, F. (2002) *Nature* 418, 159. (b) Anderson, M.S. (2003) *Appl. Phys. Lett*., **83**, 2964.

[36] Ocelic, N. and Hillenbrand, R. (2004) *Nat. Mater*., **3**, 606.

[37] Cvitkovic, A., Ocelic, N., Aizpurua, J. et al. (2006) *Phys. Rev. Lett*., **97**, 60801.

[38] (a) See f.i. Betzig, E. and Trautman, J.K. (1992) *Science*, **257**, 189. (b) Novotny, L., Pohl, D.W. and Hecht, B. (1995) *Opt. Lett*. **20**, 970. (c) Martin, O.J.F. and Girard, C. (1997) *Appl. Phys. Lett*., **70**, 705. (d) Emory, S.R. and Nie, S.M. (1997) *Anal. Chem*., **69**, 2631. (e) Hecht, B., Sick, B., Wild, U.P. et al. (2000) *J. Chem. Phys*., **112**, 7761. (f) Prikulis, J., Murty, K.V.G.K., Olin, H. et al. (2003) *J. Microsc*., **210**, 269. (g) Raschke, M.B. and Lienau, C. (2003) *Appl. Phys. Lett*., **83**, 5089.

[39] Ren, B., Picardi, G. and Pettinger, B. (2004) *Rev. Sci. Instrum*., **75**, 837.

[40] (a) Ash, E.A. and Nicholis, G. (1972) *Nature*, **237**, 510. (b) Durig, U., Pohl, D.W. and Rohner, F. (1986) *J. Appl. Phys*., **59**, 3318. (c) Furukawa, H. and Kawata, S. (1998) *Opt. Comm*., **148**, 221. (d) Azoulay, J., Debarre, A., Richard, A. et al. (2000) *Appl. Opt*., **39**, 129. (e) Stockle, R.M., Suh, Y.D., Deckert, V. et al. (2000) *Chem. Phys. Lett*., **318**, 131. (f) Hayazawa, N.N., Inouye, Y., Sekkat, Z. et al. (2002) *J. Chem. Phys*., **117**, 1296. (g) Wang, J.J., Smith, D.A., Batchelder, D.N. et al. (2003) *J. Microsc*., **210**, 330. (h) Hartschuh, A. Sanchez, E. J., Xie, X.S. et al. (2003) *Phys. Rev. Lett*., **90**, 95503. (i) Neacsu, C., Dreyer, J., Behr, N. et al. (2006) *Phys. Rev*., **B73**, 193406. (j) Zhang, W., Yeo, B.S., Schmid T. et al. (2007) *J. Phys. Chem. C*, **111**, 1733.

[41] Hartschuh, A., Beversluis, M.R., Bouhelier, A. et al. (2004) *Phil. Trans. R. Soc. Lond. A*, **362**, 807.

[42] (a) Pettinger, B., Ren, B., Picardi, G. et al. (2004) *Phys. Rev. Lett*., **92**, 96101. (b) Pettinger, B., Ren, B., Picardi, G. et al. (2005) *Angew. Chem. Int. Ed*., **44**, 139.

[43] Gerton, J.M., Wade, L.A., Lessard, G.A. et al. (2004) *Phys. Rev. Lett*., **93**, 180801.

[44] Demming, A.L., Festy, F., Huang, F. et al. (2005) *J. Korean Phys. Soc*., **47**, S1.

[45] Domke, K.F., Zhang, D. and Pettinger, B. (2006) *J. Am. Chem. Soc*., **128**, 14721.

[46] Basche, T., Kummer, S. and Brauchle, C. (1995) *Nature*, 373.

[47] Nirmal, M., Dabbousi, B.O., Bawendi, M.G. et al. (1996) *Nature*, **383**, 802.

[48] (a) Vanden Bout, D.A., Yip, W.-T., Hu, D. et al. (1997) *Science*, **277**, 1074. (b) Yip, W.-T., Hu, D., Yu, J.D. et al. (1998) *J. Phys. Chem. A*, **102**, 7564.

[49] Stefani, F.D., Vasilev, K., Bocchio, N. et al. (2007) *New J. Phys*., **9**, 21, and references therein.
[50] (a) Lakowicz, J.R., Malicka, J., Gryczynski, I. et al. (2003) *J. Phys. D: Appl. Phys*., **36**, R240. (b) Rigneault, H., Capoulade, J., Dintinger, J. et al. (2005) *Phys. Rev. Lett*., **95**, 117401. (c) Farahani, J.N., Pohl, D.W., Eisler, H.J. et al. (2005) *Phys. Rev. Lett*., **95**, 17402.
[51] (a) Shlesinger, M., Zavlasldi, G.M. and Frisch, U. (1995) *Lévy Flights and Related Topics in Physics*, Berlin: Springer-Verlag. (b) For an application to blinking quantum dots, see Jung, Y.J., Barkai, E. and Silbey, R.J. (2002) *Chem. Phys*., **284**, 181.
[52] Brokmann, X., Hermier, J.P., Messin, G. et al. (2003) *Phys. Rev. Lett*., **90**, 120601.
[53] (a) Xu, H.X., Bjerneld, E.J., Kall, M. et al. (1999) *Phys. Rev. Lett*., **83**, 4357. (b) Krug, J.T. II, Wang, G.D., Emory, S.R. and Nie, S. (1999) *J. Am. Chem. Soc*., **121**, 9208. (c) Bjerneld, E.J., Johansson P. and Kall, M. (2000) *Single Mol*., **1**, 239. (d) Weiss, A. and Haran, G. (2001) *J. Phys. Chem. B*, **105**, 12348. (e) Bizzarri, A.R. and Cannistraro, S. (2005) *J. Phys. Chem. B Lett*., **109**, 16571.
[54] Bizzarri, A.R. and Cannistraro, S. (2004) *Chem. Phys. Lett*. **395**, 222.
[55] Ramachandran, G.K., Hopson, T.J. and Rawlett, A.M. et al. (2003) *Science*, **300**, 1413.
[56] Bizzarri, A.R. and Cannistraro, S. (2005) *Phys. Rev. Lett*., **94**, 68303.
[57] Gensch, T., Bohmer, M. and Aramendia, P.F. (2005) *J. Phys. Chem*., **109**, 6652.
[58] (a) Fore, S., Laurence, T.A., Yeh, Y. et al. (2005) *IEEE J. Sel. Topics Quantum Electr*. **11**, 873. (b) Miller, A.E., Fisher, A.J., Laurence, T. et al. (2006) *Proc. Natl. Acad. Sci. USA* **103**, 11136. (c) Kiraz, A., Falth, S., Becher, C. et al. (2002) *Phys. Rev*., **B65**, 161303 (R). (d) Wenger, J., Rigneault, H., Dintinger, J. (2006) *J. Biol. Phys*., **32**, SN1.
[59] Hanbury-Brown, R. and Twiss, R.Q. (1956) *Nature* **177**, 27.
[60] Livet, F., Bley, F., Ehrburger-Dolle, F. et al. (2006) *J. Sinchrotron Rad*., **13**, 453.
[61] Haynes, C.L., Yonzon, C.R., Zhang, X. et al. (2005) *J. Raman Spectrosc*., **36**, 471.
[62] (a) Doering, W.E. and Nie, S. (2002) *J. Chem. Phys. B*, **106**, 311. (b) Barnes, L., Dereux, W.L. and Ebbsen, T.W. (2003) *Nature* **424**, 824. (c) Jackson, J.B. and Halas, N.J. (2004) *PNAS* **101**, 17930. (d) Drachev, V.P., Thoreson, M.D., Khaliullin, E.N. et al. (2005) *Surf. Sci*., **597**, 102. (e) Kuncicki, D.M., Christesen, S.D. and Velev, O.D. (2005) *Appl. Spectr*., **59**, 401. (f) Chaumet, P.C., Rahmani, A. and Nieto-Vesperinas, M. (2006) *Appl. Optics*, **45**, 5185. (g) Becker, M., Sivakov, V., Andra, G. et al. (2007) *Nano Lett*., **7**, 75.
[63] Drachev, V.P., Thoreson, M.D., Khaliullin, E.N. et al. (2004) *J. Phys. Chem. B*, **108**, 18046.

[64] Dazzi, A., Prazeres, R., Glotin, F. et al. (2006) *Infrared Phys. Technol*., **49**, 113.
[65] Okamoto, K., Niki, I., Shvartser, A. et al. (2004) *Nat. Mater*., **3**, 601.
[66] Alivisatos, P. (2004), *Nature Biotechn*., **22**, 47.
[67] Krug, J.T. II, Wang, G.D., Emory, S.R. et al. (1999) *J. Am. Chem. Soc*., **121**, 9208.
[68] Wei, A. (2006) *e-J. Surf. Sci. Nanotechnol*., **4**, 9.
[69] Wang, H., Huff, T.B., Zweifel, D.A. et al. (2005) *Proc. Natl. Acad. Sci. USA*, **102**, 15752.
[70] Thaxton, C.S., Georganopoulou, D.G. and Mirkin, C.A. (2006) *Clin. Chim. Acta*, **363**, 120.
[71] (a) Ha, T., Enderle, T., Chemla, D.S. et al. (1996) *Phys. Rev. Lett*., **77**, 3979. (b) Ha, T., Glass, J., Enderle, T. et al. (1998) *Phys. Rev. Lett*., **80**, 2093. (c) For a review on protein structural dynamics studies, see Forkey, J.N., Quinlan, M.E. and Goldman, Y.E. (2000) *Prog. Biophys. Mol. Biol*., **74**, 1–35.
[72] Yamagiwa, M., Koguchi, N., Saito, F. et al. (2006) *e-J. Surf. Sci. Nanotechnol*., **4**, 446.
[73] Yu. Latychevskaia, T., Renn, A. and Wild, U.P. (2006) *J. Luminesc*., **118**, 111.
[74] Tao, A.R. and Yang, P. (2005) *J. Phys. Chem. B*, **109**, 15689.
[75] Vannier, C., Yeo, B.S., Melanson, J. et al. (2006) *Rev. Sci. Instr*., **77**, 23104.
[76] Levene, M.J., Dombeck, D.A., Kasischke, K.A. et al. (2004) *J. Neurophysiol*., **91**, 1908.
[77] Jung, J.C., Mehta, A.D., Aksay, E. et al. (2004) *J. Neurophysiol*., **92**, 3121.
[78] Cricenti, A., Generosi, R., Perfetti, P. et al. (1998) *Appl. Phys. Lett*., **73**, 151.
[79] Cricenti, A., Generosi, R., Luce, M. et al. (2003) *Biophys. J*., **85**, 2705.
[80] Shen, Y.R. (1984) *The Principles of Nonlinear Optics*. New York: Wiley.
[81] Ichimura, T., Hayazawa, N., Hashimoto, M. et al. (2004) *Phys. Rev. Lett*., **92**, 220801.
[82] Lobo, R.P.S.M., LaVeigne, J.D., Reitze D.H. et al. (2002) *Rev. Sci. Instr*., **73**, 1.
[83] (a) Dumas, P. and Miller, L. (2002) *Rev. Sci. Instr*., **73**, 1357. (b) Miller, L.M., Smith, G.D. and Carr, G.L. (2003) *J. Biol. Phys*., **29**, 219.
[84] Erokhin, V., Berzina, T. and Fontana, M.P. (2005) *J. Appl. Phys*., **97**, 64501.
[85] Berzina, T., Erokhin V. and Fontana, M.P. (2007) *J. Appl. Phys*., **101**, 24501.
[86] Zhao, Q. and Wagner, H.D. (2004) *Phil. Trans. R. Soc. Lond*., **A362**, 2407.
[87] Dresselhaus, M.S., Jorio, A., Souza-Filho, A. et al. (2002) *Physica B*, **323**, 15.
[88] Zhao, Q. and Wagner, H.D. (2003) *Composites A*, **34**, 219.

This page intentionally left blank

Chapter 4

Conducting nanocomposite systems

Esma Sezer
Department of Chemistry, Istanbul Technical University, Istanbul, Turkey

Abstract. In order to create nanocomposite materials, well-defined nanometric objects are embedded or connected together. Functional organic molecules bound to these inorganic objects modify their colloidal behavior as well as enlarge their applications. Hybrid nanocomposites are materials that contain molecules (guests) incorporated into host lattices. The hosts include both natural materials and compounds prepared by various synthetic techniques and possessing well-defined intercalation properties. In this chapter, we shall discuss hybrid inorganic–organic materials based on conducting polymers and inorganic components (such as clay, carbon materials, metal oxides). The recent developments in the four most common conducting polymers, namely polyaniline, polypyrrole, poly(*N*-vinylcarbazole), polythiophene, and their derivatives with respect to synthesis methods, types of host materials and applications have been reviewed.

Keywords: carbon, clay, conducting polymers, conductive nanocomposites, hybrid nanocomposites, metal oxides, polyaniline, polypyrrole, poly(*N*-vinylcarbazole), polythiophene.

4.1. Introduction

During the past two decades needs and request to miniaturization makes movements towards nanodimensions in many areas of technology. A tremendous amount of research has been carried out in the field of nanoscience. The essence of nanoscience is the ability to research and work at the molecular level, atom by atom, to create large molecular architectures with fundamentally new molecular organization. The future progress in such fields of

technology will be achieved with the well documented new knowledge. Owing to numerous papers published, it is impossible to review this field completely. Up to now, several review articles have been published and they were focused on the subject in different intentions to give overview of principle concept [1–26].

Terms like 'nanoparticles' and 'nanocomposites' seem to be very trendy, and are often misused in the literature for systems that do not properly fall under the label 'nano' in the sense of advertising. In order to avoid the inappropriate use of the term 'nano', there is a strong need to understand the mechanism of the formation of such materials. The important aspects of chemistry involved in the formation of these systems are uniformity, phase continuity, domain sizes and molecular mixing at the phase boundaries, all of which have a direct influence on optical, physical and mechanical properties [27].

Nanocomposites have at least one ultrafine phase dimension, typically in the range of 1–100 nm, and exhibit improved properties when compared to micro- and macro-composites. They are especially attractive because this combination allows for the incorporation of diverse functionalities and, in certain cases, the conferring of new properties as a consequence of synergistic effects [28–30].

As suggested by Gomez-Romero [12], the term 'synergy' might sound like a modern word, but it was supposedly used by the ancient Greeks, and the idea it conveys is as old as human civilization. Indeed, among ancient materials, we could find a primitive precursor of hybrid composites with synergic properties. Adobe is a mixture of clay and straw that serves as an effective structural composite material, which has been used to make bricks and walls in arid regions throughout civilizations. As research moved towards nanocomposite materials, where components interact at the molecular level, the concept of synergy took a new dimension, a chemical dimension. Hence, composites can be designed with most desirable properties of the individual constituents, and synergistic and/or complementary behavior arises from interactions between the components [31,32].

Therefore, the development of nonomaterials is a multidisciplinary field where chemists, physicists, material scientists and engineers work together with the goal of finding advanced materials that have varieties of potential end-use applications [33,34]. Numerous research publications are already available on polymer-based organic–inorganic hybrid nanocomposites. In these publications, speciality polymers as well as conventional polymers were chosen as organic components, and various metal oxides [13,35, 36], montmorillonite clay (MMT) [37–40], various allotropes of elemental

carbon, such as carbon black (CB) [41,42], acetylene black (AB) [43–45], nano-graphite [46] and buckmin-sterfullerene (BMF) [47,48], were selected as the inorganic counterpart.

Currently, a lot of research effort is devoted to hybrid inorganic–organic materials based on conducting polymers and inorganic components (amorphous mineral phase, metal particles). The combination of conducting polymers with host materials having different characteristics opens a way to new hybrid materials [49–51]. Conducting polymer-clay [52–56] and composites of conducting polymer with inorganic nanocrystals [57–63] are the mostly investigated systems.

This chapter will survey the work developed in the field of conducting polymer nanocomposites.

4.2. Classification

Depending on the techniques of composite preparation and on the kind of materials used, one can distinguish several main groups of heterogenous electrically conductive polymer composites (CPC) and nanocomposites (CPN) [49]:

(a) non-conductive polymers or polymer blends filled with inorganic conductors,
(b) conducting colloid composites, blends of processable conducting polymers (CP) and inert matrices,
(c) reticulate doped polymers consisting of crystalline networks of low-molecular-weight organic metals penetrating inert polymer matrices.

There are several criteria for classification. In the previous reviews [12, 13], polymer nanocomposites have been clasified into two main groups: inorganic in organics (IO) and organics in inorganics (OI). IO can also be divided into two groups based on the synthesis methods: chemical and electrochemical.

Chemical methods are mainly used to obtain nanocomposites with colloidal stability, improved physical and mechanical properties, magnetic susceptibility, dielectric, energy storage, piezoresisitivity, catalytic activity and surface functionalization properties.

With electrochemical methods, it is possible to produce nanocomposites having optical, electrochemical and catalytic activites favorable for charge storage systems.

Three main electrochemical strategies have been suggested for obtaining conducting polymer nanostructures [7]:

(a) *Templateless synthesis*. Following this method, nanostructures are obtained by choosing appropriate conditions of electrosynthesis at simple chemically inert electrodes.
(b) *Template-assisted synthesis*. Nanostructured templates are created on the electrode surface, and electropolymerization occurs within the channels, holes, cavities or related nanosized structural units of a template.
(c) *Molecular template-assisted synthesis*. Some molecules having nanosized cavities are arranged in a distinct way on the electrode surface to create a template. Again, electropolymerization proceeds within these cavities, leading to nanostructures of the resulting polymers. Many aspects of electrochemical synthesis of conducting polymer nanocomposites have been reviewed recently [64–67].

On the other hand, Judeinstein and Sanchez [34] classified these hybrid materials into two groups based on the nature of the interface between organic and inorganic phases. In the first group (class I), organic and inorganic compounds are linked only by weak bonds (hydrogen or van der Waals bonds), and in the second group (class II) the two phases are linked together by strong chemical (either covalent or ionic) bonds. The chemical interactions between organic and inorganic phases are very important to understand and evaluate the properties of hybrid materials.

Since 1990s, conducting polymer nanostructures (i.e., nano-rods, -tubes, -wires and -fibers) have received increased interest both academically and commercially since they combine the advantages of organic conductors with low-dimensional systems and, therefore, create interesting physicochemical properties and potentially useful applications [68–74].

One of the most important areas of research in conducting polymers concerns with the methods for making them processable. The main approaches can be divided into three groups:

(a) preparation of composites with other polymers,
(b) synthesis of soluble derivatives, and
(c) synthesis of dispersions of insoluble conducting polymers.

Polyaniline (PANI) is one of the most intensively studied conducting polymers during the last decade; it has the following properties: (a) it can be synthesized easily; (b) it is comparatively stable in air; (c) it has high conductivity; (d) it is stable and easy to fabricate; (e) it has many

prospective applications in electrochromic devices, light-emitting diodes, chromatography, secondary batteries, electrostatic discharge protection and corrosion-resistant paint [75,76].

Polyaniline is used as a model material to systematically investigate the syntheses, properties and applications of nanocomposites of conjugated polymers. It is also a unique material among the family of conducting polymers because its doping level can be readily controlled through an acid-base doping/dedoping process [77,78].

Other conducting polymers that have attracted a great deal of interest in composite preparation due to their remarkable physical and chemical properties are polypyrrole (PPy), polyvinylcarbazole (PNVCz), polythiophene (PTh) and their derivatives.

In this chapter, we will focus on the synthesis of the four most common conducting polymers (guests), namely PANI, PPy, PNVCZ, PTh and their derivatives. The recent developments in these conducting polymer nanocomposites with respect to synthesis methods, types of host materials and applications have also been reviewed.

4.3. Host and Guest Materials for Conducting Nanocomposite Systems

Host components can be divided into two main groups: amorphous mineral phase (clay, silica, graphite, carbon nanotube (CNT), mesoporous carbon and glass, etc.) and metal particles (Al_2O_3, Fe_2O_3, V_2O_5, MnO_2, ZrO_2, TiO_2, RuO_2, CuS, CdS, CdSe, Au, Ag, Cu, $CuFeS_2$, MoS_2, MoO_3, TiS_2, $MnPS_3$, etc.). These materials may also be classified as layered (clay, graphite), channeled (nanotubes), porous (mesoporous carbon and silica), crystalline networks (metal, metalloids) and inorganic gels.

Polymeric guests having linear and rigid backbones can fit into the available pore dimensions of the hosts. These polymers include PANI [79–87], PPy [88,89], PTh [90] and poly(*N*-vinylcarbazole) [91]. Other nonconducting polymers, such as polystyrene (PS) [92–94], poly(*N*-vinyl-2-pyrolidinone) [95] and poly(ethyleneoxide) (PEO) [73], have been incorporated as well. Traditionally, intercalation involves insertion of the monomer followed by radical polymerization [80] as well as aerial oxidation (in situ polymerization) [83,84,96]. Other methods include melt polymer intercalation [93,94,97,98], exfoliation-adsorption [99], template synthesis [73] and direct intercalation from solution phase [95].

The reactions carried out within the nanometric void spaces of host materials (layers, pores, channels and cavities) along with the properties and recent applications of most common host and guest materials are given below.

4.3.1. Host Materials

Clay mineral

The polymer/layered silicate nanocomposites (PLSN) have received attention as new ionic conductive materials. The ionic conductivity of nanocomposites has been found to be several orders of magnitude higher than that of the parent silica. As compared with a polymer electrolyte, nanocomposites display enhanced conductivity, mechanical stability and improved interfacial stability towards electrode materials [100].

Smectites, belonging to a group of clay minerals (layered aluminosilicates, including two-dimensional phyllosilicates), such as MMT, hectorite, saponite [101,102], and mica-type layered silicates, find a wide spectrum of practical applications, primarily by virtue of their well-pronounced intercalation properties.

Depending on the strength of interfacial interactions between the polymer matrix and layered silicate (modified or not), three different types of PLSNs are thermodynamically achievable:

Intercalated nanocomposites

The insertion of a polymer matrix into the layered silicate structure occurs in a crystallographically regular fashion, regardless of the clay-to-polymer ratio. Intercalated nanocomposites are normally interlayered by a few molecular layers of polymer. The properties of these composites typically resemble those of ceramic materials.

Flocculated nanocomposites

Conceptually, these are the same as intercalated nanocomposites. However, silicate layers are sometimes flocculated due to hydroxylated edge–edge interactions of the silicate layers.

Exfoliated nanocomposites

The individual clay layers are separated in a continuous polymer matrix by an average distance that depends on clay loading. Usually, the clay content

of an exfoliated nanocomposite is much lower than that of an intercalated nanocomposite.

Layered aluminosilicates (also referred to as 2:1 phyllosilicates, clay minerals or smectites) and their organic modifications are an important class of industrial materials. Traditionally, they have been used as absorbents to purify and decolorize liquids, as fillers in paper and rubber materials, as rheology modifiers in paints, greases, and drilling muds, and as a basein cosmetics and medicines. Most recently, they have been widely celebrated for their performance-enhancing properties when used as a nanoscale additive in plastics to generate polymer nanocomposites. Structurally, many 2:1 phyllosilicates, such as MMT, are one-dimensional crystals comprised of covalently bonded, aluminosilicate layers, 0.92 nm thick, separated by a van der Waals interlayer (gallery) containing charge-compensating alkali metals or earth cations [15].

Since clay is hydrophilic, it is necessary to make it organophilic via cation exchange, typically with alkylammonium, imidazonium or phosphonium cations, functionalizing the aluminosilicate surface and lowering interfacial free energy [103,104].

The compatibility of these organically modified layered aluminosilicates with polymers, resins or organic solvents may be engineered depending on the composition, packing density and length of these modifiers The use of organically modified montmorillonites (OMMs) as nanofillers for polymers has motivated extensive recent efforts to elucidate the factors that dictate the structure of organic surfactant within the interlayer gallery and thus to understand better the underlying factors determining their compatibility and interfacial properties with various polymers [93,94,105].

Vermiculite, a mica-type silicate, has been used to synthesize hybrids with nanophase dimensions. It is a 2:1 layer silicate with the general formula, $M_x(Mg)_3[Al_xSi_{4-x}O_{10}](OH)_2$ where M is the exchangeable divalent cation. The layer charge is close to that of mica, but the interlayer cations are magnesium ions. The most important characteristics of these silicates are that the magnesium ions can be exchanged by other cations and, in the case of sodium, two well-defined hydrates exist. The two layer hydrates have a spacing of 14.8 Å, and the one-layer hydrate has a spacing of 11.8 Å. A typical cation exchange capacity encountered is approximately 100 milliequivalents per 100 grams of silicates. However, completely dehydrated samples give a spacing of 10 Å, similar to that of mica. Fully calcined vermiculite has a water absorption capacity of 200–500 g per gram of vermiculite depending on the particle size.

Leroux et al. present [11] an overview of systems defined strictly as the assembly of two components, a polymer and a 2D host material, more specifically a layered double hydroxide (LDH), and in the case where the bidimensional inorganic arrangement is left unmodified. The LDH structure is referred to as the natural hydrotalcite, described with the ideal formula $[M^{II}xM^{III}1-x(OH)_2]_{intra}[A^m{}_{x/m}\ nH_2O]_{inter}$, where M^{II} and M^{III} are metal cations, A is the anion, and intra and inter denote the intralayer domain and interlayer space, respectively. The structure consists of brucite-like layers constituted of edge-sharing $M(OH)_6$ octahedral [106]. Partial MII to MIII substitution induces a positive charge for the layers, balanced with the presence of interlayered anions. LDH host materials present the advantage of a large variety of compositions and a tunable layer charge density [107]. Moreover, the LDH sheets are constituted of one polyhedra-made layer, often corrugated and, therefore, more flexible than other bidimensional frameworks, such as the 2:1 layered silicate. This has been verified by computing an extended version of the discrete finite-layer rigidity model, which includes both intra- and interlayer rigidity effects [108].

A variety of conventional vinyl polymers and polycondensates, such as epoxy resins and ε-caprolactone, were used in composite preparations with layered MMT clays by in situ intercalative polymerization or by intercalation of polymer melts in layered silicates and by other procedures. The information obtained from these researches was applied to the preparation and evaluation of MMT-based nanocomposites of potentially important heterocyclic polymers. In some recent reviews, various synthesis routes for the preparation of processable polyconjugated systems were described [2,4,7,14,16,24,109], and the literature on clay-polymer intercalates and exfoliates is available [38].

To begin with, we shall review the studies on MMT nanocomposites of some vinyl polymers and resins. Later in this chapter, the studies on nanocomposites of PANI, PPy, PTh, PNVCz and their derivatives will also be reviewed.

Very recently, the synthesis of PMMA/clay nanocomposite has been reported using a variety of surfactants, dispersion techniques and polymerization conditions [110]. The synthesis of PMMA/clay nanocomposite via emulsion and in situ polymerization with 10 wt. % clay modified with zwitterionic surfactant, C18DMB, exhibited improved properties over pure polymer or conventional composites, such as enhanced mechanical and thermal properties, reduced gas permeability and improved chemical stability. A partially exfoliated nanocomposite, observed through transmission electron microscopy (TEM), was obtained by emulsion polymerization with

10 wt. % clay. The glass transition temperature (T_g) of this nanocomposite was 18°C higher than that of pure PMMA. The storage modulus of the nanocomposite was superior to that of the intercalated structure and pure polymer. Using nanocomposite technology, novel PMMA nanocomposite gel electrolytes exhibiting improved ionic conductivity and stable lithium interfacial resistance were synthesized.

Polyolefins, such as polyethylene or poly(propylene) (PP), were frequently studied matrices for MMT-containing nanocomposites [111–119]. However, their apolar character and weak interactions with other substances create problems in the intercalation of polymer chains into the MMT layers kept together by strong ionic forces. The modification of polyolefin matrix by compatibilizers [111,116,118–120] and the use of organomodified MMT [113–116,119,121] are common approaches to solve this problem.

The online dielectric sensor provides insights on how the polymer dynamics on the molecular level are altered with regard to the matrix type, the filler loading, and the morphology of nanocomposites. Dielectric data enable one to distinguish the relative degree of clay exfoliation between samples; however, the microstructure of clay cannot be identified by using dielectric spectrometer alone. Dielectric relaxation spectroscopy (DRS) is a powerful technique for obtaining dipolar relaxation as a function of temperature and frequency, from which effects due to intermolecular cooperative motion and hindered dipolar rotation can be elucidated. The relaxation time distribution was used as a rough indicator to describe the heterogeneity of the polymer/filler interface [122].

Most electrical conductors are opaque. Only a few materials, such as antimony-doped tin oxide (ATO) and tin-doped indium oxide (ITO), are optically transparent and electrically conductive [123–126]. The design of transparent, conductive nanocomposites requires the attention to several factors. Transparency is determined by reflection and absorption [127–128]. For transparency, the conductive filler itself must be transparent, and scattering at the interface between the filler and matrix must be as small as possible. Scattering can be minimized either by the matching of refractive indices of the transparent conductive fillers and the polymer matrix or by the reduction of one dimension of the conductive filler to be much smaller than the wavelength of visible light. Because refractive-index matching between a polymer and transparent ceramic conductors (e.g., ITO or ATO) is not possible, nanosized conductive particles must be used, and the concentration of conductive particles must be kept as low as possible. Several studies

were reported on the description of fabrication of conductive polymeric composites [129–134].

Recently, researchers have been interested in conducting molecular imprinting on nanostructured porous materials [135–147]. Imprinting synthesis has been carried out on mesoporous and zeolitic materials through conventional surface imprinting, hierarchical imprinting or 'ship-in-bottle' imprinting methods. The pivotal technique of all imprinting synthesis methodologies involves the incorporation of a template into a host matrix by combining it with host monomers that polymerize around the template. The subsequent removal of the template would result in a material that contains imprint cavities with a favorable size, shape and chemical environment to selectively rebind the template. The imprinting approach based on organic polymer hosts was first developed by Wulff and Sarhan, who used this technique to produce polymers for the resolution of racemic mixtures. Dai et al. [148] report a new approach for the synthesis of surface ion-imprinted sorbents using a layered nanomaterial as a host. The unique properties of layered materials are ideal for surface imprinting synthesis, which benefits from a tunable spacing but stable crystalline host. Polysilicate magadiite ($Na_2Si_{14}O_29.nH_2O$), which is composed of one or more negatively charged sheets of SiO_4 tetrahedra with abundant silanol-terminated surfaces, whose negative charges are balanced by either Na^+ or H^+ in the interlayer spacing, has resulted in a simplified experimental procedure. Dai et al. have demonstrated that the imprint-functionalized magadiite has better selectivity and higher capacity for metal-ion templates than the non-imprinted analogue. The possibility of continuous variation in basal spacing and crystalline structures of layered materials highlights a new opportunity for conducting imprinting synthesis.

A particularly interesting family of hybrid materials was obtained through the reaction of silicon alkoxides with polyethers [149,150]. PEO or poly(propylene oxide) (PPO) acts as a 'solid' solvent for many chemical species, while structural inorganic networks are obtained from the hydrolysis of reactive silicon species.

A considerable number of studies performed since 1990s aimed at reducing the crystallinity of PEO-based electrolytes, while maintaining high flexibility and mechanical stability. One of the most successful approaches relies on the preparation of ORMOLYTES (ORganically MOdified electroLYTES) [150–152].

Generally, two different approaches have been adopted for preparing organic–inorganic hybrids through sol–gel process. The first approach involves mixing an organic polymer with a metal alkoxide, such as

tetraalkoxysilane (TEOS or TMOS). In sol–gel process, the inorganic mineral is dispersed in the organic polymer matrix to develop hydrogen bonds between the organic phase and inorganic phase, and thus hybrids of class I (SiO_2-PEO or SiO_2-PPO) are obtained. In the second approach, the triethoxy silyl groups are introduced into an organic polymer prior to sol–gel reactions with metal alkoxides, and thus class II siloxane–polyether hybrids ($SiO_{3/2}$-PEO or $SiO_{3/2}$-PPO) are obtained. Two methods have been used in this approach. One method involves terminating the ethoxy silanes on both ends of the organic polymer with a covalent linkage, e.g., using 3-isocyanatopropyl triethoxysilane, to terminate poly(ethylene glycol) (PEG) through urethane linkages. The other method is to copolymerize the organic monomer with vinyl triethoxysilane.

Hybrid materials synthesized by sol–gel processes are of interest commercially as well as scientifically because of their unique properties. For example, the presence of organic phase makes the hybrid materials more flexible, and their thermal stability is greatly enhanced by the presence of inorganic phase. The addition of lithium salts and polymetalates induces interesting ionic conductivity [150–153] and photochromic properties [154], while luminescent properties can be promoted by rare earth doping [155].

Recently, Honma et al. [156–158] have synthesized a new class of hybrid composites consisting of SiO_2/polymer (PEO, PPO, polytetramethylene oxide (PTMO)) with polyurethane-linking structure through sol–gel processes.

By adopting a method similar to that of Honma et al., a series of proton-conducting membranes based on PEG/SiO_2 nanocomposites were synthesized by acid catalyzed sol–gel processes [1,3,159–164]. The details are given in the successive parts of this chapter.

Carbon

Graphite

Natural graphite (NG), which is abundant in nature, has been widely used as a conducting filler in preparing conducting polymer composites [165]. Conventional graphite fillers are usually micro-diameter powders. In order to achieve satisfactory conductivity using conventional graphite fillers, composite loadings are usually as high as 15–20 wt. % or even higher. Like many other nanocomposites, a polymer nanocomposite made from graphite nanopowder or nanosheets may have promising properties, especially good electrical conductivity.

Natural graphite is a layered structure. The carbon atoms within a layer are covalently bonded. The layers are bound by much weaker van der Waals forces. The weak interplanar forces allow certain atoms, molecules and ions to penetrate into the interplanar spaces of graphite, thereby causing the distance between layers to increase [166]. Direct dispersion of graphite carbon layers into a polymer is impossible, as no solvent or any other molecules have yet been found to delaminate the carbon layers.

Oxidized graphite or graphite oxide (GO) contains carbonyl, hydroxyl and ether groups on its surface [167,168]. Nanoscale materials based on layered GO and polymers were realized for PS [169], poly(vinyl acetate) (PVA) [170], PEO and PP [171,172].

Unlike layered silicates whose intercalation can be achieved by ion exchange reactions in the galleries, intercalation of graphite cannot be done in the same way because it does not bear any net charge. Intercalation by various chemical species leads to the preparation of graphite intercalation compounds (GIC). Expanded graphite (EG) is obtained by subjecting GIC to rapid thermal treatment at relatively high temperatures in a process called exfoliation.

The process applied to increase interplanar spacing in graphite can be summarized as follows:

$$\text{NG} \Rightarrow \text{GIC (intercalation)} \Rightarrow \text{EG (exfoliation)}$$

EG flakes expand hundreds of times along their c axis. The original graphite flake of thickness 20 μm expands up to 20–20 000 μm [166]. The microstructure of worm-like EG particles is roughly that of the irregular honeycomb network of graphite flakes with pores of different sizes ranging from 10 nm to 10 μm [173].

However, EG is somewhat a partially exfoliated graphite, because the graphite sheets interconnect with each other [174–179]. Only when the graphite sheets are fully exfoliated into polymer matrices, the resultant composites can be called delaminated nanocomposites. It should be noted that the term ‘delaminated’ used in this case does not signify a single-layer sheet, as it is used in polymer/clay nanocomposites, but refers to a separated graphite flake. As EG is fragile, it can be readily fractured by stirring the mixture of EG and monomers (or polymers).

Since the interplanar spacing is larger than that of the non-treated graphite, galleries of EG can be easily intercalated by suitable monomer molecules and/or catalysts through physical adsorption because of the porous feature of EG and polar interaction between monomer and the −OH

and −COOH groups on EG sheets. These polar groups result from chemical oxidation of the double bonds of graphite sheets during the preparation of GIC [180,181].

Many investigators have studied the properties and structure of various composites based on EG in the preparation of various fillers or matrices: metals [182], mica [183] or polymers [184–195].

A continuous insulator–conductor transition is observed in two-component systems at gradual increase of the number of conductor particles randomly dispersed in an insulator matrix. Most often, such transitions (called percolation transitions) are represented by the model of statistical percolation. The volume concentration of conducting particles (ϕ) at which the transition proceeds is called the percolation threshold or critical point (ϕ_c). EG is dependable in that only a little amount of conductive filler was required to reach the percolation threshold of conductivity [190–192,196–201].

Celzard et al. [202] first reported the conductive behavior of 100-μm-thick composite films composed of epoxy resin and ground EG flakes with an average diameter of 10 μm and an average thickness of 100 nm. Only 1.3 vol % of EG was needed to reach conductivity percolation threshold. More recently, via in situ polymerization approaches, nylon 6/EG [192], poly(styrenemethyl methacrylate)/EG [190], PS/EG [199,200] and poly(vinyl chloride)/EG [189] nanocomposites with markedly low percolation threshold value were prepared. By solution blending method, the preparation of grafted polypropylene (gPP)/EG [193,195,203] and poly(methyl methacrylate) (PMMA)/EG [194, 204,205] composites was also reported.

The physical properties, including electrical, dielectric, elastic, mechanical and thermal, surface area, pore structure as well as percolation phenomena within the composites based on compressed expanded graphites were studied [206–209]. From among these studies, Krzesinska et al. have prepared monolithic mica/EG from a mixture of EG and a fine powder of mica phlogopite [183]. The electrical conductivity and elastic moduli of about 30 samples were investigated. Among the present phases (graphite, mica and pore space), only graphite was conducting. Introducing a high amount of mica decreased conductivity; however, below 20 wt. %, the effect was rather low with respect to pure compressed EG. Hence, rigidifying the latter by making mica-based nanocomposites was possible without appreciably degrading the conducting properties.

In situ polymerization of styrene was conducted in the presence of expanded graphite obtained by rapid heating of the graphite intercalation compound (GIC) to form a polymer/EG conducting composite [190,191].

The study has shown that graphite was dispersed in the form of nanosheets in the polymer matrix. The transition from an electrical insulator to an electrical semiconductor for the composite occurred when the expanded graphite content was 1.8 wt. %, which was much lower than that of conventional conducting polymer composite. The composite exhibited a high electrical conductivity of 10^{-2} S/cm when the graphite content was 2.8–3.0 wt. %. This great improvement in conductivity could be attributed to the high aspect ratio (width-to-thickness) of graphite nanosheets. The study suggested that extensive rolling of the blend greatly affected the conductivity of the composite.

In another study, PS/graphite nanosheets were prepared via powdering the expanded graphite of thickness ranging 30–80 nm and diameter ranging 0.5–20 mm. It was an excellent nanofiller for the fabrication of polymer/graphite conducting nanocomposite [176]. The process allows to fabricate electrically conducting PS/graphite nanosheet nanocomposite films with much lower percolation threshold and much higher conductivities than those of composites made by conventional methods.

A new process was developed to fabricate electrically conducting nylon 6/graphite nanocomposites via intercalation polymerization of ε-caprolactam in the presence of EG [192,193] with low percolation threshold, and thus a great improvement in electrical conductivity was obtained.

There are also other methods for intercalating monomers or polymers into graphite. The first step in these methods is the preparation of graphite oxide (GO) by oxidation of NG [210,211]. Although the precise structure of GO is still uncertain, various structural models have been proposed, and it is assumed that the layered structure of GO consists of carbonyl, hydroxyl and ether groups on its surface, and these functional groups make intercalation of water-soluble polymers possible into GO.

Nanoscale materials based on layered GO and polymers have been realized for PS [211], PVA [212], PEO [213], poly(diallyl dimethyl ammonium chloride) [180] and poly(furfuryl alcohol) [214]. For hydrophobic polymers, such as PVA, the PVA/intercalated GO composite was prepared by in situ polymerization, in which an n-octanol (or dodecanol)-intercalated GO was first formed. The vinyl acetate monomer was then absorbed into the interlayer of GO, followed by thermal polymerization. Thermal stability of this nanocomposite was higher than that of pure PVA, and its electrical conductivity was 0.14 S/cm at room temperature [214]. MMA is a polar monomer. It can be intercalated into GO by the polar interaction between MMA molecules and polar groups on the surface of layered sheets. Ping et al. [215]

have reported the preparation of poly(methyl methacrylate)/intercalated GO composite by emulsion polymerization of MMA in the presence of GO. Various characterization techniques were used to characterize the structure and properties of the composite. Cerezo et al. have also reported the preparation of poly(ethylene-co-methyl acrylate-co-acrylicacid)-graphite oxide and EMAA-expanded graphite oxide nanocomposites by direct solution blending [216].

PMMA/graphite nanosheet composites were also fabricated via an in situ polymerization of MMA in the presence of graphite nanosheets with the aid of sonication [46]. The results have shown that the high-aspect-ratio structure of graphite nanosheets played an important role in forming conducting network in PMMA matrix. The conducting behavior of the composite was interpreted by percolation theory.

Another simple but effective procedure was developed to prepare separate graphite nanosheets from EG. The resulting foliated graphite (FG) nanosheets have been successfully incorporated into PE [217,218], PMMA [219], PS [176] and nylon 6 [201,221,222], and only 1.0 wt. % of foliated graphite was required to satisfy the critical transition in PMMA and PS cases.

A percolation threshold as low as 0.74 vol % was performed with the assistance of ultrasonic irradiation by in situ synthesis of nylon 6/FG nanocomposites [223]. In order to control the rate of crystallization, degree of crystallinity and to obtain the desired morphology and properties, a great deal of effort has been devoted to studying the crystallization kinetics and determining the change in material properties [224,225]. While there have been more papers [224–226] dealing with the crystallization behavior of neat nylon 6 and nylon 6/clay nanocomposites, little work has been done on graphite-filled nylon 6 composites [224–227] and the crystallization behavior of neat nylon 6 and nylon 6/clay nanocomposites [228–232]. It has been postulated that the conductivity change of carbon-loaded composites is related to the formation and destruction of carbon networks. Some external fields can alter the arrangement of conductive networks in the polymer matrix, resulting in a change in the overall conductivity of composites, such as the increase with temperature, which is called ‘positive temperature coefficient (PTC) effect’ [228–232]. Similar to the PTC effect, the conductivity of conducting polymer composites can also be changed with applied pressure, which is called piezoresistive property [233–241].

High-density polyethylene (HDPE)/foilated graphite (FG) nanocomposites have strong piezoresistive effects, which are induced by shear-induced orientation of FG in the HDPE matrix [217,218,242]. Time dependence of

piezoresistive behavior strongly depends on fixed pressure and FG concentration. Under a low fixed pressure, the relative resistance decreases with time; on the other hand, the composite resistance increases with time under a high fixed pressure. The shift of relative resistance changes more slowly at higher filler concentrations. The average 'nanosheet' separation in the nanocomposite changing with time under fixed pressures is the origin of the time-dependent piezoresistive behavior.

The microscopic mechanisms that result in macroscopic non-linearity in the composites can be divided into two groups. In the first group, the conducting elements can be intrinsically non-linear [243], whereas in the second group, the conducting elements are ohmic, but the appearance of additional conducting channels, arising due to the onset of tunneling or hopping across thin originally insulating layers, can lead to non-linearity in sample conductance [244]. Non-linearity increases as a fraction (ϕ) of the conducting component tends toward critical value, percolation threshold (ϕc), either from below (as in normal–superconductor mixtures) or from above (as in conductor–insulator mixtures) [245]. Chen et al. have studied [221] the non-linear conduction behavior of composite materials of foliated graphite nanosheets and nylon-6 subjected to a variable direct-current electric field. On the basis of the microscopic structures and conducting processes of the nanocomposites, it was found that a combination of models can generally account for non-linear characteristics.

Acetylene black is another type of carbon material used as a core carbon support because of its good electronic conductivity and small particle size (average diameter 44 nm). PEG with a molecular weight of 4600 Da (corresponding to a stretched chain length of 28 nm) was grafted onto carbon particles that were surface-treated to produce carboxylic functional groups to anchor the PEG chains [246,247]. The polyelectrolyte functionalized carbon or C-PEG was coated with an aqueous dispersion of V_2O_5 lamellae (sol) [248] and dried at 140°C to yield V_2O_5/C-PEG. Huang et al. had prepared nanocomposites by chemically wiring both polyelectrolytes and active metal oxide (V_2O_5) onto the surface of semigraphitic carbon black nanoparticles that serve as an electronically conductive core [249].

In the recent reviews on electrical conductivity of binary mixtures [250,251], it has been assumed that the mixing process may induce electrical charging of carbon particles and, thus, might stimulate interactions between particles and polymeric host. Recently, a lower percolation threshold was observed for carbon black filled epoxy resins [252–254] not obeying the predictions of the standard percolation model, which is suitable

for randomly dispersed but not interacting fillers. Kotsilkova et al. [255] have investigated the rheology, DC-conductivity and microwave properties of acrylic, polyurethane and epoxy composites containing 0–15 vol % of nanosized carbon particles. The percolation threshold was interpreted as a structural transition from a dispersed to an agglomerated state, and it was found to depend significantly on the type of matrix polymer. Above the percolation threshold, the presence of carbon nanoparticles produces a strong increase in the viscosity of dispersions as well as the electrical conductivity and microwave properties of solid composites. A good correlation between these three characteristics was found for systems in a wide range of carbon volume fractions.

Oxadiazole-based polymers form a class of high-performance polymers with great thermal and chemical stability and excellent mechanical strength and stiffness. Some poly(1,3,4-oxadiazole)s with substituted aromatic ring, such as poly(2,5-diphenyl-1,3,4-oxadiazole), show intense photoluminescence and electroluminescence when combined with an additional layer of electron transporter [256]. The applicability of these polymers is, however, limited because of their insolubility in common organic solvent and their difficult processability [257,258]. The introduction of certain substituents on the aromatic rings, flexible bridge in the chain or some specific units pendant to the chain has shown to improve solubility without disturbing the conjugation [259,260]. Souza et al. have developed new thermally stable conducting materials by dispersing conducting carbon black into the poly(4,4′-diphenylether–1,3,4-oxadiazole) (POD–DPE) solution in NMP [261].

It is rather difficult to prepare conductive graphite/polymer nanocomposites via direct intercalation method [262]. To achieve nanoscale dispersion of graphite in polymer matrix, certain chemical or physical modifications are generally required in the graphite [262,263]. Recently, an effective method for the preparation of poly(4,4-oxybis(benzene)disulfide)/graphite nanosheet composites via in situ ring-opening polymerization of macrocyclic oligomers was reported [264,265]. Graphite nanosheets were completely exfoliated under microwave irradiation followed by sonication in solution. The nanocomposites exhibit as both high-performance polymeric material and electrically conductive material. Therefore, they show potential applications as high temperature conducting materials.

There is a growing interest towards ion beam irradiation of polymeric materials since fine conducting micropatterns can be produced from these focused ion beams. Ion beam irradiation has been shown to produce electrical conductivity in polyimide films where conductivity has been attributed

to the inhomogeneous formation of carbonised inclusions in the polymeric medium [266,267]. Two different mechanisms have been suggested for ion-induced electrical conductivity; the first one is the formation of graphitic tracks of sufficient density resulting in the production of a graphitic-like layer [268], while the second one represents a progression of chemical modifications with irradiation resulting in a gradual modification of the band structure from semiconducting behavior at low ion fluence to metallic conduction at high fluence [268–271]. The electron transport properties of two types of carbon–polyimide (C–PI) nanocomposite thin films have been evaluated [272]. Conductive nanocomposites formed by the incorporation of 30-nm carbon particles prior to polymer cross-linking (ex situ formation) has been compared to high-energy ion beam irradiation in situ formation of nanoscale carbon clusters within the polymer composite. The addition of carbon nanoparticles has reduced resistivity by 13 orders of magnitude for 8 vol % carbon content. The irradiated in situ formed films have shown a comparable resistivity to this 8% C–PI film.

Traditionally, activated carbon has been used as an adsorbent material for water and waste water treatment [273–275]. The wide variation in functionality, surface area, porosity and ease of regeneration has made the use of polymeric resins as an alternative to activated carbon for removal of specific pollutants from contaminated water.

Another interesting carbon compound – carbon nanofibers of c. 1 μm by 20 nm dimension – has been successfully prepared by graphitization of polyacrylonitrile (PAN), previously formed inside the nanosized pores of sepiolite [276]. This natural microfibrous silicate contains structural tunnels extending along the whole fiber, which are able to include acrylonitrile (AN). AN is polymerized to give PAN, which is further thermally treated to form carbon nanofibers. The resulting solids constitute a new class of conductive carbon-clay nanocomposites having potential applications in diverse electrochemical devices such as lithium batteries, sensors or electrocatalysts.

Nanotube

The discovery of fullerenes (1985), the third form of ordered carbon, spurred the subsequent discovery of a number of related novel forms of carbon. The most famous among these carbons are the nanotubes, sometimes referred to as buckytubes.

The characterization of fullerenes by Smalley et al. [277] and Kraetschmer et al. [278], together with the discovery of carbon nanotubes

by Iijima in 1991 [279], has provided an insight into the huge potential of molecular sp^2-derived architectures of carbon.

Polymer composites based on carbon nanotubes (CNT) have received a great deal of attention because of their unique electrical properties [280–285]. The small size and high aspect ratio of CNT permit electrical percolation at very low loadings, which offers new opportunities to enhance electrical conductivity at a very low additive concentration. In addition, the presence of CNT can improve mechanical properties than the conventional composites containing carbon black.

There are two distinct types of carbon nanotubes. A single-walled carbon nanotube (SWNT or graphene tube) is made of one layer of graphene sheet, while a multiwalled carbon nanotube (MWNT or graphitic tube) is made of more than one layer [286].

In this fast-growing field of nanotechnology, SWNTs are recognized as new strong [287], electrically [288] and thermally [289] conductive materials. From the time they were discovered [290,291], many synthesis [292,293] and purification [294–296] methods have been developed to produce SWNTs of length ranging from a several hundred nanometers to a few millimeters.

Many efforts have been made to combine CNTs and polymers to produce functional composite materials with improved properties [297–299]. A detailed investigation of CP/CNT composites is of great interest nowadays. These materials find a host of applications in supercapacitors, sensors, photovoltaic cells and photodiodes, optical limiting devices, solar cells, high-resolution printable conductors, electromagnetic absorbers and, last but not least, advanced transistors. The preparation of composites requires qualifying the type of interaction between the host matrix and guest nanoparticles. In CP/CNT composites, it has been shown that either the polymer functionalizes CNTs [300,301] or the CPs are doped with CNTs, when a charge transfer between the two constituents takes place [301–304].

Three routes are used to prepare CP/CNT composites:

(a) direct mixing of the CP with CNTs,
(b) chemical synthesis of the CP in the presence of CNTs, and
(c) electropolymerization of monomers on the CNT films.

The recent studies on CNTs were reviewed in [305,306].

Carbon nanotubes and carbon nanofibers, having extremely large surface area and well-defined structure and morphology, are a key to novel composite materials with enhanced physical and chemical properties. Since the production costs are currently well above that of conventional graphite

powders and soot products, a combination of several improved properties justifies massive introduction of these relatively high-cost materials into composite production.

Hammel et al. have achieved bulk production capacities of high-purity carbon CNFs at low cost by the catalytic chemical vapor deposition (CCVD) process [307]. Reasonable low temperatures and yields of up to several g/m^2 per minute at more than 70% carbon gas-to-fiber conversion rates allow considerable reduction in costs. Polymer composites have been prepared by the dispersion of CNFs into polymer matrices by applying intensive shear via extrusion. In PP, the application of less than 10 wt. % CNFs has reduced volume resistivity from $> 10^{13}$ Ω cm to a value of c. 10^5 Ω cm. Fibers of different sizes are normally used for nylon, polycarbonate and other high-temperature applications.

Carbon nanotubes prepared by the classical CVD method with a nickel catalyst have been characterized and used as conducting anisometric objects dispersed in a polymeric matrix [308,309].

Many studies have been carried out on CNT/polymer composites [310–319]. These studies emphasize that three main factors greatly influence the reinforcement of this composite:

(a) a good dispersion of the CNTs in polymer matrix [310–313],
(b) a strong interfacial bonding between CNTs and polymer [312,314, 315], and
(c) a good alignment of CNTs in polymer matrix [316–319].

Due to weak interaction between polymer matrix and CNTs and strong van der Waals forces between CNTs themselves, CNTs tend to agglomerate in composites, and the composite strength may not be effectively enhanced.

Recently, chemical functionalization of CNTs has been realized and full solubility of CNTs was demonstrated in some solvents [307,320–323]. This offers a very important application of CNTs as additives for reinforcement of polymer materials, because functionalization of CNTs simplifies the fabrication process of CNTs/polymer composite as well as improves the interfacial bonding between polymer matrix and CNTs.

Nanotubes, mainly MWNT, belong to a large family of filamentary carbons, which were popularly known as vapor grown carbon fibers (VGCF). Depending on the experimental conditions based on catalytic cracking of hydrocarbon gases, standard fibers of micrometer diameter [324], submicron [325] or even nanometer size [326] have been produced. Their structural characteristics are related to their diameter (D), which may vary

over four orders of magnitude and aspect ratio (L/D, where L is the mean length of each filament, which may be very large; typically $L/D \sim 10^2$–10^3). This geometrical factor leads to a very low percolation threshold, i.e., a conducting-charged polymer for a very low concentration of these fillers [327].

The dispersion of CNT additive in the insulating matrix is a crucial controlling factor of the final electrical properties [281,328]. Low percolation thresholds in the 10^{-3}–10^{-1} range of weight percent of CNT have been reported in MWCNT-thermoset composites [283,285,328,329], where an extensive dispersion of the additive was achieved before the curing of resin. However, higher percolation thresholds have been observed when CNTs were dispersed in a thermoplastic polymer [282,285] unless the sample thickness was reduced to the nanometer range [280].

It is still a challenge to obtain SWNTs with a satisfying structure suitable for technological applications. Valentini et al. have reported the synthesis of supramolecular semiconducting dendrimeric structures consisting of substituted naphthalenediimides as end groups modifying commercial polyamidoamine (PAMAMC) that non-covalently interacts with single-walled carbon nanotubes [330]. The study of photoelectrical properties of this system in thin-film transistor geometry and the incorporation of PAMAMC-modified SWNTs as an electroactive component within an organic conducting polymer in order to enhance photoconductivity have been reported [331].

To date, most of the investigations on composites containing CNTs have focused on polymers, metals or metal-oxide-based composites with improved electrical, electrochemical and mechanical properties [332–335]. Few reports have considered the fabrication and property characterization of CNT–nitride composites [336]. TiN has been studied quite extensively because of its attractive properties such as oxidative stability, corrosion resistance and good electrical conductivity [336–337]. These qualities make TiN an excellent candidate for electrodes in electrochemical capacitors, which use highly corrosive electrolytes such as potassium hydroxide; for electronic conductors in electronic devices [336–338]; and in novel CNT–TiN composites with larger surface area, increased electrical conductivity and enhanced electrochemical capacitance. However, the intrinsic properties of CNTs generate particular challenges in the development of CNT-incorporated composite applications.

Treating CNTs with nitric acid or other oxidants could create acidic groups at both tips and sidewalls, which can act as nucleation sites for oxide nanoparticles. Jiang et al. have used acid treatment and nitridation

technology to fabricate TiN-immobilized CNT powders and then mixed them with pure TiN powders by ball milling [339]. The electrical conductivity and electrochemical performance of CNT–TiN composites gradually increase with increasing CNT content.

Recently, reinforcement in CNT-based composites has been investigated in numerous research works, in which different matrix materials, such as polymers, ceramics, resins, metals, etc., have been used. Although much lower in density and higher in strength, CNTs cannot replace carbon fibers in many fields immediately by virtue of unresolved hindrance of dispersion in matrix and the interface or bonding between matrix and reinforcement. As a result, aligned carbon nanotube/carbon (ACNT/C) nanocomposites were prepared by chemical vapor infiltration (CVI) technology to explore some properties of CNTs, especially the thermal properties [340].

Supronowicz et al. have designed and fabricated a novel current-conducting polylactic acid/carbon nanotube composite. They employed this composite as a substrate for exposing osteoblasts (the bone-forming cells) to electric current stimulation in vitro; and investigated the effects of electrical stimulation on select cellular/molecular functions of osteoblasts pertinent to osteogenesis [341]. These functions included osteoblast proliferation, calcium deposition in the extracellular matrix and the expression of genes for collagenous and non-collagenous bone matrix proteins.

Other layered materials like graphite, such as BN, BC_2N, $2BC_3$, C_3N_4, CN_x, MoS_2, WS_2 and V_2O_5, were predicted to form nanotubes and fullerene-like structures [342,343]. B/N/C microstructures were first observed by Bartlett et al. [344,345] in 1986 after the thermolysis of C_2H_2 and BCl_3.

Unfortunately, it could not establish any consensus with respect to the atomic location of different species within B–C–N nanotubes and other nanostructures. Both sandwich-like nanostructures composed of pure BN and C layers and those made of consecutive layers composed of B, C and N species, which somehow assembled within the single graphitic sheets, have been considered theoretically and observed experimentally using high-resolution electron energy loss spectroscopy. The production, structure and characterization of BCN nanoscale materials were discussed in detail in [342].

While C tubes can behave as either metals or semiconductors, BN tubes are expected to be insulating- and oxidation-resistant. Interestingly, hybrid B–C–N systems constitute an opportunity to tune nanotube electronic properties in a wide range. The electronic and mechanical properties of BCN

systems may be applied in nanoengineering (e.g. semiconductors with high oxidative resistance, photoluminescent materials, nanotransistors working at high temperatures, high-temperature lubricants, novel composites, etc.).

Mesoporous materials

Porous carbon materials with high surface area ($>1000\,m^2/g$) and pore volume ($>1.0\,cm^3/g$) are of great interest for catalysis, separation, purification, hydrogen storage, capacitors and other applications [346–351]. To date, zeolites and silica materials (e.g. surfactant-templated mesoporous silica [349,352–356], assembled silica nanoparticles [357,358] and silica sol–gel networks [359–362]) have been employed as templates. In 1999, two groups independently reported the fascinating synthesis of ordered mesoporous carbon by using surfactant-templated mesoporous silica as template [352a,353a].

According to the IUPAC definition, inorganic solids with pores of diameters in the range 2–50 nm are classified as mesoporous materials.

Porous silica possesses high surface area, and the size of pores can be tuned from 2 to 10 nm in a narrow diameter distribution by changing the experimental conditions. In 1992, researchers at Mobil reported the synthesis of a family of mesoporous silicates; designated as M41S, with uniform pore size distribution. Depending on the channel arrangement, mesoporous silica is further divided into hexagonal mobile composition of matter (MCM)-41, cubic MCM-48 and lamellar MCM-50.

Finally, the calcination of organic/inorganic assembly produces a hollow solid framework with large surface area and pore volumes. SBA (Santa Barbara amorphous)-15 is a silica-based mesoporous material, recently reported by a research group in the University of California at Santa Barbara, different from the Mobil products [363]. In this material, a poly(alkylene oxide) triblock copolymer with hydrophilic and hydrophobic segments is used as a structure-directing agent in a strongly acidic medium [364]. The enhanced hydrothermal stability and substantially larger pore diameter of SBA-15 are expected to produce additional potential applications.

In some recent reports, a facile and time-saving pathway towards nanoporous carbon has been demonstrated [365–368]. Among these approaches, the most promising one involves the direct formation of nanocomposites containing carbon precursors and silica followed by carbonization and subsequent silica removal. A remarkable development in this area was the synthesis of conducting polymer in the porous silica channels [365–379].

Metal and metal oxide

Polymerization of conducting polymers was studied by many authors over different inorganic hosts (e.g. SiO_2, Al_2O_3, Fe_2O_3, Fe_3O_4, V_2O_5, MnO_2, ZrO_2, TiO_2, RuO_2, α-$RuCl_3$, CuS, Cu_2S, CdS, CdSe, Fe, Co, Au, Ag, Cu, $CuFeS_2$, MoS_2, MoO_3, TiS_2, $MnPS_3$, $BaTiO_3$, molybdenum trisulfide and Nb_2O_5) for different optical and electrical applications, such as high-density information storage devices, electrochromic devices, electrorheological fluids, etc. Some of these can be used as magnetic part of the composite materials such as Ni, Fe, Fe_2O_3, Fe_3O_4, $CoFe_2O_4$, $NiFe_2O_4$, Co_3O_4 and $BaFe_{12}O$.

In a polymer nanoparticle composite, the size and shape of metal nanoparticles determine the electronic, magnetic, thermal and non-linear optical properties of the composite.

Althogh different inorganic materials can be combined with conventional polymers (thermoplastics, rubbers, etc.) mainly by blending (solution/melt) the inorganic component, it is not possible to combine inorganic nanomaterials with conducting polymers by conventional techniques because of the inherent insoluble and infusible nature of the latter. Different approaches have been suggested combining both chemical and electrochemical techniques.

Most of these methods require vigorous stirring of the solution to suspend the particles and to prevent their aggregation during the reaction.

One way to overcome this problem is to process the materials in solid state. This approach avoids thermal and solvent problems while providing infinite design flexibility. A mechanochemical reaction, which is a solid-state reaction, has been mainly employed in the study of metals and alloys.

Mechanical alloying is essentially a bulk preparation technique well established for processing metals and ceramics with fine microstructures since 1960s [380]. In 1988, Shaw [381] and Smith et al. [382,383] have proposed that mechanical alloying could be applied to the polymer field. To embrittle polymer and overcome its viscoelastic nature, ball milling of polymer was carried out under cryogenic temperature (liquid nitrogen). This adapted technology was mostly referred to as cryogenic mechanical alloying or cryomilling. Cryomilling has been recognized as an effective method to improve blending intimacy and enhance compatibility between polymers [382–385]. However, little attention has been given to fabricating polymer/metal composites via cryomilling [386,387].

Considerable investigations focusing on modifying the polymer by synthesizing novel polymer/metal oxide nanocomposites have been reported.

Among these systems, a lot of attention was paid to polymer/V_2O_5 composites due to their unique electrical and optical properties. Examples of CP-metal oxide and metal nanocomposites are given in the related part of this chapter.

Vanadium-based oxides exhibit a rich variety of interesting properties due to the multiple oxidation state of vanadium atom. In vanadium pentoxide (V_2O_5), the highest oxidation state is remarkable among all the vanadium oxide systems. Vanadium pentoxide xerogels ($V_2O_5.nH_2O$) are layered materials consisting of water in the interlayer space. The distance between two layers depends on the amount of intercalated water. The layers of xerogel consist of ribbon-like complex structure [388–390]. The water molecules are very weakly hydrogen bonded to the oxide network. Vanadium pentoxide xerogel with larger interlayer distance is suitable for intercalation of a variety of guest specimens. Acidic protons are present due to acid dissociation at oxide–water interface. Moreover, during synthesis, some V^{4+} ions are formed to initiate the formation of gel. Electronic conduction arises from the mixed valence behavior of vanadium in xerogels. Proton conduction is due to the acidic nature of xerogel [391]. Conductivity of xerogels depends mainly on the amount of water. The nanocomposites obtained from xerogel consist of both electronic and protonic conductors.

Intercalative polymerization of conducting polymers inside the layered structures requires substantial oxidizing power. Among layered materials, in particular, FeOCl [392,393], V_2O_5 [83,394] and α-$RuCl_3$ [84,395] are suitable for post-intercalation polymerization. Crystalline vanadium pentoxide has sufficiently strong oxidizing power among high-oxidation transition metal oxides. Intercalation of small ions is possible only due to strong interlayer bonding interactions.

Vanadium-based compounds, such as vanadium pentoxide and vanadyl phosphate, are the most suitable hosts for insertion of both inorganic ions and organic molecules. The physical properties of nanocomposites are completely different from that of the individual components. Some preliminary studies on intercalation of PANI into the interlamellar spaces of vanadyl phosphate have been reported [396–399]. In all these host compounds, it has been observed that intercalation and polymerization of aniline occurs through redox.

Several groups have investigated the different forms of preparing composites of V_2O_5 with polymers, including polypyrrol [400–405], PANI [394,406–411], fully sulfonated poly(aniline co-*N*-propane sulfonic acid aniline) (PAPSAH) derivative, poly (*N*-propane sulfonic acid aniline) (PSPAN) [412], PTh [415], polyethylenedioxythiophene (PEDOT) [413],

poly(2-(3-thienyloxy)ethanesulfonic acid) [414] and PEO [415,416]. Some of these approaches appear to produce composites with properties superior to the sum of those of the individual components [400,417].

CP/V_2O_5 nanocomposites had been synthesized and well studied by Kanatzidis and others [392–396,400–414]. The nanocomposite formed by PPy and V_2O_5 has shown a higher specific capacity and energy density than that of xerogel [400,402,417].

Recent literature contains numerous studies on the application of transition metal oxides as Li^+ insertion hosts in rechargeable lithium batteries. V_2O_5 xerogel is a particularly promising material with efficient and reversible insertion of lithium ions at high potentials vs. Li/Li^+, resulting in high specific capacity and energy density [23,388,410,418–420]. Thus, there is a considerable effort to enhance the overall Li^+ insertion rate in this and related materials. A substantial improvement in the overall Li^+ insertion rate was obtained for a V_2O_5 aerogel synthesized on sintered nickel fibers [421]. In another approach, more rapid Li^+ insertion was obtained by employing a supercritical drying process to produce aerogel materials with high surface areas and short diffusion path lengths [422,423]. Incorporating a conducting polymer within the xerogel matrix is another approach to improve xerogel performance [424,425]. A higher Li^+ insertion rate can be achieved in these nanocomposites, which would result in increased charge storage capacities as compared to untreated xerogel [425c]. Moreover, decreased diffusion path lengths can improve the overall rate of Li^+ insertion into the material.

While PANI is an extremely interesting conducting polymer, vanadium oxide has been extensively studied as a cathode material in lithium batteries. A number of attempts [405,407,410] have been made to produce nanocomposites from V_2O_5 and PANI with increased ion mobility and electronic conductivity of V_2O_5 in order to facilitate charge transport in battery electrodes.

Electrodeposition of V_2O_5 on the continuous PANI backbone offers the potential for regulation of porosity of macroporous composite by controlling the quantity of V_2O_5 deposited. Luca et al. have explored the possibilities for simple two-step one-pot electrochemical preparation of the novel PANI–V_2O_5 interpenetrating network by electrochemical means, which can, in principle, afford the control of dimensionality of both conductor and semiconductor [409]. The dimensionality of formed amorphous V_2O_5 can be controlled through current density during deposition; this, in turn, reduces porosity. As current density increases and more V_2O_5 is deposited, the conductivity of PANI decreases.

Buttry et al. have employed Li NMR spectroscopy to probe the local lithium environment in V_2O_5 and several nanocomposite materials comprising V_2O_5 and various PANI derivatives. The results show that charge compensation of intrinsic negatively charged ion-exchange sites in V_2O_5 xerogel by conducting polymers used to form nanocomposites is important in determining the number and type of Li^+ sites available [410].

Mechanical and electrochemical properties of CP/V_2O_5 nanocomposites depend on the preparation details. Kanatzidis et al. have shown that V_2O_5 xerogel films exposed to a dispersion containing aniline formed a nanocomposite powder with PANI intercalated within the interlayer region of V_2O_5 [83].

Huguenin et al. have employed simultaneous polymerization in forming homogeneous films from various CP and V_2O_5 [425a,425e,427].

In a recent work, Ferreira et al. have shown that PANI/V_2O_5 nanocomposites obtained by layer-by-layer (LbL) method are advantageous over those prepared by other methods [425f]. LbL films are visually uniform with a high degree of thickness control. This material exhibits a globular morphology, which is common in LbL films.

In addition, the amount of PANI distributed within the V_2O_5 matrix could be controlled, and the nanocomposite displayed a high charge capacity. Huguenin described how manipulation at the molecular level of V_2O_5/PANI nanocomposites built with LbL technique promotes enhancement of charge storage capability, new electrochromic effects and control of ionic flux [411]. By changing film architecture, one can control the amount of PANI participating in the redox processes of LbL films. As a result, the films exhibit the electrochemical profile of V_2O_5 and the chromogenic properties of PANI. It is envisaged that the molecular-level control may be exploited in producing efficient lithium batteries as well as electrochromic devices and sensors.

The synthesis and characterization of another type of water-soluble CP/V_2O_5 nanocomposites – poly(2-(3thienyloxy)ethanesulfonic acid) (PTOESA)/V_2O_5 – was reported [414]. Furthermore, both PTOESA and V_2O_5 xerogel are electrochromic materials with rich electrochemical properties. The huge interface interactions between PTOESA and V_2O_5 can create new electrochemical properties, which may not exist in organic polymer or V_2O_5 xerogel.

Electrochemical characterizations of new organic–inorganic hybrids prepared by intercalation of conducting poly(3,4-ethylenedioxythiophene) (PEDOT) into V_2O_5 and MoO_3, which have been used as electrode

materials for rechargeable lithium batteries and supercapacitor, respectively, were reported [413b].

These hybrid nanocomposites, when coupled with a large-area Li foil electrode in 1 M $LiClO_4$ in a mixture of ethylene and dimethylcarbonate (1:1, v/v), offer enhanced discharge capacity (350 mAh g^{-1}) as compared to pristine oxides. This improvement in electrochemical performance may be attributed to higher electrical conductivity, enhanced bidimensionality and increased structural disorder. Although these conducting polymer-oxide hybrids delivered more than 300 mAh g^{-1} in the potential range 1.3–4.3 V, their cycle life needs further improvements to realize their commercial potential. Similarly, the double-layer capacitance of MoO_3 increases from 40 mFg^{-1} to 300 Fg^{-1} after PEDOT incorporation in the interlayer gap under similar experimental conditions, and the nanocomposite exhibits intriguing effects with respect to electrochemical Li^+ insertion. The PEDOT–MoO_3 nanocomposite appears to be a promising electrode for non-aqueous-type supercapacitors.

4.3.2. Guest Materials

Polyaniline

Conductive PANI was considered the most perspective polymer of the future. Aniline can be polymerized electrochemically or chemically by using an oxidant in different types of acids. The chemical method has a great importance since it is very feasible for the mass production of PANI. The most common acids used are hydrochloric acid, sulfuric acid, carboxylic acid, dicarboxylic acid, sulfonic acid, etc. [426–428]. $(NH_4)_2S_2O_8$ [429, 430], $K_2Cr_2O_7$, KIO_3, $FeCl_3$ [426], H_2O_2 [431] and $KBrO_3$/KBr [432] are recommended oxidants. The yield and the conductivity of PANI depend on the acid used [76].

Thin films of PANI can also be obtained from surface polymerization of monomers [433], electrochemical deposition [434], spin coating [435], and LbL technique [436].

PANI itself is difficult to process, because it decomposes prior to melting and is insoluble in common solvents except strong acids and *N*-methylpyrrolidone (NMP). This severely restricts fabrication in the usual way, i.e., via polymer solution or melt. Therefore, in order to improve solubility, various PANI derivatives possessing substituent groups ($–CH_3$, $–OCH_3$, or $–OC_2H_5$) have been investigated [437–439]. This kind of engineering provides an excellent solubility in organic solvents even

though derivative conductivity becomes lower than that of PANI within the whole doping range due to the presence of side groups disturbing the electronic conjugation in polymer backbone.

The other way to improve PANI processability without loss in its electrical properties is composite formation. There are numerous chemical methods for preparing composites. One of the most interesting methods is 'template synthesis'. It was first demonstrated by Martin et al. and became widely used [73,440,441] for the preparation of polymers, metals and semiconductors on a nanoscopic scale.

The mechanical properties, stability of interface, thermal stability and processability of PANI would be greatly improved by nanocompositing with layered compounds. For example, electronically conductive polymer nanocomposites can have electronic conductivities of several orders of magnitude higher than that of the conventional forms (e.g. powders or thin films) of the same polymer. Besides good conductivity and excellent application perspective in rechargeable cell, this kind of nanocomposites may show many novel properties, such as photoelectric display, photoelectric transition, thermoelectricity, electromagnetism and electrorheology, through synergic interaction of PANI with layered compounds.

Three methods are available for deriving such nanocomposites [442]. The first one includes the intercalation of monomers into the host matrix followed by their polymerization due to the presence of an external oxidizing agent. In the second method, the redox properties of the host (metal oxide) ensure in situ polymerization as well as intercalation of the polymer. The third method involves direct intercalation of polymer macromolecules inside the host particles.

Water dispersion of PANI nanofibers [443], self-assembled PANI nanotube [444] formation, polymerization of aniline inside macroporous carbon [445], rod-like inclusion complex formation of cyclodextrin and PANI [446] and directed assembly of large arrays of PANI nanowires [447] are methods employed to facilitate the application of PANI in various forms. Additionally, core-shell nanoparticles consisting of metal nanoparticles as the core and polymer as the shell [448], or polymer nanoparticles as the core and metal nanoparticles deposited on the polymer surface [449], have attracted interest because of their potential applications in catalysis, controlled delivery, artificial shells, light fillers, low-dielectric-constant materials, acoustic insulation and photonic crystals. LbL is the other method useful for nanoscale integration of two polymer systems to assemble a thin film with conducting or insulating properties [450].

Compositing methods, properties and application of several kinds of layered compounds with PANI were reviewed in [5–7,13,22].

Nanomaterials based on PANI have the best functional characteristics. They can be obtained in various forms allowing fundamental aspects of different methods of preparation of nanocomposites to be investigated. A summary of host materials (mainly clay and metal oxide), preparation methods and emerging applications is included in this part.

Clay composites

Choi et al. [451] first utilized the in situ intercalative polymerization method for the preparation of polymer–clay nanocomposite consisting of conducting PANI and MMT.

The most common inorganic matrix used for PANI composites is smectite MMT [452–454] due to its capacity to swell and exchange cations, and it is naturally abundant and inexpensive. MMT, which is an important class of lamellar inorganic compounds, is composed of silicate layers 1 nm thick and measuring 200–300 nm in lateral dimensions [39,184,455,456]. A special type of nanocomposite can be obtained when anilinium (ANI) polymerization is carried out mainly between the interlayer regions, using anilinium intercalated clay (ANI-MMT) as precursor [454a,454b].

When aniline polymerization is performed in an acidic aqueous suspension of MMT having one oxidizing agent, the formation of intercalated and/or exfoliated nanocomposite is dependent on the monomer/clay ratio. At low PANI loading, conductivity of the composite is still very close to that of insulate pure MMT clay. At some critical loading, called percolation threshold [457], conductivity increases by several orders of magnitude with a very small increase in the PANI content. After this region of drastic enhancement, conductivity once again levels off and its value becomes close to that of free PANI. Nevertheless, nanocomposites of PANI-MMT [452,454] obtained by ANI-MMT polymerization show lower conductivity than free PANI [453]. The reason could be the lack of connectivity between intercalated PANI chains [452,454] or a change in the nature of polymeric chains.

One way to enhance connectivity is to use organically modified clay, which is more compatible with organic solutions or polymers. The other way is mechanochemical grinding. Ogawa et al. [458] have reported that mechanochemical reactions help to introduce organic guest species into the interlayer spaces of clay minerals. They succeeded in the solid-state intercalation of organic compounds into MMT by both cation-exchange reaction and adsorption of polar molecules.

Mechanochemical grinding allows to insert PANI chains into MMT clay nanolayers without any additive agents. PANI nanocomposites, recently prepared by this method, have attracted much attention [459].

The most noteworthy work by Choi et al. [460] has opened a new field of polymer–clay nanocomposites as electrorheological (ER) fluids, a kind of smart and intelligent material. It was the first time that polymer–clay nanocomposites were applied in ER fluids, which were originally developed by Winslow in the 1940s. The fluids are made from suspensions of an insulating base fluid and particles 0.1–100 mm in size. ER fluids exhibit a rapid, reversible and tunable transition from fluid state to solid-like state upon the application of an external electric field [461,462].

Many efforts were made to explore the various promising materials based on ER fluids, by using semiconducting polymers including poly(acene quinone) radicals [463], PANI [464], copolypyrrole [465] and copolyanilines (COPA) [466].

Clay minerals have large surface area, which gives ionic-exchange properties to PANI–clay nanocomposites [452a,460b,467].

Around the world, there has been a growing interest towards developing and implementing various techniques for removing potentially toxic organic and inorganic pollutants from water. PANI exhibits relatively high surface area and porosity [468,469] and has been well recognized as an adsorbent of proteins [470,471] and DNA [472–474]. In addition, PPy colloids stabilized by polyvinylphosphate dopant are shown to adsorb metal ions from aqueous solutions [475]. Possible interactions between charged PANI and two typical ionic dyes, namely procion red (PR), anionic in nature, and methylene blue (MB), a cationic one, were examined based on the removal of dyes as a consequence of adsorption from their aqueous solution onto PANI adsorbents [476].

Surface polymerizations of aniline and pyrrole have intuitively been used for the coating of various materials, such as glass [477–480], noble metals [481,482] and polymers [477–480,483–486]. Similar coatings have been deposited on inorganic particles [487–489], polymer microspheres [96,490–494], fibers and textiles [479,495], and even such small objects as block copolymer micelles [496] and the edges of phospholipid tubules [484]. Moreover, porous materials, such as porous glass [497], silica gel [96,490,498–500], MMT [501,502] and polymer membranes [503,504], can serve as templates for the coating.

In 1989, Gregory et al. [505] have observed that textile fibers introduced into the reaction mixture during the oxidation of aniline and pyrrole become coated with a smooth overlayer produced by the corresponding polymers.

Silica nanoparticle has attracted increasing attention for its superior properties over conventional micrometer particles [506]. It has been widely used as filler in the manufacture of paints, rubbers, plastics, binders, functional fibers, anti-virus materials and so on. There were several attempts to achieve polymer grafted nano-sized silica composites [507,508]. Carbon chain polymer grafted silica nanoparticles had been prepared successfully by one-pot method [509], free radical [510,511] copolymerization of vinyl-modified silica nanoparticles with monomers, surface-initiated free radical polymerization [512,513] and controlled/'living' radical polymerization [514–517] of monomers from the surfaces of silica nanoparticles.

Several studies demonstrate how a different composite material can be obtained from silica and PANI with a different purpose. However, its agglomeration and incompatibility with organic matrix is an impeding problem, which limits its efficient use. Surface modification by grafting of polymers onto silica nanoparticles is an effective way to improve its dispensability and compatibility with polymeric matrix, thus enhancing the properties of composite materials. A recent study demonstrates how PANI-grafted silica nanoparticles were made by the in situ chemical oxidating of aniline with ammonium peroxodisulfate (APS) from the surfaces of aminopropyl silica nanoparticles by dispersion polymerization method [518].

The objective of the research was to keep the conducting polymer in a stable colloidal form (pioneered work of Armes et al. [96]). They succeeded in incorporating large silica particles ($\sim 1\,\mu m$) into the core of PANI. The purpose of this technique was to slow down the rate and degree of polymerization and promote polymerization on the colloidal surface rather than in the bulk.

The preparation of PANI/silica composites by sol–gel process [519], ultrasonic irradiation [520], graft polymerization of aniline [521] and template method [522] were reported. The resultant hybrids had good dispersibility and self-assembly of the conductive PANI network in the inorganic network.

Porous silica possesses high surface area. The size of pores can be tuned from 2 to 10 nm in a narrow diameter distribution by changing the experimental conditions. The synthesis of PANI in porous silica channels has attracted increasing attention [80,370,371,520–524]. This composite exhibits the property of electrorheology more than that of MCM-41 or PANI alone as a result of anisotropic polarization of the PANI/MCM-41 composite.

The enhanced hydrothermal stability and substantially larger pore diameter of SBA-15 are expected to offer additional advantages in its potential applications. Various semiconducting polymers and inorganic materials have been used as particulates in ER fluids. Recently, an MCM-41-based suspension in silicone oil, showing ER properties and conducting filament of PANI, was reported [80,523]. Cho et al. have reported the preparation of an organic/inorganic nanocomposite in which PANI was located inside the channels of mesoporous SBA-15 (PANI/SBA-15) [524].

Materials with one-dimensional nanostructure and high specific surface area can find applications as humidity sensors. Li et al. have synthesized PANI in mesoporous silica SBA-15 with a two-dimensional hexagonal structure and investigated its properties from the applied science point of view. The unique features of PANI provide a basis for potential application as a humidity control sensor [369].

A conducting fluorescent poly-*N*-[5-(8-quinolinol)ylmethyl] aniline/nano $-$ SiO_2 composite was obtained by surface modification of nano-SiO_2 particles using poly-*N*-[5-(8-quinolinol) ylmethyl] (PANQ) [525]. The conductivity of this composite was 2.72×10^{-2} S cm^{-1} at 25°C, which contained approximately 50% PANQ. It has potential commercial application as a conducting film with PL property.

Lee et al. have, for the first time, reported the expansion distribution of basal spacing of silicate layers upon the increase of PANI content in the PANI/Na^+-MMT nanocomposites using the analysis of the square of full-width at half-maximum (FWHM2) of XRD patterns [526]. Nanocomposites of polydiphenylamine (PDPA) with silica nanoparticles were prepared in the presence of ultrasonic irradiation with the aid of multiple effects of ultrasound to make processable nanocomposites [527].

Metal and metal oxide composites of PANI

Polymerization of ANI was studied by many authors over different inorganic hosts, including SiO_2, Al_2O_3, MnO_2 [452 h,488,526,528, 529,530,531], CdS and Cu_2S [532], TiO_2 [488], ZrO_2 [533], $BaTiO_3$ [534], molybdenum trisulfide [535], V_2O_5 [394,406–411,536], Nb_2O_5 [537], α-$RuCl_3$ [395b,538,539] and fly ash composites [540], for applications such as electrorheological fluids [460–466], high-density information storage devices [541] and piezo resistivity [534,542,543].

It has been reported that MnO_2, PbO_2 and NH_4VO_3 act as recoverable and recyclable oxidants for aqueous polymerization of aniline. This is an advantage with respect to the conventional oxidant system $(NH_4)_2S_2O_8$ [544,545]. These composites may find wide applications in

catalysis due to the combination of redox properties of PANI and MnO_2 in one component system.

To what extent the choice of nanodimensional metal oxide may affect the stability of composite dispersion and bulk properties of various polymer-based nanocomposites is not known. Ray and Biswas [546,547] have recently shown that Al_2O_3-based nanocomposites exhibited higher conductivities and water dispersibility relative to the corresponding MnO_2- and ZrO_2-based naocomposites. It was further observed that the particle sizes of various oxides in PANI-based nanocomposite systems are in order of: $Al_2O_3 < MnO_2 < ZrO_2$.

Copper, cobalt and nickel particles embedded in PANI matrices have also been prepared by a polyol process in which the both reduction of a precursor and polymerization are achieved in one step at 180°C [548]. Cu–PANI composite materials were prepared by using a sonochemical synthetic route in which copper (II) acetate and aniline were irradiated with a high-intensity ultrasonic horn under 1.5 atm of argon at 10°C for 3 h [549]. A simple, room-temperature one-pot chemical synthesis route for the preparation of a poly-(3,5-dimethyl aniline) and copper nanoparticle composite material, in which the copper particles are embedded in the polymer [550], are the other studies carried out using copper.

The Wacker reaction is considered as a representative one because it involves the conversion of alkene to ketone or aldehyde in a single step, which is industrially important. Athawale et al. have synthesized a copper/PANI nanocomposite and utilized it as a catalytic system to bring in the oxidation of alkene to ketone, similar to that in the case of Wacker oxidation reaction [551].

Capsules and hollow spheres have broad applications in catalysis, delivery and controlled release, optoelectronics, microcavity, resonance and photonic crystals. They have been extensively synthesized using colloidal particles as template. Recently, an emulsion template method has been used to prepare micrometer-sized PANI hollow sphere [522,552].

The pumice-based composite of PAn has been reported [553] with the aim of obtaining a more thermally stable material as compared to PANI. High-temperature conductivity measurements show 'thermal activated behavior'.

Different kinds of materials are available that can be used as magnetic parts of composite materials, such as Ni [554,555], Fe [556], Co [555], Fe_2O_3, [531,557], Fe_3O_4 [558–560], $CoFe_2O_4$ [561], $NiFe_2O_4$, Co_3O_4 and $BaFe_{12}O$ [562].

Electromagnetic functionality of nanostructured conducting polymers has attracted increasing attention because of their unique magnetic, electrical and optical properties and promising potential applications in electromagnetic interference shielding [563], electrochromic devices [564] and non-linear optical systems [565].

Among many magnetic materials, spinel ferrites exhibit remarkable magnetic properties with respect to the radio-frequency region, physical flexibility, high electrical resistivity, mechanical hardness and chemical stability [566].

Until now, the preparation of PANI with ferromagnetic properties has been mostly studied by Wan's group through two approaches:

(a) blending the PANI solution with metal salt and precipitating metal cation into metal-oxide magnetic particles [567];
(b) metal salts are used as oxidants to react with aniline, followed by treatment with alkaline aqueous solution [568].

Recently, Yavuz et al. had reported a novel approach to synthesize PANI-ferrite particles with a hybrid structure via oxidative electrochemical polymerization of aniline in an aqueous solution [569].

Deng et al. have reported the preparation of PANI–Fe_3O_4 nanoparticles with core-shell structure via in situ polymerization of aniline monomer in an aqueous solution containing Fe_3O_4 nanoparticles and surfactant NaDS [570, 571].

Most of these methods require vigorous stirring of the solution to suspend magnetic particles and prevent the aggregation of nanosize magnetic particles during the reaction.

Lu et al. have reported a novel approach called aniline dimer-assisted polymerization to synthesize PANI–Fe_3O_4 nanoparticles [572]. In this approach, Fe_3O_4 nanoparticles were modified with aniline dimer–COOH by chemical precipitation method, followed by the addition of aniline monomer and oxidant to create PANI–Fe_3O_4 nanoparticles.

Zhang et al. have reported electrically and magnetically functionalized PANI composite nanostructures containing magnetic nanoparticles, which are spherical Fe_3O_4 (10 nm in diameter) or γ-Fe_2O_3 nanoneedles (30–60 nm in diameter and 500–600 nm in length), prepared by in situ doping polymerization in the presence of H_3PO_4 as a dopant in order to improve electrical properties [573].

Sulfonated polyanilines (SPANs) have more stable and reproducible electrical properties, better solubility and higher thermal stability than PANI. SPANs possess self-doping, a different phenomenon in comparison

to PANI, via the interactions of sulfonic groups in the main-chain phenylene ring and nitrogen atom in the backbone. Fe_3O_4 (magnetite) nanoparticles were incorporated into poly(aniline-co-8-amino-2-naphthalenesulfonic acid) [574].

Although many reports have been published recently on nanocomposites of PANI with magnetic nanoparticles [531,557–560,567–573], there are few reports dealing with PANI/$NiFe_2O_4$ nanocomposites [562]. $NiFe_2O_4$/PANI nanocomposites with core-shell structure were synthesized, where $NiFe_2O_4$ was the magnetic core, and PANI had the conductive shell.

The soft magnetic Li–Ni ferrites have widely been used in microwave devices, such as isolators, circulators, phase shifters and gyrators, due to their high saturation magnetization, high electrical resistivity and low eddy current losses [575,576].

Li et al. [577] have prepared La-substituted Li–Ni ferrites ($LiNi_{0.5}$-$La_{0.02}Fe_{1.98}O_4$) by a novel rheological phase-thermolyzing oxalate precursor method and fabricated the PANI-$LiNi_{0.5}$-$La_{0.02}Fe_{1.98}O_4$ nanocomposites by in situ polymerization in aqueous solution.

High-energy ball milling is also an important method in the preparation of a wide range of materials. Kaiser et al. [578] have reported that PANI-polyvinyl chloride (PVC), PAN-polyester (PET) and PAN-polymethyl methacrylate (PMMA) composites can be prepared by high-energy ball milling. Fe_3O_4–PVC nanocomposites have also been prepared by this method [579]. Bao et al. have investigated the mixture of Fe_3O_4 and PAN powders that are milled by high-energy ball milling, and microstructural evolution and phase transformation of Fe_3O_4 occurred during the milling process [387].

Core-shell nanoparticles (CSNP) consisting of metal core and polymer shell [580] or polymer nanoparticles as the core and metal nanoparticles deposited on the polymer surface [581] have attracted interest because of their potential applications in catalysis, controlled delivery, artificial shells, light fillers, low dielectric constant materials, acoustic insulation and photonic crystals.

Among inorganic materials, gold nanoparticles have received great attention because of their unique electrical and optical properties, as well as their extensive applications in diverse areas [57,582–584].

A new microemulsion-based method to form dispersed aqueous PANI as well as Au-CSNP-PANI composites by introducing aniline monomer from the vapor phase, while the reaction being performed in aqueous solution, was also reported [585]. Microemulsion-based synthesis has previously been used to obtain metal and polymer nanoparticles wherein the particle

sizes were determined by the microemulsion 'reactor' sizes [586]. In a different experimental approach, aniline was introduced into the reaction mixture from the vapor phase with slow release from a separate container kept under ambient condition. In this way, it was possible to obtain stable nanoparticles of PANI and Au-CSNP-PANI composites dispersed in aqueous solution. For the composite to develop, H_2O_2 can be used both for the reduction of $HAuCl_4$ as well as polymerization of aniline in acidic pH, thereby producing emeraldine salt of PANI in the composite.

In the resulting PAN-metal composites, metal nanoparticles are often not effectively dispersed into the polymer matrix, because metal ions and nanoparticles interact strongly with the imino groups of the polymer and are reduced at the point of contact [587]. With the aim to overcome this problem, Kinyanjui et al. have recently developed a procedure in which gold salt is used both as an oxidizing agent to polymerize aniline and as a source of metal atoms [588]. This procedure yields well-dispersed Au nanoparticles in bulk PANI. Fiber synthesis does not require templates, nor does it require large amounts of organic solvent [433] or preformed nanofiber seeds [589]. Well-dispersed fiber-noble-metal (Ag or Au) composites are produced in a single reaction set-up, and the morphology of metal nanoparticles can be controlled by varying the aniline/metal salt ratio [590]. The electrical conductivity of composites increased with the loading of metal in the nanocomposites and can be up to 50 times greater than that of PANI fibers alone.

The strong chemical affinity between CNTs and aniline has been reported to impart solubility to CNTs [591]. As a result, CNTs have been reported to be slightly soluble in aromatic amines. It has been reported that the optical and electrical properties of PANI are influenced by the interactions between CNTs and PANI [302,592–595]. An order-of-magnitude increase in the electrical conductivity of a CNT–PANI composite over that of pristine PANI has been noticed [596,597].

Metal/alloy-nanoparticle-embedded, multiwall carbon nanotubes (MWCNTs)-based composite materials are expected to find applications in molecular electronics and other applications. Composites of MWCNT and SPAN were prepared through oxidative polymerization of a mixture of aniline, 2,5-diaminobenzene sulfonic acid and MWCNTs. Fe, Pd or Fe–Pd alloy nanoparticles were embedded into the MWCNT–SPAN matrix by the reduction of Fe, Pd or a mixture of Fe and Pd ions with radiation [598]. Metal-nanoparticle-loaded MWCNT–SPAN composites (MWCNT–SPAN–M; M ¼ Fe, Pd, or Fe–Pd alloy) have shown better thermal stability than pristine polymers. The conductivity of

MWCNT–SPAN–M composites was approximately $1.5\,S\,cm^{-1}$, which was much higher than that of SPAN ($2.46 \times 10^{-4}\,S\,cm^{-1}$).

Composites of PANI and MWNT were prepared through chemical oxidative and γ-radiation-induced polymerization of aniline in the presence of functionalized MWNT, and the composites were designated as PANI/MWNTNC (c) and PANI/MWNT-NC (γ), respectively [599]. Differences in the molecular-level interactions between PANI and MWNT influence the properties of composites prepared by chemical and γ-radiation polymerization.

Polypyrrole

Polypyrrole is one of the most studied conductive polymers because of its environmental stability and unique properties, such as biocompatibility [600], redox-tunable conductivity and ease of processability. In the absence of dopant, pristine PPy ($E_g \sim 3.2\,eV$) is an insulator and has a benzoid structure [601]. However, once doped, it functions as a polymeric semiconducting material whose conductivity can be altered to varying extents via the incorporation of anionic dopants, such as perchlorate (ClO_4^-), tetrafluoroborate (BF_4^-), sulfate ($SO_4^{=}$), chloride (Cl^-), dodecylbenzenesulfonate (DBS) and *p*-toluenesulfonate (PTS) [602,603]. Additionally, depending on the charge and size of specific dopant added, the conductivity may be reversibly modulated by external parameters, such as temperature and pressure [604], as well as by 'secondary dopants', such as water molecules [605], protons [606] and reducing oxidizing gaseous molecules (NH_3, I_2) [607,608].

The main disadvantages in PPy are poor thermal stability and poor processability in states of both melt and solution due to the nature of rigidity of its backbone. The rigidity of its chain originates from the presence of strong interchain interactions [609], which greatly limits the application of PPy in many commercial fields. In 1995, Kim et al. [610] developed a new strategy in which a dopant was used to stabilize PPy as a soluble state. Soluble PPy synthesized from pyrrole monomer with no substituent group has been synthesized chemically [611,612].

Various approaches have been utilized to make PPy processable, including: (a) chemical and electrochemical modification of PPy backbone; (b) co-polymerization with appropriate functional co-monomers; (c) use of polymeric or surfactant-type dopant anions; and (d) preparation of stable colloidal dispersion of PPy particles in an aqueous or non-aqueous medium.

In the recent years, a great deal of research has focused on the latter approach and has reported the use of a wide range of polymers for the synthesis of sterically-stabilized conducting PPy. Another modification of the technique that vigorously studied recently is formation of nanocomposites. There are numerous reports describing the preparation and properties of PPy nanocomposites, which are in fact some hybrite materials of inorganic substances like porous glasses [497,613,614], inorganic oxides [615,616], three-dimensional framework materials [617], layered materials [618,619], metal nanoparticles [620] and inorganic gels [621,622].

Here nanocomposites of PPy with inorganic oxides or salts of different metals and carbon materials in nanometer dimensions will be discussed.

Clay composites

PPy/clay nanocomposite may open a novel way to construct organic–inorganic hybrid system showing good electrical conductivity and physical properties. There are two main synthetic methods to obtain PPy/clay nanocomposites. One is the intercalation of a monomer followed by subsequent chemical in situ polymerization [623–627]. The other method is direct intercalation of PPy chains into the gallery between silicate layers from the solution [628,629]. In this method, water-soluble or colloidal PPy should be first prepared for its penetration into the gallery of silicate layers. Emulsion polymerization is also used for the preparation of PPy/clay nanocomposite, where the emulsifier in polymerization system contributes to maximizing the affinity between hydrophilic host (clay) and hydrophobic guest (pyrrole) [461c,502,630–632] . Dodecylbenzene sulfonic acid (DBSA) is commonly used in such synthesis as dopant and stabilizer [624,627].

Athough, in most attempts, the intercalative structure was obtained, exfoliated nanocomposite has better physical properties, such as stiffness, strength and barrier property, with far less inorganic content than the intercalative nanocomposite. It has been rationalized that the higher the degree of exfoliation in polymer/clay nanocomposites, the greater the enhancement of these properties [633–635].

More recently, the insertion of PPy chains into clay nanolayers by a solvent-free mechanochemical route was also investigated [636]. The emulsion pathway [461c,502,630–632,637] or electropolymerization method [638,639] has been employed to introduce PPy chains into clay galleries since nonionic pyrrole cannot be intercalated by cation exchange. These methods, however, basically require additive agents, such as an emulsifier or electrolyte, and the reaction system becomes complicated

accordingly. The mechanochemical route allows to insert PPy chains without any additive agents.

Nanocrystalline silica has been incorporated into a variety of conjugated polymers due to its excellent electrical and dielectric properties, which are extensively used in dynamic random access memory and field-effect transistors [640,641]. The change in conductivity with different compositions of PPy and an understanding of the conduction process are important. The influence of PPy on the superparamagnetic behaviur of nanosized Fe_3O_4 [642,643] and conducting PPy wide-band-gap semiconducting silica (SiO_2) nanocomposites prepared by polymerizing pyrrole in the presence of colloidal silicon oxide sol was investigated to obtain better physical properties [644].

Techniques for the preparation of composites containing conducting polymers have been recently reviewed [13,645]. Silica is the most commonly used inorganic support due to two main reasons. First, the synthesis of monodispersed silica particles is quite easy to perform and well documented in the literature [645b]. Second, various potential applications of silica-based systems are involved: gas–liquid chromatography, paints, catalyst support, biosensor, etc. [645c,646]. However, since silica is initially hydrophilic, it is very difficult to form a hydrophobic PPy shell on it by direct surface polymerization. Only 'raspberry' like composite was possibly available in this case.

Recently, Armes and Maeda [647] described the synthesis of PPy-nanocomposite colloids using ultrafine silica or Ti(IV) oxide particles as particulate dispersants. It was found that only tin (IV) oxide sols act as effective particulate dispersants; the other oxide systems failed to prevent macroscopic precipitation of PPy. These PPy-tin (1V) oxide particles have a rather polydisperse 'raspberry' morphology as compared to the relatively monodisperse 'raspberry' morphology found for PPy-silica particles. The high density of tin (IV) oxide particles leads to PPy-tin (1V) oxide nanocomposites with significantly higher particle densities than PPy-silica nanocomposites. These nanocomposites are not as stable as PPy-silica colloids with respect to pH-induced aggregation, but their solid-state conductivities are higher by up to an order of magnitude. The highest conductivity obtained for PPy-tin (IV) oxide nanocomposites was $23\,S\,cm^{-1}$.

Confined polymerization is a very pertinent way to give conducting polymers controlled shape and dimension, which addresses the question of the availability of appropriate templates. The use of microtubules of PPy rather than films is much more efficient for the immobilization of

biologically active species such as glucose oxidase and, in this case, for direct electron transfer between the enzyme and conducting polymer, thus improving electrochemical detection [648]. Recently, commercially available particle track-etched membrane (PTM) templates [649], nanoporous PTM's as templates [650], microgels [651] and template-free methods [652] were applied to synthesize microtubules for such purposes.

A general overview of polymer– and biopolymer–clay nanocomposites showing attractive properties for electrochemical and electroanalytical applications, including the latest advances in this field, is discussed in [653].

Polypyrrole is one of the most extensively used conducting polymers in bioanalytical sensors as well as for other purposes. Electrochemically generated and deposited PPy is successfully exploited for the development of various types of electrochemical sensors and biosensors. Electrochemical sensors based on PPy are reviewed in Ramanavicius article [653b]. In this review, significant attention was paid to immobilization of biologically active molecules within PPy during the electrochemical deposition of this polymer. The unique properties of this polymer such as prevention of some undesirable electrochemical interactions and facilitation of electron transfer from some redox enzymes were discussed. Recent advances in the application of PPy in immunosensors and DNA sensors are presented. Some new electrochemical target-DNA and target-protein detection methods based on changes in the semiconducting properties of electrochemically generated PPy doped by affinity agents are introduced. The recent progress and problems in the development of molecularly imprinted PPy are also discussed.

Protein adsorption onto (polymeric) surfaces is very actively studied for the development of biomaterials, biological assays and biosensors in addition to fundamental research on its driving mechanisms. The primary driving force of protein adsorption seems to be the hydrophobic interactions. Electrostatic contributions also play an important role, particularly in the more hydrophilic surfaces. In addition, surface geometry and topographic considerations are likely to play a role. Other contributions to protein adsorption, such as those due to van der Waals forces, have been known, but they are much lower in magnitude. Investigations on the role of molecular forces governing protein adsorption were mainly conducted in the case of classical materials, such as metals, minerals and polymers. As far as the latter application is concerned, it has been shown that protein adsorption rather than covalent grafting can be sufficient for the development of a new assay using PPy-based material as a carrier for the antibody. PPy powder was found to be a fairly strong bioadsorbent of DNA

fragments. Electrostatic interactions were found to be the driving forces for DNA-PPy interactions since DNA is negatively charged and PPy is positively charged. Adsorption is favored on PPy-silica nanocomposites, which bear positive charges at the surfaces or strong hydrogen-bonding functional groups [654]. PPy/silica nanocomposites will have interesting biological applications (e.g. as highly colored 'marker' particles in visual agglutination immunodiagnostic assays).

Recent developments in this type of electrode make it one of the major tools for nanobiotechnological applications [655]. A novel DNA biosensor has been elaborated by means of an opposite-charged adsorption of Au-Ag nanocomposite to a conductive polymer PPy modified platinum (Pt) electrode and self-assembly of mercapto oligonucleotide probes onto the surface of modified electrode via the nanocomposite. The potential for development of reagentless DNA hybridization analysis in clinical diagnosis has been pursued.

Considerable research activity was focused on the functionalization of PPy and/or silica to developed nanocomposites for bioanalytical and other applications [656–661]. In order to increase the interaction between silica particles and pyrrole, they were modifed by aminopropyltriethoxysilane (APS) and acted as porous inorganic substrates for in situ synthesis of Py. Aminopropyl silane (aminopropyltrimethoxysilane, APS) coupling agent has been used to pretreat silica before PPy polymerization, and silica–PPy composites with PPy-rich surface were obtained [656]. Using the LBL self-assembly technique [657], the most common problem of particle aggregation upon deposition of conducting polymers could be overcome by localizing polymerization of the monomer within the polyelectrolyte multilayers resulting in the synthesis of a novel sunflower-like conducting polymer–inorganic composite [658]. For the first time, a natural biomacromolecule-chitosan was chosen as an adsorbent to alter the surface properties of silica. The acetylamino group of chitosan was considered to form hydrogen bonding with hydrogen atom on nitrogen of PPy, which ensures fixed-site growing of PPy on silica. Anchoring PPy particles uniformly on silica to obtain novel surface morphology can optimize the colloidal stability and conductivity of the silica–PPy composite particle.

The synthesis of carboxylated PPy-silica microparticles using a 3-substituted pyrrole-based co-monomer, pyrrole-3-acetic acid, in combination with a hydrogen peroxide-based oxidant system was described by Yamamoto et al. [659].

SiC is a promising material for high-temperature and high-power applications. It is also used as a filler in polymer matrices for the preparation of

composite materials [660]. Silicon carbide/PPy composites are considered as novel conducting polymer-coated fillers. SiC is a well-known ceramic material of scientific interest, because of its unique properties of high chemical and temperature stability and hardness. Non-conductive alpha modification of SiC can be modified by a conducting polymer for the preparation of a new type of filler materials [661].

Metal and metal oxide composites of PPy

Polypyrroles may be obtained from several materials, such Fe_3O_4 and Fe_2O_3 oxides [82,647d,662], FeOCl [82,663], V_2O_5 [83,394], WO_3 [664], MoO [665,666], $VOPO_4$ [396–399] and porous vycor glass (PVG) [613]. These new hybrid materials, considered as innovative advanced materials, promise new applications in many fields such as optics, electronics, mechanics and biology.

The most common method to obtain conducting polymer nanocomposite with oxide nanoparticles is the direct polymerization technique. Heterogeneous nanocomposites of conducting PPy have been synthesized from different kinds of inorganic oxides, such as NiO, SnO_2, CuO, ZnO, CeO_2, etc. [647b,d,667].

Fe_3O_4 and Fe_2O_3 oxides are good candidates to investigate PPy/oxide composite films in view of their higher oxidizing power.

Magnetic composite materials comprise a new generation of multifunctional materials that combine the properties of ordinary polymer and magnetic materials (ferri- and/or ferromagnetic particles mixed or embedded in a matrix), which are called *magnetopolymeric* materials. Although research on granular materials started as early as 1970s [668], the more recent studies on granular solids have focused on the unique magnetic properties originated from dispersed nanoparticles embedded in magnetic insulating or metallic media [669]. In this context, metal/non-metal nanogranular structures have been the subject of research interest, because magnetic composite materials with nanogranular structure have potential applications as magnetoresistance materials for high-frequency ranges. By combining the electrical conductivity of CPs and the magnetic properties of ferrite nanoparticles in a single material, new multifunctional materials may be developed.

Several groups have demonstrated the syntheses of nanometer-sized Fe_3O_4-PPy [662a,e] and γ-Fe_2O_3-PPy [82,647d,662,670] systems. However, an aqueous processing route at room temperature was commonly used for the fabrication of either Fe_3O_4 or γ-Fe_2O_3 inorganic nanoparticles in these reports. Since saturation magnetization is closely associated to

the crystallinity of an inorganic nanocomponent, Sunderland et al. [671] have replaced aqueous processing and further employed a high-temperature organic solution approach [672] to prepare inorganic nanocrystals with high crystallinity.

Chen et al. have presented a novel approach to synthesize core-shell Fe_3O_4–PPy nanocomposites, where Fe_3O_4 is the magnetic core and PPy is the conducting shell [673].

Several approaches to preparing nanocomposites consisting of magnetic nanoparticles and conducting PPy have been reported [662a].

(a) electrochemical method to prepare PPy–ferromagnetic composite films;
(b) chemical method to prepare PPy–ferromagnetic composite in the presence of sodium *p*-dodecylbenzenesulfonate (NaDS), which functions as a surfactant and dopant; $FeCl_2 \cdot 4H_2O$ and $FeCl_3 \cdot 6H2O$ are used as oxidants to react with pyrrole, followed by treatment with hot NaOH solution;
(c) simultaneous gelation and polymerization to prepare PPy and iron oxide nanocomposites;
(d) layer-by-layer self-assembly of conducting polymers and ferrite nanoparticles in aqueous solutions.

Although Fe_2O_3–PPy composites have been successfully prepared by various methods, they still have low-room-temperature conductivity (10^{-4}–10^{-1} S cm^{-1}) and low coercive force. One promising approach is the direct polymerization of pyrrole in the presence of Fe_3O_4 nanoparticles. Novel nanocomposites with a well-defined core-shell structure may be obtained [662a]. Gangopadhyay and De have reported easy chemical synthesis of a Fe_2O_3-encapsulated PPy nanocomposite [674].

Nanocomposites of iron oxide–PPy obtained by simultaneous gelation and polymerization [675] showed remarkable variation in magnetic and electrical properties with different concentrations of the monomer [59]. These thermal studies on iron oxides can help in understanding the transition behaviur of iron oxide. It is known that iron oxide exists in three forms – FeO, Fe_2O_3(γ-Fe_2O_3 and α-Fe_2O_3) and Fe_3O_4. Transformation from one form to the other is possible by oxidation or reduction mechanism [557].

A new method was applied to obtain PPy/zirconium nancomposite. PPy/zirconium oxopolymer composites, using the sol–gel polymerization process, have been prepared with five N-functionalized pyrrole derivatives including specific zirconium complexing agents (carboxylic acid

(CA) or β-diketone, acetylacetone (acac) or dibenzoylmethane (dbm) moieties) [676]. The use of functionalized pyrrole derivative group allows to control the polymerization rate of zirconium tetrapropoxide ($Zr(OPr)_4$). The organic species entrapped in the resulting hybrid materials yield conducting polymers by electropolymerization. The results show that the formation of conducting polymers depends on the nature of the monomer. Moreover, the presence of polysiloxane chains within the hybrid materials improves the properties of the latter.

The interest in the irradiation of polymers with high-energy ions initially came from their ability to register nuclear tracks and applications of polymers as particle detectors or membranes [677–679]. Conducting polymers like PANI, PPy and PTh were previously bombarded by beams of hydrogen, boron, fluorine, phosphorous and argon ions of low energy [680,681] with the aim to observe the effects of implantation on the electrical conductivity of polymers. Schiestel et al. [681] have observed the increase in resistivity by several orders of magnitude when PPy was irradiated by noble gas ions. The modification and structuring of conducting polymer blends using 14 keV argon ions have been recently studied [682]. It was shown that a lateral structure of micrometer scale can be produced using irradiation. The effects of irradiation on pure PPy and PPy–ZrO_2 nanocomposites with 12 C and 16 O beams of moderate energies were studied by the measurement of electrical conductivity and through X-ray diffraction and thermogravimetry, before and after irradiation [683]. The results indicate that the electrical conductivity of nanocomposites is very slightly affected by irradiation with heavy ions, but the conductivity of pure PPy is much more susceptible to heavy ion irradiation.

There are numerous publications describing the preparation of inorganic–organic hybrid materials, which contain PPy as the organic component. For example, yttrium oxide (Y_2O_3) nanoparticles have been intensively studied because of their good thermal stability as well as their wide applications in the host matrices of phosphors, catalyst support or even catalysts, and dielectric insulators of electroluminescent devices [684c]. Facile chemical synthesis of nano-Y_2O_3 encapsulated PPy composites was also reported [685]. Thermogravimetric analysis has shown that the composite has better thermal stability than that of pure PPy.

Conducting polymers have also been successfully prepared with the combination of noble metals, such as Pd, Pt, Ag or Au [580a], for catalitic applications.

The production of polyphenylpyrrole-coated silver nanoparticles at the liquid/liquid interface by EC-type mechanism has been reported. In

the electrochemical step of the reaction, N-phenylpyrrole facilitates the transfer of silver ion from an aqueous to an organic phase. This step was followed by a slow homogeneous electron transfer reaction from N-phenylpyrrole to the silver ion followed by polymerization and metal cluster growth [686].

As shown in literature [687], some efforts were made to enhance the conductivity and stability of PPy for practical applications. For this purpose, nanocomposite of 80 nm a Al_2O_3-incorporated PPy film was electropolymerized on a Au substrate. It was found that the nucleation and growth were instantaneous three-dimensional processes before and after nuclei overlapping for pure PPy electropolymerization. However, a distinguishable nucleation and growth mechanism before nuclei overlapping was shown for the preparation of the nanocomposite. The nanocomposite demonstrated an extremely high oxidation level. The conductivity of the nanocomposite was increased substantially ($\sim$5.4 times).

Conducting polymers have also been studied for their electronic properties. Recently, Cunnane and Evans [688] have generated conducting polymers electrochemically at the interface between two immiscible electrolyte solutions (ITIES). Furthermore, Cheng and Schirin [689] have electrodeposited metal particles at the ITIES.

Inorganic ion-exchange materials based on polyvalent metals were found to have applications in various disciplines, such as metal-ion separation, preconcentration, catalysis, environmental studies, medical science (kidney dialysis), ion-selective electrode preparation, heterogeneous solid-state membrane formation and ion-exchange fiber preparation. Systematic studies on the adsorption behavior of hydroxides and hydrous oxides of multivalent metals have indicated that crystalline antimonic acid acts as an excellent cation exchange material [690].

The antimonic acid prepared by taking potassium pyroantimonate $KSb(OH)_6$ as the starting material showed a higher ion-exchange capacity as against $SbCl_5$ [691]. Preparation characterization and analytical application of PPy–polyantimonic acid composite materials by simultaneous gelation was also reported [617,692,693].

In various cases, the encapsulation of semiconductor metal oxides into the core of conducting polymers to obtain novel core-shell nanostructures has become the most alluring aspect of nanocomposite synthesis in the past decade [12,13,694]. In this respect, well-defined nanostructures of semiconductor metal oxides (e.g. high-aspect-ratio nanorods, tubes or belts) with unique electric transporting characteristics would be more essential than irregular particles in terms of their higher carrier mobilities [12,13,75,

694,695] to be used in composite solar cell devices after the introduction of conducting polymers.

Novel core-shell micro/nanostructured and electromagnetic functionalized composites of PPy were prepared by self-assembly process in the presence of *p*-TSA as a dopant, in which spherical hydroxyl iron (Fe[OH], 0.5–5 *ím* in diameter) acted as the 'core' and self-assembled PPy nanofibers (20–30 nm in diameter) served as the 'shell' (50–100 nm in thickness). It was shown that micro/nanostructured composites exhibit high conductivity (50.6 S/cm) and superparamagnetic properties [696].

It is well known that water-in-oil (W/O) microemulsions are low-viscous, transparent, isotropic and thermodynamically stable liquid medium, which can be formed spontaneously by mixing a surfactant, a cosurfactant, oil and water. The micelles have been utilized as nanoreactors because they are fairly thermodynamically stable even though, under ultrasonic and vigorous agitation, chemical reactions may occur within the macro droplets or at oil/water interfaces. In the recent years, many studies have been conducted on the fabrication of inorganic, organic and inorganic–organic nanoparticles [697] by reverse microemulsion-mediated methods.

In blends prepared by in situ polymerization, the low solubility of the monomer in the insulating matrix can make the blend less conductive. To obtain highly conducting polymer materials and to lower the percolation threshold, different morphologies have been developed by in situ polymerization within the lamellar microdomains of block copolymers as well as inside the void space of a (micro or nano) porous polymeric matrix or inside the interstitial domains of a crystallizable host matrix. Hopkins and Reynolds [15] have analyzed electrical conductivity in blends prepared with PANI and an amorphous or a crystalline polyamide as insulating host. They observed that the conductivity of a crystalline host is 10 times higher than that of the amorphous one. Corres et al. have investigated the role of the crystallization process on the electrical conductivity of the PPy-based material [698]. Poly(3-caprolactone) (PCL) and PPy were used as crystalline and conductive polymers, respectively. Compared with amorphous matrices, considerable conductivity ($\sim$1 S/cm) was reached with the crystalline PCL matrix with a relatively low level of conductive polymer (w5%) in the blend.

Electrochemomechanical deformation of CP films is significantly affected by film morphology. Since a CP film typically has a symmetric structure, it exhibits uniform volume changes during the redox process and it cannot do bending movement as an actuator is distributed across the cross-section. Therefore, most of the CP actuators have been constructed

based on either bilayer or multilayer configuration. However, the inevitable delamination in multilayer actuators shortens their lifetime, because the physical adhesion between the inert layer and the CP layer(s) cannot sustain repeated volume alteration at their interfaces. In comparison to conventional multilayered actuators, monolithic actuators have advantages of higher efficiency and better structural stability. Although actuators have a very long lifetime ($> 3\,25\,000$ cycles), they could operate only at a high driving potential (± 2 V) in acidic medium and not do uniform bending. The main problem is low conductivity. Recently, an attempt was made to develop new materials for this purpose. A PPy film grown in a slender pipe of polytetrafluoroethylene has a considerable vertical anisotropy and can perform bending movements. High-performance actuators can also be fabricated from an anisotropic PPy-oxide nanoparticle composite film formed by direct co-deposition of PPy and nanoparticles from an electrolyte with or without TiO_2 nanoparticles [699]. The volume content of TiO_2 in the composite film, when tested, was lower than 0.9%. The actuator fabricated from this monolithic PPy film bends uniformly in two directions with an increased bending angle and has a high response rate and a long life time ($> 20\,000$ cycles) in a 1 M $LiClO_4$ aqueous solution. The high performance of this actuator resulted from non-delamination and the intrinsic asymmetric structure and high conductivity of PPy film.

Miniaturization, integration and intelligentization are notable characteristics of modern analytical chemistry, where micro electro-mechanical system (MEMS) plays an important role in fabricating various miniaturized analytical devices.

As a result of many recent advances in semiconductor manufacturing, the gap between main memory and disks is constantly increasing. This leads to significant performance bottleneck for Relational Database Management Systems. Recent advances in nanotechnology have led to the invention of based storage technology to replace disks. Many works are devoted to investigate and integrate conductive polymer nanomaterial technologies with MEMS processes for sensing applications with distinctive advantages over other approaches.

The ease of processing, mechanical flexibility and resistivity control make electrically conductive polymer films suitable for use in MEMS devices (stiction reduction).

Polypyrrole is a promising candidate for applications aimed at reducing electrostatic stiction in MEMS through reduced charge trapping because of anti-static properties [700]. In addition, the high conductivity of PPy films lends themselves well for use as electrical contacts between devices or

microwire fabrication [701]. Before PPy can be employed successfully in MEMS technology, a number of issues must be investigated, including the electrical characteristics and physiochemical stability of conductive thin films. Recently, materials based on PPy were explored as sensing materials in MEMS applications [702].

Novel immunoassays for screening of disease markers in human serum are presented by miniaturizing interdigitated array (IDA) of microelectrodes via MEMS on a silicon chip for multi-channel electrochemical measurements [702b]. Different selected antibodies are incorporated site-specifically into the electrochemically deposited PPy formed on the IDA of silicon chip.

The chip-based immunoassay shows the advantages of high sensitivity, good specificity, high throughput, low sample consumption and stability offered via batch production by MEMS as well, which is expected to benefit the multitarget screening of desired clinical analytes.

Peteu has reviewed smart materials configured for actuation, artificial channels and pore sensing. The electroactive polymers are outlined with PPy as the main example [702b]. PPy nanofabrication by template synthesis is also briefly outlined. This review concludes with several recently reported functionalized nanotube membranes as examples of artificial membrane-supported ion channels.

The layer-by-layer processing technique is used to deposit alternate layers of oppositely charged polyelectrolytes, namely sulfonated PS (polyanion) and PPy (polycation), onto a silicon or oxide substrate [702d]. This technique allows the organization of conducting polymers into multilayer films with the control of film resistivity, thickness and molecular architecture through solution chemistry and substrate preparation. Roemer et al. have reported the use of PANI and PPy for miniaturized actuators fabricated by microstructural and electrochemical technologies. The potential necessary to drive an actuator is typically less than 1 V, i.e., two to three orders of magnitude lower than that necessary for piezoelectric actuator devices. This low voltage is imperative for the future application of actuators of micrometer dimensions [702f]. The volume variation of polymers substantially exceeds that of piezoelectric materials. Different contributions to actuator characteristics are discussed and evaluated semiquantitatively.

Polythiophene

Among conducting polymers, various derivatives of PTh have been investigated extensively because of their interesting semiconducting, electronic

and optical properties, combined with processing advantages and good mechanical characteristics. Compared with many other p-conjugated polymers, they show sufficient stability for practical applications. Depending on their doping level, PThs behave either as metal-like conductors or semiconductors. When doped to metallic level, PThs become highly conducting and may find applications in batteries, electrochromic or smart windows, antistatic coatings and various types of sensors. On the other hand, in the semiconducting form, they exhibit similar electrical and optical properties as inorganic semiconductors. High-performance electrical or optoelectrical devices, such as LEDs, field-effect transistors (o-FET) and photovoltaic cells, fabricated from conjugated polymers have been demonstrated [703].

A review by Roncali [704] refers to the work on some PTh–polymer (poly (methyl methacrylate), poly (vinyl chloride), PS (PMMA, PVC, PS)) composites by direct electropolymerization of Th in the presence of the respective host polymer and on other PTh composites using multistep methods. Besides these procedures, polymethylthiophene–metal (Ag, Pt, Cu, Pd) composites were prepared by electrodeposition. More recently, in situ intercalative polymerization of Th derivatives in host matrices, such as FeOCl, zeolite or xerogels, was also reported.

Recently, the combination of semiconducting and mechanical properties of conjugated polymers with those of metals or semiconducting inorganic particles has shown new prospects for applications [12,662b,705]. A number of different metallic and metal oxide particles have been encapsulated into the shell of conducting polymers giving rise to a host of nanocomposites [13,647b,673,706].

The properties of materials produced by electropolymerization of monomers containing both transition metals and thiophene were reviewed [707].

A series of publications have reported the preparation and evaluation of nanocomposites of PTh with TiO_2 and Al_2O_3 [706a,708]. PTh nanocomposites combining both insulating and nanostructure properties, are available now. The preparation of PTh/PS/silica nanocomposite (PTh/PS/SiO_2) and PTh/SiO_2 materials by dispersing the inorganic nanomatrix SiO_2, an organic thiophene matrix, by in situ oxidative polymerization was reported [709]. TGA has revealed enhanced thermal stability of the PT/PS/SiO_2 nanocomposite as compared to that of PTh. SEMs have shown globular particles and the presence of clusters of composite particles. The conductivity of the PTh/PS/SiO_2 nanocomposite was measured to be 1.30×10^{-7} S cm^{-1}, and the conductivity value of PTh (1.02×10^{-4} S cm^{-1}) decreased with incorporation of PS and SiO_2 to PTh structure.

In view of the insolubility of Th in water, conventional procedures, such as injecting water-soluble monomers into an aqueous dispersion of metal oxide containing $FeCl_3$ [36,91,96,533,710] in the case of PY- or ANI-based systems, could not be applied for the preparation of PTh–metal oxide composites. Yet another hurdle was that, unlike PY, Th is more difficult to oxidize by $FeCl_3$, which stands in the way of achieving high yields of PTh during chemical oxidative polymerization.

Ballav et al. were able to develop a convenient procedure for the preparation of PTh with high yield in the presence of $FeCl_3$ as the oxidant. By applying this procedure, they have prepared PTh–Al_2O_3 nanocomposites [708c]. Nanodimensional Al_2O_3 was chosen as the dispersant because of its ultra-small size ($\sim$10 nm) as compared to other oxides commonly used, such as SiO_2, SnO_2, MnO_2 and ZrO_2. Dispersibility appeared to be higher when polymerization was conducted in a suspension containing a higher amount of Al_2O_3. Transmission electron micrographic (TEM) analyses revealed the particle size of the composite to be in the range of 22–74 nm. Thermal analyses (TG/DTA) revealed the outstanding stability of PTh–Al_2O_3 composites as compared to that of PTh. The conductivity of PTP and PTP–Al_2O_3 composite was of the order of 10^{-3} S cm^{-1} for samples doped with I_2.

Recently, PTh derivatives have been widely studied because of their interesting properties and possible applications [703]. For example, poly-3,4-ethylenedioxythiophene was used as a hole conductor in solid-state solar cells [711]. Polybithiophene was also used in photovoltaic devices [712]. Poly-3-methylthiophene was applied in diyotes [705c,713] and solar cells [705b,714]. Exploitation of soluble PTh derivatives like poly (3-alkylthiophene) in thin-film electronic devices, such as organic field effect transistors (o-FET) [715], LEDs [716], photovoltaic devices [717], was described. The solubility of poly (3-alkylthiophene) makes it easy to be formed on thin solid films using spin coating technique. However, the substitution may deteriorate the electric properties by steric hindrance effects or charge induction. Some applications based on insoluble PThs, such as poly-3-methylthiophene, polybithiophene and poly-3,4-ethylenedioxythiophene, have also been reported [703b,705,711–714].

Electrophoretic deposition (EPD) is essentially a two-step process. In the first step, the charged particles in a liquid migrate towards an electrode under an electric field (electrophoresis). In the second step, the particles are deposited on the electrode surface forming a homogeneous film via particle coagulation.

In recent reports [718], the possibility of using EPD for the preparation of photosensitive nanostructured layers composed of core-shell nanoparticles with TiO_2 core and about 3 nm thick PTh shell was investigated. The EPD method used for the preparation of nanostructured layers was extended to other core-shell systems based on various metal oxides and PTh with the aim to test the suitability of EPD method, the influence of core material on the EPD process and the quality of the resulting layers. The kinetics and mechanism of the EPD of metal oxide nanoparticles with a shell of conducting polymers were studied.

Poly(3,4-ethylenedithiathiophene) (PEDiTT) is completely soluble in 1-methyl-2-pyrrolidinone (NMP) and partly soluble in tetrahydrofuran (THF) and chloroform [719], and it has relatively good stability and high electrical conductivity due to the regular backbone structure. These properties make this polymer suitable for electrochemical catalytic applications.

Among the novel metals, platinum fine particles show the highest catalytic activity, but supporting materials (or matrixes) are required for their practical applications. By introducing platinum nanoparticles into the polymer matrix by doping reaction, organic/inorganic nanocomposites can be formed. Electrochemical catalytic character for methanol oxidation was investigated by adopting various electrochemical methods because it is a very important reaction in direct methanol fuel cell (DMFC), and methanol is one of the most promising fuels for the future. PEDiTT/Pt nanocomposites were prepared to give electrochemical catalytic character to the Pt fine particle for methanol oxidation and the composite showed catalytic behavior [720].

Polyfuran is known for its outstanding electrical properties [721]. However, polymerization of furan would be expected to be restricted because of its higher diene character rather than aromatic character relative to PY (nitrogen analogue of furan) or Th (sulfur analogue of furan). In this background, PF homopolymer and nanocomposite of PF with Al_2O_3 and MMT were prepared [722]. It is noteworthy that PF–MMT composite was directly obtained via intercalative polymerization of furan in MMT clay without any extraneous oxidant – a feature not reported so far in PANI–MMT or PPy–MMT composite systems.

A number of different metallic and metal oxide particles have been encapsulated into the shell of conducting polymers, giving rise to a host of nanocomposites [13,706,708a]. For example, the morphology and chemical structure of PTh/TiO_2 core-shell nanocomposite particles, prepared via Sugimoto's oxidative polymerization of thiophene in the presence of nanoscopic titanium dioxide, were studied by TEM and Raman spectroscopy [708a].

Wang et al. have used thiolates with pyrrole monomers to cap gold nanoparticles [723]. However, due to the fast and uncontrollable oxidation rate of pyrrole units, the chemical oxidation of protected gold nanoparticles leads to diffuse and disordered structure, which may hamper further applications of the material. Zhang et al. [724] have reported the two-step process of preparing poly(3-(10-mercaptodecyl)thiophene)-coated gold nanoparticle core-shell structure with uniform size of 6–8 nm. The nanoparticles can be dispersed in usual organic solvents such as ethanol. These nanoparticles can be easily processed and have potential applications in nanoscale architectures and development of novel electronic devices.

Until now, much of research works on inorganic/conducting polymer composites with good electrical and magnetic properties mainly focused on magnetic PPy nanocomposites [674] and magnetic PANI nanocomposites [49]. However, few reports on magnetic PTh nanocomposites (a novel chemical synthesis of γ-Fe_2O_3 encapsulated PTh (γ-Fe_2O_3-PTh) conducting nanocomposite [725]) are available.

There was considerable interest in the use of PTh sensors. PThs were shown to detect ppb of hydrazine gas [726].

Ram et al. have used two approaches for improving the selectivity to NO_2 gas [727]. The first approach was connected to the use of layered thin films of regioregular PThs and LBL or in situ self-assembled films of PANI, PPy, PTh and their copolymers. The second approach involved the preparation and investigation of a nanocomposite layer using in situ self-assembly technique, allowing the specific detection of NO_2 gas for the first time.

Creative designs and development strategies for new PThs have led to interesting new materials and enhanced performances in certain devices. Generally, the template synthesis method, which involves a microporous membrane as template for microtube formation, is an effective method for synthesizing conducting tubular polymers. George et al. [728] first proposed the template synthesis method, and other groups applied the method successfully to the synthesis of poly(alkylthiophene) [729], PPy [730], polyacetylene [731], and PANI [732] tubular forms.

SWNTs were coated with conducting PTh, and a new tubular material (SWNT–PTh composite) was synthesized with in situ chemical oxidative polymerization method [733].

n-doped CP/SWNT's photoconductive response is interesting for a fundamental understanding of the n-doped CP/SWNT photo-induced process and for the development of new photosensitive materials with unique optical and conductivity features. In light of current requirements for

photodegradation studies, as well as for the exploration of such composites as photovoltaic material, fundamental interactions between molecular oxygen and thin films of n-doped poly(3-octylthiophene) (P3OT)/SWNTs were studied [734].

CdS nanowires have considerable applications in optoelectronic devices, such as LEDs, and optical devices based on non-linear properties. Regioregular poly(3-hexyl thiophene) (P3HT) is an important semiconducting polymer with good luminescence properties. It was reported that CdS nanoparticles can be embedded into P3HT to form a nanocomposite in which mixed nanowire of P3HT with CdS of high aspect ratio is present [63]. Both DC and AC conductivities of P3HT and CdS–P3HT nanocomposites have shown semiconducting nature. The conductivity of CdS–P3HT was much less than that of the pure P3HT conducting polymer. The difference in the electrical behavior is attributed to the formation of nanowires in the CdS–P3HT nanocomposite. The synthesis of CdSe nanoparticles with poly(3-hexylthiophene) was also studied using microscopic, electrochemical and spectroscopic techniques [735].

Polyvinylcarbazole

Poly[3,3′(vinylcarbazole)] (PVNC) is widely used in LEDs, xerography and, in general, as an electro-optically active polymer [736].

Although this polymer has outstanding thermal stability and its photophysical characteristics might prove challenging materials, not many researches are available in this regard. The observed conductivity values for PNVC-based systems is not attractively high; however, this value can be significantly improved by modification. Recently, hybrid composite materials have attracted increased research attention due to remarkable change in their properties. Following the developments on other conducting polymers, it is possible to obtain processable aqueous dispersions of nanocomposites of PNVC. Due to the insolubility of *N*-vinylcarbazole monomer (NVC) in water unlike pyrrole or aniline, the procedures routinely adopted for these latter momoners [35,36,96] could not be applied for the preparation of water-dispersible composites of PNVC.

Sinha et al. have reported [710b] the preparation of stable aqueous dispersion of a PNVC-colloidal silica nanocomposite by using a biphasic NVC (benzene)/$FeCl_3$-impregnated silica alcohol/polymerization systems. However, in this system, the use of a polymeric stabilizer like polyvinylpyrrollidone (PVP) was essential. Relevantly, they failed to obtain a stable aqueous dispersion of a PNVC–MMT nanocomposite even by using PVP [91].

In this background, Biswas et al. have recently made an interesting finding that colloidal Mn (IV) oxide could form stable water-dispersible nanocomposites of PNVC, PPy and PANI without any polymeric stabilizer [530]. The PNVC–MnO_2 nanocomposite preparation was based on the unique behaviur of NVC monomer to be initiated directly by 3D-transition metal ions. However, direct initiation of PY or ANI polymerization by MnO was not possible.

PVCZ nanocomposites with other nanodimensional metal oxides, such as ZrO_2 [533], were also reported. TEM analyses confirmed the particle sizes to be in the 300–500 nm range for PNVC–ZrO_2 and in the 250–300 nm range for the PANI–ZrO_2 composites, respectively. TG analyses have revealed enhanced stabilities of nanocomposites relative to the base polymers. DC conductivities of PNVC–ZrO_2 composites were of the order of $(1–1.5) \times 10^{-5}$ S/cm, which were 10^7–10^{10}-fold improved with respect to the base polymer. Similarly, the conductivity of PANI–ZrO_2 composite was in the range of $(0.03–0.35) \times 10^{-2}$ S/cm, which increases with the increase of polymer loading in the composites.

In the course of our ongoing research in this area, the development of a simple method for preparing a nanocomposite of PNVC with nanodimensional alumina [737] by depositing PNVC from its solution in tetrahydrofuran (THF) on a dispersion of Al_2O_3 in water medium was also repoted.

These procedures have been extended to preparing water-dispersible nanocomposites of mixed polymer systems PPy–PNVC. Thus, by adding pyrrole monomer to a suspension of PNVC–Al_2O_3 composite in water prepared in the presence of $FeCl_3$, a PPy–(PNVC–Al_2O_3) composite could be readily prepared. Similarly, by adding preformed PNVC to a suspension of PPy–Al_2O_3 in water, a PNVC–(PPy–Al_2O_3) composite could be prepared [738].

The resulting composites from such mixed polymer systems would exhibit distinctive bulk properties of the individual polymer components.

However, the conductivity values of these PANI-, PPy- or PTP-based composites were not so high, and for the PNVC-based composites, particularly, the conductivity of 10^{-5}–10^{-7} S cm^{-1} was realized [43,530,533,708b,737–739].

In this background, Biswas et al. have reported the preparation and some properties of a highly conductive composite of PNVC with acetylene black (AB) via in situ polymerization of NVC by AB in bulk or solvent [43]. In their earlier report, they have found that several grades of CB, such as Orient black (N220) and Vulcan XC-72, were effective for NVC initiation

without any added oxidant [41,740]. Ohkita et al. [42], however, have described polymerization vis-a-vis grafting of vinyl polymers on to CB in the presence of free radical catalysts.

Among various transition metals, a distinctive feature of the chemistry of vanadium (V), molybdenum (Mo) and tungsten (W) is their capacity to form isopolymetallates (IPM) in aqueous acidic solution [741].

Colloidal molybdenum blue (MB) suspension is believed to be the oxide/hydroxide species of mixed valance, forming a series between the extremes of $MoVIO_3$ and $MoVO(OH)_3$. However, a precise explanation of their color is lacking [742]. Attempts were made to explore the interaction of NVC, PY, ANI and TP with various IPV (VV ion) and IPMo (MoVI ion) species. Ballav and Biswas [722] have observed that IPMo could act as the oxidant for polymerization of PY. During the course of interaction of PY with IPMo moieties, simultaneous reduction of IPMo led to the formation of a PPy–MB nanocomposite. Very recently, these authors [743] isolated a conducting PNVC–MB nanocomposite from the NVC–MB polymerization system.

In course of the ongoing research on molybdenum blue-based nanocomposites of polymers like PPy and PNVC, polymerization of NVC by PPy–MB nanocomposite, resulting in the formation of a PPy–MB–PNVC nanocomposite with appreciably high conductivity value, was achieved. A high conducting variety of PPy–MB nanocomposite was also prepared [32]. In this study, some relevant features on the preparation of PPy–MB, PNVC–MB and PPy–MB–PNVC nanocomposites and the results of evaluation of some bulk properties of these composites were reported.

Recently, Ballav et al. have reported a procedure for polymerization of NVC in an aqueous suspension in the presence of vanadium ion [744]. Thermogravimetric stability studies (TGA/DTA) have revealed that PNVC underwent about 60% weight loss in up to 1000°C and suggested the formation of a structure different from that of conventional PNVC homopolymer soluble in solvents. NVC-VV polymerization system was found to be intractable in nature and confirmed to be due to the formation of a cross-linked polymer structure. A possible pathway for the polymerization of NVC via coupling of aromatic rings vis-a-vis in situ formation of cross-linked PNVC (CLPNVC) has been proposed.

Among the different techniques used to obtain thin films, significant interest has been centred on the utilization of techniques such as Langmuir–Blodgett (LB), a vertical dipping method, and/or Langmuir–Schaefer (LS), a horizontal dipping method, due to their potential to build up monolayers or multilayers in which order at the molecular level can be controlled [745].

The LB/LS techniques have an advantage that it uses a very small amount of the material in contrast to the commonly used techniques, such as solution cast and spin coating. Bertoncello et al. have investigated the functionalization and photoelectrochemical characterization of PNVC-MWNT thin films prepared by the LS technique [736b]. The I/V characterization has shown an increase in the conductivity of PNVC-MWNTs and I_2-doped PNVC-MWNTs as compared with PNVC and I_2-doped PVK, respectively. The electrochemical characterization has shown the formation of an I_2-doped PNVC-MWNT complex. These nanostructured PVK-MWNT films have revealed an increase in the current density under the illumination of about 500 nA cm^{-2}.

Spange et al. have applied this technique, based on the facile and time saving pathway towards nanoporous carbon, to PNVC. They have reported cationic host–guest polymerization of *N*-vinylcarbazole and vinyl ethers in MCM-41, MCM-48 and nanoporous glasses [746]. They have observed that the molecular mass of enclosed polymer and the degree of loading of host compounds can be adjusted within certain limits. Molecular dynamics was investigated by using broadband dielectric spectroscopy. Under the conditions of constricted geometry, molecular fluctuation as well as a secondary β-relaxation was observed, which is hardly affected (in comparison with the free melt) and which corresponds to the relaxation between structural substates (dynamic glass transition). This process is several orders of magnitude faster in its relaxation rate than in the free melt and thus follows a confinement effect. This was already well known in lower-molecular-weight systems with constricted geometry.

Others

Nanocomposites for membranes

A membrane that preferentially permeates a chemical species on the basis of greater solubility, rather than mobility, is referred to as reverse selective [747] or solubility selective [748]. A solubility selective mode is especially useful in applications where a light gas stream is contaminated with a small amount of heavier species; examples include the removal of higher hydrocarbons from natural gas [749] or hydrogen [750] and the removal of volatile organic compounds (VOCs) from air [751] or water [752]. In such cases, the solubility selective mode is more economical than the mobility selective mode.

A nanocomposite material composed of an organic substance functionality attached to the mesoporous surface of an inorganic membrane would

in principle be excellent for such applications [753]. The organic groups of membrane material must be designed in terms of chemistry and structure to favorably adsorb target VOCs without permanently sequestering them.

Javaid et al. [754] have designed nanocomposites that met these design goals by manipulating molecular chemistry and structure, pore geometry and adsorbed surface density. Modified porous (5–10 nm) alumina membranes with alkyl trichlorosilanes having chain lengths ranging from C1 to C28 [753,755] were reported. Directly related [756] and similar [757] nanocomposite membranes have also been discussed recently.

Catalytic membrane reactors (CMR) offer the possibility of producing synthesis gas from methane and air while avoiding the need for either initial separation of oxygen from air or post-separation of nitrogen from synthesis gas. Dense oxide ceramic membranes with mixed ionic and electronic conductivity (MIEC) have been extensively studied because of their promising applications in oxygen separation, syngas production and oxidative coupling of methane [758].

The application of mixed-conducting membranes is limited by some disadvantages in the existing membrane materials.

Another group of membrane materials, called dual-phase composites, is comprised of a mixture of an oxide ionic conductor and an electronically conducting phase [759]. For a composite mixed conductor, it is possible to choose good ionic and electronic conductors as components and to control mixed conductivity by adjusting the fraction of constituents. Composites based on CeO_2 are considered the most promising. Gd-doped CeO_2 is a well-known oxygen-conducting electrolyte, which is receiving much attention as a model material to investigate nanoscale effects in conductivity [760].

Direct preparation of nanocomposites is possible by the Pechini process [761]. A new strategy for the design of catalytic membranes with high oxygen permeability is based on the application of the mechanochemical approach (MA) for obtaining nanosize powders and composites with a specific morphology. This technique allows superfast synthesis of mixed oxide complex peroxites and fluorites with high conductivity in high-energy planetary mills [759d,762].

The principle of fuel cell, discovered in 1839 by Sir William Grove, using hydrogen and oxygen to generate electricity and water is applied to many electrochemical devices [763]. They are promising energy-conversion devices for future transportation due to their higher energy efficiency than membrane fuel cells, a leading alternative to internal combustion and diesel engines.

Among the several kinds of fuel cells, proton-exchange membrane fuel cell (PEMFC) and DMFC are known to utilize the proton-conducting membranes. PEMFC is one of the best candidates of clean power sources for mobile and stationary applications [764]. To improve fuel cell efficiency, the polymer electrolyte should have better water retention properties especially in severe conditions. The membrane electrode assembly (MEA) is a core component of PEMFC.

In general, a proton-exchange membrane (PEM) requires the following properties:

(a) easily synthesized from available, low-cost starting materials;
(b) highly water insoluble and an ability to form films;
(c) highly proton-conducting 0.01 S/cm;
(d) chemically stable to acids and free radicals;
(e) minimized permeation to reactant gases (H_2/O_2);
(f) thermal, hydroelectric stability at high temperature 120°C;
(g) ability to survive in H_2 fuel cells for 5000 h vehicle application.

However, one limitation of the current PEMFC operating at about 80°C is that 5–10 ppm of CO in the H_2 feed gas is enough to poison the Pt anode electrocatalyst. One way to improve the CO tolerance level is to increase the operating temperature [765].

In the last decade, DMFCs have attracted considerable attention since they offer numerous potential benefits, such as high efficiency, high power density, low or zero emission and high reliability [766].

Direct methanol fuel cell is considered superior to PEMFC because of its simple liquid fuel handling and improved safety. Despite these advantages, there are several obstacles in preventing commercialization of DMFC, such as high cost, poor chemical and thermal stability, reduced conductivity of the membranes and, finally, the so-called 'methanol cross-over', i.e., methanol diffusion from anode to cathode across the polymer electrolyte membrane. Recently, there has been intensive research effort to develop new membranes for DMFC applications [767].

There were many attempts to reduce methanol permeability through polymer electrolyte membranes, namely:

(a) treatment of the membrane surface to block methanol transport;
(b) control of the size of proton transport channels using different block copolymers and cross-linkage;
(c) development of new types of electrolyte polymers;
(d) introduction of a winding pathway for methanol by making a composite with inorganic fillers.

Recently, a nanocomposite suitable for high-efficient catalysis with enhanced anti-poisoning ability for electrochemical oxidation of methanol was reported [768].

At present, the most widely used commercial PEM materials are developed by Du-Pont Nafion series and Dow. Both these materials consist of perfluorinated copolymers with sulfonic acid functionalized side chains. However, these materials limit large-scale applications, especially for DMFCs, due to their high cost, complicated synthetic procedures, thermal decomposition over 120°C and methanol crossover [769].

In recent years, many contributions have appeared in the literature dealing with alternative low-cost membranes like sulfonated aromatic polymer membranes, complexes of basic polymers with strong acids, such as poly(vinyl alcohol)/phosphotungstic acid [770], temperature-tolerant PEFC membrane materials, such as sulfonated polyethersulfone [771], or silica-based nanocomposite membranes [158,159,772–774].

Layered silicates, commonly used for PEMFC applications, are Laponite (Lp) or MMT since their composition and purity are very well controlled.

SiO_2/polymers (PEO, PPO, PTMO) are the commonly used organic–inorganic composite membranes prepared, in a method similar to that of Honma et al., by acid catalyzed sol–gel processes for PEMFC due to their enhanced mechanical and thermal properties and reduced methanol permeability with appreciable conductivity [159,770a,774e,775].

Research activities are mainly focused on two different approaches:

(a) improving the performance of perfluorosulfonic membranes by inorganic modification,
(b) finding new polymeric materials capable of replacing Nafion or even surpassing its performance.

Jones et al. and Li et al. [776] have published the most relevant findings regarding the above mentioned approaches. In their reviews, the membranes are classified into three groups: (a) modified PFSA membranes, (b) alternative sulfonated polymers and their composite membranes and (c) acid-base polymer membranes.

Interest in these nanocomposites continues on the improvement in the properties desirable for commercial applications [777].

Recently, studies on various classes of proton-conducting materials with specific emphasis on their potential use as H_2 separation membranes in the industrial processes of coal gasification, natural gas reforming, methanol reforming and water–gas shift (WGS) reaction have been reviewed. Key

material requirements for their use in these applications have also been discussed [3].

Crystal templates

Insulating polymers can be transferred into semiconducting ones by adding conductive filler particles. A majority of studies concentrated on carbon-black-based fillers, which is becoming an increasingly important source for carbon fibers [778], carbon nanotubes [328,778], conjugated polymers [779], inorganic semiconducting nanoparticles [15] and metal particles [780].

Aquocyanophthalocyaninatocobalt(III) (Phthalcon 11) is an intrinsically novel phthalocyanine semiconductive crystal, which may increase the conductivity of many polymers at low filler concentrations. Thermosets with (semi)conductive nanoparticles are of practical interest, for instance, in static dissipative flooring, (semi)conductive adhesives and thin transparent electrodes. Almost every publication on CPC containing (semi)conductive fillers is focused on thermoplastic polymer matrices [781]. The use of Phthalcon 11 as semiconductive filler in cross-linked epoxy polymer matrices has been described [782]. Homogeneously thin Phthalcon 11/epoxy layer can be made with low percolation threshold. The low percolation threshold was explained by the formation of a fractal particle network because of the large surface tension difference between the particle and matrix.

Molecular aggregates have great potential in technological applications. Recently, it was demonstrated that certain electroactive polymers doped with organic molecular nanocrystals, known as J-aggregates, can exhibit efficient electroluminescence when used as emitting layers in polymer LEDs. J-aggregates exhibit a very narrow emission band with a maximum at 815 nm. A dramatic increase in charge-carrier mobility was observed for these layers containing the J-aggregate nanocrystalline phase [783].

4.4. Conclusion

Summarizing all the above examples, it is quite clear that, within the inorganic/organic hybrid nanocomposites, speciality polymers as well as conventional polymers used as organic components and various metal oxides, MMT and allotropes of elemental carbon used as the inorganic counterpart allow nanoscale materials to exhibit properties that are distinct from those of either pure component phases or the related macro- or

microcomposites. Various possible combinations of components provide the opportunity to invent an infinite set of new materials with a large spectrum of known and unknown properties. Template guided, intercalation, sol–gel and nanoparticle incorporation are the methods used commonly for nanocomposite preparation. The properties of nanocomposites strongly depend on the type of interaction (covalent, ionic, cordination, H-bonding and van der Waals) between the host and guest materials. The great versatility of conducting nanocomposite system materials will certainly be explored in future for various potential end-use applications. We hope this overview will be a step in this long journey.

References

[1] Herring, A.M. (2006) *Polym. Rev*. **46**(3), 245–96.
[2] Jang, J. (2006) *Adv. Polym. Sci*. **199**, 189–259.
[3] Phair, J.W. and Badwal, S.P.S. (2006) *Ionics* **12**(2), 103–115.
[4] Maity, A. and Biswas, M. (2006) *J. Ind. Eng. Chem*., **12**(3), 311–51.
[5] Quadrat, O. and Stejskal, J. (2006) *J. Ind. Eng. Chem*., **12**(3), 352–61.
[6] Pomogailo, A.D. (2005) *Inorg. Mater*., **41**(Suppl. 1), S47–74.
[7] Malinauskas, A., Malinauskiene, J. and Ramanavicius, A. (2005) *Nanotechnology* **16**(10), R51–62.
[8] Kurian, M., Galvin, M.E. and Trapa, P.E. (2005) *Electrochim. Acta*, **50**(10), 2125–34.
[9] Hammond, P.T. (2004) *Adv. Mater*., **16**(15), 1271–93.
[10] Brusatin, G. and Signorini, R. (2002) *J. Mater. Chem*., **12**(7), 1964–77.
[11] Leroux, F. and Besse, J.P. (2001) *Chem. Mater*. **13**(10), 3507–15.
[12] Gomez-Romero, P. (2001) *Adv. Mater*., **13**(3), 163–74.
[13] Gangopadhyay, R. and De, A. (2000) *Chem. Mater*., **12**(3), 608–22.
[14] Ruizhitzky, E. and Aranda, P. (1997) *An. Quım*., **93**(3), 197–212.
[15] Jacobs, J.D., Koerner, H. and Heinz, H. (2006) *J. Phys. Chem. B*, **110**(41), 20143–57.
[16] Baibarac, M. and Gomez-Romero, P. (2006) *J. Nanosci. Nanotechnol*., **6**(2), 289–302.
[17] Leroux, F. and Taviot-Gueho, C. (2005) *J. Mater. Chem*., **15**(35–36), 3628–42.
[18] Terrones, M. (2004) *Int. Mater. Rev*., **49**(6), 325–77.
[19] Sunandana, C.S. and Kumar, P.S. (2004) *Bull. Mater. Sci*., **27**(1), 1–17.
[20] Njuguna, B. and Pielichowski, K. (2003) *Adv. Eng. Mater*. **5**(11), 769–78.
[21] Terrones, M. (2003) *Annu. Rev. Mater. Res*., **33**, 419–501.
[22] Yang, G., Hou, W.H., Guo, X.J. et al. (2003) *Chin. J. Inorgan. Chem*., **19**(6), 561–8.

[23] Varela, H., Huguenin, F., Malta, M. and Torresi, R.M. (2002) *Quim. Nova*, **25**(2), 287–99.
[24] Stejskal, J. (2001) *J. Polym. Mater*., **18**(3), 225–58.
[25] Kruis, F.E., Fissan, H. and Peled, A. (1998) *J. Aerosol Sci*., **29**(5–6), 511–35.
[26] Armes, S.P. (1996) *Curr. Opin. Colloid Interface Sci*., **1**(2), 214–20.
[27] Sperling, L.H. (2003) *Interpenetrating Polymer Networks and Related Materials*. New York: Plenum Press, 1981. In Guido Kickelbick *Prog. Polym. Sci*., **28**, 83–114.
[28] Ruiz-Hitzky, E. (2003) *Chem. Rec*., **3**, 88.
[29] Ruiz-Hitzky, E. (2004) In Functional Hybrid Materials, Chapter 2 (P. Gomez-Romero and C. Sanchez, eds), Weinheim: Wiley-VCH, p. 15.
[30] Aranda, P., Darder, M., Saavedra, R.F. et al. (2006) Thin Solid Films, Vol. **495**. pp. 104–112.
[31] Castro, E.G., Zarbin, A.J.G. and Galembeck, A. (2005) *J. Non Cryst. Solids* **351**, 3704–8.
[32] Ballav, N. (2005) *Mater. Sci. Eng*. B, **123**, 115–22.
[33] Pomogalio, A.D. (2000) *Russ. Chem. Rev*. **69**, 53.
[34] Judeinstein, P. and Sanchez, C. (1996) *J. Mater. Chem*., **6**, 511.
[35] Maeda, S. and Armes, S.P. (1995) *Chem. Mater*., **7**, 171.
[36] Stejskal, J., Kratochvil, I.P., Armes, S.P. et al. (1996) *Macromolecules*, **29**, 6814.
[37] Giannelis, E.P. (1996) *Adv. Mater*., **8**, 29.
[38] Biswas, M. and Ray, S.S. (2001) *Adv. Polym. Sci*., **155**, 167.
[39] Ray, S.S. and Okamoto, M. (2003) *Prog. Polym. Sci*., **28**, 1539.
[40] Ahmad, S.J.I., Huang, Y.D. and Li, W. (2004) *J. Mater. Sci*., **39**, 1919.
[41] Biswas, M. and Roy. A. (1993) *Polymer*, **34**, 2903.
[42] Ohkita, K., Tsubokawa, N. and Saittoh, E. (1978) *Carbon*, **16**, 41.
[43] Ballav, N., Maity, K.A. and Biswas, M. (2004) *Mater. Chem. Phys*., **87**, 120.
[44] Ballav, N. and Biswas, M. (2005) *Polym. Int*., **54**, 725.
[45] Maity, A. and Biswas, M. (2004) *Polym. J*., **36**, 812.
[46] Chen, G., Weng, W., Wu, D. et al. (2003) *Euro. Polym. J*., **39**, 2335.
[47] Chen, Y., Wang, J., Shen, J. et al. (1999) *J. Polym. Sci. Part A Polym. Chem*., **37**, 3745.
[48] Biswas, M. and Ray, S.S. (2001) *Synth. Met*., **123**, 135.
[49] Kryszewski, M. and Jeszka, J. (2003) *Macromol. Symp*., **194**, 75–86.
[50] Wang, Y. and Herron, N. (1992) *Chem. Phys. Lett*., **200**, 71.
[51] Dabbousi, B.O., Bawondi, M.G., Onitsuka, O. et al. (1995) *Appl. Phys. Lett*., **66**, 1316.
[52] Lee, T.W., Park, O.O., Kim, J.J et al. (2001) *Chem. Mater*., **13**, 2217.
[53] Kim, B.H., Jung, J.H., Hong, S.H. et al. (2002) *Macromolecules*, **35**, 1419.
[54] Goddard, Y.A., Vold, R.L. and Hoatson, G.L. (2003) *Macromolecules*, **36**, 1162.

[55] Kuila, A.B. and Nandi, K.K. (2004) *Macromolecules*, **37**, 8577.
[56] Kuila, A.B. and Nandi, K.K. (2006) *J. Phys. Chem. B*, **110**, 1621.
[57] Tian, S.J., Liu, J.Y, Zhu, T. et al. (2004) *Chem. Mater*., **16**, 4103.
[58] Khanna, P.K., Singh, N., Charan, S. et al. (2005) *Mater. Chem. Phys*., **92**, 214.
[59] Suri, K., Annapoorni, S. and Tandon, R.P. (2001) *Bull. Mater. Sci*., **24**, 563.
[60] Ferreira, M., Zucolotto, V., Huguenin., F. et al. (2002) *Nanosci*, *J. Nanotechnol*., **2**, 29.
[61] Liu, Y.C. and Chuang, T.C. (2003) *J. Phys. Chem. B*, **107**, 12383.
[62] Neumark, G.F., Park, R.M. and Depuydt, J.M. (1994) *Phys. Today*, **46** (6) 26.
[63] Bhattacharya, S.S., Malik, A.K. and Nandi, A. (2006) *Ghosha J. Chem. Phys*., **125**, 174717.
[64] Bao, J.C. and Xu, Z. (2002) *Chin. J. Inorg. Chem*., **18**, 965.
[65] Wallac, G.G. and Innis, P.C. (2002) *J. Nanosci. Nanotechnol*., **2**, 441.
[66] Jerome, C., Demoustier-Champagne, S., Legras, R. et al. (2000) *Chem. Eur. J*., **6**, 3089.
[67] Ge, D.T., Wang, J.X. and Wang, S.C. (2003) *Prog. Chem*., **15**, 456.
[68] Sailor, M.J. and Curtis, C.L. (1994) *Adv. Mater*., **6**, 688.
[69] Neves, S., Gazotti, W.A. and De Paoli, M.-A. (2004) In *Encyclopedia of Nanoscience and Nanotechnology*, Vol. 2 (H.S. Nalwa, ed.), pp. 133–52. Los Angeles: American Scientific Publishers.
[70] Gangopadhyay, R. (2004) In *Encyclopedia of Nanoscience and Nanotechnology*, Vol. 2 (H.S. Nalwa, ed.), pp. 105–31. Los Angeles: American Scientific Publishers.
[71] Wallace, P., Innis, G.G.C. and Kane-Maguire, L.A.P. (2004) In *Encyclopedia of Nanoscience and Nanotechnology*, Vol. 4 (H.S. Nalwa, ed.), pp. 113–30. Los Angeles: American Scientific Publishers.
[72] Epstein, A.J. (2001) In *Organic Electronic Materials: Conjugated Polymers and Low Molecular Weight Organic Solids*, Vol. 41 (R. Farchioni and G. Grosso, eds), p. 3. Amsterdam: Springer.
[73] Martin. C.R. (1995) *Acc. Chem. Res*., 28, **61**.
[74] Huang, J. (2006) *Pure Appl. Chem*., **78**, (1) 15–27.
[75] Zhang, L. and Wan, M. (2003) *J. Phys. Chem*. B, **107**, 6748.
[76] (a) Gospodinova, N. and Terlemezyan, L. (1998) *Prog. Polym. Sci*., **23**, 1443–1484. (b) Kang, E.T., Neoh, K.G. and Tan, K.L. (1998) *Prog. Polym. Sci*., **23**, 211–324.
[77] Huang, W.S., Humphrey, B.D. and MacDiarmid, A.G. (1986) *J. Chem. Soc. Faraday Trans*., **82**, 2385.
[78] Huang, J.X. and Kaner, R.B. (2004) *J. Am. Chem. Soc*., **126**, 851.
[79] Enzel, P. and Bein, T. (1989) *J. Phys. Chem*., **193**, 6270.
[80] Wu, C.G. and Bein, T. (1994) *Science* **264**, 1757.
[81] Wu, C.G. and Bein, T. (1994) *Chem. Mater*., **6**, 1109.
[82] Wu, C.G., Degroot, D.C., Marcy, H.O. et al. (1995) *J. Am. Chem. Soc*., **117**, 9229.

[83] Kanatzidis, M. and Wu, C. (1989) *J. Am. Chem. Soc*., **111**, 4139.
[84] Wang, L., Brazis, P., Rocci, M., Kannewurf, C.R., Kanatzidis, M.G. (1998) *Chem. Mater*., **10**(11), 3298.
[85] Liu, Y. and Kanatzidis, M. (1995) *Chem. Mater*., **7**, 1525.
[86] (a) Mehrotra, V. and Giannelis, E. (1992) *Solid State Ionics*., **51**, 115. (b) Mehrotra, V. and Giannelis, E. (1991) *Solid State Commun*., **77**, 155.
[87] Kanatzidis, M., Bissessur, R., De Groot, D. et al. (1993) *J. Chem. Soc. Chem. Commun*., **8**, 687.
[88] Enzel, P. and Bein, T. (1989) *Angew Chem. Int. Ed. Engl*., **12**, 28.
[89] Akelah, A., Salahuddin, N., Hiltner, A. et al. (1994) *Nanostruct Mater*., **4**, 3.
[90] Enzel, P. and Bein, T. (1989) *J. Chem. Soc. Chem. Commun*., **18**, 1326.
[91] Biswas, M. and Ray, S.S. (1998) *Polymer*, **39**, 25.
[92] Krishnamoorthy, R., Vaia, R.A. and Giannelis, E.P.Chem Mater (1996) 8, 2628.
[93] Vaia, R.A., Jandt, K.D., Kramer, E.J. et al. (1996) *Chem. Mater*., **8**, 2628.
[94] Vaia, R.A. and Giannelis, E.P. (1997) *Macromolecules*, **30**, 7990.
[95] Komori, Y., Sugahara, Y. and Kuroda, K. (1999) *Chem. Mater*., **11**, 2.
[96] Armes, S.P., Gottesfield, S., Beery, J.G., Garzon, F., Agnew, S.F. (1991) *Polymer*, **32**(13), 2325–2330.
[97] Vaia, R.A. and Giannelis, E.P. (1997) *Macromolecules*, **30**, 8000.
[98] Nisha, A., Rajeswari, M.K. and Dhamodharan, R. (2000) *J. Appl. Polym. Sci*., **76**, 1825–30.
[99] Lemmon, J. and Lerner, M. (1995) *Solid State Commun*., **94**, 533.
[100] Chen, W., Xu, Q. and Yuan, R.Z. (2001) *Composite Sci. Tech*., **61**, 935–9.
[101] Lagaly, G. (1999) *Appl. Clay Sci*., **15** (1/2) 1–9.
[102] Matsumura, A., Komori, Y., Itagaki, T. et al. (2001) *Bull. Chem. Soc. Jpn*., **74** (6) 1153–8.
[103] Vaia, R.A., Ishii, H. and Giannelis, E.P. (1993) *Chem. Mater*., **5** 1694–6.
[104] Qutubuddin, S. and Fu, X. (2002) In *Nano-Surface Chemistry* (M. Rosoff, ed.), New York: Mercel Dekker Inc., pp. 653–73.
[105] Brown, J.M., Curliss, D. and Vaia, R.A. (2000) *Chem. Mater*., **12**, 3376–84.
[106] Hofmeister, W. and Von Platen, H. (1992) *Cryst. Rev*., **3**, 3. Bender Koch, C. (1998) *Hyperfine Interact*., **117**, 131.
[107] De Roy, A., Forano, C., El Malki, K. et al. (1992) In *Synthesis of Microporous Materials*, Vol. 2 (L. Occelli and H. Robson, eds), New York: Van Nostrand Reinhold, p. 108.
[108] Solin, S.A., Hines, D., Yun, S.K. et al. (1995) *J. Non-Cryst. Solids*, **182**, 212.
[109] Pron, A. and Rannou, P. (2002) *Prog. Polym. Sci*., **27**, 135.
[110] Meneghetti, P. (2006) *Syed Qutubuddin Thermochimica Acta*, **442**, 74–7.
[111] Reichert, P., Nitz, H., Klinke, S. et al. (2000) *Macromol. Mater. Eng*., **275**, 8–17.
[112] Gopakumar, T.G., Lee, J.A., Kontopoulou, M. et al. (2002) *Polymer*, **43**, 5483–5491.
[113] Ma, J., Qi, Z. and Hu, Y. (2001) *J. Appl. Polym. Sci*., **82**, 3611–7.

[114] Pozsgay, A., Frater, T., Szazdi, L. et al. (2004) *Eur. Polym. J*., **40**, 27–36.
[115] Pozsgay, A., Frater, T., Papp, L. et al. (2002) *J. Macromol. Sci. Phys*., **41**, 1249–65.
[116] Solomon, M.J., Almusallam, A.S., Seefeldt, K.F. et al. (2001) *Macromolecules*, **34**, 1864–72.
[117] Galgali, G., Agarwal, S. and Lele, A. (2004) *Polymer*, **45**, 6059–69.
[118] Koo, C.M., Kim, M.J., Choi, M.H. et al. (2003) *J. Appl. Polym. Sci*., **88**, 1526–35.
[119] Hasegawa, N., Okamoto, H., Kawasumi, M. et al. (2000) *Macromol. Mater. Eng*., **280**, 76–9.
[120] Garcia-Lopez, D., Picazo, O., Merino, J.C. et al. (2003) *Eur. Polym. J*., **39**, 945–50.
[121] Mravcakova, M., Omastova, M., Potschke, A. et al. (2006) *Polym. Adv. Technol*., **17**, 715–26.
[122] Lee, Y-H., Bur Anthony, J., Roth Steven, C. et al. (2005) *Polym. Adv. Technol*., **16**, 249–56.
[123] Ginley, D.S. and Bright, C. (2000) *MRS Bull*., **25**, 15–8.
[124] Lewis, B.G. and Paine, D.C. (2000) *MRS Bull*., **25**, 22–7.
[125] Gorden, R.G. (2000) *MRS Bull*., **25**, 52–7.
[126] Haacke, G. (1977) *Annu. Rev. Mater. Sci*., **7**, 73–93.
[127] Bohren, C.F. and Huffman, V. (1983) *Absorption and Scattering of Light by Small Particles*. NewYork: Wiley, p. 41.
[128] Van de Hulst, H.C. (1981) *Light Scattering by Small Particles*. New York: Dover, p. 414.
[129] Grunlan, J.C., Gerberich, W.W. and Francis, L.F. (1999) *Mater. Res. Soc. Symp. Proc*., **576**, 383–7.
[130] Grunlan, J.C., Gerberich, W.W. and Francis, L.F. (2001) *J. Appl. Polym. Sci*., **80**, 692–705.
[131] Grulan, J.C., Ma, Y., Grunlan, M.A. et al. (2001) *Polymer*, **42**, 6913–21.
[132] Grunlan, J.C., Gerberich, W.W. and Francis, L.F. (2001) *Polym. Eng. Sci*., **41**, 1947–62.
[133] Grunlan, J.C., Gerberich, W.W. and Francis, L.F. (2001) *J. Mater. Sci. Lett*., **20**, 1523–6.
[134] Sun, J., Gerberich, W.W. and Francis, L.F. (2003) *J. Polym. Sci. Part B Polym. Phys*., **41**, 1744–61.
[135] (a) Dai, S. and Chem-Eur, J. (2001) **7**, 763. (b) Dai, S., Burleigh, M.C., Shin, Y.S. et al. (1999) *Chem. Int. Ed*., **38**, 1235. (c) Dai, S., Shin, Y.S., Ju, Y.H. et al. (1999) *Adv. Mater*., **11**, 1226. (d) Dai, S., Burleigh, M.C., Ju, Y.H. et al. (2000) *J. Am. Chem. Soc*., **122**, 992. (e) Zhang, Z.T., Dai, S., Hunt, R.D. et al. (2001) *Adv. Mater*., **13**, 493.
[136] Liu, J., Shin, Y., Nie, Z. et al. (2000) *J. Phys. Chem. A*., 104,8328. (b) Shin, Y.S., Liu, J., Wang, L.Q. et al. (2000) *Angew. Chem., Int. Ed*., **39**, 2702.
[137] Katz, A. and Davis, M.E. (2000) *Nature*, **403**, 286.
[138] DSouza, S.M., Alexander, C.A., Carr, S.W. et al. (1999) *Nature*, **398**, 312.

[139] Titirici, M.M., Hall, A.J. and Sellergren, B. (2002) *Chem. Mater*., **14**, 21.
[140] Ichinose, I., Kikuchi, T., Lee, S.W. et al. (2002) *Chem. Lett*., **104**. (b) He, J.H., Ichinose, I. and Kunitake, T. (2001) *Chem. Lett*., 850.
[141] Yilmaz, E., Haupt, K. and Mosbach, K. (2000) *Angew. Chem. Int. Ed*., **39**, 2115.
[142] (a) Markowitz, M.A., Deng, G. and Gaber, B. (2000) *Langmuir*, **16**, 6148. (b) Markowitz, M.A., Kust, P.R., Deng, G. et al. (2000) *Langmuir*, **16**, 1759.
[143] McKittrick, M.W. and Jones, C.W. (2003) *Chem. Mater*., **15**, 1132.
[144] (a) Wulff, G. (1995) *Angew. Chem. Int. Ed. Engl*., **34**, 1812. (b) Wulff, G. (2002) *Chem. Rev*., **102**, 1.
[145] (a) Haupt, K. and Mosbach, K. (2000) *Chem. Rev*., **100**, 2495. (b) Mosbach, K. (1994) *Trends Biochem. Sci*., **19**, 9.
[146] Shea, K.J. (1994) *Trends Polym. Sci*., **2**, 166.
[147] Sellergren, B. (2000) *Angew. Chem. Int. Ed*., **39**, 1031.
[148] Zhang, Z., Saengkerdsub, S. and Dai, S. (2003) *Chem. Mater*., **15**, 2921–5.
[149] Ravaine, D., Seminel, A., Charbouillot, Y. et al. (1986) *J. Non. Cryst. Solids*, **82**, 210.
[150] Judeinstein, P., Titman, J., Stamm, M. et al. (1994) *Chem. Mater*., **6**, 127.
[151] Croce, F., Appetecchi, G.B., Persi, L. et al. (1998) *Nature*, **394**, 456.
[152] Chaker, J.A., Dahmouche, K., Santilli, C.V. et al. (2006) *J. Non-Crystalline Solids*, **352**, 3457–62.
[153] Dahmouche, K., Atik, M., Mello, N.C. et al. (1997) *J. Sol-Gel Sci. Technol*. **8**, 711.
[154] Judeinstein, P. and Schmidt, H. (1994) *J. Sol-Gel Sci. Technol*., **3**, 189.
[155] Ribeiro, S.J.L., Dahmouche, K., Ribeiro, C.A. et al. (1998) *J. Sol-Gel Sci. Technol*., **13**, 427.
[156] Honma, I., Hirakawa, S., Yamada, K. et al. (1999) *Solid State Ionics*, **118**, 29.
[157] Honma, I., Takeda, Y. and Bae, J.M. (1999) *Solid State Ionics*, **120**, 255.
[158] Honma, I., Nomura, S. and Nakajima, H. (2001) *J. Memb. Sci*., **185**, 83.
[159] Chang, H.Y., Thangamuthu, R. and Lin, C.W. (2004) *J. Memb. Sci*., **228**, 217–26.
[160] Dahmouche, K., Santilli, C.V., Pulcinelli, S.H. et al. (1999) *J. Phys. Chem. B*, **103**, 4937–42.
[161] Chaker, J.A., Dahmouche, K., Santilli, C.V. et al. (2000) *J. Sol-Gel Sci. Tech*., **19**, 137–44.
[162] deAzevedo, E.R., Reichert, D., Vidoto, E.L.G. et al. (2003) *Chem. Mater*., **15**, 2070–8.
[163] Liu, Y., Lee, J.Y. and Hong, L. (2004) *J. Power Sources*, **129**, 303–11.
[164] Mary, K., Mary, G.E., Patrick, E. et al. (2005) *Electrochim. Acta*, **50**, 2125–34.
[165] Saunders, D.S., Gala, S.C. and Deirmendjian, G.K. (1993) *Composites*, **24**(4), 309.
[166] Herein, D., Braun, T. and Schlogl, R. (1997) *Carbon*, **35**(1), 17–29.

[167] Ramesh, P., Bhagyalakshmi, S. and Sampath, S. (2004) *J. Colloid Interface Sci*., **274**, 95.
[168] He, H., Klinowski, J., Forster, M. et al. (1998) *Chem. Phys. Lett*., **287**, 53.
[169] Ding, R., Hu, Y., Gui, Z. et al. (2003) *Polym. Degrad.Stab*., **81**, 473.
[170] Kyotani, T., Moriyama, H. and Tomita, A. (1997) *Carbon*, **35**, 1185.
[171] Matsuo, Y., Tahara, K. and Sugie, Y. (1997) *Carbon*, **35**, 113.
[172] Cerezo, F.T., Preston, C.M.L. and Shanks, R.A. (2007) *Macromol. Mater. Eng*., **292**, 155–68.
[173] Inagaki, M. and Suwa, T. (2001) *Carbon*, **39**, 915.
[174] Weng, W.-G., Chen, G.-H., Wu, D.-J. et al. (2004) *Comp Interface*, **11**(2), 131.
[175] Chen, G.-H., Wu, D.-J., Weng, W.U., Wu, C.L. (2003) *Carbon*, **41**(3), 619–621.
[176] Chen, G., Wu, C., Weng, W. et al. (2003) *Polymer*, **44**, 1781–4.
[177] Weng, W.-G., Chen, G.-H., Wu, D.-J. et al. (2004) *Carbon*, **42**, 753.
[178] Yoda, N. and Miyake, A. (1960) *J. Polym. Sci*., **43**, 117.
[179] Weng, W., Chen, G., Wu, D. et al. (2004) *J. Polym. Sci. Part B Polym. Phys*., **42**, 2844–56.
[180] Kotov, N.A., Dekany, I. and Fendler, J.H. (1996) *Adv. Mater*., **8**, 637.
[181] Fan, B. (1987) *Chem. Bull*., **10**, 24.
[182] Etter, T., Papakyriacou, M., Schulz, P. et al. (2003) *Carbon*, **41**, 1017.
[183] Krzesinska, M., Celzard, A., Grzyb, B. et al. (2006) *Mater. Chem. Phys*., **97**, 173.
[184] Alexandre, M. and Dubois, P. (2000) *Mater. Sci. Eng*., **28**, 1.
[185] Zheng, W. and Wong, S.-C. (2003) *Composites Sci. Technol*., **63**, 225.
[186] Zheng, W., Wong, S.-C. and Sue, H.-J. (2002) *Polymer*, **73**, 6767.
[187] Ishigure, Y., Iijima, S., Isto, H. et al. (1999) *J. Mater. Sci*., **34**, 2979.
[188] Celzard, A., Krzesinska, M., Begin, D. et al. (2002) *Carbon*, **40**, 557.
[189] Chen, G.H., Wu, D.J., Weng, W.G. et al. (2001) *Polym. Eng. Sci*., **41**(12) 2148.
[190] Chen, G.-H., Wu, D.J., Weng, W.G. et al. (2001) *J. Appl. Polym. Sci*., **82**, 2506–13.
[191] Chen, G.-H., Wu, D.J., Weng, W.G. et al. (2001) *Polmer Int*., **50**, 980–5.
[192] Pan, Y.-X., Yu, Z.-Z., Qu, Y.-C. et al. (2000) *J. Polym. Sci. Part B Polym. Phys*., **38**, 1626.
[193] Shen, J.W., Chen, X.M. and Huang, W.Y. (2003) *J. Appl. Polym. Sci*, **88**, 1864–9.
[194] (a) Sherman, R.D., Middleman, L.M., Jacobs, S.M. et al. (1983) *Polym. Eng. Sci*., **23**, 36. (b) 18. Dufort, M. and Deleuze, C. (1994) *Solid State Commun*., **92**, 377.
[195] Cerezo, F.T., Preston, C.M.L. and Shanks, R.A. (2007) *Macromol. Mater. Eng*., **292**, 155–68.
[196] Staufer, D. and Aharony, A. (1992) *Introduction in to Percolation Theory*. Washington, DC: Taylor & Francis, p. 198.

[197] Roldughin, V.I. and Vysotskii, V.V. (2000) *Prog. Org. Coatings*, **N39**, 81.
[198] Knite, M., Teteris, V. and Kiploka, A. (2003) *Mater. Sci. Eng. C*, **23**, 787–90.
[199] Chen, G.H., Wu, D.J., Weng, W.G. et al. (2001) *Acta Polym. Sin*., **6**, 803.
[200] Xiao, P., Xiao, M. and Gong, K. (2001) *Polymer*, **42**, 4813.
[201] Weng, W., Chen, G. and Wu, D. (2003) *Polymer*, **44**, 8119–32.
[202] Celzard, A., McRae, E., Mareche, J.F. et al. (1996) *J. Phys. Chem. Solids*, **6–8**, 715.
[203] Chen, X.M., Chen, J.W. and Huang, W.Y. (2002) *J. Mater. Sci. Lett*., **21**, 213.
[204] Zheng, W., Wong, S.C. and Sue, H. (2002) *J. Polymer*., **73**, 6767.
[205] Zheng, W. and Wong, S.C. (2003) *Compos Sci. Technol*., **63**, 225.
[206] Krzesinska, M. and Pisaroni, N. (2004) *Mater. Charact*., **52**, 195.
[207] Krzesinska, M. (2003) In *Current Topics in Acoustical Research* (R. Richard, ed.), Trivandrum: Research Trends, pp. 43–61.
[208] Celzard, A., Mareche, J.F., Furdin, G. et al. (2000) *J. Phys. D Appl. Phys*., **33**, 3094.
[209] Wei, L.U., Lin, H.F., Wu, D.J. et al. (2006) *Polymer*, **47**, 4440–4.
[210] Hummers, W.S. and Offeman, R.E. (1958) *J. Am. Chem. Soc*., **80**, 1339.
[211] Lerf, A., He, H.Y., Forster, M. et al. (1998) *J. Phys.Chem. B*, **102**, 4477.
[212] Matsuo, Y., Tahara, K. and Sugie, Y. (1998) *Chem. Mater*., **10**, 2266.
[213] Matsuo, Y., Tahara, K. and Sugie, Y. (1996) *Carbon*, **34**, 672.
[214] Liu, P.G., Gong, K.C., Xiao, P. et al. (2000) *J. Mater.Chem*., **10**, 933.
[215] Wang, W.-P. and Pan, C.-Y. (2004) *Polym. Eng. Sci*., **44** (12), 2335–2339.
[216] Cerezo, F.T., Preston, C.M.L. and Shanks, R.A. (2007) *Composites Sci. Technol*., **67**, 79.
[217] Chen, G.H., Lu, J.R., Wei Lu. et al. (2005) *Polym. Int*., **54**, 1689–93.
[218] Lu, J.R., Chen, X.F., Wei Lu, et al. (2006) *Eur. Polym. J*., **42**, 1015–21.
[219] Chen, G.H., Wu, C.L., Wu, D.J., Weng, W.G., Huang, S.X. (2003) *Acta Polym. Sin.*, **5**, 742–745.
[220] Weng, W.G.., Chen, G.H. and Wu, D.J. (2003) *Polymer*, **44**, 8119–32.
[221] Chen, G.H., Weng, W.G., Wu, D.J. et al. (2004) *J. Polym. Sci Part B Polym. Phys*., **42**, 155–67.
[222] Weng, W.G., Chen, G.H. and Wu, D.J. (2005) *Polymer*, **46**, 6250–6257.
[223] Weng, W.-G., Chen, G.-H., Wu, D.-J. et al. (2003) *Polymer*, **44**, 8119–8132.
[224] Lu, X.F. and Hay, J.N. (2001) *Polymer*, **42**, 9423.
[225] Di Lorenzo, M.L. and Silvestre, C. (1999) *Prog. Polym. Sci*., **24**, 917.
[226] Kojima, Y., Matsuoka, T., Takahashi, H. et al. (1994) *J. Appl. Polym. Sci*., **51**, 683.
[227] Mathias, L.J., Davis, R.D. and Jarret, W.L. (1999) *Macromolecules*, **32**, 7958.
[228] Boiteux, G., Fournier, J., Issotier, D. et al. (1999) *Synth. Met*., **102**, 1234–5.
[229] Park, K. (2004) *Mater. Sci. Eng. B*, **107**, 19–26.
[230] Fournier, J., Boiteux, G. and Seytre, G. (1997) *J. Mater. Sci. Lett*., **16**, 1677–9.
[231] Nicodemo, L., Nicolais, L., Romeo, G. et al. (1978) *Polym Eng Sci*., **18**, 293–8.

[232] Qi, J.Q., Zhu, Q., Wang, Y.L. et al. (2001) *Solid State Commun*, **120**, 505–8.
[233] Lundberg, B. and Sundqvist, B. (1986) *J. Appl. Phys*., **60**(3), 1074–9.
[234] Hussain, M., Choa, Y.H. and Niihara, K. (2001) *Composites Part A*, **32**, 1689–96.
[235] Aneli, J.N., Zaikov, C.E. and Khananashvili, L.M. (1999) *J. Appl. Polym. Sci*., **74**, 601–21.
[236] Pramanik, P.K., Khastgir, D., De, S.K. et al. (1990) *J. Mater. Sci*., **25**, 3848–53.
[237] Pramanik, P.K. and Khastgir, D. (1993) *J. Mater. Sci*., **28**, 3539–46.
[238] Yi, X.S., Song, Y.H. and Zheng, Q. (2000) *J. Appl. Polym. Sci*., **77**, 792–6.
[239] Sau, K.P., Chaki, T.K. and Khastgir, D. (1998) *Composites*, **29**, 363–70.
[240] Das, N.C., Chaki, T.K. and Khastgir, D. (2002) *Polym. Int*., **51**, 156–63.
[241] Taya, M., Kim, W.J. and Ono, K. (1998) *Mech. Mater*., **28**, 53–9.
[242] Lu, J.R., Weng, W.G., Wu, D.J. et al. (2005) *Adv. Funct. Mater*., **15**, 1358.
[243] Stroud, D. and Hui, P.M. (1988) *Phys. Rev. B*, **37**, 8719. (20). Ohtsuki, T. and Keys, T. (1984) *J. Phys. A*, **17**, L559.
[244] Gefen, Y., Shih, W.H., Laibowitz, R.B. et al. (1986) *Phys. Rev. Lett*., **57**, 3097.
[245] (a) Charkrabarty, R.K., Bardhan, K.K. and Basu, A. (1991) *Phys. Rev. B*, **44**, 6773.
[246] (a) Choquette, Y., Gauthier, M., Michot, C. et al. (1992) Canadian Patent CA2248304 1998, (b) Tsubokawa, N. *Prog. Polym. Sci*., **17**, 417, (c) Lin, J.-H., Chen, H.-W., Wang, K.-T. et al. (1998) *J. Mater. Chem*., **8**, 2169.
[247] R.C. Bansal and J.-B. Donnet, Chapter 4, in *Carbon Black: Science and Technology* (J.-B. Donnet, R.C. Bansal and M.-J. Wang, eds), New York: Marcel Dekker, (1993).
[248] (a) Lemerle, J., Nejem, L. and Lefebvre, J. (1978) *J. Chem. Res*., 5301, (b) Livage, J. (1991) *Chem. Mater*., **3**, 578.
[249] Huang, H. and Nazar, L.F. (2001) *Angew. Chem. Int. Ed*., **40**(20), 3880–3884.
[250] Carmona, F. (1989) *Physica A*, **157**, 461.
[251] Lux, F. (1993) *J. Mater. Sci*. **28**, 285.
[252] Flandin, L., Prasse, T., Schueler, R. et al. (1999) *J. Phys. Rev. B*., **59**, 14349.
[253] Prasse, T., Flandin, L., Schulte, K. et al. (1998) *Appl. Phys. Lett*., **72**, 2903.
[254] Rwei, S.P., Ku, F.H. and Cheng, K.C. (2002) *Colloid. Polym. Sci*., **280**, 1110.
[255] Kotsilkova, R., Nesheva, D., Nedkov, I. et al. (2004) *J. Appl. Polym. Sci*., **92**, 2220–7.
[256] (a) Kamminorz, Y., Schulz, B. and Brehmer, L. (2000) *Synth. Met*., 111–2. 75. (b) Kamminorz, Y., Schulz, B., Scharader, S. et al. (2001) *Synth. Met*., **122**, 115.
[257] Janietz, S., Anlauf, S. and Wedel, S. (2001) *Synth. Met*., **122**, 11.
[258] Song, S.Y., Ahn, T., Shim, H.K. et al. (2001) *Polymer*, **42**, 4803.
[259] Iosip, M.D., Bruma, M., Ronova, I. et al. (2003) *Eur Polym. J*., **39**, 2011.
[260] Sena, M.E. and Andrade, C.T. (1994) *Polym. Bull*., **33**, 439.

[261] Souza, F.G. Jr, Sena, M.E. and Soares, B.G. (2004) *J. Appl. Polym. Sci*., **93**, 1631–7.
[262] Xiao, M., Luyi, S., Jinging, L. et al. (2002) *Polymer*, **43**(8), 2245.
[263] Shioyama, H., Tatsumi, K. and Iwashita, N. (1998) *Synth. Met*., **96**, 229.
[264] Du, X.S., Xiao, M. and Meng, Y.Z. (2004) *Polymer*, **45**, 6713–8.
[265] Song, L.N., Xiao, M. and Meng, Y.Z. (2006) *Composites Sci. Technol*., **66**, 2156–62.
[266] Hioki, T., Noda, S., Kakeno, M. et al. (1983) *Appl. Phys. Lett*., **43**, 30.
[267] Davenas, J., Boiteux, G. and Xu, X.L. (1988) *Nucl. Instrum. Methods*, **B32**, 136.
[268] De Bonis, A., Bearzotti, A. and Marletta, G. (1999) *Nucl. Instrum. Methods*, **B151**, 101.
[269] Costantini, J.-M., Couvreur, F., Salvetat, J.-P. et al. (2002) *Nucl. Instrum. Methods*, **B194**, 132.
[270] Wolszczak, M., Kroh, J. and Abdel-Hamid, M.M. (1995) *Radiat. Phys. Chem*., **45**, 71.
[271] Sun, Y., Zhu, Z. and Lin, C. (2002) *Nucl. Instrum. Methods*, **B191**, 805.
[272] Murugaraj, P., Mainwaring, D.E., Jakubov, T. et al. (2006) *Solid State Commun*., **137**, 422–6.
[273] Weber, W.J. and van Vliet, B.M. (1980) *Activated Carbon Adsorption of Organics in Water and Waste Treatment*, Vol. I, Chapter 1. Michigan: Ann Arbor Science Publishers, p. 15.
[274] Suffet, I.H. (1980) *J. Am. Water Works Assoc*., **72**(1) 40.
[275] Eissmann, R.N. and LeVan, M.D. (1993) *Ind. Eng. Chem. Res*., **32**, 2752.
[276] Fernández-Saavedra, R., Aranda, P. and Ruiz-Hitzky, E. (2004) *Adv. Funct. Mater*., **14**, 1, 77–82.
[277] Kroto, H., Heath, J., Obrien, S. et al. (1985) C60: buckminsterfullerene. *Nature*, **318**, 162–3.
[278] Krätschmer, W., Lamb, L., Fostiropoulos, K. et al. (1990) Solid C60: a new form of carbon. *Nature*, **347**, 354–7.
[279] Iijima, S. (1991) Helical microtubules of graphitic carbon. *Nature*, **354**, 56.
[280] Kilbribe, B.E., Coleman, J.N., Fraysse, J. et al. (2002) *J. Appl. Phys*., **92**, 4024.
[281] Sandler, J.K.W., Kirk, J.E., Kinloch, I.A. et al. (2003) *Polymer*, **44**, 5893.
[282] Potschke, P., Dudkin, S.M. and Alig, I. (2003) *Polymer*, **44**, 5023.
[283] Barrau, S., Demont, P., Peigney, A. et al. (2003) *Macromolecules*, **36**, 5187.
[284] Gong, X., Liu, J., Baskaran, S. et al. (2000) *Chem. Mater*. **12**, 1049.
[285] Potschke, P., Bhattacharyya, A.R. and Janke, A. (2003) *Polymer*, **44**, 8061.
[286] (a) Dresselhaus, M.S., Dresselhaus, G. and Eklund, P. (1996) *Science of Fullerenes and Carbon Nanotubes*. San Diego, CA: Academic. (b) Ebbsen, T. (1997) *Carbon Nanotubes*. Boca Raton, FL: CRC Press. Saito, R., Dresselhaus, G. and Dresselhaus, M.S. (1998) *Physical Properties of Carbon Nanotubes*. London: Imperial College Press, (c) Pan, Z.W., Xie, S.S., Chang, B.H. et al. (1998) *Nature*, **394**, 631. (d) Vigolo, B., PØnicaud, A., Coulon,

C. et al. (2000) *Science*, **290**, (1331) (e) Qin, L.C., Zhao, X., Hirahara, K. et al. (2000) *Nature*, **408**, 50. (f) Wang, N., Tang, Z.K., Li, G.D et al. (2000) *Nature*, **408**, 50.
[287] Yu, M.F., Files, B.S., Arepalli, S. et al. (2000) *Phys. R*ev. *Lett*. **84**, 5552.
[288] Thess, A., Lee, R., Nikolaev, P. et al. *Science*, (1996) **273**, 483.
[289] Hone, J., Whitney, M., Piskoti, C. et al. (1999) *Phys. R*ev. *B*, **59**, R2514.
[290] Iijima, S. and Ichihashi, T. (1991) *Nature*, **363**, 603.
[291] Bethune, D.S., Klang, C.H., Vries, M.S. et al. (1993) *Nature*, **363**, 605.
[292] Tans, S.J. (1997) *Nature*, **386**, 474.
[293] Nikolaev, P., Bronikowski, M.J., Bradley, R.K. et al. (1999) *Chem. Phys. Lett*., **313**, 91.
[294] Chiang, I.W., Brinson, B.E., Huang, A.Y. et al. (2001) *J. Phys. Chem. B*, **105**, 8297.
[295] Zimmerman, J.L., Bradley, R.K., Huffman, C.B. et al. (2000) *Chem. Mater*., **12**, 1361.
[296] Xu, Y.Q., Peng, H.Q., Hauge, R.H. et al. (2005) *Nano Lett*., **5**, 163.
[297] Ajayan, P.M., Stephan, O., Colliex, C. et al. (1994) *Science*, **265**, 1212.
[298] Dai, L. & Mau, A.W. (2001) *Adv. Mater*., **13**, 899.
[299] Dai, L. (1999) *Polym. Adv. Technol*., **10**, 357.
[300] Zengin, H., Zhou, W., Jin, J. et al. (2002) *Adv. Mater*., **14**, 1480.
[301] Wei, Z., Wan, M., Lin, T. et al. (2003) *Adv. Mater*., **15**, 137.
[302] Baibarac, M., Baltog, I., Lefrant, S. et al. (2003) *Chem. Mater*., **15**, 4149.
[303] Chen, G.Z., Shaffer, M.S.P., Coleby, D. et al. (2002) *Adv. Mater*., **12**, 522.
[304] Lefrant, S., Baibarac, M. and Baltog, I. (2006) *Mol. Cryst. Liq. Cryst*., **447**, 75/[393]–85/[403].
[305] Subramoney, S. (1998) *Adv. Mater*., **10**, 1157–71.
[306] Dai, L. and Mau, A.W.H. (2001) *Adv. Mater*., **13**, (12 ± 13), July 4.
[307] Hammel, E., Tang, X., Trampert, M. et al. (2004) *Carbon*, **42**, 1153–8.
[308] Cui, S., Canet, R., Derre, A. et al. (2003) *Carbon*, **41**, 797–809.
[309] Dai, L. and Mau, A.W.H. (2001) *Adv. Mater*., **13**, 12–13.
[310] Gong, X.Y., Liu, J., Baskaran, S. et al. (2000) *Chem. Mater*., **12**, 1049.
[311] Jin, Z.X., Pramoda, K.P., Goh, S.H. et al. (2002) *Mater. Res. Bull*., **37**, 271.
[312] Qian, D., Dickey, E.C., Andrews, R. et al. (2000) *Appl. Phys. Lett*., **76**, 2868.
[313] Dalton, A.B., Collins, S., Munoz, E. et al. (2003) *Nature*, **423**, 703.
[314] Xu, X.J., Thwe, M.M., Shearwood, C. et al. (2002) *Appl. Phys. Lett*., **81**, 2833.
[315] Cadek, M., Coleman, J.N., Barron, V. et al. (2002) *Appl. Phys. Lett*., **81**, 5123.
[316] Tang, B.Z. and Xu, H.Y. (1999) *Macromolecules*, **32**, 2569.
[317] Andrews, R., Jacques, D., Rao, A.M. et al. (1999) *Appl. Phys. Lett*., **75**, 1329.
[318] Haggenmueller, R., Gommans, H.H., Rinzler, A.G. et al. (2000) *Chem. Phys. Lett*., **330**, 219.
[319] Jin, L., Bower, C. and Zhou, O. (1998) *Appl. Phys. Lett*., **73**, 1197.
[320] Chen, J., Hamon, M.A., Hu, H. et al. (1998) *Science*, **282**, 95.
[321] Hirsch, A. (2002) *Angew. Chem. Int. Ed*., **41**, 1853.

[322] Sun, Y.P., Fu, K.F., Lin, Y. et al. *Acc. Chem. Res*. (2002) **35**, 1096.
[323] Yang, J., Hu, J., Wang, C. et al. (2004) *Macromol. Mater. Eng*., **289**, 828–83.
[324] Tibbetts, G.G. (1983) *Appl. Phys. Lett*., **42**, 666–8.
[325] Speck, J.S., Endo, M. and Dresselhaus, M.S. (1989) *J Cryst. Growth*, **94**, 834–48.
[326] Baker, R.T.K. (1989)*Carbon*, **27**, 315–23.
[327] Carmona, F. (1987) *Ann. Chim Fr* **13**, 343–5.
[328] Sandler, J., Shaffer, M.S.P., Prasse, T. et al. (1999) *Polymer*, **40**, 5967.
[329] Nogales, A., Broza, G., Roslaniec, Z. et al. (2004) *Macromolecules*, **37**, 7669–72.
[330] Valentini, L., Armentano, I., Ricco, L. et al. (2006) *Diamond Relat. Mater*., **15**, 95.
[331] Valentini, L., Mengoni, F., Armentano, I. et al. (2006) *J. Appl. Phys*., **99**, 114305.
[332] Zhan, G.-D., Kuntz, J.D., Wan, J.L. et al. (2003) *Nat. Mater*., **2** (1), 38–42.
[333] Flahaut, E., Peigney, A., Laurent, CH. et al. (2000) *Acta Mater*., **48** (14), 3803–12.
[334] Hughes, M., Shaffer, M.S.P., Renouf, A.C. et al. (2002) *Adv. Mater*., **14** (5), 382–5.
[335] Zhan, G.-D., Kuntz, J.D., Garay, J.E. et al. (2003) *Appl. Phys. Lett*., **83** (6), 1228–30.
[336] Jiang, L.Q. and Gao, L. (2005) *J. Mater.Chem*., **15** (2), 260–6.
[337] Janes, R.A., Aldissi, M. and Kaner, R.B. (2003) *Chem. Mater*., **15** (23), 4431–5.
[338] Kim, S. and Kunta, P.N. (2003) *J. Mater. Chem*., **13**(8), 2028–35.
[339] Jiang, L.Q. and Gao, L. (2006) *J. Am. Ceram. Soc*., **89** (1), 156–61.
[340] Gong, Q.M., Li, Z., Bai, X.D. et al. (2004) *Mater. Sci. Engineer. A*, **384**, 209–14.
[341] Metzger, D.W. and Bizios, R. (2002) *Biomed. Mater. Res*., **59**, 499–506.
[342] Terrones, M., Grobert, N. and Terrones, H. (2002) *Carbon*, **40**, 1665–84 and references there in.
[343] Golberg, D., Bando, Y., Mitome, M. et al. (2002) *Chem. Phys. Lett*., **360**, 1–7 and references there in.
[344] Kaner, R.B., Kouvetakis, J.,Warble, C.E. et al. (1987) *Mater. Res. Bull*., **22**, 399–404.
[345] Kouvetakis, J., Kaner, R.B., Sattler, M.L. et al. (1986) *J. Chem. Soc. Chem. Commun*., issue (24) 1758–9.
[346] Sircar, S., Golden, T.C. and Rao, M.B. (1996) *Carbon*, **34**, 1.
[347] Che, G.L., Lakshmi, B.B., Fisher, E.R. et al. (1998) *Nature*, **393**, 346.
[348] Jiang, J.W., Klauda, J.B. and Sandler, S.I. (2003) *Langmuir*, **19**, 3512.
[349] Joo, S.H., Choi, S.J., Oh, I. et al. (2001) *Nature*, **412**, 169.
[350] Yu, J.S., Kang, S., Yoon, S.B. et al. (2002) *J. Am. Chem. Soc*., **124**, 9382.
[351] Lee, J., Han, S. and Hyeon, T. (2004) *J. Mater. Chem*., **14**, 478.

[352] (a) Ryoo, R., Joo, S.H. and Jun, S., (1999) *J. Phys. Chem. B*, **103**, 7743. (b) Ryoo, R., Joo, S.H., Kruk, M. et al. (2001) *Adv. Mater.*, **13**, 677. (c) Lee, J.S., Joo, S.H. and Ryoo, R. (2002) *J. Am. Chem. Soc.*, **124**, 1156.
[353] (a) Lee, J., Yoon, S., Hyeon, T., Oh, S.M., Kim, K.B. (1999) *Chem. Commun.*, (21) 2177. (b) Lee, J., Yoon, S., Oh, S.M. et al. (2000) *Adv. Mater.*, **12**, 359. (c) Lee, J., Kim, J. and Hyeon, T. (2003) *Chem. Commun.*, (10) 1138–9.
[354] Yu, C.Z., Fan, J., Tian, B.Z. et al. (2002) *Adv. Mater.*, **14**, 1742.
[355] Taguchi, A., Smått, J.H. and Lindén, M. (2003) *Adv. Mater.*, **15**, 1209.
[356] Lu, A.H., Schmidt, W., Spliethoff, B., Schüth, F. (2003) *Adv. Mater.*, **15**, 1602.
[357] (a) Han, S.J. and Hyeon, T. (1999) *Chem. Commun.*, (19) 1955–6. (b) Han, S.J., Sohn, K. and Hyeon, T. (2000) *Chem. Mater.*, **12**, 3337. (c) Yoon, S.B., Sohn, K., Kim, J.Y. et al. (2002) *Adv. Mater.*, **14**, 19.
[358] Li, Z. and Jaroniec, M. (2001) *J. Am. Chem. Soc.*, **123**, 9208.
[359] Han, B.H., Zhou, W.Z. and Sayari, A. (2003) *J. Am. Chem. Soc.*, **125**, 3444.
[360] Han, S., Kim, M. and Hyeon, T. (2003) *Carbon*, **41**, 1525.
[361] Kawashima, D., Aihara, T., Kobayashi, Y. et al. (2000) *Chem. Mater.*, **12**, 3397.
[362] (a) Pang, J.B., Li, X., Wang, D.H. et al. (2004) *Adv. Mater.*, **16**, 884. (b) Pang, J.B., Hu, Q.Y., Wu, Z.W. et al. (2004) *Microporous Mesoporous Mater.*, **74**, 73.
[363] Beck, J.S., Vartuli, J.C., Roth, W.J. et al. (1992) *J. Am. Chem. Soc.*, **114**, 10834.
[364] Huo, Q., Margolese, D.I., Ciesla, U. et al. (1994) *Nature*, **317**, 368.
[365] Yoon, S.B., Kim, J.Y. and Yu, J.S. (2002) *Chem. Commun.*, (14) 1536–7.
[366] Moriguchi, I., Koga, Y., Matsukura, R., Teraoka, Y., Kodama, M. (2002) *Chem. Commun.*, (17) 1844–5.
[367] Pang, J., Ford, C., Tan, G. et al. (2005) *Microporous and Mesoporous Mater.*, **85**, 293–6.
[368] Fuertes, A.B. (2005) *Macromol. Rapid Commun.*, **26**, 1055–9.
[369] Li, N., Li, X., Geng, W. et al. (2004) *J. Appl. Polym. Sci.*, **93**, 1597–601.
[370] Feng, X., Yang, G., Liu Y. et al. (2006) *J. Appl. Polym. Sci.*, **101**, 2088–94.
[371] Cho, M.S., Choi, H.J., Kim, K.Y. et al. (2002) *Macromol. Rapid Commun.*, **23**, 713–6.
[372] Nguyen, T.Q., Wu, J., Doan, V. et al. (2000) *Science*, **288**, 652–6.
[373] Molenkamp, W.C., Watanabe, M., Miyata, H. et al. (2004) *J. Am. Chem. Soc.*, **126**, 4476–7.
[374] Lin, V.S.-Y., Radu, D.R., Han, M. et al. (2002) *J. Am. Chem. Soc.*, **124**, 9040–1.
[375] Ho, S.W., Kwei, T.K. and Okamoto, Y. (2003) *Macromolecules*, **36**, 6894–7.
[376] Lu, Y., Yang, Y., Sellinger, A. et al. (2001) *Nature*, **410**, 913–917.
[377] Aida, T. and Tajima, K. (2001) Angew. Chem., 113, 3919–22; Angew. Chem. Int. Ed., 40, 3803–6.
[378] Yang, Y., Lu, Y., Lu, M. et al. (2003) *J. Am. Chem. Soc.*, **125**, 1269–77.

[379] Guo, R, Li, G., Zhang, W. et al. (2005) *Chem. Phys.Chem*., **6**, 2025.
[380] Shaw, W.J.D. and Pan, J. (1995) *J. Appl. Polym. Sci*., **56**, 557.
[381] Shaw, W.J.D. (1989) *J. Mater. Sci. Lett*., **24**, 4114.
[382] Smith, A.P., Ade, H., Smith, S.D. et al. (2001) *J. Macromol*., **34**, 1536.
[383] Smith, A.P., Ade, H., Koch, C.C. et al. (2000) *J. Macromol*., **33**, 1163.
[384] Smith, A.P., Shay, J.S., Spontak, R.J. et al. (2000) *Polymer*, **41**, 6271.
[385] Cavalieri, F., Padella, F. and Bourbonneux, S. (2002) *Polymer*, **43**, 1155.
[386] Zhu, Y.G., Li, Z.Q., Gu, J.J. et al. (2006) *J. Polym. Sci.: Part B: Polym. Phys*., 44, 3157–64.
[387] Bao, L. and Jiang, J.S. (2005) *Physica B*, **367**, 182–7.
[388] Livage, J. (1991) *Chem. Mater*., **3**, 578.
[389] Livage, J. (1998) *Coord. Chem. Rev*., **178–180**, 999.
[390] Livage, J. (1999) *Coord. Chem. Rev*., **190–192**, 391.
[391] Barboux, Ph., Baffier, N., Morineau, R. et al. (1983) *Solid State Ion*, 9–10, 1073.
[392] Kanatzidis, M.G., Wu, C.-G., Marcy, H.O. et al. (1990) *Adv. Mater*., **2**, 364.
[393] Hwang, S.R., Li, W.-H., Lee, K.C. et al. (2000) *Phys. Rev. B*., **62**, 14157.
[394] Wu, C.-G., DeGroot, D.C., Marcy, H.O. et al. (1996) *Chem. Mater*., **8**, 1992.
[395] Fletcher, J.M., Gardner, W.E., Fox, A.C., Topping, G. (1967) *J. Chem. Soc (A)*, 1038–1045.
[396] Zampronio, E.C. and Oliveria, H.P. (2003) *Mat. Res. Bull*., **39**, 1525.
[397] Nakajima, H. and Matsubayashi, G.-E. (1993) *Chem. Lett*., (3) 423–6.
[398] De Stefanis, A., Foglia, S. and Tomlinson, A.G. (1995) *J. Mater. Chem*., **5**, 475.
[399] Sukanta De, Arup Dey and De, S.K. (2007) *J. Phys Chem. Solids*, **68**, 66–72.
[400] Wong, H.P., Dave, B.C., Leroux, F. et al. (1998) *J. Mater. Chem*., **8**, 1019.
[401] Maia, G., Torresi, R.M., Ticianelli, E.A. et al. (1996) *J. Phys. Chem*., **100**, 15910.
[402] Goward, G.R., Leroux, F. and Nazar, L.F. (1998) *Electrochim. Acta*, **43**, 1307.
[403] De, S., Ashis Dey and De, S.K. (2006) *Solid State Ionics*, **177**, 245–52.
[404] De, S., Ashis Dey and De, S.K. (2006) *Solid State Communications*, **137**, 662–7.
[405] Huguenin, F., Gritto, E.M., Ruggeri, G. et al. (2003) *J. Power Source*, **114**, 133–6.
[406] Varela, H. and Torresi, R.M. (2000) *J. Electrochem. Soc*., **147**, 665.
[407] Lira-Cantú, M. and Gómez-Romero, P. (1999) *J. Electrochem. Soc*., **146**(6), 2029–33.
[408] De, S., Dey, A. and De, S.K. (2005) *Eur. Phys. J. B*, **46**, 355–61.
[409] Karatchevtseva, I., Zhang, Z. and Hanna, J. (2006) *Chem. Mater*., **18**, 4908–16.
[410] Holland, G.P., Yarger, J.L., Buttry, D.A. et al. (2003) *J. Electrochem. Soc*., **150**, **12**, 1718–22.

[411] Fritz Huguenin, Marystela Ferreira, Valtencir Zucolotto, et al. (2004) *Chem. Mater*., **16**, 2293–9.
[412] Huguenin, F., Janete Giz, M., Ticianelli, E.A. et al. (2001) *J. Power Sources*, **103**, 113–9.
[413] (a) Vadivel Murugan, A., Kale, B.B., Kwon, C.-W. et al. (2001) *J. Mater. Chem*., **11**, 2470. (b) 451-464-15 A. V.l Murugan (2006) *J. Power Sources*, **159** 312–8.
[414] Wu, C.-G. and Chung, M.-H. (2004) *J. Solid State Chem*., **177**, 2285–94.
[415] Liu, Y.-J., Schindler, J.L., DeGroot, D.C. et al. (1996) *Chem. Mater*., **8**, 525.
[416] Liu, Y.-J., DeGroot, D.C., Schindler, J.L. et al. (1991) *Chem. Mater*., **3**, 992.
[417] Leurox, F., Goward, G., Power, W.P. et al. (1997) *J. Electrochem. Soc*., **144**, 3886.
[418] Pereira-Ramos, J.-P. (1995) *J. Power Sources*, **54**, 120.
[419] Park, H.-K., Smyrl, W.H. and Ward, M.D. (1995) *J. Electrochem. Soc*., **142**, 1068.
[420] Tipton, A.L., Passerini, S., Owens, B.B. et al. (1996) *J. Electrochem. Soc*., **143**, 3473.
[421] Parent, M.J., Passerini, S., Owens, B.B. et al. (1999) *J. Electrochem. Soc*., **146**, 1346.
[422] Le, D.B., Passerini, S., Tipton, A.L. et al. (1995) *J. Electrochem.Soc*., **142**, L102.
[423] (a) Coustier, F., Passerini, S. and Smyrl, W.H. (1998) *J. Electrochem. Soc*., **145**, L73. (b). Dong, W., Rolison, D.R. and Dunn, B. (2000) *Electrochem. Solid State Lett*., **3**, 457.
[424] (a) Leroux, F., Koene, B.E. and Nazar, L.F. (1996) *J. Electrochem. Soc*., **143**, L181. (b) Lira-Cantu, M. and Gomez-Romero, P. (1999) *J. Electrochem. Soc*., **146**, 2029.
[425] (a) Huguenin, F., Torresi, R.M. and Buttry, D.A. (2002) *J. Electrochem. Soc*., **149**, A546. (b) Huguenin, F., Torresi, R.M., Buttry, D.A. et al. (2001) *Electrochim. Acta*, **46**, 3555. (c) Huguenin, F., Gambardella, M.T.D., Torresi, R.M., de Torrisi, S.I., Buttry, D.A., (2000) *J. Electrochem. Soc.*, 147(7): 2437–2444. (d) Torresi, R.M., Torresi, S.I.C.D.and Buttry, D.A. (2000) *J. Electrochem. Soc*., **147**, 2437. (e) Huguenin, F., Girotto, E.M., Torresi, R.M., et al. (2002) *J. Electroanal. Chem*., **536**, 37. (f) Ferreira, M., Huguenin, F., Zucolotto, V. et al. (2003) *J. Phys.Chem. B*, **107**, 8351.
[426] Erdem, E., Karakisla, M. and Sacak, M. (2004) *Eur. Poly. J*., **40**, 785–91.
[427] Tange, H., Kitani, A. and Shiotani, M. (1996) *Electrochem. Acta* **41**(9), 1561–7.
[428] Gok, A. and Sari, B. (2002) *J. Appl. Poly. Sci*., **84**, 1993–2000.
[429] Prokes, J., Trchova, M., Hlavata, D. et al. (2002) *J. Poly. Degrad. Stab*., **78**, 393–401.
[430] Stejskal, J., Riede, A., Hlavata, D. et al. (1998) *Synth. Met*., **96**, 55–61.
[431] Sarma, T.K., Chowdhury, D., Paul, A., Chattopadhyay, A. (2002) *Chem. Commun*., (10) 1048–9.

[432] Chowdhury, D., Paul, A. and Chattopadyay, A. (2002) *J. Phys. Chem. B*, **106**(17), 4343–6.
[433] (a) Rubner, M.F., Cheung, J.H. and Fou, A.F. (1994) *Thin Solid Films*, **244**, 985. (b) Rubner, M.F. and Fou, A.C. (1995) *Macromolecules*, **21**, 7115. (c) Zhao, B.Z., Neoh, K.G. and Kang, E.T. (2002) *J. Appl. Polym. Sci*., 86, 2099–107.
[434] Grigore, L. and Petty, M.C. (2003) *J. Mater. Sci.: Mater. Electron*., **14**, 389–92.
[435] (a) Nishimura, H., Iizuka, M., Kuniyoshi, S. et al. (2004) *Electron. Commun. Jpn. II: Electron*., **87**, 18–25. (b) Lu, W., Fadeev, A.G., Qi, B.H. et al. (2004) *J. Electrochem. Soc*., 151, H33–9. (c) Bormashenko, E., Pogreb, R., Sutovski, S. et al. (2003) *Synth. Met*., **139**, 321–5.
[436] (a) Rubner, M.F. and Stockton, W.B. (1997) *Macromolecules*, **30**, 2717–25. (b) Ferreira, M., Huguenin, F., Zucolotto, V. et al. (2003) *J. Phys. Chem. B*, **107**, 8351–4. (c) Huguenin, F., Ferreira, M., Zucolotto, V. et al. (2004) *Chem. Mater*., **16**, 2293–9. (d) Park, M.K., Onishi, K., Locklin, J., et al. (2003) *Langmuir*, **19**, 8550–4. (e) Sarkar, N., Ram, M.K., Sarkar, A. et al. (2000) *Nanotechnology*, **11**, 30–6. (f) Stepp, J. and Schenkman, J.B. (1997) *J. Electrochem. Soc*., **144**, L155–7. (g) Tian, S.J., Baba, A., Liu, J.Y. et al. (2003) *Adv. Funct. Mater*., **13**, 473–9. (h) DeLongchamp, D.M. and Hammond, P.T. (2004) *Adv. Funct. Mater*., **14**, 224–32. (i) Farhat, T.R. and Hammond, P.T. (2006) *Chem. Mater*., **18**, 41–9. (j) De Longchamp, D.M. and Hammond, P.T. (2004) *Chem. Mater*., **16**, 4799–805.
[437] Sung, J.H. and Choi, J. (2005) *J. Macromol. Sci., Part B: Physics*, **44**, 365–75.
[438] Mello, S.V., Mattoso, L.H.C., Faria, R.M. et al. (1995) *Synth. Met*., **71**, 2039–40.
[439] Macinnes, D. and Funt, B.L. (1988) *Synth. Met*., **25**, 235–42.
[440] das Neves, S., Cordoba de Torresi, S.I. and Zoppi R.A. (1999) *Synth. Metals*, **101**, 754–5.
[441] Ozin, G.A. (1992) *Adv. Mater*., **4**, 612–49.
[442] Liu, Y.J., DeGroot, D.C., Schindler, J.J. et al. (1993) *Adv. Mater*., **5**, 369.
[443] Huang, J., Virji, S., Weiller, B.H. et al. (2003) *J. Am. Chem. Soc*., **125**, 314.
[444] Wei, Z., Zhang, Z. and Wan, M. (2002) *Langmuir* **18**, 917.
[445] Lei, Z., Zhang, H., Ma, S.H., Ke, Y.X., Li, J.M., Li, F.Q. (2002) *Chem. Commun*., (7) 676–7.
[446] Yoshida, K., Shimomura, T., Ito, K. et al. (1999) *Langmuir*, **15**, 910.
[447] Liang, L., Liu, J., Windisch, C.F. Jr, et al. (2002) *Angew. Chem., Int. Ed*., **41**, 3665.
[448] (a) Liu, Y.C. and Chuang, T.C. (2003) *J. Phys. Chem. B*, **107**, 12383. (b) Shin, H.J., Hwang, I.W., Hwang, Y.N. et al. *J. Phys. Chem. B*, **107**, 4699. (c) Choi, S.J. and Park, S.M. (2000) *Adv. Mater*., **12**, 1547. (d) Marinakos, S.M., Anderson, M.F., Ryan, J.A., et al. (2001) *J. Phys. Chem. B*, **105**, 8872. (e) Cao, H., Xu, Z., Sang, H. et al. (2001) *Adv. Mater*., **13**, 121.

[449] (a) Brown, K.R. and Natan, M.J. (1998) *Langmuir*, **14**, 726. (b) Jackson, J.B. and Halas, N.J. (2001) *J. Phys. Chem. B*, **105**, 2743. (c) Ji, T., Lirtsman, V.G., Avny, Y. et al. (2001) *Adv. Mater.*, **13**, 1253. (d) Kaltenpoth, G., Himmelhaus, M., Slansky, L. et al. (2003) *Adv. Mater.*, **15**, 1113. (e) Freeman, R.G., Grabar, K.C., Allison, K.J. et al. (1995) *Science*, **267**, 1629.

[450] (a) Decher, G., Hong, J.D. and Schmitt, J. (1992) *Thin Solid Films*, **210/211**, 831–5. (b) Arys, X., Jonas, A.M., Laschewsky, A. et al. (2000) *Supramolecular Polymers* (A. Ciferri, ed.) New York: Marcel Dekker, pp 505–64. (c) Bertrand, P., Jonas, A.M., Laschewsky, A. et al. (2000) *Macromol. Rapid Commun.*, **21**, 319–48.

[451] Jhon, M.S., Choi, H.J. and To, K. (1998) *Macromol. Rapid Commun.*, **19**, 271.

[452] (a) Wu, Q., Xue, Z., Qi, Z. et al. (2000) *Polymer*, **41**(6), 2029–32. (b) Wu, Q., Xue, Z., Qi, Z. et al. (1999) *Acta Polym. Sin.*, **5**, 551–6. (c) Chang, T.C., Ho, S.Y. and Chao, K.J. (1992) *J. Chin. Chem. Soc.*, **39**(3), 209–12. (d) Feng, B., Su, Y., Song, J. et al. (2001) *J. Mater. Sci. Lett.*, **20**(4), 293–4. (e) Inoue, H. and Yoneyama, H. (1987) *J. Electroanal. Chem.*, **233**(1–2), 291–4. (f) Frisch, H.L., Xi, B., Qin, Y. et al. (2000) *High Perform. Polym.*, **12**(4), 543–9. (g) Lee, D., Char, K., Lee, S.W. et al. (2003) *J. Mater. Chem.*, **13**, 2942–7.

[453] (a) Kim, B.H., Jung, J.H., Kim, J.W. et al. (2001) *Synth. Met.*, **117**(1–3), 115–8. (b) Kim, B.H., Jung, J.H., Kim, J.W. et al. (2001) *Synth. Met.*, **121**(1–3), 1311–2. (c) Kim, B.H., Jung, J.H., Joo, J. et al. (2000) *J. Korean Phys. Soc.*, **36**(6), 366–70.

[454] (a) Do Nascimento, G.M., Constantino, V.R.L. and Temperini, M.L.A. (2002) *Macromolecules*, **35**(20), 7535–7. (b) Do Nascimento, G.M., Constantino, V.R.L., Landers, R. et al. (2004) *Macromolecules*, **37**(25), 9373–85. (c) Do Nascimento, G.M., Constantino, V.R.L. and Temperini, M.L.A. (2004) *J. Phys. Chem. B*, **108**(18), 5564–71. (d) Do Nascimento, G.M. and Temperini, M.L.A. (2006) *Quim Nova*, **29**(4), 823–8.

[455] Okamoto, K. Ray, S.S., Okamoto, M. (2003) *J. Polym. Sci. Part B – Polym. Phys.* **41**(24): 3160–3172.

[456] LeBaron, P.C., Wang, Z. and Pinnavaia, T.J. (1999) *Appl. Clay. Sci.*, **15**, 11–29.

[457] Glingerman, M.L., King, J.A., Schulz, K.H. et al. (2002) *J. Appl. Polym. Sci*. **83**(6), 1341–56.

[458] (a) Ogawa, M., Handa, T., Kuroda, K. et al. (1990) *Chem. Lett.*, (1990). (b) Ogawa, M., Shirai, H., Kuroda, K. et al. (1992) *Clays Clay Miner*, **40**, 485.

[459] (a) Yoshimoto, S., Ohashi, F., Ohnishi, Y. et al. (2004) *Synth. Met.*, **145**, 265–270. (b) Yoshimoto, S., Ohashi, F. and Kameyama, T. (2004) *Macromol. Rapid Commun.*, **25**, 1687–1691. (c) Yoshimoto, S., Ohashi, F. and Kameyama, T. (2005) *J. Polym. Sci.: Part B: Polym. Phys.*, **43**, 2705–14. (d) Krishantha, D.M.M., Rajapakse, R.M.G., Tennakoon, D.T.B. et al (2006) *Ionics*, **12**, 287–94.

[460] Kim, J.W., Kim, S.G., Choi, H.J. et al. (1999) *Macromol. Rapid Commun*., **20**, 450.
[461] (a) Park, J.H., Lim, Y.T. and Park, O.O. (2001) *Macromol. Rapid Commun*., **22**, 616. (b) Lu, J. and Zhao, X. (2002) *J. Mater. Chem*., **12**, 2603. (c) Kim, J.W., Liu, F., Choi, H.J. et al. (2003) *Polymer*, **44**, 289. (d) Kim, T.H., Jang, L.W., Lee, D.C. et al. (2002) *Macromol. Rapid Commun*., **23**, 191.
[462] (a). Block, H., Kelly, J.P., Qin, A. et al. (1990) *Langmuir*, **6**, 6. (b) Halsey, T.C. (1992) *Science*, **258**, 761. (c) Zukowski, C.F. (1993) *Ann. Rev. Mater. Sci*., **23**, 45.
[463] Choi, H.J., Cho, M.S. and Jhon, M.S. (1997) *Polym. Adv. Tech*., **8**, 697.
[464] Choi, H.J., Cho, M.S. and To, K. (1998) *Physica A*, **254**, 272.
[465] Goodwin, J.W., Markham, G.M. and Vinent, B. (1997) *J. Phys. Chem. B*, 101, 1961.
[466] Cho, M.S., Choi, H.J. and To, K. (1998) *Macromol. Rapid Commun*., **19**, 271.
[467] Yoshimoto, S., Ohashi, F., Ohnishi, Y., Nonami, T. (2004) *Chem. Commun*., (17) 1924–5.
[468] Meada, S. and Armes, S.P. (1995) *Synth. Met*. **73**, 151.
[469] Chowdhury, A.-N., Yousuf, M.A. and Rahman, M.M. (2002) *Indian J. Chem*., **41A**, 1562.
[470] Smith, A.B. and Knowles, C.J. (1990) *Biotechnol. Appl. Biochem*., **12**, 661.
[471] Miksa, B. and Slomkowski. S. (1995) *Colloid Polym. Sci*., **273**, 47.
[472] Minehan, D.S., Marx, K.A. and Tripathy, S.K. (1994) *Macromolecules*, **27**, 777.
[473] Saoudi, B., Jammul, N., Chehimi, M.M. et al. (1997) *J. Colloid Interface Sci*., **192**, 269.
[474] Saoudi, B., Jammul, N., Abel, M.-L. et al. (1997) *Synth. Met*., **87**, 97.
[475] Davey, J.M., Innis, P.C., Ralph, S.E. et al. (2000) *Colloids and Surf. A*, **175**, 291.
[476] Chowdhury, A.-N., Jesmeen, S.R. and Hossain, M.M. (2004) *Polym. Adv. Technol*., **15**, 633–8.
[477] Stejskal, J., Sapurina, I., Prokeš, J. et al. (1999) *Synth. Met*., **105**, 195.
[478] Wu, C.-G., Yeh, Y.-R., Chen, J.-Y. et al. (2001) *Polymer*, **42**, 2877.
[479] Chen, Y., Kang, E.T., Neoh, K.G. et al. (2001) *Langmuir*, **17**, 7425.
[480] Travain, S.A., Libardi, L.H., Marletta, A. et al. (2002) *Mol. Cryst. Liq. Cryst*., **374**, 439.
[481] Mazur, M. and Krysinski, P. (2001) *Electrochim. Acta*, **46**, 3963. (9) Mazur, M. and Krysinski, P. (2001) *Thin Solid Films* **396**, 131.
[482] (a) Liao, C. and Gu, M. (2002) *Thin Solid Films*, **408**, 37. (b) Chen, Y., Kang, E.T. and Neoh, K.G. (2002) *Appl. Surf. Sci*., **185**, 267.
[483] Jin, Z., Su, Y. and Duan, Y. (2001) *Sens. Actuators*, *B*, **72**, 75.
[484] Goren, M., Qi, Z. and Lennox, R.B. (2000) *Chem. Mater*., **12**, 1222.
[485] Coelho, R.A.L., Santos, G.M.P., Azevedo, P.H.S. (2001) *J. Biomed. Mater. Res*., **56**, 257.
[486] Guernion, N., Ewen, R.J., Pihlainen, K. et al. (2002) *Synth. Met*., **126**, 301.

[487] Tzou, K. and Gregory, R.V. (1992) *Synth. Met*., **47**, 267.
[488] Su, S.-J. and Kuramoto, N. (2000) *Synth. Met*., **114**, 147.
[489] Jia, W., Segal, E., Narkis, M. et al. (2002) *Polym. Adv. Technol*., **13**, 16.
[490] Bay, R.F.C., Armes, S.P., Pickett, C.J., and Ryder, K.S. (1991) *Polymer*, **32**(13), 2456–2460.
[491] Omastova, M., Pavlinec, J., Pionteck, J. et al. (1997) *Polym. Int*., **43**, 109.
[492] Orlov, A.V., Kiseleva, S.G., Yurchenko, O.Y. et al. (2000) *Polym. Sci*., *A*, **42**, 1292.
[493] Kim, B.J., Oh, S.G., Han, M.G. et al. (2002) *Polymer*, **43**, 111.
[494] Jun, J.B., Lee, C.-H., Kim, J.-W. et al. (2002) *Colloid Polym. Sci*., **280**, 744.
[495] Dhawan, S.K., Singh, N. and Venkatachalam, S. (2002) *Synth. Met*., **129**, 261.
[496] Goren, M. and Lennox, R.B. (2001) *Nano Lett*., **1**, 735.
[497] Sotomayor, P.M., Raimundo, I.M. Jr, Zarbin, A.J.G. et al. (2001) *Sens. Actuators*, *B*, **74**, 157.
[498] Stejskal, J., Quadrat, O., Sapurina, I. et al. (2002) *Eur. Polym. J*., **38**, 631.
[499] Bhattacharyya, S. and Saha, S.K. (2002) *Appl. Phys. Lett*., **80**, 4612.
[500] Stejskal, J., Trchova, M., Fedorova, S. et al. (2003) *Langmuir*, **19**, 3013–8.
[501] Lee, D. and Char, K. (2002) *Polym. Degrad. Stab*., **75**, 555.
[502] Kim, B.-H., Jung, J.-H., Hong, S.-H. et al. *Macromolecules*, **35**, 1419.
[503] Scherer, R., Bernandes, A.M., Forte, M.M.C. et al. (2001) *Mater. Chem. Phys*. **71**, 131.
[504] Tishchenko, G.A., Dybal, J., Stejskal, J. et al. (2002) *J. Membr. Sci*., **196**, 279.
[505] Gregory, R.V., Kimbrell, W.C. and Kuhn, H.H. (1989) *Synth. Met*. **28**, C823.
[506] Nalwa, H.S. (2000) *Handbook of Nanostructured Materials and Nanotechnology*. San Diego: Academic Press.
[507] Liu, P., Tian, J., Liu, W.M. et al. (2003) *Chem. Bull*., **66**, 73.
[508] Yoshinaga, K. (2002) *Bull. Chem. Soc. Jpn*., **75**, 2349.
[509] Liu, P., Tian, J., Liu, W.M. et al. (2003) *Polym. J*., **35**, 379.
[510] Liu, P., Tian, J., Liu, W.M. et al. (2003) *Mater. Res. Innov*., **7**, 105.
[511] Liu, P., Liu, W.M. and Xue, Q.J. (2004) *Des. Monom. Polym*., **7**, 253.
[512] Tsubokawa, N. and Ishida, H. (1992) *J. Polym. Sci.: Polym. Chem*. **30**, 2241.
[513] Tsubokawa, N. and Ishida, H. (1992) *Polym. J*., **25**, 809.
[514] Patten, P.E., Xia, J. and Abernathy, T. (1996) *Science*, **272**, 866.
[515] Pyun, J. and Matyjaszewski, K. (2001) *Chem. Mater*., **13**, 3436.
[516] Carrot, G., Diamanti, S. and Manuszak, M. (2001) *J. Polym. Sci.: Polym. Chem*., **39**, 4294.
[517] Liu, P., Tian, J., Liu, W.M. et al. (2004) *Polym. Int*., **53**, 127.
[518] Liu, P., Liu, W. and Xue, Q. (2004) *Mater. Chem. and Phys*., **87**, 109–13.
[519] Wang, Y.J., Wang, X.H., Li, J. et al. (2001) *Adv. Mater*. (Weinheim, Germany), **13**, 1582.
[520] Xia, H.S. and Wang, Q. (2003) *J. Appl. Polym. Sci*., **87**, 1811.
[521] Liu, P., Liu, W.M. and Xue, Q. (2004) *J. Mater. Chem. Phys*., **87**, 109.
[522] Niu, Z.W., Yang, Z.Z., Hu, Z.B. et al. (2003) *Adv. Funct. Mater*., **13**, 949.

[523] Choi, H.J., Cho, M.S., Kang, K.K. et al. (2000) *Microporous Mesoporous Mater*., **39**, 19.
[524] Cho, M.S., Choi, H.J., Kim, K.Y. et al. (2002) *Macromol. Rapid Commun*., **23**, 713–6.
[525] Li, X., Li, X. and Wang, G. (2006) *Mater. Lett*., **60**, 3342–5.
[526] Lee, D (2000) *Macromol. Rapid. Commun*., **21**, 1136–9.
[527] Lee, K.P., Gopalan, A.I., Lee, S. et al. (2006) *Appl. Polym. Sci*., **102**, 3912–8.
[528] Ballav, N. and Biswas, M. (2004) *Synth. Met*., **142**, 309.
[529] Jia, W., Segal, E., Kornemandel, D. et al. (2002) *Synth. Met*., **128**, 115.
[530] Biswas, M., Ray, S.S. and Liu, Y.P. (1999) *Synth. Met*., **105**, 99.
[531] Yang, S.M. and Chen, K.H. (2003) *Synth. Met*., **135**, 151.
[532] Chandrakanthi, R.L.N. and Careem, M.A. (2002) *Thin Solid Films*, **417**, 51 (171-215-10 da).
[533] Ray, S.S. and Biswas, M. (2000) *Synth. Met*., **108**, 231.
[534] Somani, P., Kale, B.B. and Amalnerkar, D.P. (1999) *Synth. Met*., **106**, 53.
[535] Fusalba, F. and Belangar, D.J. (1999) *Mater. Res*., **14**, 1805.
[536] Gautu, M.L. and Romero, P.J.G. (1999) *Solid State Chem*., **147**, 601.
[537] Ravikiran, Y.T., Lagare, M.T., Sairam, M. et al. (2006) *Synth. Met*., **156**, 1139–47.
[538] Wang, L., Rocci-Lane, M., Brazis, P., et al. (2000) *J. Am. Chem. Soc*., **122**, 6629.
[539] Inzelt, G. and Puskas, Z. (2006) *J. Solid State Electrochem*., **10**, 125–33.
[540] Raghavendra, S.C., Syed Khasim, Revanasiddappa, M. et al. (2003) *Bull. Mater. Sci*., **26**, 101.
[541] Wang, C., Zang, Y.H., Gao, J.B. et al. (1999) *Chem. J. Chin. Univ*., **20**, 1491.
[542] Patil, R.C., Radhakrishna, Pethkar, S. et al. (2001) *J. Mater. Res*., **16**, 1982.
[543] Khasım, S., Raghavendra, S.C., Revanasıddappa, M. et al. (2005) *Ferroelectrics*, **325**, 111–9.
[544] Nirmalya, B. (2004) *Mater. Lett*. **58**, 3257.
[545] Gemeay, A.H., Rehab, I.A.M., El-Sharkawy, G. et al. (2005) *Euro. Polym. J*., **41**, 2575.
[546] Ray, S.S. (2002) *Mater. Res. Bull*., **37**, 813–824 and references therein.
[547] Biswas, M. and Ray, S.S. (2000) *J.Appl. Polym. Sci*., **77**(13), 2948–56.
[548] Deschamps, A., Lagier, J.P., Fievert, F. et al. (1992) *J. Mater. Chem*., **2**, 1213.
[549] Vijaya Kumar, R., Mastai, Y., Diamant, Y. et al. (2001) *J. Mater.Chem*., **11**, 1209.
[550] Mallick, K., Witcomb, M.J. and Scurrell, M.S. (2005) *Mater. Sci. Eng. B*, **123**, 181–6.
[551] Athawale, A.A. and Bhagwat, S.V. (2003) *J. Appl. Polym. Sci*., **89**, 2412–7.
[552] (13) Wei, Z. and Wan, M. (2002) *Adv. Mater*., **14**, 1314.
[553] Gok, A., Gode, F. and Turkaslan, B.E. (2006) *Mater. Sci. and Eng. B*, **133**, 20–5.
[554] Houdayer, A., Schneider, R., Billaud, D. et al. (2005) *Synth. Met*., **151**, 165.

[555] Sarkar, A., Kapoor, S., Yashwant, G. et al. (2005) *J. Phys. Chem. B*., **109**, 7203.
[556] Sazou, D. (2001) *Synth. Met*., **118**, 133.
[557] Suri, K., Annapoorni, S., Tandon, R.P. et al. (2003) *Curr. Appl. Phys*., **3**, 209.
[558] Chen, A., Wang, H., Zhao, B. et al. (2003) *Synth. Met*., **139**, 411.
[559] Caruso, F., Susha, A.S., Giersig, M., Mohwald, H. (1999) *H. Adv. Mater.*, 11, 950.
[560] Novakova, A.A., Lanchinskaya, V.Y., Volkov, A.V., Gendler, T.S., Kiseleva, T.Y., Moskvina, M.A., Zezin, S.B. (2003) *J. Magnetism Magnetic Mater*., **354**, 258–259.
[561] Singh, R.N., Lal, B. and Malviya, M. (2004) *Elec. Acta*, **49**, 4605.
[562] Aphesteguy, J.C. and Jacobo, S.E. (2004) *Phys. B*., **354**, 224.
[563] Miyauchi, S., Aiko, H., Sorimashi, Y. and Tsubata, I. (1989) *J. Appl.Polym. Sci*., **37**, 289.
[564] Shen, P.K., Huang, H.T. and Tseung, A.C.C. (1992) *J. Electrochem. Soc*., **139**, 1840.
[565] Peng, X., Zhang, Y., Yang, J., Zou, B.S., Xiao, L.Z., Li, T.J. (1992) *J. Phys. Chem*., **96**, 3412–15.
[566] Huang, X. and Chen, Z. (2005) *Mater. Res. Bull*., **40**, 105.
[567] Wan, M.X. and Fan, J.H. (1998) *J. Polym. Sci. Part A: Polym. Chem*., **36**, 2749.
[568] Wan, M.X. and Li, W.C. (1997) *J. Polym. Sci. Part A: Polym. Chem*., **34**, 2129.
[569] Yavuz, O., Ram, M.K., Aldissi, M., et al. (2005) *J. Mater. Chem*., 15, 810.
[570] Deng, J., He, C., Peng, Y. et al. (2003) *Synth. Metals*, **139**, 295–301.
[571] Deng, J., Ding, X., Zhang, W. et al. (2002) *Polymer*, **43**, 2179–2184.
[572] Lu, X., Yu, Y., Chen, L. et al. (2005) *Nanotechnology*, **16**, 1660–5.
[573] Zhang, Z., Wan, M. and Wei, Y. (2005) *Nanotechnology*, **16**, 2827–32.
[574] Reddy, K.R., Lee, K.-P., Gopalan, A.I. and Md Showkat, A. (2007) *Polym. Adv. Technol*., **18**, 38.
[575] Schloeman, E. (2000) *J. Magn. Magn. Mater*., **209**, 15.
[576] Pardavi-Horvath, M. (2000) *J. Magn. Magn. Mater*., **215–216**, 171.
[577] Li, L., Jiang, J. and Xu, F. (2006) *Euro. Polym. J*., **42**, 2221–7.
[578] Kaiser, A.B., Subramaniam, C.K., Gilberd, P.W. et al. (1995) *Synth. Met*., **69**(1–3), 197.
[579] Chen, C.X., Qian, S.M., Gong, F.F. et al. (2000) *Chin. J. Mater. Res*., **14**(3), 334.
[580] (a) Liu, Y.C. and Chuang, T.C. (2003) *J. Phys. Chem. B*, **107**, 12383. (b) Shin, H.J., Hwang, I.W., Hwang, Y.N. et al. (2003) *J. Phys. Chem. B*, **107**, 4699. (c) Choi, S.J. and Park, S.M. (2000) *Adv. Mater*., **12**, 1547. (d) Marinakos, S.M., Anderson, M.F., Ryan, J.A. et al. (2001) *J. Phys. Chem. B*, **105**, 8872. (e) Cao, H., Xu, Z., Sang, H. et al. (2001) *Adv. Mater*., **13**, 121.
[581] (a) Brown, K.R. and Natan, M.J. (1998) *Langmuir*, **14**, 726. (b) Jackson, J.B. and Halas, N.J. (2001) *J. Phys. Chem. B*, **105**, 2743. (c) Ji, T., Lirtsman,

V.G., Avny, Y. et al. (2001) *Adv. Mater*., **13**, 1253. (d) Kaltenpoth, G., Himmelhaus, M., Slansky, L. et al. (2003) *Adv. Mater*. **15**, 1113. (e) Freeman, R.G., Grabar, K.C., Allison, K.J. et al. (1995) *Science* ***267***, 1629.

[582] Antonietti, M., Forster, S., Hartmann, J. et al. (1996) *Macromolecules*, **29**, 3800.

[583] Liu, Y.C. and Jang, L.Y. (2002) *J. Phys. Chem. B*, **106**, 6748.

[584] Feng, X., Yang, G., Xu, Q. et al. (2006) *Macromol. Rapid Commun*., **27**, 31–6.

[585] Sarma, T.K. and Chattopadhyay, A. (2004) *J. Phys. Chem. A*, **108**, 7837–42.

[586] (a) Kuramoto, N. and Genies, E.M. (1995) *Synth. Met*., **68**, 191. (b) Kinlen, P.J., Liu, J., Ding, Y. et al. (1998) *Macromolecules*, **31**, 1735. (c) Riede, A., Helmstedt, M., Riede, V. et al. (1998) *Langmuir* **14**, 6767. (d) Premachandran, R., Banerjee, S., John, V.T. et al. (1997) *Chem. Mater*. **9**, 1342. (e) Cason, J.P., Miller, M.E., Thompson, J.B. et al. (2001) *J. Phys. Chem. B*, **105**, 2297.

[587] Smith, J.A., Josowicz, M. and Janata, J. (2003) *J. Electrochem. Soc*., **150**, E384.

[588] Kinyanjui, J.M., Hatchett, D.W., Smith, J.A. et al. (2004) *Chem. Mater*., **16**, 3390.

[589] Zhang, X.Y., Goux, W.J. and Manohar, S.K. (2004) *J. Am. Chem. Soc*., **126**, 4502.

[590] Pillalamarri, S.K., Blum, F.D., Tokuhiro, A.T. et al. (2005) *Chem. Mater*., **17**, 5941–4.

[591] Sun, Y., Wilson, S.R. and Schuster, D.I. (2001) *J. Am. Chem. Soc*., **123**, 5348.

[592] Zengin, H., Zhou,W.S., Jin, J.Y. et al. (2002) *Adv. Mater*. **14**, 1480.

[593] Michael, L., Graciela, B. and Rogers, J.A. (2003) *Adv. Mater*., **15**, 1188.

[594] Feng, W., Bai, X.D., Lian, Y.Q. et al. (2003) *Carbon*, **41**, 1551.

[595] Du, X.S., Xiao, M. and Meng, Y.Z. (2004) *J. Polym. Sci. Part B:Polym. Phys*. **42**, 1972.

[596] Ramamurthy, P.C., Harrel, W.R., Gregory, R.V., et al. (2003) *Synth. Met*., **137**, 1497.

[597] Cochet, M., Maser, W.K., Benito, A.M. et al. (2001) Chem. Commun., **16**, 1450.

[598] Reddy, K.R., Lee, K.P.I., Gopalan, A.I., et al. (2006) *J. Polym. Sci. Part A: Polym. Chem*., **44**, 3355–64.

[599] Gopalan, A.I., Lee, K.P., Santhosh, P., et al. (2007) *Composites Sci. Technol*., **67**, 900–5.

[600] Wong, J.Y., Langer, R. and Ingber, D.E. (1994) *Proc. Natl Acad. Sci. USA*, **91** 3201–4.

[601] Nalwa, H.S. (ed) (2001) *Handbook of Surfaces and Interfaces of Materials: Biomolecules, Biointerfaces, and Applications*, vol. 5, Chapter 11. New York: Academic. pp 445–94.

[602] Smela, E., Kallenbach, M. and Holdenried, J. (1999) *J. Microelectromech. Syst*., **8**, 373–83.

[603] Skotheim, T.A., Elsenbaumer, R.L. and Reynolds, J.R. (1998) *Handbook of Conducting Polymers*. New York: Dekker.
[604] Orgzall, I., Lorenz, B., Dunsch, L. et al. (1996) *Synth. Met*., **81**, 59–63.
[605] Teh, K.S. and Lin, L. (2003) *Technical Digest: 7th Int. Conf. On Micro Total Analysis Systems*. USA: Squaw Valley, 5–9 October, pp 1195–8.
[606] Qian, R., Pei, Q. and Li, Y. (1993) *Synth. Met*., **61**, 275–8.
[607] Gustafsson, G., Lundstrom, I., Liedberg, B. et al. (1989) *Synth. Met*., **31**, 163–79.
[608] Pfluger, P., Krounbi, M., Street, G.B. et al. (1983) *J. Chem. Phys*., **78**, 3212–8.
[609] Chen, S.A. and Liao, C.S. (1993) *Macromolecules*, **26**, 2801.
[610] Kim, D.Y., Lee, J.Y., Kim, C.Y. et al. (1995) *Synth. Met*., **72**, 243.
[611] Bjorklund, R.B., Armes, S.P., Maeda, S. et al. (1998) *J. Colloid Interface Sci*., **197**, 179.
[612] Song, M.K., Kim, Y.T., Kim, B.S. et al. (2004) *Synth. Met*., **141**, 315.
[613] Zarbin, A.J.G., De Paoli, M.-A. and Alves, O.L. (1999) *Synth. Met*. **99**, 227.
[614] Maia, D.J., Zarbin, A.J.G., Alves, O.L. et al. (1995) *Adv. Mater*., **7**, 792.
[615] Schnitzler, D.C., Meruvia, M., Hummelguen, I.A. et al. (2003) *Chem. Mater*., **15**, 4658.
[616] Schnitzler, D.C. and Zarbin, A.J.G. (2004) *J. Braz. Chem. Soc*., **15**, 378.
[617] Beleze, F.A. and Zarbin, A.J.G. (2001) *J. Braz. Chem. Soc*., **12**, 542.
[618] Zarbin, A.J.G., Maia, D.J., De Paoli, M.-A. et al. (1999) *Synth. Met*., **102**, 1277.
[619] Gonçalves, A.B., Mangrich, A.S. and Zarbin, A.J.G. (2000) *Synth. Met*., **114**, 119.
[620] Oliveira, M.M., Zanchet, D., Ugarte, D. et al. (2004) *Prog. Colloid Polym. Sci*., **128**, 126.
[621] Amorim, M.S., Galembeck, A., Bazin, H. et al. (2002) *Mol. Cryst. Liq. Cryst*., **374**, 267.
[622] Galembeck, A., Silva, S.B.C. and Silva, J.A.P. (2004) *J. Del Nero*, *Opt. Mater*. **24**, 637.
[623] Peter, W.F., Wanli, M., Alan, J.L., et al. (1994) *J. Mater. Chem*., **4**(5), 771.
[624] Faguy, P.W., Lucas, R.A. and Ma, W.L. (1995) *Colloids Surf A: Physicochem. Eng. Aspects*, **105**(1), 105.
[625] Zeng, Q.H., Wang, D.Z. and Yu, A.B. (2002) *Nanotechnology*, **13**(5), 549.
[626] Omastova, M., Mravcakova, M., Chodak, I. et al. (2006) *Polym. Eng. Sci*., **46**, 1069–1078.
[627] (a) Kim, B.H., Hong, S.H., and Joo, J. (b) Park, I.-W., Epstein, A.J., Kim, J.W. and Choi, H.J. (2004) *J. Appl. Phys*., **95**, 5.
[628] Orikakhi, C.O. and Lerner, M.M. (1995) *Mater. Res. Bull*., **30**(6), 723.
[629] Sinha Ray, S. and Biswas, M. (1999) *Mater. Res. Bull*., **34**(8), 1187.
[630] Kim, J.W., Kim, S.G., Choi, H.J. et al. (2001) *Int. J. ModPhys. B*, **15**, 657.
[631] Sohn, J.I., Kim, J.W., Kim, B.H. et al. (2002) *Mol. Cryst. Liq. Cryst*., **377**, 333–336. 121-150-6.

[632] Kim, J.W., Liu, F., Choi, H.J., Hong, S.H., Joo, J. (2003) *J. Joob Polymer*, **44**, 289–293.
[633] Bae, W.J., Kim, K.H., Park, Y.H. et al. (2004) *Macromolecules*, **37**, 9850.
[634] Bae, W.J., Kim, K.H., Park, Y.H. et al. (2005) *Macromolecules*, **38**, 1044.
[635] Baea, W.J., Kima, K.H., Joa, W.H. et al. (2005) *Park Polymer*, **46**, 10085–91.
[636] Yoshimoto, S., Ohashi, F. and Kameyama, T. (2005) *Macromol. Rapid Commun*., **26**, 461–6.
[637] Hong, S.H., Kim, B.H., Joo, J. et al. (2001) *J. Curr. Appl. Phys*., **1**, 447–50.
[638] Liu, Y.C. and Tsai, C. (2003) *J. Chem. Mater*., **15**, 320–6.
[639] Liu, Y.C. and Ger, M.D. (2002) *Chem. Phys. Lett*., **362**, 491–6.
[640] Kingon, A.I., Maria, J.P. and Streiffer, S.K. (2000) *Nature* **406**, 1032.
[641] Wilk, G.D., Wallace, R.M. and Anthony, J.M. (2001) *J. Appl. Phys*., **89**, 5243.
[642] Sharma, R., Lamba, S. and Annapoorni, S. (2005) *J. Phys. D. Appl. Phys*., **38**, 3354.
[643] Dey, A., De, A. and De, S.K. (2005) *J. Phys. Condens. Mater*., **17**, 5895.
[644] Dutta, K. and De, S.K. (2006) *Solid State Commun*., **140**, 167–71.
[645] (a) Caruso, F. (2001) *Adv. Mater*., **13**, 11–22. (b) Stober, W., Fink, A. and Bohn, E. (1968) *J. Colloid Interface Sci*., **26**, 62–9. (c) Xia, Y.N., Gates, B. and Yin, Y.D. (2000) *Adv. Mater*., **12**, 693–713. (d) Cen, L., Neoh, K.G., Li, Y.L. et al. (2004) *Biomacromolecules* **5**, 2238–46.
[646] (a) Christian, P., Mohamed, M.C., Michel, D. et al. (1997) *J. Colloid Interface Sci*. **193**, 190–9. (b) Saoudi, B., Jammul, N., Chehimi, M.M. et al. (1997) *J. Colloid Interface Sci*. **192**, 269–73.
[647] (a) Maeda, S. and Armes, S.P. (1994) *J. Mater. Chem*., **4**, 935. (b) Maeda, S. and Armes, S.P. (1995) *Synth. Met*., **73**, 151. (c) Maeda, S., Gill, M., Armes, S.P. et al. (1995) *Langmuir*, **11**, 1899. (d) Butterworth, M.D., Corradi, R., Johal, J. et al. (1995) *J. Colloid Interface Sci*., **174**, 510.
[648] Koopal, C.G., Feiters, M.C., Notle, R.J. et al. (1992) *Biosens. Bioelectron*., **7**, 461.
[649] (a) Martin, C.R. (1961) *Science*, **266**. (b) Martin, C.R. (1996) *Chem. Mater*., **8**, 1739. (c) Hulteen, J.C. and Martin, C.R. (1997) *J. Mater. Chem*., **7**, 1075. (d) Menon, V.P., Lei, J. and Martin, C.R. (1996) *Chem. Mater*., **8**, 2382.
[650] Jerome, C., Demoustier-Champagne, S., Legras, R. et al. (2000) *Chem. Eur. J*., **6** (17), 3089.
[651] Picha, A., Lua, Y., Boykob, V. et al. (2003) Polymer, **44**, 7651–9.
[652] Liu, J. and Wan, M. (2001) *J. Polym. Sci. Part A Polym. Chem*., **39**, 997.
[653] Ramanavicius, A., Ramanaviciene, A. and Malinauskas, A. (2006) *Electrochim. Acta*, **51**, 6025–37.
[654] (a) Azioune, A., Chehimi, M.M., Miksa, B. et al. (2002) *Langmuir*, **18**, 1150–6 and reference there in. (b) Saoudi, B., Despas, C., Chehimi, M.M. et al. (2000) *Sens. Actuators B*, **62**, 35–42.
[655] Fu, Y.Z., Yuan, R., Chai, Y.Q. et al. (2006) *Anal. Lett*., **39**, 467–82.

[656] Perruchot, C., Chehimi, M.M. and Delamar, M. (1998) *Surf. Interface Anal*., **26**, 689–98.
[657] Shi, X.Y., Briseno, A.L. and Sanedrin, R.J. *Macromolecules*, (2003) **36**, 4093–8.
[658] Yang, X., Dai, T.Y. and Lu, Y. (2006) *Polymer*, **47**, 441–7.
[659] (a) Liu, C.F., Maruyama, T. and Yamamoto, T. (1993) *Polymer*, **25**, 363. (b) McCarthy, G.P., Armes, S.P., Greaves, S.J. et al. (1997) *Langmuir*, **13**, 3686–92.
[660] Martensson, E. and Gafvert, U. (2004) *J. Phys. D Appl. Phys*., **37**, 112.
[661] Omastova, M., Boukermab, K., Chehimi, M.M. et al. (2005) *Mater. Res. Bull*., **40**, 749–65.
[662] (a) Deng, J., Peng, Y., He, C. et al. (2003) *Polym. Int*., **52**, 1182. (b) Garcia, B., Lamzoudi, A., Pillier, F. et al. (2002) *J. Electrochem. Soc*., **149** (12), B560–6. (c) Turcu, R., Peter, I., Pana, O. et al. (2004) *Mol. Cryst. Liq. Cryst*., **417**, 235/[719]–243/[727]. (d) Mallouki, M., Tran-Van, F. Sarrazin, C. et al. (2007) *J. Solid State Electrochem*., **11**, 398–406. (e) Chang, B.H., Liu, Z.Q., Sun, L.F. et al. (2000) *Low Temp. Phys*., **119**, (1–2).
[663] Kanatzidis, M.G., Tonge, L.M., Marks, T.J. et al. (1987) *J. Am. Chem. Soc*., **109**, 3797.
[664] Srinivasan, S. and Pramanik, P. (1994) *J. Mater. Sci. Lett*., **13**, 365.
[665] Kerr, T.A., Wu, H. and Nazar, L.F. (1996) *Chem. Mater*., **8**, 2005.
[666] Bissessur, R., DeGroot, D.C., Schindler, J.L., Kannewurf, C.R., Kanatzidis, M.G. (1993) *J. Chem. Soc. Chem. Commun*., (8) 687–9.
[667] Huang, C.L. and Matijevi, E. (1995) *J. Mater. Res*., **10**, 1327.
[668] Abeles, B., Sheng, P., Coutts, M.D. and Arie, Y. (1975) *Adv. Phys*., **24**, 407.
[669] (a) Chien, C.L. (1991) *J. Appl. Phys*., **69**, 5267. (b) Barzilai, S., Goldstein, Y., Balberg, I. et al. (1981) *Phys. Rev. B*, **23**, 1809. (c) Murillo, N., Ochoteco, E., Alesanco, Y. et al. (2004) *Nanotechnology*, **15**, S322–7.
[670] Yang, X., Xu, L., Ng, S.C. et al. (2003) *Nanotechnology*, **14**, 624.
[671] Sunderland, K., Brunetti, P., Spinu, L. et al. (2004) *Mater. Lett*., **58**, 3136–40.
[672] (a) Hyeon, T., Lee, S.S., Park, J. et al. (2001) *J. Am. Chem. Soc*., **123**, 12798. (b) Ji, T., Jian, W.-B. and Fang, J. (2003) *J. Am. Chem. Soc*., **125**, 8448. (c) Fang, J., Stokes, K.L., Zhou, W.L., Wang, W.D., Lin, J. (2001) *Chem. Commun*., (18) 1872–3.
[673] Chen, W., Li, X., Xue, G., Wang, Z., Zou, W. (2003) *Appl. Surface Sci*., **218**, 215–21.
[674] Gangopadhyay, R. and De, A. (1999) *Eur. Polym. J*., **35**, 1985–92.
[675] Suri, K., Annapoorni, S., Tandon, R.P. et al. (2002) *Synth. Met*., **126**, 137.
[676] (a) Roux, S., Audebert, P., Pagetti, J. et al. (2000) *New J. Chem*., **24**, 877. (b) Roux, S., Audebert, P., Pagetti, J. et al. (2003) *Sol-Gel Sci. Technol*., **26**, 435–439.
[677] Ferain, E. and Legas, R. (1994) *Nucl. Instrum. Meth. B*, **84**, 331.

[678] Fleischer, R.L., Price, P.B. and Walker, R.M. (1975) *Nuclear Tracks in Solids: Principles and Applications*, Berkeley, CA: University of California Press.
[679] Spohr, R. (1990) *Ion Tracks and Microtechnology: Basic Principles andApplications*. Braunsweig: Vieweg.
[680] Zhu, J., Liu, Z., Yu, Z. et al. (1994) *Nucl. Instrum. Meth. B*, **91**, 469.
[681] Schiestel, S., Ensinger, W. and Wolf, G.K. (1994) *Nucl. Instrum. Meth. B*, **91**, 473–7.
[682] Asmus, T. and Wolf, G.K. (2000) *Nucl. Instrum. Meth. B*, **166–167**, 732–6.
[683] De, A., Das, A. and Lahiri, S. (2004) *Synth. Metals*, **144**, 303–7.
[684] (a) Cho, K.G., Kumar, D., Holloway, P.H. et al. (1998) *Appl. Phys. Lett*., **73**, 3058. (b) Tanabe, K., Misono, M., Ono, Y. et al. (1989) *New Solid Acids and Bases*. New York: Elsevier, p. 41. (c) Wang, S.Y. and Lu, Z.H. (2002) *Mater. Chem. Phys*., **78**, 542.
[685] Cheng, Q., Pavlinek, V., Li, C. et al. (2006) *Appl. Surf. Sci*., **253**, 1736–40.
[686] Johans, C., Clohessy, J., Fantini, S. et al. (2002) *Electrochem. Commun*. **4**, 227–30.
[687] (a) Wan, X., Liu, X., Xue, G. et al. (1999) *Polymer*, **40**, 4907. (b) Cairns, D.B., Armes, S.P. and Bremer, L.G.B. (1999) *Langmuir*, **15**, 8052. (c) Liu, Y.C. and Hwang, B.J. (2001) *J. Electroanal. Chem*., **501**, 100. (d) Liu, Y.C. and Tsai, C.J. (2002) *J. Electroanal. Chem*., **537**, 165–71.
[688] (a) Cunnane, V.J. and Evans, U. (1998) *Chem. Commun*., (19) 2163–4. (b) Gorgy, K., Fusalba, F., Evans, U. et al. (2002) *Synth. Met*., **125**, 365–73.
[689] (a) Cheng, Y.F. and Schirin, D.J. (1996) *J. Chem. Soc. Faraday Trans*., **92**, 3865. (b) Johans, C., Lahtinen, R., Kontturi, K. et al. (2000) *J. Electroanal.Chem*., **488**, 99–109.
[690] (a) Abe, M. and Ito, T. (1967) Nippon Kagaku Zasshi **87**, 1174. (b) Abe, M. and Ito, T. (1969) *Bull. Chem. Soc. Jpn*., **42**, 2683.
[691] Abe, M. and Ito, T. (1968) *Bull. Chem. Soc. Jpn*., **41**, 333.
[692] Lefebvre, J., Maria, H., Hebd, C.R. et al. (1963) *Seanc. Acad. Sci. Paris*, **256**, 3121.
[693] (a) Khan, A.A., Alam, M.M., Inamuddin, and Mohammad, F. (2004) *J. Electroanal. Chem*., **572**, 67–78. (b) Khan, A.A., Inamuddin, and Alam, M.M. (2005) *Mater. Res. Bull*., **40**, 289–305.
[694] (a) Biswas, M. and Mukherjee, A. (1994) *Adv. Polym. Sci*., **115**, 89–123. (b) Deronzier, A. and Moutet, J.-C. (1996) *Coord. Chem. Rev*., **147**, 339–71.
[695] Xu, J., Li, X.L., Liu, J.F. et al. (2005) *J. Polym. Sci. Part A Polym. Chem*., **43**, 2892–900.
[696] Li, X., Wan, M., Wei, Y. et al. (2006) *J. Phys. Chem. B*, **110**, 14623–6.
[697] (a) Shi, H.T., Ma, J.M. and Cheng, H.M. (2002) *Chem. Commun*., **1704**. (b) Zhang, D.B., Qi, L.M., Ma, J.M. et al. (2002) *J. Mater. Chem*., **12**, 3677. (c) Li, M., Lebeau, B. and Mann, S. (2003) *Adv. Mater*., **15**, 2032. (d) Jang, J. and Yoon, H. (2003) *Chem. Commun*., **6**, 720–721. (e) Sun, W.D., Xu, L.P., Chu, Y. et al. (2003) *J. Colloid Interface Sci*. **266**, 99. (f) Xing, S.X., Chu, Y.,

Sui, X.M. et al. (2005) *J. Mater. Sci*., **40**, 215. (g) Sui, X.M., Chu, Y., Xing, S.X. et al. (2004) *Mater. Lett*., **58**, 1255. (h) Sui, X.M., Chu, Y., Xing, S.X. et al. (2004) *Colloids Surf. A Physicochem. Eng. Asp*., **251**, 103. (i) Han, D.X., Chu, Y., Yang, L.K. et al. (2005) *Colloids Surf. A Physicochem. Eng. Asp*., **259**, 179. (j) Han, M., Chu, Y., Han, D. et al. (2006) *Colloid Interface Sci*., **296**, 110–7.

[698] Corres, M.A., Mugica, A., Carrasco, P.M. et al. (2006) *Polymer*, **47**, 6759–64 and references there in.

[699] He, X. and Shi, G. (2006) *Sens. Actuators B* **115**, 488–93.

[700] (a) Kuhn, H.H and Child, A.D. (1998) *Handbook of Conducting Polymers*, 2nd ed., New York; Marcel Dekker Inc., pp. 993–1013. (b) Kuhn, H.H., Child, A.D. and Kimbrell, W.C. (1995) *Synth. Met*., **71**, 2139.

[701] Dong, B. et al. (2005) *Small*, **1** (5), 520–4.

[702] (a) Teh, K.S. and Lin, L. (2005) *J. Micromech. Microeng*, **15**, 2019–27. (b) Shi, M.H., Peng, Y.Y., Zhou, J. et al. (2006) *Biosens. Bioelectron*., **21** (12), 2210–6. (c) Peteu, S.F. (2007) *J. Intell. Mater. Syst. Struc*., **18** (2), 147–52. (d) Bush, B., Xu, G., Carraro, C. et al. (2006) *Sens. Actuators A*, **126**, 194–200 (e) Roemer, M., Kurzenknabe, T.,·Oesterschulze,·E. et al. (2002) *Anal Bioanal Chem*. **373**, 754–7.

[703] (a) Chandrasekhar, P. (1999) *Conducting Polymer*, *Fundamentals and Applications*. Boston: Kluwer Academic Publishers. (b) Fichou, D. (1999) *Handbook of Oligo – and Polythiophene*. Weinheim: Wiley-VCH. (c) Dionigi, C., Stoliar, P., Porzio, W. et al. (2007) *Langmuir*, **23**, 2030–6.

[704] Roncali, J. (1992) *Chem. Rev*., **92**, 711 and references cited therein.

[705] (a) Nguyen, P.T., Rammelt, U. and Plieth, W. (2002) *Macromol. Symp*., **187**, 929. (b) Nguyen Cong, H., Dieng, M., Sene, C. et al. (2000) *Solar Energy Mater. Solar Cells* **63**, 23. (c) Tagmouti, S., Outzourhit, A., Oueriagli, A. et al. (2000) *Thin Solid Films*, **379**, 272.

[706] (a) Hebestreit, N., Hofmann, J., Rammelt, U. et al. (2003) *Electrochim. Acta*, **48**, 1779. (b) Hofmann, J., Diplomarbeit, Dresden, T.U. (2000) (c) Plieth, W. and Hebestreit, N. (1991) German Patent Application No. 261.8.

[707] Michael, O. (2001) *Wolf Adv. Mater*., **13**, 8.

[708] (a) Vu, Q.T., Pavlik, M., Hebestreit, N. et al. (2005) *Reactive Funct. Polym*., **65**, 69–77. (b) Ballav, N. and Biswas, M. (2003) *Polym. Int*., **52**, 179.

[709] Gok, A., Kocak, E.D. and Aydogdu, S. (2005) *J. Appl. Polym. Sci*., **96**, 746–52.

[710] (a) Sinha Ray, S. and Biswas, M. (1999) *J. Appl. Polym. Sci*., **73**, 2971. (b) Sinha Ray, S. and Biswas, M. (1998) *Mater. Res. Bull*., **33**, 105.

[711] Saito, Y., Kitamura, J., Wada, Y. et al. (2002) *Synth. Met*. **131**, 185.

[712] (a) Too, C.O., Wallace, G.G., Burrell, A.K. et al. (2001) *Synth. Met*. **123**, 53. (b) Kajihara, K., Tanaka, K., Hirao, K. et al. (1997) *Jpn. J. Appl. Phys*., **36**, 5537.

[713] Jones, G.W., Taylor, D.M. and Gomes, H.L. (1999) *Synth. Met*. **101**, 431.

[714] Glenis, S., Horowitz, G., Tourillon, G. et al. (1984) *Thin Solid Films*, **111**, 93.

[715] (a) Torsi, L., Tafuri, A., Cioffi, N. et al. (2003) *Sens. Actuators B*, **93**, 257. (b) Park, S.K., Kim, Y.H., Han, J.I. et al. (2003) *Synth. Met*., **139**, 377.
[716] (a) Zagorska, M., Sanetra, J. and Barta, P. (1998) *Synth. Met*. **94**, 119. (b) Wang, X.J., Andersson, M.R., Thompson, M.E. et al. (2003) *Synth. Met*. **137**, 1019. (c) Bolognesi, A., Botta, C., Cecchinato, L. et al. (1999) *Synth. Met*. **106**, 183.
[717] (a) Spiekermann, S., Smestad, G., Kowalik, J. et al. (2001) *Synth. Met*., **121**, 1603. (b) Gebeyehu, D., Brabec, C.J., Sariciftci, N.S. et al. (2002) *Synth. Met*. **125**, 279. (c) Grant, C.D., Schwartzberg, A.M., Smestand, G.P. et al. (2002) *J. Electroanal. Chem*., **522**, 40.
[718] (a) Pfleger, J., Pavlik, M., Hebestreit, N. et al. (2004) *Macromol. Symp*., **212** (1), 539. (b) Vu, Q.-T., Pavlik, M., Hebestreit, N. et al. (2005) *Electrochim. Acta*, **51**, 1117–24.
[719] Wang, C., Schindler, J.L., Kannewurf, C.R. et al. (1995). *Chem. Mater*., **7**, 58.
[720] Son, Y., Lee, J., Kim, J. et al. (2006) *Mol. Cryst. Liq. Cryst*., **444**, 275–82.
[721] Glenis, S., Benz, M., LeGoff, E. et al. (1993) *J. Am. Chem. Soc*., **115** (12), 519.
[722] Ballav, N. and Biswas, M. (2004) *Polym. Int*., **53**, 1467–72.
[723] Wang, T.X., Zhang, D.Q., Xu, W. et al. (2002) *Langmuir*, **18**, 8655.
[724] Zhang, Z., Wang, F., Chen, F. et al. (2006) *Mater. Lett*., **60**, 1039–42.
[725] Yin, H.R.and Jiang, J.S. (2005) *J. Mater. Sci*., **40**, 3013–5.
[726] (a) Penza, M., Milella, E. and Anisimkin, V.I. (1998) *Sens. Actuators B*, **47**, 218. (b) Collins, G.E. and Buckley, L.J. (1996) *Synth. Met*. **78**, 93. (b) Bauerle, P. and Scheib, S. (1993) *Adv. Mater*., **5**, 848. (c) McQuade, D.T., Pullen, A.E. and Swager, T.M. (2000) *Chem. Rev*., **100**(7): 2537–2574.
[727] Ram, M.K., Yavuz, O. and Aldissi, M. (2005) *Synth. Met*., **151**, 77–84.
[728] Georger, J.H., Singh, A., Price, R.P. et al. (1987) *J. Am. Chem. Soc*., **109**, 6169.
[729] Cai, Z. and Martin, C.R. (1989) *J. Am. Chem. Soc*., **111**, 4138.
[730] Cai, Z., Lei, J., Liang, W. et al. (1990) *Chem. Mater*., **3**, 960.
[731] Liang, W. and Martin, C.R. (1991) *J. Am. Chem. Soc*., **112**, 9666.
[732] Martin, C.R., Parthasarathy, R. and Menon, V. (1993) *Synth. Met*., **55**, 1165.
[733] Karim, M.R., Lee, C.J. and Lee, M.S. (2006) *J. Polym. Sci. Part A Polym. Chem*., **44**, 5283–90.
[734] Valentini, L., Armentano, I., Kenny, J.M. et al. (2005) *Thin Solid Films*, **476**, 162.
[735] Sonar, P., Sreenivasan, K.P., Madddanimath, T. et al. (2006) *Mater. Res. Bull*., **41**, 198–208.
[736] (a) Baba, A., Onishi, K., Knoll, W. et al. (2004) *J. Phys. Chem. B*, **108**, 18949. (b) Bertoncello, P., Notargiacomo, A., Erokhin, V. et al. (2006) *Nanotechnology*, **17**, 699–705.
[737] Maity, A. and Biswas, M. (2002) *J. Appl. Polym. Sci*., **88**, 2233.
[738] Maity, A. and Biswas, M. (2003) *J. Appl. Polym. Sci*., **90**, 1058–65.

[739] Ballav, N. and Biswas, M. (2003) *Synth. Met*., **132**, 213.
[740] Biswas, M. and Haque, S.A. (1983) *J. Polym. Sci. Polym. Chem*., **21**, 1861.
[741] Cotton, F.A., Wilkinson, G., Murillo, C.A., Bochmann, M. (1999) *Advanced Inorganic Chemistry, sixth edn*. John Wiley & Sons Inc. Pub. Ltd. New York, USA.
[742] Greenwood, N.N. and Earnshaw, A. (1998) *Chemistry of Elements, second edn*. A Div. of Reed Ed. and Professional Pub. Ltd.
[743] Ballav, N. and Biswas, M. (2005) *Synth. Met*., **149**, 109.
[744] Ballav, N. and Biswas, M. (2006) *J. Polym. Res*., **13**, 115–9.
[745] (a) Ulman, A. (1991) *Ultrathin Organic Films*. New York: Academic. (b) Petty, M.C. (1996) *Langmuir–Blodgett Films: An Introduction*. Cambridge: Cambridge University Press.
[746] Spange, S., Gräser, A., Huwe, A. et al. (2001) *Chem. Eur. J*., **7**, 17, 3722.
[747] Merkel, T.C., Freeman, B.D., Spontak, R.J. et al. (2002) *Science*, **296**, 519–22.
[748] Freeman, B. and Pinnau, I. (1997) *Trends Polym. Sci*., **5**, 167–73.
[749] Schultz, J. and Peinemann, K.-V. (1996) *J. Membr. Sci*., **110**, 37–45.
[750] Rao, M.B. and Sircar, S. (1993) *J. Membr. Sci*., **85**, 253–64.
[751] (a) Baker, R.W., Yoshioka, N., Mohr, J.M. et al. (1987) *J. Membr. Sci*., **31**, 259–71. (b) Leemann, M., Eigenberger, G. and Strathmann, H. (1996) *J. Membr. Sci*., **113**, 313–22.
[752] Sikdar, S.K., Grosse, D. and Rogut, I. (1998) *J. Membr. Sci*., **151**, 75–85.
[753] Javaid, A., Hughey, M.P., Varutbangkul, V. et al. (2001) *J. Membr. Sci*., **187**, 141–50.
[754] Asad Javaid a,1, Sergio, O. Gonzalez b, Eric, E. Simanek b, David, M. Ford (2006) *J. Memb. Sci*., **275**, 255–60.
[755] (a) Javaid, A. and Ford, D.M. (2003) *J. Membr. Sci*., **215**, 157–68. (b) Javaid, A., Krapchetov, D.A. and Ford, D.M. (2005) *J. Membr. Sci*., **246**, 181–91.
[756] (a) Leger, C. and Lira, H.D.L. (1996) *R. J. Membr. Sci*., **120**, 187–95. (b) Alami-Younssi, S., Kiefer, C., Larbot, A. et al. (1998) *J. Membr. Sci*., **143**, 27–36. (c) McCarley, K.C. and Way, J.D. (2001) *Sep. Purif. Technol*., **25**, 195–210. (d) Van Gestel, T., Van der Bruggen, B., Buekenhoudt, A. et al. (2003) *J. Membr. Sci*. **224**, 3–10.
[757] (a) Nagale, M., Kim, B.Y. and Bruening, M.L. (2000) *J. Am. Chem. Soc*., **122**, 11670–8. (b) Lee, S.B., Mitchell, D.T., Trofin, L. et al. (2002) *Science*, **2002**, 2198–200. (c) Perez, G.P., Yelton, W.G., Cernosek, R.W. et al. (2003) *Anal. Chem*., **75**, 3625–30.
[758] (a) Teraoka, Y., Zhang, H.M., Furukawa, S., Yamazoe, N. (1985) *Chem. Lett*., (11) 1743–1746. (b) Teraoka, Y., Nobunaga, T., Okamoto, K. et al. (1991) *Solid-Sate Ionics*, **48**, 207. (c) Dyer, P.N., Richards, R.E., Russek, S.L. et al. (2000) *Solid-State Ionics*, **134**, 21. (d) Lu, Y., Dixon, A.G., Moser, W.R. et al. (2000) *Catal. Today*, **56**, 297. (e) Sammels, A., Schwartz, M., Mackay, R.A. et al. (2000) *Catal. Today*, **56**, 325.

[759] (a) Takamura, H., Kawai, M., Okumura, K. et al. (2003) *Mater. Res. Soc. Symp. Proc*., **756**, EE8.111. (b) Kharton, V.V., Kovalevsky, A.V., Viskup, A.P. et al. (2000) *J. Electrochem.Soc*., **147**, 2814. (c) Nigge, U., Wiemhofer, H.-D., Romer, E.W.J. et al. (2002) *Solid-State Ionics*, **146**, 163. (d) Zyryanov, V.V., Uvarov, N.F., Kostrovskii, V.G. et al. (2001) *Mater. Res. Soc. Symp. Proc*., **755**, DD6.27.1. (e) Meen, J.K., Goksen, O.A., Lin, I.-C. et al. (2001) *Mater. Res. Soc. Symp. Proc*., **658**, GG9.14.1-6. (f) Goksen, O.A., Meen, J.K., Jacobson, A.J. et al. (2001) *Mater. Res. Soc. Symp. Proc*., **658**, GG4.7.1–5. (g) Li, C., Hu, T., Zhang, H. et al. (2003) *J. Membr. Sci*., **226**, 1–7. (h) Kharton, V.V., Kovalevsky, A.V., Viskup, A.P. et al. (2003) *Solid-State Ionics*, **160**, 247.

[760] (a) Mogensen, M., Sammes, N.M. and Pompsett, G.A. (2000) *Solid-State Ionics*, **63**, 129. (b) Knauth, P. and Tuller, H.L. (2000) *Solid-State Ionics*, **1215**, 136–7.

[761] Pechini, M.P. (1967) US Patent 3,330,697.

[762] (a) Zyryanov, V.V. and Uvarov, N.F. (2004) *Inorg. Mater*., **40**(7), 729. (b) Zyryanov, V., Uvarov, N., Sadykov, V. et al. (2003) *Proceedings of the X APAMTopical Seminar "Nanoscience and Technology"*. Russia: Novosibirsk. p. 173. (c) Zyryanov, V.V., Uvarov, N.F., Sadykov, V.A. et al. (2005) *Catal. Today*, **104**, 114–9.

[763] (a) Stone, C. and Morrison, A.E. (2002) *Solid State Ionics*, (152), Part A Sp. Iss, 1–13. (b) Flint, S.D. and Slade, R.C.T. (1997) *Solid State Ionics*, **97**, 299.

[764] (a) Song, C. (2002) *Catal. Today*, **77**, 17–49. (b) Costamagna, P. and Srinivasan, S. (2001) *J. Power Sources*, **102**, 242.

[765] Formato, R.M., Osenar, P. and Kovar, R.F. (1999) *DOE/ONR Fuel Cell Workshop Presentation Documents*. Baltimore, MD, Oct 6–8, 1999.

[766] (a) Hogarth, M.P. and Hards, G.A. (1996) *Platinum Met. Rev*., **40**, 150. (b) Surampudi, S., Narayanan, S.R., Vamos, E. et al. (1994) *J. Power Sources*, **47**, 377. (c) Wang, J., Wasmus, S. and Savinell, R.F. (1995) *J. Electrochem. Soc*., **142**, 4218.

[767] (a) Kalappa, P. and Lee, J.-H. (2007) *Polym. Int*., **56**, 371–5. (b) Kima, Y., Lee, J.S., Rhee, C.H. et al. (2006) *J. Power Sources*, **162**, 180–5; and references therein.

[768] Jiang, C. and Lin, X. (2007) *J. Power Sources*, **164**, 49–55.

[769] (a) Nagy, G., Gerhardt, G.A., Oke, A.F. et al. (1985) *J. Electroanal. Chem*., **188**, 85. (b) Kristensen, E.W., Khur, W.G., and Wightman, R.M. (1987) *Anal. Chem*., **59**, 1752. (c) Baur, J., Kristensen, E.W., May, L.J. et al. (1988) *Anal. Chem*., **60**, 1268. (d) Wiedemann, D., Kawagoe, K.T., Kennedy, R.T. Ciolkowski, E.L., Wightman, R.M. (1991) *Anal. Chem*., **63**, (24): 2965–2970. (e) Gunasingham, H. and Tan, C. (1989) *Analyst. Cambridge, U.K*., 114, 695. (f) Hoyer, B., Florence, T.M. and Bately, G.E. (1987) *Anal. Chem*., 59, 1608. (g) Harrison, D.J., Turner, R.F.B. and Bates, H.P. (2002) *Anal. Chem*., 60, 1988.

[770] (a) Kreuer, K.D. (2001) *J. Membr. Sci*., **185**, 29. (b) Rikukawa, M. and Sanui, K. (2000) *Prog. Polym. Sci*., **25**, 1463. (c) Kerres, J.A. (2001) *J. Membr. Sci*., **185**, 3. (d) Jones, D.J. and Roziére, J. (2001) *J. Membr. Sci*., **185**, 41. (e) Bae, J.-M., Honma, I., Murata, M. et al. (2002) *Solid-State Ionics*, **147**, 189. (f) Li, L., Xu, L. and Wang, Y. (2003) *Mater. Lett*., **57**, 1406.

[771] (a) Kim, J.-D. and Honma, I. (2004) *J. Electrochem. Soc*., **151**, 9 A1396–401 (2004); and references therein. (b) Prashantha, K. and Park, S.G. (2005) *J. Appl. Polym. Sci*., **98**, 1875–8.

[772] (a) Staiti, P. (2001) *Mater. Lett*., **47**, 241. (b) Staiti, P., Freni, S. and Hocevar, S. (1999) *J. Power Sources*, **79**, 250. (c) Staiti, P., Minutoli, M. amd Hočevar, S. (2000) *J. Power Sources*, **90**, 231.

[773] (a) Nakajima, H. and Honma, I. (2002) *Solid State Ionics*, **148**, 607. (b) Honma, I., Nakajima, H. and Nomura, S. (2002) *Solid State Ionics*, **707**, 154–5. (c) Honma, I., Nakajima, H., Nishikawa, O. et al. (2002) *Electrochemistry*, **70**, 920. (d) Honma, I., Nakajima, H., Nishikawa, O. et al. (2002) *J. Electrochem. Soc*., **149**, A1389. (e) Nakajima, H., Nomura, S., Sugimoto, T. et al. (2002) *J. Electrochem. Soc*., **149**, A953. (f) Honma, I., Nakajima, H., Nishikawa, O. et al. (2003) *J. Electrochem. Soc*., **150**, A616. (g) Honma, I., Nakajima, H., Nishikawa, O. et al. (2003) *Solid State Ionics*, **162**, 237.

[774] (a) Wu, Q., Tao, S., Lin, H. et al. (2000) *Mater. Sci. Eng. B*., **68**, 161. (b) Lavrencic Stangar, U., Groselj, N., Orel, B. et al. (2000) *Chem. Mater*., **12**, 3745. (c) Lavrencic Stangar, U., Groselj, N., Orel, B. et al. (2001) *Solid State Ionics*, **145**, 109. (e) Chang, H.Y. and Lin, C.W. (2003) *J. Membr. Sci*., **218**, 295. (d) Tadanaga, K., Yoshida, H., Matsuda, A. et al. (2003) *Electrochem. Commun*., **5**, 644. (e) Dahmouche, K., Atik, M., Mello, N.C. et al.. (1997) *J. Sol–Gel Sci. Technol*., **8**, 711. (f) Damay, F. and Klein, L.C. (2003) *Solid State Ionics*, **162–3**, 261. (g) Mauritz, K.A. (1998) *Mater. Sci. Eng. C*, **6**, 121. (h) Slade, R.C.T. and Varcoe, J.R. (2001) *Solid State Ionics*, **145**, 127. (l) Halim, J., Buchi, F.N., Hans, O. et al. (1994) *Electrochim. Acta*, **39**, 1303.

[775] (a) Brinker, C.J., Scherrer, G. (1989) *Sol–gel Science—The Physics and Chemistry of Sol–gel Processing*. San Diego: Academic Press. (b) Kreuer, K.D. (1996) *Chem. Mater*., **8** 610. (c) Thangamuthu, R. and Lin, C.W. (2005) *Solid State Ionics*, **176**, 531–8. (d) Lin, C.W., Thangamuthu, R. and Chang, P.H. (2005) *J. Membran. Sci*., **254**, 197–205.

[776] (a) Jones, D.J. and Roziere, J. (2003) In *Handbook of Fuel Cells – Fundamentals,Technology and Applications*, vol. 3 (W. Vielstich, A. Lamm, H.A. Gasteiger, eds). Chichester: Wiley-VCH. pp. 447. (b) Li, Q., He, R., Jensen, J.O. et al. (2003) *Chem. Mater*., **15**, 4896.

[777] (a) Higuchia, E., Uchidab, H., Fujinami, T. et al. (2004) *Solid State Ionics*, **171**, 45–9. (b) Colicchio, I., Keul, H., Sanders, D. et al. (2006) *Moeller Fuel Cells*, 06, **3–4**, 225–36. (c) Bebin, P, Caravanier, M. and Galiano, H. (2006) *J Membr. Sci*., **278**, 35–42.

[778] (a) Clingerman, M.P., Weber, E.H., King, J.A. et al. (2003) *J. Appl. Polym. Sci*., **88**, 2280. (b) Flandin, L., Verdier, M., Boutherin, B. et al. (1999) *J. Polym. Sci., Part B*, **37**, 805.

[779] (a) Reghu, M., Yoon, C.O., Yang, C.Y. et al. (1993) *Macromolecules*, **26**, 7245. (b) Reghu, M., Yoon, C.O., Yang, C.Y. et al. (1994) *Phys. Rev. B*, **50**, 13931.

[780] (a) Saatweber, D., Klostermann, P., Rekowski, V. Patents: DE19933098-A1, (2001) WO200105897-A1, (2001) EP1216278-B1, (2005). (b) Gonon, P. and Boudefel, A. (2006) *J. Appl. Phys*., **99**, 024308.

[781] (a) Othmer, K. (1994) (2000) *Encyclopedia of Chemical Technology*. New York: John Wiley and Sons. (b) (2003) *Encyclopedia of Polymer Science and Technology*. New York: Third edn, John Wiley and Sons. (c) Singh, N. (2001) *Handbook of Advanced Electronic and Photonic Materials*. London: Academic Press. (d) Chandrasekdar, P. (1999) *Conducting Polymers, Fundamental and Applications, A Practical Approach*. Dordrecht: Kluwer Academic. (e) Gul, V.E. (1996) *Structure and Properties of Conducting Polymer Composites*, The Netherlands, Brill Academic Publishers.

[782] (a) Chen, Z., Brokken-Zijp, J.C.M. and Michels, M.A.J. (2006) *J. Polym. Sci., Part B: Polym. Phys*., **44**, 33. (b) Chen, Z., Brokken-Zijp, J.C.M., Huinink, H. et al. (2006) *Macromolecules*, **39**, 6115–24. (c) Huijbregts, L.J., Brom, H.B., Brokken-Zijp, J.C.M. et al. (2006) *J. Phys. Chem. B*, **110**, 23115–22.

[783] (a) Maltsev, E.I., Lypenko, D.A., Bobinkin, V.V. et al. (2002) *Appl. Phys. Lett*., **81**, **16**, 14.

This page intentionally left blank

Chapter 5

Electrochemically assisted scanning probe microscopy: A powerful tool in nano(bio)science

Andrea Alessandrini

CNR-INFM-S3; Department of Physics, University of Modena and Reggio Emilia, Modena, Italy

Paolo Facci

CNR-INFM-S3, Modena, Italy

Abstract. Nanosciences in general and nanobiophysics, in particular, have taken much advantage of the advent of scanning probe microscopies. These instruments have enabled real space visualization of atoms and molecules allowing the retrieval of unprecedentedly accurate information. Nevertheless, the most powerful implementations of scanning probe microscopies should also enable a full control of the phenomena taking place at solid–liquid interfaces (e.g., electrochemical reactions). In this chapter, we will review the applications of scanning probe microscopies (STM and SFM) under electrochemical control. In particular, we will firstly present the fundamentals of electrochemically controlled scanning tunnelling microscopy, as far as basic concepts and possible set-ups are concerned, and proceed to the basic applications involving characterization of clean surfaces, study of underpotential deposition of metals, potential-induced phase transitions in molecular layers. The further paragraphs will be devoted to reviewing biophysical applications of electrochemical scanning tunnelling microscopy (EC-STM) as far as investigation on redox metalloproteins is concerned. A discussion on the state-of-the-art video rate EC-STM is provided. In the last sections, we will present the current and future efforts aimed at further developing electrochemically assisted scanning probe microscopy towards the implementation of an electrochemically controlled current sensing atomic force microscope with the fundamental contribution of state-of-the-art nanotechnology.

Keywords: ECSTM; AFM; redox molecules; electron tunneling in water

5.1. Introduction

The introduction of scanning probe microscopy (SPM) techniques in the early 1980s [1] has represented a genuine revolution in surface science and solid-state physics. For the first time, the atoms, until then only postulated and studied just by indirect spectroscopic evidences or in ordered lattices in the Fourier space, were available for observation and manipulation in the direct space. This remarkable achievement gave access to a large number of novel experimental evidences and approaches in those disciplines. However, the most relevant effect of the introduction of the scanning probe microscopies has been probably not on the disciplines that gave rise to them. Rather, it was that of paving the way to completely new topics: those gathered under the umbrella of Nanosciences and Nanotechnologies [2]. It is, in fact, possible to date back the beginning of the nowadays interest and vigorous development of nanosciences to the introduction and rapid spreading of that class of novel microscopes. Visualization and manipulation of molecular and atomic details of surfaces and surface adsorbates are since then available, and the introduction of novel imaging techniques and operating modes appears, to date, almost endless.

Soon after the first exciting results were obtained typically in ultra high vacuum on conducting or semiconducting substrates by the scanning tunnelling microscope (STM), the early advent of the atomic force microscope (AFM) [3] paved the way, among others, to biological applications.

Particularly, the investigations of single biomolecules both at conformational and functional levels are among the most intriguing opportunities available to nanobioscientists. For the first time, it became possible to visualize important biomolecules in an environment very similar to that present in living beings. By imaging biomolecular adsorbates in a proper, water-based buffer, it made it possible to preserve not only their structure but also their functional features often connected to the modulation of molecular conformation. Molecular interactions (e.g., protein-DNA interaction) were real time visualized and studied in great detail.

One remarkable feature of the SPM techniques is that they can probe a large ensemble of different sample properties according to the physicochemical parameters that are measured in the particular experiment. The range of measurable parameters spans from tunnelling current, to surface repulsive or attractive interactions, to local temperature, surface potentials, friction force, specific biointeractions, etc. In light of the large set of measurable physical characteristics, the term ‘microscope’ for this kind of instruments appears at least inadequate. Rather, one should regard scan-

ning probe instruments as complete tools for space-resolved spectroscopy, microscopy and single molecule/atom manipulation.

In the described general frame, one more aspect enters the game in a very crucial way: the electrochemical control of electrode potentials at the solid–liquid interface. When metal or semiconductor electrodes are placed in an electrolytic solution, their potential *vs* a reference electrode can be controlled by using an external source of free energy, say a potentiostat, connected to a sacrificial (counter) electrode. Such a setup configures an electrochemical cell whose general features are those of being able to force the electrochemical potential of electrons in a metal electrode (i.e., its Fermi level, at $T = 0\,\mathrm{K}$) at a desired value. As a consequence, it is possible to drive electrochemical reactions (electron exchange or ion adsorption/desorption) at that electrode.

Particularly, such kind of control enables also the possibility of acting on the redox state of molecules adsorbed at an electrode surface, whose electronic coupling to the metallic states of the substrate is strong enough.

The coupling of electrochemical control with the capability of scanning probe microscopes to produce high-resolution images of surfaces allowed to visualize the surface of electrodes at atomic scale and to perform a large variety of investigations at the single molecule level. Moreover, electrochemically assisted scanning probe microscopes can be used for nanostructuring surfaces by exploiting deposition and/or dissolution [4]. Apart from the investigation of typical electrochemical systems, the liquid environment prompted the extension of the researches also to biomolecules on surfaces. For example, by performing SPM experiments on redox metalloproteins adsorbed at metal electrodes in an electrochemical cell (i.e., proteins whose physiological functional tasks consist in exchanging electrons with molecular partners by changing their oxidation state reversibly), it is possible to learn much on the fine mechanisms ruling electron transport through these crucial life-sustaining molecules.

In this chapter, along with a general description of the operating principles and techniques of the electrochemically assisted SPMs, their potentialities in imaging electrochemical interfaces and molecules of different nature adsorbed on atomically flat metal surfaces will be reviewed. We will concentrate on electrochemically assisted STM, where the probe can play an active role. Furthermore, a full account on the achievements regarding the behaviour of redox metalloproteins at surfaces will be provided as studied by EC-STM. The recent instrumental developments and future trends, as enabled by the advent of nanotechnology, will be taken into consideration; particular emphasis will be given to those attempts

which tend to empower scanning force microscopy with the possibility of measuring electronic and ionic currents in water-based environments and which are likely to represent the future of these exciting techniques in the electrochemical environment.

5.2. Electrochemical Scanning Tunnelling Microscope (EC-STM)

Soon after the first demonstrations of the enormous potentiality of STM imaging on conductive surfaces in vacuum and air, the possibility of operating in a liquid environment for the STM was demonstrated [5]. Afterwards, STM imaging in water was also operated in a three electrode electrochemical cell in which the substrate acted as a working electrode and a reference plus a counter electrode completed the cell [6]. This configuration resembled the usual three electrode configuration equipped with a potentiostat, in which the potential of the working electrode can be controlled with respect to a high-impedance reference electrode, while the current is allowed to flow between the working and the counter electrode. In this case, the tip was not an active electrode in the cell, but was used only to image the surface morphology, even if it had to be under potential control in order to apply a voltage drop to drive the tunnelling current. The implementation of a liquid STM represented a great breakthrough for the in situ study of surface electrodes, which was till then mainly limited to optical spectroscopic techniques, which are unable to supply real-space information with high spatial lateral resolution. Since the beginning of liquid STM imaging, the technical problem of collecting mainly the tunnelling current flowing between the tip and the sample, keeping other current sources (Faradaic currents) to a negligible level, had to be faced. This fundamental technical problem will be extensively discussed in Section 5.2.2. An improvement in the control of the in situ STM has been obtained with the introduction of the bipotentiostatic approach, in which both tip and sample potentials are independently controlled with respect to a reference electrode in solution [7,8]. The following section deals with some basic concepts about electrochemical scanning tunnelling microscopy (EC-STM), including the bipotentiostatic approach, some technical aspects such as tip preparation and characterization and electrode substrate preparation, and some features specific to tunnelling in water which are of fundamental interest to understand contrast formation mechanism.

5.2.1. Bipotentiostatic Approach

In a standard potentiostatic approach, the potential of a working electrode is controlled with respect to a reference electrode by injecting current through a low-impedance auxiliary or counter electrode. In such a configuration, the potential of the working electrode is well defined. When applied to in situ STM, the potentiostatic approach is able to control the potential of the substrate with respect to a reference electrode in order to control electrochemical reactions taking place at its surface, but it is not able to control the potential of the other polarizable electrode present in solution, i.e., the tip. In the STM configuration, it is assumed that the only relevant charge transfer mechanism which enters the current measuring system is the electron tunnelling current between the tip and the substrate. If the potential of one of the two electrodes is not controlled in the electrochemical cell, then electrochemical charge transfer mechanisms might become relevant and contribute to the measured currents. This phenomenon implies a strong source of noise in the STM control circuit. Besides involving unwanted electrochemical currents, the absence of control on the electrochemical potential of one electrode in an electrochemical cell might lead to phase variation in the surface composition of the electrode. In this framework, the use of a bipotentiostatic approach, with an independent control on the potential of both the tip and the substrate with respect to a reference electrode in solution, represented a milestone in the development of the in situ STM (Fig. 5.1).

The basic operating concept of a potentiostat is the possibility of controlling the potential of an electrode in an electrochemical cell independently from the variations in the impedances connecting the other two electrodes. Usually, the system operates to maintain the potential of the reference with respect to the working electrode, which is virtually grounded being connected to the inverting end of a current follower. Due to this configuration, the potential of the working electrode with respect to the reference is exactly opposite to the controlled potential, which is independent of the fluctuations of the impedances. The simultaneous control of the potential of two electrodes with respect to a reference electrode is performed by a bipotentiostat. One possible approach to realize this situation is that of controlling the potential of one electrode in the same way as in a potentiostat, while measuring the current through the second working electrode to control its potential with respect to the first one [9]. While setting the potential of one electrode, it is possible to independently set the potential of the second working electrode with respect to the first one. The second

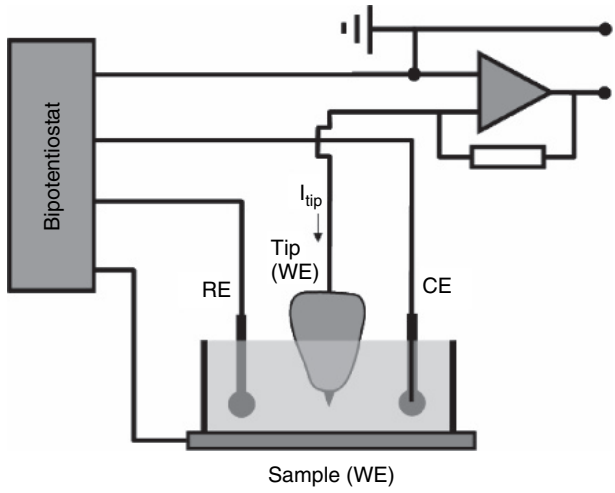

Figure 5.1: Schematic representation of the EC-STM setup based on a bipotentiostatic approach. The four electrodes in the cell are the sample (working electrode, WE), tip (WE), reference electrode (RE) and counter electrode (CE).

electrode will also have a defined potential with respect to the reference electrode, and the counter electrode will support the sum of the currents through the two electrodes. The circuitry in the case of the bipotentiostat is designed in such a way that applying a potential to one of the two working electrodes does not interfere with the potential of the other one (Fig. 5.2). In the context of EC-STM, the bipotentiostatic approach has been applied according to different strategies [7,10,11]. Usually, the tip is virtually grounded and the tunnelling current is measured via a high-gain current follower or it is fed to the STM control unit via a preamplifier. In all configurations, the tip and substrate potentials are controlled with respect to a currentless reference electrode. Usually, the counter (sacrificial) electrode in EC-STM setup is obtained by a Au or Pt wire which assures enough stability. The choice of a suitable reference electrode is instead limited by the cell design of the microscope. Ideally, a good reference electrode is obtained when a metal is used in electrochemical equilibrium with the corresponding metal cation in solution. For example, a silver wire in equilibrium with a solution containing Ag^+ could be a good choice [12]. The use of reference electrodes like saturated calomel electrode (SCE) or the classical reversible hydrogen electrode (RHE) is in most cases unsuitable for an STM setup, whereas an Ag/AgX electrode, where X^- is an

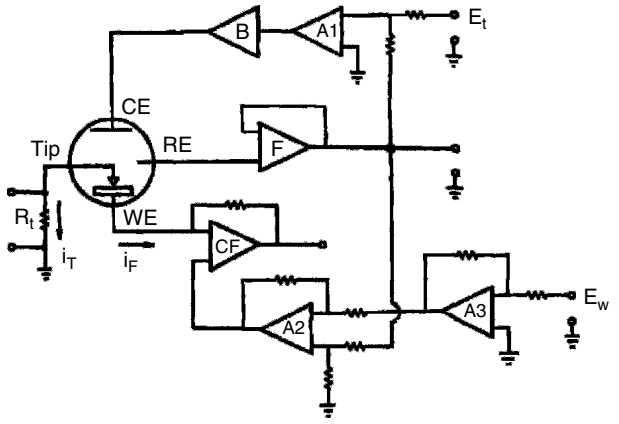

Figure 5.2: Schematic illustration of the electric circuit connections for a bipotentiostat. CE: counter electrode; WE: working electrode; RE: reference electrode; i_F: electrochemical current, i_T: tunnelling current. Reprinted from [7]. With permission of Elsevier.

anion forming a limited soluble salt phase with Ag, appears more suitable. In EC-STM setups, an Ag/AgCl electrode in equilibrium with a Cl^- containing solution is currently used with the sample cell separated from the reference electrode solution by a double frit-shielded salt bridge which allows to reduce the diffusion potential arising from different concentrations of the two solutions. Another strategy is that of using Pt or Ag wires as 'quasi reference' electrodes, which means that the wires are directly immersed in the sample solution. This situation is acceptable if in the cell solution no change occurs during the imaging process. This circumstance assures that, even if the potential of the electrode is not known, it does not change during the experiment. The actual potential of the 'quasi reference' electrode must be calibrated *vs* a true reference electrode by using a redox couple whose standard potential is known with respect to that of reference electrode under the same conditions. Typically, the ferrocene/ferrocenium couple is used to calibrate the electrode.

5.2.2. Tip Preparation

A crucial aspect of the operating principle of EC-STM is that of being in the situation in which the current entering the STM feedback circuit is

mainly due to tunnelling electrons flowing between the tip and the sample. In an electrochemical cell, both the substrate and the tip are prone to electrochemical charge transfer reactions. When these Faradaic charge transfer mechanisms occur at the tip surface, they will contribute to the current measured by the feedback system. If their contribution is relevant with respect to the current setpoint, instabilities will occur and the imaging capability of the microscope will be corrupted. Moreover, if electrochemical reactions at the tip and the substrate entail transport of chemical species involved in both reactions, then the current arising from this process will enter the feedback system too. The latter contribution will be strongly dependent on the separation between the two electrodes accordingly to the diffusion models for the involved species. Typically, the presence of dissolved O_2 could give rise to steady-state currents disturbing the imaging process. The bipotentiostatic approach described earlier can be exploited to control electrochemical reactions at the sample surface and the tip. However, in order to reduce the Faradaic contribution to the current as much as possible, the tips used for EC-STM are coated with an insulating layer which leaves only the very apex of tip exposed to the solution. Moreover, a coating of the tip results also in a decrease of the capacitance associated with the interface between the tip and the electrolyte, which would contribute a capacitive noise to the current. The thickness of the coating layer can greatly reduce the capacitance of the interface allowing to perform experiments in which the voltage or distance between the tip and the surface is modulated.

Different approaches have been exploited for coating the tips for EC-STM. The first step in the tip preparation procedure is the electrochemical etching of metal wires in order to obtain sharp tips [13] using the same techniques developed for the preparation of tips for vacuum or air STM. Usually, the electrochemical etching involves the anodic dissolution of the metal wire at the air–electrolyte interface using an alternating-current (ac) or a direct-current (dc) approach. In most of the cases, these techniques result in a tip with a conical shape which has several asperities at the very apex. It is the asperity closest to the surface which establishes a tunnelling current with the sample surface. Typically, tips for in situ STM are fabricated from metal wires: tungsten (W), platinum–iridium (Pt/Ir) or gold. The etching solution differs according to the metal wire. In the case of W tips, an aqueous base (typically 1 M NaOH or KOH) is used for the electrochemical etching, whereas for Pt/Ir, different strategies have been used. Hazardous chemicals such as a mixture of NaOH and NaCN [14] can be used for etching Pt–Ir tips or, alternatively, electrochemical solu-

tion based on $CaCl_2$ [15] or molten salt etchants can be used. For gold tips, either cyanide solutions or HCl solutions can be used to perform the electrochemical etching.

After conferring a conical shape to the tip, it has to be coated in order to leave only the very apex exposed. At the beginning of the in situ STM activity, the tips were coated with melting glass [16]. This technique requires the tips to be heated to over 1000 °C, limiting the choice of the materials which can be used. Gewirth et al. [17] developed a method to coat the tip by an epoxy coating. In this case, an electrochemically etched Pt/Ir tip is dipped into an epoxy varnish solution and returned upright in order to obtain a dewetting of the very apex of the tip. Dewetting is obtained as a consequence of the surface tension of epoxy solution. So, by adjusting the solvent/epoxy ratio, it is possible to control the degree of dewetting and the final portion of the tip which remains exposed to the solution. A very important requirement for every coating material is the range of potential which can be applied to the tip in solution without decomposition of the insulating material. For example, glass-insulated tips cannot be used in concentrated alkali solutions and epoxy-insulated tips cannot be used at tip potentials less than −200 mV *vs* SCE. Apiezon wax is another material which can be efficiently used to insulate the tips [14,18]. This procedure consists in letting the tip go through a film of melted wax. The dewetting properties of the wax–metal tip system at the very apex of the tip are controlled by the temperature of the wax. Moreover, the Apiezon wax appears to be inert in most electrolytes and stable in a potential range between the oxygen and hydrogen evolution of typical electrolytes used in EC-STM experiments.

Another strategy which is currently exploited to insulate the tips is that of using insulating polymer films which are electropainted (typically by anodic deposition) on the STM tip [19,20]. Electrodeposition occurs as a result of oxygen evolution induced by the tip potential. After the deposition, heating of the tip leads to a further polymerization and hardening which assures better stability to the insulating coating. It is probably the heating of the polymer with the induced polymer film shrinking which leads to the exposure of the very apex of the tip. A scanning electron microscopy (SEM) inspection of the coated tips has shown that the polymer coating thickness is in the order of a few microns. The small thickness means that the capacitor established between the biased tip and the electrolyte might have a very high capacitance which increases the noise pickup of the system. In order to reduce the capacitance of the system, the dielectric

layer thickness can be increased by coating the tip with an Apiezon wax layer after the electropolymerization step.

5.2.3. Tip Characterization

Characterization of the coating quality refers to an assessment of the residual Faradaic current of the tip in the electrolyte solution along with the leakage currents due to capacitance modulation. The aim of the characterization procedure is that of establishing if the residual current, measured as a function of different tip voltages, is negligible with respect to the tunnelling current setpoint value. Different tip characterization techniques can be used to evaluate the exposed tip area, such as microscopic inspection by SEM and experiments based on the ultramicroelectrodes (UME) theory. Moreover, techniques based on the tip current noise measurement can be used to in situ characterize the exposed tip area [21].

In order to evaluate the quality of a coated tip, the electrochemical steady-state tip current as a function of the tip potential outside the tunnelling region (tip far from the sample) can be measured (Fig. 5.3). A full characterization allows to establish the potential range which assures an electrochemical contribution to the tunnelling current below a certain threshold, assuming that the electrochemical current is not influenced by the tip/sample distance [10]. For example, in establishing a tolerance limit of ± 10 pA, a corresponding potential range for the tip potential was found as shown by the marked interval in Fig. 5.3.

Scanning electron microscopy images can be used to inspect the exposed tip area for a coated tip. Figure 5.4 shows two images of Pt/Ir tips coated with Apiezon wax (Fig. 5.4(a)) and with an electrophoretic paint (Fig. 5.4(b)). Both images have been acquired exploiting back-scattered electrons, obtaining a strong compositional contrast. The different scattering between the coating and the tip material is responsible for the observed contrast.

To establish the exposed tip area, methods based on the steady-state Faradaic current cannot be used because the current is not proportional to the area, but, due to geometrical considerations, it depends linearly on the radius of the hemispherical terminal part of the tip. According to the UME theory, in the presence of an electroactive species, the current in the electrochemical cell as a function of the tip potential reaches a stationary value which is given by:

$$I_S = nFCD2\pi r$$

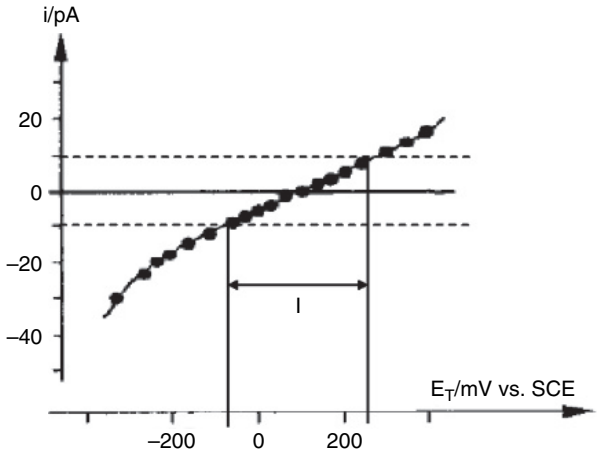

Figure 5.3: Steady-state current–voltage plot measured for a Au epoxy-coated tip in electrolyte solution with the tip outside the tunnelling regime. If the residual current has to remain inside the range ±10 pA, then the corresponding potential window for the tip is defined by the interval *I*. Reprinted from [10] (slightly modified). With permission of Elsevier.

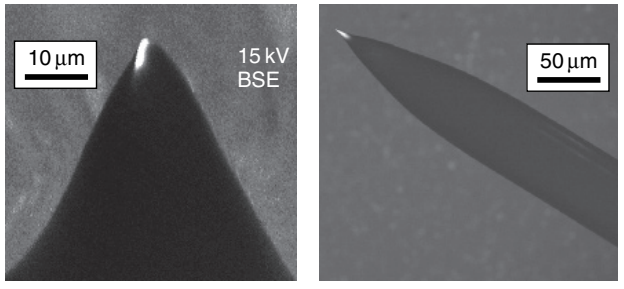

Figure 5.4: SEM images of Pt/Ir coated tips. (a) Back-scattered electron image of an Apiezon wax coated tip; (b) Back-scattered electron image of a tip coated by an electropolymerized layer.

where n is the number of electrons involved in the oxidation or reduction reaction, F is the Faraday constant, D is the diffusion coefficient of the electroactive species, C is its concentration in the solution, and r is the radius of the hemispherical exposed tip. This behaviour is due to non-linear

diffusion effects which lead to sigmoid-shaped cyclic voltammograms. By measuring the limiting current, it is possible to determine the exposed tip area as $2\pi r^2$. Also, capacitance measurements of the tip–electrolyte interface can be used to characterize insulated tips. Coating a tip by an insulating layer leads to a dramatic decrease of the capacitance associated with the interface. A high value of the measured capacitance can be an indication that a significant area of the tip is left exposed to the solution or a penetration of the electrolyte between the insulating layer and the tip. It is to be stressed again that a low capacitance of the interface also means a low pickup noise of the system during normal operation.

5.2.4. Substrate Electrode Preparation

The development of in situ EC-STM relied on the development of techniques to prepare well-defined surfaces which had to remain outside UHV environment. Methods developed for UHV analysis of surfaces, based on ion sputtering and/or high-temperature annealing, could not be used in this case.

Different electrode substrate can be used in EC-STM experiments depending on the aim of the particular study. Most of the studies involving EC-STM concentrate on the behaviour of an electrode surface at atomic resolution level in contact with an electrolyte or on the behaviour of single molecules adsorbed on a substrate electrode. Both applications require an electrode surface which is flat at atomic level, because only in this case atomic resolution is attainable and single molecules can be imaged over the surface. Moreover, most of the studies by EC-STM involve ideal electrode surfaces to carry out fundamental analysis of electrochemical processes. Based on these considerations, it is clear that the electrode surfaces of choice are monocrystalline surfaces which can be obtained according to different procedures.

To obtain single crystal electrode surface, the technique of choice is the flame-annealing technique, which has been pioneered by Clavilier et al. for Pt [22] and then extended to Au by Hamelin [23]. The technique is based on the melting of the extremity of metal wires such as Pt, Au, Rh and Pd in an appropriate flame (usually hydrogen–oxygen flame) in order to obtain single crystal faces with wide atomically flat areas in the order of hundreds of nanometers separated by monoatomic steps. In the case of gold, it is possible to obtain Au(111) surfaces by thermal evaporation of the metal on freshly cleaved mica [24]. By exploiting flame annealing after gold

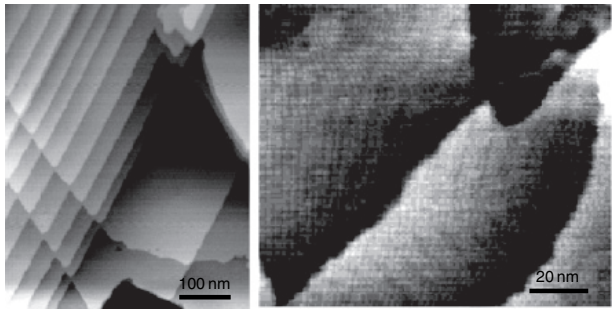

Figure 5.5: (a) EC-STM image of a Au(111) surface obtained by thermal evaporation of 150-nm Au film on freshly cleaved mica and flame annealing. (b) EC-STM image of the Au(111) $(\sqrt{3} \times 22)$ surface reconstruction.

evaporation, larger terraces can be obtained. Figure 5.5 reports an example of an Au(111) substrate prepared by the thermal Au evaporation and flame annealing imaged by STM. After the flame annealing step, the surface structure of Au(111) usually shows the $(\sqrt{3} \times 22)$ reconstruction pattern [25]. Surface reconstruction is a phenomenon which has been extensively studied in vacuum. It is due to reorganization of surface atoms with respect to bulk atoms to minimize their surface energy. Electrochemistry offers an invaluable opportunity to vary the surface electronic state and so to study surface rearrangements at the atomic scale by means of EC-STM. The $(\sqrt{3} \times 22)$ reconstruction involves a compression of the lattice so that 23 atoms on the surface fit into the space of 22 atoms in the bulk (every 23rd atom, the surface is in register with the underlying bulk). Due to this discrepancy, the surface appears with waves forming paired rows which make turns at multiple of 60°. At sufficiently positive potential, this surface reconstruction is lifted and, due to extra amount of surface atoms in the reconstructed surface with respect to the non-reconstructed one, monoatomic Au islands are formed resulting in an increase of the surface roughness. Under water, the lifting of the reconstruction is not reversible and care should be taken when the interest is to study adsorbates on the gold surface.

The flame annealing procedure can be applied only to a limited set of metals such as Au, Pt, Rh and Pd. For other less-noble metals such as Ni, Co and Cu, exposure to a flame would lead to a strong oxidation of the surface. For these metals, electrochemical etching methods can be used to

produce atomically flat terrace-step structures even if the dimensions of the terraces are restricted to the order of some nanometers [26].

Especially, if the focus of the in situ EC-STM investigation is on molecular adsorbates, layered materials such as graphite (highly oriented pyrolytic graphite, HOPG) can be used, providing at the same time conductivity and an atomically flat surface.

5.2.5. Tunnelling in Water

Electrochemical scanning tunnelling microscopy operates by tunnelling electrons across solvent molecules. Experiments made in order to measure apparent barrier height for electrons tunnelling between tip and substrate established that the barrier height is lower than that found in UHV [27–30]. Typical heights for the barrier are about 1–2 eV in water, whereas a feature of about 4–5 eV is found for vacuum. Figure 5.6 shows the behaviour obtained by Vaught et al. for the tunnelling resistance as a function of the distance when the tip was moved towards the substrate (negative displacements) starting from a position corresponding to a tunnelling resistance of 10^9 Ω. The tunnelling barrier can be characterized by the associated inverse

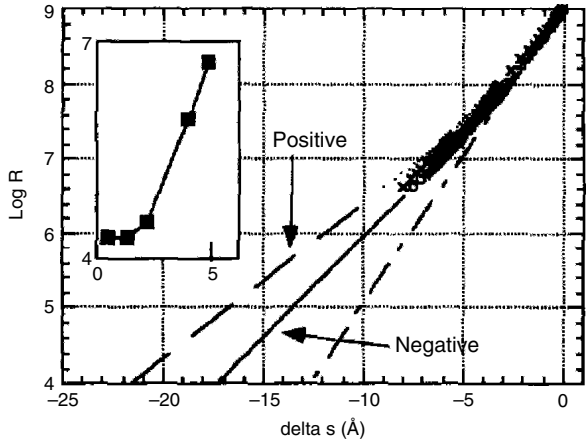

Figure 5.6: Plot of the tunnelling resistance as a function of the distance the tip has moved from the position at which $R = 10^9$ Ω. Negative displacements means approaching the surface. The inset shows the data obtained for vacuum tunnelling. Reprinted from [30]. With permission of Elsevier.

decay length κ, which is related to the tunnelling current as $\exp(-\kappa s)$, where s is the distance of the tunnelling gap. The first theoretical approaches considered the solvent as a continuous dielectric medium in which the tunnelling electrons interact with the medium polarizability, predicting a decrease in the inverse decay length of about $0.03\,\text{Å}^{-1}$ with respect to the vacuum value ($1.9\,\text{Å}^{-1}$), corresponding to a lowering of the barrier by about 1 eV. The feature experimentally obtained by Vaught et al. [30] depends on the tunnelling resistance, and it is about 0.92 or $0.76\,\text{Å}^{-1}$. Depending on the polarity of the barrier, at $10^9\ \Omega$, the first feature corresponded to tunnelling from the substrate to the tip, almost independent of the substrate potential *vs* SCE. Moreover, the junction was found to be almost Ohmic in the limit of low bias, making it possible to consider the single parameter of the tunnelling resistance in the plot of Fig. 5.6. In this figure, two data sets, for the positive and negative substrate potentials, are shown, which both have a change in the resistance slope as a function of tip–substrate separation at about $10^8\ \Omega$. The comparison of the extrapolation to $10^4\ \Omega$ for the $10^9\ \Omega$ region with the extrapolation for the two cases in the $10^8\ \Omega$ region shows how the change in κ leads to a change in the tunnelling gap. In practice, the inverse decay length for tunnelling in water decreases to about $0.5\,\text{Å}^{-1}$ when the tunnelling resistance is in the order of $10^8\ \Omega$. As a result, the tunnelling behaviour has a non-exponential trend which extends to distances of several Angstroms, at variance with the behaviour in vacuum, where the non-exponential trend is restricted to a few Angstroms.

The theoretical interpretation of this behaviour is still not completely understood. It has been clarified that a continuum dielectric model for the medium separating the tip and the substrate is able to give a reasonable description of the tunnelling behaviour, but it cannot take into account the effects due to the discrete nature of the separating medium at this separation distance. Moreover, the presence of localized electronic states in water has to be taken into consideration. Some theoretical investigations considered the possibility of tunnelling via intermediate states. The decrease in the apparent tunnelling barrier can be understood by considering that in a sequence of tunnelling steps, the overall tunnelling probability will be governed by the smaller one of the two tunnelling probabilities. If the overall distance between the two electrodes is changed by a certain amount, the distance among the minima in the intervening medium will change by a quantity which is a fraction of the overall variation, explaining the apparently reduced barrier height. Schmickler [28] simulated the tunnelling region between two metal plates through an aqueous solution composed of

three layers of water molecules by molecular dynamics and by numerical calculations of the scattering of electrons by a three-dimensional potential energy barrier. The simulation results in a distribution profile for the particle density which has three maxima both for the hydrogen and the oxygen atoms, with the two maxima nearest to the two surfaces higher than the one in the middle, and with a small net orientation of the water molecules. The resulting potential surface in the gap has maxima corresponding to the position of oxygen atoms and minima near hydrogen atoms. Tunnelling of electrons through the water layer proceeds throughout a barrier represented by a three-dimensional grid endowed with maxima and minima. The positions of the minima, corresponding to the hydrogen positions, represent localized states for the electrons which can enhance the tunnelling probability. Tunnelling is represented by the scattering of an incoming wavepacket by this potential configuration. The model is based on the assumption that the characteristic time for electron tunnelling is negligible with respect to the time scale of water movements, and the water configuration can be considered static. Peskin et al. [31] considered a narrow water barrier between two Pt surfaces and obtained, by molecular dynamics simulation, an enhancement of the tunnelling due to the presence of molecular cavities between repulsive oxygen cores promoting transient resonances. The simulation was further improved by considering a more realistic geometric configuration for the STM tip and the substrate, by introducing the presence of a bias voltage between the two metal electrodes and by considering the image effect between tunnelling electrons and electrons in the metal [32]. In this model, the calculated order of magnitude of the tunnelling current is in good agreement with the experimental values, and the decrease of the tunnelling barrier as a consequence of the water presence is properly reproduced. Moreover, it has been found that the tunnelling electron flux is not influenced by the scattering of water molecules in the off-resonance regime, but the scattering can be of relevance in the case of resonance, leading to an effect on the STM resolution.

In this context, it is worthwhile to note that the presence of oxygen in the EC-STM cell has a strong influence on the obtained contrast. This has been demonstrated especially in the case in which the imaged system is oxygen sensitive [33]. The presence of oxygen disturbs EC-STM imaging, sometimes preventing the imaging of the real structure on the surface. This effect could be due to oxygen-bound species acting as centres for inelastic electron scattering and oxidation/reduction reactions which could introduce barrier features for the tunnelling electrons. In the case of oxygen-free imaging, in situ EC-STM is able to reproduce the same sur-

face features observed for UHV STM imaging, demonstrating that water molecules represent a transparent medium for the tunnelling electrons.

5.3. EC-STM for Studying Underpotential Deposition

Underpotential deposition (UPD) refers to the deposition of (sub)monolayers of metals on foreign metal substrates occurring at a potential more positive than that predicted by the Nernst equation. From a thermodynamic point of view, UPD arises when the free energy of the interaction between the deposited metal and the metal substrate is less than the free energy involved between two of the atoms to be deposited (bulk deposition). In the opposite situation, nucleation and bulk phase growth of the metal takes place [34]. The work function difference between the two metals plays a fundamental role in the UPD determining the potential shift. Usually, UPD occurs for the deposition of lower work function metal on higher work function metal. The phenomenon has been studied since a long time by electrochemical techniques such as cyclic voltammetry [35], where the occurrence of UPD is inferred from the presence of two separated peaks, one corresponding to bulk deposition and the other one, more positive, corresponding to monolayer formation. The mechanism of UPD is controlled by (a) the metallic substrate, (b) the metal to be deposited, (c) the presence of dipoles due to the solvent and (d) the presence of adsorbed ionic species. The investigation of UPD by EC-STM appeared immediately as a means to retrieve structural information at the atomic level about the (sub)monolayer formation controlled by the substrate electrochemical potential [36]. The presence of regular structures on the surface of single crystal metal substrates has been inferred by diffraction techniques, but it has been only with the introduction of in situ scanning probe techniques that atomic structure in the real space has been observed. The interest in the deep comprehension of this phenomenon is dictated also by the fact that the deposition of foreign metal layers may cause a considerable change in the electrochemical behaviour of the surfaces, leading to positive or negative catalytic effects. For example, it has been demonstrated that the UPD of Bi and Pb adlayers considerably accelerate the electroreduction of H_2O_2 and O_2 on Au surfaces, the surface coverage also having a dominant role.

The deposition of Cu on low-index Au single crystal substrates was one of the first systems studied by EC-STM [37,38]. Cyclic voltammograms of Au(111) in the presence of Cu show two well-defined pair of peaks

corresponding to different processes for adsorption and desorption. Specifically, cyclic voltammetry in $H_2SO_4 + 1\,mM\ CuSO_4$ shows two different waves for UPD before starting the bulk deposition. Hence, there is an electrochemical evidence that two different Cu adlayer structures are present corresponding to the two deposition peaks. In situ diffraction techniques demonstrated the presence of a (1×1) structure after the second UPD peak, corresponding to a surface coverage of 1. The surface structure of Cu atoms after the first UPD peak was studied by EC-STM [39]. Ordered structures have been identified in this case corresponding to a $(\sqrt{3} \times \sqrt{3})R30°$ pattern with respect to a surface coverage of 0.33 for the Cu atoms if the maxima seen in the image are to be interpreted as Cu atoms. However, complementary studies using different techniques (EC Quartz Crystal Microbalance and chronocoulombmetry) had shown that the surface coverage for Cu was 0.67 in this potential range. The apparent contradiction was later solved by observing that the surface has a $(\sqrt{3} \times \sqrt{3})R30°$ structure in which the coverage is 0.67, and the (bi)sulfate anions occupy the centres of the honeycomb protruding well above the Cu plane [40]. This finding explained that the maxima observed by EC-STM corresponded to (bi)sulfate anions and not to Cu adatoms.

The important role played by the presence of coadsorbed anions on the Au(111) surface for Cu UPD has been demonstrated by EC-STM [41]. In the presence of Cl^- anions, EC-STM images showed the formation of an incommensurate structure identified as (5×5) after the first UPD peak. At a more negative potential, with a low concentration of Cl ions (below 10^{-5} M), the structure transforms to a (2×2) pattern corresponding to the appearance of an additional peak in the cyclic voltammogram (Fig. 5.7).

Other UPD systems have been studied by in situ STM. Among them are Cu on Au(100) [42], in which the role of both the crystal surface and the presence of anion species in the electrolyte has been elucidated, as well as Ag on Au(h,k,l) electrodes [43,44]. In situ STM investigation of the silver deposition on Au(111) from sulfuric acid solution revealed the presence of ordered structures of increasing surface coverage as the potential was changed to lower values in the UPD region [45]. Figure 5.8 shows the $(\sqrt{3} \times \sqrt{3})R30°$ structure due to silver adatoms observed on Au(111) in $0.05\,M\ H_2SO_4 + 1\,mM\ Ag_2SO_4$ at a potential of 500 mV *vs* Ag/Ag^+ corresponding to the region immediately after the first UPD peak observed by cyclic voltammetry.

Herrero et al. [36] have published an extensive review on many UPD systems, in which many references to in situ STM works on this topic can be found. As a general rule, in situ STM investigation of UPD systems

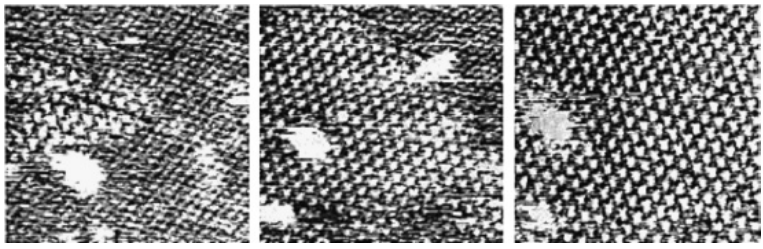

Figure 5.7: EC-STM images of Cu UPD on Au(111) in 0.1 M $HClO_4 + 0.01$ M $Cu(ClO_4)_2$ solution containing small amount (10^{-6} M) of Cl^- ions. The three images correspond to a time sequence of images on the same area over a period of 25 s following a change in potential of the substrate from +0.3 V to +0.13 V *vs* SCE. The strucure evolves starting form (2×2) islands in a (5×5) pattern (first image on the left) to a complete (2×2) pattern. Reprinted from [41]. With permission of Elsevier.

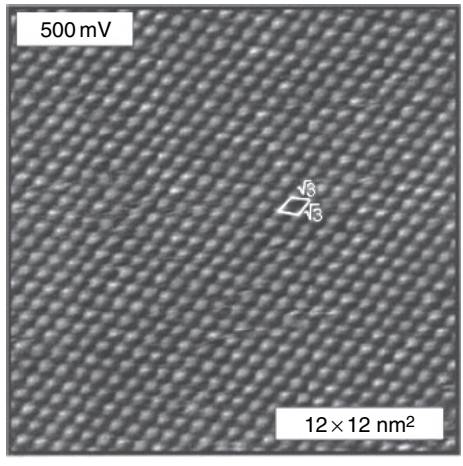

Figure 5.8: EC-STM image of silver adatoms structure on Au(111) in 0.05 M $H_2SO_4 + 1$ mM Ag_2SO_4 obtained for a substrate potential immediately after the first UPD peak. Reprinted from [45]. Permission of Royal Society of Chemistry.

allows to visualize the surface structures in the real space and to understand the role played by the presence of anions, but care must be paid to the interpretation of the maxima observed in the images. Depending on the particular case, metal adatoms or coadsorbed anions are visualized by STM.

5.4. Visualization of Potential-Induced Molecular Assembling and Phase Transitions

Control of the molecular assembly on surfaces has recently received a great deal of attention, both from fundamental and technological points of view [46]. The capability of controlling the ordering of molecules at the atomic scale deals with the understanding of the adsorbate/adsorbate interaction and adsorbate/surface interaction. When the assembling is performed at the liquid–solid interface, the overall structure of the molecular edifices is the result of the interplay of several different types of contributions in which the solvent and the substrate play a pivotal role together with the intermolecular interactions. The electrolyte–solid interface offers the unique opportunity to control the adsorbate/surface interaction by means of the electrochemical potential. This possibility can be considered as an external control to induce different types of 2D molecular organization on the surface simply by changing the surface potential, i.e., the surface charge density [47]. In this context, in situ scanning tunnelling microscopy is the technique of choice to induce and visualize 2D phase transitions of molecular adsorbates in the real space and at atomic level.

Cunha and Tao have visualized the order/disorder reversible phase transition of 2,2′-bipyridine on Au(111) induced by changing the surface potential in an electrochemical cell [48]. Intermolecular interaction is in this case due to stacking between π electrons, and the molecules assemble each other forming roll of coins whose main axis is randomly oriented on the surface for low surface charges but align following surface atomic orientation for surface charges above a certain threshold. Ordered domains start to form by increasing the surface charge, and the ordered domains component increases with the potential. The phase transition has been interpreted to have a consequence of the increased interaction between molecules and the substrate at high surface charge, which leads to an increased surface concentration and the assembly of the molecule to avoid the hard-core repulsion between rods.

Potential control of the surface charge represents a method to modulate the surface mobility of adsorbates in the same way high temperature

induces surface reorganization in vacuum. Systems that have been studied comprehend large planar structures composed of π systems, such as porphyrins and phthalocyanine, and polar molecules, such as 2,2′-bipyridine or 4,4′-bipyridine, which can undergo orientational transitions with respect to the substrate at different values of the surface potential. In the first case, molecules are expected to lie always flat on the surface independently of the surface charge [49] due to their tendency to maximize π interactions with the substrate. Moreover, due to polarizability of these systems, it is possible to modulate adsorbate/surface interaction by means of a variation in the surface charge (i.e., potential), controlling in these ways their surface mobility. With this type of molecules, it is, therefore, possible to concentrate mainly on adsorbate/surface interaction to understand the mechanism of self-assembly, neglecting intermolecular interactions by π stacking which may arise if the molecules would change their orientation. He et al. [49] have studied the self-assembling of porphyrin molecules on Au(111) electrodes and they have found a strong dependence of the substrate/adsorbate interaction on the surface potential. The capability of modulating the interaction leads to a control of the surface mobility of the molecules, which assemble according to an ordered structure only in the case of potentials between −0.2 and +0.2 V *vs* SCE. This situation is intermediate between the case in which molecules are weakly bound to the surface and cannot be visualized by EC-STM due to their high mobility, and the case in which molecules are too strongly bound to the surface can be visualized by EC-STM, but do not assemble in an ordered structure. The role played by the different redox state of the adsorbed molecules at the different values of substrate potential is not clear.

Yoshimoto et al. [50] have studied the molecular assembly of a mixed layer of porphyrins (copper octaethylporphyrin: CuOEP) and phthalocyanine (cobalt phthalocyanine: CoPc) molecules on Au(111) as a function of the substrate potential and history. Both types of molecules lie flat on the surface, but different surface structures were observed by EC-STM by changing the substrate potential. Figure 5.9 shows two images obtained for the same mixture of CuOEP and CoPc at two different substrate potential values. The different electronic configurations of the two transition metals allow for a strong contrast between the molecules, and it is easily possible to discriminate between the species in an EC-STM image. From Fig. 5.9, it is evident that at 0.45 V *vs* RHE (Fig. 5.9(a)) domains constituted by bright spots in a squared lattice and domains of darker spots in a quasi-hexagonal structure are present. Brighter spots are associated to CoPc. At 0.65 V *vs* RHE (Fig. 5.9(b)), one-dimensional chains of darker spots are found

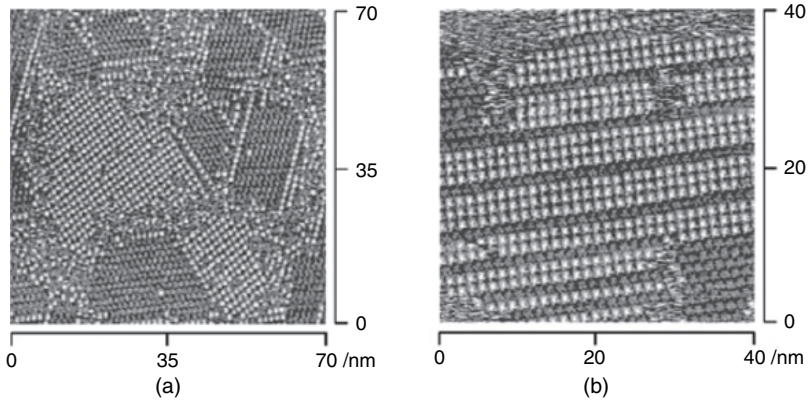

Figure 5.9: Two EC-STM images obtained on the same mixture of CuOEP and CoPc (see text) at different substrate potential: (a) 0.45 V *vs* RHE, (b) 0.65 V *vs* RHE. Reprinted from [50]. With permission of the American Chemical Society.

between the brighter rows of CoPc with square unit cell. These results show that the surface structure of mixed adsorbates and phase separation between them is controlled by surface potential, even if the mechanism by which this happens is not completely understood.

Dealing with molecules which are able to modify their orientation with respect to the substrate, Mayer et al. [51] have studied the structure adopted by 4,4′-bipyridine, a bifunctional molecule employed as a bridging ligand in coordination chemistry, on Au(111) surfaces as a function of the applied substrate potential. They have found that the molecules may exist in three different types of organization on the surface. Starting from a high surface coverage with densely packed molecular stacks, by decreasing the surface potential, a first-phase transition corresponds to a loss of parallel stacking rows and an orientational transition from perpendicular to a tilted position of the molecules. This phase implies a lower surface coverage. A third surface phase is found by further decreasing the surface potential. With these molecules, a pivotal role is played by intermolecular interactions (π-stacking), solvent molecules, hydrogen bonding and metal-ion-ligand coordination. Figure 5.10 shows two EC-STM images obtained in the high-surface coverage phase for different values of the bias voltage, obtaining a sort of molecular switch, being the contrast inverted in the two images.

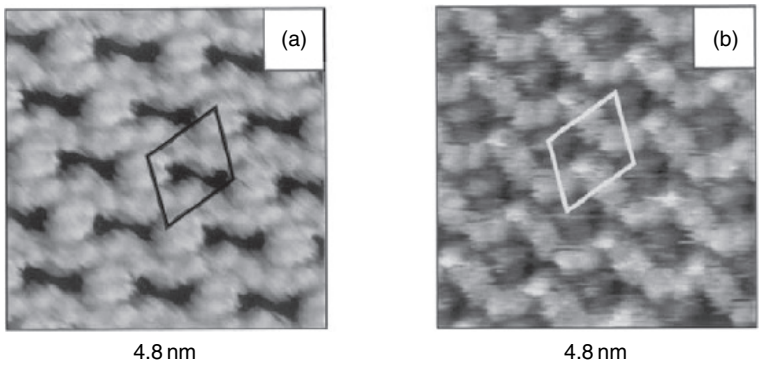

Figure 5.10: Two EC-STM images of the high-surface coverage phase of 4, 4′-bipyridine for two different applied biases: (a) −0.40 V, (b) −0.60 V. Reprinted from [51]. With permission of Elsevier.

It is clear from this behaviour that the electron transfer between the tip and the sample is mediated by the π system via through-bond tunnelling.

5.5. EC-STM on Redox Adsorbates: First Evidences

Electrochemical scanning tunnelling microscopy can also be exploited for its capability of probing electronic properties of molecules. This capability endows the microscope with spectroscopic abilities. However, to be able to extract molecular electronic information from EC-STM, the imaging mechanism of the microscope has to be understood, which is particularly appealing in the case of redox active adsorbates.

The first experimental study of electron tunnelling via a redox active molecule by EC-STM was performed by Tao [52]. In his pioneering work, Tao investigated a peculiar molecular system: Fe(III)-protoporphyrin (FePP) with respect to a protoporphyrin (PP) reference molecule adsorbed on a highly oriented pyrolytic graphite electrode. The difference between the sample and the reference lies in the presence of a Fe ion which is able to change its oxidation state reversibly from Fe(III) to Fe(II) as a function of the substrate potential value. The possibility of distinguishing between FePP and PP appears to depend, at a given constant bias voltage, upon the

value of the substrate potential. When the substrate potential was held close to the redox potential of FePP (−0.48 V *vs* SCE), the molecular species bearing Fe appeared brighter than the reference ones (Fig. 5.11).

Tao has outlined that the dependence of the imaging contrast on the substrate potential was due to the redox level made available by the Fe ion. The presence of this redox level assists, in a way which has to be inferred, the electron tunnelling between the tip and the substrate. This experiment has shown, for the first time, a new spectroscopic feature of the STM, confirming the possibility of exploring the density of states of a surface-adsorbed redox molecule, as proposed first by Schmickler [53]. Moreover, Tao has measured the apparent height increment of FePP *vs* PP as a function of substrate potential. The observed resonance-like trend reached its maximum at a substrate potential value very close to the redox potential of FePP, and was interpreted in terms of resonant tunnelling between the tip and the substrate, assisted by molecular levels. In a later work, Schmickler and Tao [54] have translated the apparent height changes in current changes assuming constant height imaging and a suitable value for the exponential tunnelling decay constant. They have also interpreted Tao's experimental work according to a resonant tunnelling phenomenon using Gerischer's terminology of density of oxidized states. According to this theory, electrons flow via the molecule without being trapped in it, and the maximum in the tunnelling current should occur when the density of oxidized states is centred between the tip and the substrate Fermi levels. The difference in energy between the centre of the density of oxidized states and the standard reduction potential of a redox species is given by the reorganization energy λ, which is, in turn, related to the extent of thermal fluctuations of the redox level and thus determines the width of the $i(V_s)$ curve, where V_s is the substrate potential.

The use of the resonant tunnelling model to explain this experiment had led to an inconsistency: λ obtained by the width of the $i(V_s)$ curve is 0.2 eV, which should lead to a maximum in the tunnelling current for a substrate potential equal to −0.73 V *vs* SCE instead of the experimentally obtained value of −0.42 V *vs* SCE. This discrepancy was attributed both to an uncertainty in the 'quasi reference' electrode potential and to the uncertainty in the decay constant which has to be considered to obtain a fitted value for λ. The reorganization energy for a redox species in these conditions is small as compared to that of the same species in solution, due to both solvent exclusion from the tip–substrate gap and the high electric field experienced by the molecules in this particular configuration. More recently, Schmickler and Kuznetsov have re-interpreted the results of this

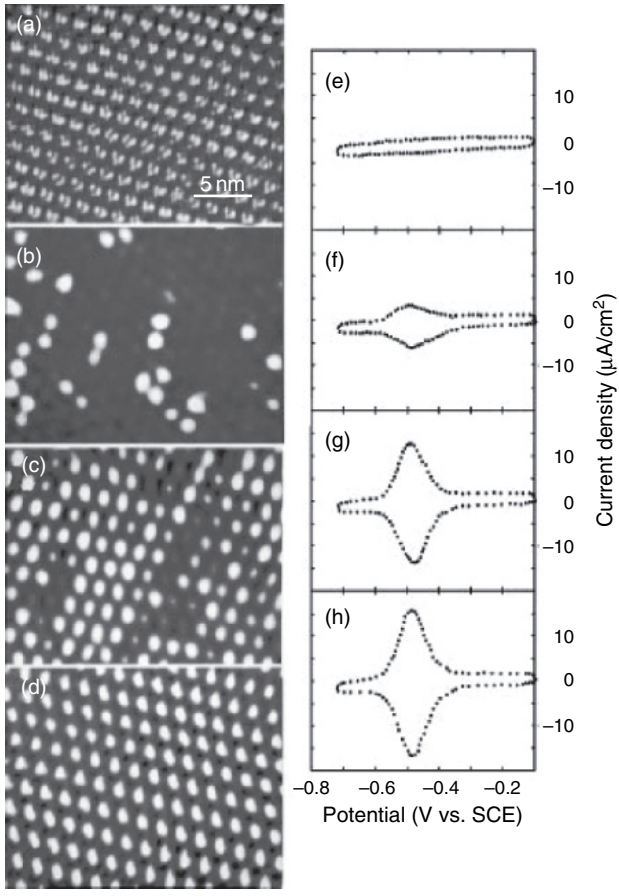

Figure 5.11: EC-STM images of FePP/PP adsorbed on a HOPG substrate from solutions containing FePP and PP at the ratio of 0:1 (a), 1:4 (b), 4:1 (c) and 1:0 (d). All the images were acquired at a substrate potential of −0.41 V *vs* SCE with a tunnelling current of 30 pA and a tip-substrate bias of −0.1 V. The percentage of brighter spots increases from (a) to (d) accordingly with the increase in the presence of FePP in the solution. From (e) to (h), the corresponding cyclic voltammograms of the adsorbed samples are reported. Clearly, the redox current increases with the presence of FePP. Reprinted from [52]. With permission of the American Physical Society.

experiment in the framework of stochastic adiabatic model, according to which the maximum in tunnelling current takes place at a substrate potential corresponding to the redox midpoint of the couple [55].

5.6. EC-STM on Biological Redox Adsorbates: Metalloproteins

FePP is the prosthetic group of many heme-based proteins such as cytochrome *c* and hemoglobin. One of the first applications of the EC-STM technique directly to a metalloprotein is that by Friis et al. [56], where the authors have investigated the behaviour of azurin chemisorbed on Au(111) under double potentiostatic control in aqueous solution. Azurin is a redox metalloprotein belonging to the family of blue copper proteins, whose functional task is to shuttle electrons between molecular partners along a free energy cascade involved in the oxidative phosphorilation of the bacterium *Pseudomonas aeruginosa* [57]. In situ STM images showed that azurin is able to form a submonolayer on gold which can sustain repeated scans of the STM tip. Moreover, a submolecular feature in the images, represented by a central brighter spot on each molecule, was attributed to electron tunnelling enhancement due to the presence of copper in the active site. Remarkably, even if the theories for sequential and coherent electron transfer between the tip and the substrate predict a contrast dependence on the substrate potential, no such effect was reported in the work. The authors have interpreted the lack of such a result as a consequence of competing tunnelling mechanisms and the reduced value for the reorganization energy in this particular configuration.

5.6.1. First Evidences of Potential Dependent EC-STM Contrast in Metalloproteins

The first evidence of potential-dependent EC-STM contrast in azurin was provided by an experiment in which azurin was chemisorbed on Au(111) substrates grown by thermal evaporation on a freshly cleaved mica sheet and studied by EC-STM and EC-SFM [58]. CV measurements were recorded on sub-monolayers of azurin to confirm that protein retained its redox activity once chemisorbed (Fig. 5.12).

The marked peak separation suggests a certain slowness in the ET process [9], likely due to redox-induced conformational changes or to an

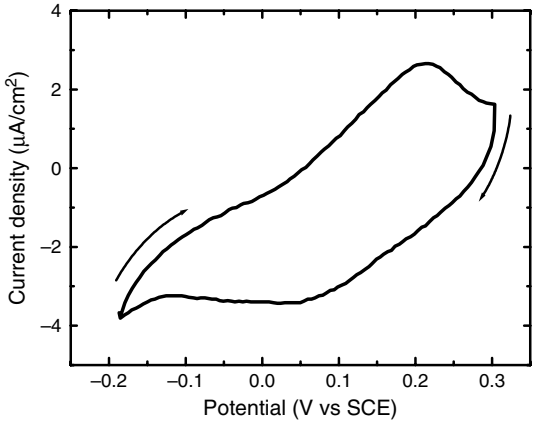

Figure 5.12: Cyclic Voltammogram of an azurin (sub)monolayer chemisorbed on a Au(111) electrode in NH_4Ac 50 mM, pH 4.6 at a sweeping rate of 5 mV s^{-1}. Redox midpoint +120 mV *vs* SCE, peak separation 160 mV. Reprinted from [57]. With permission of the Royal Society of Chemistry.

oxidation state-dependent mobility of the redox centre with respect to the working electrode. This could be due to electrostatic coupling between charged or polar groups of the proteins and the charged substrate. Nonetheless, the resulting redox potential (+120 mV *vs* SCE) matches well with that measured in diffusion experiments, confirming the retention of azurin native redox properties.

Afterwards, EC-STM imaging was performed showing a bumpy structure above the atomic terraces of the Au(111) film (Fig. 5.13). The imaged features, 3–4 nm in lateral size, could be ascribed to single azurin molecules chemisorbed on the gold surface. In order to provide a deeper insight into the mechanism ruling, the appearance of the aforementioned features and previously reported in the literature [56,59,60] when imaging azurin by in situ EC-STM, a parallel STM–SFM experiment under electrochemical control was carried out. Figure 5.14 shows a sequence of SFM (upper set) and STM (lower set) images acquired at −225, −125, −25 and +75 mV, i.e., on the negative side of the redox midpoint of azurin and in a potential range where the Au(111) surface structure is not affected by buffer ion adsorption [61].

While the SFM images showed spots corresponding to azurin adsorbates in the whole set of potential values, the STM data appeared completely

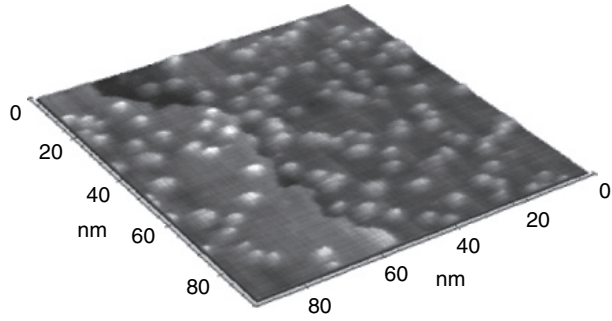

Figure 5.13: EC-STM image of azurin molecules adsorbed on a Au(111) substrate. The image has been obtained with a substrate potential value of −25 mV *vs* SCE, a tunnelling current setpoint of 2 nA with a bias voltage of 400 mV (tip positive). Scan area, $92.7 \times 92.7\,nm^2$. Vertical range, 1, 7 nm. Reprinted from [57]. With permission of the Royal Society of Chemistry.

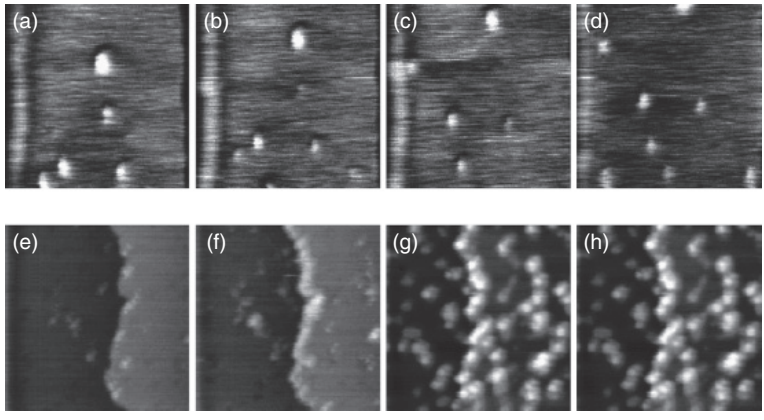

Figure 5.14: Upper set: EC-SFM images obtained in contact mode at different values of substrate potential with respect to SCE: −225 mV (a), −125 mV (b), −25 mV (c) and +75 mV (d). Scan area $200 \times 200\,nm^2$. Vertical range, 1 nm. Lower set: EC-STM images of the same sample recorded at the same substrate potential as for EC-SFM: −225 mV (e), −125 mV (f), −25 mV (g) and +75 mV (j). Imaging conditions: tunnelling current 2 nA, bias 400 mV tip positive. Scan area $70 \times 70\,nm^2$. Reprinted from [57]. With permission of the Royal Society of Chemistry.

different. In fact, the typical bright spots which were repeatedly imaged when tuning the substrate potential to the proper region appeared to be markedly potential-dependent, switching on only between −125 and −25 mV. Therefore, while the topographic SFM images were not affected by changes in the electrochemical potential of the substrate, STM images appeared to be unambiguously dependent on tuning its value with respect to that of the azurin redox midpoint. The limitations imposed by the particular experimental system did not allow to follow the sample behaviour at more positive substrate values.

Interestingly, it can be noted that as far as the potential remained in the aforementioned range, it was possible to step back and forth its value and switch on and off the visible spots, accordingly. Figure 5.15 reports such an example, in which the potential was stepped by 100 mV to a more negative value (from −25 to −125 mV) and then the original value was re-established. The molecular features, clearly visible in the first image (a), disappeared in the second (b) for reappearing only once the potential was re-established (c). It is also remarkable that in the image at −125 mV, some darker zones appeared in correspondence to the brighter spots in the other two images. These effective depressions could be interpreted as a consequence of the STM feedback response to the local variation in sample conductivity, suggesting that when the substrate potential is not tuned to the redox midpoint of azurin, the protein itself cannot elicit a current flow

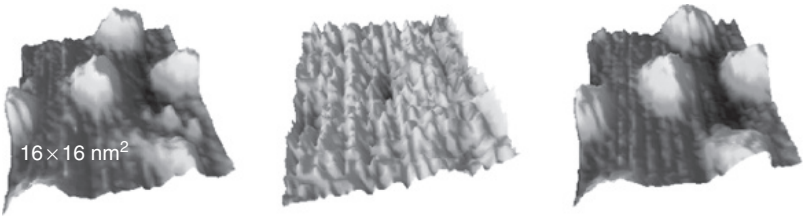

Figure 5.15: Sequence of consecutive EC-STM images obtained on the same sample area for three different values of the substrate potential with respect to SCE: −25 mV (a), −125 mV (b) and −25 mV (c). (Other imaging conditions: tunnelling current setpoint 2 nA, bias 400 mV tip positive). Azurin molecules are clearly visible only at −25 mV. Even if at −125 mV the molecules appear as darker spots, they again reappear if the substrate potential is brought back to −25 mV, highlighting that the molecules are not removed by the tip. Reprinted from [57]. With permission of the Royal Society of Chemistry.

through it; rather, it behaves as an insulating barrier. This evidence was also confirmed by the occurrence of a sort of blurring in Fig. 5.15(c), which was consistently due to the interaction of the tip apex with the protein globule when scanning the surface at de-tuning potentials.

5.6.2. Further Evidences

A further experiment [62] has confirmed the role of the particular metal ion at the redox-active site in determining the dependence of the contrast upon substrate potential. In this work, a reference sample represented by azurin molecules bearing a Zn ion instead of Cu in the active site was mixed with the usual Cu-azurin. Due to the fact that Zn is not electroactive in the potential range explored, the performed experiment represents a situation very similar to that of Tao's first experiment. A spectroscopic-like imaging at different substrate potential was performed on a mixture of Cu and Zn azurin molecules (Fig. 5.16).

When the substrate potential value was varied, some of the proteins changed their apparent height while others remained unchanged. Being the percentage of varying *vs* non-varying spots equal to that of the Cu *vs* Zn azurin molecules, the varying ones were attributed to Cu-azurin, also in light of previous investigations [58]. To further confirm that spots not varying their intensity were due to Zn counterparts, a control experiment with a sample consisting of only Zn azurin was carried out. This test has shown no dependence of the apparent height of the spots on the substrate potential, corroborating the aforementioned interpretation of the experiment with the mixed sample. Focussing just on a single contrast-varying spot, the behaviour of its apparent height with respect to non-varying ones highlights a resonance-like behaviour with a maximum at -0.21 V *vs* SCE. The location of the maximum in the tunnelling current *vs* substrate potential is considerably different from the redox halfway potential of azurin immobilized on gold ($+120$ mV *vs* SCE), in contradiction to Tao's experiment. The position of the current maximum, in principle, provides a criterion which helps to clarify the involved electron transfer mechanism. In fact, the different mechanisms proposed for the electron transfer between the tip and the substrate through the redox adsorbate lead to different equations for the position of the current maximum [57]. However, from the experimental data, the authors were unable to assess the exact mechanism for the electron transfer. The uncertainty was mainly ascribed to the unknown value of the azurin reorganization energy in their experimental configuration. A

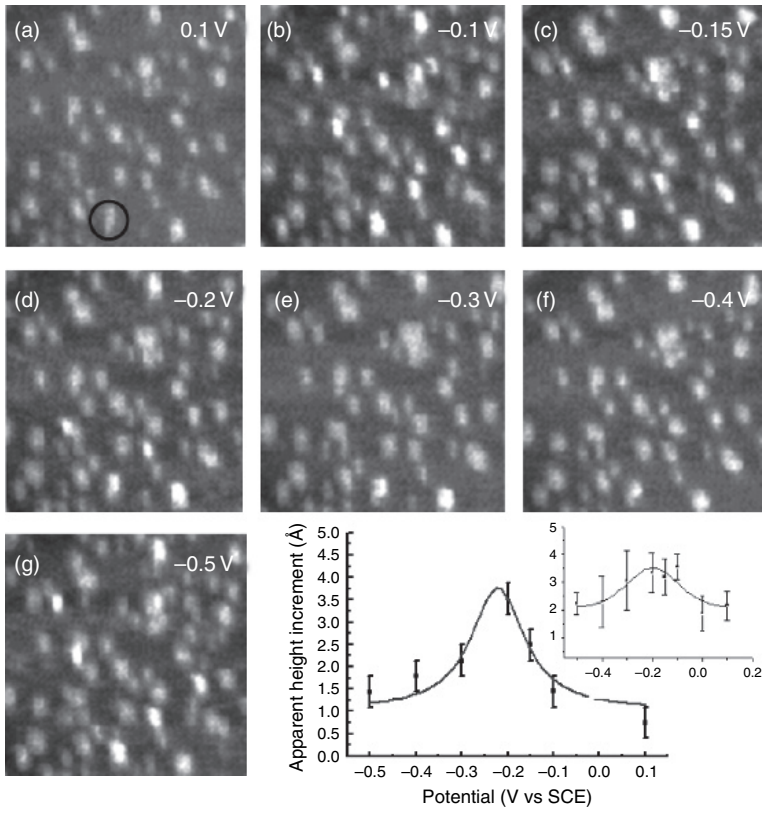

Figure 5.16: (a)–(g) EC-STM spectroscopy-like-imaging of a mixture of Cu- and Zn-azurin molecules adsorbed on a Au(111) substrate. The value of the substrate potential with respect to SCE is reported in each image. Some molecules do not change their apparent height upon substrate potential, whereas others do. In (h) the apparent height increment of a spot (in the black circle in (a)) with respect to the non-varying ones is reported. The inset to (h) reports the apparent height increment averaged over six molecules. (Other imaging conditions: tunnelling current setpoint 1 nA, bias 400 mV tip positive, scan range $130 \times 130\,nm^2$). Reprinted from [57]. With permission of the Royal Society of Chemistry.

theoretical investigation aimed at evaluating the reorganization energy of azurin in the particular configuration of an EC-STM experiment reported a value which makes a two-step electron transfer mechanism more plausible than resonant tunnelling [63].

5.6.3. A Novel Setup for Direct Access to Current

In order to achieve a direct access to tunnelling current, thus enabling an effective comparison between experimental results and theoretical estimates, a different experimental configuration was needed, always referring to EC-STM-based setup.

In a further experiment [64], a modified configuration with azurin molecules chemisorbed on an EC-STM gold tip facing a Au(111) substrate (Fig. 5.17(a)) was adopted. The gold tip, bearing azurin molecules on its surface, was brought within tunnelling distance from the gold substrate and stabilized at a set-point current of 100 pA. Afterwards, the feedback was switched off in order to measure the current as a function of the tip potential at constant bias voltage and distance from the substrate. This configuration allowed the authors to investigate directly the dependence of tunnelling current on tip potential for different values of the bias voltage. Moreover, given the exponential dependence of the tunnelling current on distance, it is conceivable that the current flows just through the single, most protruding

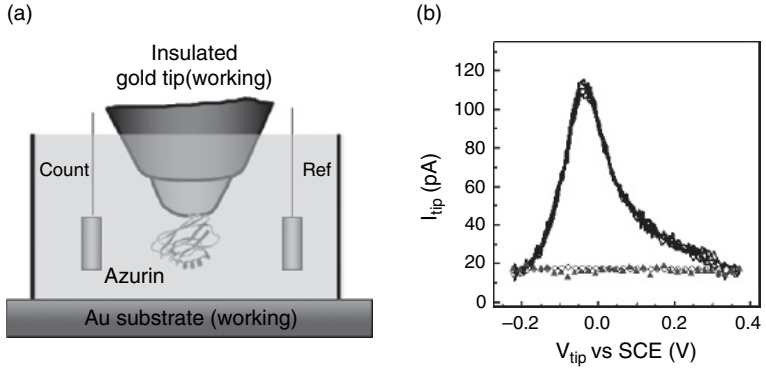

Figure 5.17: (a) Schematic representation of the setup in which azurin molecules are chemisorbed on an EC-STM gold tip facing a Au(111) substrate. Electrically biased tip and substrate are fed by a bipotentiostat that controls their potential in an electrochemical cell with respect to the reference electrode. The fourth electrode in the cell is the counter electrode. (b) Black lines: six repeated tip potential sweeps (initial conditions: $V_{bias} = +100$ mV, tunnelling current = 15 pA, tip potential = −225 mV *vs* SCE) showing current peaks compared to the behaviour of a bare insulated gold tip (hollow circles) and to that of a Zn azurin-coated tip (triangles). Reprinted from [57]. With permission of the Royal Society of Chemistry.

molecule, being the contribution of molecules positioned away from the tip apex negligible. The behaviour of the tunnelling current via the azurin as a function of tip potential showed a marked current maximum (Fig. 5.17(b)) due to temporary population of azurin redox states aligned with the Fermi levels of the gold electrodes. It is to be stressed that the measured current maximum was reproducible and reversible, assuring that the phenomenon was not related to irreversible structural modifications of the molecule. The experimental setup allowed to study the dependence of the observed behaviour on the bias voltage, simply repeating the measurement for different bias voltages. This investigation showed that the current maximum and the width of the curve increased with bias, while the position of the maximum shifted to positive tip potential values. The behaviour of the tunnelling current in this experiment gave insight into some theoretical aspects of the electron transfer mechanism. In particular, the experimental $I/(V_{\text{tip}})$ results are nicely fitted by the sequential two-step curve (see Fig. 5.18).

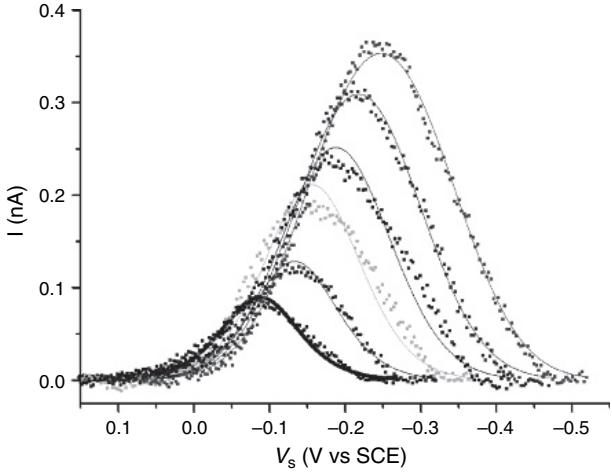

Figure 5.18: Current intensity as a function of tip potential for azurin in the EC-STM setup [64]. Dots: experimental data; Lines: fitting to the sequential two-step model. The different curves refer to different V_{bias} (from 50 to 300 mV via 50 mV steps). For each curve, a different $\varepsilon_0{}^{\text{loc}}$ and a different electronic coupling matrix element has been used in the fit, while reorganization energy is the same for all the curves ($\lambda = 0.13$ eV). The electronic couplings (taken equal for tip and substrate) range in the interval $\pm 15\%$ around their mean value. Reprinted from [57]. With permission of the Royal Society of Chemistry.

The resulting ε_0^{loc} (abscissa of the maximum of the curves in Fig. 5.18) is linearly dependent on V_{bias}, as expected. However, the results of the fitting leave some doubts on the transport mechanism: first, the fitted value of λ is quite small (0.13 eV) and second, the range of values of ε_0^{loc} (60–100 meV *vs* SCE) is relatively far from the known redox midpoint for azurin; even if one extrapolates ε_0^{loc} to $V_{bias} = 0$, it remains ~0.15 eV more positive than what expected. Regarding λ we remark that the fit is not very sensitive on its value (larger values give fit of reasonable quality). As for ε_0^{loc}, one possibility is that the local environment modifies the protein redox midpoint via other effects (e.g., conformational changes due to protein squeezing, electrostatic effects of the applied voltages). Another plausible explanation is that the two-step vibrationally coherent mechanism is working. In fact, the position of the current maximum appears, in this model, at $\varepsilon_0^{loc} + \lambda$ which would be consistent with the data assuming λ to be about 0.2 eV (again a quite small value). A pure resonant tunnelling mechanism is unlikely, if one considers that the mean residence time of the electrons on the protein (estimated from the values of the tunnelling current) is about 10 ns, which is much larger than typical water longitudinal relaxation times (tens of ps). It is to be stressed that no loss of functionality has been observed up to an applied bias voltage of 350 mV. However, this value should not be considered as the true voltage bias felt by the protein, because in EC-STM setup much of the voltage drop occurs very close to the polarizable electrodes. After the first demonstration of the possibility of controlling the tunnelling current through a metalloprotein by means of electrochemical potential in solution, configuring a wet biomolecular transistor, another work by Chi et al [65] has reported a similar behaviour, characterized by a resonance-like curve of the tunnelling current as a function of substrate potential. In this case, azurin was immobilized exploiting its hydrophobic patch located around the copper site on a gold substrate functionalized with a self-assembled monolayer of methyl-terminated alkanethiols. The resonance-like behaviour was, in this case, interpreted in terms of a two-step electron transfer process in the limit of weak electronic coupling between the redox centre and the electrodes. Remarkably, the value of the reorganization energy of azurin obtained as a fit to the experimental curve of the tunnelling current is in the range 0.35–0.45 eV and is consistent with the theoretical prediction of 0.43 eV performed by Corni [63].

It is worthwhile to note that, depending on the particular experimental conditions, a different type of response is observed for the tunnelling current-substrate potential dependence. In fact, in the first work of Facci

et al. [58], a sigmoidal behaviour of the tunnelling current has been reported, with an increase followed by a saturation level. In the subsequent experiment [62], a resonance-like behaviour was reported in which the tunnelling current decreased after reaching a maximum. In light of the sequential two-step electron transfer process, the different behaviour can be rationalized. In fact, the relative values of the bias voltage and reorganization energy for the azurin molecule in the EC-STM configuration determine which is the relationship between tunnelling current and substrate or tip potential. When the bias voltage is small with respect to the reorganization energy, the two-step electron transfer mechanism predicts a resonance-like behaviour. When the azurin redox level is brought near the Fermi level of one of the two electrodes (depending on the polarity of the bias), an electron flows from the metal to the vacant redox level of the molecule. The molecule relaxes to its reduced configuration, and, after a second thermally activated transition, the electron is passed to the second electrode. When the bias voltage becomes higher than the reorganization energy, once the redox level of the molecule is near the Fermi level of one electrode, the first electron transfer takes place. However, at this point, the energy of the molecular redox level is still within the Fermi level of the second electrode, and the molecule transmits electrons without the need of a second thermally activated transition. This means that, upon further variation of the substrate or tip potential, the current intensity does not change, reaching a plateau. However, if the overpotential continues to increase, a situation in which the reduced level begins to lie below the Fermi level of the second electrode will be reached and the current will decrease. Different experimental conditions may shift the conditions between one of the two situations. In the first experimental investigation [58], a setpoint current of 2 nA was used along with a bias voltage of 400 mV, at variance with a setpoint current of 1 nA that was used in the second one [64]. A higher setpoint current requires a lower tip–surface distance. Decreasing the tip–substrate distance can lower the reorganization energy for the azurin molecule [63], thus leading to the situation where a plateau, rather than a peak, is obtained. In addition, when the tip–surface distance is lowered, the electrostatic coupling of the molecular redox level to the electrodes increases, and the effective overpotential decreases accordingly. This means that a larger overpotential must be applied to reach the point where the current starts decreasing, leading to a more extended plateau (Fig. 5.19). In light of these considerations, the different observed behaviours in the two experiments can be understood. It is worthwhile to note that in a recent paper, Wandlowski et al. [66] have shown that a redox active molecule (a viologen derivative) can follow

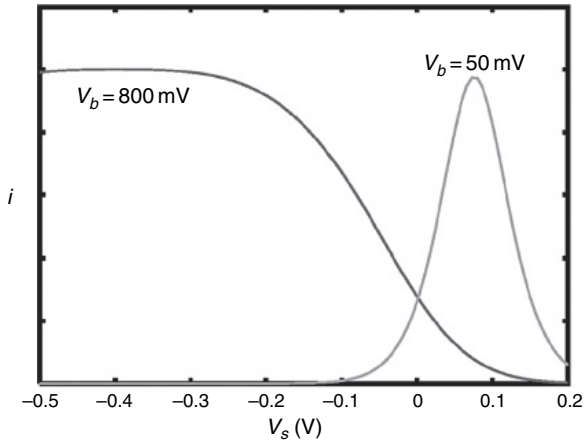

Figure 5.19: Current intensity i as a function of the substrate potential V_s for different choice of V_b (sequential two-step model). Parameters of the calculations: $\lambda = 200$ meV, $T_s\rho_s = T_t\rho_t$, $E_0 = 100$ mV. Currents have been scaled to give the same maximum value. Reprinted from [57]. With permission of the Royal Society of Chemistry.

both a resonance-like behaviour and a sigmoidal trend upon increasing the coupling of the molecule to one electrode.

Recently, in the case of small redox molecules, it has been possible to analyze the ET mechanism in the EC-STM setup in a more quantitative manner [67]. Albrecht et al. measured for the conductance of a single pyridyl-based Os complex a feature of 9 nS for 100-mV bias. The occurrence of a maximum in the tunnelling current close to the redox potential of the redox active species is explained by assuming that the electron transfer mechanism occurs via a two-step electron hopping with full vibrational relaxation in between (V_{bias} smaller than the reorganizational energy). The behaviour of single molecules observed in the EC-STM configuration was compared to the behaviour of a monolayer obtained by electrochemical methods confirming again that the transfer mechanism is a two-step electron tunnelling. A quantitation of the maximum tunnelling current obtained allowed to establish that the current for a single molecule is 0.32 nA. In the limit of strong electronic coupling between the redox molecules and the electrodes, the number of electrons exchanged in a single nuclear relaxation time is $>> 1$. By measuring the tunnelling current per molecule for different values of the current setpoint (which establishes the distance between

the tip and the molecule, decreasing with an increase in the setpoint), it was possible to establish the maximum current per molecule (for a bias of 0.1 V) and, assuming a rate constant for the molecule/substrate interaction similar to that determined by electrochemical measurements, a figure for the number of electrons exchanged in the range between 60 and 600 was obtained. Even if the procedure used by Albrecht et al. for determining the number of electrons exchanged and the electronic transmission coefficient can be considered as a crude approximation for several aspects, it represents the first attempt to compare the theories of electron transfer in the EC-STM setup with experiments in a quantitative manner.

The electron transfer properties of biological molecules can be probed also by conductive atomic force microscopy (C-AFM). This technique has been extensively applied to the study of the conduction properties of single alkanethiols and other organic molecules with impressive results [68–70]; it has also helped elucidating the role of contacts to the electrodes in the quantitative measurements of the current. Even if currently available experimental techniques prevent these experiments from being performed in an aqueous environment, useful information can be obtained on the electron transport properties of metalloproteins in spite of the lack of control on the molecule's oxidation state. Using a conductive AFM [71,72], Davis et al. have measured the dependence on the applied force of the tunnelling barrier on an azurin molecule immobilized on a gold electrode. Under low force conditions ($<$2–3 nN), azurin molecules are highly insulating due to the lack of a reliable electrical contact to the protein by the AFM tip. By increasing the applied force ($>$3 nN), the current through azurin increases with bias, showing a linear relationship for low-bias regime, while the overall current–voltage behaviour is well described by a Simmons tunnelling model where the protein resembles a featureless continuum tunnelling barrier. Upon further increase of the applied force (5–50 nN), the current is enhanced till a breakdown takes place, pointing out a direct contact between the tip and the sample. However, these experiments usually reveal a lack of measurement reversibility. After a cycle in which the force is increased to the breakdown limit, the electron transport does not go back to the initial value upon force releasing. Interestingly, the variation of the transported current upon the applied force can be deconvoluted into a contribution from the variation of the barrier height and the variation of the tunnelling distance. More relevant to the presence of an active redox site and to the redox properties accessibility is the case in which a negative differential resistance (NDR) is observed by C-AFM for low applied force and high bias ($\pm$3–4 V) [73]. This behaviour is related to the presence of

the copper ions as evidenced by a control experiment with Zn-substituted azurin molecules for which no such phenomenon was observed. However, a clear correlation between the potentials at which NDR happens and the potentials typically encountered in electrochemical investigations of azurin has not been established and the phenomenon is still poorly understood.

5.7. Video Rate EC-STM

In the study of surface reactions at an electrified interface, many phenomena occur on a time scale which is too fast to be followed by conventional STMs. This is true, for example, for surface reconstruction phenomena or for dissolution/deposition reactions. The coupling of high spatial and time resolution in EC-STM is of great interest for the investigation of many electrochemical surface events. Magnussen et al. [74] have developed a high-speed EC-STM which is capable of 25 frames per seconds. They have used this microscope to study the mechanism of Cu(100) surface dissolution in diluted HCl solution and have demonstrated that the metal dissolution proceeds via removal of atoms at atomic kinks on the crystal surface. The local kink structure and the dynamics of the dissolution mechanism have been studied with the high spatial and time resolution afforded by their microscope. The dissolution rate can be controlled by the surface potential, and it takes place when the surface is covered by an ordered Cl adlayer with a $c(2 \times 2)$ structure, which induces a faceting of the Cu steps and stable and straight steps along the {001} direction. On this surface, the STM images show the corresponding Cl adlayer rather than Cu atoms. When the potential is higher than -0.25 V *vs* SCE, Cu dissolution as $CuCl_2^-$ and redeposition start. The process proceeds both in a row-by-row fashion and in a way involving collective $(\sqrt{2} \times \sqrt{2})$R45° rows wide segments of terraces. Figure 5.20 shows a sequence of high-speed EC-STM images in which the collective growth and dissolution are clearly visible.

In another work, Magnussen et al. [75] have studied the Cu(100) dissolution/deposition in Cu-containing solution under equilibrium conditions showing fluctuations at the Nernst potential.

High-speed EC-STM has been exploited also to investigate adsorbate diffusion at metal–electrolyte interface [76], for which it is known that the diffusion behaviour depends on the liquid phase and the surface potential. Surface 'tracer diffusion' (corresponding to the case in which adsorbate/adsorbate interactions can be ignored) of adsorbed sulfide on Cu(100)

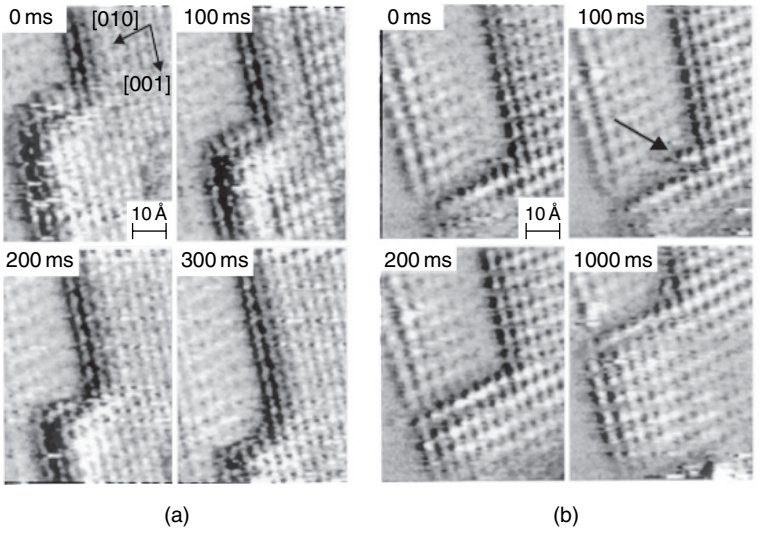

Figure 5.20: Two series of high-speed EC-STM images of a Cu(100) surface in diluted HCl solution at −0.23 V *vs* SCE showing the collective dissolution (a) and the collective growth of a several $(\sqrt{2} \times \sqrt{2})$R45° rows wide segment of a terrace (b). Reprinted from [74]. With permission of Elsevier.

has been studied in HCl solution. For this system, the Cu(100) is covered by an ordered chloride adlayer for a large potential range, and the adsorbate diffusion is sufficiently low due to the strong interaction with the surface. EC-STM images allowed to establish that the surface diffusion phenomenon is a thermally activated hopping between neighbouring adsorption sites with an activation energy dependent on the surface potential. In particular, it has been found that the diffusion barrier increases linearly with the surface potential probably due to a change in the adsorbate dipole moment and the contributions from coadsorbates.

5.8. Possible Future Trends and Developments

The future of SPM with full electrochemical control relies on the development of suitable nanotech-based probes for implementing the electrochemically controlled current sensing AFM: EC-AFM. This device would gather the advantages of both EC-STM and those of current sensing AFM. In particular, it would be able to measure electronic features out of a single

molecular adsorbates (as EC-STM can do), allowing a fine control of the force (pressure) applied by the probe to the molecule, as can be achieved by AFM. Such kind of instrument would enable molecular investigation of electron transfer properties without the unknown aspect related to the structure of the probe-molecule interaction region in terms of reorganization energy as well as preservation of molecular conformation.

To achieve such an implementation, however, several crucial steps have to be overcome, namely:

- Fabrication of insulated conductive AFM probes, i.e., probes which have a conductive apex and leads but which are largely insulated as the aforementioned STM counterparts.
- Implementation of a bipotentiostat setup similar to that used in EC-STM experiments.

In scanning probe microscopies, the demand for studying not only topography but also other local properties of surfaces has prompted the development of different techniques, able to probe a rich set of different interactions between tip and sample [77]. Critical items to the development of these new applications is the design of specific probes, having improved spatial resolution, sensing the desired sample properties and operating in different environments. In this respect, focused ion beam (FIB) has proven to be a powerful tool. Its capability of removing and adding material with sub-micrometre resolution, by ion milling and beam-induced deposition, respectively, has allowed probe tailoring in many SPM fields [78–81].

Several SFM applications exist taking advantage of conductive probes, for instance electric force microscopy (EFM) [82], which probes the electric force between a conductive cantilever tip and the sample, Kelvin probe force microscope (KPFM) [83], which maps the local surface potential, and current sensing AFM (cAFM) in air, controlled atmosphere, and possibly in liquid. Usually, EFM, KPFM and cAFM cantilevers have a uniform metal coating on the tip side. With this configuration, not only the interaction between the whole tip and the sample plays a role in forming the image contrast but also the cantilever–sample interaction [84,85]. The latter interaction is a limiting factor for resolution, especially when working at large (tenths of nanometers) tip–sample distances [86]. In fact, it is well known that capacitive forces can affect EFM cantilever deflection [87] when operating in the static mode. Reducing the capacitive force on the cantilever could also find useful application in other SPM implementations requiring a conductive tip, such as local oxidation nanolithography [88].

A crucial step for improving conductive cantilever performance for any of the above mentioned applications is to develop a procedure for obtaining probes with a sensing area limited at the very tip and a reduced cantilever contribution to the contrast. This task can be accomplished by means of FIB milling and FIB metal deposition steps, integrating a nanoelectrode at the tip apex and drawing the electrical connection to the cantilever backside through the inner of the tip [89].

5.9. Fabrication of EFM Probes

To obtain EFM probes with conductive area limited at the tip apex, Facci et al. have developed a FIB-based nanomachining technique on conventional AFM cantilevers. The FIB apparatus is incorporated in a FEI 235M Dual Beam workstation, combining a Ga^+ FIB and a thermal field emission SEM working at coincidence on the sample. The system is equipped with a gas injector system, supplying $(CH_3C_5H_4)(CH_3)_3Pt$ (methylcyclopentadienyl-trimethyl-platinum) metallorganic molecules for beam-assisted (either electrons or ions) Pt deposition. All milling and deposition steps were performed with an ion beam energy of 30 keV and with the sample normal to the beam. Silicon nitride cantilevers, V-shape type, were coated on both sides with a 5-nm chromium layer and 20-nm gold layer in a thermal metal evaporation system, to prevent charging during the FIB machining. A sketch of the probe design and the different steps of the probe processing are shown in Fig. 5.21. The overall process was divided in back-side (Fig. 5.21(b–d)) and front-side (Fig. 5.21(e,f)) processing, where frontside means that the tip is facing the ion beam. By using a 10-pA beam current, the pyramidal tip was milled through at the apex to enable an electrical connection between back- and frontside of the cantilever. As shown in Fig. 5.21(b), a circular aperture with a diameter of 170 nm was obtained. Then, with the same beam current and a $(0.3 \times 0.3)\ \mu m^2$ rastering pattern, a Pt pillar was deposited onto the aperture to fill in the hole. Afterwards, a Pt connection was brought from the bottom of pyramid up to the surface of cantilever along an inner edge to ensure the electrical connection (Fig. 5.21(c)). To reduce the capacitive force component, the metal layer coating the cantilever backside was removed by FIB milling, leaving only a narrow conductive line between the tip and the cantilever chip, as shown in Fig. 5.21(d). For front-side processing, the chip was mounted with the pyramidal tip facing the beam. As the first step, a (0.2×0.2)-μm^2 trench was milled at the tip apex until the backside deposited material was reached.

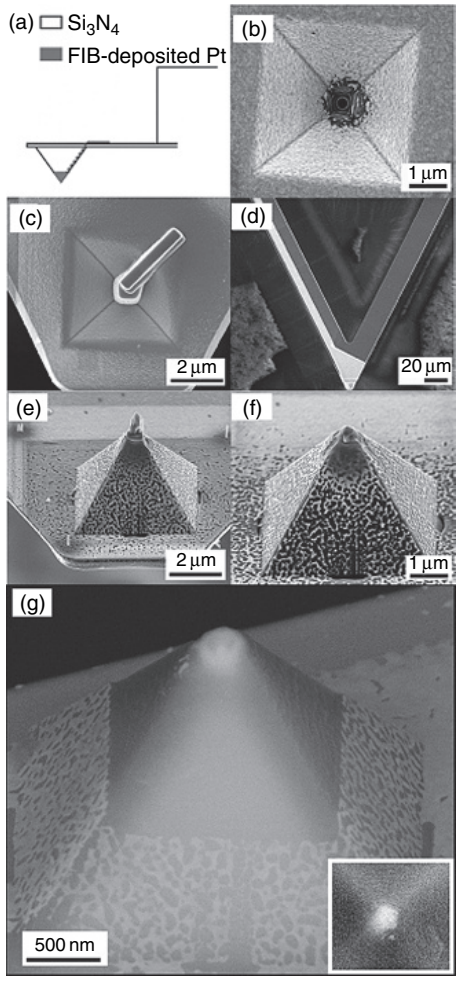

Figure 5.21: (a) Sketch of the modified AFM tip. (b), (c) and (d) are normal-view SEM images of backside processing, (e) and (f) are tilted-view images of front-side processing. (b) Aperture milled at the centre of the tip; (c) Pt depositions over the hole and along an inner edge of the reversed pyramid; (d) conductive line between the tip region and the chip left after gold removal; (e) deposition of the Pt nanoelectrode at the tip apex; (f) final tip shape after remodelling the deposited material by FIB cutting; (g) back-scattered electron image of the tip (tilted view) which shows the presence of platinum confined to the very apex of the tip. Inset: top view of the same tip (scale bar: 200 nm). Reprinted from [89]. With permission of Elsevier.

Then, a nanoelectrode was deposited by rastering a 10-pA beam within the trench, over a (0.1×0.1)-μm^2 area, obtaining the protruding pillar shown in Fig. 5.21(e). Deposition into the trench ensured a firm mechanical basis and a good electrical contact for the metal electrode. The following step was a tip-shaping procedure. The deposited material was machined such that the pyramid tip was restored to its original shape. To this end, the FIB was aligned along each of the four walls of the pyramid, and a line milling pattern was superimposed onto each side of the square basis, at the middle, in order to intersect the deposited pillar and to cut away the material above the line. The result (Fig. 5.21(f)) is a shape very similar to the original one, before processing. Finally, the topmost region of the tip was cleaned of the gold layer around the apex to cut any electrical connection between the electrode and the cantilever. Figure 5.21(g) shows a top view back-scattered electrons image of the same tip.

5.10. Conductive Probe Performance Test

The probes nanofabricated so far can be used for various SPM techniques among those requiring a conductive tip. The first task, therefore, was that of testing their performances as conductive probes per se.

Scanning probe microscopy measurements were performed using a Pico SPM (Molecular Imaging), as far as cAFM was concerned (0.1 nA V^{-1} preamp. Module) and a Bioscope Nanoscope IIIa (Veeco Instruments) for EFM measurements and force volume imaging. Silicon nitride cantilevers with a spring constant of 0.06 N m^{-1} (Veeco Instruments) were used as the starting point for FIB nanomachining.

To try out the improved performances of the FIB-modified cantilevers and tips over uniformly coated probes for electric force measurements, a test sample was prepared. A glass substrate was coated with 5-nm chromium layer and 100-nm gold layer by thermal evaporation. After coating, the sample was processed with FIB in order to obtain conductive lines on an insulating substrate. Line structures were 15 μm wide with 30 μm periodicity.

The tip was characterized by different techniques. Using C-AFM, *I-V* curves recorded on an evaporated gold film have confirmed the presence of the electrical connections between the apex of the tip and the cantilever chip. The curves were reproducible even after several contact mode scanning of the tip on the sample surface, confirming the mechanical stability of the deposited Pt at the tip apex. In Fig. 5.22, C-AFM image of a

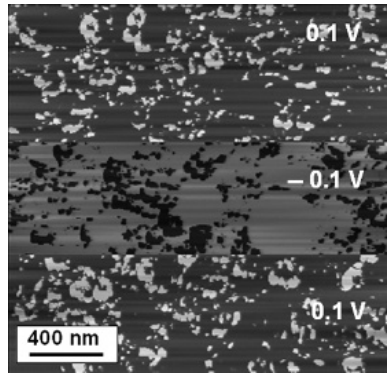

Figure 5.22: Current contrast image on a polycrystalline gold sample with 0.1 and −0.1 V bias applied. Reprinted from [89]. With permission of Elsevier.

polycrystalline gold film is shown. The current contrast is due to the shape of gold grains causing a variation of the tip–sample contact area and, consequently, a variation in contact resistance. The image contrast, as expected, reverses upon voltage bias reversal.

To show the reduced capacitive force between the modified probe and a conductive sample, the electric force above a biased gold-coated substrate was compared, at the same distance, to that of the electric force probed by a uniformly coated probe. In Fig. 5.23, the cantilever deflection, measured with respect to the zero-bias force curve, is reported for the modified probe (squares) and for a uniformly coated one (triangles) as a function of the applied bias voltage at the same distance of 15 nm above the sample surface. The data have been fitted with a parabola as expected for a bias-dependent capacitive force. The spring constant of the two cantilevers used has been measured using the thermal method [90] and has been found to be the same ($k = 0.09\,\mathrm{N\ m^{-1}}$) within experimental errors. Due to the equal spring constant, the difference in the deflection can be translated into a difference in the probed force. It is clear that the capacitive force in the case of the FIB-machined cantilever is greatly reduced due to the fact that only the tip apex is sensitive to electric forces and the capacitive force on the cantilever is strongly decreased.

To show the improvement in EFM performances, gained with the FIB-modified probe, we mapped the electric forces on the FIB-patterned sample. Bias voltage (3 V) was applied between the conductive lines and the cantilever, and the electric force was mapped by the force volume (FV)

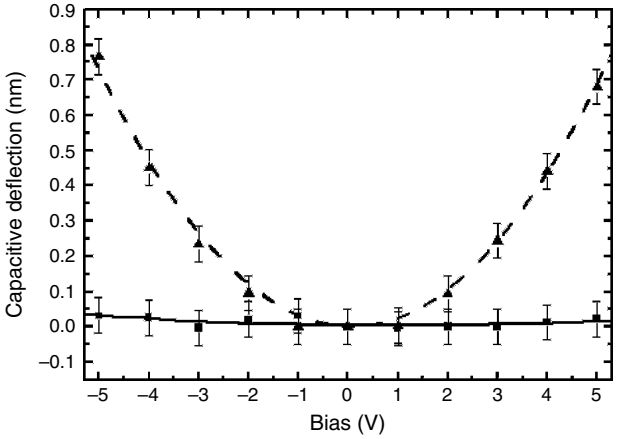

Figure 5.23: Capacitive-induced deflection for a uniformly coated tip (triangles) and a FIB-machined tip (squares) as a function of the applied bias voltage. The capacitive deflection reported is the difference with respect to the zero-bias deflection of the cantilever at a constant distance of 15 nm above the sample surface. Reprinted from [89]. With permission of Elsevier.

technique [91]. In a force volume image, a two-dimensional matrix of force curves is acquired. Each force curve can be assigned to a defined pixel of a topographic image acquired at the same time as a result of the z-position at which a predefined force setpoint is reached. Recording all the force curves, it is possible to recover a map of the cantilever deflection at a specific constant distance from the point of maximum applied force, which, in the case of a rigid sample, means a constant distance from the sample surface. The measurement setup is reported in Fig. 5.24(a). In Fig. 5.24(b), the topographic AFM image of the structure is shown. The FV images at a distance of 15 nm from the point of maximum force and with a bias voltage of 3 V are reported in Fig. 5.24(c,d) with the same deflection scale for the uniformly coated and FIB-machined cantilevers, respectively. Each FV image is displayed along with its averaged cross section, centred around the mean value. It is quite evident that, in the case of uniformly coated probes, the border between electrically biased regions and insulating regions are rounded, whereas, in the case of the FIB-modified tips, the borders are sharper and the contrast between conductive and non-conductive areas is higher.

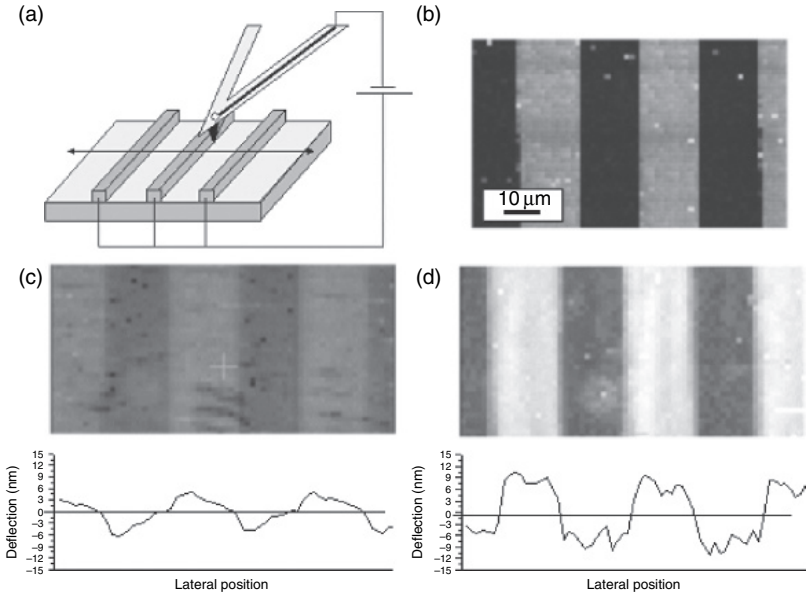

Figure 5.24: (a) Scheme of the test structure used to characterize the FIB-modified tip in EFM; (b) topographic AFM image of the test structure; (c) force volume image relative to a distance of 15 nm from the point of maximum force (approach portion of the force curve considered) and 3 V bias voltage for a uniformly coated cantilever. In the bottom, the averaged cross section of the force volume image is reported. (The ordinate reports the deflection in nm of the cantilever centred around its mean value); (d) same as (c) for the FIB-modified cantilever. Reprinted from [89]. With permission of Elsevier.

So far, SPM cantilevers with tiny conductive pathways through the probe and along the back of the cantilever arms have been implemented by FIB nanofabrication. These probes show improved performances over completely metallized ones in terms of reduced capacitive coupling as well as improved imaging contrast. However, they are not yet suitable for EC-SFM applications, since they require to be insulated in order to minimize leakage currents in liquid cells. This task is partially accomplished by the particular design chosen for the conductive pathway (running through the tip pyramid) but requires the back lead to be insulated from the contact with the liquid. Technological efforts are still underway against this problem since insulation, performed with a solid-state or organic flexible coating, have to preserve mechanical properties of the cantilever. Among the most

promising approaches, that are however both underway, we can recall the use of a electropolymerizable organic varnish which can be deposited just on the conductive leads of the cantilever exposed to the solution and insulation with inorganic oxides deposited by chemical vapour deposition [92]. Both the approaches show advantages and disadvantages. The first one coats only the conductive pathway and, therefore, can in principle preserve the mechanical characteristics of the cantilevers more effectively; it is, however, more difficult to optimize and standardize its features at the technological level. The second one is a well-established approach, but it tends in general to cause alteration in the mechanical and geometrical properties of the cantilever and so far has not given acceptable results.

References

[1] Binnig, G., Rohrer, H., Gerber, C. et al. (1982) *Phys. Rev. Lett*., **49**, 57.
[2] Gimzewski, J.K. and Joachim, C. (1999) *Science*, **283**, 1683.
[3] Binnig, G., Quate, C.F. and Gerber, C. (1986) *Phys. Rev. Lett*., **56**, 930.
[4] Kolb, D.M. and Simeone, F.C. (2005) *Curr. Opin. Solid State Mater. Sci*., **9**, 91.
[5] Schneir, J., Sonnenfeld, R., Hansma, P.K. et al. (1986) *Phys. Rev. B*, **34**, 4979.
[6] Sonnenfeld, R. and Schardt, B.C. (1986) *Appl. Phys. Lett*., **49**, 1172.
[7] Itaya, K. and Tomita, E. (1988) *Surf. Sci. Lett*., **201**, L507.
[8] Lustenberger, P., Rohrer, H., R. Christoph et al. (1988) *J. Electroanl. Chem*., **243**, 225.
[9] Bard, A.J. and Faulkner, L.R. (2001) *Electrochemical Methods. Fundamentals and Applications*. Second edition. New York: Wiley.
[10] Cristoph, R., Siegenthaler, H., Rohrer, H. et al. (1989) *Electrochim. Acta*, **34**, 1011.
[11] Uosaki, K. and Kita, H. (1988) *J. Electroanal. Chem*., **259**, 301.
[12] Höpfner, M., Obretenov, W., Jüttner, K. et al. (1991) *Surf. Sci*., **248**, 225.
[13] Ibe, J.P., Bey, P.P., Brandow, S.L. et al. (1990) *J. Vac. Sci. Technol. A*, **8**, 3570.
[14] Nagahara, L.A., Thundat, T. and Lindsay, S.M. (1989) *Rev. Sci. Instrum*., **60**, 3128.
[15] Libioulle, L., Houbion, Y. and Gilles, J.-M. (1995) *Rev. Sci. Instrum*., **66**, 97.
[16] Sonnenfeld, R. and Hansma, P.K. (1986) *Science*, **232**, 211.
[17] Gewirth, A.A., Craston, D.H. and Bard, A.J. (1989) *J. Electroanal. Chem*., **261**, 477.
[18] Wiechers, J., Twomey, T., Kolb, D.M. et al. (1988) *J. Electroanal. Chem*., **248**, 451.
[19] Bach, C.E., Nichols, R.J., Beckmann, W. et al. (2005) *Nature*, **437**, 671.

[20] Slevin, C.J., Gray, N.J., Macpherson, J.V. et al. (1999) *Electrochem. Comm.*, 1, 282.
[21] Abadal, G., Pérez-Murano, F., Barniol, N. et al. (2003) *IEEE Trans. Instrum. Meas.*, **52**, 859.
[22] Clavilier, J., Faure, R., Guinet, G. et al. (1980) *J. Electroanal. Chem.*, **107**, 205.
[23] Hamelin, A., Doubova, L., Wagner, D. et al. (1987) *J. Electroanal. Chem.*, **220**, 155.
[24] Trevor, D.J., Chidsey, C.E.D. and Loiacono, D.N. (1989) *Phys. Rev. Lett.*, **62**, 929.
[25] Tao, N.J. and Lindsay, S.M. (1991) *J. Appl. Phys.*, **70**, 5141.
[26] Itaya, K. (1998) *Prog. Surf. Sci.*, **58**, 121.
[27] Pan, J., Jing, T.W. and Lindsay, S.M. (1994) *J. Phys. Chem.*, **98**, 4205.
[28] Schmickler, W. (1995) *Surf. Sci.*, **335**, 416.
[29] Sass, J.K. and Gimzewski, J.K. (1991) *J. Electroanal. Chem.*, **308**, 333.
[30] Vaught, A., Jing, T.W. and Lindsay, S.M. (1995) *Chem. Phys. Lett.*, **236**, 306.
[31] Peskin, U., Edlund, A., Bar-On, I. et al. (1999) *J. Chem. Phys.*, **111**, 7558.
[32] Galperin, M., Nitzan, A. and Benjamin, I. (2002) *J. Phys. Chem. A*, **106**, 10790.
[33] Zhang, J. and Ulstrup, J. (2007) *J. Electroanal. Chem.*, **599**, 213.
[34] Conway, B.E. (1984) *Prog. Surf. Sci.*, **16**, 1.
[35] Kolb, D.M., Przasnyski, M. and Gerischer, H. (1974) *J. Electroanal. Chem.*, **54**, 25.
[36] Herrero, E., Buller, L.J. and Abruna, H.D. (2001) *Chem. Rev.*, **101**, 1897.
[37] Magnussen, O.M., Hotlos, J., Nichols, R.J. et al. (1990) *Phys. Rev. Lett.*, **64**, 2929.
[38] Magnussen, O.M., Hotlos, J., Beitel, G. et al. (1991) *J. Vac. Sci. Technol.*, **9**, 969.
[39] Hachiya, T., Honbo, H. and Itaya, K. (1991) *J. Electroanal. Chem.*, **315**, 275.
[40] Toney, M.F., RicHoward, J.N., Richer, J. et al. (1995) *Phys. Rev. Lett.*, **75**, 4472.
[41] Hotlos, J., Magnussen, O.M. and Behm, R.J. (1995) *Surf. Sci.*, **335**, 129.
[42] Möller, F.A., Magnussen, O.M. and Behm, R.J. (1995) *Phys. Rev. B*, **51**, 2484.
[43] Endo, K., Sugawara, Y., Mishima, S. et al. (1991) *Jpn. J. Appl. Phys.*, **30**, 2592.
[44] Ogaki, K. and Itaya, K. (1995) *Electrochim. Acta*, **40**, 1249.
[45] Esplandiu, M.J., Schneeweiss, M.A. and Kolb, D.M. (1999) *Phys. Chem. Chem. Phys.*, **1**, 4847.
[46] Barth, J.V., Costantini, G. and Kern, K. (2005) *Nature*, **437**, 671.
[47] Lipkowski, J., Stolberg, L., Yang, D.-F. et al. (1994) *Electrochim. Acta*, **39**, 1045.
[48] Cunha, F. and Tao, N.J. (1995) *Phys. Rev. Lett.*, **75**, 2376.
[49] He, Y., Ye, T. and Borguet, E. (2002) *J. Am. Chem. Soc.*, **124**, 11964.
[50] Yoshimoto, S., Higa, N. and Itaya, K. (2004) *J. Am. Chem. Soc.*, **126**, 8540.
[51] Mayer, D., Dretschkow, Th., Ataka, K. et al. (2002) *J. Electroanal. Chem.*, **20**, 524–5.

[52] Tao, N.J. (1996) *Phys. Rev. Lett*., **76**, 4066.
[53] Schmickler, W. (1990) *J. Electroanal. Chem*., **296**, 283.
[54] Schmickler, W. and Tao, N.J. (1997) *Electrochim. Acta*, **42**, 2809.
[55] Kuznetsov, A.M. and Schmickler, W. (2002) *Chem. Phys*., **282**, 371.
[56] Friis, E.P., Andersen, J.E.T., Kharkats, Y.I. et al. (1999) *Proc. Natl. Acad Sci. USA*, **96**, 1379 and references therein.
[57] Alessandrini, A., Corni, S. and Facci, P. (2006) *Phys. Chem. Chem. Phys*., **8**, 4383.
[58] Facci, P., Alliata, D. and Cannistraro, S. (2000) *Ultramicroscopy*, **189**, 291.
[59] Chi, J., Zhang, Nielsen, J.U. et al. (2000) *J. Am. Chem. Soc*., 122, 4047, and references therein.
[60] Friis, E.P., Andersen, J.E.T., Madsen, L.L. et al. (1998) *Electrochim. Acta*, **43**, 2889.
[61] Kolb, D.M., Dakkouri, A.S. and Batina, N. (1995) *Nanoscale Probes of the Solid/Liquid Interface* (A.A. Gewirth and H. Siegenthaler eds). Dordrecht: Kluwer Academic Publishers, NATO ASI Series, **288**, pp. 263–84.
[62] Alessandrini, A., Gerunda, M., Canters, G.W. et al. (2003) *Chem. Phys. Lett*., **376**, 625.
[63] Corni, S. (2005) *J. Phys. Chem. B*, **109**, 3423.
[64] Alessandrini, A., Salerno, M., Frabboni, S. et al. (2005) *Appl. Phys. Lett*., **86**, 133902.
[65] Chi, Q., Farver, O. and Ulstrup, J. (2005) *Proc. Natl. Acad. Sci. USA*, **102**, 16203.
[66] Li, Z., Han, B., Meszaros, G. et al. (2006) *Faraday Discuss*., 131, 121.
[67] Albrecht, Guckian, A., Kuznetsov, A.M. et al. (2006) *J. Am. Chem. Soc*., **128**, 17132.
[68] Wold, D.J. and Frisbie, C.D. (2000) *J. Am. Chem. Soc*., 122, 2970.
[69] Cui, X.D., Primak, A., Zarate, X. et al. (2001) *Science*, **294**, 571.
[70] Xu, B., Xiao, X. and Tao, N.J. (2003) *J. Am. Chem. Soc*., **125**, 16164.
[71] Zhao, J. and Davis, J.J. (2003) *Nanotechnology*, **14**, 1023.
[72] Zhao, J.W., Davis, J.J., Sansom, M.S.P. et al. (2004) *J. Am. Chem. Soc*., **126**, 5601.
[73] Davis, J.J., Wang, N., Morgan, A. et al. (2006) *Faraday Discuss*., **131**, 167.
[74] Magnussen, O.M., Zitzler, L., Gleich, B. et al. (2001) *Electrochim. Acta*, **46**, 3725.
[75] Magnussen, O.M., Polewska, W., Zitzler, L. et al. (2002) *Faraday Discuss*., **121**, 43.
[76] Tansel, T. and Magnussen, O.M. (2006) *Phys. Rev. Lett*., **96**, 026101.
[77] Alessandrini, A. and Facci, P. (2005) *Meas. Sci. Technol*., **16**, R65.
[78] Kageshima, M., Ogiso, H., Nakano, S. et al. (1999) *Jpn. J. Appl. Phys*., **38**, 3958.
[79] Folks, L., Best, M.E., Rice, P.M. et al. (2000) *Appl. Phys. Lett*., **76**, 909.
[80] Veerman, A.J., Otter, A.M., Kuipers, L. et al. (1998) *Appl. Phys. Lett*., **72**, 3115.

[81] Lugstein, A., Bertagnolli, E., Kranz, C. et al. (2002) *Appl. Phys. Lett*., **81**, 349.
[82] Martin, Y., Abraham, D.W. and Wickramasinghe, H.K. (1988) *Appl. Phys. Lett*., **52**, 1103.
[83] Nonnenmacher, M., O'Boyle, M.P. and Wickramasinghe, H.K. (1991) *Appl. Phys. Lett*., **58**, 2921.
[84] Belaidi, S., Girard, P. and Leveque, G. (1997) *J. Appl. Phys*., **81**, 1023.
[85] Jacobs, H.O., Leuchtmann, P., Homan, O.J. et al. (1998) *J. Appl. Phys*., **84**, 1168.
[86] Belaidi, S., Girard, P. and Leveque, G. (1997) *Microelectron. Reliab*., **37**, 1627.
[87] Wittpahl, V., Behnke, U., Wand, B. et al. (1998) *Microelectron. Reliab*., **38**, 981.
[88] Cui, X.D., Zarate, X., Tomfohr, J. et al.. (2002) *Ultramicroscopy*, **92**, 67.
[89] Menozzi, C., Alessandrini, A., Gazzadi, G. et al. (2005) *Ultramicroscopy*, **104**, 220.
[90] Butt, H-.J. and Jaschke, M. (1995) *Nanotechnology*, **6**, 1.
[91] Radmacher, M., Cleveland, J.P., Fritz, M. et al. (1994) *Biophys. J*., **66**, 2159.
[92] Frederix, P.L.T.M., Gullo, M.R., Akiyama, T. et al. (2005) *Nanotechnology*, **16**, 997.

Chapter 6

Polymer-based adaptive networks

Victor Erokhin

Department of Physics, University of Parma, Parma, Italy; Institute of Crystallography, Russian Academy of Sciences, Moscow, Russia

Abstract. This chapter describes a strategy for the realization of adaptive networks based on polymer molecules and electrochemical mechanisms. As biological benchmark, the main elements of the nervous system are considered. The basic principles of neuron network realization are also presented. Constructions of individual elements are discussed. Finally, demonstration circuits and perspective developments are described.

Keywords: conducting polymers; solid electrolyte; electrochemistry; adaptive networks

6.1. Introduction

Despite the fact that adaptive networks have features similar to neuron networks, we will avoid calling them in this manner, because the name neuron networks is mainly used considering software realization of adaptive systems, capable of learning and decision-making. In this chapter, we are more interested in the hardware realization of such systems, both from the fundamental point of view, allowing better understanding of the architecture and working principles of nervous systems of living organisms, and from the application point of view, suggesting new ways of computational paradigms and entirely new computer organization architectures.

Systematization of chaos and new knowledge creation are among the most miraculous events in the world. Processes involving accumulation of information, which appears to be a random event, and its processing, leading to the performance of generalized conclusions and decision-making, are among the greatest mysteries ever existed.

Modern progress in computer science can be considered as a new tool allowing to understand the processes that are essential in information processing, at least to some extent, in the living systems, even if the direct parallel is quite questionable. Starting from the simplest single-task processing of task-specific algorithms, the current status of computer hardware and software allows multi-task problem solutions, where certain priority can be attributed to an individual task or a group of tasks. Moreover, neuron network algorithms are widely used in modern software for the execution of several specific tasks, such as image and voice recognition, analysis and forecasting, etc.

The area of neuron networks had attracted the attention of numerous researchers for more than two decades and, at the beginning, they were used mainly in the framework of hardware realization. A fundamental reason for this was the attempt to understand how living objects, even the simplest ones, can treat information obtained from outside and perform decision-making. The progress in biophysics and biochemistry has allowed to reconstruct the scheme of organization of nervous system circuit responsible for the treatment of signals coming from the sensoristic elements (eyes, ears, nose), accumulation of information, learning, and producing adequate signals to the executive elements (muscles, for example). It was established that the system must contain numerous nonlinear elements with very complicated network of interconnections capable of signal transfer. In other words, the system must provide many possible pathways for signal propagation from each input to each output.

An essential difference in biological nervous systems with respect to usual electronic circuits is the possibility to transfer adaptively and reversibly certain signal pathways in preferential ones. It means that the whole system, during its operation, can accumulate the experience, establishing preferential pathways, by decreasing the resistance of the 'wires', connecting defined sets of nonlinear elements (neurons), according to the frequency of their involvement into the signal transmission process. Such a property is known as the Hebbian rule [1], which states that 'When an axon of cell A is near enough to excite cell B and repeatedly or persistently takes part in firing it, some growth process or metabolic change takes place in one or both cells such that A's efficiency, as one of the cells firing B, is increased'. Probably, this property can be considered as a fundamental difference of the nervous system form the traditional electronic circuits. If we consider the circuit as one containing active elements (transistors, for instance) and wires, the wires, in the case of nervous system, must be much more intelligent than transistors. The nervous system of real biological

objects can be considered as a reference point. Nonlinear elements ('transistors') are neurons. The neuron body plays a rather simple role. It can be considered even more simple than a transistor, namely, as a trigger. Its function is to allow any signal input, while its further propagation will be performed only when some threshold level will be overcome. Axons and dendrites are also rather simple elements (they can be considered as electrolytic conductors). However, there are some specific objects (synapses) that cannot be considered as simple elements and that have no analogies in the traditional electronic devices. They can be considered as variable electrochemical bridges between 'wires', which can be established and then they can exist for long time periods. Synapse provides the change to the signal passing from one possible pathway to the other, allowing, therefore, the possibility of experience accumulation (learning) and external forced training (teaching). The realization of such 'bridges', which must permit multiple adaptations also, is a rather difficult technical task for the available materials and technologies. Therefore, the alternative approach, based on the variation of 'wire' conductivity according to the frequency of its involvement into signal transmission, was considered for adaptive network realization. This property was taken as the basis for the organization of systems capable of learning and decision-making. Frequently used pathways, according to the previous experience resulting into correct decision-making, will be more probably used for signal transfer when the new decision must be done.

Learning, or the accumulation of processed experience, is one, but not the single, essential feature of adaptive systems. The entire system must include elements and systems allowing the possibility of the external training – 'teaching', which is usually referred to as supervised learning. In fact, even the simplest animal, such as a pond snail, can be externally trained.

Last but not least, a feature necessary for adaptation and, moreover, any living system's existence is bringing the whole system out of equilibrium even in steady-state environmental conditions. To understand the fundamental importance of the above statement, we must again make parallels with living organisms. According to Schrödinger, life is a situation that is far from thermodynamic equilibrium. He wrote, 'Living matter evades the decay to equilibrium' [2]. Similar statements were also claimed by Prigogine [3], emphasizing that each living system must have at least one element, performing rhythmic features at fixed environmental conditions, providing, therefore, living cycles necessary for maintaining the organism out of equilibrium.

This chapter is organized in the following manner. We will often refer to the organization of nervous system of simple animals, particularly; we will consider the pond snail *Lymnaea stagnalis* as a representative example. The main reason for this choice is that the system of *L. stagnalis* is simple enough to be considered as a model, on one hand, and it is rather complicated to allow learning, on the other hand. Moreover, the role of its constituent elements is already studied and well defined, simplifying, therefore, the attempts to substitute them with synthetic analogs. It is also important that adequate theoretical models of the system behavior are developed, which will make easier comparisons of the artificially realized elements with those exhibited by real biological structures. However, we will not consider the organization of pond snail nervous system in detail here, as it is beyond the scope of this chapter. Readers interested in knowing more details can find them elsewhere [4]. However, some concepts of neuron system organization will be presented in Section 6.2.

After considering the structure and properties of biological benchmarks briefly, we shall proceed to the principles and basic features of the modern status of neuron network architectures. Much attention will be paid to their similarities and differences with features provided by biological systems.

A significant portion of this chapter will be devoted to the realization of polymer-based electrochemical element, which is supposed to be used as the principal node of adaptive network. The choice seems to be well grounded. In fact, all living systems are organized from organic materials, and they use electrochemistry as the main tool for signal transfer, its processing, decision-making, and generation of actions. Therefore, we will describe the structure, fabrication methods and properties of such elements.

The subsequent section will be dedicated to the realization of simplest model systems that can represent some learning features demonstrated by living organisms. It will also be considered as a network capable of demonstrating multiple adaptive behaviors in response to external training actions (supervised learning).

The successive part of this chapter will give some ideas and possible approaches for the development of adaptive networks. It will describe an alternative approach to the straight line of device fabrication, based on the realization of mesoscopic structures, having sizes comparable with that of the fundamental blocks of cell biology that can bring to the realization of intellectual systems, at least comparable with existing silicon-based electronic devices. This approach will be based on the formation of statistically organized polymeric fiber structures that, due to extremely high number

of elements and interconnections, are expected to form a system that can demonstrate more complicated adaptive behaviors.

Finally, the conclusion summarizes the perspectives of applications of polymer-based electrochemical elements for the realization of networks with adaptive behavior. A comparison of structure and properties of these elements and networks based on them in biological systems will be performed.

6.2. Biological Benchmark

The nervous system of living organisms is, of course, the most effective adaptive network that we know. Despite the fact that each operation of signal processing is very slow compared to that performed by a computer (as it is based on rather slow electrochemical processes), the overall performance of the system is so high that it is much more superior to the latest generation computers. Our brain is able to perform image and sound recognition even when the signal is superimposed to the significant noise level. This is due to the very high level of parallel processes in the brain.

Neuron is the key element of the nervous system [5]. It is schematically shown in Fig. 6.1. It contains the neuron body, axon, and dendrites. Dendrites provide signal income to the neuron body, while the axon serves as a drain signal wire. Signals from dendrites are summarized in the neuron body and, if this sum is more than some threshold value, the neuron generates an output signal and allows further propagation through the axon. It is important to note that each neuron has only one axon. Signal transfer from one neuron to the other takes place in points where the axon of one neuron is connected with a dendrite of the other. This contact point is called synapse. This element seems to be extremely important in the nervous system as it can change the signal pathway, which will consequently result in the variation of properties of the network as well as the system output. New synapses can be created during the learning process. Moreover, no synapse is equal to the other. Efficiency of signal transfer from the axon to dendrite depends on the state of a particular synapse (which corresponds to the weight function in terms of artificial neuron networks) and can be varied during the system working.

We are still very far from fully understanding the learning mechanisms in the brain. However, we have some ideas about the pond snail *L. stagnalis*, which we will refer to throughout this chapter. It is well known that the flexibility of synapses is one of the most important properties allowing

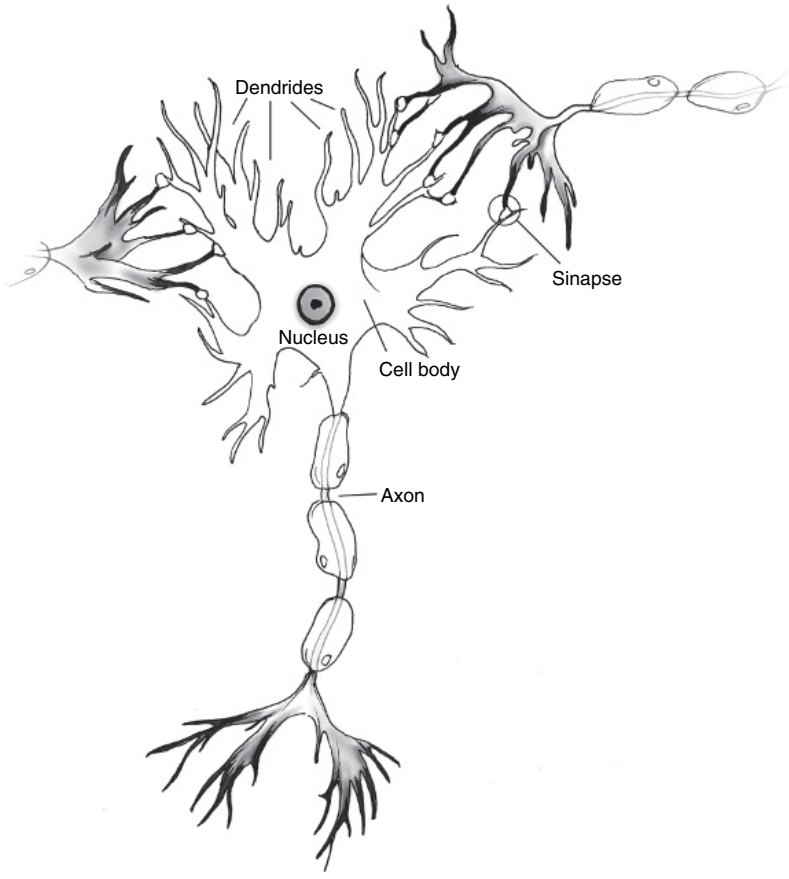

Figure 6.1: Schematic representation of the part of the nervous system. Numerous dendrites provide the income of signals to the neuron body. Income signal is summarized in the neuron body and, when the threshold value is reached, the signal is transmitted further through a single axon. Transfer of the signal from one neuron to the other takes place in synapses that can be considered as contact points of axons and dendrites.

learning in the system. One may say that it adjusts the weight functions of the efficiency of signal transfer from one neuron to the other based on the experience gained during the previous events of information processing. Thus, while considering artificial systems that must mimic the properties

of the nervous system, significant attention must be paid to the realization of some elements that will be able to imitate the properties of synapses.

6.3. Some Aspects of Artificial Neural Networks

In this section, we will consider some specific features of artificial neuron networks. Of course, we limit ourselves to present only the material that will be necessary for further considerations. We cite here some books [6] from the numerous literatures available on this topic.

Let us begin with the initial studies in this field and proceed to the very popular works of Minsky and Papert [7]. These researchers have demonstrated the limited learning capabilities of the single-layer neuron organization. In the beginning of 1980s, the interest on artificial neuron networks increased as a result of the many new approaches developed in this period. A detailed description of the problem is available in [6].

The term 'neuron' means that the network must imitate some features of the nervous system based on neurons. In order to correspond to the biological neuron networks, artificial neuron networks must have several properties that a usual computer does not have. One of the main properties that these networks must have is the capability to perform parallel execution of a large number of tasks. Therefore, the execution of a single task can be rather slow, just like how the brain performs even simple calculations slower than a simple computer or a calculator. This drawback will be compensated by the very large number of operations executed simultaneously. Comparing again the computer with a human brain, we can claim that such parallel data processing results in a fact that even the most powerful computer cannot perform, for example, the recognition function faster and more efficient than a man and even animals. The second important property is that the system must have the intelligence to learn. This property is closely connected to an other important property, namely the integration and mutual influence of memory and processing functions. It means that the processing of information results in the modification of the state of local processors (learning), and the next processing events will be performed by the processors whose properties are varied based on the previous experience (memorization of processed information). Finally, the system must be self-protected from errors in a generic sense. It means that errors unavoidable during complex parallel processing of information will not result in the blocking of the system, and they can be corrected during successive processing events.

Currently, most of the artificial networks are realized on the software level. A rapid development in this field has resulted in wider applications of neuron networks in such fields as image recognition, forecasting, optimization, and management.

The key element of the neuron network must play a role similar to that of the neuron body – it accumulates the incoming signals and provides further propagation of information if the sum of the signals is more than some threshold level. According to McCulloch and Pitts [8], this mathematical neuron must summarize all incoming signals and generate signal 1 (otherwise 0) when the predetermined threshold level is reached. A schematic representation of artificial neuron is shown in Fig. 6.2.

Mathematical models that are used for such neuron behavior description employ the sigmoid (or logic) function to describe the signal pass through the neuron. This function is described by the following formula (Eqn 6.1).

$$y = \frac{1}{1 + e^{-x}} \tag{6.1}$$

A graphical representation of this function behavior is shown in Fig. 6.3. As you see, the function can be considered as 0 and 1 value with rather high coincidence in practically the whole range of parameters, performing some smoothing of the break near the threshold level. Artificial neuron networks are constructed from elements (artificial neurons) having the described properties and capable of generating output signals.

There are several possible architectures of neuron networks; however, some important features are common for all of them. The network must have layered structure where each neuron of the lower level is connected to all neurons of the successive layer. The earliest artificial networks were based on single-layer organization. However, such structures were shown

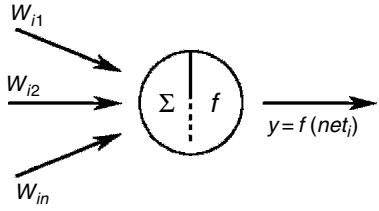

Figure 6.2: Schematic representation of the artificial neuron. Input signals multiplied on weight coefficients are summarized and output signal '1' is generated when the threshold level is reached, otherwise its value is '0'.

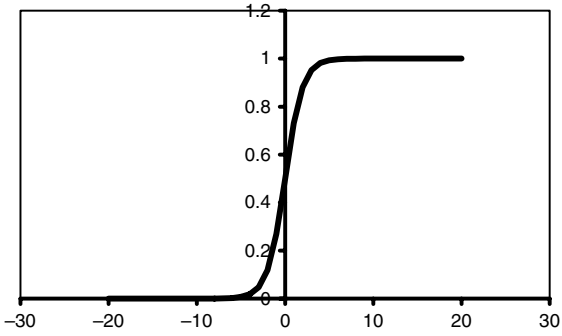

Figure 6.3: Graphic behavior of sigmoid function.

to have significant limitation in signal processing. Therefore, multilayer architectures are considered now in artificial neuron networks. An example of such an organization of artificial neuron network is shown in Fig. 6.4. As you see, the signal from any neuron of the lower level can be transferred further through the network choosing one of the numerous possible pathways, because it was connected to practically all neurons of the successive layer. However, this possible signal transfer is not equally probable between all pairs of neurons. Weight functions must be attributed for each neuron pairs. Considering these weight functions, we assume that the characteristics of the system will be more closer to that of a real nervous system when the connections between neurons are performed with 'smart' wires that are able to increase conductivity if the previously performed

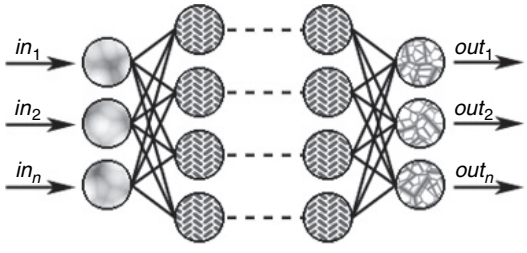

Figure 6.4: Schematic representation of the layered organization of the neuron networks. Input receptors transfer the signals to all neurons of the first layer. Each of these neurons is connected to all neurons of the successive layer. Number of layers depends on the complexity of the task that must be solved. Finally, a set of outputs is generated as a result of the processing.

connection has resulted in the correct response, or decrease conductivity if this connection has resulted in wrong output. Special procedures have been developed for the software realization of this property (weight function adjustment). However, as we are interested in hardware adaptive network, these procedures will not be considered here. Making parallels with biological objects, we can say that this feedback, in the simplest case, plays the role of a sensoristic system. In living organisms, the input signal comes from biological sensors (eyes, ears, noise). The signal must be processed by the nervous system for some decision making. Some actions will be generated according to this decision. A correct decision will mean that some good response appears as a result of the action (clear vision, good taste, pleasant smell, etc.), while pain, for example, can be considered as a result of wrong decision. As a result of the accumulated experience, the weight functions of signal transfer between neurons of different layers will be adjusted by modifying the signal pathways of the whole system resulting in a new decision at the same input conditions.

In the simplest case of artificial neuron networks, there is only one direction of signal transfer. A more complicated network involves the possibility of back signal propagation, which is mainly used as the feedback allowing to perform more effective learning in the system.

We must underline the principle difference of architecture described in this part with respect to that considered later based on polymeric electrochemical elements. Neuron analogs are the key elements for a network as shown in Fig. 6.4. Weight function variation in this case can be realized only at the software level. Instead, as it was mentioned in the previous part, in biological systems and in networks that will be considered later, neuron analogs play rather passive role. The key elements are synapse analogs, which can vary their properties according to the learning or external training. Thus, we intend to realize a system whose performance is connected to not only the possibility of further signal propagation after overcoming the threshold level after the summarization of income signals at the neuron body analog, but also varying the conductivity of the 'wires' connecting different neuron analogs. It will imitate the synapses behavior (variation of weights of transfer functions) at the hardware level as it occurs during the interactions of axon with different dendrites. These conductivity variations must be rather stable, on the one hand, but they must be flexible enough to allow multiple adaptations, on the other hand.

Learning paradigms can be divided into three main types, namely supervised learning (with teacher), unsupervised learning (without teacher) and combined learning, which has some features of the two former methods. It

is clear that combined learning is the most perspective one as it seems to be similar to the human learning.

There are four main roles in the organization of a system capable of learning. In this chapter, we will consider only one of them, the oldest one – the Hebbian role. Hebbian role was postulated based on the data obtained from neurophysiology. It highlights that the force of the synaptic bond (or, in terms of artificial neuron networks, the value of weight functions) increases when the neurons involved into this synapse are activated frequently and simultaneously. Reformulating the role to be more suitable to the strategy used in this chapter, we can say that the more frequently (or longer in time) the pathway between two neurons is involved into signal propagation, the more probably it will be used, among all other possibilities, as a pathway of new signal propagation.

To summarize, the following properties of artificial neuron networks are most essential for further considerations of hardware realization of adaptive networks constructed from polymer molecules and based on electrochemical working principles – the systems that seem to be the most similar, at least considering the composition and working mechanisms, to natural biological adaptive systems – nervous systems:

- **Very high level of parallel processing**: Multiple inputs, or analogs generated by sensory systems in living organisms (vision, sound, taste, smell, touch), are connected to the network of neuron analogs organized into a complicated layered network and interconnected through smart wires (synapses analogs), capable of increasing their conductivity (weight function analogs) according to the frequency of the signal passing through them. Thus, the input information will be processed simultaneously providing complex mutual variations of possible signal pathways and, therefore, generating the output signal (organ activation) as a result of the processing of the whole input information.
- **Integration of processing and memory properties for network elements**: This property implies that variations in the processing element characteristics will take place during the learning process (increase or decrease in the conductivity of smart wires or, in terms of neuron networks, the variation of weight functions). These variations must be temporally stable. Therefore, the processors will act in different ways according to the experience (processed information) accumulated during previous acts of processing, thus performing the memory functions.
- **Learning procedure of the developed network must be based on combined learning paradigm**: It allows for both supervised learning (with teacher) and unsupervised learning (without teacher) algorithms.

In fact, learning of rather complicated systems (children, for example) implies critical analysis of the environmental situation by themselves and establishing causal relationship (unsupervised learning) as well as forced external teaching (supervised learning). In the successive portions of the chapter, 'with teacher' learning will be called 'training'.

- **Hebbian role**: It will be used as the main learning role for developed adaptive networks based on polymer molecules.

Note that one other essential property will be considered later in the discussion on polymer-based adaptive network realization. This property is essential for some internal elements in the system to perform nonlinear rhythmic signals in steady-state environmental conditions. In biological nervous systems as well as in artificial neuron networks, signal propagation takes place in the form of pulses. However, in the case of artificial neuron networks, we do not need to fabricate a special element that will bring the system out of equilibrium. This function can be performed through a simple external generator. In our case, however, such an element must be realized within the system as we intend to mimic, at least at the qualitative level, the features of the nervous system of living organisms, and if we allow to use some external element, the system will no longer be a closed one. The processes in the nervous system of biological organisms are of electrochemical origin (ionic currents). Thus, the information signals must be in the form of pulses; otherwise, mass transfer will occur (the accumulation of some ions in particular restricted areas). In the case of pulse propagation of information, however, no mass transfer will take place, and only the excitation will be transmitted. Therefore, we must realize the element preferentially with the composition that is rather similar to other elements in the network, which will act as a generator in fixed environmental conditions, preventing the system from saturation and avoiding mass transfer (selective ion redistribution) during network functioning.

6.4. Electrochemical Element

6.4.1. Molecular Layers

All devices and elements considered in this chapter are based on diffusion-controlled ionic flow processes. Therefore, the thickness of their working layers is an extremely important parameter. It means that the working structure must be thick enough to allow a macroscopically high value

of conductivity, much higher with respect to the noise level at working (room) temperature, on the one hand. On the other hand, the thickness must be as thin as possible to allow ionic drift through the whole depth of working molecular layers, providing rationally fast response during signal processing.

Two main methods are currently used to realize molecular layer assembling. The first method, called self-assembling (SA), is based on the properties of some classes of molecules to be organized in regular arrays on solid surfaces. The other method, called Langmuir–Blodgett (LB) technique, is based on successive transferring of monomolecular layers, previously formed at the water surface, onto the surfaces of solid supports as they pass the air/water interface.

Both these techniques allow the fabrication of structures with molecular resolution in one direction (thickness); however, there are significant differences between the techniques. The SA method is based on the chemical and biochemical affinity of different molecules and parts of molecules to the solid substrate surface and to each other. The method is rather general, simple and, therefore, widely used. It allows the statistical organization of materials on thin films. To some extent, the resultant layers have some features similar to biological membrane-like systems. The LB technique, on the other hand, is a more artificial method. Nevertheless, it allows manipulation at the molecular scale with long-chain amphiphilic molecules, allowing the realization of very complicated structures with desirable alteration of functionally active molecular layers. (Readers may find more details on these techniques in [9], [10] and [11] and other chapters of this book.) However, we would like to present in brief the very basic features of these approaches with respect to their advantages and disadvantages as well as the areas of their applicability.

Self-assembling

Generally speaking, SA involves the utilization of molecules that have affinity to the adequately modified solid substrate surface, on the one hand, and provide the binding site for the next molecular layer deposition, on the other hand. A typical SA process is illustrated in Fig. 6.5. Different approaches have been developed taking into account the different properties of various surfaces and a wide variety of molecules considered for immobilization. However, we can consider at least two different approaches generally used for SA layer formation on the surfaces of different materials.

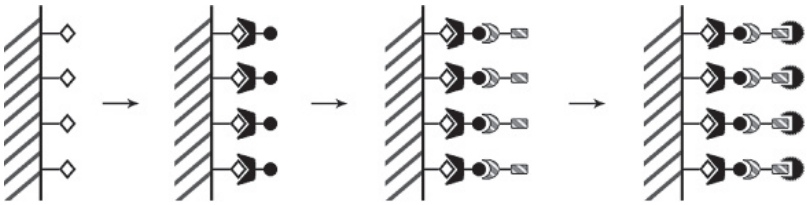

Figure 6.5: Schematic representation of the SA process. The first layer molecules have special groups with the affinity to the substrate surface, and other functional groups served for providing binding sites for the attachment of the successive molecular layer.

Suppose we wish to assemble a layer of some molecules on the oxide-terminated substrate surface. Glass or silicon may be a typical example of such substrate (silicon always has the native oxide layer on its surface). In working with such surfaces, we need molecules containing some reactive groups that must interact with the surfaces of those materials. Let us consider silicon or glass surface as example. From the surface composition point of view, they are very similar, thus terminating the silicon oxide layer. In normal conditions, the surface oxygen is hydrated, thus terminating the –OH groups, as shown in Fig. 6.6. Suppose we wish to transfer the initially hydrophilic glass or silicon substrate surface into a hydrophobic state. Thus, on the one hand, we must take a molecule that can react anisotropically with the terminal –OH group of the surface and to have hydrocarbon hydrophobic groups, on the other hand. Dimethyldichlorosilane is one example of such kind of molecules (of course, other molecules may be used, but they must have groups capable of providing the reaction of covalent

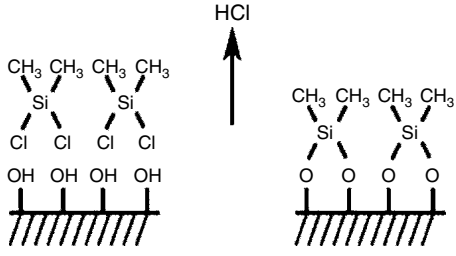

Figure 6.6: SA of dimethyldichlorsilane layer at the glass or silicon surface. The molecules are attached covalently to the substrate surface and make it hydrophobic.

bonding to the substrate surface and must be terminated with hydrocarbon or fluorocarbon chains of any length from the opposite side). Thus, if we treat the surface of oxide-terminated material with such molecules, we can achieve surface modification according to the scheme shown in Fig. 6.6. Note that the properties of the modified surface will practically be maintained forever. Methyl groups are attached covalently to the surface, and its properties can be reversed to their initial hydrophilic state only by mechanical polishing of the surface. This method was successfully used to prepare surfaces for successive deposition of patterned layers of nanoengineered polymeric capsules [12].

An other example of SA process is connected to the assembling of layers on conducting surfaces composed mainly of gold, silver or platinum [13]. The assembling, performed generally using thiol-containing molecules, is based on the high affinity of these groups to the surfaces of noble metals. Some examples of self-assembling using S-containing compounds are shown in Fig. 6.7. The main characteristic feature of all these processes is the final modification of metal substrate surfaces with groups that will be successively used for the attachment of molecules or particles, which cannot be directly placed onto metal surface or regular arrays with definite orientation of functionally active groups. One important example of the application of this method is the immobilization of proteins, as in most cases the direct contact of protein molecules with metal surfaces will result in protein denaturation.

The SA process based on biotin–streptavidin interactions [14] is widely used due to the extremely high level of affinity between these two biological molecules. Streptavidin is a protein molecule having four binding sites for biotin attachment. Biotin is a rather small molecule, which allows effective attachment to practically any molecule or nanosized object. Thus, a layer of molecules derivatized by the specific attachment of biotin to allow desirable orientation can be assembled on the surface where streptavidin layer is already formed. It is worthwhile to mention that streptavidin can form two-dimensional crystals permitting regular organization of practically any

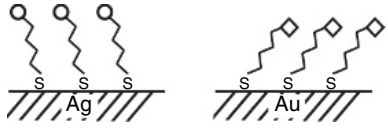

Figure 6.7: SA of thiol containing molecular layers on metal surfaces.

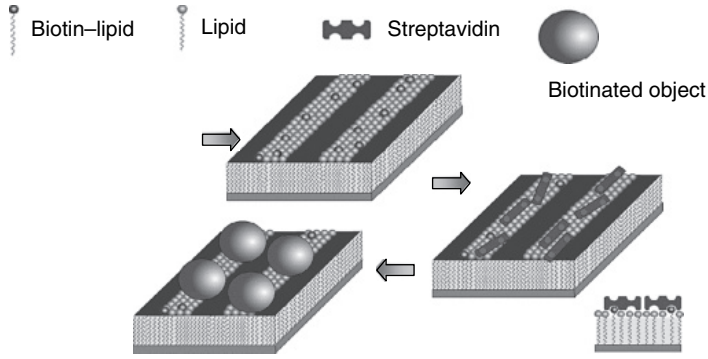

Figure 6.8: Example of the SA process based on biotin-streptavidin interactions. Biotinated molecules are mixed in a desirable concentration with nonbiotinated ones. Such mixed layer is deposited onto the specially prepared substrate surface, forming particular features (in the case shown in the figure – lines). Streptavidin layer is assembled on this substrate, forming the desirable density of the binding sites for the next layer. The next layer can be formed from any other objects (molecules, including proteins, particles). The only requirement is their performed modification by biotin. If the biotin will be attached to the well-defined part of the object, we will have not only the predetermined density of objects on the sample surface, by also their desirable orientation.

substance conjugated with biotin. The streptavidin-biotin based SA process is schematically presented in Fig. 6.8.

Currently, a large variety of applications is based on the polyelectrolyte self-assembly [14], involving sequential adsorption of polyanions and polycations on the solid support surface. The process is schematically presented in Fig. 6.9.

The polyelectrolyte SA technique is based on the deposition of successive layers of oppositely charged polymers onto a solid support by placing it into solutions of these polymers. With every step, the charged molecules are adsorbed on the surface due to electrostatic interactions. The thickness of each successive layer is limited to 1 nm. Further layer growth does not occur due to electrostatic repulsion of charged polymer molecules from that already adsorbed on the solid surface. Placing the sample into the solution of oppositely charged polymers would result in the adsorption of molecules that compensate the surface charge induced by the previously deposited layer. The main advantage of this technique is its simplicity and the possibility to cover solid substrates of any shape. The main disadvantage with respect to the LB technique, which will be discussed later,

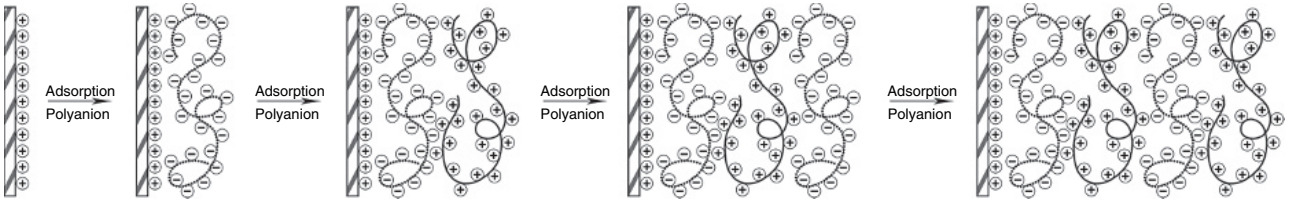

Figure 6.9: Polyelectrolyte self-assembling (the other frequently used name of the technique is 'layer-by-layer self-assembling'). Successive dipping of the sample into solutions containing polyanions and polycation with washing of the sample after each successive layer adsorption allows to deposit films with thickness resolution control of about 1 nm.

is the statistical nature of the structure of deposited layers. There is no sharp boundary between adjacent monolayers, and we can consider only the statistical increase of the total film thickness. Moreover, even mutual interpenetrations of deposited layers can take place.

Langmuir–Blodgett technique

The LB technique was developed by Irving Langmuir, who studied the behavior of insoluble monolayers at the air/water interface [15]. However, its practical application was taken into serious consideration after the suggestion of K. Blodgett to use the technique for the monolayer successive transfers onto solid substrates [16]. A slightly modified method of film deposition was developed by V. Schaefer [17]. Initially, this last method was applied mainly for the deposition of protein layers. Later, it found a lot of applications, such as the transfer of rigid and polymer monolayers. Despite the obvious usefulness of the LB method, it attracted enormous attention only after the popular works of Kuhn et al. [18], where all possibilities of the technique were demonstrated. In particular, systems with adequate molecular orientation to allow energy and electron transfer were realized and studied. These works laid the basis of future molecular architecture.

More details on this technique are available in [9,12,19]. Here, we present the very basic features useful to introduce the method of electrochemical element realization.

Surfactants or amphiphilic molecules are a wide class of molecules, which reveal an interesting behavior when placed at the air/water interface. Fatty acids are classic representatives of this kind of molecules (Fig. 6.10). Their general formula is written as shown in (Eqn 6.2):

$$CH_3(CH_2)_nCOOH \tag{6.2}$$

where $14 < n < 20$ for acids forming stable monolayers at the air/water interface. Too short chains would result in the significant solubility of molecules, while too long chains make it very rigid and, therefore, not processible.

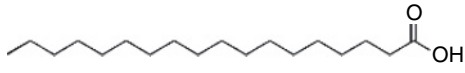

Figure 6.10: Stearic acid as an example of amphiphilic molecules.

After spreading at the air/water interface, the polar hydrophilic head-group of these molecules penetrates the water volume, as there is a very strong interaction of these head-groups with water molecule dipoles. Hydrophobic chains, on the other hand, cannot penetrate into water; otherwise, the surface energy must be increased.

Suppose we have spread some rather small amount of a solution of such molecules in organic volatile solvent at the water surface in a special device called Langmuir trough (the same results may be obtained practically on any water surface, but with a Langmuir trough we have possibility of control and directed manipulation with the molecules spread at the air/water interface). After the solvent evaporates, we will observe the situation, which may be considered as a two-dimensional gas. The molecules are far away from each other and practically do not interact. In order to manipulate such layer, we need two devices: a system of compression, allowing to induce phase transitions in such layer, and a monitoring device to reveal some parameters characterizing the monolayer state. Surface pressure (difference of the surface tension of pure water surface with that covered with monolayer) can be considered as the monitoring parameter. Wilhelmy balance is the most frequently used tool to measure this parameter. The construction and working principles of this device can be found elsewhere [20]. One or two barriers moving along the trough length can be used as a compression system. Characteristics, that can be considered as 2D analog of the phase diagram for 3D materials for the monolayer at the water surface, was called compression isotherm or, more frequently, π-A isotherm, where π is a surface pressure and A is the area per one molecule, usually expressed in $Å^2$ or nm^2. A typical π-A isotherm for stearic acid monolayer at air/water interface is shown in Fig. 6.11 (for other fatty acids, the isotherm will be same).

A comparison of this curve with phase diagrams for three-dimensional systems reveals several similar features. At the beginning of compression, we have very small variation of surface pressure, which can be described with linear dependence of the surface pressure upon the area per molecule as it occurs in the case of an ideal gas (pressure volume relationship). This 2D state is called the two-dimensional gas – the situation when distances between molecules are much higher with respect to the actual dimensions of the molecules. Further compression would result in the more or less pronounced (depending on the type of molecules and the composition of the subphase) phase transition (it is clearly visible in the case of stearic acid isotherm (Fig. 6.11)). Diminishing the area per molecule in this phase reveals significant variations of surface pressure.

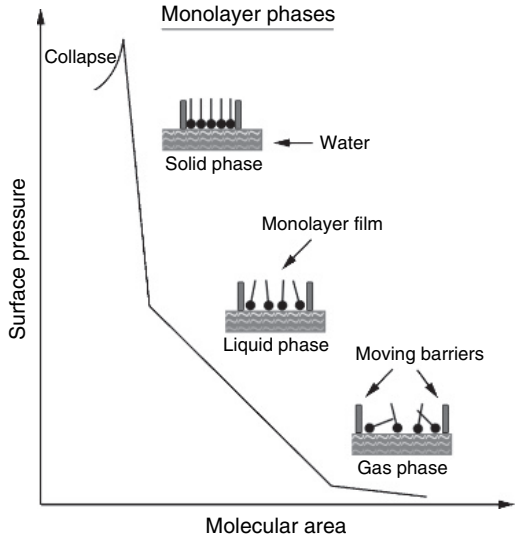

Figure 6.11: Compression isotherm (π-A isotherm) of the stearic acid monolayer at the air/water interface. Two-dimensional phase transitions are clearly visible in the isotherm. It must be mentioned that the shape of this characteristics is very sensitive to the water subphase composition and pH.

Molecules begin to interact with each other in the monolayer. This state is called two-dimensional liquid. Further compression would result in another phase transition. The new state is characterized by the very sharp increase of surface pressure as a result of very small variation of the area per molecule. This phase is called the two-dimensional solid state. Molecules are closely packed at the air/water interface. In practice, we can even form (for some kinds of compounds) a 2D crystal. This crystal exists in the form of domains, separated by boundaries, very similar to the case of normal 3D crystals. The sizes of the domains may be large or small depending on the purity of the initial compounds and conditions of monolayer preparation. Further compression would result in the layer collapse – no monomolecular layer anymore. Noncontrollable structures of three or more layers can be formed at the air/water interface.

When comparing with biological systems, it is interesting to note that practically all lipids must be considered as amphiphilic molecules (the only exception is bipolar lipids from membranes of extremophile bacteria that have two hydrophilic head-groups on opposite sides of the molecule), and

their monolayer can be formed and studied at the air/water interface. In other words, the Langmuir monolayer at air/water interface is a model representation of half of the biological membranes. Variations of its composition and surface pressure under feedback control can be used for the organization of some specific conditions useful in studying the different aspects occurring during membrane functioning and their further utilization in, for example, drug design investigations.

An important step toward various possible technical applications of this method was performed after the discovery of the possibility of transfer of such monolayers from the air/water interface onto the surfaces of solid surfaces. Two main methods are used for layer transferring onto the solid substrate surface, namely Langmuir–Blodgett (LB, vertical lift) method [16] and Langmuir–Schaefer (LS, horizontal lift) technique [17]. These methods are schematically presented in Fig. 6.12. The difference between these methods is in the geometry of air/water interface passing. Initially, the

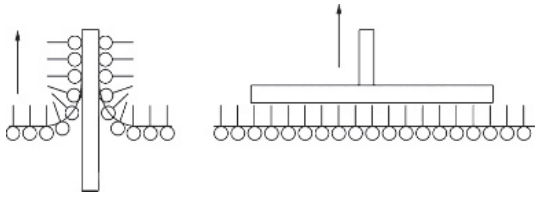

Figure 6.12: Methods of the Langmuir monolayer transfer onto the solid substrate surface. (a) Langmuir–Blodgett (LB, vertical lift) technique. The sample is passing vertically the interface covered by the monolayer in the 2D solid state phase at a surface pressure rather far from that of the collapse. The sample can move upward and downward. The deposited films have bilayer structure ('head-to-head' and 'tail-to-tail'). (b) Langmuir–Schaefer (LS, horizontal lift) method. The monolayer is in a very rigid solid state 2D phase and the surface pressure is only slightly less than the collapse pressure. After the monolayer formation, it is better to divide the layer into sections with sizes corresponding to the sample sizes with a special grid in order to prevent the formation of breaks and defects during the transfer of the layers. The sample touches the layer horizontally. The technique is used not only for the rigid monolayers deposition. This method is often used also for the transfer of layers that cannot be deposited by the LB technique, such as films of proteins, some lipids, polymers, etc. For both deposition techniques, the surface pressure must be maintained at the certain fixed value by the feedback system, compensating by the compression the area already deposited onto the solid support, during the layer transfer onto solid supports.

LB method was mainly used for deposition. However, the LS technique has currently found a lot of applications due to its applicability in the deposition of practically all types of substances and the possibility to significantly increase the speed of sample formation.

A very important property of these methods is the possibility of so-called molecular architecture. We can use multisectional trough and even multiple troughs for the deposition of LB and LS films. In this case, monolayers of different molecules will be formed in different sections and/or troughs. After their formation and activation of the feedback, a specially developed dipping system will be required to pass from one trough (or section) to the others in a programmed sequence. This possibility will allow to realize heterostructures containing predetermined sequences of monomolecular layers of different molecules. Consequently, very complicated molecular structures can be realized. The potentialities of this approach were demonstrated as early as 1980s through the works Kuhn et al. [18], when heterostructures of donor and acceptor molecules were realized and the importance of their mutual orientation and spacing between them was demonstrated.

It seems interesting and useful to compare LB (including LS) and SA methods. The main advantages of SA methods are their simplicity and readiness to industrial applications. In fact, these methods allow to cover any number of samples simultaneously with practically all possible surface shapes. However, significant difficulties can arise at the stage of chemical synthesis of adequate molecules that must guarantee the expected structure and properties of the resultant layers. The LB technique, on the other hand, especially concerning the vertical dipping method, is rather time consuming and demands several strong requirements to the solid support properties. On the other hand, in the case of LB method, we are dealing with crystal-like 2D structures. Thus, when depositing heterostructures, we can, to some extent, be sure of the mutual arrangement and orientation of functional groups in adjacent layers. In the case of SA, especially polyelectrolyte layer-by-layer deposition, we cannot expect perfectly distinct boundaries between different functional layers. We can only claim the realization of some average layer thickness during each cycle of film formation. The orientation of molecules can be random. Therefore, we must always consider the objectives when deciding what method must be used for molecular structure realization. If we wish to fabricate a structure with fixed mutual orientation of functional groups and well-defined spacing between different layers, we must use the LB technique, even if it consumes more time, requires special equipment and can limit the class of possible solid supports. If the mutual arrangement of active groups is not necessary, and

we need only to have the statistical distribution of molecules in the layer with their preferential orientation and averaging of the structure properties for the desired performance of the structure, SA is the preferred method.

6.4.2. Building Blocks

As mentioned earlier, the only known effective hardware realization of adaptive network is the nervous system of biological organisms. It is constructed with organic molecules and is based on electrochemistry principles, in particular, redox reactions. All living organisms are mainly constructed of a water-containing material that is a very effective medium for carrying out such kinds of reactions. Unfortunately, with the present status of technology development, we cannot allow the utilization of quasi-liquid elements for the construction of working systems dedicated to practical applications. Thus, the choice of appropriate materials is of crucial importance. We can a priori claim that we need at least two materials, one of which must have rather high electrical conductivity and the possibility to vary it by appropriate redox reactions. Conducting polymers are the best candidates for playing the required role. The electrochemical properties of thin polymer layers are rather well studied [21]. However, there are not so many examples when the electrochemical variation of polymer conductivity was used for device fabrication [22]. The second material must provide a suitable medium for carrying out electrochemical reactions. Therefore, it must be an electrolyte in any case and a solid electrolyte, in particular, if we wish to realize the whole system in the solid state. In this chapter, we will concentrate on the elements constructed from two particular polymers – polyaniline (PANI) and polyethylene oxide (PEO). PANI is a well-studied conducting polymer, whose conductivity can reach several tens of S/cm, and PEO is often used as a matrix for solid electrolyte realization, in particular, for solid-state lithium batteries. However, other materials can also be used for element construction, and we will not consider them here.

Some derivatives of the PANI molecule structure are shown in Fig. 6.13. Such derivatization is performed in order to give special properties to the molecule (for example, improving the solubility in standard organic solvent) for practical reasons.

Several different forms of PANI (Fig. 6.14) were considered beginning from a completely reduced one (pernigraniline form) to a completely oxidized one (leucoemeraldine form [23]). However, not all of them revealed a high value of conductivity. Significant values of electrical conductivity

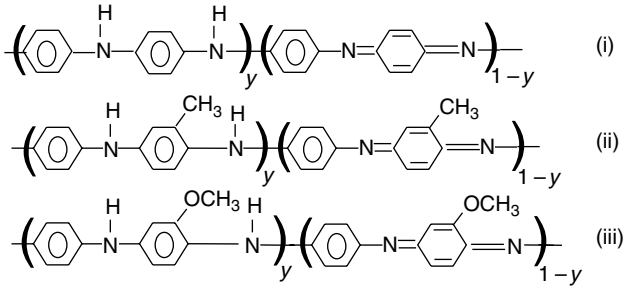

Figure 6.13: Different derivatives of the polyaniline molecule.

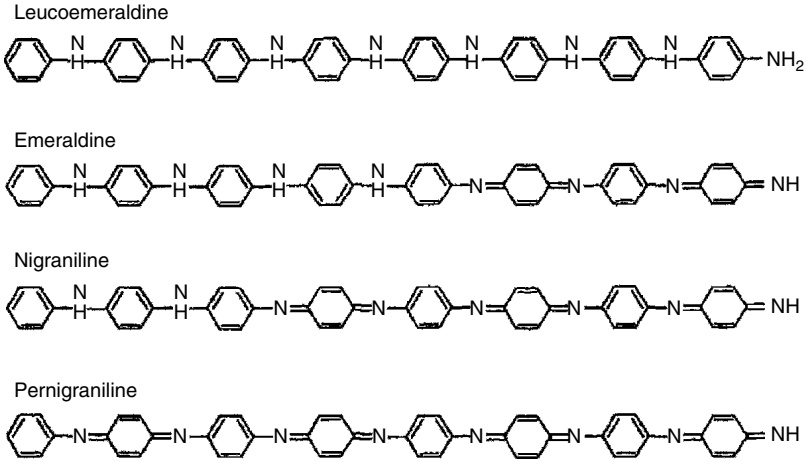

Figure 6.14: Different states of PANI molecule starting from the completely reduced one (pernigraniline form) to completely oxidized one (leucoemeraldine form). (Reprinted from *Progress in Polymer Science*, Vol. 23, E.T. Kang, K.G. Neoh, and K.L. Tan, 'Polyaniline' pp. 277–324, Copyright 1998, with permission from Elsevier.)

were obtained only on the emeraldine form of PANI. However, even the emeraldine base does not conduct. The specific resistance of the material in its native undoped form is about $10^9\ \Omega\,\text{cm}$. The material must be doped in order to transfer it into a conducting state. The difference in conductivity between the conducting and insulating states of PANI can reach about 10 orders of magnitude. Acids are usually used as doping agents.

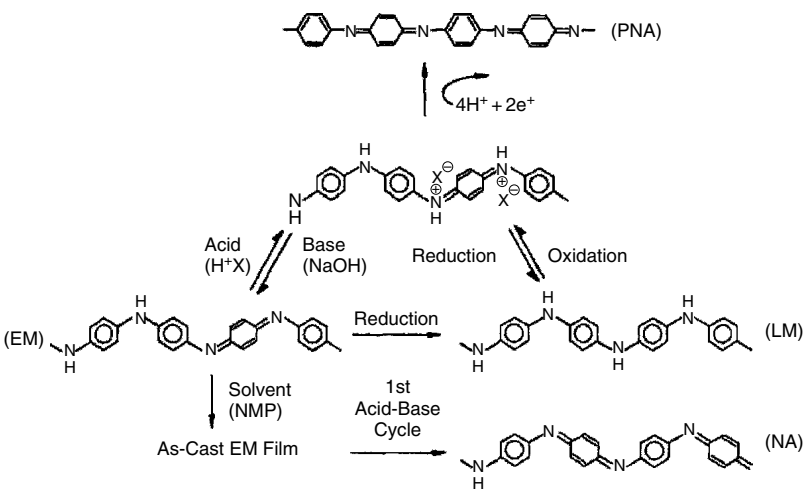

Figure 6.15: Doping induced and redox controlled changing of the electrical property of the PANI layers [23]. The molecular state that we are working with is in the second line from above. The basic principle of our electrochemical element functioning is illustrated by the right double arrow in the right part of the reaction cycle. (Reprinted from *Progress in Polymer Science*, Vol. 23, E.T. Kang, K.G. Neoh, and K.L. Tan, 'Polyaniline' pp. 277–324, Copyright 1998, with permission from Elsevier.)

If, for example, the emeraldine base is treated with hydrochloride acid, it can be transferred into a conducting emeraldine salt form (Fig. 6.15, left double arrow).

As reported in the literature, the specific resistance of highly conducting forms of PANI is about 0.01 Ω cm. However, in our experiments, we found that the reported value is hardly reachable and the real value of conductivity is about one order of magnitude less with respect to the reported one. The conductivity of PANI is due to the delocalized pi-electrons (polarons and bipolarons). It may be understood as the displacement of electron from the polymer chain due to doping. One event of such displacement is called polaron. The presence of two correlated polarons in the same chain is called bipolaron. Electrical current through the PANI chain is due to the motion of polarons and bipolarons in the electric field. As the electrons are displaced, the conductivity can be considered as the conductivity of p-type in comparison with inorganic semiconductors.

For our purposes, the very important characteristic of PANI is its ability to vary conductivity not only due to performed doping but also electrochemically. The different transitions varying the conductivity of PANI are illustrated in Fig. 6.15. After doping (left double arrow), the initially insulated molecular film transfers itself into the conducting form. The conducting state corresponds to the oxidized form. However, when the appropriate reduction potential is applied to the material that is placed into the electrolyte environment, it will be reduced and its conductivity will diminish for at least seven orders of magnitude. Generally, the vanishing of conductivity can be illustrated by Eqn 6.3 (of course, this formula represents a case when the lithium ions are present in the electrolyte medium):

$$PANI^{+} : Cl^{-} + Li^{+} + e^{-} \Leftrightarrow PANI + LiCl \tag{6.3}$$

Metal ions (in the particular case of Eqn 3, Li^{+} ions) from the electrolyte can penetrate the PANI layer and bind the Cl^{-} ions. Thus, the Cl^{-} ions cannot perform doping properties anymore. Such behavior was directly demonstrated using spectroscopy techniques, in particular, micro-Raman spectroscopy [24]. This possibility to vary the conductivity of the layer for several orders of magnitude due to the redox state of the material is an intrinsic property of conducting polymers. No material of traditional semiconductor electronics has this property. On the other hand, all biological objects are constructed from organic (including polymer) molecules. Therefore, the processes of signal generation, transmission and processing are based on redox reactions. The slow kinetics of these processes is compensated by extremely high degree of parallelism in signal elaboration. A huge number of tasks can be performed simultaneously. Thus, being slow in individual task execution, the system is very fast when multiple tasks are carried out for a fixed time interval.

The other essential counterpart of the structure we intend to realize is solid electrolyte. Why do we need electrolyte? We need an electrolyte to serve as a suitable medium where all redox reactions can be performed. Why must it be a solid one? As it was stated above, currently, we are too far from the natural capabilities, allowing a system, where water is the main compound (like nervous systems of biological organisms, including human bodies) to operate effectively for a rational period of time not only without degradation of main properties but even accumulating the experience after all essential events.

Polyethylene oxide was taken as a matrix for solid-state electrolyte construction (the formula of the molecule is shown in Eqn 4):

$$(-CH_2CH_2O-)_n \tag{6.4}$$

This material was considered as a very perspective one for the construction of secondary lithium batteries [25]. It was also tested for high-value capacitor realization with very good performance [26]. Therefore, it was considered as a suitable matrix for solid-state electrolyte realization. However, we need to have a matrix that contains ions. Li^+ has the highest mobility among available ions. Therefore, it seems rational to take lithium ions for solid electrolyte realization.

The transport of lithium ions from one polymeric chain to the other can occur spontaneously or due to temperature or concentration gradients as well as in the applied electric field. Several oxygen atoms from one or more polymeric chains must coordinate the lithium ion.

Models of ion transport are based on hopping of ions between allowed states separated from each other by potential barriers of different height and width.

Lithium chloride and lithium perchloride were tested in the present study as doping agents of PEO layers. Even if lithium chloride has several advantages, lithium pechloride was taken for its working structure formation; it is much less hydroscopic. Therefore, its properties are more stable in time and less affected by environmental conditions.

As we intend to construct elements based on electrochemical principles that are rather slow in kinetics, we need to make our elements of effective size (thickness of the active layer, where lithium ions will go in and out due to the diffusion processes in order to provide conductivity variations according to Eqn 3) as small as possible in order to increase the velocity of signal processing. Ideally, the active area must be composed of one or few molecular layers. There are several methods to form ultrathin organic layers. The LB technique is among the most frequently used methods. Active PANI layers are deposited by LB technique. The details of the applicability of this method for depositing PANI layers are described in literature [27]. The LB technique was also applied for PEO layer formation [28]. However, it demands the functionalization of molecules or formation of mixed monolayers. Moreover, the thickness of PEO layer is not so critical. Thus, the solution casting method is used for solid electrolyte layer formation.

6.4.3. Neuron Body Analog

As mentioned in a previous section, the neuron body must summarize all input signals and generate the output signal when this sum overcomes some threshold level. There are many devices to perform this function. In our case, we are interested in the realization of an element that can be incorporated in a natural way into a whole system composed of polymers.

Among different physical phenomena that can be used as the basis of neuron body analog realization, we have taken Schottky effect, as it is rather easy.

Since we use PANI for active channel realization, we need to make a junction to provide anisotropy of the current flow. Thus, we need a material whose work function will be higher than that of PANI (4.5 eV [29]). Gold can serve as this material (work function is 5.1 eV). The voltage/current (V/A) characteristics of the structure composed of PANI film with attached gold and indium electrodes is shown in Fig. 6.16.

From Fig. 6.16, we understand the possibility to design an element that will perform the function of neuron body in a rather simple way. Suppose the signal is in a form of current (or current pulses) flowing in one direction. Several molecular wires realized from PANI (dendrite analogs) will be contacted to bring the signals to the gold particle. In order to pass the particle and to perform further propagation of the signal to the output wire (axon analog), some threshold potential on the particle must be

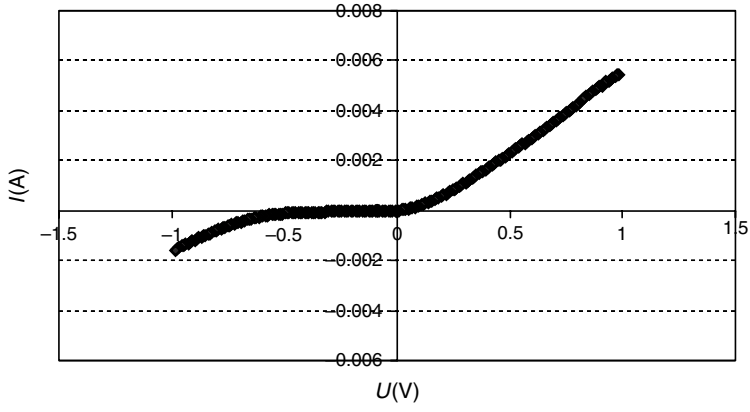

Figure 6.16: V/I characteristics of the In–PANI–Au structure. Anisotropic rectifying behavior of the structure is due to the Schottky effect.

reached (equal to the Schottky barrier). The potential on the particle will be determined by Eqn 6.5:

$$V = \frac{q}{C} \tag{6.5}$$

where q is the charge accumulated on the particle and C is its capacity.

The charge on the particle will be determined by the input currents coming to the particle. Its value will correspond to the complete time integral of all current pulses arrived to the particle, according to Eqn 6.6:

$$q = \int_{t_1}^{t_2} i \, \mathrm{d}t \tag{6.6}$$

where t_1 is the moment when the previous drain of the signal through the axon analog was finished and t_2 is the moment when the new drain of signal through the axon analog will begin.

When the particle is charged till the value, providing a potential higher than the Schottky barrier, the output signal will be transmitted from the particle. An interesting feature of the suggested approach is the possibility of varying the threshold value by just changing the size of gold particle. In fact, the capacity of the particle is connected to its geometrical dimensions. Thus, taking rather small particle, we can observe desirable characteristics even for very low current values. It is important that the present level of technology allows the fabrication of monodisperse gold nanoparticles even at nanometer scale. The possible realization of the device is schematically presented in Fig. 6.17.

The suggested scheme must permit rather simple organization of nonlinear elements playing the role of neuron body. It can be specifically useful for the construction of statistical adaptive networks. In that case, we can expect adequate performance of the system when micro- and nanoparticles of gold are added to the starting polymer solution before network fabrication.

6.4.4. Polymeric Electrochemical Element

This section is dedicated to a more complicated element, namely, the synapse analog [30]. This material must provide weight function variations according to the learning of the system. In other words, the element that we

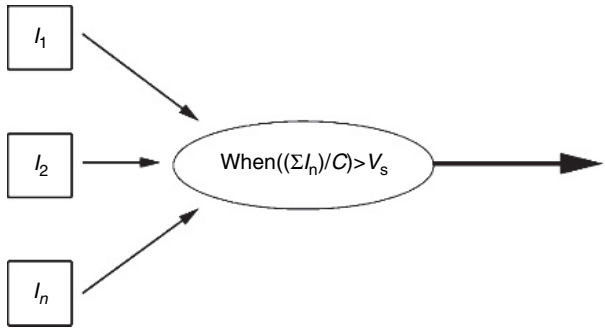

Figure 6.17: Schematic representation of the neuron body analog. Input currents from the dendrite analogs enter the gold particle charging it by income currents. The potential on the particle depends on the current sum and the capacitance of the particle. When the potential will be higher than the Schottky barrier, the signal drain will take place through the axon analog.

plan to use as a basic node of our adaptive network must have a property to increase its conductivity with the frequency (or time) of its involvement into the signal propagation process. If the synapse analog is based on PANI, it means that its active area (in a contact with electrolyte) must be exposed to the oxidation potential during signal propagation. Therefore, first of all, we need to form an active PANI channel.

A PANI channel was formed by LB technique. Forty-eight monolayers of PANI were deposited onto solid substrates (glass) with already formed two metal (Cr) evaporated electrodes. These electrodes are called source (S) and drain (D) in analogy to the field effect transistor. The prescribed thickness of the active layer (channel) is very important. On the one hand, this thickness provides already rather high value of conductivity, and, on the other hand, it is thin enough to guarantee effective electrochemical transformations, as ion motion into and from this layer occurs rather fast and on the whole thickness.

Thus, the structure contains the PANI channel connected to two metal electrodes. One of these electrodes (S) will be maintained at ground potential level, and external voltage will be applied to the other electrode (D). However, we need to realize an active zone where all the electrochemical reactions can take place. Thus, thin Li salt (lithium perchloride)-doped PEO stripe was deposited by casting and drying in the central part of the PANI layer and perpendicular to it. The concentration of Li salt in the electrolyte is also rather critical. It must be rather low, on the one hand,

in order to demonstrate the ionic conductivity much less than that of the PANI channel. However, it must be rather high, on the other hand, to provide enough lithium ions for effective electrochemical transformations. The concentration of 0.01 M was found to be optimal. Thus, we have the structure with active area (contact of PANI with PEO stripe) where redox reactions can occur. However, in all electrochemical cells, the reference potential must be provided. Therefore, we need to have an additional electrode maintained at a potential, which will be considered as a reference. We have attached a silver wire to the PEO-based solid electrolyte as this electrode. It was called gate (G) even if its function is more closed to that of the reference electrode. This electrode was also connected to the ground potential. Thus, when we apply a voltage to electrode D, the active area of the PANI channel will have a potential with respect to the reference electrode G. The polarity of this potential will be the same as that applied to electrode D, while its value will be less, as the potential is distributed on the whole channel length. The scheme of the element, together with electrical connections used for the characterization, is shown in Fig. 6.18.

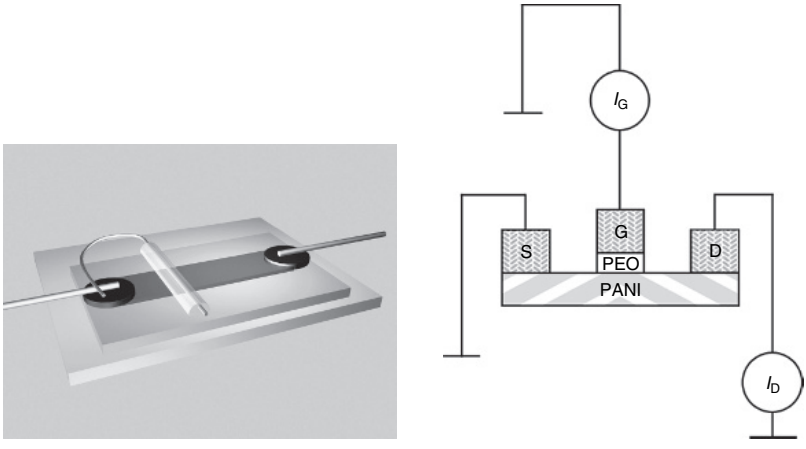

Figure 6.18: Schematic view (a) and electrical connections (b) of the polymer-based electrochemical element that will be used as the synapse analog. Both S and G electrodes are connected to the ground potential level, while the external voltage is applied to the D electrode. Two currents will be measured for the element characterization: I_D – drain current (the total current passing the element) and I_G – gate current (current occurring in the active area due to the electrochemical reactions).

The element was characterized by measuring simultaneously two V/I characteristics of the dependences of the drain and gate currents on the variation of applied drain voltage. These characteristics are shown in Fig. 6.19(a, b). The third characteristic, as shown in Fig. 19(c), is the dependence of differential current (drain–gate) on the applied voltage. This characteristic seems to be important because it demonstrates conductivity variation in the active area of PANI channel. In fact, the drain current contains both ionic current in the electrolyte and electron current in the channel.

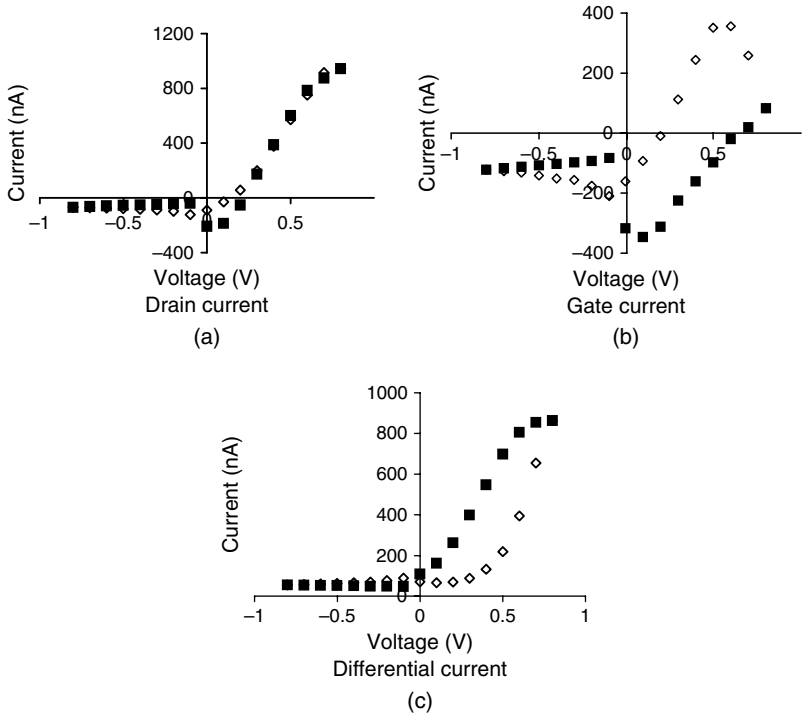

Figure 6.19: *V/I* characteristics for drain (a), gate (b) and differential (c) currents of the polymer-based electrochemical element (synapse analog) shown in Fig. 6.18. Empty squares represent the acquisitions during the voltage increase (in absolute value) scans, while the filled squares correspond to the voltage decrease in absolute value. (Reprinted with permission from V. Erokhin, T. Berzina, and M.P. Fontana, 'Hybrid electronic device based on polyaniline–polyethylenoxide junction', *J. Appl. Phys*, **97**, 064501 (2005); Copyright 2005, American Institute of Physics.)

Let us consider first the V/I characteristics for the gate (b) and differential (c) currents. The measurement starts at 0 V drain voltage. Then, it was increased in the direction of positive polarity, coming to its maximum value. This voltage cannot be too high (more than +1.5 V) as irreversible decrease of conductivity due to 'overoxidation' may occur. Then, the voltage sweep was performed in the decrease direction passing through zero and increase in absolute value in the negative polarity till its maximum negative value (−1.5 V) that was taken equal to that for the positive bias. After this, the voltage was swept back to zero in order to close the cycle. An essential feature of reported acquisitions of these curves is the delay between the application of the voltage and readout of the current value. This delay is very important, especially for the voltage values close to the potentials of oxidation and reduction, because transient processes take place in these voltage ranges, and the current values undergo significant variations at this time. For suggested configuration, the optimal value of delay was found to be 1 min. The current values became to be practically saturated within this time period.

Immediately after the deposition of the solid electrolyte layer, the conductivity of active PANI area decreases significantly due to ionic flows resulting from the gradient of Li ion concentration between PANI and PEO layers. Lithium ions enter the active layer and, according to the scheme shown in Eqn 3, perform reduction (dedoping) of the PANI molecules in this area. As a result, active PANI area is in the insulating state when the measurements of the V/I characteristics begin from zero voltage. We can observe very low values of differential current during the increase of the D voltage till about 0.4 V. Then, both G and differential currents begin to increase significantly, and G current comes to its maximum value at about 0.6 V of the applied voltage. Such behavior is connected to the oxidation of PANI molecules in the active zone. It is interesting to note that the observed voltage for G current maximum is somewhat higher than the oxidation potential of PANI measured with traditional cyclic voltammogramms performed in solutions [31]. This discrepancy will not seem strange if we take into account that the applied D voltage is distributed over the whole PANI channel length, and the actual potential in the active area is always less than the applied one.

By approaching the value of oxidation potential, the conductivity of active area increases significantly. During the back sweeping of voltage, differential current exhibits linear Ohmic behavior till approximately 0.1 V, when the reduction of layer molecules begins to take place. The G current passes its minimum (maximum, considering the absolute negative value),

transferring the active PANI layer into the reduced insulating state. The negative branch of the V/I characteristics exhibits very low values for both currents, because all the electrochemical processes are completed, and active PANI area is in an insulating state.

The V/I characteristics for G current is very similar to cyclic voltammogramms usually registered for the investigation of redox processes. We must note that it depends also on the speed of applied voltage sweeping, again in absolute agreement with similar behaviors of cyclic voltamogramms due to diffusion limited redox processes.

For the purposes of the present chapter (construction of the adaptive networks), it is much more important to investigate the temporal dependences of currents at fixed drain voltages, corresponding to the cases when the active area must be completely oxidized or reduced. In the case of reduction process, the choice of voltage value is rather easy. Any negative voltage of the drain potential must induce reduction of the active area of the PANI channel. Therefore, this value was chosen to be $-0.2\,V$, even if it can be varied (remaining negative) without significant variations of the observed results. In the case of oxidation process, the value of the potential was chosen to be $+0.6\,V$. First, these values correspond to the position of the maximum of gate current during the voltage sweep increasing branch of the V/I characteristics. Second, this value is sufficiently higher than the oxidation potential in the bulk and significantly lower with respect to the irreversible overoxidation potential. Thus, we can expect that all zones of the active area will be oxidized without irreversible modifications after adequate time interval.

Temporal dependences of the drain current at fixed drain voltages equal to $+0.6\,V$ and $-0.2\,V$ are shown in Fig. 6.20(a, b).

The dependences are very important; as they are the basic properties allowing to conclude that the adaptive systems can be constructed using the described polymer-based electrochemical element as a key node of the network. Let us study the presented dependencies in more detail. The characteristics shown in Fig. 6.20 (a) verifies the possibility of accumulation of experience and, therefore, of learning (without supervising). In fact, elements of the network involved into the formation of signal transfer pathways will increase their conductivity (more involved elements will increase the conductivity till reaching the saturation level). Thus, next time when the system will be in a situation similar to the previously occurring one, the signal will propagate through the same pathway, that was successfully used in the solving of similar task (low resistance of the elements establishing it). Summarizing, the probability of signal

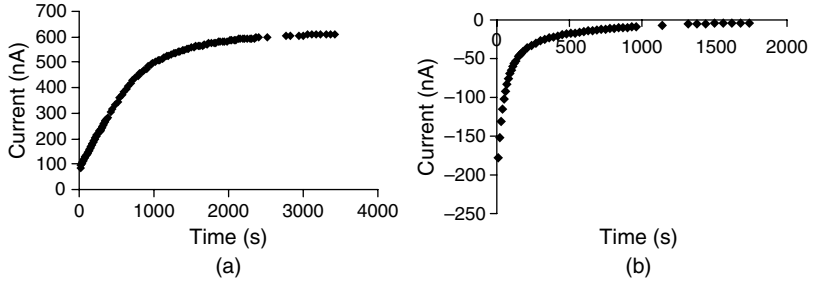

Figure 6.20: Temporal behavior of the drain current at fixed drain voltage of +0.6 V (a) and −0.2 V (b). Both dependences reveal the saturation. However, time constants are significantly different for these processes. (Reprinted with permission from V. Erokhin, T. Berzina, and M.P. Fontana, 'Hybrid electronic device based on polyaniline–polyethylenoxide junction', *J. Appl. Phys*, **97**, 064501 (2005); Copyright 2005, American Institute of Physics.)

propagation through one of the numerous possible pathways will depend on the frequency (or duration) of the involvement of elements, establishing this pathway, in the previous events of signal propagation. We can say that the accumulated experience will be a key parameter responsible for the mode of processing the input signal. In other words, we see the process of unsupervised learning here. It means that the previously performed decisions, resulting in the correct answer, will have a dominant influence on the elaboration of new input signals.

However, the dependence shown in Fig. 6.20(b) is also of fundamental importance for two reasons. First, the increase of element conductivity at positive bias is rather slow, but it is better to keep it even much slower. This increase of conductivity finally brings the system to saturation, when no further learning is possible. It means that, if the network composed of the described polymer-based electrochemical elements will be maintained at appropriate positive potential difference between the systems of input and output electrodes, all possible signal pathways will become preferential, when the time of exposition is long enough. Thus, if we will hold the system to work for a relatively long time, all the elements establishing the network will be in the high conducting (saturated) oxidized state, corresponding to the thermodynamic death of the system. Thus, we need to have some special tools to perform necessary actions that prevent the system to decay to equilibrium. The dependence shown in Fig. 6.20(b) can serve as the characteristics of this tool. In fact, short-scale temporal

application of inversed (negative) bias to all input-output pairs will result in the decrease of conductivity of all the elements involved previously in signal pathway formation. With the exception of synapses analogs that are already in the insulating state, all others will diminish their conductivity in a programmable way, according to the duration of inverted bias application. After this event, elements really (not occasionally) involved into the preferential signal pathway formation (and, therefore, in the right decision-making) will come back to their high conducting state very soon, after being involved into several signal transfer events, while those occasionally formed will be suppressed.

The second reason why the characteristics in Fig. 6.20(b) is important is that it gives us the possibility of 'supervised learning' (training) of the system. In other words, if the system by its own decision (unsupervised learning) finds some solution, but it is *a priori* wrong according to the superior system; it can be depressed by just applying the reversed potential difference between the input-output pair that has resulted in the making of this wrong decision. Thus, the action will adjust the conductivity of all elements involved into the establishing of the wrong pathways of signal propagation to the low conductivity state (it will be very similar to the variation of weight functions during signal back propagation in the case of artificial neuron networks). It implies as if we make explanations (or supervision) to a child that the decision he made is wrong.

Summarizing, the characteristics shown in Fig. 6.20 are the main basic features to consider the described polymer-based electrochemical element as one of the most suitable key node in adaptive network formation.

From the very basic point of view, it seems rather strange that the temporal behaviors of curves shown in Fig. 20(a, b) do not coincide, as both of them must depend on the diffusion of Li^+ ions from PEO to PANI and vice versa. In order to understand the observed difference in the kinetics of characteristics shown in Fig. 20 (a, b) qualitatively, let us make the following considerations. First, we will consider the reduction of active area (negative drain potential is applied to the drain electrode, Fig. 6.20(b)). In this case, the whole active area is at a potential that allows the reduction of PANI molecules in the active area of the channel (reduction potential in the bulk is about $+0.1$ V; therefore, any negative potential will be less than this value). In the case of positive drain voltage, the applied potential is distributed along the whole channel length. Therefore, only some areas of the active zone can be at a potential equal or more than the oxidizing one. In order to explain the observed behavior, the following model was considered. Let us divide the active area into small stripes as shown in

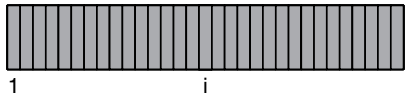

Figure 6.21: Active area of the PANI channel (real length is about 1 mm) was divided into n stripes (number of divisions was varied for different models developed for the explanation of the difference in the kinetics of the conductivity variation for different applied voltage polarities and for the non-linear rhythmic generating element (will be considered later)).

Fig. 6.21. We assume that all the materials within the same stripe behave in the same mode.

The active area in the starting time moment, before voltage application, is in a reduced insulating state due to the lithium gradient between PEO and PANI. We assume that all conductivity variations take place only in the active zone, and thus all other areas of the PANI channel (out of the active zone) remain in a conducting state. Thus, we can claim that the potential difference will be located mainly in the active zone. Let us suppose that +0.6 V was applied as the drain voltage. The profile of the applied potential distribution at the starting moment (immediately after voltage application) is shown in Fig. 6.22(a). Let us consider that the oxidation potential of thin PANI layer is the same as in a case of bulk material and is equal to +0.3 V [31]. Taking into account that the main part of the potential difference is located in the active part of the channel, we can suppose that the half of this active area, close to the D electrode, will be at the oxidation potential or higher, what is the same for the beginning of oxidation process). Thus, the transformation of zones within this half of the active area into the oxidized conducting state will occur.

After the transfer of half of the active area that was initially in the reduced insulating state into the oxidized conducting form, the redistribution of potential profile along the active area will take place. Practically, all the applied potentials will be distributed in the residual insulating area, as shown in Fig. 6.22(b). Repeating the above considerations, we will arrive to the conclusion that half of this new insulating area (again in the direction of drain electrode) will be at the potential allowing oxidation. Therefore, it will be successively transferred into the oxidized conducting state. Whenever this happens, the potential will be redistributed again, according to the situation, shown in Fig. 6.22(c), which will result in the appropriate conditions for further transition of the half length of residual reduced insulating area into the conducting state. The previous considerations were the

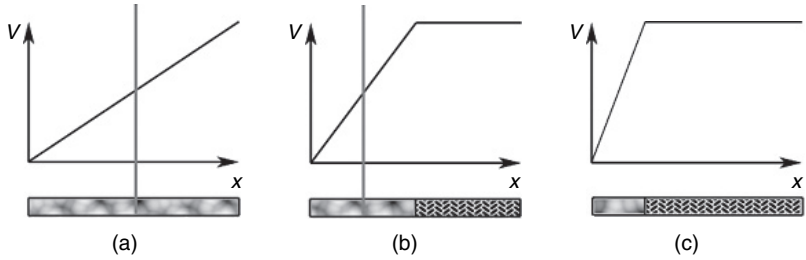

Figure 6.22: Potential distribution profile and the state (conducting-insulating) of the active area of the PANI channel after application of the positive (+0.6 V) drain potential. After the PEO stripe formation and before the application of the positive D potential, the active area is in an insulating reduced state due to the concentration gradient of Li ions. The potential is distributed linearly mainly in this insulating zone. Material, localized in the half of this area (closed to the drain electrode; the boundary is shown as a vertical line), is at a potential allowing the oxidation reaction (a). After the oxidation reaction was finished in the area marked in (a), this zone was transferred into the oxidized conducting state. Therefore, the potential distribution profile was varied and the potential difference now is located in the residual reduced area of the PANI active zone. Thus, the boundary of the film coordinate at the potential higher than the oxidation one was displaced in left (towards the source electrode) direction (indicated again as a vertical line). Therefore, the film located at the right of the line can be oxidized (b). The presented considerations can be further repeated (c) till all the active area will be transferred into the oxidized conducting state.

basis of mathematical modeling to explain the observed experimental data. The results of the modeling of conductivity variation at fixed applied bias drain voltage of +0.6 V to the described electrochemical element is shown in Fig. 6.23.

The model is based on the suggestion that each stripe, shown in Fig. 6.21, behaves independently, according to the actual potential difference between it and the reference potential level (let us recall that the gate potential is maintained at the ground level). The stripe is insulating when its potential is rather low with respect to the reference one. Conductivity variations begin to take place when this potential difference becomes more than the oxidizing potential (+0.3 V). When it happens (the potential difference is more than the oxidizing potential), the stripe begins to transfer itself into the oxidized conducting state with the kinetics, experimentally obtained for the transition of the conducting zone into the insulating state

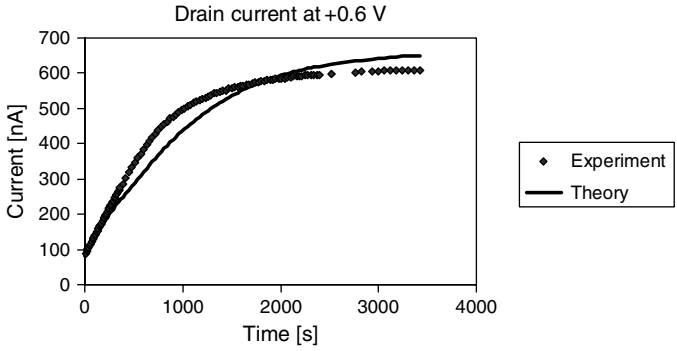

Figure 6.23: Experimental (squares) and theoretical (solid line) temporal behavior of the drain current at the constant drain voltage of 0.6 V. As it is clear from the dependences, the suggested model explain qualitatively the difference of the kinetics of the transformation of the active area of the PANI channel into the oxidized state with respect to the same transition into the reduced state at the negative potential.

(Fig. 6.20(b)). The conductivity variation and new potential distribution profile are calculated after fixed time intervals (the intervals were varied during modeling). A comparison of the calculated dependence, obtained from the model described above, and the curve of experimental results are shown in Fig. 6.23. Good coincidence of theoretical and experimental results allows to conclude that the fundamental mechanism of conductivity variation in the case of positive and negative drain potential is the same. The difference of kinetics has resulted from the difference in the relative distribution of potentials along the active zone with respect to the reference potential. In the case of negative drain voltage, the whole active under-electrolyte PANI channel area is at the reduction potential. Therefore, its transformation into the insulating state takes place simultaneously in the whole area. In the case of positive drain voltage, only the part of active zone is at the oxidizing potential in each determined time moment, which makes its transformation into the oxidized conducting state possible. As a result of this transformation, redistribution of the potential profile occurs, bringing the other zones of active area of the PANI channel to the potential allowing their oxidation.

Thus, we can conclude that the difference in the kinetics is due to the fact that, for the negative potential, the transformation from the conducting to

the insulating state takes place simultaneously for all sections of the active PANI area, while in the case of positive drain voltage, the transformation takes place gradually, shifting the boundary of the conducting area, step by step, into the direction of the source.

6.4.5. Out-of-equilibrium Element

Living means to be out of equilibrium even in fixed environmental conditions. In fact, thermodynamic equilibrium is possible only for the dead (or inorganic) matter. Probably, we can even claim that the most essential feature of the living system is the capacity to produce nonlinear rhythmic behavior even if the surrounding conditions are maintained at the fixed level. In real biological systems, such behavior can be easily recognized, for example, the breath or heart pulsing. Similar features, although not so obvious, can be observed in the case of cell splitting. Interesting features can be observed if we revisit our biological benchmark of the pond snail. In its nervous system, we can recognize one neuron, namely N1M neuron, whose behavior is absolutely different from all the other neurons [4]. This neuron, being activated once, produces a sequence of potential pulses rather long in time duration. Thus, we can consider this element as a clock generator analog. These pulses, being interfered with the signals propagating in the nervous system, result in the decision-making and the generation of adequate command signals to the executive organs. Thus, if we indent to approach the natural way of signal processing and decision-making, we need to have some elements capable of performing rhythmic response in steady-state conditions. Moreover, for our purposes, this response must be of an electrical origin. Thus, we can approach closely to the natural situation.

The important question is whether we can fabricate the element allowing such behavior starting from the polymeric electrochemical element? In this case, we are able to organize the whole system composed from similar elements. The answer is yes. The only property we need to vary is the possibility of having the reference potential not fixed anymore. The easiest way is to apply the periodically modulated potential to the gate electrode. However, if we permit such action, our system will not be a closed one anymore. Thus, we need to fix some element inside the system that will result in the variation of gate potential. The simplest element can be a capacitor, connected between the gate electrode and the ground level. In fact, in this case, the potential of the gate will be varied during element

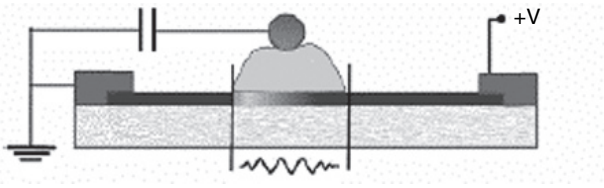

Figure 6.24: Scheme of the modified polymer-based electrochemical element capable to the rhythmic nonlinear response generation. The capacitor between the gate electrode and ground level allows the potential variation in the G electrode.

functioning. The current flow in the electrolyte will result in the accumulation of charge at the capacitor that will successively vary the gate potential. A schematic representation of the polymer-based electrochemical element is shown in Fig. 6.24.

The results of the response for both drain and gate currents at fixed applied voltage are shown in Fig. 6.25 [32].

As we can see, both currents exhibit oscillation behavior, and these oscillations are shifted in phase. This temporal shift corresponds to about 100 s delay of drain current oscillations with respect to that of the gate. This time is comparable with the characteristic time of conductivity variations recorded in simpler structures without capacitor [30]. Thus, our aim was reached. The described element can be the basis for the construction of a system capable of performing rhythmic electrical response at fixed environmental conditions. The only drawback in this element is the necessity of inserting an external component – the capacitor. However, we can avoid it considering the ability of some materials to accumulate charges. This property is well known and is used, in particular, for the construction of rechargeable battery. The first candidate that must be considered is graphite, as it is the most frequently used material for the electrodes of lithium batteries [33]. Ions of lithium can be stored in it due to their intercalation between layers of the hexagonally packed carbon atoms. Temporal behavior of the drain current for the element, similar to that shown in Fig. 6.18 with the only difference that the gate electrode is made not from the silver wire but from the graphite stripe, is shown in Fig. 6.26. As in the previous case (with the external capacitor), the oscillations are clearly visible. Thus, we can avoid any external element for having out-of-equilibrium

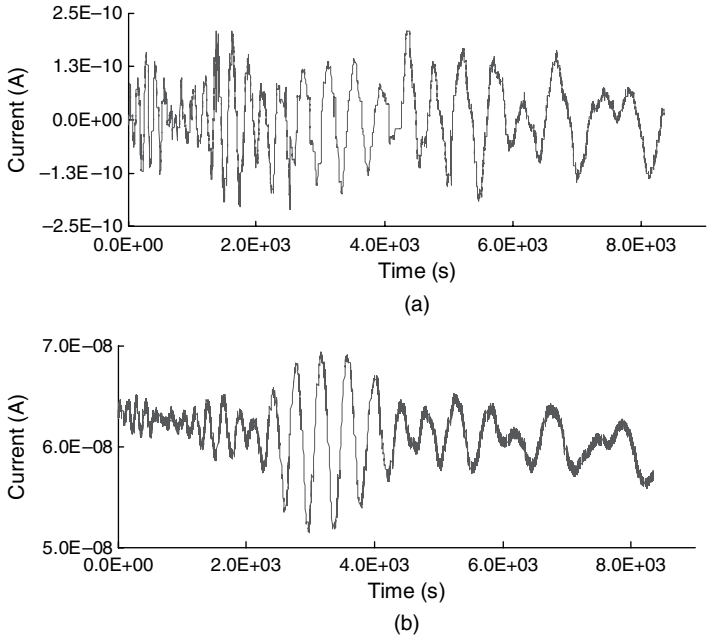

Figure 6.25: Gate (a) and drain (b) current temporal behavior of the element shown in Fig. 6.24 at fixed drain voltage of 1.0 V. The capacitance of the external capacitor in the element of Fig. 6.24 was 1.0 μF (reproduced from V. Erokhin, T. Berzina, P. Camorani, and M.P. Fontana, *Journal of Physics: Condensed Matter*, 19, 20511 (2007) with the permission from IOP Publishing Limited.)

rhythmic electrical response. However, we need to use adequate materials for the construction of the element.

In order to explain the observed results, the following model was developed. The active area of the PANI layer (under PEO area) was divided, as shown in Fig. 6.27.

It was suggested that the behavior of the material within each single stripe is the same, and all transformations due to redox reactions take place simultaneously. The total drain current is determined by Eqn 6.7:

$$I_{\mathrm{d}} = \frac{V_{\mathrm{d}}}{\sum_i R_i} + I_{\mathrm{g}} \tag{6.7}$$

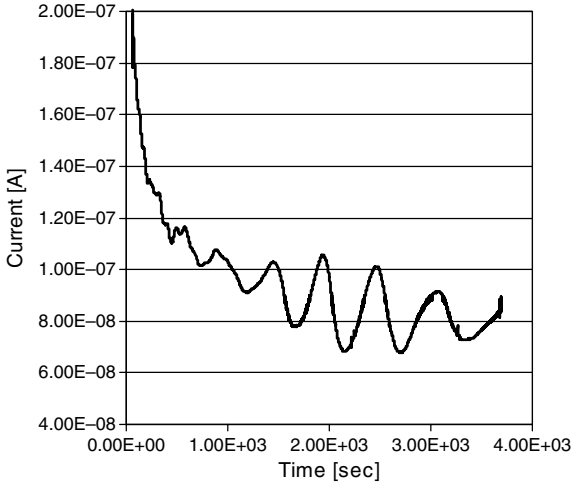

Figure 6.26: Temporal behavior of the drain current at positive (+1.5 V) voltage for the element shown in Fig. 6.18 where the gate electrode is a stripe of graphite.

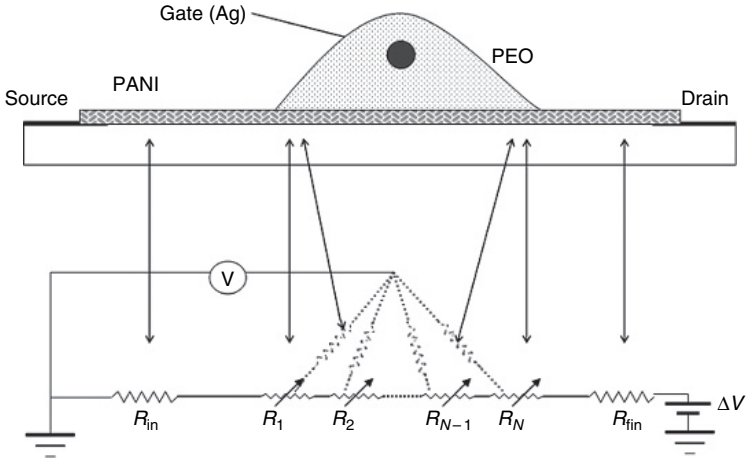

Figure 6.27: The model explaining the rhythmic output of the current. In the model we have two fixed resistances R_{in} and R_{fin} corresponding to the PANI channel zones, not covered by PEO, before (in the direction from S to D) and after the active area. The active area of the PANI channel was divided into narrow stripes. These stripes are characterized by the resistance R_N and the potential with respect to the reference one (G potential). Lines between the stripes of the active area and the G electrode represent ionic flow.

where V_d is the applied voltage, R_i is resistance of the stripe i, and I_g is the total gate current determined with Eqn 6.8:

$$I_g = \sum_{i=1}^{N} i_i^g \tag{6.8}$$

We can claim that gate current from the point *i* to the G electrode must have two components, active and passive (Eqn 6.9):

$$i_i^g = i_{i_{pas}}^g + i_{i_{act}}^g \tag{6.9}$$

The passive component of the gate current is determined by actual potential difference and resistance of the electrolyte between stripe *i* of the active area and the gate electrode. The difference in the passive gate current of different stripes is due only to the resistance difference resulting from the difference in the electrolyte length from the stripe to the gate electrode. The active component, on the other hand, must be time dependent, and we need to make some suggestions about this dependence. Being in the positive branch of potential difference, and making the voltage sweep from zero to the maximum positive voltage, the active component of gate current must begin to increase when the potential difference overcomes 0.3 V (oxidation potential) with the kinetics, experimentally measured and shown in Fig. 6.20(b). In the decreasing voltage branch, the active component of gate current begins to go to negative values when the potential difference passes 0.1 V (reduction potential).

The behavior of the resistance of each PANI stripe according its actual potential with respect to G electrode is summarized in Table 6.1.

The modeling was performed in the following way. At each time period (the temporal step was variable, starting from 1 s), the following parameters were calculated: actual potential at the gate electrode with respect to the

Table 6.1: Behavior of the resistance in each individual stripe in the active area as a function of its potential with respect to the G electrode

	$V < V_{reduction}$	$V_{reduction} < V < V_{oxidation}$	$V > V_{oxidation}$
V increasing	No changes	No changes	Decrease in the resistance
V decreasing	Increase in the resistance	No changes	No changes

ground level, the distribution of potentials between each stripe of the active area length and the gate electrode, conductivity of each stripe, and actual values of the drain and gate currents. The following parameters were varied during modeling: number of stripes, R_{in} and R_{fin} values, specific conductivity of the electrolyte, value of the external capacitor, time constants of the PANI stripe conductivity variation, and applied drain voltage. Some results of the modeling are shown in Fig 6.28. Fig. 6.28(a, b) show the dependences of drain and gate currents for the element without capacitor, respectively.

The comparison of the data, calculated within the developed model, with the experimental results (Fig. 6.19(a, b)) concludes that the suggested approach has permitted to perform a rational qualitative explanation of the observed phenomenon.

Figure 6.29 represents the temporal behavior of the gate current at fixed applied drain voltage for the element containing the capacitor.

As we can see, the model forecasts the oscillating behavior of the system at fixed applied potential. It is interesting to note that, according to the model, the appearance of oscillations depends strongly on the conditions of the junctions. The value of the capacitor, applied voltage, and mutual ratio of the active area resistance with respect to the rest zones of the PANI channel are very critical. This fact is also in agreement with experimentally observed data. In some cases, the model did not allow the appearance of oscillations, which is also in agreement with the experimental data. In fact, not all realized structures revealed oscillating behavior.

The described model was based on the formal consideration of different electrical and electrochemical processes occurring in the fabricated device. However, the obtained results can be explained using the other approach that was successfully applied for the explanation of cyclic chemical reactions, such as Belousov–Zhabotinsky (BZ) reaction, as there are several features common to these reactions and our system. The BZ reaction describes a complex behavior of the system, very far from equilibrium [34]. At least three reactions (much more in real particular systems) must occur. An example of the reaction is shown in the Eqn 6.10:

$$\begin{aligned}
BrO_3^- + Br^- &=> HBrO_2 + HOBr \ \text{Rate} = k_1[BrO_3^-][Br^-] \\
HBrO_2 + Br^- &=> 2HOBr \ \text{Rate} = k_2[HBrO_2][Br^-] \\
BrO_3^- + HBrO_2 &=> 2HBrO_2 + 2Ce^{4+} \ \text{Rate} = k_3[BrO_3^-][HBrO_2] \\
2HBrO_2 &=> BrO_3^- + HOBr \ \text{Rate} = k_4[HBrO_2]^2 \\
B + Ce^{4+} &=> 1/2f Br^- \ \text{Rate} = k_c[Z][Ce^{4+}]
\end{aligned} \quad (6.10)$$

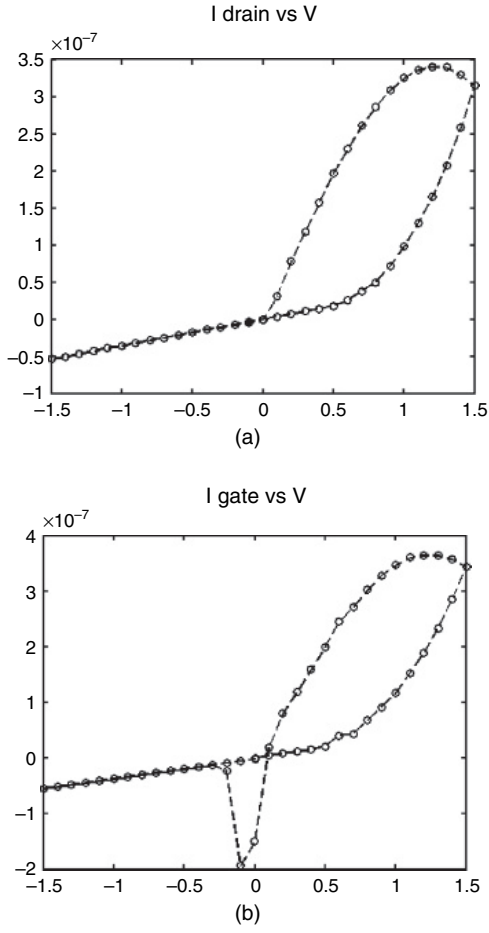

Figure 6.28: Result of the modeling of the dependence of the drain (a) and gate (b) currents on the applied drain voltage. These data were obtained without external capacitor.

Cyclic behavior can be observed if at least three reactions go simultaneously in the system. The first of these reactions must be an oxidation reaction. The second one must be a reduction reaction with the production of the catalyzer. Therefore, this reaction is autocatalytic. The third reaction closes the loop inhibiting the catalyzer. Visually, this reaction demonstrates the periodic changes of the solution color. Prigogine had evaluated the

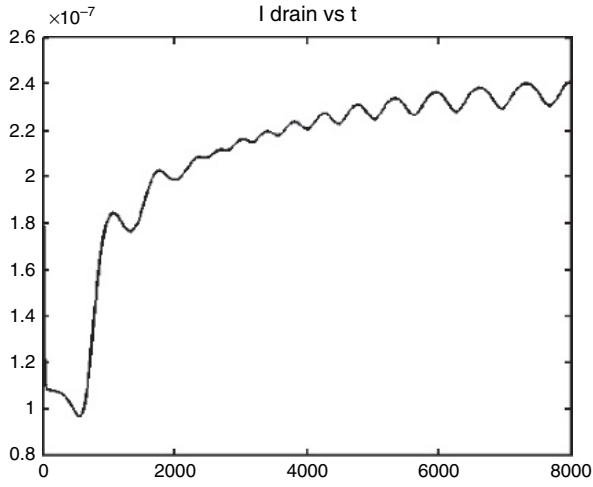

Figure 6.29: Temporal behavior of the drain current of the element with the external capacitor of 1 μF at fixed (+1.5 V) drain voltage. Period, amplitude and duration of the oscillations were found to be strongly dependent on the parameters of the model.

discovery of such reactions as an extremely important one, as it was the first experimental confirmation of nonequilibrium thermodynamics [3]. Similar processes must also occur in living systems. However, all literatures dealing with cyclic chemical reactions report mainly the rhythmic variations of the optical (color) or viscoelastic properties of the reaction media. On the other hand, in the nervous systems of living organisms, we need to have oscillating output of the electrochemical parameters, as it was previously considered for the N1M neuron of pond snail.

If we consider our element with the capacitor, exhibiting the oscillating behavior, we will find similar features with BZ reaction. First of all, the variations of conductivity in the active area of the PANI channel are due to the oxidation and reduction processes. In parallel, we have the variation of reference potential (charging–discharging of the capacitor) and the variation of the profile of the applied drain voltage distribution along the active area coordinate. The latter two processes can be considered as the production/inhibition of the catalyzer. Thus, processes taking place in our element and resulting in the rhythmic electrical output are characterized by features necessary for the BZ reaction to occur. Therefore, we can try to apply the formalism developed for BZ reactions to our systems.

BZ reactions can be described using Lotka–Volterra equations. These equations were previously used for the description of closed ecological systems, such as predator–victim system. The system of equations is shown in Eqn 6.11.

$$\frac{dX}{dt} = aX - bXY$$
$$\frac{dY}{dt} = -dY + hXY \tag{6.11}$$

Y is the population of predators and X is the population of victims. We assume that all victims are eaten by predators. Therefore, the rate of variation of victims is proportional (positively) to the actual population value (more new members may be born) and it is (negatively) proportional to the probability of their direct contact with predators (the product of X and Y). In the case of predator population variation rate, we must consider the death of individuals, which is proportional to the actual population, and the birth of new ones, which depends on the availability of food and, therefore, on the probability of the contact of predator/victim pairs (again the product of X and Y). These assumptions result in Eqn 6.11, which describes the behavior of such closed system. The solution of equations is shown in Fig. 6.30.

As we can see, there is an oscillating behavior of both populations, shifted in time one from the other. It is important to note that the solution is

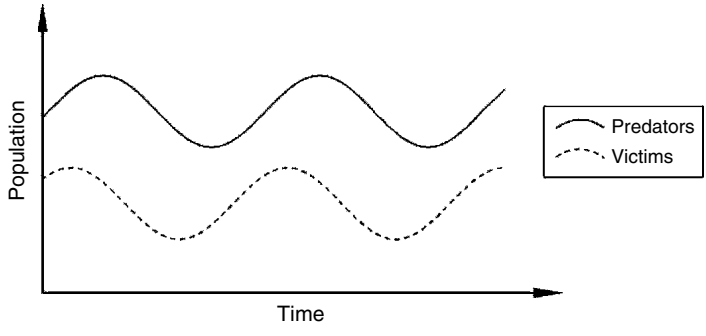

Figure 6.30: Graphic representation of the solution of Lotka-Volterra equations, describing the temporal variation of the predator and victim populations. The solution depends strongly on the initial state of the system and gives the stable solution with oscillation of both populations shifted in phase with respect to each other.

extremely dependent of the initial conditions. For some cases, we can have the behavior without oscillations, resulting in the complete disappearance of the predator population (or both of them, if victims were eaten before).

This approach was applied successfully for the description of the BZ reaction. The appropriate equations are presented in Eqn 6.12:

$$\begin{aligned}\frac{dX}{dt} &= k_3AY - k_2XY + k_5AX - 2k_4X^2 \\ \frac{dY}{dt} &= -k_3AY - k_2XY + 0.5k_6BZ \\ \frac{dZ}{dt} &= 2k_5AX - k_6BZ\end{aligned} \tag{6.12}$$

The equations connect the variation of the amount of three compounds involved into the reaction. The solution of these equations gives the oscillating behavior of these compounds (used coefficients are related to the time constants of reactions).

A comparison of our oscillations with those in the case of BZ reaction gives several points of coincidence. First, in both cases, redox reactions are the driving forces of system behavior. Second, in the case of BZ reaction in its classic form, the essential part is responsible for the cyclic behavior due to the production and inhibition of the catalyzer. In our case, two processes can play the same role. First, we have the variation of the reference potential due to the charge accumulation or release at the capacitor (or graphite stripe as G electrode) of the structure. Second, we have continuous redistribution of the applied potential profile along the active area with respect to the variable reference potential. Therefore, we can assume that the same formalism, based on the Lotka–Volterra equations, can be applied for describing the behavior of our system.

Formally, the equations can be written as those in system (Eqn 6.13):

$$\begin{aligned}\frac{dA}{dt} &= k_1I_gB - k_2A \\ \frac{dB}{dt} &= -k_3I_gA - k_4B \\ \frac{dV_g}{dt} &= \frac{I_g}{C}\end{aligned} \tag{6.13}$$

where A and B are the amounts of oxidized and reduced PANI in the active area; C is the value of capacitance and V_g is the actual gate potential at

certain moment. From the first two equations, we can understand that the variation of the amount of oxidized and reduced matter in the active area is proportional to the reduced and oxidized matter amounts, respectively, that can be transformed into other form. The proportional coefficient is equal to the gate current as it is responsible for bringing the carriers necessary for these reactions. The latter terms in these equations indicate that the already oxidized (or reduced) material cannot be oxidized (reduced) anymore. Unfortunately, in its present form, Eqn 6.13 cannot be solved, as the third one has a parameter absent in the first two equations. Therefore, the third equation must be rewritten to the form shown in Eqn 6.14:

$$\frac{dI_g}{dt} + \frac{dB}{dt} = \frac{k_8 I_g}{C} \tag{6.14}$$

Thus, we have a system of three differential equations with three independent parameters. A comparison of the system with that already applied for the description of the cyclic behavior of chemical reactions reveals their similarity. Therefore, even their solutions must be similar.

The last result seems to be extremely important. Up to now, all observed cyclic behaviors were registered on the variation of optical or viscoelastic properties of the reaction medium. Instead, in order to mimic the processes in biological systems, we need to have the rhythmic output of electrical characteristics. Thus, the presented data have provided a direct observation of the behavior, which can be considered as a model for intrinsic processes within living systems, allowing to avoid decay to equilibrium.

6.5. Demonstrative Circuits

6.5.1. Simple Mimicking Element

The simplest utilization of the described electrochemical element in order to mimic the behavior of biological systems was performed considering again the pond snail digestion nervous system as a natural benchmark. The learning in snail was studied in detail by neurophysiologists and the appropriate model of this process was developed [3]. Touching the snail lips with sugar was used as the 'training' action (supervised learning). After several acts of this 'training', the snail begun to open its mouth and started the digestion process after touching the mouth even without sugar. In the case of the real animal, 6 neurons are involved in this learning action. Probably, this is due to the fact that same neurons can be used for the other

processing events. The same feature can be realized, as we will see, using only one electrochemical element described in earlier sections. In order to mimic the learning behavior of pond snail, the realized circuit must contain two inputs, corresponding to the main (touching) and training (feeding) signals. The circuit must also contain one output, performing the executive signal (opening of the mouth and start of the digestion process). This last signal must be more than some threshold level; otherwise it will be not able to start executive organs. Action of the main input signal itself must not provide enough intensity of the output signal. Instead, when both, main and training, signals act together, the executive signal must be significantly increased, and, after such action, application of only the main input signal must provide output signal with a higher intensity.

The scheme of the circuit used for mimicking this learning behavior [35] is shown in Fig. 6.31.

The summator plays partially the role of the neuron body, providing at its output the sum of the two applied voltages. The circuit also contains two inputs corresponding to the main (touch) and teaching (taste) signals (both of them are +0.3 V) and one output (current between S electrode and the ground), providing a signal to executive elements. Let us suppose that the threshold level of the output signal, enough for performing executive actions, is 0.2 μA. Temporal characteristics of the output current behavior of the circuit is shown in Fig. 6.32.

Let us consider the learning imitation performed by the circuit shown in Fig. 6.31. Initially (0 V applied), the electrochemical element PANI active area is in reduced insulating state. Point A of the Fig. 6.32 corresponds to the application of the main signal, imitating the touch event. As the active area is still in the reduced insulating state, the value of the output

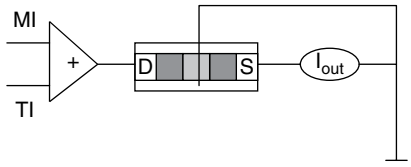

Figure 6.31: Electrical circuit used to mimic learning behavior of the pond snail. Main (MI) and training (TI) inputs (each of them was +0.3 V), imitating taste and touch signals of the snail sensoristic system, are connected to the summator. Sum of the MI and TI is applied to the D electrode of the polymeric electrochemical element. Current measured between the S electrode and the ground was the output signal.

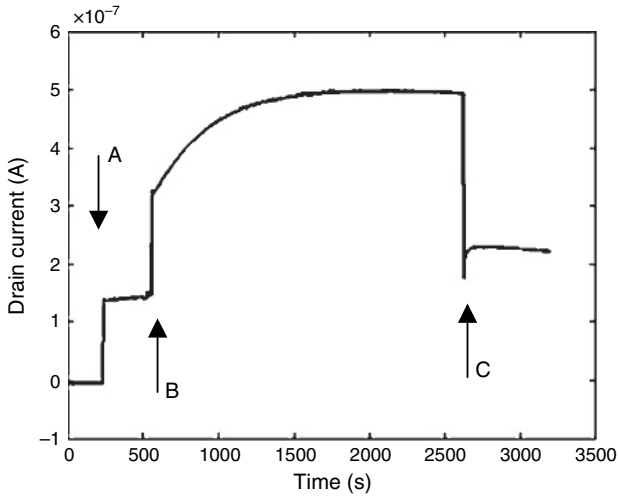

Figure 6.32: Temporal behavior of the circuit shown in Fig. 6.31. Main input (touch) was applied to the circuit at the point A. The application of this signal has resulted in the output current of 0.14 μA, that is below the threshold level. TI (taste) was applied together with MI at the point B. The action has resulted in the increase of the element conductivity coming to the saturation in about 2000 s. In the point C the TI was switched off and only MI was applied to the circuit. As a result, we have observed the output current of 0.23 μA, that is higher than the threshold level and, therefore, can perform execution actions.

current is rather low (0.14 μA) and, therefore, cannot activate executive mechanism (we have determined the threshold level to be equal to 0.2 μA). Training signal (taste imitation) is applied at the moment corresponding to point B in the figure. It results in the beginning of the continuous increase of the output current value, arriving to the saturation. This behavior is due to the transformation of the active area of the PANI channel into its oxidized conducting state. After switching off the teaching signal (point C), the active area is still in oxidized state and the output current value, corresponding to the only main input, is about twice more with respect to that before the training event and, therefore, is higher than the threshold level allowing the activation of the executive mechanisms.

It is interesting to note that even this simplest circuit has demonstrated the necessity of parallel working of processing and memorizing events. In fact, during the signal processing, learning took place when the properties of

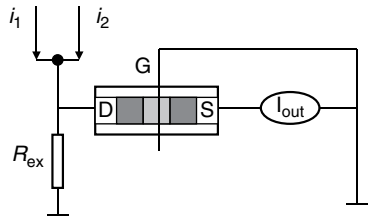

Figure 6.33: Scheme of the circuit capable for learning. Summator is substituted with the inputs from two current generators.

the active area of the PANI channel were modified and these modifications were saved and used for the successive signal processing.

This simple scheme has demonstrated the possibility to mimic simple learning behavior with artificial circuits, using the described electrochemical polymeric element as the main node. In this circuit, we have to use the external electrical element – summator. Probably, it is possible to avoid it if we use current generators as the input signals instead of fixed voltages, as it was used in the earlier circuit. Scheme of the connections in this case is shown in Fig. 6.33.

In this case, the potential on the input (D electrode) of the electrochemical element will depend on the potential difference on the loading resistor R_{ex}, that can be realized also from PANI or other conducting polymer and integrated in the element. It is important to make the value of the resistance R_{ex} more much less than that of the electrochemical element both in conducting and insulating states. Thus, we will be able to consider that the drain electrode is loaded only with the potential. We will have the increased potential on the electrochemical element when both, main and training, currents are applied. Thus, as in the previous case, learning will take place when the active area of the PANI channel will be transferred into the oxidized conducting state, and this state will provide the higher output signal even after the training signal will be switched off.

6.5.2. Adaptive Circuit

Next step is to demonstrate the possibility of the construction of more complicated circuit [36] that is capable to learn according the external training process (supervised learning). The scheme of such circuit is shown in Fig. 6.34.

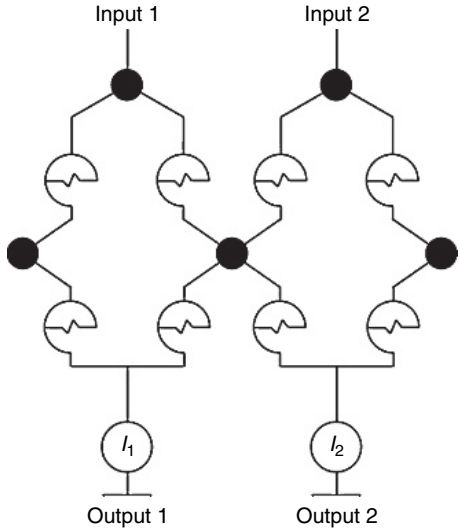

Figure 6.34: Adaptive circuit realized from eight polymeric electrochemical elements and containing two inputs (voltages) and two outputs (currents).

The circuit contains two input and two output electrodes. Eight polymeric electrochemical elements provide different signal pathways from each input to each output. Potentials of 1.0 V were used as input, while currents measured between S electrodes and the ground were taken as output signals. Initially, the signal was applied to the first input electrode and both output currents were registered and analyzed. The results of the measurements are shown in Table 6.2.

As can be seen from the table, the properties of individual electrochemical elements, constituting the circuit, have resulted in the fact that the application of the signal to the first input resulted in the higher signal at the first output. It is necessary to note that such behavior was obtained

Table 6.2: Results on the adaptive behavior of the circuit shown in Fig. 6.34

	Out 1 (nA)	**Out 2 (nA)**
Before training	150	31
After training	45	144

occasionally, as elements, constituting the circuit, were not identical. Let us suppose that we want to train the system (supervised learning) to provide higher current value at the second output when the signal is applied to the first input. In order to have such possibility, we need to recall the characteristics of the individual element, shown in Fig. 6.20(b). As it was claimed before, these characteristics can be considered as key properties for performing external training (supervised learning). Thus, we need to apply inverted voltage to the input–output pairs where we want to decrease occasionally appeared high conductivity. Therefore, the external training of the circuit was performed in the following way. Positive voltage was maintained between the first input and the second output electrodes, while it was negative between the first input and the first output simultaneously. Such action was performed in 5 min. After this, the circuit was tested again. Here, the signal was applied to the first input and both output signals were measured and analyzed. The results of the measurements are also shown in Table 6.2. As can be seen, the external training process turned out to be successful. We were able to teach the system that the application of the signal to the first input must provide a higher second output signal. It is very important to note that no modification of the circuit was performed. Training was done only by the application of the adequate potentials. As in the case of simple mimicking circuit (previous section), the proposed network combines processing function with memory properties. Being trained, the circuit memorizes the properties of constituting elements, and these properties are used during successive signal processing. The other important characteristic of the circuit is its flexibility and possibility of multiple adaptations. Properties of the elements and, therefore, the whole network can be further modified by successive training actions. We can suppress the value of the first output more, we can return to the initial situation or we can suppress the value of the second output signal more.

This simple circuit has demonstrated the validity of the chosen approach of the adaptive networks realization. Of course, really complex systems must contain much more elements with numerous mutual interconnections. Therefore, following the main road of the circuit fabrication, each discrete element must be miniaturized and special technological approaches must be developed, allowing the fabrication of the entire circuit, similar to the current situation in semiconductor micro- and nanoelectronics industry. However, alternative approaches can be developed. These approaches must follow bottom-up way of the device realization based on the self-assembling. We can expect that they will allow the fabrication of networks with a statistical distribution of functional elements. If the network will

be complex enough, we can expect the formation of adequate functional elements providing different signal pathways, connecting numerous input and output electrodes. Then, the network must be trained in order to realize some preferential pathways of the signal propagation. After such training, we can expect that the system will modify its own properties during functioning according to the acquired experience (non-supervised learning). The next part is dedicated to the description of the method of fabrication of simple statistical network based on the fibers of conducting polymers and solid electrolytes.

6.5.3. Perspectives: Network of Polymer Fibers

The capacity of PEO to form fibers is well known [37]. One of the main methods of the fiber formation is based of the application of electric field. The scheme of the electric field-assisted fiber formation process is shown in Fig. 6.35.

PEO solution was placed in the container with a capillary outlet. The support, where fibers were planned to be deposited, was placed at 5–10 cm from the PEO container and the voltage value in the range of 5–20 kV was applied between them. Typical example of the fibrillar structure, obtained by this method is shown in Fig. 6.35(b). However, for our reasons (formation of statistical network allowing adaptive behavior) this approach seems to be not completely adequate. First, it allows to form fibers of only one compound. Instead, we need to have fibers of at least two different polymers. Second, we can obtain 2D organization of fibers; but for the

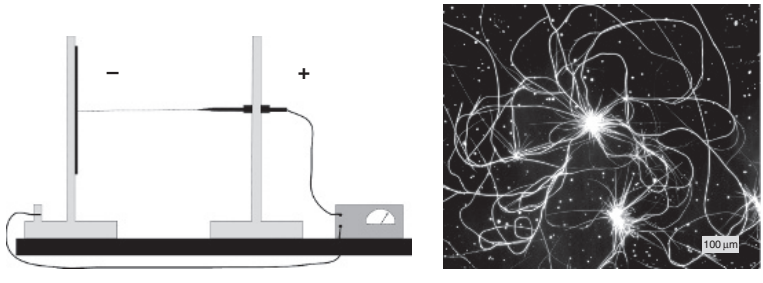

Figure 6.35: Scheme of the electric-field assisted polymer fiber deposition (a) and image of the realized structure (b).

realization of really complicated network, it is better to have 3D structures. Therefore, alternative approach was performed. This approach was based on the capability of PEO to form fiber structure after exposing its solution to vacuum treatment by rather fast pumping [38].

The following procedure was performed. As the first step, drop of PEO solution in water (concentration range 5–20 mg/ml) was casted on the solid support and placed in vacuum chamber with successive pumping till 10^{-2} Torr during 10–20 minutes. A 3D fibrillar structure was formed as a result of such treatment. This PEO network was then used as a template for the formation of superimposed PANI fiber structure. For these reasons, PANI solution (0.2–0.5 mg/ml in NMP) was casted onto the formed structure and the same vacuum treatment was repeated. Optical images of the formed structure are shown in Fig. 6.36.

Of course, optical microscopy does not allow to estimate fiber diameter when it is in a submicron range. Therefore, TEM imaging was performed. Representative image of fibrillar structure is shown in Fig. 6.37.

Analysis of the images concludes that fibers of different diameter (from some tens of nanometers till several microns) and length (up to several mm) were formed. Also, a 3D organization of the formed network is clearly visible. Thus, the statistical network with occasional crossing of fibers of two necessary materials (conducting polymer (PANI) and solid electrolyte (PEO)) is possible to realize. The key question is whether this network is complex enough to provide the required configurations in a statistical way, similar to those fabricated in a predefined way during discrete single electrochemical element preparation?

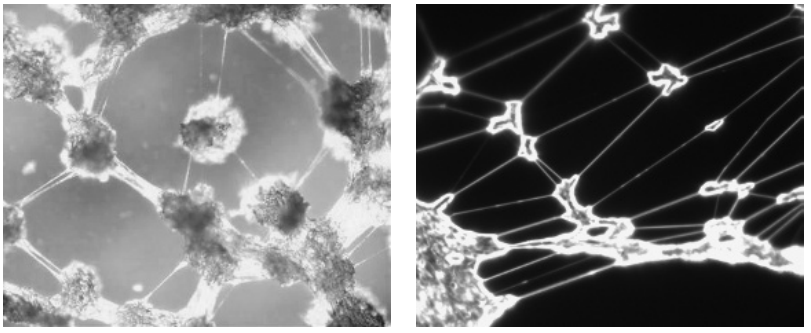

Figure 6.36: Optical images of different realized structures of PEO–PANI fibers [37].

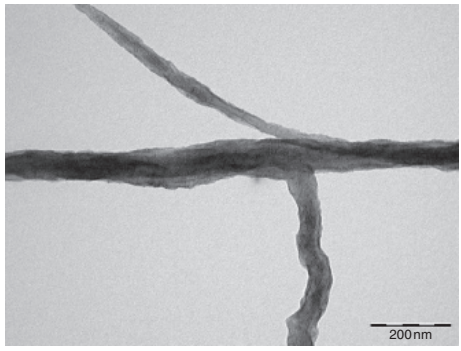

Figure 6.37: TEM image of the fibrillar structure.

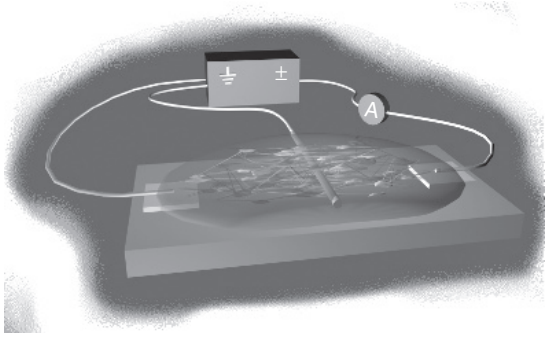

Figure 6.38: Model structure for testing properties of the network formed from PEO and PANI fibers. Gate electrode (silver wire) was placed into the network and was used to provide the reference potential (ground level).

In order to check this hypothesis, the following structure, shown in Fig. 6.38, was realized and tested.

PEO drop was casted onto the surface of glass support, where two metal electrodes, that will be used as source and drain electrodes, respectively, were already evaporated. Gate (reference) electrode (silver wire) was placed into the PEO drop before the vacuum treatment. Thus, after the pumping, the reference electrode was inside the fibrillar network, and was maintained there after the formation of successive PANI fiber structure in the same way as it was described earlier for PEO. If the network is complex enough, we can expect the existence of the statistically formed configurations, where PANI and PEO fibers are connected to the reference electrode (silver wire),

forming junctions similar to the single electrochemical element (Fig. 6.18). If this is the case, then electrical characteristic of such structure must reveal behavior, similar to that of discrete element (as that shown in Fig. 6.19). In particular, rectifying characteristic must be observed in the appropriate configuration. Let us refer once more to the scheme shown in Fig. 6.38. As in the case of the discrete element, source and reference electrodes were connected to the ground potential, while the voltage was applied to the drain electrode and the current value was registered. Also, in this case, current measurements were taken after 1 min delay after the voltage application in order to equilibrate electrochemical processes. The resultant voltage-current characteristic is shown in Fig. 6.39.

Expected rectifying behavior is clearly visible in the figure, confirming, therefore, the possibility of the realization of necessary working configurations of functional units in a statistical way. This result seems to be very important. In fact, it allows to believe that even very complicated networks can be realized in a statistical way, bypassing time-consuming and complicated lithography processes at each stage of the structure formation. It is worth to mention that the sizes of the elements of the formed structure are comparable with sizes of elements of the nervous systems of living organisms.

However, the presented results have demonstrated only the principal applicability of the statistical fibrillar structure approach for the adaptive network realization. Of course, we are only in the beginning stage and this work must be continued. One of the possible ways of this approach

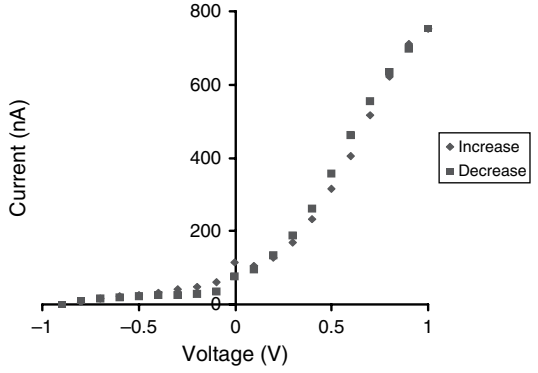

Figure 6.39: Voltage-current characteristics measured on the statistically formed fibrillar network in a configuration shown in Fig. 6.38 [37].

continuation will be based on the utilization of the silver wire networks as a framework for the fibrillar structure formation. The network will contain a large number of input and output electrodes (gold wires, for example) connected to the structure. After the formation, the network will be trained, suppressing undesirable input–output pathways. The choice of the pathways that must be suppressed will be taken attributing to each input the feature of some sensoristic element from living systems (vision, smell, touch, etc.) and to each output some executive organs (muscles, digestion, etc.).

6.6. Conclusions

In this chapter, I have tried to draw some perspective lines to develop for the construction of adaptive networks. Of course, we are in a very beginning of such works. If we make a comparison with electronics, we are still in a pre-silicon epoch. Further developments can result in the utilization of others, more effective materials, methods of the structures formation, and architecture of elements and networks. However, even the already available results are rather promising, the attempt to make the system whose working principals and main properties are similar to those of biological systems – ideally working adaptive networks – also seems to be important.

We can underline the importance of the realization of polymeric electrochemical element that is supposed to be used as a key node of the system. This synapse analog uses similar electrochemical principles that are the basis for the functioning of nervous system. The other important feature of the element is that it combines the functions of the processor with those of the memory. As we have underlined in the previous sections, this feature must be a very important property of the system that is planned to perform adaptive behavior.

The other important element that has been realized is the auto-generating element that must prevent the whole system from the equilibrium. There are also biological analogs for this element. Moreover, it seems that without such elements, capable of performing rhythmic nonlinear responses even in the fixed environmental conditions, biological organisms cannot exist.

Simple model circuits have demonstrated the possibility of the construction of systems capable to learn. Finally, as the possible alternative way of the adaptive network realization, it was suggested the approach, based on the realization of statistical networks of fibers of different polymers.

Acknowledgement

I wish to thank Filippo Romani and Konstantin Erokhin for their help in preparation of the artworks.

References

[1] Hebb, D.O. (1949) *The Organization of Behavior: A Neuropsychological Theory, 2nd edn (1961)*. New York: Wiley and Sons.

[2] Schrödinger, E. (1944) *What is Life? Physical Aspect of the Living Cell*. Cambridge University Press.

[3] Glansdor, P. and Prigogine, I. (1971) *Thermodynamic Theory of Structure, Stability and Fluctuations*. New York: John Wiley.

[4] (a) Feng, J.F. (ed.) (2003) *Computational Neuroscience: A Comprehensive Approach*. Boca Raton: Chapman and Hall/CRC Press. (b) Feng, J.F., Jost, J. and Qian, M.P. (eds) *Networks: From Biology to Theory*. Berlin, New York: Springer-Verlag.

[5] Carnevale, N.T. and Hines, M.L. (2006) *The Neuron Book*. Cambridge: Cambridge University Press.

[6] (a) Caudill, M. (1989) *Neuron Networks Primer*. San Francisco: Miller Freeman Publications. (b) Takefuji, Y. (1992) *Neural Network Parallel Computing*. Berlin, New York: Springer. (c) Wasserman, P.D. (1993) *Advanced Methods in Neural Computing*. New York: Van Nostrand Reinhold. (d) Hagan, M.T., Demuth, H.B. and Beale, M.H. (1996) *Neural Network Design*. Boston: PWS Publishing. (e) Parks, R.W., Levine, D.S. and Long, D.L. (1998) *Fundamentals of Neural Network Modeling: Neurophychology and Cognitive Neuroscience*. Cambridge: MIT Press.

[7] Minsky, M. and Papert, S. (1969) *Perceptrons: An Introduction to Computational Geometry*. MIT Press, Cambridge.

[8] McCulloch, W.S. and Pitts, W. (1943) *Bull. Math. Biophys*., **5**, 115–33.

[9] (a) Ulman, A. (1991) *An Introduction to Ultrathin Organic Films*. Boston: Academic Press. (b) Roberts, G. (1990) *Langmuir–Blodgett Films*. New York: Plenum Press. (c) Tredgold, R.H. (2004) *Order in Organic Thin films*. Cambridge: Cambridge University Press.

[10] (a) Kawakatsu, T., Kawasaki, K., Furusaka, M. et al. (1994) *J. Phys. Condensed Matt*., **6**, 6385–408. (b) Gomez-Lopez, M., Preece, J.A. and Soddart, J.F. (1996) *Nanotechnology*, **7**, 183–92. (c) Fray, H., Lach, C. and Lorenz, K. (1998) *Adv. Mater*., **10**, 279–93. (d) Abetz, V. and Goldacker, T. (2000) *Macromol. Rapid Commun*., **21**, 16–34. (e) Gale, P.A. (2000) *Phylos. Trans. Royal Soc. London A*, **358**, 431–53. (f) Kawaguchi, H. (2000) *Progr. Polymer Sci*., **25**, 1171–210 (2000). (g) Vogtle, F., Gestermann, S., Hesse, R. et al. (2000) *Progr. Polymer Sci*., **25**, 987–1041. (h) Sherrington, D.C. and Taskinen, K.A. (2001) *Chem. Soc. Rev*., **30**, 83–93. (i) Okada, M. (2001)

Progr. Polymer Sci., **26**, 67–104. (j) Motta, N. (2002) *J. Phys. Condens. Matt*., **14**, 8353–78. (k) Mamula, O. and A. von Zelewsky (2003) *Coord. Chem. Rev*., **242**, 87–95. (l) Castelvetro, V. and De Vita, C. (2004) *Adv. Colloid Interface Sci*., **108**, 167–85. (m) Ratner, B.D. and Bryant, S.J. (2004) *Ann. Rev. Biomed. Engineer*., **6**, 41–75. (n) Segalman, R.A. (2005) *Mater. Sci. Engineer. R*, **48**, 191–226. (o) Ishi-i, T. and Shinkai, S. (2005) *Topics Curr. Chem*, **258**, 119–60. (p) Choi, H.S. and Yui, N. (2006) *Progr. Polymer Sci*., **31**, 121–44. (q) Borovkov, V.V. and Inoue, Y. (2006) *Topics Curr. Chem*., **265**, 89–146. (r) Nishio, Y. (2006) *Adv. Polymer Sci*, **205**, 97–151.

[11] (a) Leger, L. and Joanny, J.F. (1992) *Rep. Progr. Phys*., **55**, 431–86. (b) Arslanov, V.V. (1992) *Adv. Colloid Interface Sci*., **40**, 307–70. (c) Nalwa, H.S. and Kakuta, A. (1992) *Appl. Organomet. Chem*., **6**, 645–78. (d) Möhwald, H. (1993) *Rep. Progr. Phys*., **56**, 653–85. (e) Blinov, L.M. (1996) *J. Nonlin. Opt. Phys. Mater*., **5**, 165–87. (f) Petty, M.C. (2006) *Mater. Sci. Technol*., **7**, 725–37. (g) Tsukruk, V.V. (1997) *Progr. Polymer Sci*., **22**, 247–311. (h) Diederich, F. and Gomez-Lopez, M. (1999) *Chem. Soc. Rev*., **28**, 263–77. (i) Ashwell, G.J. (1999) *J. Mater. Chem*., **9**, 1991–2003. (j) Palacin, S. (2000) *Adv. Colloid Interface Sci*., **87**, 165–81. (k) Basu, J.K. and Sanyal, M.K. (2002) *Phys. Rep*., **363**, 1–84. (l) McCreery, R.L. (2004) *Chem. Mater*., **16**, 4477–96. (m) Metzger, R.M. (2004) *Chem. Rec*., **4**, 291–304. (n) He, L.Z., Dexter, A.F. and Middelberg, A.P.J. (2006) *Chem. Engineer. Sci*., **61**, 989–1003. (o) Ariga, K., Nakanishi, T. and Michinobu, T. (2006) *J. Nanosci. Nanotechnol*., **6**, 2278–301.

[12] Troitsky, V., Berzina, T., Shchukin, D. et al. (2004) *Colloids and Surfaces A*, **245**, 163–8.

[13] Kimura, K., Yao, H. and Sato, S. (2006) *Synth. React. Inorg. Metal Org. Nano Metal Chem*., **36**, 237–64.

[14] (a) Haussling, L., Knoll, W., Ringsdorf, H. et al. (1991) *Makromol. Chem. Macromol. Symp*., **46**, 145–55. (b) Spinke, J., Liley, M., Schnitt, F.J. et al. (1993) *J. Chem. Phys*., **99**, 7012–9. (c) Avila-Sakar, A.J. and Chui, W. (1996) *Biophys. J*., **70**, 57–68. (d) Edmiston, P.L. and Saavedra, S.S. (1998) *J. Am. Chem. Soc*., **120**, 1665–71. (e) Larsson, C., Rodahl, M. and Hook, F. (2003) *Anal. Chem*., **75**, 5080–7. (f) Zheng, M. and Huang, X.Y. (2004) *J. Am. Chem. Soc*., **126**, 12047–54. (g) Liu, Z. and Amiridis, M.D. (2005) *J. Phys. Chem. B*, **109**, 16866–72. (h) Wenz, G. and Liepold, P. (2007) *Cellulose*, **14**, 89–98.

[15] (a) Langmuir, I. (1916) *J. Am. Chem. Soc*., **38**, 2221–95. (b) Langmuir, I. (1917) *J. Am. Chem. Soc*., **39**, 1848–906. (c) Langmuir, I. (1917) *J. Franklin Inst*., **184**, 445–6. (d) Langmuir, I. (1917) *Proc. Natl. Acad. Sci. USA*, **3**, 251–7. (e) Langmuir, I. (1920) *Trans. Faraday Soc*., **15**, 62–74. (f) Langmuir, I. and Langmuir, D.B. (1927) *J. Phys. Chem*., **31**, 1719–31. (g) Langmuir, I. (1933) *Chem. Rev*., **13**, 147–91. (h) Langmuir, I. (1934) *J. Franklin Inst*., **218**, 143–71. (i) Langmuir, I. (1938) *Science*, **87**, 493–500. (j) Langmuir, I. (1938) *J. Am. Chem. Soc*., **60**, 1190–4. (k) Langmuir, I. and Waugh, D.F. (1940) *J. Am. Chem. Soc*., **62**, 2771–93.

[16] (a) Blodgett, K.B. (1934) *J. Am. Chem. Soc*., **56**, 495. (b) Blodgett, K.B. (1935) *J. Am. Chem. Soc*., **57**, 1007–22. (c) Blodgett, K.B. and Langmuir, I. (1937) *Phys. Rev*., **51**, 964–82. (d) Blodgett, K.B. (1937) *J. Phys. Chem*., **41**, 975–84. (e) Blodgett, K.B. (1939) *Phys. Rev*., **55**, 391–404. (f) Blodgett, K.B. (1940) *Phys. Rev*., **57**, 921–4.

[17] (a) Langmuir, I. and Schaefer, V.J. (1936) *J. Am. Chem. Soc*., **58**, 284–7. (b) Langmuir, I. and Schaefer, V.J. (1937) *Science*, **85**, 76–80. (c) Langmuir, I. and Schaefer, V.J. (1937) *J. Am. Chem. Soc*., **59**, 1406. (d) Langmuir, I., Shaefer, V.J. and Sobotka, H. (1937) *J. Am. Chem. Soc*., **59**, 1751–9. (e) Langmuir, I and Schaefer, V.J. (1937) *J. Am. Chem. Soc*., **59**, 1762–3. (f) Langmuir, I. and Schaefer, V.J. (1937) *J. Am. Chem. Soc*., **59**, 2400–14. (g) Langmuir, I. and Schaefer, V.J. (1938) *J. Am. Chem. Soc*., **60**, 1351–60. (h) Langmuir, I. and Schaefer, V.J. (1938) *J. Am. Chem. Soc*., **60**, 2803–10. (i) Langmuir, I. and Schaefer, V.J. (1939) *Chem. Rev*., **24**, 181–202. (j) Langmuir, I. and Schaefer, V.J. (1943) *J. Franklin Inst*., **235**, 119–62.

[18] (a) Bücher, H., Wiegand, J., Sanavely, B.B. et al. (1969) *Chem. Phys. Lett*., **3**, 508–11. (b) Kuhn, H. (1970) *J. Chem. Phys*., **53**, 101. (c) Inacker, O., Kuhn, H., Bücher, H. et al. (1970) *Chem. Phys. Lett*., **7**, 213–8. (d) Bücher, H. and Kuhn, H. (1970) *Chem. Phys. Lett*., **6**, 183–5. (e) Mann, B., Kuhn, H. and Szenpály, L.v. (1971) *Chem. Phys. Lett*., **8**, 82–4. (f) Mann, B. and Kuhn, H. (1971) *J. Appl. Phys*., **42**, 4398–405. (g) Kuhn, H. and Mobius, D. (1971) *Angew Chem., Int. Ed. Engl*., **10**, 620–37. (h) Kuhn, H. (1972) *Chem. Phys. Lipids*, **8**, 401–4. (i) Kuhn, H., Möbius, D. and Bücher, H. (1972). 'Determination of chemical composition and molecular structure' in Physical methods of chemistry. (A. Weissberger and B.W. Rossiter, eds). New York: John Wiley and Sons, Part III B, Chapter VII. (j) Sugi, M., Nembach, K., Möbius, D. et al. (1973) *Solid State Commun*., **1**3, 603–6. (k) Schoeler, U., Tews, K.H. and Kuhn, H. (1974) *J. Chem. Phys*., **6**1, 5009–16. (l) Inacker, O. and Kuhn, H. (1974) *Chem. Phys. Lett*., **27**, 317–21. (m) Inacker, O. and Kuhn, H. (1974) *Chem. Phys. Lett*., **27**, 471–4. (n) Inacker, O. and Kuhn, H. (1974) *Chem. Phys. Lett*., **28**, 15–6. (o) Sugi, M., Nembach, K., Möbius, D. et al. (1974) *Solid State Commun*. (1974) **1**5, 1867–70. (p) Polymeropoulos, E.E., Möbius, D. and Kuhn, H. (1978) *J. Chem. Phys*., **68**, 3918. (q) Kuhn, H. (1979) *Pure Appl. Chem*., **51**, 341–52. (r) Kuhn, H. (1979) *J. Photochem*., **10**, 111–32. (s) Petrov, J.G., Kuhn, H. and Mobius, D. (1979) *J. Colloid Interface Sci*., **73**, 66–75. (t) Polymeropoulos, E.E., Möbius, D. and Kuhn, H. (1980) *Thin Solid Films*, **68**, 173–90. (u) Kuhn, H. (1981) *Pure Appl. Chem*., **53**, 2105–22. (v) Kuhn, H. (1983) Energy transfer mechanisms. In *Biophysics* (H.W. Lohman, W. Markl, H. Ziegler, H.S. Verlag, eds). NY. (w) Kuhn, H. (1983) *Thin Solid Films*, **99**, 1–16. (x) Nakahara, H., Fukuda, K., Möbius, D. et al. (1986) *J. Phys. Chem*., **90**, 6144–8. (y) Yonezawa, Y., Möbius, D. and Kuhn, H. (1986) *Ber. Bunsen-Ges. Phys. Chem*., **90**, 1183–8. (z) Kuhn, H. (1988) *Adv. Experim. Medicine Biol*., **238**, 279–90. (aa) Kuhn, H. (1989) *Thin Solid Films*, **178**, 1–16.

[19] (a) Agarwal, V.K. (1975) **2**, 1–31, 75–107. (b) Giles, C.H. (1978) *J. Soc. Dyers Colour*, **94**, 4–12. (c) Berton, M. (1981) *J. Macromol. Sci., Rev. Macromol. Chem*., **C21**, 61–87. (d) Roberts, G.G. (1983) *Sensors and Actuators*, **4**, 131–45. (e) Sugi, M. (1985) *J. Mol. Electron*., 1, 3–17. (f) Roberts, G.G. (1985) *Adv. Phys*., **34**, 475–512. (g) Möhwald, H. (1988) *Thin Solid Films*, **159**, 1–15. (h) Petty, M.C. (1988) *Acta Polytechnica Scandinavica, Electr. Engineer. Ser*., 116–37. (i) Mohwald, H. (1990) *Annu. Rev. Phys. Chem*., **41**, 441–76. (j) Richard, J., Delhaes, P. and Vandevyver, M. (1991) *New J. Chem*., **15**, 137–48. (k) Petty, M.C. (1992) *Thin Solid Films*, **210/211**, 417–26. (l) Möhwald, H. (1993) *Rep. Prog. Phys*., **56**, 653–85. (m) Chien-Hsiang, C. and Franses, E.I. (1995) *Colloids and Surfaces A: Physicochemical and Engineering Aspects*, **100**, 1–45. (n) Möhwald, H., Menzel, H., Helm, C.A. et al. (2004) *Adv. Polymer Sci*., **165**, 151–75.

[20] (a) Wilhelmy, L. (1863) *Ann. Phys. Chem*., **119**, 177–217. (b) Gains, G.L. Jr (1977) *J. Colloid Interface Sci*., **62**, 191–2. (c) Barrow, R.E. and Hills, B.A. (1979) *J. Physiol*., **295**, 217–27. (d) Sato, S. and Kishimoto, H. (1979) *J. Colloid Interface Sci*., **69**, 188–91. (e) Halperin, K., Ketterson, J.B. and Dutta, P. (1989) *Langmuir*, **5**, 161–4. (f) Murphy, O.J. and Wainright, J.S. (1989) *Langmuir*, **5**, 519–23. (g) Martin, D.A. and Vogler, E.A. (1991) *Langmuir*, **7**, 422–9. (h) Buontempo, J.T. and Novak, F.A. (1992) *Rev. Sci. Instrum*., **63**, 5707–13. (i) Vogler, E.A., Spencer, K.B., Montgomery, D.B. et al. (1993) *Langmuir*, **9**, 2470–7. (j) Welzel, P.B., Weis, I. and Schwartz, G. (1998) *Colloids and Surfaces A*, **144**, 229–34. (k) Abe, K., Takiguchi, H. and Tamada, K. (2000) *Langmuir*, **16**, 2394–7. (l) Biswas, S.C., Dubreil, L. and Marion, D. (2001) *J. Colloid Interface Sci*., **244**, 245–53. (m) Gutiérrez, H.M., Castillo, J.A., Chirinos, J.R. et al. (2005) *Rev. Sci. Instrum*., **76**, 045112.

[21] (a) Fujihira, M. and Araki, T. (1986) *J. Electroanal. Chem*., **205**, 329–33. (b) Iyoda, I. Ando, M., Kaneko, T. et al. (1986) *Tetrahed. Lett*., **27**, 5633–6. (c) Bilewicz, R. and Majda, M. (1991) *J. Amer. Chem. Soc*., **113**, 5464–6. (d) Cammarata, V., Atanasoska, L., Miller, L.L. et al. (1992) *Langmuir*, **8**, 876–86. (e) Goldenberg, L.M., Petty, M.C. and Monkman, A.P. (1994) *J. Electrochem. Soc*., **141**, 1573–6. (f) Mello, S.V., Mattoso, L.H.C., Santos, J.R. Jr et al. (1995) *Electrochimica Acta*, **40**, 1851–5. (g) Aoki, A. and Miyashita, T. (1996) *Macromolecules*, **29**, 4662–7. (h) Ashton, P.R., Boyd, S.E., Ballardini, R. et al. (1997) *Chemistry – A European J*., **3**, 152–70 (1997). (i) Goldenberg, L.M. (1997) *Russian Chem. Rev*., **66**, 1033–52. (j) Ram, M.K., Joshi, M., Mehrotra, R. et al. (1997) *Thin Solid Films*, **304**, 65–9. (k) Rikukawa, M., Nakagawa, M., Nishizawa, N. et al. (1997) *Synth. Met*., **85**, 1377–8. (l) Dabke, R.B., Dhanabalan, A., Major, S. et al. (1998) *Thin Solid Films*, **335**, 203–8. (m) Goldenberg, L.M., Lévesque, I., Leclerc, M. et al. (1998) *J. Electroanal. Chem*., **447**, 1–3. (n) Aoki, A. and Miyashita, T. (1999) *J. Electroanal. Chem*., **473**, 125–31. (o) Kim, Y.-H. and Kim, Y.T. (1999) *Langmuir*, **15**, 1876–8. (p) Lu, W., Gao, J.P., Wang, Z.Y. et al. (1999) *Macromolecules*, **32**, 8880–5. (q) Kumpumbu-Kalemba, L. and Leclerc, M.

(2000) *Chem. Commun*., 1847–8. (r) Leclerc, M. (2000) *Sensors Update*, **8**, 21–38. (s) Tang, Z.Y., Liu, S.Q., Wang, E.K. et al. (2000) *Langmuir*, **16**, 5806–13. (t) Wong, E.W., Collier, C.P., Behloradsky, M. et al. (2000) *J. Am. Chem. Soc*., **122**, 5831–40. (u) Zotti, G., Zecchin, S., Berlin, A. et al. (2001) *Chem. Mater*., **13**, 43–52. (v) Ferreira, M., Wohnrath, K., Torresi, R.T. et al. (2002) *Langmuir*, **18**, 540–6. (w) Fichet, O., Tran-Van, F., Teyssie, D. et al. (2002) *Thin Solid Films*, **411**, 280–8. (x) Ferreira, M., Wohnrath, K. and Oliveira, O.N. (2003) *Synth. Met*., **135**, 455–6. (y) Fushimi, T., Oda, A., Ohkita, H. et al. (2005) *Thin Solid Films*, **484**, 318–23. (z) Hays, M.E. and Abbott, N.L. (2005) *Langmuir*, **21**, 12007–15. (aa) Sussuchi, E.M., A.A. de Lima and De Giovani, W.F. (2006) *Polyhedron*, **25**, 1457–63. (ab) Cabaj, J., Soloducho, J., Nowakowska, A. et al. (2006) *Electroanalysis*, **18**, 801–6.

[22] (a) Pei, Q., Yu, G., Zhang, C. et al. (1995) *Science*, **269**, 1086. (b) Chen, M., Nilsson, D., Kugler, D. et al. (2002) *Appl. Phys. Lett*., **81**, 2011. (c) Nilsson, D., Robinson, N., Berggren, M. et al. (2005) *Adv. Mater*., **17**, 353.

[23] Kang, E.T., Neoh, K.G. and Tan, K.L. (1998) *Progr. Polymer Sci*., **23**, 277–324.

[24] Berzina, T., Erokhin, V. and Fontata, M.P. (2007) *J. Appl. Phys*., **101**, 024501.

[25] (a) Mendolia, M.S. and Farrington, G.C. (1995) *Adv. Chem. Ser*., **245**, 107–30. (b) Song, J.Y., Wang, Y.Y. and Wan, C.C. (1999) *J. Power Sources*, **77**, 183–97. (c) Stephan, A.M. (2006) *Eur. Polymer J*., **42**, 21–42. (d) Stephan, A.M. and Nahm, K.S. (2006) *Polymer*, **47**, 5952–64.

[26] Erokhin, V., Raviele, G., Glatz-Reichenbach, J. et al. (2002) *Mater. Sci. Engineer. C*, **22**, 381–5.

[27] (a) Agbor, N.E., Petty, M.C., Monkman, A.P. et al. (1993) *Synth. Met*., **55–57**, 3789–94. (b) Ram, M.K., Sundaresan, N.S. and Malhotra, B.D. (1993) *J. Phys. Chem*., **97**, 11580–2. (c) Cheung, J.H. and Rubner, M.F. (1994) *Thin Solid Films*, **244**, 990–4. (d) Goldenberg, L.M., Petty, M.C. and Monkman, A.P. (1994) *J. Electrochem. Soc*., **141**, 1573–6. (e) Suwa, T., Kakimoto, M.-A., Imai, Y. et al. (1994) *Mol. Cryst. Liq. Cryst. A*, **255**, 45–54. (f) Quint, P., Hara, M., Knoll, W. et al. (1995) *Macromolecules*, **28**, 4019. (g) Ramanathan, K., Ram, M.K., Malhotra, B.D. et al. (1995) *Mater. Sci. Ingeneer. C*, **3**, 159–63. (h) Riul, A. Jr, Mattoso, L.H.C., Telles, G.D. et al. (1995) *Synth. Met*., **71**, 2067–8. (i) Rebattet, L., Pinéri, M., Escoubes, M. et al. (1995) *Synth. Met*., **71**, 2133–7. (j) Porter, T.L., Thompson, D. and Bradley, M. (1996) *Thin Solid Films*, **288**, 268–71. (k) Ram, M.K., Annapoorni, S. and Malhotra, B.D. (1996) *J. Appl. Polym. Sci*., **60**, 407–11. (l) Riul, A. Jr, Mattoso, L.H.C., Telles, G.D. et al. (1996) *Thin Solid Films*, **284–285**, 177–80. (m) Lavrik, N.V., De Rossi, D., Kazantseva, Z.I. et al. (1996) *Nanotechnology*, **7**, 315–9. (n) Agbor, N.E, Cresswell, J.P., Petty, M.C. et al. (1997) *Sensors and Actuators B*, **41**, 137–41. (o) Dhanabalan, A., Riul, A. Jr, Mattoso, L.H.C. et al. (1997) *Langmuir*, **13**, 4882–6. (p) Dhanabalan, A., Dabke, R.B., Kumar, N.P. et al. (1997) *Langmuir*, **13**, 4395–400. (q) Dhanabalan, A., Dapke, R.B., Datta, S.N. et al. (1997) *Thin Solid Films*, **295**, 255–9. (r) Granholm, P.,

Paloheimo, J. and Stubb, H. (1997) *Synt. Met*., **84**, 783–4. (s) Mello, S.V., Faria, R.M., Mattoso, L.H.C. et al. (1997) *Synt. Met*., **84**, 773–4. (t) Ram, M.K., Gowri, R. and Malhotra, B.D. (1997) *J. Appl. Polym. Sci*., **63**, 141–5. (u) Ram, M.K., Carrara, S., Paddeu, S. et al. (1997) *Thin Solid Films*, **302**, 89–94. (v) Ram, M.K., Carrara, S., Paddeu, S. et al. (1997) *Langmuir*, **13**, 2760–5. (w) Barker, P.S., Monkman, A.P., Petty, M.C. et al. (1997) *IEE Proc.-Circuits Devices Syst*., **144**, 111–6. (x) Granholm, P., Paloheimo, J. and Stubb, H. (1997) *Phys. Scripta*, **T69**, 146. (y) Dabke, R.B., Dhanabalan, A., Major, S. et al. (1998) *Thin Solid Films*, **335**, 203–8. (z) Dhanabalan, A., Riul, A. Jr, Gonçalves, D. et al. (1998) *Thin Solid Films*, **327–329**, 60–4. (aa) Dhanabalan, A., Riul, A. Jr and Oliveira, O.N. Jr (1998) *Supramol. Sci*., **5**, 75–82. (ab) Dhanabalan, A., Malmonge, J.A., Riul, A. Jr et al. (1998) *Thin Solid Films*, **327–329**, 808–12. (ac) Riul, A. Jr, Dhanabalan, A., Mattoso, L.H.C. et al. (1998) *Thin Solid Films*, **327–329**, 576–80 (1998). (ad) Granholm, P., Paloheimo, J. and Stubb, H. (1998) *Physica Status Solidi B*, **205**, 315–8. (ae) Ram, M.K., Adami, M., Sartore, M. et al. (1999) *Synt. Met*., **100**, 249–59. (af) Dhanabalan, A., Talwar, S.S., Contractor, A.Q. et al. (1999) *J. Mater. Sci. Lett*., **18**, 603–6. (ag) Dimitriev, O.P. and Lavrik, N.V. (1999) *Synth. Met*., **98**, 173–5. (ah) Kosonen, H., Ruokolainen, J., Knaapila, M. et al. (2001) *Synth. Met*., **121**, 1277–8. (ai) Wu, C.-G., Yeh, Y.-R., Chen, J.-Y. et al. (2001) *Polymer*, **42**, 2877–85. (aj) Ferreira, M., Wohnrath, K., Torresi, R.T. et al. (2002) *Langmuir*, **18**, 540–6. (ak) Kulesza, P.J., Chojak, M., Miecznikowski, K. et al. (2002) *Electrochem. Commun*., **4**, 510–5. (al) Troitsky, V.I., Berzina, T.S. and Fontana, M.P. (2002) *Synth. Met*., **129**, 39–46. (am) Xie, D., Jiang, Y., Pan, W. et al. (2002) *Sensors and Actuators B*, **81**, 158–64. (an) Jiang, Y.D. and Xie, G.Z. (2006) *Rare Metal Mater. Engineer*., **35**, 59–60. (ao) De Souza, N.C., Ferreira, M., Wohnrath, K. et al. (2007) *Nanotechnology*, **18**, 075713.

[28] (a) Cárdenas-Valera, A.E. and Bailey, A.I. (1993) *Colloids and Surfaces A*, **79**, 115–27. (b) Henderson, J.A., Richards, R.W., Penfold, J. et al. (1993) *Macromolecules*, **26**, 4591–600. (c) Joanny, J.F. (1998) *Macromolecules*, **31**, 2198–211. (d) Rother, G. and Findenegg, G.H. (1998) *Colloid Polymer Sci*., **276**, 496–502. (e) Sadev, R. (1999) *Colloids and Surfaces A*, **156**, 65–70. (f) Lheveder, B. (2000) *Macromolecules*, **32**, 8538–50. (g) Sano, M., Kamino, A., Okamura, J. et al. (2001) *Langmuir*, **17**, 5125–8. (h) Yang, Z. and Sharma, R. (2001) *Langmuir*, **17**, 6254–61. (i) Ahmed, F., Hategan, A., Discher, D.E. et al. (2003) *Langmuir*, **19**, 6505–11. (j) Chen, C., Even, M.A. and Chen, Z. (2003) *Macromolecules*, **36**, 4478–84. (k) Kim, C. and Yu, H. (2003) *Langmuir*, **19**, 4460–4. (l) Wesemann, A., Ahrens, H., Steitz, R. et al. (2003) *Langmuir*, **19**, 709–16. (m) Hambardzumyan, A., Aguié-Béghin, V., Daoud, M. et al. (2004) *Langmuir*, **20**, 756–63. (n) Peleshanko, S., Jeong, J., Gunawidjaja, R. et al. (2004) *Macromolecules*, **37**, 6511–22. (o) Blomqvist, B.R., Wänheim, T. and Claesson, P.M. (2005) *Langmuir*, **21**, 6373–84. (p) Cheyne, R.B. and Moffitt, M.G. (2005) *Langmuir*, **21**, 5453–60. (q) Park, Y., Choi, Y.-W., Park, S. et al.

(2005) *J. Colloid Interface Sci*., **283**, 322–8. (r) Dynarowitz-Latka, P., Rosilio, V., Boullanger, P. et al. (2005) *Langmuir*, **21**, 11941–8. (s) Gunawidjaja, R., Peleshanko, S. and Tsukruk, V.V. (2005) *Macromolecules*, **38**, 8765–74. (t) Noskov, B.A., Lin, S.-Y., Loglio, G. et al. (2006) *Langmuir*, **22**, 2647–52. (u) Gunawidjaja, R., Peleshanko, S., Genson, K.L. et al. (2006) *Langmuir*, **22**, 6168–76. (v) Rieger, J., Dubois, P., Jérome, R. et al. (2006) *Langmuir*, **22**, 7471–9. (w) Hodges, C.S., Neville, F., Konovalov, O. et al. (2006) *Langmuir*, **22**, 8821–5. (x) Hlady, V. and Jogikalmath, G. (2007) *Colloids and Surfaces B*, **54**, 179–87.

[29] Liess, M., Chinn, D., Petelenz, D. et al. (1996) *Thin Solid Films*, **286**, 252–5.

[30] Erokhin, V., Berzina, T. and Fontana, M.P. (2005) *J. Appl. Phys*., **97**, 064501.

[31] Rossberg, K., Paasch, G., Dunsch, L. et al. (1998) *J. Electroanal. Chem*., **443**, 49.

[32] Erokhin, V., Berzina, T., Camorani, P. et al. (2007) *J. Phys.: Condens. Matter*, **19**, 205111.

[33] (a) Tarascon, J.M. and Guyomard, D. (1993) *Electrochim. Acta*, **38**, 1221–31. (b) Noel, M. and Santhanam, R. (1998) *J. Power Sources*, 72, 53–65. (c) Noel, M. and Suryanarayanan, V. (2002) *J. Power Sources*, 111, 193–209. (d) Aubach, D. (2005) *J. Power Sources*, 146, 71–8. (e) Balakrishnan, P.G., Ramesh, R. and Kumar, T.P. (2006) *J. Power Sources*, **155**, 401–14.

[34] (a) Scott, S.K., Johnson, B.R., Taylor, A.F. et al. (2000) *Chem. Engineer. Sci*., **55**, 209–15. (b) Ivanitskii, G.R. (1999) *Biofizika*, **44**, 773–95. (c) Boccaletti, S., Grebogi, C., Lai, Y.C. et al. (2000) *Phys. Rep. Rev. Sec. Phys. Lett*., **329**, 103–97. (d) Meron, E. (2000) *Discrete Dynam. Nat. Soc*., **4**, 217–30. (e) Taylor, A.F. (2002) *Progr. React. Kin. Mech*., **27**, 247–325. (f) Yoshida, R. (2005) *Curr. Org. Chem*., **9**, 1617–41. (g) Mikhailov, A.S. and Showalter, K. (2006) *Phys. Rep. Rev. Sec. Phys. Lett*., **425**, 79–194. (h) Taylor, A.F. and Britton, M.M. (2006) *Chaos*, **16**, 037103. (i) Toth, R. and Taylor, A.F. (2006) *Progr. React. Kin. Mech*., **31**, 59–115.

[35] Smerieri, A., Erokhin, V., Berzina, T. et al. (2007) *Mater. Sci. Engineer. C*., published online doi:10.1016/j.msec.2007.04.037.

[36] Erokhin, V., Berzina, T. and Fontana, M.P. (2007) *Cryst. Rep*., **52**, 159–66.

[37] (a) Norris, I.D., Shaker, M.M., Ko, F.K. (2000) *Synth. Met*., **114**, 109. (b) Kidoaki, S., Kwon, I.K. and Matsuda, T. (2005) *Biomaterials*, **26**, 37.

[38] Erokhin, V., Berzina, T., Camorani, P. et al. (2006) *Soft Matter*, **2**, 870–74.

This page intentionally left blank

Chapter 7

Nanostructured materials for enzyme immobilization and biosensors

Silvana Andreescu, John Njagi and Cristina Ispas
Department of Chemistry and Biomolecular Science, Clarkson University, Potsdam, NY, USA

Abstract. The unique electrical, optical, catalytic and magnetic properties of materials in which the structural elements are in the nanometer size (broadly defined as nanostructured materials) have attracted considerable interest for designing powerful enzyme-based biocatalytic systems. This paper discusses recent advances in the study and use of various classes of nanostructured materials (carbon nanotubes, nanofibers and nanowires, nanoparticles and nanocrystals, mesoporos silica and composite materials) for enzyme immobilization and describes selected examples of their application in the development of biologically active systems and biosensors. Different strategies used for the functionalization of nanostructures with enzymes, development and characterization of the nanostructure assembly, evaluation of biological activity and generation of response and sensing function are also discussed.

Keywords: nanomaterials, enzyme immobilization, composites, carbon nanotubes, mesoporous silica

7.1. Introduction

The development of nanostructured materials for enzyme immobilization with applications in biotechnology, biocatalysis, protein delivery systems and biological sensors is currently becoming an emerging area of research. In this complex system, the material chemistry, its structure and composition have a critical role on the binding, orientation and biological activity of proteins. By definition, nanostructured materials are those materials whose structural elements (i.e., crystallites or molecules) have dimensions of the

order of or below 100 nm [1]. The uniqueness of these materials is due to their electrical, optical and magnetic properties which offer distinctive prospects for designing powerful biocatalytic systems. For instance, their high surface area provides a large number of binding points for biomolecule attachment, while their electrocatalytic properties could facilitate direct and fast electron transfer between oxido-reduction species and a physical transducer. The immobilization of enzymes on nanometer-size materials is a very promising concept for biosensing and biotechnological applications. Furthermore, gaining a fundamental understanding of the biomolecular events between the enzyme and the nanoscale environment is essential for the success of these applications.

Enzymes are efficient catalysts that accelerate the rate of chemical reactions without themselves being consumed in the process. Typically, enzymes function in an aqueous environment with a low ionic strength at near neutral pH and physiological temperatures. An important feature of enzymes is that they possess specific 3D configurations that are essential for their catalytic action. The most important part of an enzyme is its active site, located at a precise position in the molecule, which stabilizes the transition state between the substrate and its products. Alteration of the overall conformation of the molecule could affect its biological activity.

The commonly used lyophilized freeze-dried enzyme powders often exhibit low activity and stability. As an alternative, enzymes immobilized onto a support could offer advantages such as higher catalytic activity, enzyme recycling and continuous operation [2–5]. Other advantages include resistance to environmental changes (i.e., wider pH range than in solution), easy separation from the product, rapid termination of reactions, increased stability, generation of a defined diffusion region and reduced cost of operation [2,3,6,7]. A study published in 1978 showed that 60% of studied proteins showed an increased stability upon immobilization, 24% were unaffected and 16% presented a decreased stability [8]. Enzyme immobilization is now a popular strategy used in many practical applications. However, in some cases, immobilized enzymes have poor biocatalytic efficiency, which often limits the development of large-scale bioprocessing that could compete with traditional chemical technologies. A schematic representation showing the main strategy that could be used as a guide in the development of immobilized enzyme biocatalyst is shown in Fig. 7.1 (from [9] with permission).

The main challenge is to design functional biocompatible materials and interfacial structures which allow stable attachment of enzymes while maintaining their activity and function as close as possible to their native state.

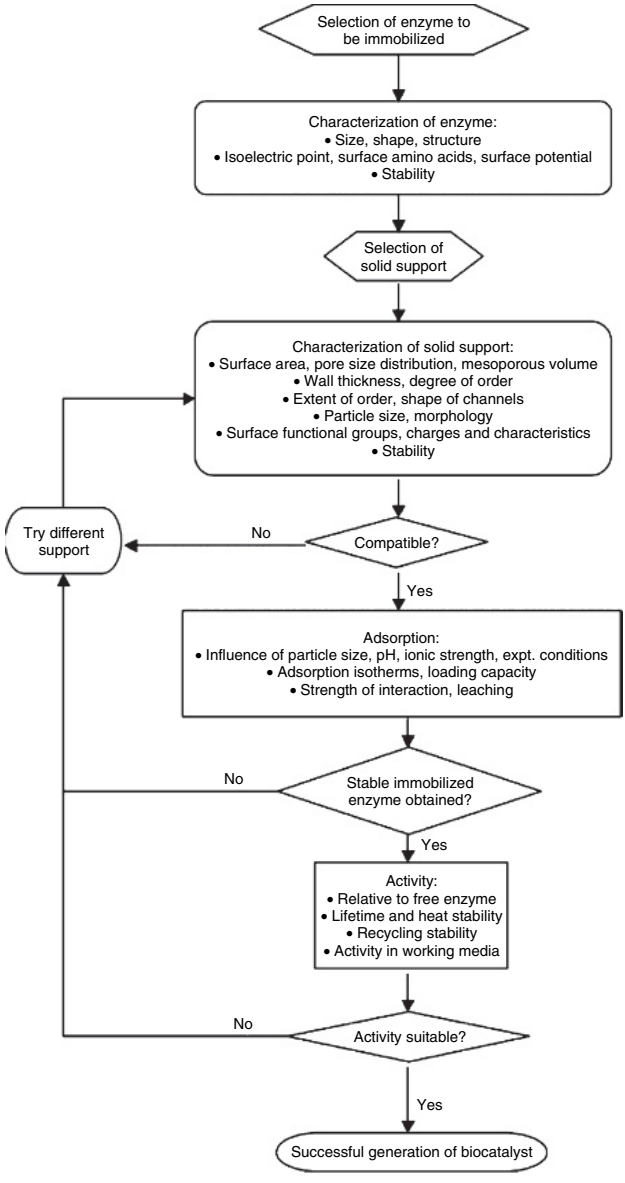

Figure 7.1: Schematic representation of the main strategy that could be used in the development of an immobilized enzyme biocatalyst (from Ref. [9] with permission).

Recent trend is to use nanostructured materials for the purpose of enhancing enzyme retention while providing high biocatalytic activity and efficiency. Examples of nanostructured architectures used for enzyme immobilization include carbon nanotubes (CNTs) [10–13], nanoparticles [14–16], magnetic nanoparticles [15,17], mesoporous media [18,19], nanofibers [20,21], nanocomposites [22,23], nanorods and sol-gel materials containing nanometer-size particles [24–26] and single-enzyme nanoparticles [27]. These materials have attracted considerable attention due to their biocompatibility and high accessible surface area which greatly enhance the stability and the amount of immobilized enzymes. In addition, the reduced mass transfer limitation of substrates and inhibitors leads to improved sensitivities when compared to conventional macroscale matrices [2].

Fabrication of active biological systems consisting of interacting nanostructures with enzymes requires the development and characterization of an appropriate nanostructure assembly, enzyme attachment, evaluation of biological activity, generation of response and sensing function. This chapter discusses recent advances in the study and use of nanostructured materials for enzyme immobilization. A short overview of enzyme immobilization techniques and application to the development of enzyme sensors with focus on those with electrochemical transduction mechanism is also discussed.

7.2. Properties of Materials for Enzyme Immobilization

The activity of immobilized enzymes depends on the available surface area, porosity, hydrophilic character, reaction conditions and the method chosen for the immobilization [28]. Although it is generally recognized that there is no unique and ideal material for the immobilization of all enzymes, some basic requirements should be desirable: (a) biocompatibility with the enzyme, (b) availability of reactive functional groups necessary for enzyme attachment or should be easily functionalized, (c) stability with changes in the microenvironment (pH, ionic strength), (d) ensure enzyme stability and avoid leaching, (e) allow free diffusion of substrates and reaction products, (f) selectivity and sensitivity for the detected species, (g) ease of preparation and low cost [3,6,29] and, in addition, (h) the immobilization method should not involve toxic or denaturing reagents that can alter the activity of the enzyme. In a typical configuration, the sensor material is a planar surface with a limited number of anchoring

points available for biofunctionalization. Advances have been made by using nanostructured architectures, such as nanoparticles, single-walled CNTs and nanocomposite films. These materials fulfill many of the 'ideal' requirements for enzyme immobilization. For instance, these have been shown to provide enhanced binding efficiency and increased stability and might improve the performance of enzyme systems and devices.

7.3. Methods for Enzyme Immobilization

The method used to attach the enzyme is the key step in the development of many practical applications and devices involving immobilized biocatalysts. This process is governed by various interactions between the biological component and the material interface [30]. Starting with the first demonstration of an immobilized enzyme in 1950, considerable efforts have been directed toward the development of new and more efficient methods that do not affect the activity or the conformation of native protein and that could be applicable to a broad range of surfaces. Various strategies have been employed including physical adsorption [31,32] covalent binding, [33,34] physical entrapment [32,33] Langmuir–Blodgett films [35], self-assembly [36] and affinity methods [33,37]. Figure 7.2 illustrates the general approaches of several enzyme immobilization methods. Nanostructured materials were first used as support matrices for direct enzyme attachment. This is achieved almost exclusively through physical adsorption via the weak bonds such as van der Waals forces, ionic binding or hydrophobic interactions. More recent methods involve the use of physical entrapment, covalent and affinity-based methods. Engineering the enzyme by adding a functional group at a precise location in its structure (usually the amino or carboxyl terminal group) was also used in the binding process. An appropriate selection of the method is dictated by several parameters such as the nature of enzyme, the type and properties of material and/or the final application of the enzymatic system. In the following section, we briefly discuss the main and the most widely used enzyme immobilization methods.

7.3.1. Physical Adsorption

Generally, physical adsorption is the easiest, inexpensive and the least denaturing immobilization method. The procedure consists of simple deposition of the enzyme onto the support or electrode material. It does not

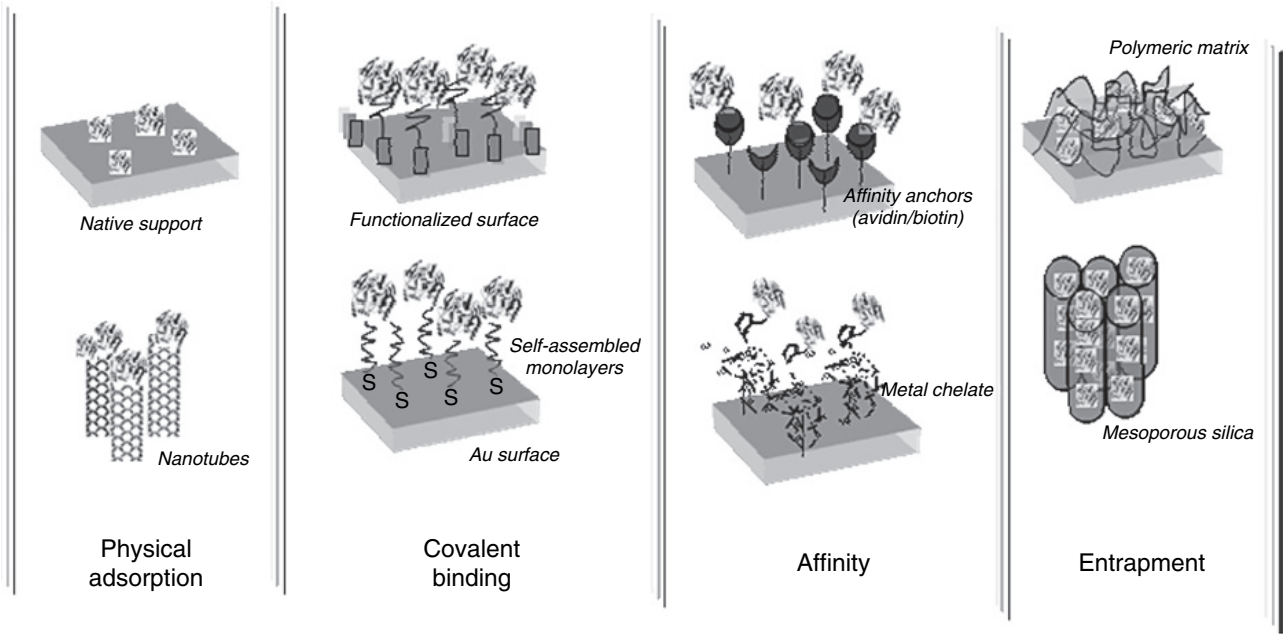

Figure 7.2: Schematic representation of various enzyme (E) immobilization strategies.

involve additional reagents, sequential steps or enzyme modifications that could affect its activity. However, due to the fact that the binding forces involved are weak, the enzyme immobilized in this way is susceptible to pH, temperature, solvent and ionic strengths changes and does not provide increased enzyme activity and long-term operational and storage stability [28,38,39]. As mentioned earlier, this is the most popular strategy to immobilize enzymes onto nanostructures. As compared to macroscale materials, enzymes appear to bind stronger to nanomaterials. An example is the adsorption onto CNTs [40] and gold nanoparticles [41].

7.3.2. Covalent Coupling

The attachment of an enzyme by covalent linkage consists of two steps. The first step involves activation of the material to provide useful chemical reactivity for subsequent binding of the biomolecule. Typically, this is achieved with bifunctional groups or spacers such as glutaraldehyde, carbodiimide/succinimide, self-assembled monolayers or multilayers (SAM) and aminopropyltriethoxysilanes. The second step consists of binding the enzyme to a chemically activated support. The chemistry involved in the immobilization process depends upon the type of material used and its surface characteristics. In general, this method has been successfully developed for noble metals and carbon-based materials. This procedure has some advantages such as the increased stability of the enzyme due to the strong chemical binding, but has poor reproducibility, requires the use of large amounts of enzyme and the immobilized enzyme has relatively low activity due to the fact that the process can involve groups that are essential for its activity [28,38,39,42,43]. Covalent methods using SAM have a special interest in biological sensors due to the fact that they provide orientation and spatial control of the enzyme. It is also possible to design SAM with specific functional groups and use them as a communication relay between the electrode surface and redox active enzymes [44–46].

7.3.3. Affinity Immobilization

Increasing efforts have been focused on the development of new and innovative techniques which can ensure controlled spatial orientation/conformation, without loss of enzyme activity during the immobilization procedure [47,48]. A recent trend is to create (bio)affinity bonds

between an activated support and a specific group of the protein sequence. When these groups are not present in the native enzyme, they can be engineered at a specific location which does not affect the activity or the folding of the protein [49]. Specific examples of affinity interactions include cellulose–cellulose binding domain bearing enzymes, immobilized metal ions for histidine-bearing enzymes [33,50], polyclonal/monoclonal antibodies for specific enzymes and lectins – glycoenzymes bearing appropriate oligosaccharides [51–53]. The method is usually reversible facilitating the reuse of support matrix [54,55] and provides stable enzyme attachment. In addition, it provides a basis for controlled and oriented immobilization of the enzyme on different supports, opening the way for new approaches to enzyme immobilization.

These procedures are gaining increasing acceptance in the construction of sensitive enzyme-based analytical devices. However, enzymes immobilization onto nanostructures using bioaffinity bonds is still relatively unexplored and represents an important research direction for future developments. A very interesting recent example is the immobilization of His-tagged peptides onto nickel/gold/nickel nanowires. In this example, in addition to the controlled immobilization of the protein, the use of nickel nanowires also allows control of directionality of the nanoassembly by an external magnetic field [56].

7.3.4. Entrapment

One of the most convenient methods of enzyme immobilization is by physical entrapment in an inert material (i.e., photopolymerized monomers, sol-gel matrices). This method has some advantages over the other procedures such as mild conditions, easy one-step fabrication, low cost and high stability of encapsulated enzyme. The limitations of the method are diffusional barriers of the transport of substrate and/or product resulting in long response times, difficulties in controlling the pores dimensions and possible enzyme leaching [38,42,57,58]. In some cases, the activity of the enzyme can be affected by the physical and chemical properties of the immobilization matrix. The process, however, can be considered as general applicable for all enzymes.

Examples of materials used for encapsulation include photopolymerizable polymers, chemically generated polymers (i.e., alginate, latex),

electrochemically generated polymers (polypyrrole, polyaniline polyacetylene, polythiophene, polyindole) [58,59], inorganic clays and sol-gels. In this process, enzymes can be immobilized together with activators or artificial mediators such as ferrocene, quinoline derivates, tetrathiafulvalene and organic salts that facilitate the transport of the electrons from the redox center of the enzyme to the surface of the electrode. This feature is particularly important for biosensing. Among these, the most attractive method is perhaps by electrodeposition of a conducting polymer in the presence of the enzyme [28,59]. The principal advantages of this method are that the resulting materials are easily prepared in a single-step procedure and the possibility to control the thickness of the polymeric layer. The main limitation is the high amount of biomolecule and monomer necessary for the immobilization. A more straightforward method is to retain the enzyme behind a thin semi-permeable membrane such as dialysis tubing or negatively charged perflourinated sulfonate polymer Nafion (DuPont-NEN, Boston, MA, USA) [38].

Chemically synthesized PPy using chloroauric acid ($HAuCl_4$) as oxidizing agent can also be used for enzyme immobilization and biosensors. The procedure consists of a simple single-phase reaction between $HAuCl_4$ and pyrrole (Py) in phosphate buffer (PB) solution. $HAuCl_4$ acts as an oxidizing agent for the polymerization of Py [60]. As the polymerization proceeds, metallic gold (of a diameter of $\sim$24 nm) is formed simultaneously with the PPy, which finally results in the formation of an Au–PPy nanocomposite material. The synthesis occurs in mild aqueous conditions and does not involve application of an electrical potential, surfactants or solvents that could affect the biological activity. Since the synthesis is carried out in an aqueous solution, enzymes could be included during or after synthesis of this nanocomposite. The enzymes (polyphenol oxidase, glucose oxidase (GOX) and a redox protein, cytochrome *c* (Cyt *c*)) immobilized on this material remained fully active during manufacturing, storage and use ($\sim$15 days at room temperature and more than 6 months at 4°C). In addition to enzyme entrapment, the presence of gold nanoparticles in the polymeric layer enhances the conductivity, and thus this nanostructured material has a particular interest for electrochemical biosensors. Their nanometer size and high surface area has the ability to facilitate direct and fast electron transfer between the oxido-reduction species and the transducer, and allows minimum diffusion of the substrate and/or product when compared to macroscale conventional matrices [2,16,61]. In this case, PPy has a dual function: it serves as a matrix for the incorporation of metal

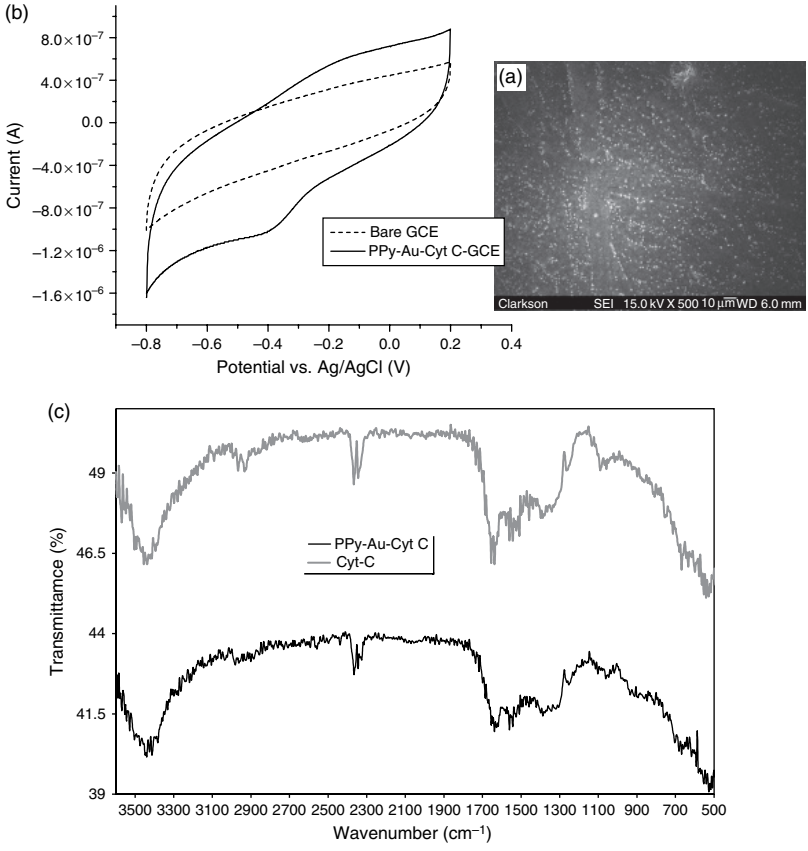

Figure 7.3: (a) Field-emission scanning electron microscopy (FE-SEM) of Au-PPy-GCE electrode. (b) Cyclic voltammograms of bare GCE and GCE-Au-PPy-Cyt *c* electrode in 0.1 M PB at pH 7.4 at a scan rate of 50 mV/s. (c) FTIR spectra of native and immobilized Cyt *c*.

nanoparticles and for the immobilization of the enzyme. The scanning electron microscopy of a glassy carbon electrode (GCE) modified with this Au–PPy composite shows the presence of gold nanoparticles uniformly distributed within the PPy film (Fig. 7.3(a)). The cyclic voltammogram (CV) of Cyt *c* entrapped in this material and deposited onto the surface of a GCE confirms that the redox activity of Cyt *c* is conserved after immobilization. CV measurements reveal a pair of redox peaks corresponding to

a quasi-reversible electrode behavior due to electrochemical activity of the Au–PPy-bound protein (Fig. 7.3(b)). In addition, Fourier-transform infrared spectroscopy (FTIR) indicated no major structural changes when the protein is bound to the composite. The FTIR spectrum of Cyt *c* immobilized onto the Au–PPy is similar to that of the native Cyt *c*, and the amide vibrational bands I and II of the Cyt *c* did not change upon immobilization (Fig. 7.3(c)).

7.4. Classes of Nanostructured Materials for Enzyme Immobilization and Biosensors

Since the discovery of CNTs in 1991, nanomaterials have been the target of numerous investigations for both fundamental and practical applications [62] including the immobilization of enzymes. The type of nanomaterials, the structure, composition and morphology are of critical importance in creating active and efficient supported enzyme catalysts. In this chapter, the properties and characteristics of different classes of nanomaterials and their use for enzyme immobilization are discussed.

7.4.1. Carbon Nanotubes

Two main types of CNTs have been used for biomodification: single-walled (SW)CNTs (a single graphitic sheet with a tubular structure) and multi-walled (MW)CNTs (an array of nanotubes) [63]. These structures offer an easy and versatile way for enzyme attachment [64]. Two main procedures can be used to immobilize enzymes onto CNTs: physical adsorption and covalent attachment. A schematic representation of these methods onto a SWCNT is illustrated in Fig. 7.4. Because of their high electrochemically accessible surface and high electronic conductivity, these materials are especially attractive for electrochemical enzyme sensors. Moreover, CNT-based biosensors present a direct electrical communication between the redox-active biomolecule and the delocalized π system of CNT system [65,66].

Barone et al. showed that, by using the inherent fluorescence from SWNTs, it is possible to construct a simple optical solution-phase biosensor that can be used to monitor glucose level in blood [67]. SWNTs modulate their emission in response to the adsorption of specific biomolecules. These results opened new opportunities for optical sensors that operate in strongly

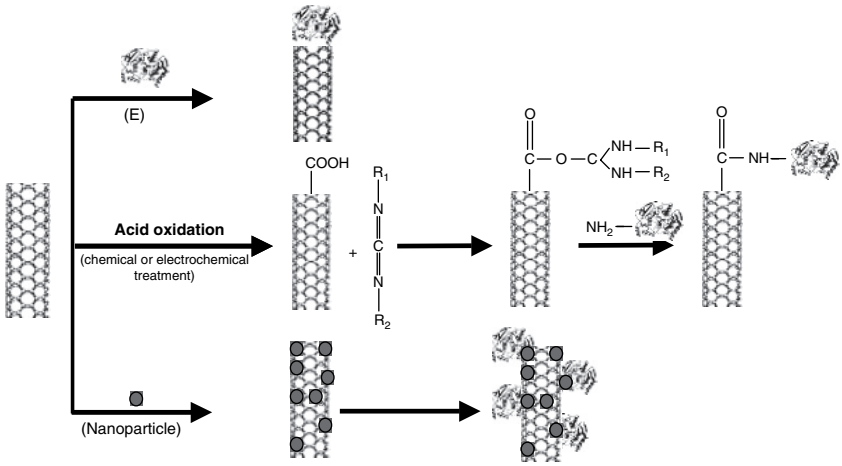

Figure 7.4: Strategies for the immobilization of enzymes (E) onto carbon nanotubes.

absorbing media of relevance to medicine or biology. This solution-phase biosensor presents some important advantages over the substrate-based types, because they do not require electrode deposition, minimizing the problems related to biocompatibility and biofouling. However, the SWNTs and immobilization procedure should be carefully optimized in order to conserve their optical activity [68].

Physical adsorption

The surface acidic sites of CNTs (as a result of their purification with oxidizing acids), high surface area and tubular structure may enhance the binding of biomolecules by simple adsorption [69]. For instance, both GOX and flavine adenine dinucleotide (FAD) were found to spontaneously adsorb onto SWCNTs [70]. GOX was mixed within CNTs to generate a needle microsensor for monitoring glucose [71]. In other configurations, enzymes were adsorbed onto a CNT composite obtained by mixing CNTs with a linker such as mineral oil [72], epoxy resin [73], chitosan biopolymer [74] or Teflon [75]. Such biocomposites were used for the construction of amperometric biosensors for the detection of glucose and ethanol and for the determination of β-nicotineamide adenine dinucleotide (NADH), which is the cofactor of more than 300 dehydrogenase enzymes [76,77]. The use of

CNTs favorized a direct communication between the biomolecule and the nanotube and allowed a non-mediated detection of hydrogen peroxide and NADH detection at a low applied potential. Another example is the immobilization of the enzyme acetylcholinesterase (AChE) by simple deposition and drying of the enzyme in solution onto the working electrode surface of a screen-printed electrode containing acid-purified CNTs [78,79]. The sensor exhibited enhanced electrocatalytic activity toward thiocholine and facilitated operation at low applied potential without the use of electronic mediators. Figure 7.5 shows the electrochemical responses of an AChE biosensor to the injection of acetylthiocholine substrate in the presence and absence of CNTs. The enzyme was immobilized by entrapment in a chitosan layer with/without CNTs. The use of CNTs clearly indicates an enhancement of the amperometric response with more than one order of

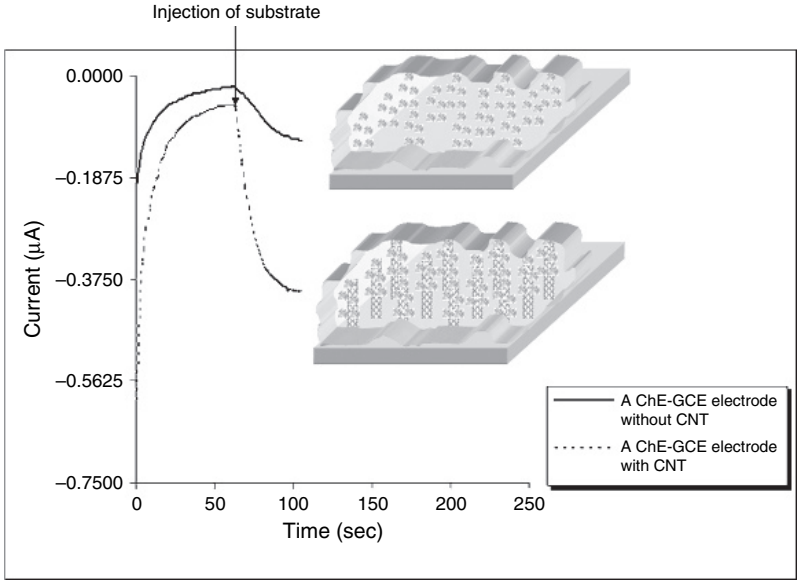

Figure 7.5: Amperometric responses of a AChE-GCE electrode with and without CNTs at an applied potential of 410 mV vs a Ag/AgCl reference electrode. The enzyme and the CNTs were physically entrapped in a chitosan layer. The response corresponds to the oxidation of thiocholine, the product of the AChE reaction of acetylthiocholine substrate.

magnitude (in the same experimental conditions) than that obtained when the enzyme was entrapped only in the chitosan matrix.

Functionalized MWCNTs have been used as dopant within a conducting polymer such as Py to create an amperometric enzyme electrode. The CNTs were deposited by electropolymerization of Py in the presence of CNTs and enzyme [12]. In another approach, CNTs were simply grown in a silicon layer covered with a thin gold film [80]. Etching of the silicon layer left the vertical nanotubes attached to the gold film which then provided an excellent electron transfer material. These sensors have shown superior performance in terms of sensitivity, applied potential and surface fouling as compared to those based on macroscale materials.

Covalent biofunctionalization

The CNTs can be functionalized with carboxylic acid groups before covalently attaching the enzyme [12,80,81]. The most commonly used chemical modification procedure involves treatment (i.e., sonication) under oxidizing conditions (sulfuric acid, nitric acid, piranha) to generate oxygenated functionalities such as carboxylic acids, anhydrides, quinones and esters. Other procedures include fluorination, electrophilic attack with chloroform, reduction of aryl diazonium salts, dissolved metal reduction [82], but these have not so far been used for the immobilization of enzymes. For instance, electrochemical reduction of nitro groups at the surface of a CNT produces terminated $–NH_2$ groups [34] that could serve as binding point for further covalent attachment of enzymes. In some cases, such a 'pre-activation', treatment is necessary to increase the functionalized surface of the nanotube for further biomolecule binding. Another advantage of this strategy is that it increases the electrochemical responses, which are otherwise weak [65].

An example of covalent immobilization method is the use of carbodiimine chemistry (Fig. 7.4(b)) by forming amide linkage between the amine residues and the carboxylic acid groups of the CNT tips [83]. These functionalities were formed by employing an electrochemical pre-treatment in 1 M NaOH at 1.5 V for 90 s. The immobilization consisted of immersing the activated CNTs-COOH in an aqueous solution of 1-ethyl-3-(3-dimethylaminopropyl)carbodiimide) (EDC, 10 mg/mL) and N-Hydroxy-sulfo-succinimide (sulfo-NHS). The pH of the solution was adjusted to 7 and then the entire assembly was washed with water and immediately immersed in a GOX solution (2 mg/mL) prepared in PB

solution. The immobilization reaction occurred at room temperature for ~2 h. The system performed a selective electrochemical analysis of glucose avoiding the generation of an overlapping signal for common interferences (acetaminophen, uric and ascorbic acid).

Another feature of CNTs structures is the possibility to attach colloidal particles (gold nanoparticles, magnetic nanoparticles, quantum dots) or polyelectrolyte layers to mediate the attachment of nanoparticles along their sidewalls [84–86]. These systems have been so far studied for their physical and electrochemical properties, but their applications could be extended to enzyme immobilization (Fig. 7.4(c)). For instance, enzymes could be entrapped within a CNT-polymer-nanoparticles multilayer assembly. In addition, by attaching magnetic nanoparticles, electrocatalytic and magnetic properties can be combined in a unique 'magneto-nanotubes' which makes it possible to control the entire assembly in a magnetic field and creates magneto-switchable devices [86].

7.4.2. Nanofibers and Nanowires

Enzymes immobilized in nanofibrous materials show apparent high activity which is indicative of high catalytic efficiency compared to other forms of immobilized enzymes. The use of nanofibers offers the advantage of reduced diffusional limitation of substrate to the enzyme active sites. In addition, these materials are durable, can be manufactured in a highly porous form and have a high degree of biologically accessible surface area [20,87,88]. Their use overcomes the problem of dispersion and recovery in reaction solutions encountered in the case of nanoparticles, while still keeping the advantageous features of nanometer-sized materials. Enzyme can be either physically adsorbed or covalently bound to functionalized nanofibres. The types of fibers that have been most commonly used for bioimmobilization are carbon nanofibers and polymeric nanofibers (polystyrene, poly(styrene-co-maleic anhydride), polyvinylpyrrolidone, polyacrilonitrile-co-maleic acid – PANCMA).

Carbon nanofibers (CNs) are well-defined cylindrical structures consisting of graphene layers arranged as cones, cups or plates [40]. Several forms of CNs of various dimensions (in the order of ~10–200 nm diameter) are commercially available and can be used for the immobilization of enzymes. CNs have a larger functionalized surface area as compared to that of CNTs. In a recent study, CNs have been shown to provide a

better matrix for the immobilization of GOX (selected as model protein) compared to that of CNTs and graphite [40]. The enzyme was immobilized by adsorption at 4°C for 24 h. The resulting biofunctionalized material was used for the construction of a glucose biosensor with high sensitivity, long lifetime and good reproducibility. In another study, the redox-active protein, Cyt *c* was immobilized onto photochemically carboxyl and amino functionalized vertically aligned CNs [88]. Two procedures were used in this work for CNs functionalization: (a) methyl ester-protected undecylenic acid was used during a UV reaction and then deprotected using a methyl-ester, followed by rinsing with 0.1 M HCl and deionized water. This strategy generated COOH groups. (b) To produce CNs with primary amine, tert-butyloxy-carbamate (tBOC) was linked to the surface during a UV reaction and then deprotected in a trifluoroacetic acid/methylene chloride (1:1) mixture followed by immersion in 10% ammonium hydroxide. In this work, the authors highlighted the importance of the surface functionalization and provided a comprehensive discussion on the complexity of the system involving a number of biological, chemical and electrical factors. A combination of these parameters, rather than only the 'increased surface area effect' contributed to the enhanced electrochemical detection of Cyt *c*. The disadvantage of these systems was the increased capacitive current.

Polymeric nanofibers are usually prepared by electrospinning. Enzyme can be coated onto the nanofibres using covalent procedures such as the glutaraldehyde or carbodiimide chemistry. In this way, the enzyme is immobilized onto the external surface of the electrospun fibers. This type of immobilization resulted in highly active and stabilized enzyme systems which are cost-effective and inexpensive [87,89]. For instance, Ye et al. immobilized lipase onto PANCMA fibers and compared the properties of the immobilized enzyme with that of hollow fibers. They found that the enzyme loading and activity retention increased from 2.3 (for the hollow fiber) to 21.2 mg/g (for the nanofibers) and that the Michaelis–Menten kinetic constant k_m decreased from 1.36 (for the hollow fiber) to 0.98 mmol/L for the nanofiber. These results demonstrate that the nanofiber architecture provides an enhanced biocatalytic activity and a higher efficiency for the immobilization of enzymes. A covalent immobilization procedure of GOX onto polystyrene/poly(styrene-co-maleic) anhydride nanofibers via glutaraldehyde was also used to produce enzyme aggregate [87].

In another strategy, enzymes can be immobilized by direct electrospinning of the enzyme together with the polymer to construct enzyme

nanofibers in a single-step process. Such an example is the immobilization of urease to construct a urease biosensor [90]. The fabrication procedure consisted in mixing 30% urease solution (prepared in PB) with 70% polymer solution (4.6×10^{-5} M polyvinylpyrrolidone (PVP) dissolved in ethanol). Then, the mixture was electrospun at a voltage of 20 kV at room temperature and a flow rate of 15 L/min. By direct electrospinning, the enzyme is confined inside the fiber and thus could cause diffusion limitation of the substrate/product to/from the catalytic active site. An additional limitation of this procedure is the weak stability, non-reusability and the enzyme leaching due to a possible swelling of the polymer.

More recently, fibers of other types of materials have been developed. For example, Patel et al. used nanoporous sol-gel silica fibers to encapsulate horseradish peroxidase (HRP) via a combined method involving direct encapsulation of enzymes and electrostatic nanofiber spinning [91]. The fibers produced had a diameter of ~100–200 nm, high porosity (2–4 nm), high mechanical flexibility and high thermal stability. In another work, silicon nanowires provided a platform for the immobilization of GOX for high-sensitivity glucose detection [92]. These nanowires have been prepared by thermal evaporation of silicon monoxide powder, which resulted in a crystalline Si core of ~15–20 nm in diameter and a Si oxide shell of ~3–5 nm. In this case, the enzyme was linked covalently via the carboxyl groups of the nanowires.

7.4.3. Metal Nanoparticles and Nanocrystals

Another class of nanomaterials currently investigated as carriers for enzyme immobilization comprises metal nanoparticles (NPs) and nanocrystals. In general, solid, colloidal, polymer-stabilized and protein-coated NPs have been used in enzyme stabilization. The advantages offered by these materials are the high enzyme loading and a large surface area available to facilitate reaction kinetics. For instance, effective enzyme loading can be achieved up to 6.4 or 10 wt. % [14]. By means of theoretical and experimental studies, Jia et al. demonstrated that particle mobility affected the intrinsic activity of the particle-attached enzymes [14]. In general, reducing the size of enzyme-carrier materials improves the efficiency of immobilized enzymes and the subsequent catalysis of their corresponding substrates [87]. Surface area is inversely proportional to the size of NPs. Therefore, smaller particles provide a larger surface area for the attachment of enzymes, leading to higher enzyme loading per unit mass of particles. This feature is

expected to enhance the sensitivity of the device and reduce the mass transfer resistance. The unique properties of NPs render biomolecule–NPs conjugates attractive labels for biosensing applications.

By far, the most commonly used NPs are the gold NPs, which have attracted an enormous attention due to their unique optoelectronic and catalytic properties [16,93]. Several research groups have studied the immobilization and enzymatic activity of Au–NPs biofunctionalized with enzymes such as HRP, GOX and pespine [93–95]. Au–NPs have been used to enhance the amount of immobilized enzyme and allow direct electrical contact between redox center of the enzyme and electrode surface [96]. Enzyme–Au–NPs have been immobilized onto the surface of electrodes to fabricate biosensors for H_2O_2, glucose, xanthine and hypoxanthine [66]. Gold–colloids bienzyme conjugates consisting of GOX and HRP have been developed for the detection of glucose using surface-enhanced Raman scattering (SERS) [95]. This method is based on the enhancement of Raman signal for molecules adsorbed on metallic surfaces. In the strategy, both enzymes were adsorbed onto the surface of Au–NPs by simple mixing of GOX and HRP for about 1 h. The immobilized GOX catalyzes the oxidation of glucose liberating hydrogen peroxide. In a subsequent stage, HRP in the presence of H_2O_2 oxidizes *o*-phenylenediamine to azoaniline, an azo compound with strong Raman scattering when adsorbed onto the surface of the gold colloids. The detection of glucose is then indirectly achieved from the intensity of the SERS signal which is proportional with the concentration of glucose. A schematic representation of the detection principle from Ref. [95] is presented in Fig. 7.6.

More recently, magnetic particles such as magnetite (Fe_3O_4) and quantum dots (QDs, colloidal inorganic semiconductor nanocrystals) have received a considerable attention. Magnetic nanoparticle bioconjugates have been used for the fabrication of nanometric glucose sensors [97]. QDs are characterized by a high size-dependent photoluminescence, broad excitation spectra and narrow emission bandwidths. These characteristics make them versatile photoelectrochemical labels for biomolecules [98–100]. For instance, CdS–NPs have provided an ideal environment for retaining GOX activity via simple adsorption and for facilitating electron transfer, resulting in an increase of the reduction peak of dissolved oxygen when used in an electrochemical glucose biosensor [101]. Katz et al. reported on the photocurrent generation by coupling reduced or oxidized Cyt *c* to CdS–NPs linked to an electrode [99]. The same research group reported the use of AChE-labeled CdS for the photochemical sensing of enzyme inhibitors. For this purpose, AChE was covalently linked to CdS–NPs of

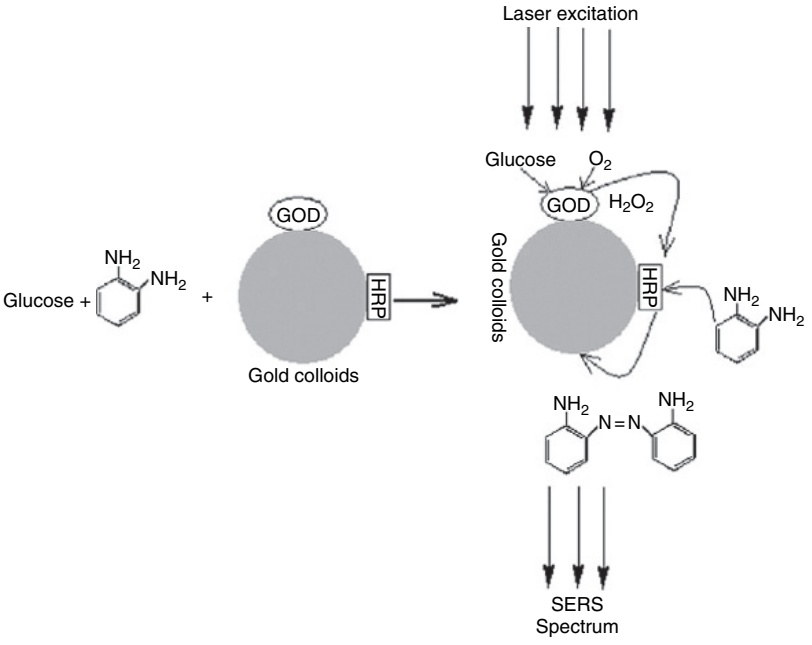

Figure 7.6: Indirect SERS detection of glucose using a GOD/HRP bienzymatic system with the enzymes immobilized on Au-NPs (from Ref. [95] with permission).

3 nm diameter using glutaric dialdehyde as a bifunctional unit. Microgravimetric measurements indicate that the surface coverage of enzyme was 3.9×10^{-12} mol/cm^2 and that ~2.4 NPs were associated with each AChE unit [98].

In addition to simple QDs–NPs, core-shell type QDs such as (CdSe)ZnS have been used in biosensing applications. It has been proven that by coating the QDs with higher band gap inorganic semiconductor materials, it is possible to increase the photoluminescence quantum yield and the chemical and photostability of these NPs. Core-shell QDs were recently used for bioconjugation with organophosphate hydrolase (OPH). The resulting biohybrid was used as the biological sensing element for the detection of organophosphorus pesticides. In this example, the (CdSe)ZnS core-shells were first modified with 2-mercapto acetic acid to achieve water solubility in basic conditions and a high photoluminescence. These QDs were

negatively charged. Then, the OPH was attached through electrostatic interactions. The OPH was positively charged at pH 7.3 (the isoelectric point is 7.6) and thus at this pH, it can be attached to the negatively charged QDs. These complexes were formed by simply mixing the OPH with QDs at room temperature. Figure 7.7 shows the schematic representation of the QDs/OPH bioconjugates from Ref. [100]. The detection of paraoxon was then achieved by photoluminescence quenching of the OPH–QDs bioconjugate in the presence of paraoxon. The quenching of the photoluminescence intensity was attributed to the conformational changes in the enzymes, which was confirmed by circular dichroism spectroscopy.

One of the limitations of NPs–enzyme systems is their rapid agglomeration and aggregation. For this reason, many efforts are focused on developing methods to assemble NPs in useful structures and functional devices. For example, they can be incorporated in polymeric matrices to form nanocomposites with high particle distribution and high conductivity. In this case, the polymer serves as a matrix for the incorporation of NPs and for enzyme immobilization. Such materials have been used for the fabrication of a variety of enzyme sensors and will be discussed in detail in the next section. A popular technique involves functionalizing of the NPs with a fluorescent chromophore for fluorescence detection, or chemically/electrostatically attaching biomolecules for subsequent electrochemical detection [17,102]

Another problem of NPs is the difficult recovery and reuse after being dispersed in the reaction medium. As a possible solution to this problem, Dyal et al. proposed to use magnetic nanoparticles, which can be easily separated from the reaction medium by use of a magnet [17]. For example, lipase was covalently attached to γ-Fe_2O_3 nanoparticles (with an average size of 20 ± 10 nm in diameter) resulting in up to $\sim$5.6 wt. % enzyme loading. Although the immobilized enzyme displayed much lower apparent activity than the native enzyme (less than 1%), the operational stability was greatly improved [17]. In another study, superparamagnetic polyacrylamide–Fe_3O_4 coated nanoparticles have been synthesized and used to covalently attach a model enzyme, α-chymotrypsin, to produce magnetic enzyme nanoparticles [103]. The preparation of the amine-functionalized nanogel and enzyme immobilization is schematically presented in Fig. 7.8. In this procedure, Fe_3O_4–NPs have been first modified to contain exposed amino functionalities for subsequent covalent binding using the EDC/NHS chemistry. The binding capacity determined by thermogravimetric analysis and standard BCA assay was found to be

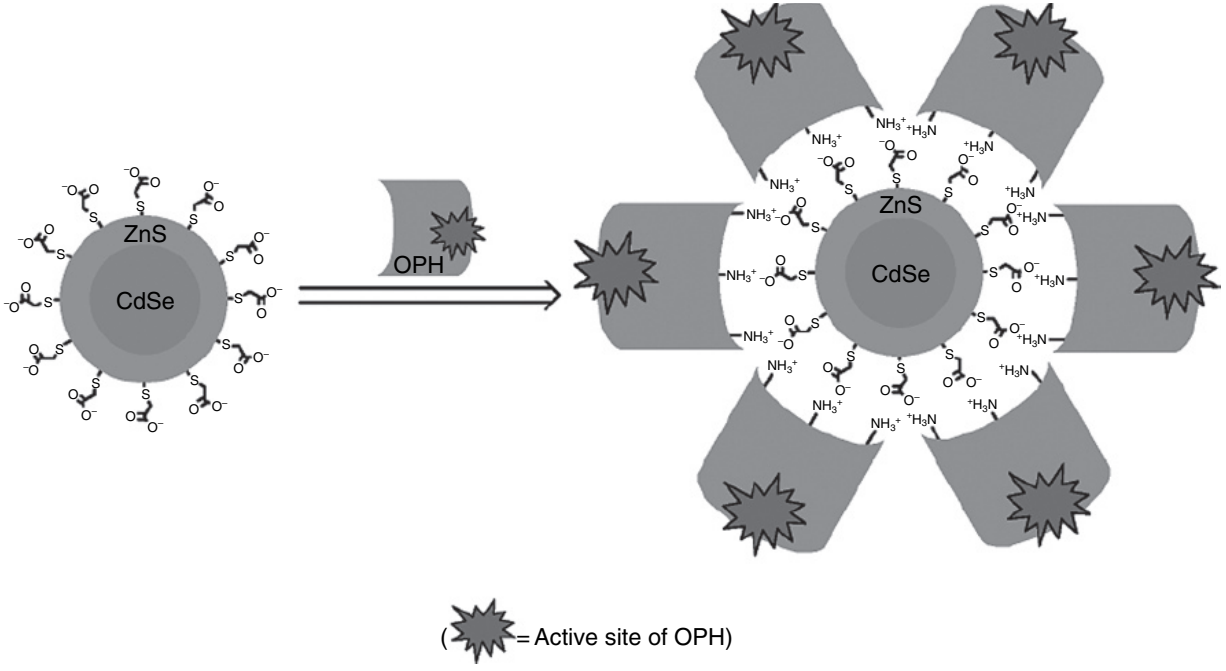

Figure 7.7: Immobilization of OPH on (CdSe)ZnS core-shell QDs (from Ref. [100] with permission).

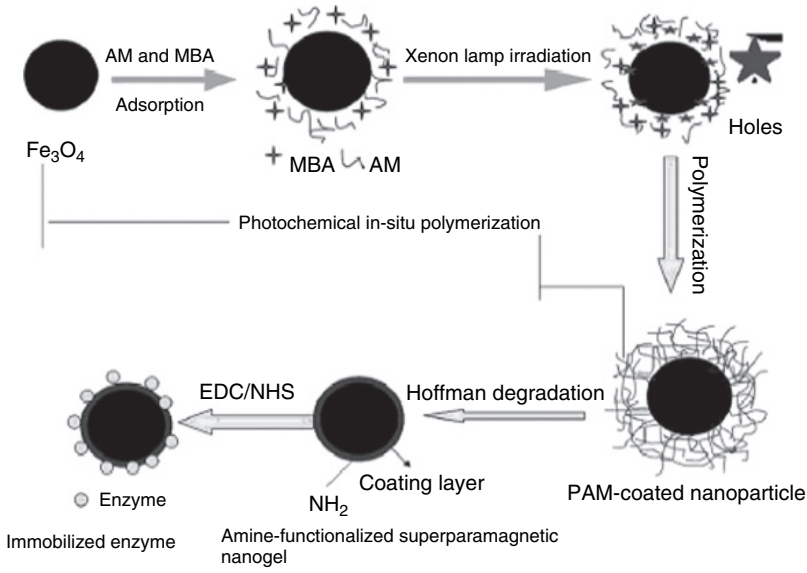

Figure 7.8: Immobilization of α-chymotrypsin on amino-functionalized magnetic nanogels (from Ref. [103] with permission).

69 mg of enzyme per gram of nanogel, while the specific activity was 0.39 U/mg/min.

7.4.4. Nanocomposite Materials

A new trend in enzyme immobilization and biosensor manufacturing is to use nanocomposite materials. These materials can contain free functional groups precisely located on the surface and available for specific biomolecule binding in a controlled and oriented manner or can be used as a platform for simple adsorption. Typically, nanocomposites are prepared from materials such as carbon, sol-gels, polymers [104] and nanometer-size materials. The composite can also contain cofactors, catalysts, mediators or stabilizers which might be necessary for the enzyme activity and function. In the process, enzymes could be incorporated (a) in a single step together with the other components to form a so-called biocomposite paste/ink or

(b) after nanocomposite preparation using classical attachment procedures. This can then be applied to a substrate/electrode to form a biosensor. Even though the method offers rapidity and simplicity, it also requires a rigorous and complex optimization due to the fact that the materials involved are of different nature and characteristics. In addition, it is important to conserve the initial properties of these materials during the fabrication process. With careful optimization, nanocomposite materials might provide better characteristics than their individual constituents.

Polymer nanocomposites

Most nanocomposites reported in the literature for the immobilization of enzymes are based on a mixture of polymers and gold nanoparticles. Examples include epoxy resins, polyurethanes, silicone, methacrylates, Teflon, polystyrenes, polythiophene, polypyrrole, polyacetylene, polyaniline and polyindole [105,106]. Their main advantage is the easy one-step preparation. The most commonly used are the composites based on conducting polymers, which offer excellent characteristics especially with respect to rigidity and mechanical stability. An example of such a configuration is the incorporation of Au nanoparticles during the electropolymerization of the monomer in the absence/presence of enzyme to form an enzyme Au–PPy composite. The main application of this type of materials is in biosensing [106,107]. Xiang et al. [22] synthesized an Au–NPs/polyaniline (Au–PANI) composite and used it to immobilize GOX via entrapment in Nafion. They found that the high conductivity coupled with the large surface area as well as the excellent electroactivity of the Au–PANI film were responsible for the low detection limit and rapid response time for the detection of glucose. The biosensor also exhibited high stability and excellent reproducibility.

Polymers such as epoxy resins have also been used. However, in some cases, the curing process requires high temperatures for polymerization that can be fatal to the enzyme. If the polymers are to be cured at room temperature, the process takes longer. For example, the optimal curing of the Epo-Tek H77 resin (Epoxy Technology, MA, USA) is 1 h at 150°C. For the same resin, the curing time is 1 week at 40 °C [105].

In other works, natural biopolymers such as chitosan and alginate have been used as matrix for the entrapment of nanoparticles and enzymes. These nanocomposites provided a suitable microenvironment for enzymes;

enzyme biosensors based on these materials with high stability and sensitivity have been described [23]. This is due to the biocompatibility of both Au nanoparticles and biopolymers. A phenol biosensor based on chitosan/laponite hybrid nanocomposite has been reported [108]. Laponite is a synthetic cationic clay of formula $(Mg_5 \cdot 5LiO_5)Si_4O_{10}(OH)_2(Na^+ \cdot 0.73 \cdot nH_2O)$ which appears as a colloidal suspension when suspended in water at a concentration $<10\,g/L$. This material was used to immobilize polyphenol oxidase on the surface of a GCE. The biosensor exhibited high sensitivity ($674\,mA/M/cm^2$ for catechol), stability (88% of the original activity after 60 days) and reproducibility. Polymers containing TiO_2 nanoparticles have been recently studied for the same purpose [109,110]. These materials have shown a particular interest for the construction of third-generation biosensors based on a direct electron transfer in the absence of mediators. For instance, the electron exchange between the enzyme (GOX and HRP have been used as model) and the electrode was greatly enhanced when TiO_2-nanostructured microenvironment which was used as immobilization matrix. Enhanced electrical properties can be further obtained by adding CNTs to the composite material. For example, by adding MWCNTs to a conducting polymer matrix containing poly(*o*-anisidine), TiO_2 and carbon black, it was possible to decrease the charge transfer resistance and the mass transfer impedance, which provided superior characteristics for biosensing [111].

Biofunctionalized membranes

Biofunctionalized membranes typically involve the random immobilization of enzymes to porous, polymeric membranes [112] and represent excellent candidates for enzyme immobilization [113–115]. Example of such materials include: porous silicone, dendrimers and TiO_2 nanofilms. The utilization of porous materials with nanometer pore size presents several advantages including: the pore size can be controlled and the enzyme is protected against leaching by entrapment inside the pores, thereby increasing the stability. One major disadvantage is that the activity of the immobilized enzyme could be affected due to the random distribution and non-specific multiple binding points of the enzyme. To avoid this limitation, one approach is site-specific immobilization in conjunction with molecular methods such as site-directed mutagenesis, gene fusion technology and post-translational modification methods. These methods have been reviewed by Butterfield et al. [112]. The real success of this interdisciplinary approach depends on the results of combined efforts of

scientists from different fields including molecular biologists, chemists and engineers.

Biofunctionalized membranes have found many applications for biosensing and bioreactors. Shoning et al. immobilized penicillinase on the surface of porous silicon and used it to construct a penicillin biosensor, with a sensitivity of ~90 mV mmol/L and a linear concentration range from 0.01 to 1 mM [116]. In another application, Darder et al. encapsulated GOX in a homemade alumina membrane using a chitosan network with two different pore diameters: 30 and 200 nm and studied their applications for the construction of a glucose biosensor [115,117]. The resulting sensor had a short response time and a wider linear range for the 30-nm pores and, a long response time and a narrower linear range for the 200 nm size. In another work, poly(amidoamine) dendrimers and cobalt-hexacyanoferrate-modified gold nanoparticles were deposited in a layer-by-layer configuration with poly(vinylsulfonic acid) as alternating unit [118]. The entire assembly was then used to immobilize GOX. The developed biosensor showed a sensitivity of 33.2 nA mmol/L/cm^2 and a detection limit of 17 μmol/L for glucose. In this case, cobalt hexacyanoferrate was used as an electronic mediator and the enzymatic detection of hydrogen peroxide was carried out at 0 V. Piletsky et al. demonstrated that a PANI-coated polypropylene (PANI/PP) membrane possessed high affinity for proteins. HRP immobilized on this membrane retained 70% of its activity after 3-month storage at 5°C [119].

7.4.5. Mesoporous Silica

Mesoporous silicas (MPS) are porous materials with controlled and well-ordered porosity (in an open-pore structure) and extremely high surface area [120,121]. The surface area improves the amount of enzyme immobilized, while the porosity is important in controlling the leaching and activity/stability [122]. The most widely used method to immobilize enzymes on mesoporous materials is simple adsorption in the silica pores via hydrogen bonding and electrostatic and hydrophobic interactions between the enzyme and the silica support [120,121]. Covalent binding inside the pores to create functionalized MPS [81] could also be used, but this involves a rigorous optimization in order to prevent the complete closure of the mesopores which can lead to mass-transfer limitation of the substrate [2,123]. Other methods involve physical entrapment by polyelectrolyte multilayers in a layer-by-layer assembly [120,121].

Enzyme immobilization and stability on these materials is highly dependent on the pore size and pH. Ideally, the pore size of the MPS should be similar to or slightly larger than that of the enzyme. Size matching between pore size and the molecular diameter of enzymes is important in achieving high stability and loading of adsorbed enzymes [81,124]. Enzymes with molecular diameter larger than the pore size cannot be adsorbed on the MPS. On the other hand, pores larger than the diameter of the enzymes result in rapid enzyme leaching [87]. To prevent leaching, the pores could be partially closed with silane or with alginate biocomposites [125]. A second approach would be to covalently bind enzymes to the MPS.

Another factor that contributes to the success of the immobilization is the charge interaction. With this respect, the pores should posses a charge that is opposite to the net surface charge of the enzyme [81,126]. This will stabilize the enzyme due to the attractive interaction forces between two opposite charges. On the other hand, when enzymes and mesopores have the same charge, enzyme stability diminishes due to the repulsion between the enzyme and the internal surface of mesopores, leading to enzyme leaching. In this situation, the charge can be controlled by changing the pH of the buffer solution [81] and/or by functionalizing the MPS with amino or carboxyl groups.

The first MPS used to immobilize an enzyme was a MCM-41, reported by Diaz and Balkus [127]. The MCM-41 was originally discovered by the Mobil research group in 1992 [9,127]. The MCM-41 is a unidimensional system with narrow pore-size distribution, where access to the enzymes might be restricted to the end of the channel [127]. Other MPS used are the MCM-48 (a tridimensional cubic phase pore structure), SBA-15 (highly ordered large pores MPS) [128], FSM-15 [129], SBA-1 (a cage-type structure) and several hexagonal, cellular foams and other FSM- and MCM-type structures as summarized recently by Hartmann [3]

The majority of MPS reported in the literature have a rather small pore size (usually less than 7 nm) which restrict their applications to the immobilization of small proteins such as Cyt *c* (molecular weight of 13 000 Da), lysozyme (13 930 Da), α-chymotrypsin (21 600 Da) [9,127]. Larger mesopores are rarely described. A recent example was the synthesis of ordered large mesopores of ∼13 nm diameter with 100–200 nm in length and 50–80 nm in width [130]. These structures have shown an unusual 'ultrafast enzyme adsorption' as compared to smaller pore-size MPS. Immobilization of Cyt *c* on MCM-48 and SBA-15 generated a biocatalyst that was stable for several months under conditions that would denature the protein in

solution [128]. In another application, enzymes immobilized in MPS have shown high enzyme activity in the presence of an organic solvent (toluene), in which native enzymes are inactive or exhibit low activity [129].

As an alternative to the small pore-size MPS for the immobilization of large enzymes, Yang et al. [131] proposed the use of macroporous cages connected by uniform mesoporous channels. Several enzymes (fumarase, trypsin, lipase and porcine liver esterase) were encapsulated in this material. One of the important characteristics of this material is that once the water was introduced in the channels, the environment in the interior of the cage was similar to that of native enzymes in aqueous solution. As a result, the encapsulated enzymes showed good activity, long-term stability and excellent recycling characteristics. In the system, the enzymes served as templates for the formation of macroporous cage. The connecting mesoporous channels protect the enzymes from leaching while allowing the diffusion of substrate/reactant to/from the catalytic active sites during the biocatalytic reaction.

7.5. Conclusions and Future Perspectives

Nanoarchitectural materials (nanoparticles, nanofibers, nanotubes, nanoporous silica, nanocrystalline films, etc.) have made a major impact in the field of enzyme immobilization, biotechnology and biosensors. This chapter provided an overview of the various nanomaterials used for enzyme immobilization and biosensors fabrication. Table 7.1 summarizes several examples of nanomaterials, enzyme immobilization and detection methods and their practical applications. New classes of composite materials which include almost all the discussed classes of nanomaterials are rapidly emerging. For example, Yang et al. functionalized CNTs with nickel hexacyanoferrate NPs using histidine, glutaraldehyde and chitosan to immobilize cholesterol oxidase [132]. It seems that blending of these components together may result into materials with interesting properties which can be useful for enzyme immobilization. In the future, these materials could lead to a new class of powerful biocatalysts and biosensors that could be used for identifying and quantifying a large diversity of analytes with application in quality control, clinical diagnosis, environmental monitoring and other types of analysis. However, while several nanostructure-based systems have been reported in literature, their implementation into routine functional devices still remains a great challenge.

Table 7.1: Examples of nanomaterials used for enzyme immobilization and detection methods and their practical applications.

Material	Immobilization method	Enzyme	Detection method/ Applications	Analytical performances				Reference
				Detection Limit (μM)	Linear Range	Sensitivity	Stability	
Carbon nanotubes	Physical adsorption	GOX	Electrochemical detection of glucose	–	–	–	86% after 4 months	[133]
	Electrochemical entrapment of nanotubes/GOX in a PPy film	GOX	Electrochemical detection of glucose	200	0–50 mM	2.33 nA/mM	–	[12]
	Covalent attachment on -COOH modified CNTs	GOX	Electrochemical detection of glucose, uric acid, ascorbic acid and acetaminophen	80	Up to 30 mM	–	–	[79]
Gold nanoparticles and quantum dots	Crosslinking atop Au-NPs modified carbon paste electrode	Xanthine Oxidase	Electrochemical detection of hypoxanthine in sardines and chicken meat	0.2	0.5–10 μM	22.9 mA/M	15 days	[134]
	Covalent binding using 1,4-benzene dithiolate as linker	Cyt *c*	Photoelectrochemical measurement of photocurrent generated after irradiation with UV light	–	–	–	–	[99]

Magnetic nanoparticles	Covalent bonding on γ-Fe_3O_4 magnetic nanoparticles	Candida rugosa lipase	AFM and UV–VIS spectroscopy (measurement of the reaction product, p-nitrophenol butyrate at 450 nm)	–	–	–	85% activity after 14 days	[17]
	Covalent binding of α-chymotrypsin on amine modified superparamagnetic NPs	α-chymotrypsin	IR spectroscopy, X-ray diffraction	–	–	–	59.3% of the free enzyme	[103]
	Covalent immobilization to core-shell ($MgFe_2O_4$–SiO_2) magnetic NPs attached to an electrode surface via a magnet	Tyr	Electrochemical detection of phenol & UV-VIS spectroscopy	0.6	1–250 μM	52 μA/mM	70% after 1 month	[102]
Nanofibers	Chemical attachment to electrospun polystyrene fibers	α-Chymotrypsin	UV-Vis spectroscopy (measurement of the reaction product, p-nitroaniline at 410 nm) and GC-FID	–	–	–	–	[20]

(*Continued*)

Table 7.1: (*Continued*)

Material	Immobilization method	Enzyme	Detection method/ Applications	Analytical performances				Reference
				Detection Limit (μM)	Linear Range	Sensitivity	Stability	
	Covalent attachment via glutaraldehyde	α-Chymotrypsin	UV-Vis spectroscopy (measurement of the reaction product, p-nitroaniline at 410 nm)	–	–	–	9 days	[21]
	Adsorption on the nanofibers (dimension ~10–200 nm) at 4°C for 24 h	GOX	Electrochemical detection of glucose	–	–	–	83–93% after 100 h	[40]
Biofunctionalyzed membranes	Adsorption on porous silicon	Penicillinase	Capacitance/ measurement of pH	–	0.01–1 mM	90 mV/mM	–	[116]
Polymers nanocomposites	Entrapment within a hybrid polysaccharide-silica hydrogel	Endo-1,3-β-D-gluconases (luminarinases)	HPLC, TLC, C NMR (for the substrates) and GPC for the products or hydrolysis of luminaran and synthesis of translam	–	–	–	–	[135]

	Adsorption on chitosan/laponite	Tyr	Electrochemical detection of catechol	–	–	674 mA/M	88% after 60 days	[108]
Mesoporous silica	Encapsulation within the porous pores	Cyt *c*, catalase and protease	UV-VIS spectroscopy	–	–	–	–	[120]
	Covalent attachment on the silica pores (1–15 nm) via glutaraldehyde chemistry.	Glutaryl-7-ACA acylase	UV-VIS spectroscopy	–	–	–	–	[136]
Sol-gels nanocomposites	Adsorption in a nanocomposite of silver nanoparticles, methylene blue, enzyme and sol-gel	HRP	Electrochemical detection of hydrogen peroxide	0.4	0.001–1 mM	–	82% in two weeks	[137]
	Entrapment of enzyme in a sol-gel doped with super paramagnetic Fe_3O_4 NPs	Lipase	HPLC and calorimetry	–	–	–	50% in 4 months at 40°C	[138]

Polypyrrole (PPy), Glucose oxidase (GOX), Horseradish peroxidase (HRP), Tyrosinase (Tyr), Cytochrome *c* (Cyt *c*)

High performance liquid chromatography (HPLC), Nuclear magnetic resonance (NMR), Thin layer chromatography (TLC), Gel permeation chromatography (GPC), Atomic force microscopy (AFM), Gas chromatography with flame ionization detector (GC-FID) Carbon nanotubes (CNTs), nanoparticles (NPs)

References

[1] Moriarty, P. (2001) Nanostructured materials. *Rep. Prog. Phys.*, **64**, 297–381.

[2] Kim, J., Grate, J.W. and Wang, P. (2006) Nanostructures for enzyme stabilization. *Chem. Eng. Sci.*, **61**, 1017–26.

[3] Hartmann, M. (2005) Ordered mesoporous materials for bioadsorption and biocatalysis. *Chem. Mater.*, **17**, 4577–93.

[4] Tischer, W. and Kasche, V. (1999) Immobilized enzymes: crystals or carriers? *Trends Biotechnol.*, **17**, 326–35.

[5] David, A.E., Wang, N.S., Yang, V.C. et al. (2006) Chemically surface modified gel (CSMG): an excellent enzyme-immobilization matrix for industrial processes. *J. Biotechnol.*, **125**, 395–407.

[6] Krajewska, B. (2004) Application of chitin- and chitosan- based materials for enzyme immobilizations: a review. *Enzy. Microb. Technol.*, **35**, 126–39.

[7] Böyükbayram, A.E., Kiralp, S., Toppare, L. et al. (2006) Preparation of biosensors by immobilization of polyphenol oxidase in conducting copolymers and their use in determination of phenolic compounds in red wine. *Biolectrochemistry*, **69**, 164–71.

[8] Chibata, I. (1978) *Immobilized Enzymes: Research and Development A Halsted Press Book ISBN 0470265310*. New York: John Wiley & Sons.

[9] Hudson, S., Magner, E., Cooney, J. et al. (2005) Methodology for the immobilization of enzyme onto mesoporous materials. *J. Phys. Chem. B*, **109**, 19496–506.

[10] Sljukic, B., Banks, C.E., Salter, C. et al. (2006) Electrochemically polymerised composites of multi-walled carbon nanotubes and poly(vinylferrocene) and their use as modified electrodes: application to glucose sensing. *Analyst*, **131**, 670–7.

[11] Pan, D., Chen, J., Yao, S. et al. (2005) An amperometric glucose biosensor based on glucose oxidase immobilized in electropolymerized poly(o-aminophenol) and carbon nanotubes composite film on a gold electrode. *Anal. Sci*, **21**(4), 367–71.

[12] Wang, J. and Musameh, M. (2005) Carbon-nanotubes doped polypyrrole glucose biosensor. *Anal. Chim. Acta*, **539**, 209–13.

[13] Luo, X.-L., Xu, J.-J., Wang, J-L. et al. (2005) Electrochemically deposited nanocomposite of chitosan and carbon nanotubes for biosensor application. *Chem. Comm.*, **16**, 2169–71.

[14] Jia, H., Zhu, G. and Wang, P. (2003) Catalytic behaviors associated with enzymes attached to nanoparticles: the effect of particle mobility. *Biotechnol. Bioeng.*, **84**, 406–14.

[15] Chen, J.-P. and Su, D.-R. (2001) Latex particles with thermo-flocculation and magnetic properties for immobilization of α-chymotrypsin. *Biotechnol. Prog.*, **17**, 369–75.

[16] Mena, M.L., Yanez-Sedeno, P. and Pingarron, J.M. (2005) A comparison of different strategies for the construction of amperometric biosensors using gold nanoparticles-modified electrodes. *Anal. Biochem*., **336**, 20–7.
[17] Dyal, A., Loos, K., Noto, M. et al. (2003) Activity of *Candida rugosa* lipase immobilized on gamma-Fe_2O_3 magnetic nanoparticles. *J. Am. Chem. Soc*., **125**, 1684–5.
[18] Liu, B., Cao, Y., Chen, D. et al. (2003) Amperometric biosensor based on a nanoporous ZrO_2 matrix. *Anal. Chem. Acta*, **478**, 59–66.
[19] Heilmann, A., Teuscher, N., Kiesow, A. et al. (2003) Nanoporous aluminum oxide as a novel support material for enzyme biosensors. *J. Nanosci. Nanotechnol*, **3**, 375–9.
[20] Jia, H.F., Zhu, G.Y., Vugrinovich, B. et al. (2002) Enzyme-carrying polymeric nanofibers prepared via electrospinning for use as unique biocatalysts. *Biotechnol. Prog*., **18**, 1027–32.
[21] Kim, B.C., Nair, S., Kim, J. et al. (2005) Preparation of biocatalytic nanofibers with high activity and stability via enzyme aggregate coating on polymer nanofibers. *Nanotechnology*, **16**, S382–8.
[22] Xiang, Y., Hu, Y., Liu, F. et al. (2006) Glucose biosensor based on Au nanoparticles – conductive polyaniline nanocomposites. *Biosens. Bioelectron*., **21**, 1996–2000.
[23] Xu, Q., Mao, C., Liu., N.-N. et al. (2006) Direct electrochemistry of horseradish peroxidase based on biocompatible carboxymethyl chitosan–gold nanoparticle nanocomposites. *Biosens. Bioelectron*., **22**, 768–73.
[24] Yang, M., Yang, Y., Liu, Y. et al. (2006) Platinum nanoparticles-doped sol – gel/carbon nanotubes composite electrochemical sensors and biosensors. *Biosens. Bioelectron*., **21**(7), 1125–31.
[25] Yang, M., Yang, Y., Yang, Y. et al. (2005) Microbiosensor for acetylcholine and choline based on electropolymerization/sol – gel derived composite membrane. *Anal. Chim. Acta*., **530**(2), 205–11.
[26] Tan, X.-C., Tian, Y.-X., Cai, P.-X. et al. (2005) Glucose biosensor based on glucose oxidase immobilized in sol – gel chitosan/silica hybrid composite film on Prussian blue modified glass carbon electrode. *Anal. Bioanal. Chem*., **381**(2), 500–7.
[27] Kim, J. and Grate, J.W. (2003) Single enzyme nanoparticles armored by a nanometer a nanometer-scale organic/inorganic network. *Nano Lett*., **3**, 1219–22.
[28] Gerard, M., Chaubey, A. and Malhotra, B.D. (2002) Application of conducting polymers to biosensors. *Biosens. Bioelectron*., **5**, 345.
[29] Andreescu, S. and Marty, J.-L. (2006) Twenty years research in cholinesterase biosensors: from basic research to practical applications. *Biomol. Eng*., **23**, 1–15.
[30] Andreescu, S. and Sadik, O.A. (2004) Trends and challenges in biochemical sensors for clinical and environmental monitoring. *Pure Appl. Chem.* **76**(4), 861.

[31] Bonnet, C., Andreescu, S. and Marty, J.-L. (2003) Adsorption: an easy and efficient immobilisation of acetylcholinesterase on screen-printed electrodes. *Anal. Chim. Acta*., **481**, 209.
[32] Collings, A.F. and Caruso, F. (1997) Biosensors: recent advances. *Rep. Prog. Phys*., **60**(11), 1397.
[33] Andreescu, S., Barthelmebs, L. and Marty, J.L. (2002) Immobilization of acetylcholinesterase on screen-printed electrodes: comparative study between three immobilization methods and applications to the detection of organophosphorus insecticides. *Anal. Chim. Acta*., **464**(2), 171.
[34] Baker, S.E., Tse, K.Y., Hindin, E. et al. (2005) Covalent functionalization for biomolecular recognition on vertically aligned carbon nanofibers. *Chem Mater*., **17**(20), 4971.
[35] Loscher, F., Ruckstuhl, T., Jaworek, T. et al. (1998) Immobilization of biomolecules on Langmuir–Blodgett films of regenerative cellulose derivatives. *Langmuir*, **14**(10), 2786.
[36] Senaratne, W., Andruzzi, L. and Ober, C.K. (2005) Self-assembled monolayers and polymer brushes in biotechnology: current applications and future perspectives. *Biomacromolecules*., **6**(5), 2427.
[37] Sigal, G.B., Bamdad, C., Barberis, A. et al. (1996) A self-assembled monolayer for the binding and study of histidine tagged proteins by surface plasmon resonance. *Anal. Chem*., **68**(3), 490.
[38] Scouten, W.H., Luong, J.H.T. and Brown, R.S. (1995) Enzyme or protein immobilization techniques for applications in biosensors design. *Tibtech*., **13**, 178–85.
[39] Thévenot, D.R., Toth, K., Durst, R.A. et al. (2001) Electrochemical biosensors: recommended definitions and classification. *Biosens. Bioelectron*., **16**, 121–31.
[40] Vamvakaki, V., Tsagaraki, K. and Chaniotakis, N. (2006) Carbon nanofiber-based glucose biosensor. *Anal. Chem*., **78**, 5538–42.
[41] Phadtare, S., Vinod, V.P., Wadgaonkar, P.P. et al. (2004) Free-standing nanogold membranes as scaffolds for enzyme immobilization. *Langmuir*, **20**, 3717–23.
[42] Andreescu, S. and Marty, J.L. (2006) Twenty years research in cholinesterase biosensors: from basic research to practical applications. *Biomol. Eng*., **23**, 1–15.
[43] Gooding, J.J. and Hibbert, D.B. (1999) The application of alkanethiol self-assembled monolayers to enzyme electrodes. *Trends Anal. Chem*., **18**(8), 525.
[44] Chaki, N.K. and Vijayamohanan, K. (2002) Self-assembled monolayers as a tunable platform for biosensor applications. *Biosens. Bioelectron*., **17**, 1–12.
[45] Wink, Th., van Zuilen, S.J., Bult, A. et al. (1997) Self-assembled monolayers for biosensors. *Analyst*, 122, 43R–50R.
[46] Fink, S., van Veggel, F.C.J.M. and Reinhoudt, D.N. (2000) Sensor functionalities in self-assembled monolayers. *Adv. Mater*., **12**, 1315–28.

[47] Saleemuddin, M. (1999) Bioaffinity based immobilization of enzymes. *Adv. Biochem. Eng. Biotechnol*., **64**, 203–26.
[48] Kumada, Y., Tokunaga, Y., Imanaka, H. et al. (2006) Screening and characterization of affinity peptide tags specific to polystyrene supports for the orientated immobilization of proteins. *Biotechnol. Prog*., **22**, 401–5.
[49] Andreescu, S., Bucur, B. and Marty, J.-L. (2006) Affinity immobilization of tagged enzymes. In *Immobilization of Enzymes and Cells*, Second edition (J.M. Guisan, ed.). Series: *Methods in Biotechnology*. *Humana Press* (ISBN 1-58829-290-8) pp. 97–106.
[50] Andreescu, S., Magearu, V., Lougarre, A. et al. (2001) Immobilization of enzymes on screen-printed sensors via an histidine tail. Application to the detection of pesticides using modified cholinesterase. *Anal. Lett*., **34**(4), 429.
[51] Hsiao, H. and Royer, G.P. (1979) Immobilization of glycoenzymes through carbohydrate side chain. *Arch. Biochem. Biophys*., **198**, 379–85.
[52] Woodward, J. and Wiseman, A. (1978) The involvement of salt linkages in the stabilization of bakers yeast invertase. *Biochim. Biophys. Acta*., **527**, 8–16.
[53] Saleemuddin, M. and Husain, Q. (1991) Concanavalin A: a useful ligand for glycoenzyme immobilization. *Enzyme Microbiol. Technol*., **13**, 290–9.
[54] Song, J.M. and Vo-Dinh, T. (2004) Miniature biochip system for detection of Escherichia coli O157:H7 based on antibody-immobilized capillary reactors and enzyme-linked immunosorbent assay. *Anal. Chim. Acta*, **507**, 115–21.
[55] Oh, B.K., Chun, B.S., Park, K.W. et al. (2004) Fabrication of protein G LB film for immunoglobulin G immobilization. *Mater. Sci. Eng*. C, **24**, 65–9.
[56] Wang, A.A., Lee, J., Jenikova, G. et al. (2006) Controlled assembly of multi-segment nanowires by histidine-tagged peptides. *Nanotechnology*, **17**, 3375–9.
[57] Cosnier, S., Mousty, C., Gondran, C. et al. (2006) Entrapment of enzyme within organic and inorganic materials for biosensor applications: Compartive study. *Mater. Sci. Eng. C*, **26**, 442–7.
[58] Cosnier, S. (2005) Affinity biosensors based on electroplymerized films. *Electroanal*., **17**(9), 1701–5.
[59] Brahim, S., Narnesigh, D. and Guiseppi-Elie, A. (2002) Polypyrrole-hydrogel composites for the construction of clinically important biosensors. *Biosens. Bioelectron*., **17**, 53–9.
[60] Njagi, J., Andreescu, D. and Andreescu, S. (2006) Nanostructures for enzyme immobilization and biosensors. 34th Northeast Regional Meeting of American Chemical Society at Binghampton October 5–7.
[61] Wang, J. (2005) Nanomaterial-based electrochemical biosensors. *Analyst*., **130**, 421–6.
[62] Rao, C.N.R., Satishkumar, B.C., Govindarai, A. et al. (2001) Nanotubes. *Chemphyschem*, **2**(2), 78–105.
[63] Baughmman, R.H., Zaknidov, A.A. and Heer, W.A. (2002) Carbon nanotubes-the route toward applications. *Science*, **297**, 787–92.

[64] Wang, J. (2005) Carbon-nanotube based electrochemical biosensors: a review. *Electroanalysis*, **17**(1), 7.
[65] Davis, J.J., Coleman, K.S., Azamian, B.R. et al. (2003) Chemical and biochemical sensing with modified single walled carbon nanotubes. *Chem. Eur. J*., **9**, 3732.
[66] Jianrong, C., Yuqing, M., Nongyue, H. et al. (2004) Nanotechnology and biosensors. *Biotechnol. Advances*., **22**, 505–18.
[67] Barone, P.W., Baik, S., Heller, D.A. et al. (2005) Near-infrared optical sensors based on single-walled carbon nanotubes. *Nat. Mater*., **4**(1), 86–92.
[68] Ziegler, K.J. (2005) Developing implantable optical biosensors. *Trends in Biotechnol*., **23**(9), 440–4.
[69] Sotiropoulou, S., Gavalas, V., Vamvakaki, V. et al. (2003) Novel carbon materials in biosensors systems. *Biosens. Bioelectron*., **18**, 211–5.
[70] Guiseppi-Elie, A., Lei, C. and Baughman, R.H. (2002) Direct electron transfer of glucose oxidase on carbon nanotubes. *Nanotechnology*, **13**, 559–64.
[71] Wang, J. and Musameh, M. (2003) Enzyme dispersed carbon-nanotube electrodes: a needle microsensor for monitoring glucose. *Analyst*., **128**, 1382.
[72] Rubianes, M.D. and Rivas, G.A. (2003) Carbon nanotubes paste electrodes. *Electrochem. Comm*., **5**, 689–94.
[73] Perez, B., Pumera, M., del Valle, M. et al. (2005) Glucose biosensor based on carbon nanotube epoxy composites. *J. Nanosci. Nanotechnol*., **5,10**, 1694–8.
[74] Liu, Y., Wang, M., Zhao, F. et al. (2005) The direct electron transfer of glucose oxidase and glucose biosensor based on carbon nanotubes/chitosan matrix. *Biosens. Bioelectron*., **21**, 984–8.
[75] Wang, J. and Musameh, M. (2003) Carbon nanotube/Teflon composite electrochemical sensors and biosensors. *Anal. Chem*., **75**, 2075.
[76] Zhang, M. and Gorski, W. (2005) Electrochemical sensing based on redox mediation at carbon nanotubes. *Anal. Chem*., **77**, 3960–5.
[77] Musameh, M., Wang, J., Merkoci, A. et al. (2002) Low-potential stable NADH detection at carbon-nanotube-modified glassy carbon electrodes. *Electrochem. Comm*., **4**, 743–6.
[78] Joshi, K.A., Tang, J., Haddon, R. et al. (2005) A disposable biosensors for organophosphorus nerve agents based on carbon nanotubes modified thick film strip electrodes. *Electroanalysis*, **17**, 54–8.
[79] Lin, Y.H., Lu, F. and Wang, J. (2004) Disposable carbon nanotube modified screen-printed biosensor for amperometric detection of organophosphorus pesticides and nerve agents. *Electroanalysis*, **16**, 145–9.
[80] Wang, S.G., Zhang, Q., Wang, R. et al. (2003) A novel multi-walled carbon nanotube-based biosensor for glucose detection. *Biochem. Biophys. Res. Comm*., **311**, 572–6.
[81] Lei, C., Shin, Y., Liu, J. et al. (2002) Entrapping enzyme in a functionalized nanoporous support. *J. Am. Chem. Soc*., **124**, 11242–3.

[82] Bahr, J.L. and Tour, J.M. (2002) Covalent chemistry of single-wall carbon nanotubes. *J. Mater. Chem*., **12**, 1952.
[83] Lin, Y., Lu, F., Tu, F. et al. (2004) Glucose biosensors based on carbon nanotubes nanoelectrode ensemblies. *Nano Lett*., **4**(2), 191–5.
[84] Ravidran, S., Chaudhary, S., Colburn, B. et al. (2003) Covalent coupling of quantum dots to multiwalled carbon nanotubes for electronic device applications. *Nano Lett*., **2**(4), 447–53.
[85] Carrillo, A., Swartz, J.A., Gamba, J.M. et al. (2003) Non-covalent functionalization of graphite and carbon nanotubes with polymer multilayers and gold nanoparticles. *Nano Lett*., **3**(10), 1437–40.
[86] Musameh, M. and Wang, J. (2005) Magnetically induced carbon nanotube-mediated control of electrochemical reactivity. *Langmuir*, **21**, 8565–8.
[87] Kim, J., Jia, H. and Wang, P. (2006) Challenges in biocatalysis for enzyme-based biofuel cells. *Biotechnol. Advances*, **24**, 296–308.
[88] Baker, S.E., Colavita, P.E., Tse, K-Y. et al. (2006) Functionalized vertically aligned carbon nanofibers as scaffolds for immobilization and electrochemical detection of redox-active proteins. *Chem. Mater*., **18**, 4415–22.
[89] Ye, P., Xu, Z.K., Wu, J. et al. (2006) Nanofibrous membranes containing reactive groups: electrospinning from poly(acrylonitrile-co-maleic acid) for lipase immobilization. *Macromolecules*, **39**(3), 1041–5.
[90] Sawicka, K., Gouma, P. and Simon, S. (2005) Electrospun biocomposite nanofibers for urea biosensing. *Sens. Actuators B*., **108**, 585–8.
[91] Patel, A.C., Li, S.X., Yuan, J.M. et al. (2006) In situ encapsulation of horseradish peroxidase in electrospun porous silica fibers for potential biosensor applications. *Nano Lett*., **6**(5), 1042–6.
[92] Chen, W.W., Yao, H., Tzang, C.H. et al. (2006) Silicon nanowires for high-sensitivity glucose detection. *Appl. Phys. Lett*., **88**, 21.
[93] Mukhopadhyay, K., Padtare, S., Vinod, V.P. et al. (2003) Gold nanoparticles assembled on amine-functionalized Na–Y zeolite: a biocompatible surface for enzyme immobilization. *Langmuir*, **19**, 3858–63.
[94] Lei, C.X., Hu, S.Q., Shen, G.L. et al. (2003) Immobilization of horseradish peroxidase to a nano-Au monolayer modified chitosan-entrapped carbon paste electrode for the detection of hydrogen peroxide. *Talanta*, **59**(5), 981–8.
[95] Wu, Z.S., Zhou, G.Z., Jiang, J.H. et al. (2006) Gold colloid-bienzyme conjugates for glucose detecting surface-enhanced raman Scatterring. *Talanta*, **70**(3), 533–9.
[96] Katz, E., Willner, I and Wang, J. (2004) Electroanalytical and Bioelectroanalytical systems based on metal and semiconductor nanoparticles. *Electroanalysis*, **16**, 1–2, 19.
[97] Rossi, L.M., Quach, A.D. and Rosenzweig, Z. (2004) Glucose oxidase-magnetite nanoparticle bioconjugate for glucose sensing. *Anal. Bioanal. Chem*., **380**(4), 606.

[98] Pardo-Yissar, V., Katz, E., Wasserman, J. et al. (2003) Acetylcholine esterase-labeled CdS nanoparticles on electrodes: photoelectrochemical sensing of the enzyme inhibitors. *J. Am. Chem Soc*., **125**(3), 622–3.
[99] Katz, E., Zayats, M., Willner, I. et al. (2006) Controlling the direction of photocurrents by means of CdS nanoparticles and cytochrome c-mediated biocatalytic cascades. *Chem. Comm*., **13**, 1396–7.
[100] Ji, X.S., Zheng, J.Y., Xu, J.M. et al. (2005) (CdSe)ZnS quantum dots and organophosphorus hydrolase bioconjugate as biosensors for detection of paraoxon. *J. PhysChem. B*, **109**(9), 3793–9.
[101] Huang, Y.X., Zhang, W.J., Xiao, H. et al. (2005) An electrochemical investigation of glucose oxidase at a CdS nanoparticles modified electrode. *Biosens. Bioelectron*., **21**(5), 817–21.
[102] Liu, Z., Liu, Y., Yang, H. et al. (2005) A phenol biosensor based on immobilizing tyrosinase to modified core-shell magnetic nanoparticles supported at a carbon paste electrode. *Anal. Chim. Acta*, **533**, 3–9.
[103] Hong, J., Gong, P.-J., Yu, J.H. et al. (2006) Conjugation of alfa-chymotrypsin on a polymeric hydrophobic nanolayer covering magnetic nanoparticles. *J. Mol. Catal. B-Enzym*, **42**(3–4), 99–105.
[104] Albareda-Sirvent, M., Merkoci, A. and Alegret, S. (2000) Configurations used in the design of screen-printed enzymatic biosensors. a review. *Sens. Actuators. B*, **69**(1–2), 153–63.
[105] Cespedes, F. and Alegret, S. (2000) New materials for electrochemical sensing II. Rigid carbon-polymer biocomposites. *Trends in Anal. Chem*., **19**(4), 276–84.
[106] Cosnier, S. (1999) Biomolecule immobilization on electrode surfaces by entrapment or attachment to electrochemically polymerized film. A review. *Biosens. Bioelectron*., **14**, 443–56.
[107] Yuqing, M., Jianrong, C. and Xiaohua, W. (2004) Using electropolymerized non-conducting polymers to develop enzyme amperometric biosensors. *Trends in Biotechnol*., **22**(5), 227–31.
[108] Fan, Q., Shan, D., Xue, H. et al. (2007) Amperometric phenol biosensor based on laponite clay–Chitosan nanocomposite matrix. *Biosens. Bioelectron*, **22**, 816–21.
[109] Vitcoli, M., Curulli, A., Cusma, A. et al. (2006) Third-generation biosensors based on TiO_2 nanostructured films. *Mater. Sci. Eng. C*, **26**(5–7), 947–51.
[110] Curulli, A., Valentini, F., Padeletti, G. et al. (2005) Smart (nano) materials: TiO_2 nanostructured films to modify electrodes for assembling of new electrochemical probes. *Sens. Actuators. B*., **111–112**, 441–9.
[111] Carrara, S., Bavastrello, V., Ricci, D. et al. (2005) Improved nanocompotite materials foir biosensor applications investigated by electrochemical impedance spectroscopy. *Sens. Actuators, B*., **109**, 221–6.
[112] Butterfield, D.A., Bhattacharyya, D., Daunert, S. et al. (2001) Catalytic biofunctional membranes containing site-specifically immobilized enzyme arrays: a review. *J. membrane science*., **181**(1), 28–37.

[113] Delouise, L.A. and Miller, B.L. (2005) Enzyme immobilization in porous silicon: Quantitative analysis of the kinetic parameters for glutathione-S-transferases. *Anal. Chem*., **77**(7), 1950–6.

[114] Myler, S., Collyer, S.D., Bridge, K.A. et al. (2002) Ultra-thin-polysiloxane-film-composite membranes for the optimisation of amperometric oxidase enzyme electrodes. *Biosens. Bioelectron*., **17**, 35–43.

[115] Hernandez-Velez, M. (2006) Nanowires and 1D arrays fabrication: an overview. *Thin Solid Films*., **495**, 51–63.

[116] Schöning, M.J., Kurowski, A., Thust, M. et al. (2000) Capacitive microsensors for biochemical sensing based on porous silicon technology. *Sens Actuators*, **64**, 59–64.

[117] Darder, M., Aranda, P., Hernández-Vélez, M. et al. (2006) Encapsulation of enzymes in alumina membranes of controlled pore size. *Thin Solid Films*., **495**, 321–6.

[118] Crespilho, F.N., Ghica, M.E., Florescu, M. et al. (2006) A strategy for enzyme immobilization on layer-by-layer dendrimer–gold nanoparticle electrocatalytic membrane incorporating redox mediator. *Electrochem. Commun*., **8**, 1665–70.

[119] Piletsky, S., Piletska, E., Bossi, A. et al. (2003) Surface functionalization of porous polypropylene membranes with polyaniline for protein immobilization. *Biotectnol. Bioeng*., **82**(1), 86–92.

[120] Wang, Y. and Caruso, F. (2004) Enzyme encapsulation in nanoporous silica spheres. *Chem. Comm*., issue 13, 1528–9.

[121] Wang, Y. and Caruso, F. (2005) Mesoporous silica spheres for enzyme immobilization and encapsulation. *Chem. Mater*., **17**, 953–61.

[122] Sotiropoulou, S., Vamvakaki, V. and Chaniotakis, N.A. (2005) Stabilization of enzymes in nanoporous materials for biosensor applications. *Biosens. Bioelectron*., **20**, 1674–9.

[123] Ma, H., He, J., Evans, D.G. et al. (2004) Immobilization of lipase in a mesoporous reactor based on MCM-41. *J. Mol. Catal. B Enzym*., **30**, 209–17.

[124] Blanco, R.M., Terreros, P., Fernandez-Perez, M. et al. (2004) Functionalization of mesoporous silica for lipase immobilization characterization of the support and the catalysts. *J. Mol. Catal. B-Enzym*, **30**, 83–93.

[125] Avnir, D., Coradin, T., Lev, O. et al. (2005) Recent bio-applications of sol-gel materials. *J. Mater. Chem*., **16**, 1013–30.

[126] Vinu, A., Murugesan, V., Tangermann, O. et al. (2004) Adsorption of cytochrome c on mesoporous molecular sieves: influence of pH, pore diameter, and aluminum incorporation. *Chem. Mater*., **16**, 3056–65.

[127] Diaz, J.F. and Balkus, K.J. (1996) Enzyme immobilization in MCM-41 molecular sieve. *J. Molec. Catal. B. Enzymatic*, **2**, 115–26.

[128] Washmon-Kriel, L., Jimerez, V.L. and Balkus, K.J. (2000) Cytochrome c immobilization into mesoporous molecular sieves. *J. Molec. Catal. B. Enzym*., **10**, 453–69.

[129] Takahashi, H., Li, B., Sasaki, T. et al. (2001) Immobilized enzymes in ordered mesoporous silica materials and improvement of their stability and catalytic activity in an organic solvent. *Micropor. Mesopor. Mater*., **44–45**, 755–62.

[130] Sun, J., Zhang, H., Tian, R. et al. (2006) Ultrafast enzyme immobilization over large-pore nanoscale mesoporous silica particles. *Chem. Comm*., issue 12, 1322–4.

[131] Yang, X.-Y., Li, Z.-Q., Liu, B. et al. (2006) 'Fish in net' encapsulation of enzymes in macroporous cages as stable, reusable and active heterogeneous biocatalysts. *Adv. Mater*., **18**, 410–4.

[132] Yang, M., Yang, Y., Qu, F. et al. (2006) Attachment of nickel hexacyanoferrates nanoparticles on carbon nanotubes: preparation, characterization and bioapplication. *Anal. Chim. Acta*., **571**(2), 211–7.

[133] Wang, S.G., Zhang, Q., Wang, R. et al. (2003) A novel multi-walled carbon nanotube-based biosensor for glucose detection. *Biochem. Biophys. Res. Commun*., **311**, 572–6.

[134] Agui, L., Manso, J., Yáñez-Sedeño, P. et al. (2006) Amperometric biosensor for hypoxanthine based on immobilized xanthine oxidase on nanocrystal gold–carbon paste electrodes. *Sens. Actuators B*., **113**, 272–80.

[135] Shchipunov, Y.A., Burtseva, Y.V., Karpenko, T.Y. et al. (2006) Highly efficient immobilization of endo-1, 3-β-d-glucanases (laminarinases) from marine mollusks in novel hybrid polysaccharidesilica nanocomposites with regulated composition. *J. Mol. Catal. B: Enzym*., **40**, 16–23.

[136] Kim, J.-K., Park, J.-K. and Kim, H.-K. (2004) Synthesis and characterization of nanoporous silica support for enzyme immobilization. *Colloids Surf. A Physicochem. Eng. Aspects*., **241**, 113–7.

[137] Xua, J.-Z., Zhangb, Y., Lia, G.-X. et al. (2004) An electrochemical biosensor constructed by nanosized silver particles doped sol-gel film. *Mater. Sci. Eng. C*., **24**, 833–6.

[138] Chen, J.-P. and Lin, W.-S. (2003) Sol-gel powders and supported sol-gel polymers for immobilization of lipase in ester synthesis. *Enzyme Microb. Technol*., **32**, 801–11.

Chapter 8

Design of the solid phase for protein arrays and use of semiconductor nanoparticles as reporters in immunoassays

Olena Tsvirkunova
Research Scientist, Align Technology, Inc., Santa Clara, CA, USA

Tim Dubrovsky
Senior Group Manager, BD Biosciences, San Jose, CA, USA

Abstract. A fundamental problem encountered while using polymer solid phase in immunoassays is non-specific protein adsorption from blood or serum. Grafting of functionalized poly(ethylene glycol) (PEG) to microparticles and planar quartz surface induces protein resistance. In this chapter, we review several methods of PEG modification of micro- and nanoparticles and discuss the behavior of non-ionic polymers at solid/liquid interfaces. We have demonstrated that microparticles coated with PEG can be used as a solid phase in immunoassays, both for immobilization of antibodies and for presentation of various antigens. We have also devised a convenient method for grafting functionalized PEG monolayers to polymer surfaces. Here, we review the photophysical properties of available fluorescent labels potentially useful as reporters in immunoassays and cell analyses, and discuss recent advances in the development of luminescent semiconductor quantum dots (Qdots). In comparison with organic dyes and fluorescent proteins, Qdots represent a new class of fluorescent labels with unique spectral properties. The photophysical properties of semiconductor Qdots and the fluorescence intensity of a single nanocrystal species (Qdot-655) were investigated in the context of a panel containing conventional fluorophores.

Keywords: Protein arrays, Quantum dots, Nanoscale modification of polymer surface, Reporters for immunoassay, Fluorescent proteins

8.1. Introduction

Immunoassays are a form of macromolecular binding reaction between an antibody and an antigen. Antibodies recognize specific epitopes, small organic molecules or amino acid residues on the surface of an antigen, by weak hydrogen bonding and van der Waals forces. This phenomenon of specific recognition has been widely exploited over the last 50 years, for the development of various quantitative analytical techniques. In many modern immunological methodologies, the specific binding of antigens is carried out on solid surfaces such as polystyrene (PS) plates, nitrocellulose membranes, quartz optical waveguides, and various microparticles. In particular, polymer microparticles with covalently linked antibodies have been used to efficiently separate antigens from heterogeneous samples.

Despite significant advances in the design of solid-phase immunoassays, two surface-related problems have yet to be overcome. The first challenge is to prevent conformational changes of antibodies bound to solid surfaces. The adsorption of an antibody onto a solid phase may lead to its partial denaturation due to changes in the microenvironment of the antibody. Experimental data suggest that antibodies adsorbed or immobilized directly to polymers through short-chain linkers change their native conformation, which in turn decreases their avidity. Stenberg and Nygren reported that the antibody avidity measured at the solid/liquid interface did not reflect the avidity measured for the same antigen/antibody system in solution [1,2]. The second major challenge is the 'matrix effect' that occurs when an extremely complex and variable mixture of proteins, carbohydrates, lipids, small molecules, and salts constitutes a sample, seriously affecting analytical measurements. The matrix effect may be defined as the sum of the effects of all of the components in a system with the exception of the analyte to be measured [3,4]. Non-specific adsorption of endogenous proteins like albumin, rheumatoid factors (these are autoantibodies directed against the Fc portion of IgG), complement, fibrinogen, and the reporter (i.e., the labeled antibody) are known to be the major interfering factors. The common strategy of coating/blocking the solid phase with bovine serum albumin (BSA) suffers from poor reproducibility in antibody adsorption and from limited stability of the protein layer.

Criteria for solid-phase features are: (a) resistance to non-specific adsorption of proteins and other components of serum and (b) availability

of functional groups that can be used for covalent immobilization of antibodies or antigens. This chapter reviews the use of grafted poly(ethylene glycol) (PEG) monolayers to control the interactions of proteins with solid-phase polymer materials. Specific antigen binding requires a certain degree of physical accessibility of immobilized antibodies, which can be achieved by tethering antibodies to the solid-phase surface by flexible, long chain, hydrophilic linker molecules. Modification of the solid phase with PEG is one approach to providing immobilized antibodies with additional degrees of freedom. Through PEG's action as a hydrophilic spacer, antibodies are separated from the hydrophobic polymer surface and have enhanced avidity.

In Section 8.2, we illustrate how and why the properties of PEG-modified surface can be remarkably different from other polymer/liquid interfaces. We discuss the mechanism behind the effective repulsion of proteins and define the structural parameters that make the grafted PEG monolayer inert to protein adsorption. Methods of PS magnetic particle synthesis and PEG-particle surface grafting are discussed in Section 8.2.3. In Section 8.2.4, we report the data on the performance of PEG-modified particles employed as a solid phase in multiplexed immunoassays.

In a later part of this chapter, we review the photophysical properties of available fluorescent labels potentially useful as reporters in immunoassays and cell analyses, and discuss the recent advances in luminescent semiconductor quantum dots (Qdots). In comparison with organic dyes and fluorescent proteins, Qdots represent a new class of fluorescent labels with unique spectral properties: they can be excited by a broad range of wavelengths and, most importantly, their emission spectra can be continuously tuned by changing the crystal size. Recent developments indicate that the first practical applications of Qdots are occurring in imaging and flow cytometry. The photophysical properties of semiconductor Qdots and the fluorescence intensity of a single nanocrystal species (Qdot-655) were investigated in the context of a panel containing conventional fluorophores.

8.2. Nanoscale Modification of Polystyrene Particles

Although PS is widely used as a solid phase for protein-based analysis, this material has several disadvantageous characteristics. The hydrophobicity of PS, for instance, usually requires that the PS surfaces be modified with carboxy- or amine-functionalized co-polymers to make them more

hydrophilic. One promising technique includes covalent grafting of PEG polymers and block copolymers of PEG and poly(propylene glycol) (PEG–PPG) to the surface of PS. PEG's ability to resist the adsorption of proteins at the solid/liquid interface and strategies for tailoring solid surfaces with these polymers has been extensively investigated over the years. PEG-grafted planar silicon and quartz surfaces have demonstrated very low protein adsorption, provided that the PEG polymer chains are long enough and the density of the grafted layer at the solid/liquid interface is sufficiently high [5–7].

Some authors have concluded that only high-molecular-weight PEGs can be used for surface grafting and that short-chain PEGs lose their ability to repel proteins [5,8]. In the patent that has been assigned to the Nektar Corp., Harris et al. claim to have used a broad spectrum of functionalized PEG polymers with molecular weights ranging from 2000 to 176 000 Da for tethering proteins to a surface and conjugation [9]. These parameters are represented by the general structure below:

$$R–(OCH_2CH_2)_{44–4000}–Z–(CH_2)_{2–3}–COO–Q$$

where R is selected from the group including hydrogen, alkyl, amine, etc; Z is –O–, –S–, –CONH; and Q is selected from the group including hydrogen, tert-butyl, N-succinimide, etc.

On the other hand, results by Prime and Whitesides have convincingly shown that even very short-chain PEGs (up to 2–6 ethylene glycol units) could succeed in preventing protein adsorption [10,11]. In their studies, they employed short-chain PEGs conjugated to alkanethiols [12,13]. Self-assembled monolayers are formed upon the adsorption of long-chain alkanethiols (11–18 methylene groups) from organic solution to a gold surface. When alkanethiols are conjugated to small ligands, terminal ligand functional groups are presented at the surface and determine the properties of the interface [14,15]. An important outcome of these studies was recognition of the fact that the surface density of grafted PEGs, and not the chain length, is the parameter that controls the interfacial properties of the monolayer and its ability to repel proteins.

Sofia and Merrill studied adsorption of cytochrome *c*, albumin, and fibronectin to surfaces grafted with three linear PEGs (from 3000 to 20 000 Da) at different densities [16]. All three proteins were found to reach zero adsorption at the highest grafting densities on all PEGs. They also found that there is no specific PEG molecular weight that is necessary for the prevention of protein adsorption. Rather, there is a defined minimum in grafting density for a given PEG chain length, above which the

desired protein adsorption resistance is achieved. They concluded that protein adsorption behavior on PEG-grafted surfaces seems to be independent of protein size and charge.

Based on data available in the literature, we concluded that defining the relationship between density, length, and flexibility of PEG chains to protein adsorption resistance would lead to the elaboration of a model and provide the knowledge necessary for the design of PEG monolayer at the solid/liquid interface. Thus, the first objective of our study was to provide theoretical considerations of PEG–protein interaction. Second, we wanted to establish the feasibility of making grafted monolayers of short-chain PEGs with 20–30 monomer units at high densities (i.e., a brush regime) on planar surfaces and microparticles. Finally, we proceeded to examine the impact of coupling protocols on protein adsorption at the solid/liquid interface and assayed the specific activity of antibodies tethered to the surface via PEG linkers.

8.2.1. Why PEG Monolayer Grafted to a Surface Repels Proteins from Bulk Solution?

In his monograph published in 1979, de Gennes laid out the case for what became to be known as the scaling theory [17]. The theory describes the interactions between non-ionic polymers in a good solvent within a range of distances between 1 and 100 nm. de Gennes considered protein–PEG interactions as a system governed by: (a) van der Waals forces, (b) hydrophobic interactions between protein molecules and the monolayer, and (c) steric repulsion between neighboring chains of PEG [18]. In the model further developed by Jeon, it was shown that a brush (overlapping, stretched chains attached to the surface at a very high density) or a mushroom (chains grafted close to each other at lower density) conformation could be obtained, depending on the PEG layer density. The brush conformation is presented as the highest steric protection against protein adsorption due to the steric hindrance of heavily hydrated chains of PEG molecules and their flexibility, in terms of free rotation of individual polymer units, around inter-unit linkage [19,20].

Polymer chain flexibility correlates with the ability to squeeze non-linked water molecules out of the PEG monolayer formed over a solid-phase surface, making the surface impermeable for plasma proteins, which require free water for diffusion. Structured water molecules that are hydrogen bonded to the ether oxygens of PEG are believed to form a protective

hydration shell around the PEG molecule, creating an excluded volume. When a protein from the bulk solution interacts with a monolayer, it is rejected due to a steric repulsion force that is generated from the loss of configurational entropy, as the PEG chains are compressed by approaching protein [19,21]. Furthermore, in order to adsorb directly at the underlying surface, a protein would have to penetrate the interfacial PEG monolayer, which could be achieved only by increasing the polymer concentration within the monolayer. This is energetically unfavorable and, therefore, the monolayer repels an approaching protein. The structural parameters of PEG monolayers that make them inert to protein adsorption are still not well understood.

Auroy et al. demonstrated that the scaling theory fits experimental data [22], indicating that the properties of a monolayer can be modeled by a rather simple theoretical approach. Let us consider a system that consists of a densely packed monolayer of PEG_{30} grafted to a planar surface. Figure 8.1 represents the brush regime when the chains are attached to

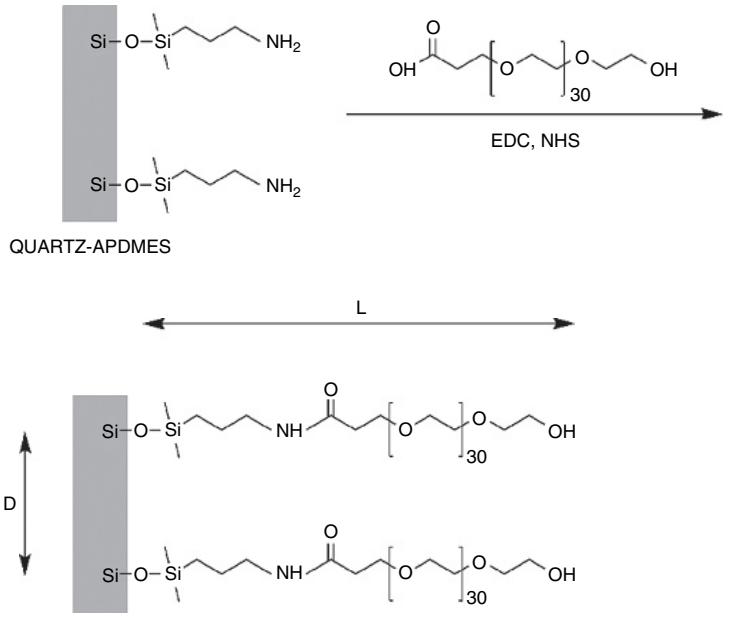

Figure 8.1: A monolayer of 3-aminopropyldimethylethoxysilane (APDMES) formed on a quartz surface by vapor-phase transport. This APDMES monolayer was used as a primer for anchoring the functionalized COOH-PEG_{30}.

the surface at the high density. The chains are stretched out to the bulk solution and repel each other. In the range of distances from 1 to 100 nm, a relatively simple scaling analysis could be used to describe the polymer behavior in a good solvent. de Gennes' scaling analysis starts by a representation of a self-similar grid, in which the mesh size ξ is a decreasing function of a polymer fraction Φ:

$$\xi = a\Phi^{-3/4} \tag{8.1}$$

where Φ is the polymer volume fraction, ξ is the mesh size of the bulk polymer solution with overlapping chains, and a is a monomer size.

Typically, a is around 3 Å and ξ is in the range 0–100 Å. In order to predict the properties of a bulk solution in a close proximity to the surface, we should define the number of monomers, g, in the subunit of size ξ:

$$g = \Phi^{-5/4} \tag{8.2}$$

where g is the number of monomers in the subunit of size ξ.

In the case of low grafting densities, the polymer extends up to the Flory radius of the chain, given by the equation:

$$R_F = aN^{3/5} \tag{8.3}$$

where R_F is the Flory radius and N is the degree of polymerization (which is about 30 in our case).

Such regime is referred to as polymer mushroom conformation [18]. With increasing the grafting density, D (an average distance between grafting points as shown on Fig. 8.1), the polymer chains start to interact at $D \sim R_F$. This causes their extension into the 'brush' conformation. The 'brush' builds up a region of uniform concentration and the mesh size in this regime is equal to D:

$$\xi(\Phi_d) \approx D \tag{8.4}$$

where Φ_d is the uniform PEG concentration in the densely packed monolayer.

The chains in the brush regime are stretched out and could be described as a linear sequence of subunits each of size D and number of PEG monomers g_D:

$$g_D = \Phi^{-5/4} = (D/a)^{5/3} \tag{8.5}$$

Therefore, the overall thickness of the PEG monolayer using volume fraction of polymer Na^3/LD^2 is given as follows:

$$L = ND/g_D = Na(a/D)^{2/3} \tag{8.6}$$

Using the above arguments, many properties of PEG monolayer can be calculated. For instance, osmotic pressure is simply

$$\Pi = kT/\xi^3 \tag{8.7}$$

where Π is osmotic pressure, k is the Boltzmann constant and T is temperature.

Therefore, we can estimate the repulsive force between two densely packed PEG monolayers. The same approach can be used for calculating the repulsive force between a monolayer and an approaching protein globule. When two hypothetical monolayers come in contact at the distance

$$h = h_c = 2L$$

then the polymer concentration in the monolayer increases upon the compression as

$$\Phi \approx \Phi_d(h_c/h)$$

resulting in increased osmotic pressure inside the monolayer and decrease of elastic restoring forces (as entropy prefers non-stretched chains). While in an uncompressed monolayer the osmotic and elastic terms balance each other at the equilibrium thickness L, the compressed PEG monolayers exhibit repulsion. The repulsion force can be calculated as follows:

$$F \approx (kT/D^3)[(h_c/h)^{9/4} - (h/h_c)^{3/4}] \tag{8.8}$$

In this equation, D is the average distance between grafting points. The first term in the bracket is the osmotic term and the second one is an elastic term. When these two monolayers interact with each other, or when approaching protein globules compress the monolayer, then the osmotic term should dominate completely.

8.2.2. PEG Monolayer Grafted to a Planar Surface – A Working Model

The influence of molecular weight, surface density and conformation of PEG dramatically affects the protein adsorption pattern. The Jeon and de Gennes model discussed earlier is applicable to a densely packed PEG monolayer (or stretched chain brush regime), which is extremely difficult to achieve experimentally. Generally, it has been found that maximum grafting densities achieved with solvated PEG chains correlates to chain spacings on the order of the radius of gyration of the PEG molecule [21–23]. This raised the question of whether it would be possible to obtain a densely packed PEG monolayer using common immobilization strategies [24,25]. A simple model that we decided to start with consisted of a round quartz support having a polished surface coated with a layer of functionalized siloxane polymer (Fig. 8.1). The quartz support fit into a standard 96-well plate and was suitable for a protein adsorption study. PEG_{20} or PEG_{30} were grafted to the surface by a covalent reaction with the siloxane polymer as described in [26]. In the following experiments, we quantitatively monitored adsorption of antibodies and europium-labeled HSA to the surface at different grafting densities.

Experimental design and methods

Silanization of quartz supports and grafting of PEG monolayers

Quartz supports with chemically polished surfaces were wiped with an acetone-soaked cotton swab and sonicated in dichloromethane to remove traces of the polishing agent (an epoxy resin) from the surface. Pretreated supports were then placed in a freshly prepared 'piranha' solution of 70:30 (v/v) concentrated sulfuric acid and 30% hydrogen peroxide for an hour at 60°C. The supports were then rinsed with DI water and dried under a nitrogen stream. Monolayers of 3-glycidoxypropyltrimethoxysilane (GOPTS) and 3-aminopropyldimethylethoxysilane (APDMES, Gelest, Inc. Morrisville, PA) were formed on the quartz surface, either by silanization in gas phase, as described in [26], or by vapor-phase transport [27,28]. The latter method is based on the vapor-phase transport of silane in an organic solvent to the surface bearing silanol groups. Briefly, quartz supports were placed on a sample rack 5–10 cm above a refluxing solution of alkoxysilane, in toluene in a flask fitted with a condenser for 4 hours. After heating the supports in the silane/toluene vapor, they were rinsed with toluene and dried in a steam of nitrogen. This technique promotes the –Si–O–Si– condensation

reaction, but prevents the contact of silane oligomers from the stock solution to the surface. Formed monolayers of GOPTS and APDMES were used as primers for anchoring functionalized PEGs to the quartz surface. Amino and carboxyl PEG_{20} or PEG_{30} intermediates were grafted to silane monolayers from 5–20 mM organic solutions.

Labeling of proteins with europium

To assess the ability of a planar surface coated with PEG to resist the non-specific adsorption of proteins from patient samples, we used antibodies and human serum albumin (HSA) labeled with a stable europium chelate [29,30]. Europium labeling was achieved by derivatizing proteins with europium-charged N^1-(*p*-isothiocyanatobenzyl)-diethylenetriamine-N^1, N^2, N^3, N^3-tetraacetic acid (DTTA), a tetraacetic acid lanthanide chelator, through the formation of isothiocyanates as described in [29]. Being attached to a protein through the DTTA linker, the europium atom is very weakly fluorescent. The degree of europium incorporation (or labeling ratio) was determined by releasing the europium from a known amount of protein and measuring the released Eu in a time-resolved fluorometer. Detected Eu signals were quantified by linear regression to a standard curve. Similarly, when europium-labeled proteins adsorbed to planar surfaces or particles, the amount of adsorbed protein could be determined by releasing the europium to a standard volume of the enhancement solution [30] and quantifying the released Eu in a time-resolved fluorometer. In our experiments, the labeling ratio was two europium atoms per one antibody and one europium atom per one HSA.

Measuring protein adsorption to planar surfaces

Interfering proteins of general relevance include albumin, rheumatoid factors (these are autoantibodies directed against the Fc portion of IgG) and immunoglobulins. The concentration of albumin in healthy individuals is expected to be in the range between 3.5 and 4.5 g/dL and the concentration of IgG1 is typically below 1.2 g/dL [31]. Therefore, in the adsorption study, we used europium-labeled HSA at 45 mg/mL (0.68 mM solution in PBS) and monoclonal antibody (anti-TSH, Biospacific A21170136P) at 12 mg/mL (80 μM solution in PBS). Labeled proteins were adsorbed to the PEG-grafted quartz supports using established protocols [26]. When washing steps were completed, the supports were immersed in the enhancement solution, which contained β-diketone and detergents at low pH [29]. In acidic conditions, the europium ion is released from the DTTA chelator

and forms a new, highly fluorescent complex with β-diketones and detergents. Released europium was measured in a fluorometer and quantified by linear regression analysis to a europium standard. The energy transfer to the europium ion from β-diketones allows a very sensitive detection of the label at concentrations up to 0.1 pM, translating to a detection limit of 10^{-16} mol of europium per 1 mL. The sensitivity of this time-resolved fluorescence technique compares favorably with that of ^{125}I.

In our first experiment, PEG_{20} or PEG_{30} were grafted to an APDMES monolayer through the reaction of their carboxyl groups to amines on the solid-phase surface in the presence of (1-ethyl-3(3-dimethylaminopropyl)carbodiimide (EDC) and N-hydroxysuccinimide (NHS), as depicted in Fig. 8.1. The surface density of amine groups was found to be 250–300 amines per 100 nm^2. The detected value was somehow lower than the calculated density of a closely packed silane monolayer (around 400 amines/100 nm^2), which was indicative of a random orientation of APDMES molecules on the surface. The results shown in Fig. 8.2(a) demonstrate that PEG monolayers grafted directly to APDMES surface were not effective at preventing protein adsorption. In our opinion, this could be related to the sub-optimal density of the grafted PEG layer. As previously discussed in Section 8.2.1, depending on the size of the polymer (L) and the distance between grafting points (D), PEG polymers can have different conformations. At very low surface coverages ($D >> L$), the polymer forms pancake like structures. At $D > L$, the so-called 'mushroom conformation' is present, while for $D \leq L$, polymer chains start to interact, forcing their extension into the brush conformation [32]. Short-chain PEG_{20} or PEG_{30} have a more extended chain conformation, as compared to the randomly coiling long-chain PEGs [33] and, therefore, the surface concentration of the short-chain PEG should be relatively higher in order to get to a brush regime.

In order to achieve a sufficient density of PEG molecules in the monolayer, we modified the quartz surface with a primer. First, the surface was silanized with GOPTS and then poly(allyl amine) (PAA) was applied. PAA with a molecular weight of 17 000 serves as a graft primer that provides plenty of additional amine groups for PEG grafting. This experimental design is depicted in Fig. 8.3. Silanization of the quartz surface with GOPTS introduced active epoxy groups that could react directly with amines on PAA. As we predicted, this approach yielded a densely packed PEG layer, which reduced the protein adsorption almost tenfold (Fig. 8.2(b)). Our results suggest that the density of the grafted PEG monolayer governs its ability to repel proteins from the bulk solution. Our data correlates well with the

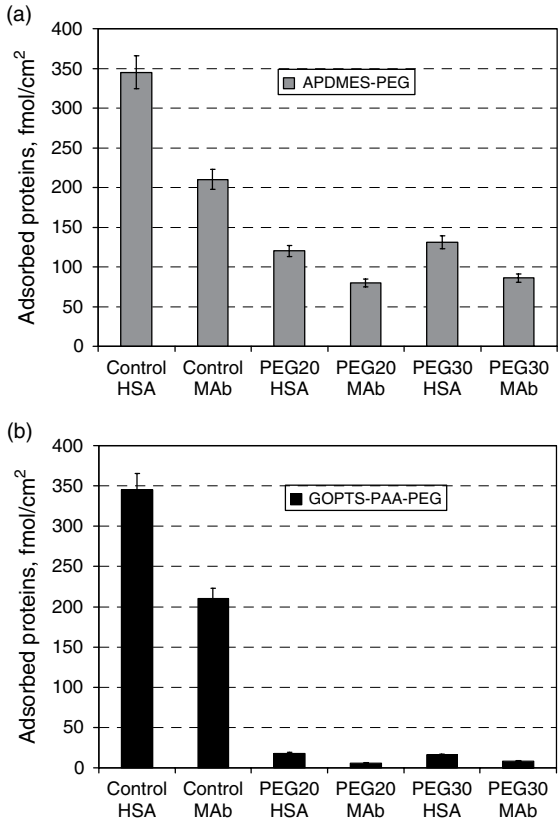

Figure 8.2: Adsorption of europium-labeled human serum albumin (HSA) and monoclonal antibody to the PEG grafted quartz supports. In the first experiment COOH-PEG_{20} or COOH-PEG_{30} were grafted directly to APDMES monolayers through the reaction of their carboxyl groups to amines on the surface (a). In the following experiment the quartz surface was modified with GOPTS and poly(allyl amine) primer, PAA, which provides plenty of additional amine groups for PEG grafting. The later approach yielded a densely packed PEG layer, which reduced protein adsorption almost tenfold (b).

findings of Whitesides' group [10–13] and the results of Sofia and Merrill [16]. Wazawa and Aoyama used a similar approach to graft PEG to a poly(acrylic acid) precursor, thereby increasing the density of PEG monolayer [34]. Both PEG_{20} and PEG_{30} were able to prevent the adsorption of

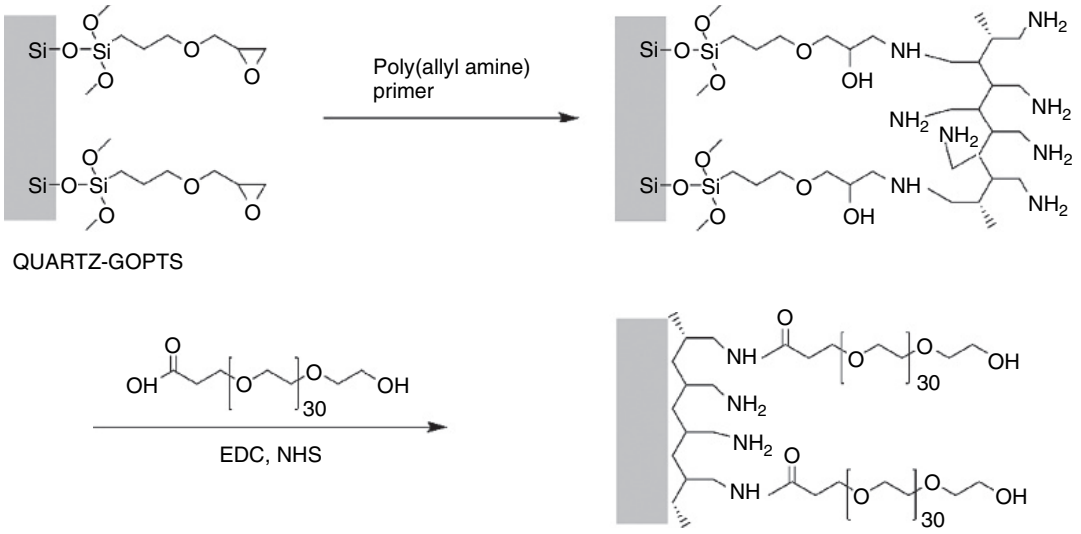

Figure 8.3: New experimental design using poly(allyl amine), PAA. In order to achieve a sufficient density of PEG molecules in the monolayer, we modified the quartz surface. First, the surface was silanized with GOPTS and then PAA was applied. PAA serves as a graft primer that provides plenty of additional amine groups for PEG grafting. Functionalized COOH-PEG_{20} or COOH-PEG_{30} was grafted to the PAA primer through the reaction of their carboxyl groups to amines on the surface.

proteins when grafted to PAA primer at high grafting densities. These findings were of particular significance when applied to the design of polymer microparticles used as a solid phase in immunoassays (details in the next section).

These model surfaces could be used to study the properties of various materials tailored with PEG, such as silicon chips and quartz waveguides. Additional considerations that make this system well suited for studies of protein interactions at solid–liquid interface include the use of PEG chains as linkers for immobilization of proteins. For instance, the chains can be activated using routine synthetic methods and antibodies can be covalently attached to these monolayers. The terminal hydroxyl groups on the PEG monolayer could be readily activated and used for reactions with protein amines (Fig. 8.4). Introduction of active ester moieties can also be carried out using 4-nitrophenyl chloroformate, which reacts directly with hydroxylic species in the presence of a catalyst such as 4-(dimethylamino)pyridine, DMAP, to introduce a good leaving group [35]. The stability of PEG monolayers to organic solvents is sufficient to allow the reaction to be carried out under non-aqueous conditions in acetonitrile (30 min at room temperature), obviously an advantage in terms of avoiding competitive hydrolysis. Active carbonate groups can further react with lysine amino groups on antibody at pH 7.4–8.2 to form N-substituted carbamate bonds [36].

8.2.3. Tailoring of Microparticles with PEG – Immunoassay Development

Our next step was to develop a methodology for grafting PEG to the surface of microparticles that are widely used as a solid phase in bead-based microarrays. Multiplexing immunoassays employ a suspension of microparticle sets in which each set represents an individual analytical test. This system is sometimes referred to as a liquid array. Microparticles are internally encoded by fluorescent dyes and individually addressed to a specific test in the multiplexed analysis. The common synthesis strategy of 8-μm polymer particles widely used for assay development (e.g., Luminex and Bio-Rad Laboratories bead-based microarrays) is presented in Fig. 8.5. The standard bead is a polymer of styrene, cross-linked with divinylbenzene and ethyleneglycol dimethacrylate. The particle core composed of 94% styrene, cross-linked with 6% divinylbenzene, and is magnetized through the application of a layer of magnetite (Fe_2O_3/Fe_3O_4). The coating layer is more complex and is typically composed of three monomers.

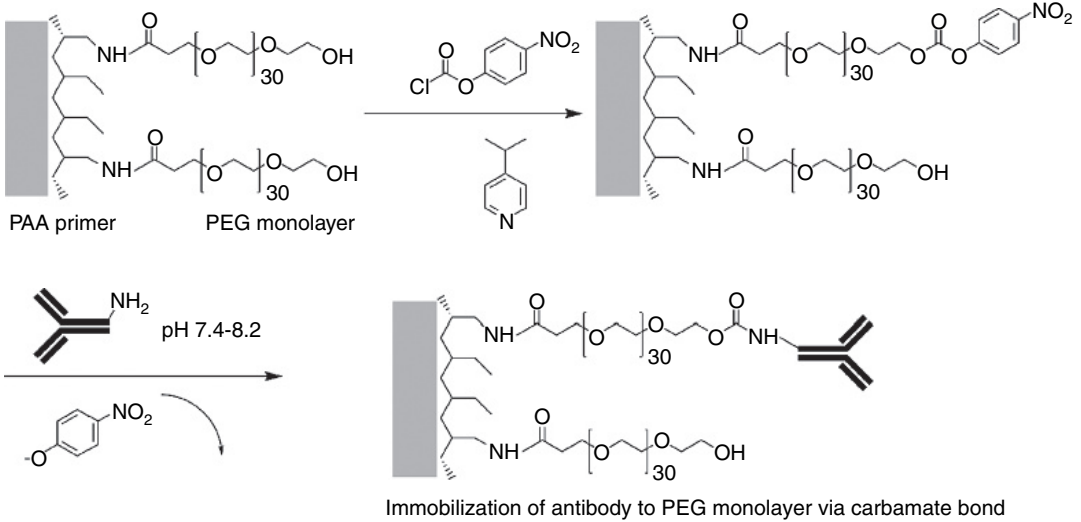

Figure 8.4: The terminal hydroxyl groups on the PEG monolayer could be readily activated and used for reactions with protein amines.

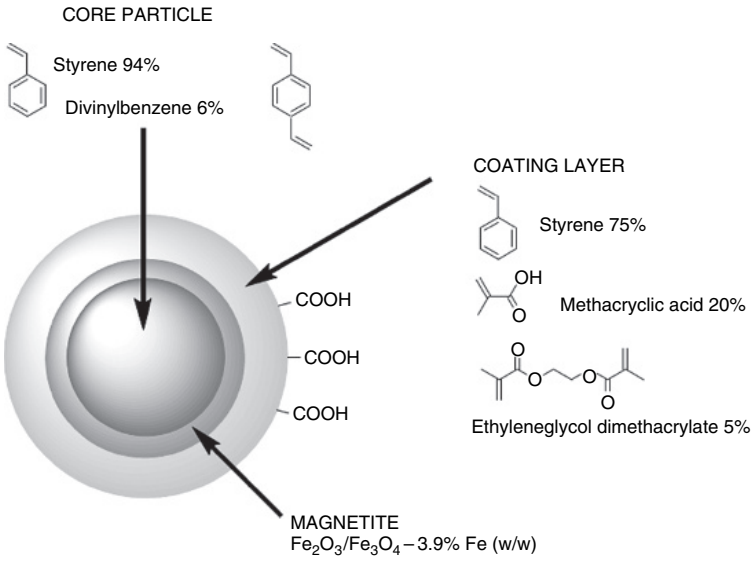

Figure 8.5: Standard bead architecture. The particle core is a polymer of styrene stabilized by cross-linking with divinylbenzene. The particle is magnetized through the application of a layer of magnetite. The particle surface is stabilized by co-polymerization of styrene, methacrylic acid, which provides the carboxyl functionality, and ethyleneglycol dimethacrylate – the cross linker. All three coating monomers have vinyl moieties, which provide chemical handles for polymerization. Bead dyeing is accomplished by the infusion of two hydrophobic dyes in organic solvents.

Styrene makes up the bulk of the coating layer and contributes a significant hydrophobic character to the bead surface. Methacrylic acid provides the carboxyl functionality that is used for amine coupling and contributes a negative charge, which helps to keep the beads disperse in aqueous suspension. Ethyleneglycol dimethacrylate cross-links the polymers in the coat and reduces the bulk hydrophobicity of the particle. All three coating monomers have vinyl moieties, which provide chemical handles for polymerization initiated with potassium persulfate. Because $K_2S_4O_8$ is used to generate radicals for polymerization, all the polymers formed are terminated with a sulfonate anion (SO_3^-). The surface of a standard bead is thus a nodular mosaic of hydrophobic fields of styrene with islands of negative charge from methacrylic acid and sulfonate. Small polymeric nanoparticles formed in the bulk solution during emulsion polymerization could also

adsorb to the outer surface of big particles, making the surface pattern even more complex. The SEM image of the particle presented in Fig. 8.6 gives a good representation of the morphology of a bead's outer layer. Prepared beads are subsequently dyed with two classification dyes, according to the method developed by Chandler at al. [37,38].

We developed a novel strategy of bead coating using long-chain PEG diamine grafted to microparticles by reaction with glycidyl groups on the surface. The structure of the particle core and magnetite layer was similar to the standard bead. The coating layer was composed of styrene and glycidyl methacrylate, cross-linked with ethyleneglycol dimethacrylate. Glycidyl methacrylate provides the epoxy functionality that is used for grafting PEG diamine (Fig. 8.7). Positively charged terminal amines on PEG were converted to carboxyl groups by succinylation at pH 9.5. The beads were subsequently dyed with two classification dyes using the lowest possible concentrations of these dyes to minimize the autofluorescence [37,38].

To convert carboxyl groups to a stable and reactive ester, particles were reacted with (1-ethyl-3(3-dimethylaminopropyl)carbodiimide (EDC) and N-hydroxysuccinimide (NHS) according to the method described in [35,36]. This is accomplished by including two to three equivalents of NHS relative to the carbodiimide, or 2000 to 3000 equivalents relative to the concentration of bead surface carboxyls in the activation reaction.

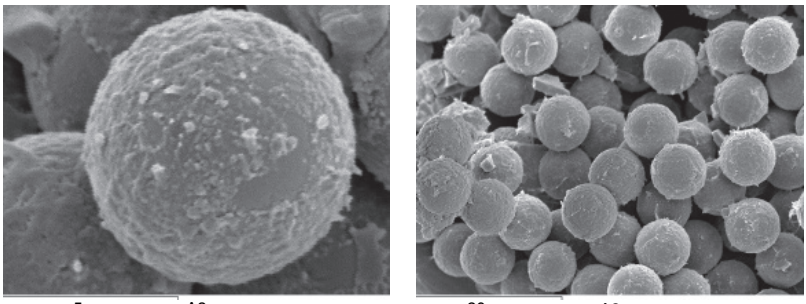

Figure 8.6: Scanning electron micrographs showing the morphology and texture of magnetic particles. The surface of a bead is a nodular mosaic of hydrophobic fields of styrene with islands of negative charge from methacrylic acid and sulfonate. Small polymeric nanoparticles formed in the bulk solution in the course of emulsion polymerization can adsorb to the outer surface of big particles and become a part of it, which makes the surface pattern even more complex.

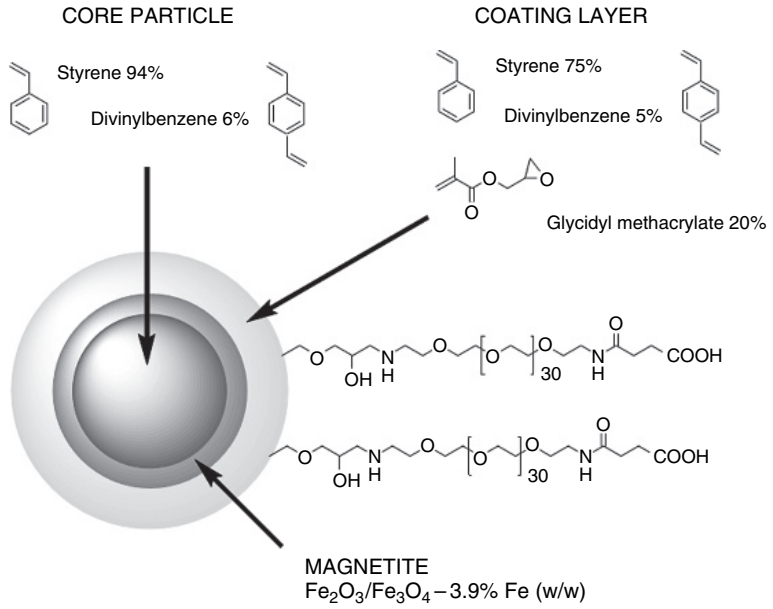

Figure 8.7: The new strategy of grafting the short chain PEG_{30} to the particle surface. The particle core is a polymer of styrene stabilized by cross-linking with divinylbenzene. The particle is magnetized through the application of a layer of magnetite. The coating layer is composed of styrene, glycidyl methacrylate and divinylbenzene. Epoxy groups are embedded on the particle surface by co-polymerization with glycidyl methacrylate and used for grafting of PEG_{30} diamine. Positively charged terminal amines on PEG are converted to carboxyl groups by succinylation at pH 9.5.

The magnetic nature of the beads affords a significant luxury that allows rapid and easy removal of particles from the reaction mixture. It is worthy to note that carboxyl activation in EtOH is more efficient than activation in aqueous buffer because of the general effect of EtOH on elevating the pKa of acids. Furthermore, the bead classification dyes do not leak in EtOH as they do in some other organic solvents. Hence, activated microparticles were used for the conjugation with antibodies.

Coupling of antibodies to carbodiimide-activated carboxyl groups relies on condensation with deprotonated primary amines. A typical target amine is the epsilon amine of lysine; however, amino groups on arginine and

the amino terminus of the protein can also serve as coupling partners for the activated carboxyls. For successful conjugation of lysine, the pH of the coupling buffer should be in the range between 8 and 10 to match the pKa of amine groups. Elevating the pH of the coupling reaction does not always improve coupling efficiency because the half-life of the activated ester decreases as the pH increases. At pH 8.0, the half-life of an NHS ester is 10 min, thus in 50 min, there is virtually no carboxyl reactivity left on the bead surface. Non-specific protein adsorption can be difficult to dissect from covalent coupling unless appropriate control reactions are conducted (e.g., no carbodiimide used in the activation step, stringent washing with 1% Tween 20 or 1% SDS after coupling or application of high salt and chaotropic reagents (2 M urea, for instance)).

This system, consisting of dyed magnetic particles with antibodies attached via long-chain PEG linkers, was far more complicated than the planar models we had previously employed. Accurate experimental characterization of a PEG monolayer grafted to a polymer particle is extremely difficult to accomplish. Therefore, we decided to limit the scope of the study to: (a) quantitative measurement of carboxyl groups available on the surface and (b) characterization of protein adsorption. The concentration of carboxyl groups was measured by covalent coupling of Ala-*para*-nitroaniline to particles using the EDC/NHS method, as described earlier, with subsequent hydrolysis of nitroaniline at high pH [15]. This method estimates the concentration of carboxyl groups on the surface that is available for covalent binding to proteins. The concentration of carboxyl groups on a standard particle (Fig. 8.5) was found to be 12.7 μEq/g, whereas on a PEG-grafted particle (Fig. 8.7), it dropped almost five times to 2.8 μEq/g.

Figure 8.8 shows typical adsorption profiles of Eu-labeled albumin on standard and PEG-grafted particles. The specific surface area of the 8-μm standard particles was estimated to be around 20 cm^2/mg of beads. Given the nodular nature of the bead surface (Fig. 8.6), however, this is likely to be a gross underestimation. The bead capacity for HSA loading was found to be 150–250 pmol of HSA per milligram of standard particles, which may be a more relevant statistic. This concentration corresponds to 1–3 albumin monolayers on the surface. PEG-grafted beads demonstrated a significantly lower level of non-specific adsorption of HSA (40–50 pmol/mg), suggesting that only a few hydrophobic sites remained exposed at the polymer/liquid interface. The concentration of COOH–PEG_{30} on particles was estimated to be 100–200 molecules per 100 nm^2. Given our current data, grafting bead surfaces with hydrophilic PEG polymers could potentially resolve the ‘matrix effects’ associated with non-specific adsorption

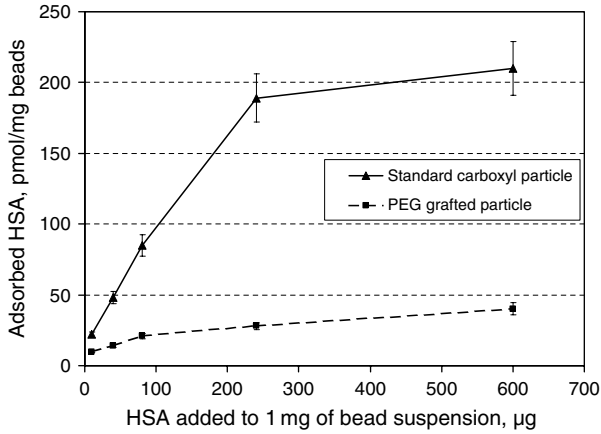

Figure 8.8: Typical adsorption profiles of Eu-labeled albumin (HSA) on standard and PEG-grafted particles.

of proteins and/or phospholipid aggregates from patient samples, thereby, limiting cross-reactivity with immunoassay reporters and increasing the overall detection sensitivity of immunoassays.

The concept of assay sensitivity

The minimum detectable dose (MDD) of an analyte in a patient sample, or detection limit of the system, is primarily determined by the precision with which an analyte concentration is measured at zero [31,39,40]. The precision of an assay, which is usually determined in terms of standard deviation (SD) or coefficient of variation (CV), is governed by the precision of the analyzer (i.e., by the accuracy of sample dispensing, temperature control, detector limitations, etc.) and the design of the solid phase.

Non-specific binding of serum proteins including the reporter antibody during the assay contributes to the precision of the zero-dose estimate and, therefore, could limit the sensitivity of the system. As shown earlier, grafting PEG to surfaces offers the benefit of reduced non-specific adsorption. Functionalized PEGs bearing carboxyl groups that remain available for conjugation to antibodies further improves this methodology by introducing hydrophilic spacers, or tethers, for minimizing surface effects and steric interactions. Production of solid-phase particles

uniformly coated with a PEG monolayer and having the same concentration of capture antibodies on the surface are of crucial importance in minimizing of random detection errors and increasing immunoassay sensitivity.

Principle of multiplexed assay

An illustration of multiplexed assays can be found in the development of the new solid phase for the measurement of thyroid stimulating hormone (TSH), an important regulatory hormone involved with thyroid function. The solid phase for the reaction comes in the form of 8-μm PS particles, as depicted in Fig. 8.9. Each particle has a unique combination of two fluorescent dyes, excitable by a red laser, which serve as a spectral 'barcode' allowing the creation of a set of up to 100 color-coded particle populations. Each population of particles may be coated with antigens indicative of specific bacteria, viruses, capture antibodies or other specific markers. These protein-coated particles serve as the center of the reactions and as the backbone of the chemistry.

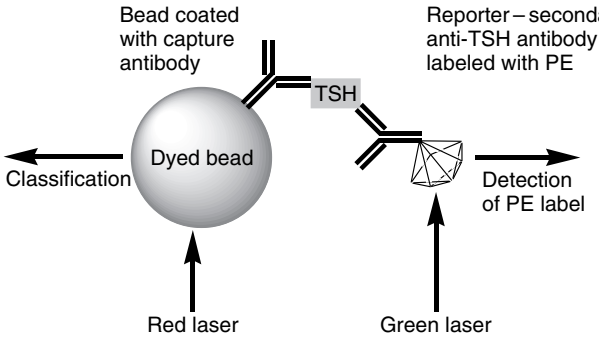

Figure 8.9: Principle of multiplexed assay. The solid phase for the reaction comes in the form of 8 μm polystyrene particle as depicted. Each particle has a unique combination of two fluorescent dyes, which serve as a spectral 'barcode'. In TSH assay, the capture anti-TSH antibody is anchored to the solid phase by binding to carboxyl functionalized PEG. By using a complement anti-TSH antibody, which is 'tagged' with PE, TSH could be sandwiched and captured on the solid phase. The detection system involves a solid state green laser. It excites reporters that are bound on the particle surface after the immunoreaction is completed. (See colour plate section).

In the TSH assay, the capture anti-TSH antibody is anchored to the solid phase by binding to carboxyl-functionalized PEG. A diluted patient sample is added to the solid phase and a set amount of time is allowed for the reaction. If the specific antigen (i.e., TSH) is present in the sample, the bead-anchored antibodies bind to the antigens, forming antigen–antibody complexes on the solid phase. Several wash steps follow to remove any unbound sample. By using a complement anti-TSH antibody which is 'tagged' with PE, TSH can be sandwiched and captured on the solid phase, thus allowing direct measurement.

A solid-state green laser excites reporters that are bound to the particle surface after the TSH immunoreaction is completed. The laser illuminates the particles as they move in laminar flow through the flow cell. Fluorescent signals are discriminated with a digital signal processor and using high-speed digital signal processing, about $1–2 \times 10^5$ beads can be screened per minute. Using this assay, up to 10–15 different analytes can be determined in the patient sample in seconds. Extrapolating to a standard curve allows the qualification and/or quantification of each analyte in the sample. This type of liquid array technology has been simultaneously developed by Luminex Corporation (LX100 platform) and BD Biosciences (FACSArray platform) and, in our opinion, has been one of the major advances in immunoassay since 1990s.

8.2.4. Performance of PEG-Grafted Particles with Immobilized Antibodies in TSH Assay

Thyroid stimulating hormone is a glycoprotein with a molecular weight of 26 600 Da, made up of two non-covalently attached subunits, α and β. The α subunit is similar to the corresponding subunit of follicle stimulating hormone, human chorionic gonadotropin (hCG) and luteinizing hormone (LH). The β subunit is immunologically unique among these hormones which contain epitopes used in the TSH assay [41].

The effect of the linker on the sensitivity of the TSH assay was studied as described in the Section 8.2.3. Magnetic particles of 8 μm (Polymer Laboratories, UK) were first grafted with PEG and then succinylated (Fig. 8.7). These particles, along with standard particles dyed in two 'dim' regions, were then coated with capture TSH antibody (Fitzgerald M94205). A complementary anti-TSH antibody (Biospacific A21170136P) labeled with PE was employed to test the functional performance of both particles in sandwich format. An assay was performed at 37°C and run in multiplex mode

on the LX100 (Luminex Corp). A comparison of the assay curves is shown in Fig. 8.10.

The use of particles with grafted PEG linkers substantially lowered non-specific binding and had a considerable effect on the assay sensitivity. Comparison of the S/N for the PEG-grafted particles (S/N for the $0.5\,\mu\text{IU/mL}$ standard $= 232.1$) with the S/N for the standard particle, where

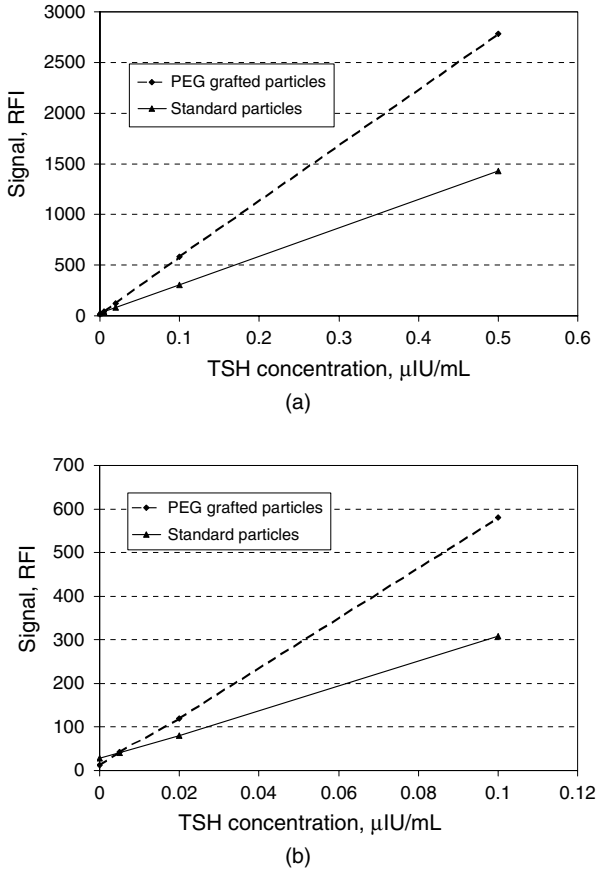

Figure 8.10: A comparison of the assay curves for the PEG grafted particles and the standard particles where the capture antibody directly attaches to the surface without PEG [(b) represents a comparison of the low end of the TSH assay curves].

the capture antibody directly attaches to the surface without PEG (S/N for the 0.5 μIU/mL standard = 51.1) illustrates this use. Since the TSH assay is a sandwich assay, any increase in background fluorescence in the RP1 channel decreases the sensitivity of the assay. A comparison of the low end of the assay curves demonstrated that hydrophilic linkers were capable of yielding good S/N ratios due to low background signals ($N = 12$ RFI for PEG-grafted particle versus $N = 28$ RFI for the standard particle, Fig. 8.10(b)). The analytical sensitivity of this system (i.e., the concentration corresponding to the signal 2 SDs greater than the 0 standard; 25 replicates) in a multiplex assay was estimated to be 0.002 μIU/mL. The SD at zero provides a simple and unambiguous indication of the lowest concentration of analyte, which can be measured with good precision using this assay design.

A simple titration of the capture antibody on EDC/NHS-activated particles can be used to establish the optimal concentration of antibody on the solid phase, thereby yielding maximum precision of measurements of any target analyte concentration. The higher the concentration of capture antibody on the surface, the better the solid phase is able to extract and isolate THS from patient samples. We also found that the dynamic range of the TSH immunoassay could be significantly improved by employing two beads: (a) a bead with the highest concentration of capture antibodies on the surface (designed for maximum sensitivity) and (b) a bead with less antibody concentration (intended for measurement of TSH at the high end of the assay curve).

8.3. Semiconductor Nanoparticles as Reporters in Immunoassay and Cell Analysis

In the previous section, we have discussed issues surrounding non-specific adsorption in solid-phase immunoassays and the novel strategies we have developed to reduce non-specific adsorption and enhance assay sensitivity. Background 'noise' is certainly the most critical parameter of the system that governs the sensitivity of immunoassay, but what about the 'signal'? In this section, we review the photophysical properties of conventional fluorescent labels and discuss the recent advances in luminescent semiconductor Qdots. These crystalline nanoparticles have optical and structural properties that are not available in either isolated molecules or bulk solids. Recent developments indicate that the first practical applications of Qdots are occurring in imaging and flow cytometry.

In comparison with organic dyes and fluorescent proteins, Qdots represent a new class of fluorescent labels with unique spectral properties: they can be excited at almost any wavelength and, most importantly, their emission spectra can be continuously tuned by changing their crystal size. The first systematic studies of the size-dependent, optical properties of semiconductor crystals in colloidal solutions were performed two decades ago by Henglein [42] and Brus [43]. A major advancement in increasing the quantum yield was accomplished by introducing the passivation shell on the crystalline core. The large surface-to-volume ratio in a nanosized crystal (about 50% of all atoms are on the surface) affects the emission of photons. The shell helps to confine the excitation to the CdSe core and prevents non-radiative relaxation. Photochemical oxidation and surface defects in a crystal with no shell may lead to a broad emission and lower quantum yields. One of the first core-shell syntheses was performed by Spanhel et al. [44]. Major improvements leading to highly fluorescent Qdots were made in the mid-1990s [45–47]. Subsequently, CdSe crystals with silane-modified hydrophilic surfaces were introduced as reporters for biological applications [48,49].

Conventional fluorescent-labeled immunoassay techniques have detection limits in the range of 0.1–1.0 nmol/L (which translates into 10^{14}–10^{15} molecules/L) because of high background signals, light scattering and certain limitations of fluorescent probes [50]. Two of the most sensitive probes available today, radioisotope labels (e.g., ^{125}I) and time-resolved lanthanide labels (e.g., Europium, Terbium and Samarium), could potentially achieve a detection limit of 10^{-14}–10^{-15} mol/L in a non-competitive format [51,52]. The use of semiconductor Qdots as reporters could theoretically yield methods capable of detecting about 10^{6}–10^{8} molecules/L, up to six orders of magnitude in increased detection limit.

8.3.1. Unique Photophysical Properties of Quantum Dots

Fluorescence in CdSe Qdots is due to the radiative recombination of an excited electron–hole pair, or exciton. The excitonic energy levels and quantum yields of fluorescence, (i.e., the ratios describing how many absorbed photons are emitted) depend on exciton–photon interaction in the crystal and the size of the crystalline core. Each Qdot has a characteristic, singlet emission peak. With increasing crystal size (from 2–3 to 10–12 nm), emission maxima shift from 500 to 800 nm. In addition, Qdots have very broad absorption spectra and can be excited over the entire visual wavelength

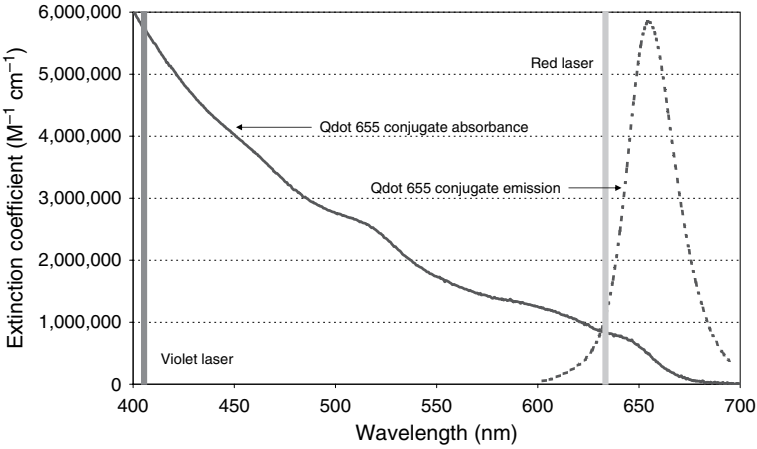

Figure 8.11: Absorption and emission spectra of Qdot-655 conjugate. Bars represent laser lines of the violet and red lasers. The shape of the absorption spectrum reveals that the Qdots can be excited by several commonly used visible-range emission lasers. Although the extinction coefficient is much lower at the red laser line than at the violet, it can be seen that it is still quite high (∼1 000 000). (See colour plate section).

range, as well as far into the UV (Fig. 8.11). Due to their exceptionally large Stokes shifts (up to 400 nm), Qdots may be used for multicolor detection with a single-wavelength excitation source.

Quantum dots with a regular crystalline CdSe core and uniform ZnS shell have large extinction coefficients and high quantum yields in organic solvents [45,46]. These parameters describe the capacity of the system to capture and subsequently re-release light. However, in aqueous buffers, quantum yields of Qdots are comparable with those of conventional fluorophores (20–50%), but the excitation efficiency of Qdot conjugates is still much higher. The Qdot-655 conjugate has an absorption maximum of $6 \times 10^6\,M^{-1}\,cm^{-1}$ at 405 nm (Fig. 8.11). This makes these Qdot conjugates about two orders of magnitude more efficient at absorbing excitation light than organic dyes and fluorescent proteins.

Qdots have a fluorescence lifetime of 20–30 ns, about ten times longer than the background autofluorescence of proteins. The lifetime characterizes a delay between the moment in which the Qdot absorbs a photon from the light source and the moment of radiative recombination of the exciton. Fluorescence from single CdSe crystals has been observed much longer

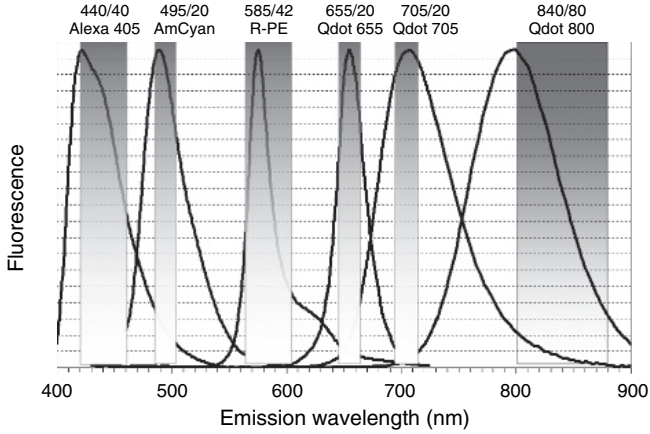

Figure 8.12: A panel of conventional fluorophores and quantum dots that might be used in a single laser platform design. (See colour plate section).

than from other fluorophores, thereby resulting in high turnover rates and a large number of emitted photons [53]. These unique optical properties of Qdots were used to overcome the autofluorescence problem associated with most cells and tissues. For most biological samples, autofluorescence exhibits a decay time of nanoseconds and a broad spectrum, with a maximum at about 500 nm. The emission peaks of Qdot-655, Qdot-705 and Qdot-800 are shifted to the right from this maximum due to large Stokes shifts (Fig. 8.12).

8.3.2. Recent Developments in Surface Chemistry of Quantum Dots

Two important obstacles to biological applications of commercially available Qdots were low quantum yields in aqueous buffers and strong aggregation of protein-Qdot conjugates. Surface chemistry of CdSe particles and the design of linkers for protein immobilization played a major role [54] in overcoming these obstacles. For the use of Qdots as reporters in immunoassay, their outer layer must perform multiple functions. It must insulate the CdSe/ZnS core structure from the aqueous environment, it must prevent the non-specific adsorption of Qdots to cells, and it must provide the functional groups necessary for covalent attachment of antibodies. Recent improvements in both nanocrystal core and shell technologies have enabled

production of Qdot conjugates with exceptional brightness and low non-specific adsorption [55]. Quantum Dot Corporation has introduced a new surface chemistry, where the polymeric shell is modified with long-chain amino-functionalized polyethyleneglycols. This new generation of Qdot nanocrystals has a low non-specific binding to cells and can be directly conjugated to antibodies (see Fig. 8.13). CdSe/ZnS core-shell nanocrystals were encapsulated into carboxylated polymer, followed by a chemical modification of the surface with long-chain functionalized polyethyleneglycols [56]. The properties of the grafted layer can be controlled further by formation of 'mixed' layers from solutions of two PEGs.

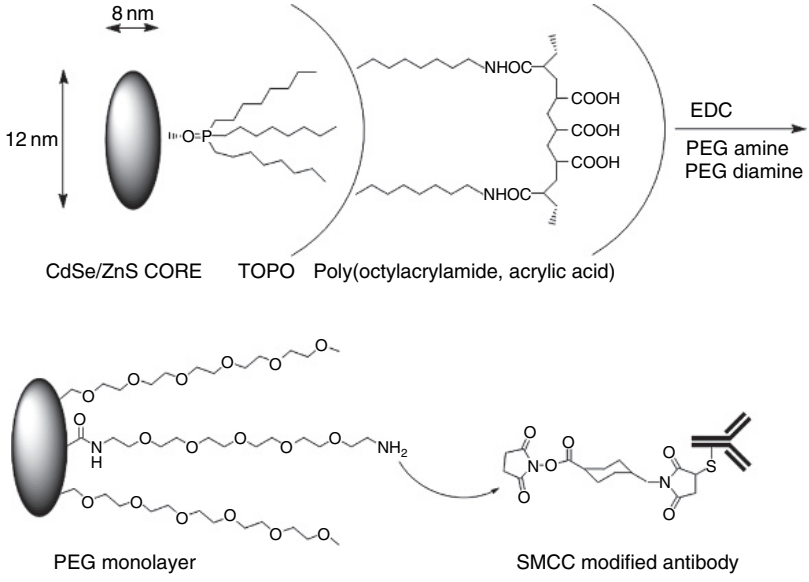

Figure 8.13: Structure of Qdot-655 core and the outer layer. The typical quantum dot consists of the CdSe core and ZnS shell overcoated with tri-*n*-octylphosphine oxide (TOPO) coordinating layer. As revealed by high-resolution TEM, the quantum dots are not smooth spheres, but are faceted crystals with planes and edges. To convert these hydrophobic cores to water soluble and biocompatible crystals the surface is modified with amphiphilic co-polymer of octylacrylamide and polyacrylic acid, introducing about 300–500 carboxyls per Qdot. The resulting carboxyl surface is further modified with a mixture of PEG mono- and diamines (MW 2000) in the presence of EDC. Finally, SMCC-activated antibodies are attached to Qdot-655 by reaction with amine functionalized PEG.

8.3.3. Spectrophotometric Characterization of Quantum Dots

Excitonic fluorescence is dependent on crystal size and, theoretically, should yield a very sharp peak. Chan and Nie reported that the emission spectra of single CdSe/ZnS-capped Qdots are as narrow as 13 nm [49]. However, research in several groups has demonstrated that brightness and emission peak width of identically sized crystals from different manufacturers may vary significantly [57–60]. For example, phospholipid-coated EviTag crystals manufactured by Evident Technologies demonstrated broader emission peaks than PEG-modified Qdot crystals manufactured by the former Quantum Dot Corporation. Differences in emission peaks might be attributed to defect states in the crystal interior or on its surface. These defects can trap the electron–hole pairs, or excitons, thereby leading to a broad emission peak that is red-shifted from the excitonic peak. It would appear reasonable that crystals with a large number of trap states have low quantum yields. Figure 8.14 shows the comparison of relative brightness of Qdot-655 and Qdot-705 following excitation by violet, blue and green lasers.

Since the data on relative brightness and width of Qdot emission peaks varied depending on the manufacturer, the first objective of our study

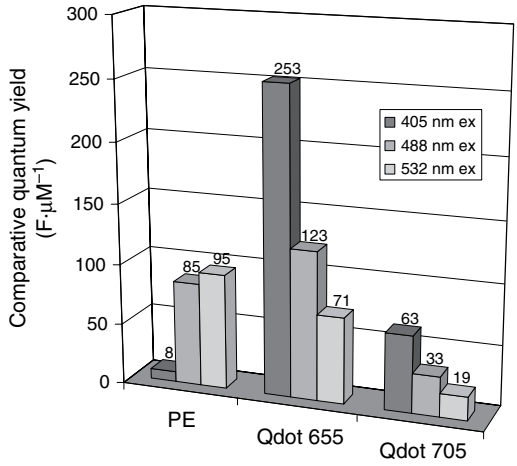

Figure 8.14: Comparative quantum yields of PE, Qdot-655 and Qdot-705, excited at 405, 488 and 532 nm. (See colour plate section).

was to dispel this ambiguity via direct comparison of the photophysical properties of Qdots with conventional fluorophores. Fluorescence emission spectra, normalized to a full scale, reveal similar peak widths at half-height between Qdot-655 nanocrystals and conventional fluorophores (Fig. 8.12). However, the common 'tailing' seen with organic dyes and fluorescent proteins is virtually absent with Qdots, making them better suited to multicolor detection due to decreased 'spillover' between neighboring colors. It should be noted, though, that emission peaks of IR crystals Qdot-705 and Qdot-800 are much wider than those of organic dyes.

Spectrophotometric analysis of Qdot-655, Qdot-705 and R-PE (all excited at 405, 488 and 532 nm in a spectrofluorometer) demonstrated that Qdot nanocrystals are extremely bright fluorophores (Fig. 8.14). When excited at 405 nm, Qdot-655 is about 30 times brighter than R-PE and about 100 times brighter than Pacific Blue [57]. When excited by blue or green lasers at 488 and 532 nm, the Qdot-655 was as bright as R-PE.

8.3.4. Multicolor Labels in Cell Analysis

One major drawback of Qdots is that the binding of these crystals to antibodies, or actually coating the crystal with antibodies adversely affects the avidity of the antibody. The size of the crystal is about twice as large as the antibody molecule itself (Fig. 8.13). It is important, therefore, when employing Qdots in an immunoassay to insure that conjugated antibodies have high avidity towards the target antigen and to design the surface of the Qdot crystal to minimize the non-specific binding. The introduction of a hydrophilic coating (functionalized PEGs) has been used to overcome problems of insolubility of crystals and introduction of functional groups for covalent immobilization of antibodies (Fig. 8.13). To demonstrate the potential of Qdots in cell analysis, we assembled a panel of conventional fluorophores: AmCyan; fluorescein (FITC); phycoerythrin (PE); allophycocyanine (APC); and the tandem dye APC-Cy7 conjugated to CD4 antibody (Table 8.1). Antibody-conjugated Qdot-655 and fluorophores were used for the detection of cell-surface antigens by multicolor flow cytometry [61].

Overview of methods and applications

Basic cell-surface staining methodology involves incubation of whole blood with a fluorescently labeled antibody, followed by lysis of the red cells, washing, and analyzing on a flow cytometer. The labeling and detection

Table 8.1: Characteristics of phycobiliproteins, fluorescent proteins and tandem fluorophores

Fluorophore	Subunit composition	Abs. max. (nm)	Em. max. (nm)	Extinction coefficient (M^{-1} cm^{-1})	Molecular weight (Da)
R-phycoerythrin (PE)	$(\alpha\beta)_6\gamma$	496–564	578	2 000 000 at 564 nm	270 000
Allophycocyanine (APC)	$(\alpha\beta)_3$	650	660	700 000	110 000
APC-Cy7 (tandem fluorophore)	$(\alpha\beta)_3$	650	785	700 000	110 000
AmCyan (fluorescent protein)	α_4	457	491	39 000	110 000
FITC	Organic dye	494	519	68 000	389
Pacific Blue	Organic dye	416	451	46 000	340

techniques presented are equally applicable to organic dyes, fluorescent proteins, and Qdot nanocrystal reagents and were developed for immune function testing involving cytokine flow cytometry [61–63]. To assess the brightness of Qdot conjugates and determine the stain index (SI), we used Qdot-655 in conjunction with conventional fluorophores being analyzed on a three-laser system.

The panel of conventional fluorophores conjugated to the same antibody (monoclonal anti-CD4 antibody, clone SK3, BD Biosciences) consisted of CD4 AmCyan, CD4 FITC, CD4 PE, CD4 APC and CD4 APC-Cy7. Both allophycocyanin and R-phycoerythrin are light-harvesting phycobiliproteins derived from *Spirulina platensis* and red algae, respectively. In algae, phycobiliproteins are incorporated into supramolecular complex called the phycobilisome, which, in turn, is a part of photosynthetic complex (see Table 8.1). APC has an absorption maximum at 650 nm, making it a good choice for red-laser (633 nm) excitation, while PE has absorption peaks at 496 and 565 nm, thereby making it compatible with either blue (488 nm) or green (532 nm) excitation. AmCyan is one of the reef coral fluorescent proteins derived from *Anemonia Majano* [64,65]. The AmCyan that we used for conjugation is a recombinant protein that is composed of four subunits. The chromophore consists of three oxidized amino acid residues Met–Tyr–Gly. All fluorescently labeled antibodies were from BD Biosciences. Quantum Dot-655 (Quantum Dot Corp.) consists of CdSe/ZnS

core-shell nanocrystals (ITK 2152-1) with 655 nm emission, coated with an amphiphilic carboxylated polymer and further modified with amino-functionalized polyethyleneglycols (Fig. 8.13). Antibody attachment to the Qdot surface occurs through the PEG 2,000-diamine spacer [56].

A flow cytometer equipped with violet, blue, and red lasers, and at least 10 parameter detection, was used in the Qdot assay (LSR II, BD Biosciences). The target concentration of CD4 Qdot-655 reagent to use for cell staining was determined from titration, in which the Qdot concentration is varied over a range of 8.3–0.13 nM final concentration in the staining mix. For subsequent studies, a target final concentration of 5 nM was employed. The surface concentration of CD4 antigen (~47 900 molecules per CD4+ lymphocyte) was measured using QuantiBRITE PE beads [66]. The sample processing, cell staining and data analyses were performed as described in our early work [57].

Separation of positive and negative cell populations

It is important to determine whether covalent attachment of an antibody to a nanometer size QD impacts the avidity and non-specific binding of the conjugate. A comparative titration of CD4 Qdot-655 and CD4 AmCyan reagents reveals that the concentration of reagent required to achieve half saturation is 1–2 nM for either fluorophore and, therefore, the affinity of antibodies does not appear to be affected by conjugation to Qdot nanocrystals.

The signal-to-noise ratio (S/N) is one approach to quantifying the separation between two stained cell populations. For most flow cytometry applications, though, S/N alone is insufficient to judge performance. The reason for this is that the spread of the negative or 'noise' population will also strongly impact the ability to distinguish the signal and noise populations. Therefore, we used stain index (SI) to quantify the separation between positive and negative lymphocytes. Stain index [67,68] measures the ability of the assay to distinguish between cell populations by incorporating both the spread of the negative peak and the difference of the means of the positive and negative populations. The negative population (also referred to as 'background') may be defined according to the application (e.g., the negative peak of a stained sample, unstained cells, a cell type other than the target population in the sample, etc.).

When CD4 Qdot-655-stained cells are excited with a violet laser at 405 nm and compared with CD4 PE-stained cells excited with the blue laser

Table 8.2: Relative brightness of CD4 Qdot-655 compared with typical fluorophore conjugates used in cell-surface staining

Fluorophore sample	**FITC**	**Pacific Blue**	**PE**	**APC**	**Qdot-655**
Positive lymphocytes	1641	2729	24 861	48 477	85 729
Negative lymphocytes	38	45	37	26	35

at 488 nm, the cells stained with Qdot-655 are about 3.5 times brighter than PE-stained cells, on the basis of positive lymphocytes (see Table 8.2). An SI comparison also demonstrates the superior separation of the Qdot reagent, the CD4 Qdot-655 having an SI of 2.7 times that of CD4 PE. (Fig. 8.15). When CD4 Qdot-655-stained cells are excited with a violet laser at 405 nm and compared with CD4 APC stained cells excited with the red laser at 633 nm, Qdot-655 is about two times brighter than APC (see Table 8.2). This is reflected in data demonstrating that the SI comparison is similar,

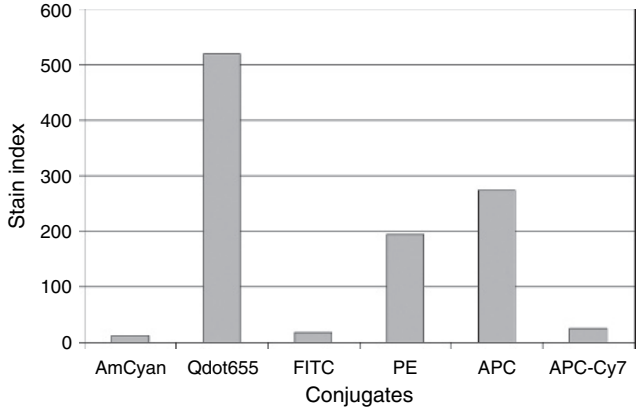

Figure 8.15: Stain Index of CD4 Qdot-655 compared with conventional fluorophores. Stain index (SI) is a measure of how well a signal is distinguished from background. SI takes into account the spread of the negative population and describes positive and negative population separation.

with CD4 Qdot-655 having an SI of 1.9 times higher than that of CD4 APC (see Fig. 8.15).

8.3.5. Future Prospects for Quantum Dots in Immunoassay

Widespread penetration of DVD recording technology will make violet diode lasers available at a low market cost ($\geq$\$500) in the very near future. In turn, this will allow the practical, widespread implementation of Qdot technology in immunoassays. Bead array-multiplexed assays using PS particles is emerging as an extremely attractive alternative to microarrays and microplates, particularly for multi-parameter analysis of proteins in immunology and cell biology applications (e.g., cytokine and chemokine analysis; cell apoptosis research; study of inflammation responses, etc.). Rather than preparing probes in pixels on a microarry, probes or antibodies will be attached to PS particles 6–8 μm in diameter, as illustrated in Section 8.2.3 above. Each particle will have a unique combination of two fluorescent dyes, which will serve as a spectral barcode. Dual-channel barcoding will allow the creation of a set of up to 100 color-coded particle populations. The next step, as we foresee it, will be the replacement of organic dyes with IR quantum dots: Qdot-705 and Qdot-800, in bead classification for the multi-analyte detection. Due to their large Stokes shift (in the range of 300–400 nm), these two Qdots should not have any emission in the detection channels. Thus, the autofluorescence signal would be reduced to a minimum. Figure 8.12 illustrates a panel of conventional fluorophores and Qdots that might be used in a single laser platform design.

Further improvements on the CdSe nanocrystal core technology have enabled production of Qdots, which are substantially brighter than previously evaluated materials. We have obtained experimental verification that initial surface chemistry issues have been resolved and, therefore, one of the brightest dots, Qdot-655, can be used as an additional reporter. As shown in Section 8.3.3, Qdot-655 is about 30 times brighter than PE and about 100 brighter than Pacific Blue dye when excited at 405 nm. Qdot-655 also has a Stokes shift of 250 nm and, thus, the background fluorescence, which comes from the components of serum like NADH and bilirubin, will not affect the detection system. R-PE may serve as an additional reporter in immunoassays, whereas Alexa 405 and AmCyan conjugates can be used for the detection of cell-surface antigens by multicolor flow cytometry. Finally, in using the single violet laser platform, we obtain two great advantages:

(a) the instrument is inexpensive to produce and (b) this platform enables multiplex analysis of biological samples using beads as a solid phase, as well as cell analysis.

8.4. Conclusions and Outlook

In this chapter, we present key findings from our investigation of the dependence of protein adsorption on density of PEG monolayers grafted to solid-phase surfaces. Planar quartz supports grafted with a PEG monolayer, europium-labeled HSA and antibodies provided a model system for the study of protein adsorption. Our results suggest that the density of grafted PEG monolayers governs the ability of a solid phase to repel proteins from a bulk solution. This chapter also describes a simple, generally applicable procedure for coating solid-phase surfaces with PAA polymer, used in our research as a primer for grafting short-chain PEGs to the surface. This approach yields PEG monolayers with a high grafting density, successfully preventing the adsorption of HSA and antibodies to the surface.

Understanding mechanisms of protein–polymer interactions allows a rational approach to the design and improvement of analytical techniques. Here, we have described the use of functionalized PEG monolayers in immunoassay. We have demonstrated that microparticles grafted with PEG can be used as a solid phase in immunoassay, both for immobilization of antibodies and for presentation of various antigens. We have also devised a convenient method for grafting functionalized PEGs to polymer surfaces. This method allows for the fabrication of a densely packed PEG layer on the solid-phase surface in a brush regime. PEG-coated particles were shown to be remarkably resistant to protein adsorption and had a very low background signal at zero standard; a critical property for use in quantitative assays. TSH assays on particles with the new coating chemistry have yielded significantly higher sensitivity values, compared to those obtained on conventional solid phases. In combination, the above results have allowed the design of novel solid-phase surfaces for immunoassays, and will certainly be important in work that follows.

The development of new fluorophores has experienced a tremendous advance over the last two decades. Here, we have discussed the photophysical properties of traditional fluorescent labels and the comparatively advantageous properties of Qdots. The unique spectral properties of Qdots, such as their large Stokes shifts and exceptional brightness, make them attractive probes in biological applications and prime candidates for further

research and development in the field of solid-phase immunoassay and cell analysis.

Acknowledgements

We would like to express sincere thanks to our colleagues, Drs Renato del Rosario and Richard Bruehl, from Bio-Rad Laboratories, as well as, Drs James Bishop, Barnaby Abrams and Majid Mehrpouyan from BD Biosciences, who have kindly given their valuable time to contribute to this chapter. The support of Drs Graham Margetts, Jane Wheeler and Peter Brown from Polymer Laboratories (UK) in custom synthesis of magnetic particles is gratefully acknowledged.

References

[1] Stenberg, M. and Nygren, H. (1988) *J.Immunol. Meth*., **113**, 3–15.
[2] Nygren, H. and Stenberg, M. (1989) *Immunology*, **66**, 321–7.
[3] Wood, W.G. (1991) *Scand. J. Clin. Lab. Invest. Suppl*., **205**, 105.
[4] Selby, C. (1999) *Ann. Clin. Biochem*., **36**, 704.
[5] Bergstrom, K., Osterberg, E., Holmberg, K. et al. (1994) *J. Biomater. Sci. Polym. Ed*. **6**, 123.
[6] Tan, J.S., Butterfield, D.E., Voycheck, C.L. et al. (1993) *Biomaterials*, **14**, 823.
[7] Malmsten, M. (ed.) (1998) *Biopolymers at Interfaces*. New York: Marcel Dekker.
[8] Ostenberg, E., Berstrom, K., Holmberg, K. et al. (1993) *Coll. Surf. A: Phys. Eng. Aspects*, **77**, 159.
[9] Harris, J.M. and Kozlowski, A. (1997) Poly(ethylene glycol) and related polymers monosubstituted with propionic or butanic acids and functional derivatives thereof for biotechnical applications. US Patent 5,672,662.
[10] Prime, K.L. and Whitesides, G.M. (1991) *Science*, **252**, 1164.
[11] Prime, K.L. and Whitesides, G.M. (1993) *J. Am. Chem. Soc*., **115**, 10714.
[12] Mrksich, M., Sigal, G.B. and Whitesides, G.M. (1995) *Langmuir*, **11**, 4383.
[13] Mrksich, M. and Whitesides, G.M. (1997) Using self-assembled monolayers that present oligo(ethylene glycol) groups to control the interactions of proteins with surfaces. In *Poly(ethylene glycol) Chemistry and Biological Applications* (J.M. Harris and S. Zalipsky, eds). Washington, DC: ACS Symposium Series.
[14] Gupta, V.K., Skaife, J.J., Dubrovsky, T.B. et al. (1998) *Science*, **279**, 2077.
[15] Dubrovsky, T.B., Hou, Z., Stroeve, P. et al. (1999) *Anal. Chem*., **71**, 327.

[16] Sofia, S.J. and Merrill, E.W. (1997) Protein adsorption on poly(ethylene oxide)-grafted silicon surfaces. In *Poly(ethylene glycol) Chemistry and Biological Applications*. (J.M. Harris and S. Zalipsky, eds). Washington, DC: ACS Symposium Series.
[17] de Gennes, P.G. (1979) *Scaling Concepts in Polymer Physics*. Ithaca: Cornell University Press.
[18] de Gennes, P.G. (1987) *Adv. Colloid. Interface Sci*., **27**, 189.
[19] Jeon, S.I., Andrade, J.D. and de Gennes, P.G. (1991) *J. Colloid. Interface Sci*., **142**, 149.
[20] Jeon, S.I. and Andrade, J.D. (1991) *J. Colloid. Interface Sci*., **142**, 159.
[21] Golander, C.G., Herron, J.N., Lim, K., Claesson, P., Stenius, P., Andrade, J. D. (1992) Protein adsorption on PEG surfaces. In *Poly(Ethylene Glycol) Chemistry: Biotechnical and Biomedical Applications* (J.M. Harris, ed). New York: Plenum Press.
[22] Auroy, P., Auvray, L. and Leger, L. (1991) *Phys. Rev. Lett*., **66**, 719.
[23] Huang, S.C., Caldwell, K.D., Lin, J.N. et al. (1996) *Langmuir*, **12**, 4292.
[24] Weetall, H.H. (1993) *Appl. Biochem. Biotechnol*. **41**, 157.
[25] Plueddemann, E.P. (1991) *Silane Coupling Agents*. New York: Plenum Press.
[26] Dubrovsky, T. (2000) Immobilization of protein monolayers on planar solid supports. In *Protein Architecture* (Y. Lvov and H. Mohwald, eds). New York: Marcel Dekker.
[27] Haller, I. (1978) *J. Am. Chem. Soc*., **100**, 8050.
[28] Dunaway, D.J. and McCarley, R.L. (1994) *Langmuir*, **10**, 3598.
[29] Hemmila, I., Mukkala, V-M., Dakubu, S. et al. (1984) *Anal. Biochem*., **137**, 335.
[30] Soini, E. and Kojola, H. (1983) *Clin. Chem*., **29**, 65.
[31] Ekins, R.P. (1999) J. Clin. Lig. Assay, **22**, 61.
[32] Lasic, D.D. (1997) The conformation of polymers at interfaces. In *Poly(ethylene glycol) Chemistry and Biological Applications* (J.M. Harris and S. Zalipsky, eds). Washington, DC: ACS Symposium Series.
[33] Abbott, N.L., Blankschtein, D. and Hatton, T.A. (1992) *Macromolecules*, **25**, 3917.
[34] Wazava, T., Ishizuka-Katsura, Y., Nishikawa, S. et al. (2006) *Anal. Chem*., **78**, 2549.
[35] Aslam, M. and Dent, A. (1998) *Bioconjugation. Protein Coupling Techniques for the Biomedical Sciences*. New York: Grove's Dictionaries.
[36] Wong, S.S. (1991) *Chemistry of Protein Conjugation and Cross-linking*. Boca Raton: CRC Press.
[37] Chandler, D.J., Lambert, B.A., Reber, J.J., Phipps, S.L. (2003) Precision fluorescently dyed particles and methods of making and using same. US Patent 6,514,295.
[38] Chandler, V.S., Fulton, R.J. and Chandler, M.B. (2003) Multiplexed analysis of clinical specimens apparatus and method. US Patent 6,524,793.

[39] Ekins, R.P. (1991) Immunoassay design and optimization. In *Principles and Practice of Immunoassay* (C.P. Price and D.J. Newman, eds). New York: Stockton Press.
[40] Tijssen, P. (1985) Practice and theory of enzyme immunoassay. In *Laboratory Techniques in Biochemistry and Molecular Biology*, volume 15 (R.H. Burdon and P.H. van Knippenberg, eds). Amsterdam: Elsevier.
[41] Midgley, J.E.M. (2001) *Clin. Chem*., **47**, 1353.
[42] Henglein, A. (1982) *J. Phys. Chem*., **86**, 2291.
[43] Brus, L.E. (1983) *J. Chem. Phys*., **79**, 5566.
[44] Spanhel, L., Haase, M., Weller, H. et al. (1987) *J. Amer. Chem. Soc*., **109**, 5649.
[45] Hines, M.A. and Guyot-Sionnest, P. (1996) *J. Phys. Chem*., **100**, 468.
[46] Dabbousi, R.O., Rodriguez-Viejo, J., Mikulec, F.V. et al. (1997) *J. Phys. Chem. B*, **101**, 9463.
[47] Peng, X., Schlamp, M.C., Kadavanich, A.V. et al. (1997) *J. Amer. Chem. Soc*., **119**, 7019.
[48] Bruchez, M., Moronne, M., Gin, P. et al. (1998) *Science*, **281**, 2013.
[49] Chan, W.C.W. and Nie, S. (1998) *Science*, **281**, 2016.
[50] Wood, P. (1991) Heterogeneous fluoroimmunoassay. In *Principles and Practice of Immunoassay* (C.P. Price and D.J. Newman, eds). New York: Stockton Press.
[51] Jackson, T.M. and Ekins, R.P. (1986) *J. Immunol. Meth*., **87**, 13.
[52] Ekins, R.P. (1985) Current concepts and future developments. In *Alternative Immunoassays* (W.P. Collins, ed.). New York: John Wiley and Sons.
[53] Doose, S. (2003) Single molecule characterization of photophysical and colloidal properties of biocompatible quantum dots. Ruprecht-Karls University, Heidelberg: Dissertation.
[54] Abrams, B. and Dubrovsky, T. (2003) Evaluation of the new Qdot-655 conjugates. Unpublished results.
[55] Larson, D.R., Zipfel, W.R., Williams, R.M. et al. (2003) *Science*, **300**, 1434.
[56] Wu, X., Liu, H., Liu, J. et al. (2002) *Nat. Biotechnol*., **1038**, 1.
[57] Abrams, B. and Dubrovsky, T. (2006) Quantum dots in flow cytometry. In *Methods in Molecular Biology, volume 374: Quantum Dots: Applications in Biology* (M.P. Bruchez and C.Z. Hotz, eds) Totowa, NJ: Humana Press.
[58] Alivisatos, A.P. (2004) *Nat. Biotechnol*., **22**, 47.
[59] Dubertret, B., Skourides, P., Norris, D.J. et al. (2002) *Science*, **298**, 1759.
[60] Han, M., Xiaohu, G., Su, J.Z. et al. (2001) *Nat. Biotechnol*., **19**, 631.
[61] Maino, V.C. and Maecker, H.T. (2004) *Clin. Immunol*., **110**, 222.
[62] Maecker, H.T. (2004) Cytokine flow cytometry. In *Methods in Molecular Biology: Flow Cytometry Protocols* (T.S. Hawley and R.G. Hawley, eds). Totowa, NJ: Humana.
[63] Suni, M.A., Dunn, H.S., Orr, P.L. et al. (2003) *BMC Immunol*., **4**, 9.
[64] Matz, M.V., Fradkov, A.F., Labas, Y.A. et al. (1999) *Nat. Biotechnol*., **17**, 969.

[65] Yanushevich, Y.G., Staroverov, D.B., Savitsky, A.P. et al. (2002) *FEBS Lett.*, **511**, 11.
[66] Davis, K.A., Abrams, B., Iyer, S.B. et al. (1998) *Cytometry*, **33**, 197.
[67] Bigos, M., Stovel, R. and Parks, D. (2004) *Cytometry*, **59**, 42.
[68] Maecker, H.T., Frey, T., Nomura, L.E. et al. (2004) *Cytometry*, **62**, 169.

List of Abbreviations

PS	polystyrene
PEG	poly(ethylene glycol)
PEG-PPG	poly(ethylene glycol) and poly(propylene glycol) copolymer
D	the grafting density or an average distance between grafting points
L	the overall thickness of the PEG monolayer
GOPTS	3-glycidoxypropyltrimethoxysilane
APDMES	3-aminopropyldimethylethoxysilane
DTTA	N^1-(*p*-isothiocyanatobenzyl)-diethylenetriamine-N^1,N^2,N^3,N^3-tetraacetic acid
EDC	(1-ethyl-3(3-dimethylaminopropyl)carbodiimide
NHS	N-hydroxysuccinimide
PAA	poly(allyl amine)
DMAP	4-(dimethylamino)pyridine
MDD	minimum detectable dose
SD	standard deviation
CV	coefficient of variation
TSH,	thyroid stimulating hormone
Qdot	semiconductor quantum dot
FITC	fluorescein
PE	phycoerythrin
APC	allophycocyanine
APC-Cy7	tandem fluorophore
S/N	signal-to-noise ratio
SI	stain index

This page intentionally left blank

Chapter 9

Electromagnetic applications of conducting and nanocomposite materials

Özlem Yavuz, Manoj K. Ram and Matt Aldissi
Fractal System Inc., Safety Harbor, FL, USA

Abstract. This chapter reviews our previous studies and summarizes the research on electromagnetic interference (EMI) shielding studies with conductive polymers (CPs): polyaniline (PANI), polypyrrole (PPy), and their composites in various frequency ranges. As the use of electronic products and communication devices increases, the need for EMI shielding materials increases as well. CPs are new alternative candidates for EMI shielding applications due to their lightweight, corrosion resistance, ease of processing, and tunable conductivities as compared with typical metals; however, very high level of shielding efficiency cannot be achieved by using CPs only. Therefore, this chapter highlights, reviews, and shows the usage of magnetic particles (MnZn-ferrites (MZFs)) together with CPs. The results show that chemical and electrochemical polymerization techniques yield homogenous coatings onto ferrites particles, which is important to generate electromagnetic waves from magnetic sources, especially at low frequencies, together with those generated from electric sources by CPs having a single coating with desired shielding properties. CP coated textile studies are also included in this chapter to demonstrate that CP-coated fabrics offer several advantages including increased flexibility, access to a wide range of structures, and have a high absorption level to shielding, which is lacking in traditional shielding materials.

Keywords: Conductive polymers, nanocomposite materials, electromagnetic interference shielding (EMI), electromagnetic applications, magnetic particles, polyaniline (PANI), and polypyrrole (PPy)

9.1. Introduction

Conductive polymers (CPs) were the subject of intensive research starting from the end of 1980s [1], with foreseeable applications in such diverse fields as rechargeable batteries [2], biological and chemical sensors [2,3], transducers [4–6], antistatic coatings [6], corrosion-inhibiting films [6], and electromagnetic interference (EMI) shielding [6]. Although conducting polymers have interesting properties, brittleness and lack of processability can inhibit their commercial applications. However, when coated on substrates such as fabrics, flexible conductive sheets with infinite structural variations are obtained. Synthetic materials can achieve high conductivity values upon doping. For example, films of doped polyacetylene [7] have conductivities approaching those of conventional metals. However, there are some limits. For example, the conductivity of polyacetylene can be extremely high (10^5 S cm^{-1}), but it suffers from severe atmospheric instability, and thus, it is not suitable for device applications. A lot of recent studies concentrated on polypyrrole (PPy), polyaniline (PANI), and polythiophene (PTh) because of their superior oxidative stabilities as compared with other inherently conducting polymers. PPy can be synthesized either by an electrochemical oxidative process or by chemical oxidation of pyrrole [6,8]. It is an intractable, brittle solid. However, many products with usable mechanical properties can be made by blending PPy with another polymer [9]. PANI, one of the most stable CPs, is also well suited for electrochemical applications because its conductivity can be switched from low to high to low within the electrochemical potential range of aqueous electrolytes, and the films of PANI can be readily prepared from aqueous electrolytes.

Electromagnetic interference implies that all unwanted, spurious, conducted, and/or radiated signals of electrical origin can cause unacceptable degradation of system or equipment performance and contain components with frequencies ranging from 50, 60 and 400 Hz up to the microwave region, as manmade or natural, which may be either narrowband or broadband [10]. Shielding of EMI is not a new concept. However, we can see its increased visibility with the spread of digital electronics, in aerospace, terrestrial applications, portable consumer devices and appliances, as well as ongoing miniaturization and the increasing sensitivity and importance of these electronic devices. In addition, shielding of EMI is of critical use due to health concerns, such as symptoms of languidness, insomnia, nervousness, headache, etc., on exposure to electromagnetic waves [11], the dangerousness of electromagnetic field on health [12], and

the lack of convincing biological evidence for such adverse health effects in humans [13].

Traditional approach for EMI shielding relies on the use of metallic materials, which supply excellent shielding effectiveness (SE). However, the conventional metallic shields, in the form of bulk sheets, meshes, plating coatings, [14,15] powders (or whiskers) and/or fibers (or filaments) in filled polymer composites or coatings, impose severe weight difficulties, especially in aerospace applications such as spacecrafts and satellite systems. Several approaches were undertaken to solve the weight problems, such as the coating of ceramic microballoons [16] and carbon fibers [17] with metals for conductive fillers.

Carbons are also used in EMI shielding applications, mainly as conductive fillers (fibers, particles, powders, filaments, tubes) in composite materials, due to their electrical conductivity, chemical resistance and low density. Unfortunately, with the exclusive use of carbon fillers, the conductivity and resulting EMI shielding performance was not sufficient, in addition to the drawback of 'sloughing' of carbon fillers, which can otherwise contaminate or damage the electronic devices. Great efforts have been made to increase the conductive and electromagnetic performances of carbon-based materials. For instance, the novel class of vapor-grown carbon nanotubes [18] and nanofibers [19] imparts a broad range of conductivity to plastics at far lower loadings than conventional carbon-based additive and simultaneously provides reinforcement and enhanced thermal conductivity. However, the potential of these nanocarbon products is currently limited due to high cost.

Electrical conductivity and processability of CPs can be tuned by chemical manipulation of the polymer backbone by the nature of the dopant, by the degree of doping, and by blending with other polymers. Nowadays, multifunctionalized micro/nanostructures of CPs have attracted great attention due to their unique properties and technological applications in electrical, optical, and magnetic materials and devices, such as electromagnetic shields and microwave-absorbing materials [20–25]. Previous reports have also demonstrated that conducting polymers are responsible for their electrical properties, while magnetic properties are induced by magnetic materials in the composites [26]. Thus, the molecular structure of the component in micro/nanostructured composites is the key parameter affecting the electromagnetic properties of micro/nanostructured composites. As CPs have several merits such as low weight, physical flexibility, ease of control of properties through processing [27–29], and a tunable shielding response, materials such as doped PANI or PPy are considered

as promising candidates for replacement of (or for use in conjunction with) metallic materials for EMI shielding applications. Conducting materials can effectively shield electromagnetic waves generated from an electric source, whereas electromagnetic waves from a magnetic source, especially at low frequencies, can be effectively shielded only by magnetic materials. Thus, if films having both conducting and magnetic components were used as EMI shielding materials, good SE can be achieved for various electromagnetic sources with a single coating.

Based on the survey of work available in literature, this chapter briefly describes the shielding theory, EMI shielding results of PANI, PPy, other conducting polymers including poly(3-octyl thiophene) (POTh) and poly(phenylene-vinylene) (PPV), and includes some of the authors' own studies demonstrating the synthesis of multifunctional particles with a novel composition for the production of lighter materials.

9.2. Shielding Theory

Electromagnetic energy consists of a magnetic (H-field) and an electric (E-field) component perpendicular to each other and propagating at right angles to the plane containing the two components. The ratio of E to H is defined as the wave impedance (Z_w, in ohms) and depends on the type of source and distance from the source. Large impedances characterize electric fields and small ones characterize magnetic fields. Far from the source, the ratio of E to H remains constant and is equal to 377 Ω (intrinsic impedance of free space). In EMI shielding, there are two regions we should consider: the near field shielding region and the far field shielding region. When the distance between the radiation source and the shield is larger than $\lambda/2\pi$ (where λ is the wavelength of the source), it is in the far field-shielding region. The electromagnetic plane wave theory is generally applied for EMI shielding in this region. When the distance is less than $\lambda/2\pi$, it is in the near field shielding region, and the theory based on the contribution of electric and magnetic dipoles is used for EMI shielding.

SE in decibel (dB) is a measure of the reduction of EMI at a specific frequency achieved by a shield, such as a coating, and it is defined as in Eqn (9.1):

$$\mathrm{SE} = 10\log P_o/P_t = 20\log E_o/E_t = 20\log H_o/H_t \qquad (9.1)$$

where P_o, E_o and H_o are the incident intensities of the power, the electric and magnetic fields, and P_t, E_t and H_t are the counterparts transmitted through the shield.

A part of the incident electromagnetic wave is generally attenuated through reflection from the surface of a material, by way of absorption by the material or multiple internal reflections inside the material. The rest of the wave energy is transmitted. The total EMI shielding effectiveness (EMI SE) of the material is, therefore, the sum of SE resulting from the three shielding mechanisms. The relative shielding efficiency by reflection and absorption is an important determinant of practical application. EMI shielding by absorption rather than reflection is currently more important for a lot of applications. Materials coated with metals possess very high EMI SE, ranging from 40 to 100 dB. However, they cannot be used as an electromagnetic wave absorbent because their shallow skin depth helps shield EMI mainly through surface reflection [30]. On the other hand, electrically conducting polymers are capable for reflecting and absorbing electromagnetic waves and, therefore, exhibiting a significant advantage over metallic shielding materials. EMI shielding by absorption may be enhanced by increasing the skin depth, which is controlled by changing the electrical conductivities or dielectric constants of electrically conducting polymers.

9.3. CPs and EMI Shielding Studies

To prevent undesirable effects of EMI, various EMI shielding techniques and materials have been developed. For example, a functional EMI shielding material, such as metal complex or multilayered metal coatings, has been introduced. A conducting or magnetic material can be used as EMI shielding material. CPs have many functional properties suitable for their application in EMI shielding, such as an absorption-dominant EMI shielding characteristics, good processability, low mass density, etc. The physical properties of typical metals and conducting polymers such as the EMI shielding materials are summarized in Table 9.1. Conductivity is one of the most important characteristics for the calculation of SE of metals due to their higher microwave frequency loss tangent ((tan δ), far higher than 1). However, in the case of CPs, both permittivity and tan δ are important for the calculation of SE due to lower (tan δ) of CPs (between 0.5 and 7.0 [31]). The thickness also affects the shielding behavior of polymers, and SE increases linearly with thickness [32]. Furthermore, the temperature, especially in the room temperature range, has negligible effect on

Table 9.1: Physical properties of typical metal and conducting polymer

Properties	Metal	Conducting polymer
Electrical conductivity	$\geq 10^5$	$1–10^2$ S cm^{-1}
Mass density	High (Cu $\cong$ 8.9 g/cm^3)	Low (PPy$\sim$1.2 g cm^3)
Metal stiffness	Good	Poor
Flexibility	Poor	Good
Processability	Poor	Good
Dominant shielding characteristics	Reflection	Absorption

SE. In addition to the above-mentioned extrinsic parameters of conducting polymers, there are intrinsic parameters, such as permittivity (both real and imaginary parts and the absolute value of complex permittivity), tan δ, absorption and reflection effects, responsible for shielding behaviors.

9.3.1. EMI Shielding Studies with PANI

The first systematic study of PANI for EMI shielding applications was reported by Shacklette et al. [33,34]. PANI was melted and blended with polyvinyl chloride (PVC) to form a composite having a conductivity of 20 S cm^{-1}. The SE of PANI composites, with metal fillers, was measured over a frequency range from 1 MHz to 3 GHz and calculated theoretically for both near and far fields. It was found that SE increases with the increase of conductivity. The far field SE was found to be as high as 70 dB for PANI composites.

Mixtures of PANI and conducting powders, including silver, graphite and carbon-black [35–37], were prepared with the aim to increase conductivity of PANI and SE. According to these studies, thin films of emaraldine base of PANI dissolved in N-methyl-2-pyrrolidone (NMP) were prepared and doped with HCl (denoted as ES/Ag, ES/graphite, and ES/carbon-black). The EMI measurements were performed at room temperature in the frequecy range of 10 MHz to 1 GHz. The SE of ES/Ag and ES/graphite (with PANI thickness of c. 75 mm) was c. 46 dB and c. 27 dB, respectively, which were higher than the c. 17 dB for pure ES. The SE of EB/Ag was c. 3.5 dB, indicating that chemical doping enhances EMI SE by more than 10 times. Moreover, it was verified that SE increased with the DC conductivity of films [35–37].

The microwave parameters, such as complex permittivity, absorption, and reflection and SE of bulk PANI (doped with two sulfonate dopants), were measured over a broadband range of 4 to 18 GHz for the first time using coaxial line techniques [38]. Permittivity decreased monotonically with the increase of frequency. The real part varied from 188 at 4 GHz to c. 32 at 10 GHz and 10 at 18 GHz; the imaginary part varied from about 35 at 4 GHz to c. 2 at 18 GHz. The microwave SE of PANI, calculated on the basis of measured complex permittivity, was lower than −15 dB over the frequency range.

Shielding effectiveness studies of conducting PANI and acrylonitrile-butadiene-styrene (ABS) composites, processed at 180–190°C at 101 GHz, have revealed that a loading of 5% PANI in the composite has resulted in a 6.23 dB SE. These cannot be used for EMI shielding in the millimeter band but can be used for dissipation of static charges. With the increase of PANI concentration, SE was increased. The best SE, larger than 60 dB, has been achieved in 50% PANI. Similar results were reported by Dhawan et al. [39] on a composite of PANI with polystyrene (PS), which was prepared by melt blending DBSA and TSA-doped PANI with PS in the 180–220°C temperature range (with slight decrease of SE). The best SE at 50% concentration of PANI in PS composite was about 58–59 dB (lower than that for the ABS composite [40]).

The SE of HCl-doped PANI and poly(vinylalcohol) (PVA) composites was measured within the 8.2–12 GHz frequency range, which has shown that SE increased with the increase of conductivity and thickness. A 10 dB was observed with 16% PANI concentration. According to Wessling [41], highly conductive blends of PANI with PVC and polymethylmethacrylate (PMMA), having conductivities of c. 20 S cm^{-1} (in some cases up to 100 S cm^{-1}), have exhibited EMI SE in the range of 40–75 dB for both near and far fields.

Other types of composites were prepared by Wojkiewicz et al. [42]. The first among them was a PANI and PVC composite. It was prepared in NMP, processed over a fiber glass, and doped with HCl. The second one was CSA doped PANI in m-cresol. The SE results have indicated that a composite of the second type may have higher conductivity and SE efficiency. In the low frequency range (50 MHz to 1 GHz), a polyurethane (PU) composite with 40% PANI exhibited 50–70 dB; over the microwave band, 60–70 dB was obtained (higher than that of other composites). A large increase in SE can be achieved with successive addition of CSA-doped PANI layers (similar to the increase observed on multilayer PANI films [43,44]).

Jing et al. have studied different concentrations of TSA-doped PANI mixed with polyacrylate powders. The results have shown that an SE of 30–79 dB can be reached in the frequency range of 14 kHz to 1 GHz, with the highest of 79 dB at 200 MHz [43]. The SE of the coatings was found to increase with PANI percentage and conductivity of the coatings.

Free-standing PANI films of different thicknesses, prepared by solution cast of EB in NMP and doped with HCl thereafter, were tested for EMI shielding in broadband ranges from 50 MHz to 13.5 GHz. An SE of 70 dB was measured in the range of 50 MHz to 1.5 GHz, corresponding to the theoretical SE calculations based on conductivities. The thicker the films, the higher the SE values obtained [44].

9.3.2. EMI Shielding Studies with PPy

Yashino et al. have first reported the EMI shielding properties of PPy [45], and found that the shielding electric field was higher than 30 dB over the 3–300 MHz range. However, it was not effective in magnetic field shielding. Later, another group prepared PPy membranes from PU, polyethylene, poly(propylene), etc., to overcome the poor adhesion resistance of ICP coatings on various substrates, and has tested EMI shielding over 10 kHz to 1000 MHz. PPy-based membranes have shown higher SE. Electropolymerized PPy films have shown different microwave reflection, transmission, and absorption at 10 GHz. Microwave transmission decreased with the increase of dopant concentration, while microwave reflection increased with the increase of dopant concentration. The far field EMI shielding measurements at 1 GHz have shown that SE increased with the conductivity of the film. A significant SE of 38 dB was achieved with highly doped conductive films, while lightly doped semiconductive films exhibited small SE values [46]. Similar EMI SE results were reported on freshly electrosynthesized PPy films over 300 MHz to 2 GHz by using different measurement techniques, and 40 dB was achieved [47,48].

Polypyrrole-based conducting hot-melt adhesives were prepared by mixing appropriate amounts of ethylene-co-vinyl acetate (EVA) copolymer and PPy, which was synthesized with oxidative polymerization technique. Both near and far field EMI shielding properties of the adhesives were determined at room temperature, according to the expressions derived by Colaneri and Shacklette [49], on experiment-measured conductivities. Both the values increased with the loading of PPy [50]. A near field SE in excess of 80 dB was determined at 1 MHz and above 30 dB at 300 MHz, revealing

a decrease with the increase of frequency. The far field SEs of [51,52] (30 dB) were determined over the range of 1–300 MHz for PPy loadings of 15, 20 and 25%.

9.3.3. EMI Shielding Studies with Poly(3-octyl thiophene) (POTh) and Poly(phenylene-vinylene (PPV)

Poly(3-octyl thiophene) composites were tested for EMI shielding within the frequency range from 100 kHz to 1 GHz [53]. The EMI SE of composites increased with polymer loadings; c. 45 dB (from 100 kHz to 10 MHz) was achieved with a polymer loading of 20% in the PVC matrix. However, this EMI SE was lower than that of nickel coated samples (c. 80 dB). The composites with 20% loading or less of POTh were not readily applicable as EMI shielding materials, and no EMI studies were performed with PTh or its derivatives. In the case of poly-*p*-phenylene-benzobisthiazole (PBT) [54,55], the early results indicated potential usefulness of the polymer as an EMI shield over the microwave frequency range of 2 GHz to 10 GHz; however, no other results were reported thereafter.

Poly(phenylene-vinylene is another CP with attractive properties such as resistance to oxidation, high thermal decomposition temperature, and high electroluminescence. It was found that highly doped PPV provides high conductivity and permittivity resulting in very low absorbance and reflectivity of the polymer (up to 5 GHz [56]).

9.4. Experimental Results

According to the authors' own studies, polymer/composite synthesis can be performed in three ways: (a) using ferrite particles, (b) using a thin coating of nickel, or (c) using a thin layer of conducting polymer (Fig. 9.1). Due to the unprocessability of conducting polymers, materials may be processed in the form of coatings, films, or sheets, as well as by blending of conventional polymers, such as PU, wherein the composites retain the mechanical properties of conventional polymers and electrical conductivity of conducting polymers. In this chapter, we shall discuss the synthesis, electrical, magnetic and shielding properties, and applications of these materials.

Several approaches for preparing nanocomposites with magnetic nanoparticles and conducting PPy and PANI have been reported, including: (a) electrochemical method [57]; (b) chemical method with sodium

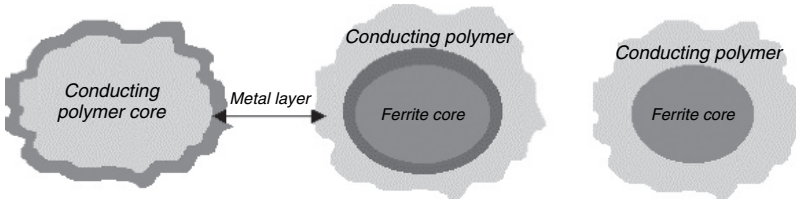

Figure 9.1: Schematic representation of the multifunctional particle for shielding materials.

p-dodecylbenzenesulfonate (NaDS) used as surfactant and dopant; $FeCl_2 \cdot 4H_2O$ and $FeCl_3 \cdot 6H_2O$ are used as oxidants to react with pyrrole, followed by the treatment with hot NaOH solution [58,59]; (c) simultaneous gelation and polymerization to prepare PPy and iron oxide nanocomposites [60]; and (d) layer-by-layer self-assembly (LBL-SA) of conducting polymers and ferrite nanoparticles in aqueous solutions [61]. Wan et al. have investigated PANI with magnetic properties using two approaches: (a) $FeCl_2 \cdot 4H_2O$ and $FeCl_3 \cdot 6H_2O$ were used as oxidants to react with aniline, followed by the treatment with KOH aqueous solution [62]; and (b) blending PANI in *N*-methyl-2 pyrrolidone (NMP) with iron(II) sulfate aqueous solution, and precipitating Fe^{2+} into maghemite [63]. A poly(aniline-co-aminobenzenesulfonic acid (PAOABSA)) copolymer containing γ-Fe_2O_3 magnetic particles was prepared by this approach [64].

The authors have applied two approaches in their laboratory to synthesize MnZn ferrite/PPy and MnZn ferrite/PANI particles by electrochemical and chemical oxidative polymerization techniques with high conductivity and coercive force suitable for antistatic applications [65,66].

9.4.1. Chemical Synthesis of PANI and PPy in the Presence of MnZn Ferrite and Ni/MnZn Ferrite

Polyaniline was prepared by chemical oxidative polymerization (COP) technique as described in literature [66]. Yavuz et al. have applied this technique for the synthesis of PANI-covered MnZn ferrite (MZF) [65]. According to the method, in the presence of ferrite particles and aniline, aqueous ammonium persulfate solution was slowly added to an acidic (pH 1.0) aqueous solution (c. 0°C) and mixed with a stirrer. For each reaction, 4 g of MZF was immersed in 200 ml of an aqueous solution

containing different percentages of anilines. The reaction time was kept as 4 h for each preparation.

Polypyrrole was also prepared by COP technique of pyrrole in the presence of MnZn ferrite and/or Ni/MnZn ferrite, *p*-toluensulfonic acid monohydrate (*p*-TSA), and $FeCl_3$ at (c. 0°C), and kept for 4 h. The PPy-coated particles were collected on a filter paper, washed using an aqueous acid solution and methanol until they turned colorless, and then dried in a vacuum oven at 60°C.

9.4.2. Electrochemical Synthesis of PANI and PPy in the Presence of MnZn Ferrite and Ni/MnZn Ferrite

In the electrochemical method, the setup is used to deposit polymer and Ni over MnZn ferrite particles (Fig. 9.2). The setup consists of a rectangular stainless steel container with a flat bottom acting as anode. Pt was used as cathode. The slurry has to be stirred to form a suspension every 2 min by applying 1.2 V in order to achieve an efficient coating. Since deposition time is critical to determine the coating thickness and polymer to ferrite ratio, it is varied. The resulting materials are washed several times using ethanol and dried under vacuum.

9.4.3. Ni Coating over PANI and PPy

Metal coating may be performed electrochemically using the same setup as electropolymerization technique (Fig. 9.2). The polymer particles are

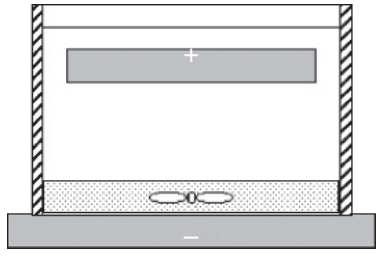

Figure 9.2: Electrochemical setup for metal coating of MnZn ferrite and polymer particles.

synthesized by both COP and electrochemical polymerization (ECP) techniques. The polarity is reversed as compared to the polymer coating because of the anodic oxidation nature of CPs. The aqueous metal (nickel) precursor solutions – $NiSO_4 \cdot 6H_2O$ 0.171 mol l^{-1}, $NiCl_2 \cdot 6H_2O$ 0.063 mol l^{-1}, H_3BO_3 0.404 mol l^{-1}, $KH_2PO_4 \times 0.33$ mol l^{-1} – are mixed with PPy and PANI particles by adjusting and forming a slurry (pH 3.0–3.5), which is in direct contact with the cathode plate. Several short stirrings (few tens of seconds) and electrodeposition cycles are performed to achieve the desired coating thickness using an applied current (5–10 mA). Longer process times are not desirable, as the particles tend to precipitate in the bottom. Therefore, repetitive short coating times with stirring after each coating pulse would provide more homogeneous materials. The coated particles are washed with water several times, rinsed with methanol and dried in a vacuum oven. The whole coating process can be achieved within few minutes as a low percentage of metal is required for shielding applications.

9.4.4. Dispersion Preparations and Processing

Three types of dispersions are possible: nickel-coated PPy and/or PANI core, the two-layer particles of ferrites and PPy/PANI, and the three-layer particles of NiMZF with PPy and PANI. PPy and PANI act as interfacial modifier for the nickel surface. In all cases, the material is lightweight and has a density equivalent to that of the CP. PUs of different grades are mixed in the dispersion solution. Initially, the ferrite particles comprise 75% (the rest 25% are mixtures of PU). The dispersion contains multilayer particles within the polymer matrix, and is prepared by using polymeric particles together with PU in the presence of NMP as a solvent. Polymer-coated ferrite as well as Ni-coated polymer particles are added in different percentages and stirred continuously until the mixture is homogenized. The film/sheet is casted on glass plates and removed after 48–72 h of drying in air.

9.5. Material Characterization

9.5.1. FTIR Measurements

PANI/MnZn ferrite

The characteristic bands in the IR spectrum of PANI occur at 1574, 1490, 1371, 1296, 1234, 1135, and 797 cm^{-1} [67]. The bands at 1296 and

1234 cm^{-1} correspond to the N-H bending and asymmetric C−N stretching modes of the benzenoid ring, respectively. The band at 1490 cm^{-1} is assigned to the C−N stretching of quinoid ring, which arises due to the protonation of PANI by the dopant. These bands at 1574 and 1490 cm^{-1} are the characteristic bands of nitrogen benzenoid and quinoid forms and are present due to the conducting state of the polymer. The peaks observed at 800–900 cm^{-1} are characteristic of para substitution of the aromatic ring and reveal that polymerization has proceeded via head-to-tail mechanism. The peak values at 1603 and 1637 cm^{-1} are due to the conjugated system and presence of an aromatic C−H out of the plane band. The absorption bands ν_1 and ν_2 around 600 and 400 cm^{-1} are attributed to the stretching vibration of tetrahedral and octahedral group complexes of ferrites, respectively. The IR absorption bands of solids in the 100–1000 cm^{-1} range are usually assigned to vibrations of ions in the crystal lattice. In ferrites, the metal ions are situated in two different sub-lattices, designated as tetrahedral and octahedral according to the geometrical configuration associated to the stretching of metal ions (Me=O). Waldron [68] has attributed the ν_1(400–450 cm^{-1}) band to the intrinsic vibrations of tetrahedral groups, the ν_2 (520–560 cm^{-1}) band to the octahedral groups, and the ν_3 (800 cm^{-1}) band is associated with the vibration of metal ions in the isotropic force fields of the octahedral or tetrahedral environments of ferrites. Figure 9.3 shows PANI-coated ferrite with different concentrations of aniline. A small band appears at 441 cm^{-1} due to the vibrations of $Mn^{2+} - O_2{}^2$ bond, indicating the incorporation of Mn. Figure 9.3 also shows that a decrease of aniline concentration causes lower absorption peak intensity. Table 9.2 shows the comparative assignment of FT-IR spectra of PANI and Ni-PANI particles. New peaks appear at 1287 and 1394 cm^{-1} and they are assigned to Ni−O, whereas the intensity of peaks at 785 and 873 cm^{-1} was greatly diminished.

PPy/MnZn ferrite

Characteristic absorption bands of PPy are observed at 1652, 1560, and 1459 cm^{-1}. The absorption peaks at 1652, 1560, and 1459 cm^{-1} were induced in the PPy−MZF composite by the interaction of MZF and PPy backbone. The C−H in-plane vibrations at 1309, 1044, and 1190 cm^{-1} and C−H out-of-plane vibrations at 786 and 922 cm^{-1} were observed in Fe_3O_4–PPy, and were found to shift to a lower wave number. The IR absorption bands in the range between 100 and 1000 cm^{-1} are usually assigned to vibrations of ions in the crystal lattice. The metal ions in

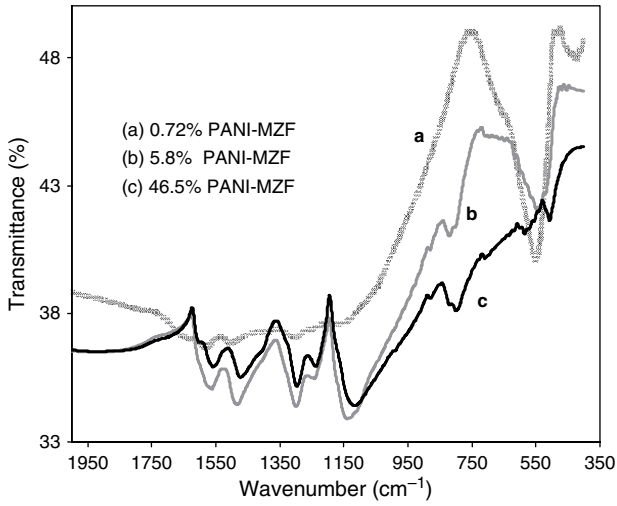

Figure 9.3: FT-IR spectra of (a) 0.72%, (b) 5.8% and (c) 46.5% aniline-coated MZF particles.

Table 9.2: FT-IR peaks of electrochemically Ni-coated PANI at different current conditions

PANI (cm^{-1})	**Ni/PANI, 10 mA (cm^{-1})**	**Ni/PANI, 15 mA (cm^{-1})**	**Peak assignment**
785	–	777	
873	–	–	
1135	1111	1013,1099	Quinoid–NH
1234,1296	1212,1217	1218,1243	–CN benzoid
–	1287	1295	–C–N str.
–	1394	–	Ni–O
1489,1574	1438,1496	1440,1467,1496	Quinoid ring, –C=C– benzoid ring
1603,1630	1645	1637	

ferrites are situated in two different sub-lattices designated as tetrahedral and octahedral according to the geometrical configuration of the oxygen nearest neighbors. Intrinsic vibrations of tetrahedral and octahedral groups of ferrites are observed in PANI/MZF structures.

9.5.2. X-ray Diffraction (XRD)

PANI/MnZn ferrite

X-ray diffraction is used to determine the crystalline structure of metal oxides and polymer-coated metal oxides by comparing the diffraction angle (2Theta) with that of metal oxides of known compositions. Figure 9.4 shows the XRD patterns of PANI/MZF composites (curve c) as well as PANI (curve a), Ni/PANI (curve b), and PANI/Ni/MZF (curve d) particles. The main diffraction peaks are at 18.13, 29.78, 35.10, 36.73, 42.63, 56.33, and 61.83 degrees for PANI-MZF powder, whereas MZF shows 2Theta peaks at 29.78, 35.10, 36.70, 42.58, 52.825, 56.33, 61.83, and 73.13 degrees. The broad ferrite peaks indicate very small crystallite size in the sample. The pattern for PANI (curve a) itself does not show sharp peak, suggesting the quasi-amorphous nature of the material. However, the polymer displays a diffuse broad peak ranging from 20 to 35° in consistent with the results obtained by others [69–72]. The PANI/MZF composite shows a high degree of crystallinity due to either the presence of high amount of ferrite in the composite or the more homogeneous protonation of PANI by synthesis with ferrite. During the process of composite formation of PANI with ferrite, it shows the change in the amorphous nature of PANI as a result

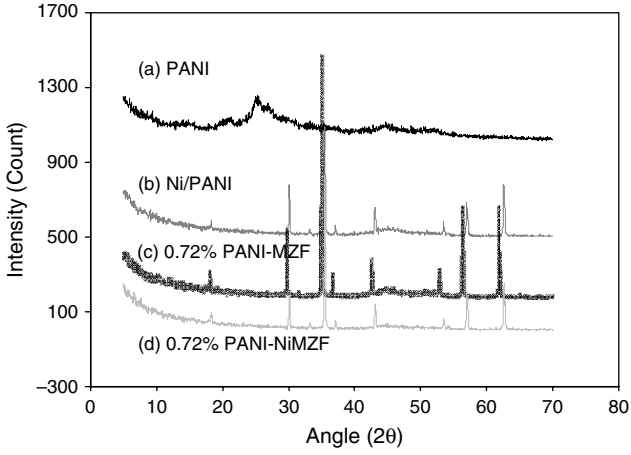

Figure 9.4: XRD spectra of PANI (a), Ni-coated PANI (Ni/PANI) (b), 0.72% PANI-coated MZF (PANI/MZF) (c), and 0.72% PANI-coated 3% Ni-coated MZF (PANI/NiMZF) (d).

of the interaction with ferrite. For Ni-coated PANI, crystallinity increases as a result of incorporation/addition of Ni coating to the PANI lattice as observed in Ni-coated MZF.

PPy/MnZn ferrite

X-ray powder diffraction measurements of PPy particles and PPy (weight 1% pyrrole monomer to Ni/MZF) coated over Ni/MZF were performed (Fig. 9.5). The X-ray pattern of PPy does not show sharp peak, suggesting no ordered structure in PPy CP. In fact, the polymer displays a diffuse broad peak ranging from 20 to 50° and broad peaks centered around 45–55° similar to the one observed for electrochemically synthesized PPy doped with *p*-TSA [73], which can be interpreted as the ordering in PPy chains at interplanar spacing [74]. PPy has been reported to be a 95% amorphous material where the controlling of synthesis and types of dopant can result in slight ordering. Figure 9.5 shows the crystalline structure of PPy coated over Ni/MZF particles. MnZn ferrite shows the spinel crystal structure [75]. PPy-coated Ni/MZF shows similar characteristic peaks as observed for MZF particles, indicating that the crystalline structure can be maintained by coating PPy CP. The composite formation of PPy with ferrite shows the spinel structure of MZF, which can be maintained by making each particle of PPy to interact.

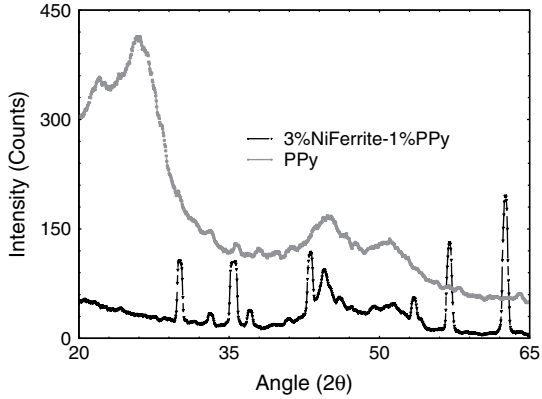

Figure 9.5: XRD spectra of PPy and 1% PPy coated 3% Ni-MZF.

9.5.3. Electrical Properties

DC measurements of PANI/MnZn ferrite

The DC conductivity results of chemically polymerized PANI coated over MZF and PANI coated over Ni/MZF are shown in Table 9.3. These results suggest that the aniline percentage significantly affects the conductivity of the resulting PANI composite particles. The increment of PANI over NiMZF particles would result in higher conductivity in comparison to MZF particles. However, there may not be much appreciable change in conductivity for containing a lower concentration of aniline monomer under chemical polymerization of PANI over NiMZF particles. Based on the conductivity measurements, 3% of aniline is sufficient to obtain PANI coating over MZF particles.

The conductivity results on electrochemically formed PANI over coated MZF particles are shown in Table 9.4. The monomer, varying from 2 to 10%, does not significantly affect the value of PANI-coated MZF particles

Table 9.3: Conductivity results of chemically polymerized aniline over MnZn ferrite (MZF) and 3% Ni-coated MZF particles

Aniline (%)	**PANI/MZF** (Ω^{-1} **cm**$^{-1}$)	**PANI/NiMZF** (Ω^{-1} **cm**$^{-1}$)
46	0.92	3.28
23	0.51	0.75
11.5	0.74	1.93
5.75	0.62	1.36
2.8	0.16	1.80
1.43	0.08	0.22
0.72	0.05	0.21

Table 9.4: Conductivity results of electrochemically PANI coated MZF (in ACN at 1.2 V)

Monomer (%)	**Conductivity** (Ω^{-1} **cm**$^{-1}$)
2	0.29
3	0.30
5	0.26
10	0.21

electrochemically. In fact, it was known that a 3% coating of polymer makes homogenous composite material for both chemical and electrochemical synthesis techniques.

DC measurements of PPy/MnZn ferrite

The DC conductivities of 'chemically polymerized PPy over MZF particles' and 'PPy over Ni/MZF particles' are shown in Table 9.5. These results suggest a significant change in the conductivity values of composite particles by varying the percentage of pyrrole monomer and amount of oxidant and electrolyte (used for doping PPy). In general, Ni/MZF particles reveal significant conductivity values. The increment of PPy over Ni/MZF particles shows better conductivity than MZF particles. However, the change in conductivity may be observed by varying 1 or 2% of pyrrole monomer over the weight of Ni/MZF particles for obtaining PPy/Ni/MZF composite particles. Table 9.6 shows the results of Ni-coated PPy particles. Interestingly, a decrease in conductivity may be observed in PPy/Ni/MZF composite particles by varying the amount of dopant (*p*-TSA), indicating that the concentration of dopant is an important parameter for repositioning Ni anions on PPy surface.

The conductivities of PPy and Ni/MZF with increasing PPy content in PU are summarized in Table 9.7. The conductivity of the 1% PPy coated MZF containing PU composites shows higher conductivity compare to 2% PPy ones. Pure PPy is a very lightweight polymer and has poor compactness. Therefore, 2% pyrrole-containing composites are very randomly

Table 9.5: Conductivity results of polymers obtained chemically in the presence of MnZn ferrite (MZF) and 3% Ni/MnZn ferrite (Ni/MZF)

Pyrrole (%)	**PPy-MZF (Ω^{-1} cm^{-1})**	**PPy-Ni-MZF (Ω^{-1} cm^{-1})**
1[a]	0.29	4.24
1[b]	0.43	1.98
1[c]	1.02	2.08
2[a]	0.25	4.07
2[b]	1.13	1.98
2[c]	1.47	2.18

[a] *p*-TSA: 0.026 M, $FeCl_3$: 0.006 M.
[b] *p*-TSA: 0.052 M, $FeCl_3$: 0.012 M.
[c] *p*-TSA: 0.104 M, $FeCl_3$: 0.104 M.

Table 9.6: Conductivity results of electrochemical Ni coating of PPy particles (synthesis conditions: PPy1: 0.1 M Py, 0.2 M *p*-TSA, 0.2 M $FeCl_3$; PPy2: 0.1 M Py, 0.1 M *p*-TSA, 0.2 M $FeCl_3$)

Sample	Applied current (mA)	$\delta(\Omega^{-1}\ cm^{-1})$
Ni/PPy1	3	0.21
Ni/PPy1	10	0.18
Ni/PPy2	3	1.47
Ni/PPy2	10	1.28

Table 9.7: Conductivity results of Ni-coated PPy and PPy-coated MZF and Ni/MZF containing PU sheets

Sample	$\delta(\Omega^{-1}\ cm^{-1})$
1% PPy/MZF, 99% PU	8.15×10^{-6}
2% PPy/MZF, 98% PU	1.64×10^{-6}
5% PPy/Ni, 95% PU	2.9×10^{-5}
2% PPy/Ni, 98% PU	4.01×10^{-5}
1% PPy/Ni, 99% PU	4.87×10^{-5}

oriented. Its interaction with polymer particles through grain boundaries is very poor, resulting in lower conductivity. As the PPy content is lowered in the samples, the change in compactness becomes more significant and the weak links between the grains are increasingly improved. The coupling through grain boundaries becomes stronger, resulting in the improvement of conductivity [76].

AC measurements of PANI/MnZn ferrite

Figure 9.6 shows the Bode plot of MZF, Ni/MZF, PANI-coated MZF, and PANI-coated NiMZF particles. The impedance of either MZF or Ni/MZF decreases by coating PANI over the particles. In the low frequency region, there is not so much appreciable change in the value of impedance as shown in Fig. 9.6. Impedance was also measured for electrochemically PANI-coated MZF particles. The Bode plot shows that a composite made at 1.2 V has lower impedance than a PANI made at lower potential.

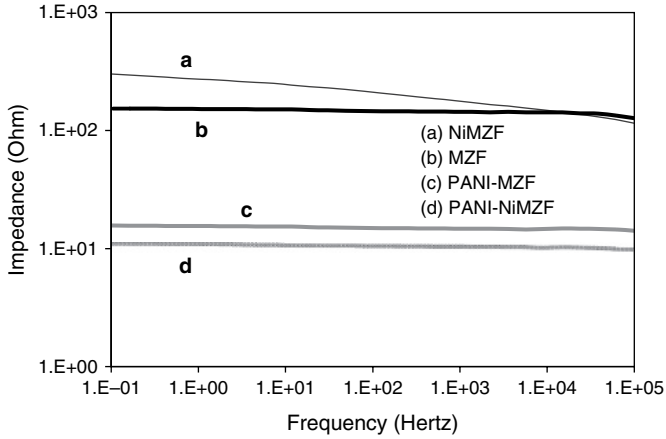

Figure 9.6: Bode plot of Ni/MZF (a), MZF (b), chemically 2.8% PANI-coated MZF (c), and 2.8 % PANI-coated NiMZF (d).

AC measurements of PPy/MnZn ferrite

Figure 9.7 shows the plot of log f (frequency, Hz) vs. log Z (impedance, Ω) for the chemically PPy-coated over MZF (a), PPy (b), and Ni-MZF (c) particles. It has earlier been shown that impedance measurements were performed in two-electrode setup by compacting the powder in a cylinder

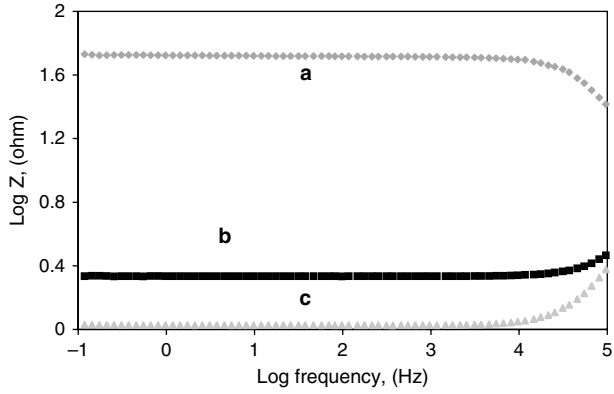

Figure 9.7: Bode plot of chemically PPy coated MZF (a), PPy (b), and chemically PPy coated 3% Ni/MZF (c),

between the two steel rods. The force (5 N) between the steel electrodes was kept constant in the measurement process. The impedance decrease by increasing the PPy over Ni-MZF was similar to the conductivity increase by four-point probes. No appreciable change in impedance was observed at frequency below 10^3 Hz to 10^4 Hz similar to that observed in the films studied by Beladakere et al. [77]. Conductivity was always attributed to the PPy systems. Interestingly, the PPY–Ni–MZF composite does not reveal any appreciable change in impedance in the low frequency region.

Figure 9.8 shows the plot of log (f) vs. log (Z) of MZF (a) and the results of electrochemically PPy coated MZF particles (3% (b), 8% (c), 10% (d)) by using 0.1 M $TEATFBO_4$ as an electrolyte in acetonitrile (ACN) at 10 mA.

ACN has been chosen as a solvent for PPy coated over ferrite. The results show that the dispersion of ferrite particles in ACN is very close to the dispersion of water, resulting in similar conductivity of the electrochemical system. The decrease in Z as a function of PPy coated over the particles indicates the increment in dopant content in the polymer.

The impedance of electrochemically PPy-coated Ni/MZF particles is measured in the presence of different electrolytes ($LiTFBO_4$ and $TEATFBO_4$). The results show that the size of dopant significantly affects the polymer properties. The impedance studied for various composites by varying the PPy has not revealed the dependence, showing that PPy does not perform any polarization effect and that the solvent or water effects

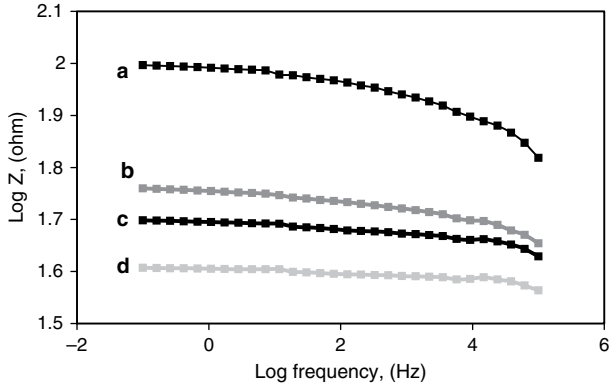

Figure 9.8: Bode plot of MZF (a) and electrochemically 3% (b), 8% (c), 10% (d) PPy coated MZF by using 0.1 M $TEATFBO_4$ as an electrolyte in ACN at 10 mA.

have been trapped at the junction of PPy and Ni-MZF particles. PPy shows stability till 10^3 kHz.

Based on impedance measurements, 1% and 2% of pyrrole is sufficient to obtain the PPy coating over MZF particles, as already observed from FTIR and X-ray measurements, respectively.

9.5.4. Magnetic Properties

Magnetic properties of PANI/MnZn ferrite, Ni/PANI/MnZn ferrite, and Ni/MnZn ferrite

Saturation magnetization vs. temperature measurements were performed over the 10–300 K temperature range. With the aim to study the magnetic properties, as-synthesized powdered samples were filled in gelatin capsules having a small diamagnetic background. The PANI sample reveals a paramagnetic behavior at lower H values at 300 K; whereas at higher magnetic fields the diamagnetic contribution is dominant over paramagnetic contribution. Due to the soft ferromagnetic properties of manganese zinc ferrite, we did not observe any measurable coercivity and remnant magnetization. At 10 K, the paramagnetic contribution was dominant over the temperature-independent diamagnetic contribution for paramagnetic materials. According to Curie–Weiss law, magnetic susceptibility increases with decreasing temperature.

A comparative measurement of M-H curves for MZF and PANI-coated MZF is shown in Fig. 9.9. The results suggest that none of the samples show appreciable coercivity even at 10 K within the resolution of our measurement; these results are consistent with the soft ferromagnetic nature of MZF. The coating of PANI reduced the magnetization value pertaining to the dominant diamagnetic nature. At 300 K, the MZF samples showed saturation magnetization (M_S) of 66 emu g^{-1}, which increased up to 140 emu g^{-1} at 10 K, indicating that MZF samples saturate much faster.

The M_S of MZF reduced to 64.2 emu g^{-1} after PANI coating, which raised up to 135.8 emu g^{-1} at 10 K. The values of M_S for these samples are tabulated in Table 9.8.

The M-H curves for Ni-coated MZF and PANI-Ni-coated MZF particles are shown in Fig. 9.10. It can be noted that the magnetization of MZF particles increased after coating with Ni. A thin coating of Ni over micron-sized particles of MZF can affect the moments of surface atoms leading to an increase in saturation magnetization or Curie temperature of the Ni-coated MZF particle with respect to MZF particles. It is well known that the

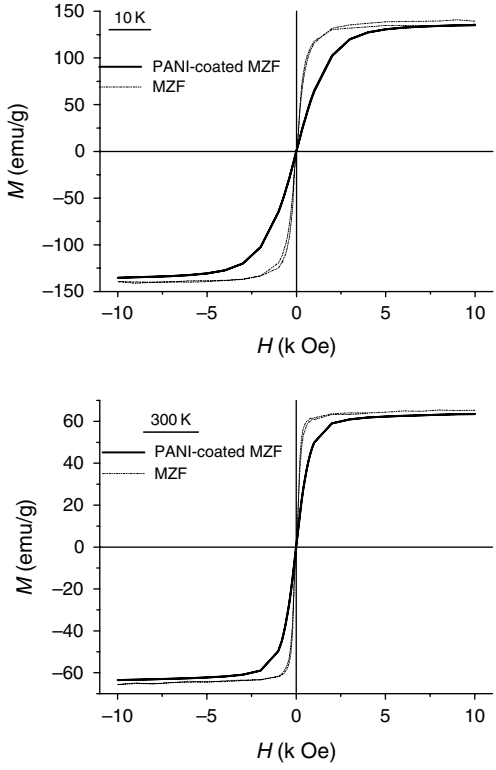

Figure 9.9: Comparison between magnetization vs. magnetic field results on MZF and PANI-coated MZF particles at 10 K and 300 K.

Table 9.8: Summary of magnetic characterization

Sample	**Saturation magnetization at 15 kOe (emu g^{-1})**	
	300 K	**10 K**
PANI	0.1	0.17
MZF	66	140
PANI/MZF	64.2	135.8
Ni/MZF	72.7	78.2
Ni/PANI/MZF	67.7	72.7

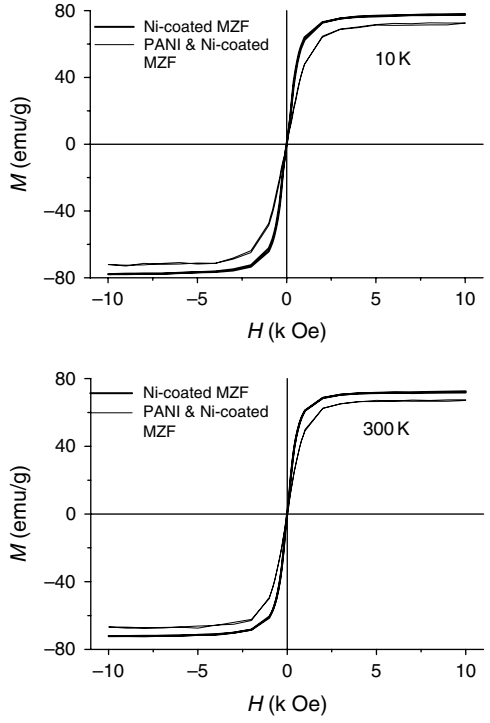

Figure 9.10: Comparison between magnetization vs. magnetic field results on Ni-coated MZF and PANI- and Ni-coated MZF particles at 10 K and 300 K.

surface chemistry highly affects the magnetic properties of fine magnetic particles due to relatively larger surface area. After coating with PANI, the magnetization of these particles strongly reduced. This was due to its diamagnetic contribution. Interestingly, none of these samples showed any detectable coercivity. At 300 K, the Ni-coated MZF has shown the M_S of 72.7 emu g^{-1}, which increased to 78.2 emu g^{-1} at 10 K. The weak temperature dependence of Ni-coated MZF particles pratically supports the fact that the Curie temperature of Ni-coated MZF is much higher than that of uncoated MZF. A high-temperature magnetization study is required to understand the effect of Ni coating on the Curie temperature of MZF. The PANI-Ni-coated MZF particles showed an M_S of 67.7 emu g^{-1}, which increased to 72.7 emu g^{-1} at 10 K.

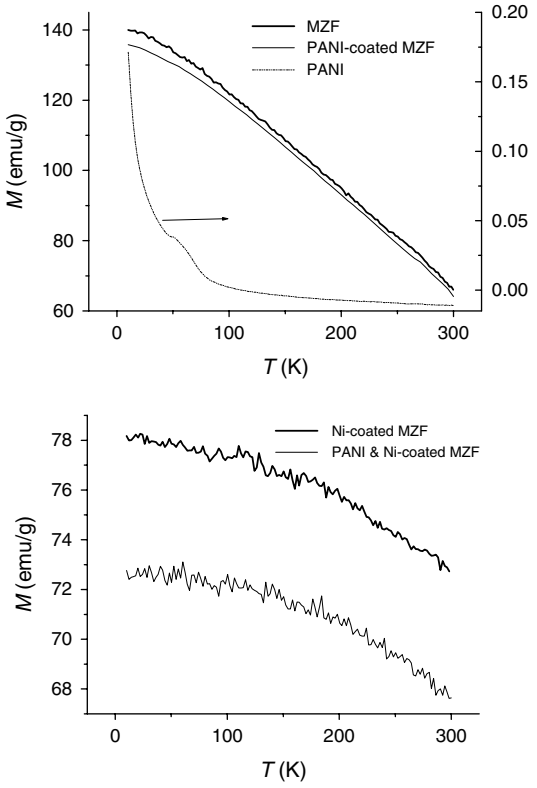

Figure 9.11: In the top panel, we have compared magnetization vs. temperature (M-T) curves between PANI, MZF and PANI/MZF. In the bottom panel, we have compared magnetization vs. temperature (M-T) curves between Ni/MZF and PANI- and Ni-coated MZF.

The magnetization vs. temperature curves at 15 kOe magnetic fields are shown in Fig. 9.11. This field was sufficient to magnetically saturate all the studied samples. The temperature dependence of M_S is quite strong for MZF and PANI-coated MZF samples. On the other hand, the temperature dependence is relatively weak for Ni-coated and PANI/Ni-coated MZF samples. This fact establishes again the role of Ni coating over surface magnetic moments.

Magnetic properties of PPy/MnZn ferrite Ni/PPy/MnZn ferrite, and Ni/MnZn ferrite

Saturation magnetization vs. temperature measurements were performed over the 10–300 K-temperature range. With the aim to study the magnetic properties, as-synthesized powdered samples were filled in gelatin capsules having a small diamagnetic background. Figure 9.12 shows the M-H loop measurements on PPy and Ni-coated PPy samples at 300 K and 10 K. The PPy sample reveals a weak ferromagnetic behavior at lower H values at 300 K, whereas at higher magnetic field the diamagnetic contribution is dominant over ferromagnetic contribution. At 10 K, the M-H curve shows primarily weak ferromagnetic behavior, masking the temperature-independent diamagnetic contribution. In principle, magnetically pure PPy should show a diamagnetic signal. We assume that the present behavior is due to small ferromagnetic impurities mixed in our PPy samples due to the processing technique, as it is evident from Fig. 9.12. In the inset of this figure, we have shown the temperature dependence of magnetic moments that show evidence of ferromagnetic impurity.

Comparative measurements of M-H curves at 300 K and 10 K were performed for MZF, MZF coated with PPy, MZF coated with Ni, and MZF coated with both Ni and PPy (Fig. 9.13). The results suggest that none of the samples show appreciable coercivity even at 10 K within the resolution of

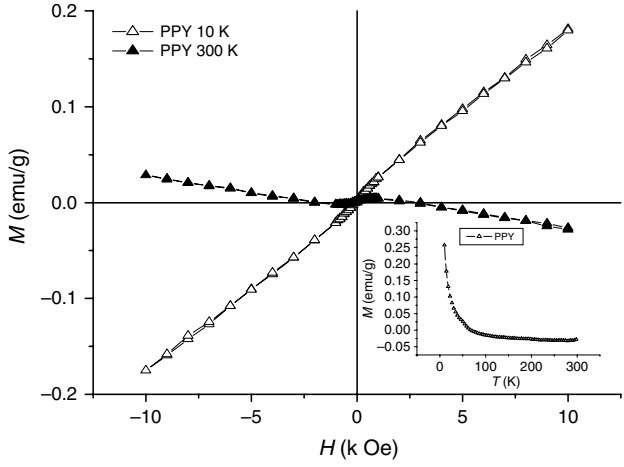

Figure 9.12: M-H loop measurements on PPy at 10 K and 300 K. In the inset, we have shown the temperature dependence of magnetization.

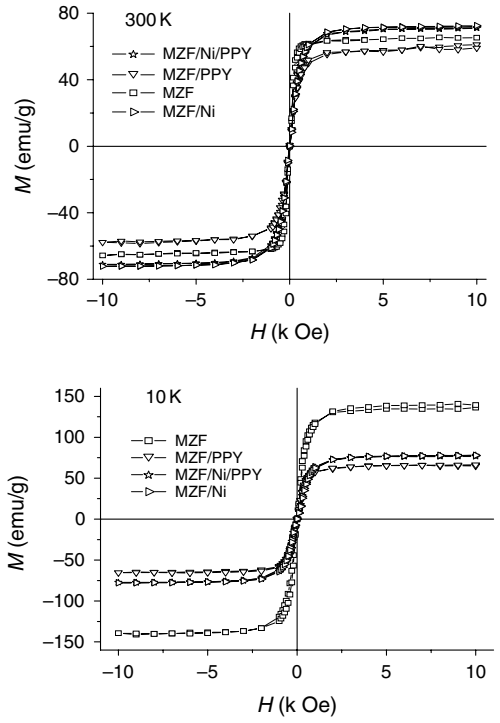

Figure 9.13: Comparison between magnetization vs. magnetic field results for MZF, PPy/MZF, Ni/MZF and both PPy and Ni-coated MZF particles at 10 K and 300 K.

our measurement. These results are consistent with the soft ferromagnetic nature of MZF. The magnetization values are summarized in Table 9.9. The coating of PPy reduces the magnetization value pertaining to the dominant diamagnetic nature. At 300 K, MZF samples show an M_S of 66 emu g^{-1}, which increases up to 140 emu g^{-1} at 10 K indicating that MZF samples saturate much faster. The M_S of MZF reduced to 61.7 emu g^{-1} after PPy coating, which increased to 121.3 emu g^{-1} at 10 K. It can also be noted that the magnetization of MZF particles increased after its coating with Ni. A thin coating of Ni over micron-sized particles of MZF can affect the moments of surface atoms leading to an increase in saturation magnetization or Curie temperature of the Ni-coated MZF particle. After coating with PPy, the magnetization of these particles significantly reduced, and this was due to its diamagnetic contribution. These results are rather similar to those

Table 9.9: Summary of the magnetic characterization

Sample	Magnetization at 15 kOe (emu g^{-1})	
	300 K	**10 K**
PPy	−0.025	0.257
MZF	66	140
PPy/MZF	61.7	121.27
Ni/MZF	72.7	78.20
PPy/Ni/MZF	71.93	78.07

obtained for PANI coating. The PPy-Ni-coated MZF particles showed an M_S of 71.93 emu g^{-1}, which increased to 78.07 emu g^{-1} at 10 K.

Studies have revealed that the temperature dependence of M_S is quite strong for MZF and PPy-coated MZF samples. On the other hand, the temperature dependence is relatively weaker for Ni-coated and PPy-Ni-coated MZF samples. This fact again establishes the role of Ni-coating over surface magnetic moments.

9.6. Conducting Polymers and EMI Shielding Applications for Textiles

The main limitations of chemically or electrochemically produced conducting polymers in commercial applications are their poor mechanical properties and lack of processability. A thin homogeneous coating of conducting polymer can be formed on the surface of the fabric by direct polymerization. This enables the combination of a wide range of structural and mechanical properties of fabrics with the electrical properties of conducting polymers, providing infinite possibilities in the design of conductive composites. Synthetic fibers have been occupying a great part of textile and industrial materials, but their undesirable hydrophobic and electrically insulating properties bring about inevitable disadvantages, such as static charge accumulation under dry conditions and transmission of electromagnetic waves. A spark due to static charge may cause a fire or an explosion. The transmission of electromagnetic waves may cause EMI; it is harmful to human body as well [78,79]. To overcome these problems in synthetic fibers, a number of methods have been suggested, including

spinning of electrically conducting fibers [80,81], and coating fibers with electrically conducting materials such as metals [82,83] or intrinsically conducting polymers [84–87]. Instead of synthesizing conducting polymer fibers and their blends, a homogenous coating of conductive PANI and PPy samples on the insulating woven–non-woven fabrics is another promising method to prepare mechanically strong, flexible, and conducting fabrics. The use of functional fabrics coated with CPs and/or metals maximizes the processability for various EMI shielding situations of both commercial and military purposes.

9.6.1. PANI as a Shielding Material for Textiles

Conducting PANI-coated fabrics, including polyester fabric and silica fabric, were evaluated for EMI shielding properties at 101 GHz by Dhawan et al. [88]. The EMI shielding measurements have suggested that the SE of PANI-coated fabrics increased with the thickness of PANI. For instance, a coated polyester fabric, with a resistivity of 160 Ω cm, has shown an SE of 6.3 dB. However, with the thickness doubled and trebled, SE of 25.52 and 29.1 dB, respectively, was achieved. In the case of a TSA-doped PANI-coated polyester fabric (resistivity of 40 Ω cm), the SEs for single-fold, two-fold, and three-fold samples were 17.77, 28.26, and 47.63 dB, respectively. Similar results were obtained for a HCl-doped PANI-coated polyester fabric (resistivity of 26 Ω cm), and the SEs were 21.48, 40, and 48.72 dB for single-, two-, and three- fold samples, respectively. Moreover, the higher SE of coated silica fabric (35.61 dB) than that of coated polyester fabric (21.48 dB) under identical conditions implies that the conductive silica fabric retains more PANI in their interstices than did polyester fabric. According to Dhawan et al. [89], the PANI-coated fabric exhibited an SE of the order of 30–40 dB over the 100–1000 MHz range measured by coaxial transmission line method. The values of resistivities are given in Table 9.10. From the measurements, we understand that a resistivity of 10–10^8 Ω cm can be achieved depending upon the doping level of dopant attached. Observe that a single coating of PANI on silica cloth gave a resistivity of 1.6 kΩ cm. A second coating gave an electrical resistivity of 150–170 Ω cm, whereas a third coating gave a resistivity of 10–28 Ω cm. However, undoped silica cloth gave a resistivity of 10^8 Ω cm. Similarly, PPy-coated fabrics show a resistivity of 292–5300 Ω cm.

The SE, as measured by coaxial transmission line method from 100 to 1000 MHz, is shown in Fig. 9.14. The figure shows that the use of

Table 9.10: Resistivity data of conducting polymer coating on fabrics

Conducting polymer coating	Resistivity (Ω cm^{-1})
PANI on silica fabrics	$10–10^8$
PPy on glass fabric	292–5300
PANI on glass fabrics	300
PANI on glass fabrics by indirect method	$10^4–10^8$

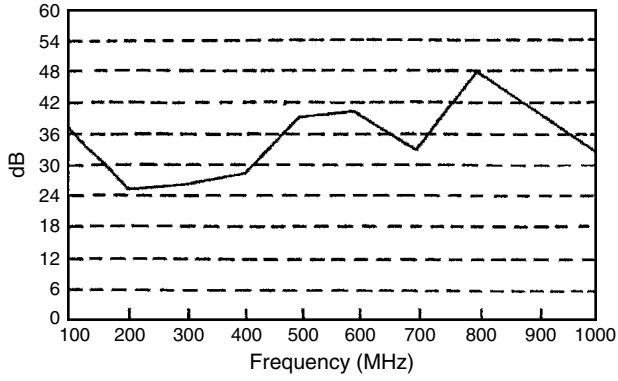

Figure 9.14: SE of PANI-coated fabrics in the frequency range 100–1000 MHz. (Reprinted from *Synthetic Metals*, Vol. 129, Dhawan S.K., Singh N., Venkatachalam S. 'Shielding behavior of conducting polymer-coated fabrics in X-band, Wband and radio frequency range' pp. 261–267, Copyright 2002 Elsevier; with permission from Elsevier.)

conducting PANI-coated fabric resulted in a SE of the order of 30–40 dB. However, for most industrial applications, a SE of 30 dB is a useful attenuation value because it will prevent 99.9% of EMI. The microwave absorption studies of conducting polymer-coated fabrics were carried out in the range of 8–12 GHz and are presented in Fig. 9.15. The measurements suggest that conducting PANI-coated fabrics show a SE of -3 to -11 dB in the range of 8–12 GHz.

The reflectance/transmittance of CP-coated fabrics was also studied to see the percentage of energy absorbed by the fabric. The studies have

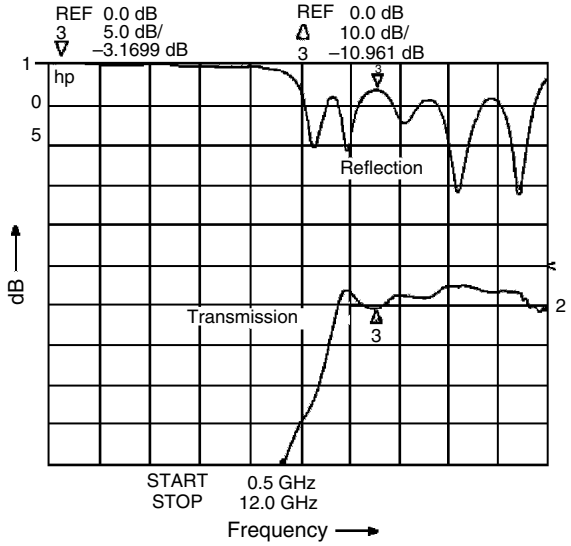

Figure 9.15: Microwave absorption studies of conducting PANI-coated fabrics in the frequency range 8–12 GHz (Reprinted from *Synthetic Metals*, Vol. 129, Dhawan S.K., Singh N., Venkatachalam S. 'Shielding behavior of conducting polymer-coated fabrics in X-band, Wband and radio frequency range' pp. 261–267, Copyright 2002 Elsevier, with permission from Elsevier.)

shown that, in the UV-Vis-NIR range, 98% of the energy was absorbed by the PANI-coated fabrics, which is larger than the absorbed energy percentage of PPy-coated fabrics (95%), leaving only 2% of the energy being reflected.

9.6.2. PPy as a Shielding Material for Textiles

In preparing conductive composite fabrics, many researchers have focused on COP. Li et al. have prepared a PPy–carbon fabric composite by coating PPy onto carbon fibers [90]. In addition to this conductive substrate, a conductive composite fabric was prepared using the COP of pyrrole in the presence of a nonconductive matrix, such as nylon 6 fabric, nonwoven fabric, and acryl fabric [90,91]. However, its application to EMI shielding is limited, because the conductive composite fabric from the COP process

has a low level of conductivity. There were some reports on the preparation of conductive composite fabrics using ECP, which is a common method for producing conductive films [87,92]. The ECP technique is simple and inexpensive and it provides ease in controlling the film thickness by an electrical current or potential. Kim et al. have compared PPy-N composite nylon 6 fabrics prepared by COP and ECP techniques for use in EMI shielding applications. Measurements were performed in the frequency range from 50 MHz to 13.5 GHz [93]. The stability of the composite prepared by ECP was better than that of the composite prepared by the COP process, because the sodium salt of anthraquinone-2-sulfonic acid (AQSA) dopant was able to interact strongly with the PPy main chain.

The temperature dependence of the conductivity of composites was verified over four heating and cooling cycles. The change in conductivity over four repeated cycles was affected by the interaction between the thermal stability of the dopant and the rearrangement of PPy main chain. The EMI SE values were in the range of 5–40 dB and depended on the conductivity and layer array sequence of the conductive fabric. The composites with high conductivity represented reflection-dominant EMI shielding characteristics, which are typical for the EMI shielding characteristics of metals. However, composites with low conductivity have shown absorption-dominant EMI shielding characteristics.

Joo et al. [94–96] have extensively studied the EMI shielding performances of PPy-coated ethylene terephthalate (PET)-woven fabric, or polyester, chemically or electrochemically. The PPy sample doped with naphthalene sulfonic acid (NSA) was chemically coated on the PET-woven fabrics (one to eight times). By using the electrochemical coating of PPy-doped AQSA on PPy-NSA/PET complexes, the PPy-AQSA/PPy-NSA/PET complexes were synthesized. Silver was thermally evaporated on the surface of PPy–AQSA/PPy-NSA/PET complexes (AgIPPy-AQSA/PPy-NSA/PET). The EMI SE and DC conductivity (σ_{dc}) of fabric complexes were measured for EMI shielding characteristics and theoretical simulations. The SEs of PPy-AQSA/PPy-NSA/fabric and Ag/fabric were c. 22 and 55 dB, respectively, over 1 MHz to 1 GHz, while the SE of Ag/PPy-AQSA/AgPd/fabric was c. 80 dB, signifying the potential military applications of the fabrics [95,96]. The contribution of absorption to the total EMI SE was higher for PPy-AQSA/PPy-NSA/fabric without Ag and lower for those with Ag, and vice versa for the contribution of reflection to the total EMI SE of the fabric [94], confirming the EMI shielding characteristics of PPy as an excellent radio frequency and microwave absorber due to the deeper skin depth of PPy (or PANI) than metals [92]. The EMI SE

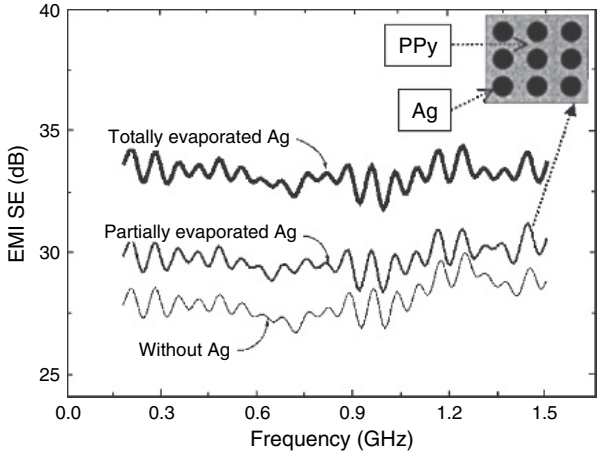

Figure 9.16: EMI SE of fabric complex various Ag evaporation layer, (Reprinted from *Current Applied Physics*, Vol. 1, Hong Y.K., Lee C.Y., Jeong C.K., Sim J.H., Kim K., Joo J., Kim M.S., Lee J.Y., Jeong S.H., and Byun S.W. 'Electromagnetic interference shielding characteristics of fabric complexes coated with conductive polypyrrole and thermally evaporated' pp. 439–447, Copyright 2001 Elsevier; with permission from Elsevier.)

of PPy/PET fabric increased with conductivity, and the same relationship was reported for many ICP-based systems [97–102]; the increase resulted dominantly from reflection rather than absorption. The EMI SEs of PPy-AQSA/PPy-NSA/PET and Ag/PPy-AQAS/PPy-NSA/PET complexes are shown in Fig. 9.16. When Ag was partially (c. 37%) evaporated on one side of fabric complexes, the EMI SE was 29 dB at 0.5 GHz, while the EMI SE of the sample with Ag evaporation on the whole area was 33 dB at 0.5 GHz.

9.7. Concluding Remarks

The use of electronic devices for communication, computation, and automation is rapidly increasing, and it enhances working capability. As the operating frequency and the integration of electronic devices increase, EMI has become a major problem, which reduces the lifetime and efficiency of electronic devices and electrical products. An example of a potential

application of conducting polymers in EMI is the control and modification of indoor wireless channel for minimization of interference by fabricating frequency-selective absorbers and shields based on multilayer conducting polymer composites. Electrically conductive materials, especially PANI and PPy, are used to protect electronic equipment from EMI. These products could have specific absorption and reflection properties intended for radiation shields in electronic equipment.

The main advantages in using electrically conductive materials for shielding applications include lightweight, which is of critical importance in aerospace applications, corrosion resistance, ease of processing, and tunable conductivities as compared with typical metals. In addition, the dominant shielding characteristics of absorption for these materials, other than that of reflection for metals, render ICPs more useful in applications requiring not only high EMI SE but also shielding by absorption, such as in stealth technology.

Conductive polymers with relatively high conductivity and dielectric constant are promising materials for EMI shielding applications; however, a very high level of SE cannot be achieved by using only CPs. Therefore, in this chapter, we have shown some possible synthesis techniques and material characterization for applications. PANI/MZF, PPy/MZF, PANI/NiMZF, and PPy/NiMZF hybrid-type particles can effectively shield electromagnetic waves generated from electric and magnetic sources. A combination of both conducting and magnetic components can be successfully synthesized for shielding applications. The results show that chemical and electrochemical polymerization techniques yield homogenous coatings onto ferrite particles, which is important to generate electromagnetic waves from magnetic sources, especially at low frequencies, together with those generated from electric sources by CPs with a single coating. In addition to these results, the conductivity of nanocomposites can be varied by relative composition of used materials. The particles were stable during two years. It was also found that the annealing temperature affects the conductivity of samples starting from 493 K, resulting in restructured composition together with decomposition of the polymer backbone. The M_S values of MZF increases in the 10–300 K temperature range by the addition of thin Ni coatings, while the addition of polymer decreases M_S.

Shielding from EMI using conducting polymer-coated fabrics also offers several advantages including flexibility, access to a wide range of structures, reduced weight and lower cost. Conducting fabrics provide an absorption-dominant interaction with microwave radiation.

Acknowledgment

This work was sponsored by the Missile Defense Agency (MDA/IST), and managed by the U.S. Army Space and Missile Defense Command, contracts number DASG60-01-C-0085 and number DASG60-02-C-0010.

References

[1] Bott, D.C. and Skotheim, T.J. (ed.) (1986) In *Handbook of Conducting Polymers*. New York: Marcel Dekker, vol. 2.

[2] Roncali, J. (1992) Conjugated poly(thiophenes): synthesis, functionalization, and applications. *Chem. Rev*., **92**, 711–38.

[3] Salaneck, W.R., Lundstron, L.I. and Ranby, B. (ed.) (1993) *Conjugated Polymers and Related Material*. Oxford University Press: New York.

[4] Bredas, J.L. and Chance, R.R. (ed.) (1989) *Conjugated Polymeric Materials: Opportunities in Electronics, Optoelectronics and Molecular Electronics*. Dordrecht, The Netherlands: Kluwer Academic Press.

[5] Barisci, J.N., Conn, C. and Wallace, G.G. (1996) Conducting polymer sensors. *Trends Polym. Sci*., **4**, 307–9.

[6] Rodriguez, J., Grande, H.J. and Otero, T.F. (1997) In *Handbook of Organic Conductive Molecules and Polymers: Conductive Polymers: Transport, Photophysics and Applications*, 1st edn (H.S., Nalwa, ed.). New York: John Wiley and Sons, vol. 4.

[7] MacDiarmid, A.G. (2002) Synthetic metals: a novel role for organic polymers. *Synth. Met*., **125**, 11–22.

[8] Walker, J.A., Warren, L.F. and Witucki, E.F. (1988) New chemically prepared conducting pyrrole blacks. *J. Polym. Sci. A: Polym. Chem*. **26**, 1285–9.

[9] De Jesus, M.C., Fu, Y. and Weiss, R.A. (1997) Conductive polymer blends prepared by in situ polymerization of pyrrole: a review. *Polym. Eng. Sci*., **37**, 1936–9.

[10] Violette, J.L.N, White, D.R.J and Violette, M.F. (1987) *Electromagnetic Compatibility Handbook*. New York: Van Nostrand Reinhold Company.

[11] Jang, J.O. and Park, J.W. (2002) *Coating Materials for Shielding Electromagnetic Waves*. US Patent No. 6355707 B1, March 12.

[12] Miller, H.K. (1997) EMF controversy: are electromagnetic fields dangerous to your health? *Mater. Eval*., **55**, 994–5.

[13] Sienkiewicz, Z. (1998) Biological effects of electromagnetic fields. *Power. Eng. J*., **12**, 131–9.

[14] Mandich, N.V. (1994) EMI shielding by electroless plating of ABS plastics. *Plat. Surf. Finish*., **81**, 60–3.

[15] Stefecka, M., Kando, M., Matsuo, H. et al. (2004) Electromagnetic shielding efficiency of plasma treated and electroless metal plated polypropylene nonwoven fabrics. *J. Mater. Sci*., **39**, 1919–2273.
[16] Radford, D.W. and Cheng, B.C. (1993) Ultra-lightweight composite materials for EMI shielding. *SAMPE Quart*, **24**, 54–5.
[17] Huang, C.Y., Mo, W.W. and Roan, M.L. (2004) Studies on the influence of double-layer electroless metal deposition on the electromagnetic interference shielding effectiveness of carbon fiber/ABS composites. *Surf. Coat. Technol*., **184**, 163–9.
[18] Kim, H.M., Kim, K., Lee, C.Y. et al. (2004) Electrical conductivity and electromagnetic interference shielding of multiwalled carbon nanotube composites containing Fe catalyst. *Appl. Phys. Lett*., **84**, 589–91.
[19] Kim, M.S., Lee, B.O., Woo, W.J. et al. (2002) Influence of aspect ratio and skin effect on EMI shielding of coating materials fabricated with carbon nanofiber/PVDF. *J. Mater. Sci*., **37**, 1715–921.
[20] Kawaguchi, H. (2000) Functional polymer microspheres. *Prog. Polym. Sci*., **25**, 1171–210.
[21] Kalinina, O. and Kumacheva, F. (1999) A 'core-shell' approach to producing 3d polymer nanocomposites. *Macromolecules*, **32**, 4122–29.
[22] Pedro, G.R. (2001) Hybrid organic-inorganic materials-in search of synergic activity. *Adv. Mater*., **13**(3), 163–74.
[23] Marchessault, R.H., Rioux, P. and Raymond, L. (1992) Magnetic cellulose fibres and paper: preparation, processing and properties. *Polymer*, **33**, 4024–28.
[24] Ziolo, R.F., Fiannelis, E.P., Weistein, B.A. et al. (1992) Matrix-mediated synthesis of nanocrystalline γ-Fe_2O_3: a new optically transparent magnetic material. *Science*, **257**, 219–23.
[25] Dhanabalan, A., Talwar, S.S., Contractor, A.Q. et al. (1999) Polyaniline-CdS composite films obtained from polyaniline–cadmium arachidate multilayers. *J. Mater. Sci. Lett*., **18**, 591–658.
[26] (a) Wan, M.X. and Li, J.C. (1999) Electrical and ferromagnetic behavior of polyaniline composites. *Synth. Met*., **101**, 844–5. (b) Deng, J.G., Peng, Y.X., He Ch. et al. (2003) Magnetic and conducting Fe_3O_4-polypyrrole nanoparticles with core-shell structure. *Polym. Int*., **52**, 1182–7.
[27] Dhawan, S.K., Singh, N. and Rodrigues, D. (2003) Electromagnetic shielding behaviour of conducting polyaniline composites. *Sci. Technol. Adv. Mater*., **4**, 105–13.
[28] Koul, S., Chandra, R. and Dhawan, S.K. (2000) Conducting polyaniline composite for ESD and EMI at 101 GHz. *Polymer*, **41**, 9305–10.
[29] Chandrasekhar, P. and Naishadham, K. (1999) Broadband microwave absorption and shielding properties of a poly(aniline). *Synth. Met*., **105**, 115–20.
[30] Chung, D.D.L. (2000) Materials for electromagnetic interference shielding. *J. Mater. Eng. Perform*., **9**, 350–3.

[31] Epstein, A.J. and MacDiarmid, A.G. (1995) Polyanilines: from solitions to polymer metal, from chemical curiosity to technology. *Synth. Met*., **69**, 179–82.
[32] Joo, J. and Epstein, A.J. (1994) Electromagnetic radiation shielding by intrinsically conducting polymers. *Appl. Phys. Lett*., **65**, 2278–80.
[33] Colaneri, N.F. and Shacklette, L.W. (1992) EMI shielding measurements of conductive polymer blends. *IEEE Trans. Instrum. Meas*., **41**, 291–7.
[34] Shacklette, L.W., Colaneri, N.F., Kulkarni, V.G. et al. (1992) EMI shielding of intrinsically conductive polymers. *J. Vinyl Technol*., **14**, 118–20.
[35] Joo, J., Lee, C.Y., Song, H.G. et al. (1998) Enhancement of electromagnetic interference shielding efficiency of polyaniline through mixture and chemical doping. *Mol. Cryst. Liq. Cryst. Sci. Technol., Sect. A: Mol. Cryst. Liq. Cryst*., **316**, 19–22.
[36] Lee, C.Y., Song, H.G., Jang, K.S. et al. (1999) Electromagnetic interference shielding efficiency of polyaniline mixtures and multilayer films. *Synth. Met*., **102**, 1346–9.
[37] Joo, J. and Lee, C.Y. (2000) High frequency electromagnetic interference shielding response of mixtures and multilayer films based on conducting polymers. *J. Appl. Phys*., **88**, 513–8.
[38] Chandrasekhar, P. and Naishadham, K. (1999) Broadband microwave absorption and shielding properties of a poly(aniline). *Synth. Met*., **105**, 115–20.
[39] Dhawan, S.K., Singh, N. and Rodrigues, D. (2003) Electromagnetic shielding behaviour of conducting polyaniline composites. *Sci. Technol. Adv. Mater*., **4**, 105–13.
[40] Koul, S., Chandra, R. and Dhawan, S.K. (2000) Conducting polyaniline composite for ESD and EMI at 101 GHz. *Polymer*, **41**, 9305–10.
[41] Wessling, B. (1998) Dispersion as the link between basic research and commercial applications of conductive polymers (polyaniline). *Synth. Met*., **93**, 143–69.
[42] Wojkiewicz, J.L., Fauveaux, S. and Miane, J.L. (2003) Electromagnetic shielding properties of polyaniline composites. *Synth. Met*., **127**, 135–6.
[43] Wang, Y. and Jing, X. (2005) Intrinsically conducting polymers for electromagnetic interference shielding. *Polym. Adv. Technol*., **16**, 344–51.
[44] Hong, Y.K., Lee, C.Y., Jeong, C.K. et al. (2003) Method and apparatus to measure electromagnetic interference shielding efficiency and its shielding characteristics in broadband frequency ranges. *Rev. Sci. Instrum*., **74**, 1098–102.
[45] Yoshino, K., Tabata, M., Kaneto, K. et al. (1985) Application and characteristics of conducting polymer as radiation shielding material. *Jpn. J. Appl. Phys., Part 2: Lett*., **24**, 693–9.
[46] Kaynak, A., Unsworth, J., Clout, R. et al. (1994) A study of microwave, reflection, absorption, and shielding effectiveness of conducting polypyrrole films. *J. Appl. Polym. Sci*., **54**, 269–72.

[47] Kaynak, A., Mohan, A.S., Unsworth, J. et al. (1994) Plane-wave shielding effectiveness studies on conducting polypyrrole. *J. Mater. Sci. Lett*., **13**, 1121–3.

[48] Kaynak, A. (1996) Electromagnetic shielding effectiveness of galvanostatically synthesized conducting polypyrrole films in the 300–2000 MHz frequency range. *Mater. Res. Bull*., **31**, 845–60.

[49] Colaneri, N.F. and Shacklette, L.W. (1992) EMI shielding measurements of conductive polymer blends. *IEEE Trans. Instrum. Meas*., **41**, 291–7.

[50] Pomposo, J.A., Rodriguez, J. and Grande, H. (1999) Polypyrrole-based conducting hot melt adhesives for EMI shielding applications. *Synth. Met*., **104**, 107–11.

[51] Wiznerowicz, F. (1994) Conductive polymers instead of carbon black? *Wire*, **44**, 102–3.

[52] Mäkelä, T., Pienimaa, S., Taka, T. et al. (1997) Thin polyaniline films in EMI shielding. *Synth. Met*., **85**, 1335–6.

[53] Taka, T. (1991) EMI shielding measurements on poly(3-octyl thiophene) blends. *Synth. Met*., **41**, 1177–80.

[54] Chen, C. and Naishadham, K. (1990) Plane wave shielding effectiveness of conductive polymer films. *Conference Proceedings-IEEE SOUTHEASTCON*, **1**, 38.

[55] Naishadham, K. and Kadaba, P.K. (1991) Measurement of the microwave conductivity of a polymeric material with potential applications in absorbers and shielding. *IEEE Trans. Microwave Theory Technol*., **39**, 1158–64.

[56] Courric, S. and Tran, V.H. (1998) Electromagnetic properties of poly(pphenylene-vinylene) derivatives. *Polymer*, **39**, 2399–408.

[57] Jarjayes, O., Fries, P.H. and Bidan, G. (1995)_New nanocomposites of polypyrrole including γ-Fe_2O_3 particles: electrical and magnetic characterizations. *Synth Met*, **69**, 343–4.

[58] Yan, F., Xue, G., Chen, J. et al. (2001) Preparation of a conducting polymer/ferromagnet composite film by anodic-oxidation method. *Synth. Met*., **123**, 17–20.

[59] Liu, J. and Wan, M.X. (2000) Composites of polypyrrole with conducting and ferromagnetic behaviors. *J Polym Sci, Part A: Polym Chem*, **38**, 2734–9.

[60] Suri, K., Annapoorni, S., Tandon, R.P. et al. (2002) Nanocomposite of polypyrrole-iron oxide by simultaneous gelation and polymerization. *Synth. Met*., **126**, 137–42.

[61] Kim, H.S., Sohn, B.H., Lee, W. et al. (2002) Multifunctional layer-by-layer self-assembly of conducting polymers and magnetic nanoparticles. *Thin Solid Films*, **419**,173–7.

[62] Wan, M.X. and Li, W.C. (1997) A composite of polyaniline with both conducting and ferromagnetic functions. *J. Polym. Sci., Part A: Polym. Chem*., **34**, 2129–36.

[63] Wan, M.X. and Fan, J.H. (1998) Synthesis and ferromagnetic properties of composites of a water-soluble polyaniline copolymer containing iron oxide. *J. Polym. Sci., Part A: Polym. Chem.*, **36**, 2749–55.
[64] Wan, M.X. and Li, J.C. (1998) Synthesis and electrical-magnetic properties of polyaniline composites. *J. Polym. Sci., Part A: Polym. Chem.*, **36**, 2799–805.
[65] Yavuz, Ö., Ram, M.K., Aldissi, M. et al. (2005) Polypyrrole composites for shielding applications. *Synth. Met.*, **151**, 211–7.
[66] Yavuz, Ö., Ram, M.K., Aldissi, M. et al. (2005) 'Synthesis and the physical properties of MnZn ferrite and NiMnZn ferrite–polyaniline nanocomposite particles. *J. Mater. Chem.*, **15**, 810–7.
[67] Chiang, J.C. and MacDiarmid, A.G. (1986) 'Polyaniline': protonic acid doping of the emeraldine form to the metallic regime. *Synth. Met.*, **13**, 193–205.
[68] Waldron, R.D. (1955) Infrared spectra of ferrites. *Phys. Rev.*, **99**, 1727–35.
[69] Wang, F.S., Tang, J.S., Wang, L. et al. (1988) Study on the crystallinity of polyaniline. *Mol. Cryst.Liq.Cryst.*, **160**, 175–84.
[70] Chaudhari, H.K. and Kelkar, D.S. (1997) Investigation of structure and electrical conductivity in doped polyaniline. *Polym. Int.*, **42**, 380–4.
[71] Luzny, W. and Banka, E. (2000) Relations between the structure and electric conductivity of polyaniline protonated with camphorsulfonic acid. *Macromol*, **33**, 425–9.
[72] Xia, Y., Wiesinger, J.M. and MacDiarmid, A.G. (1995) Camphorsulfonic acid fully doped polyaniline emeraldine salt: conformations in different solvents studied by an ultraviolet/visible/near-infrared spectroscopic method. *Chem. Mat.*, **7**, 443–5.
[73] Quyang, J. and Li, Y. (1997) Great improvement of polypyrrole films prepared electrochemically from aqueous solutions by adding nonaphenol polyethyleneoxy ether. *Polymer*, **38**(15), 3997–9.
[74] Wang, H.L. and Fernandez, J.E. (1993) Blends of polypyrrole and poly(vinyl alcohol). *Macromolecules*, **26**, 3336–9.
[75] Wang, J., Zeng, C., Peng, Z. et al. (2004) Synthesis and magnetic properties of $Zn_{1-x}Mn_xFe_2O_4$ nanoparticles. *Physica B*, **349**, 124–8.
[76] Maeda, S. and Armes, S.P. (1995) Preparation and characterization of polypyrrole-Tin(IV) oxide nanocomposite. *Colloids Chem. Mater.*, **7**, 171–8.
[77] Beladakere, N.N., Misra, S.C.K., Ram, M.K. et al. (1992) Interfacial polarization in semiconducting polypyrrole thin films. *J. Phys.: Condens. Matter.*, **4**, 5747–56.
[78] Chandrasekhar, P. and Naishadham, K. (1999) Broadband microwave absorption and shielding properties of a poly(aniline). *Synth. Met.*, **105**, 115–20.
[79] Shinn, S.T. and Fa, Y.C. (2001) EMI shielding effectiveness of metal-coated carbon fiber-reinforced ABS composites. *Mat. Sci. Eng. A*, **302**, 258–67.

[80] Pomfret, S.J., Adams, P.N., Comfort, N.P. et al. (1999) Advances in processing routes for conductive polyaniline fibres. *Synth. Met*., 101 724–5.
[81] Kincal, D., Kumar, A., Child, A.J. et al. (1998) Conductivity switching in polypyrrole-coated textile fabrics as gas sensors. *Synth. Met*., **92**, 53–6.
[82] Cioffi, N., Torsi, L., Sabbatini, L. et al. (2000) Electrosynthesis and characterisation of nanostructured palladium-polypyrrole composites. *J. Electroanal. Chem*., **488**, 42–7.
[83] Huang, C.Y. and Wu, C.C. (2000) The EMI shielding effectiveness of PC/ABS/nickel-coated-carbon-fibre composites. *Eur. Polym. J*., **36**, 2729–37.
[84] Kuhn, H.H. (1992) *Intrinsically Conducting Polymers*. Kluwer London: Academic Press, p. 25.
[85] Zarbin, J.G., Paoli, M.-A.D. and Alves, O.L. (1999) Nanocomposites glass/conductive polymers. *Synth. Met*., **99**, 227–35.
[86] Min, G. (1999) Conducting polymers and their applications in the film industry – polyaniline/polyimide blended films. *Synth. Met*., **102**, 1163–6.
[87] Iroh, J.O. and Williams, C. (1999) Formation of thermally stable polypyrrole-naphthalene/benzene sulfonate-carbon fiber composites by an electrochemical process. *Synth. Met*., **99**, 1–8.
[88] Dhawan, S.K., Singh, N. and Venkatachalam, S. (2001) Shielding effectiveness of conducting polyaniline coated fabrics at 101 GHz. *Synth. Met*., **125**, 389–93.
[89] Dhawan, S.K., Singh, N. and Venkatachalam, S. (2002) Shielding behavior of conducting polymer-coated fabrics in X-band, Wband and radio frequency range. *Synth. Met*., **129**, 261–7.
[90] Li, H., Shi, G., Ye, W., Li, C., Liang, Y. (1997) Polypyrrole–Carbon fiber composite film prepared by chemical oxidative polymerization of pyrrole. *J. Appl. Polym. Sci*., **64**(11), 2149–54.
[91] Oh, K.W., Kim, S.H. and Kim, E.A. (2001) Polypyrrole-carbon fiber composite film prepared by chemical oxidative polymerization of pyrrole. *J. Appl. Polym. Sci*., **81**, 684.
[92] Bhadani, S.N., Gupta, S.K.S., Sahu, G.C. et al. (1996) Electrochemical formation of some conducting fibers. *J. Appl. Polym. Sci*., **61**, 207–12.
[93] Kim, S.H., Jang, S.H., Byun, S.W. et al. (2003) Electrical properties and EMI shielding characteristics of polypyrrole–nylon 6 composite fabrics. *J. Appl. Polym. Sci*., **87**, 1969–74.
[94] Hong, Y.K., Lee, C.Y., Jeong, C.K. et al. (2001) Electromagnetic interference shielding characteristics of fabric complexes coated with conductive polypyrrole and thermally evaporated Ag. *Curr. Appl. Phys*., **1**, 439–47.
[95] Lee, C.Y., Lee, D.E., Joo, J. et al. (2001) Conductivity and EMI shielding efficiency of polypyrrole and metal compounds coated on (non) woven fabrics. *Synth. Met*., **119**, 429–30.

[96] Lee, C.Y., Lee, D.E., Jeong, C.K. et al. (2002) Electromagnetic interference shielding by using conductive polypyrrole and metal compound coated on fabrics. *Polym. Adv. Technol*., **13**, 577–9.
[97] Mäkelä, T., Pienimaa, S., Taka, T. et al. (1997) Thin polyaniline films in EMI shielding. *Synth. Met*., **85**, 1335–6.
[98] Colaneri, N.F. and Shacklette, L.W. (1992) EMI shielding measurements of conductive polymer blends. *IEEE Trans. Instrum. Meas*., **41**, 291–7.
[99] Lee, C.Y., Kim, H.M., Park, J.W. et al. (2001) AC electrical properties of conjugated polymers and theoretical high frequency behavior of multilayer films. *Synth. Met*., **117**, 109–13.
[100] Chandrasekhar, P. and Naishadham, K. (1999) Broadband microwave absorption and shielding properties of a poly(aniline). *Synth. Met*., **105**, 115–20.
[101] Koul, S., Chandra, R. and Dhawan, S.K. (2000) Conducting polyaniline composite for ESD and EMI at 101 GHz. *Polymer*, **41**, 9305–10.
[102] Gangopadhyay, R., De, A. and Ghosh, G. (2001) Polyaniline-poly(vinyl alcohol) conducting composite: material with easy processability and novel application potential. *Synth. Met*., **123**, 21–31.

This page intentionally left blank

Index

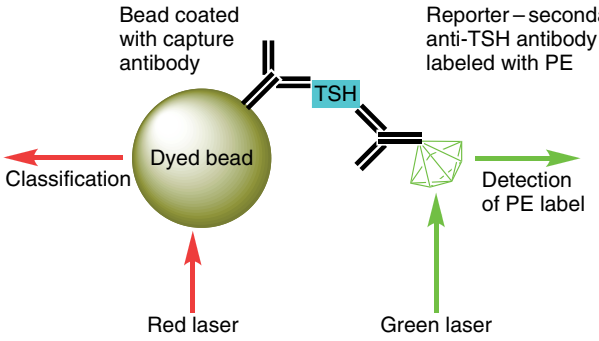

Colour plate 1: Principle of multiplexed assay. The solid phase for the reaction comes in the form of 8 μm polystyrene particle as depicted. Each particle has a unique combination of two fluorescent dyes, which serve as a spectral 'barcode'. In TSH assay, the capture anti-TSH antibody is anchored to the solid phase by binding to carboxyl functionalized PEG. By using a complement anti-TSH antibody, which is 'tagged' with PE, TSH could be sandwiched and captured on the solid phase. The detection system involves a solid state green laser. It excites reporters that are bound on the particle surface after the immunoreaction is completed. (See Figure 8.9, pp. 415).

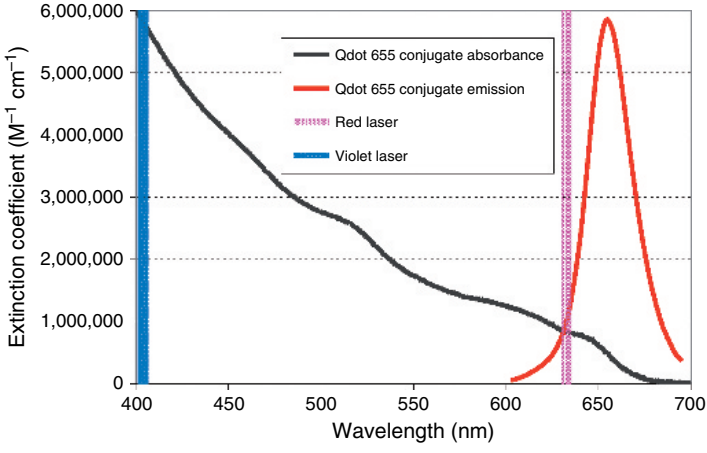

Colour plate 2: Absorption and emission spectra of Qdot-655 conjugate. Bars represent laser lines of the violet and red lasers. The shape of the absorption spectrum reveals that the Qdots can be excited by several commonly used visible-range emission lasers. Although the extinction coefficient is much lower at the red laser line than at the violet, it can be seen that it is still quite high (~1 000 000). (See Figure 8.11, pp. 420).

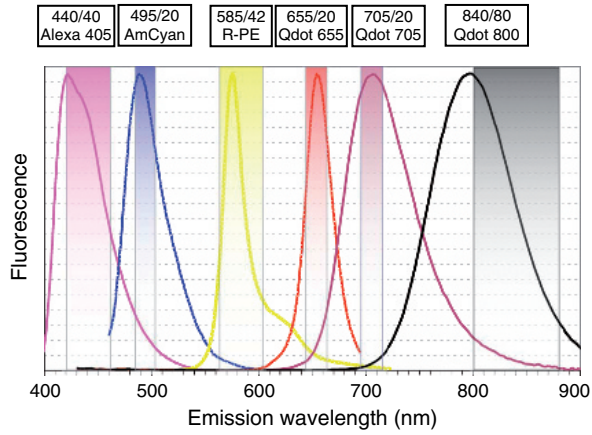

Colour plate 3: A panel of conventional fluorophores and quantum dots that might be used in a single laser platform design. (See Figure 8.12, pp. 421).

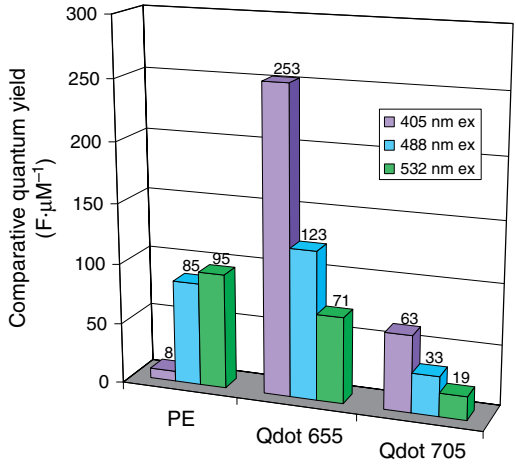

Colour plate 4: Comparative quantum yields of PE, Qdot-655 and Qdot-705, excited at 405, 488 and 532 nm. (See Figure 8.14, pp. 423).